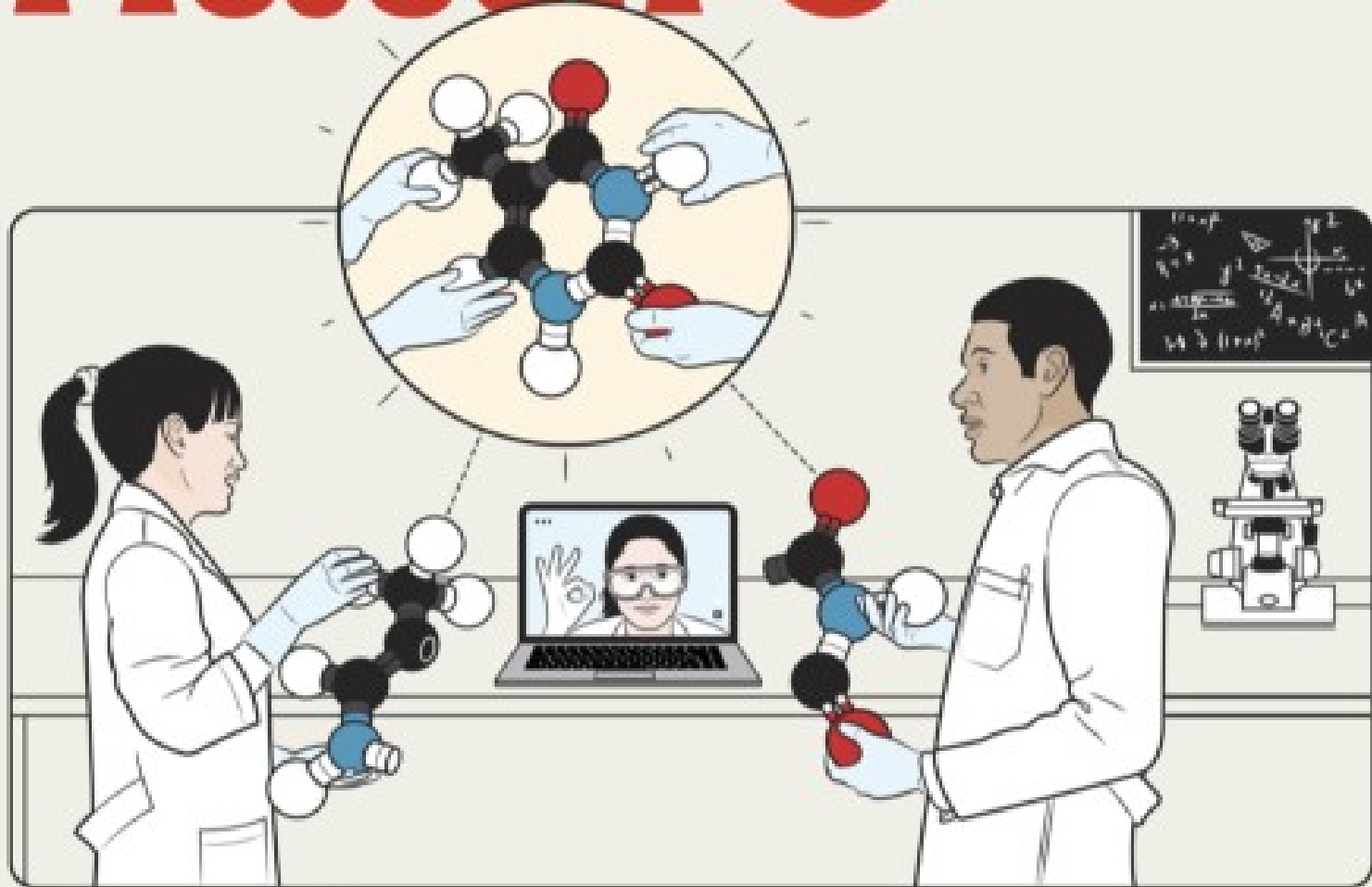


nature



HOW TO COLLABORATE

The promise and pitfalls of partaking in team science

Cross-examination
Ethical issues beset DNA database used to help solve crimes

Flow diagram
Mapping the rivers and streams that run dry for part of the year

Coronavirus
Contact-tracing app helps slow the spread of COVID-19

Vol. 594 No. 7869
DOI: 10.1038/nature23099

Nature.2021.06.19

[Sat, 19 Jun 2021]

- [Collaborations](#)
- [This Week](#)
- [News in Focus](#)
- [Books & Arts](#)
- [Opinion](#)
- [Research](#)

| [Next section](#) | [Main menu](#) |

Donation

| [Next section](#) | [Main menu](#) |

Collaborations

- **[Research collaborations bring big rewards: the world needs more](#)** [16 June 2021]
Editorial • A special issue on COVID-era research collaboration highlights the benefits to science and society of working across borders, cultures and disciplines.
- **[COVID has shown the power of science–industry collaboration](#)** [16 June 2021]
Editorial • But a thriving relationship needs clearer rules around data ownership and intellectual property – and public trust in the process.
- **[How the COVID pandemic is changing global science collaborations](#)** [16 June 2021]
News Feature • The pandemic and political tensions might slow the march towards more globalized science.
- **[Community–academic partnerships helped Flint through its water crisis](#)** [15 June 2021]
Comment • A city that faced a public-health emergency shows how collaborations with neighbourhood advocates can advance health equity.
- **[A white-knuckle ride of open COVID drug discovery](#)** [14 June 2021]
Comment • In early 2020, a spontaneous global collaboration came together to design a new, urgent antiviral treatment. There are lessons in what happened next.
- **[The authorship rows that sour scientific collaborations](#)** [14 June 2021]
Career Feature • Team science suffers when junior researchers see their career-defining contributions to a paper downplayed. Here's how to tackle disputes.
- **[‘We need to talk’: ways to prevent collaborations breaking down](#)** [15 June 2021]
Career Feature • Scientists who plan to partner on a research project should identify pressure points and consider a team charter at the outset.
- **[Tapping local knowledge to save a Papua New Guinea forest](#)** [14 June 2021]
Where I Work • Villagers who know the land help Jason Paliau to survey the region's insects.

| [Next section](#) | [Main menu](#) | [Previous section](#) |

- EDITORIAL
- 16 June 2021

Research collaborations bring big rewards: the world needs more

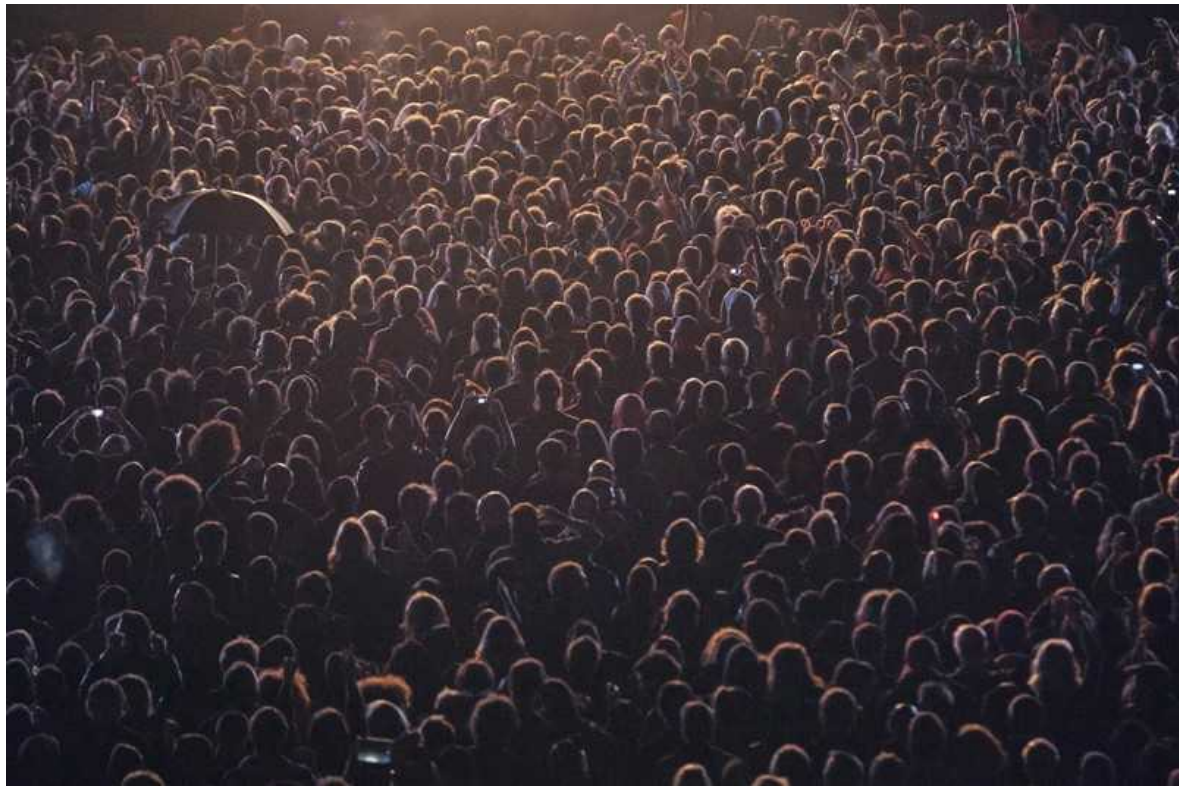
A special issue on COVID-era research collaboration highlights the benefits to science and society of working across borders, cultures and disciplines.





•

[Download PDF](#)



Group theory: international collaborations are at risk from geopolitical tensions.Credit: Getty

“The most important ingredient in making collaborations work is commitment: to producing research that is relevant, and to understanding many angles and perspectives.”

Yvonne Lewis and Richard Sadler make this point in a piece in this issue that describes how [universities and community organizations worked in concert](#) to find solutions to water contaminated with lead in Flint, Michigan. Their advice: spend less time and attention meeting metrics of performance, such as papers published and grants procured, and more time nurturing relationships.

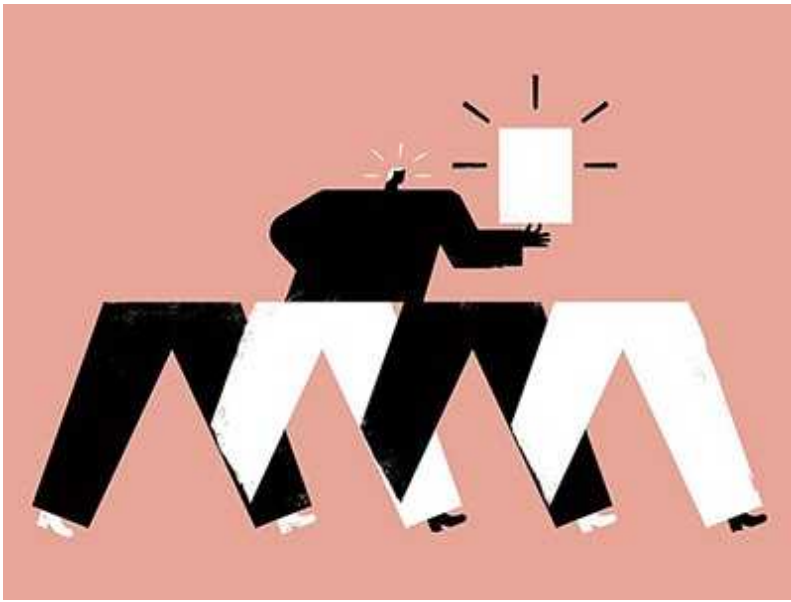


How the COVID pandemic is changing global science collaborations

Yet that, as Anna Hatch at the San Francisco Declaration on Research Assessment explains, is hard, because many of the structures and mechanisms that evaluate and reward science [are still those of the age of the lone scientist.](#)

Recognition — the naming of labs, and the awarding of national-academy fellowships and Nobel prizes — is still given to individuals, often on the basis of individual, rather than collective, performance measures. Few Nobels have explicitly rewarded scientific and technological collaboration. Two notable examples — for climate change and nuclear non-proliferation — have been Nobel peace prizes.

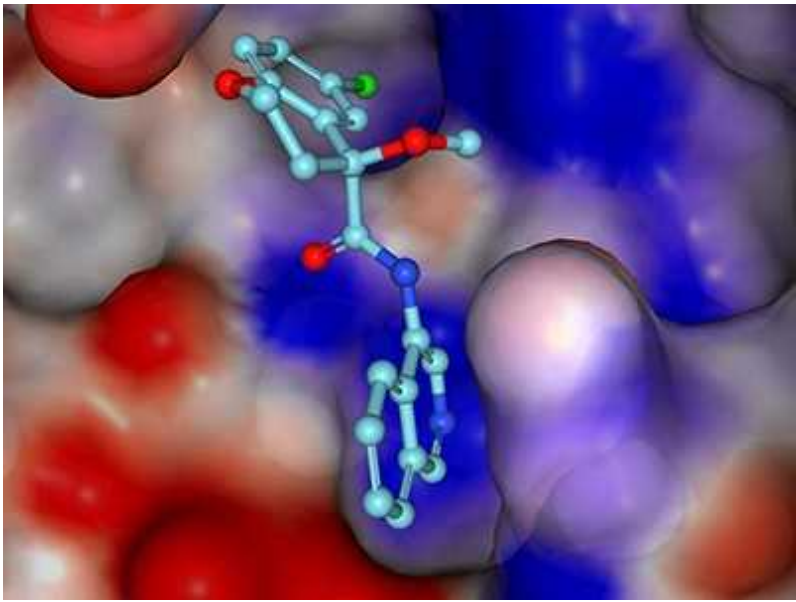
This special issue of *Nature* shines a spotlight on collaborations in science today, particularly in the wake of the coronavirus pandemic. It reveals that such cooperation, although complex, is thriving in many ways. It is clearly essential, both to the progress of research and for the betterment of society. But, at the same time, international collaboration is under pressure, partly as a result of geopolitical tensions. And science's historical conventions continue to hinder such team-based working.



The authorship rows that sour scientific collaborations

The pandemic has seen a host of inspiring stories of scientists stopping in their tracks and joining forces across borders and disciplines, whether to sequence viral genomes or describe protein structures and other features of SARS-CoV-2. In this issue, members of one of many such groups — those behind the COVID Moonshot project, which involves scientists scattered across continents — tell their story of [pulling together to design antiviral drugs](#). They write of juggling spectrometers, chemistry hoods, computer models, courier companies and Zoom calls, and of an “inexhaustible wellspring of goodwill”.

Analyses of bibliometric data reveal that [international collaborations were less common on COVID-19-related papers](#) in 2020 than they were for research on other coronaviruses in previous years. Moreover, as the pandemic has progressed, papers in which the authors are all in the same country have occupied a greater share of the COVID-19 literature. Looking at 2020 as a whole, the rate of international collaboration for COVID-19-related science was similar to that for all recorded research.



A white-knuckle ride of open COVID drug discovery

Indicators that some international collaboration is waning are evident when looking at data for China and the United States. The fraction of China's international collaborations that involve US authors has been falling since 2017. Such trends are likely to continue if geopolitical tensions with the United States worsen.

That would be regrettable. Successful collaboration relies on trust and long-standing relationships, as researchers at Dunhuang Academy in China and the University of Oxford, UK, told *Nature* in a specially commissioned short film on their collaboration on heritage conservation. Team members at the two institutions are studying how climate and weather affect ancient structures at cultural heritage sites on the Silk Road route in northwest China, and how natural methods might be used to better protect such sites ([J. Richards et al. Sci. Rep. 10, 16419; 2020](#)).

Among other things, the film explores how the team members approach and resolve differences of opinion, including the order of authors on joint publications, because China and the United Kingdom have different conventions. Qinglin Guo at Dunhuang Academy says that they were able to reach consensus “because we have the same goal — which is to protect the cultural heritages which belong to all of mankind”. ([Authorship disputes](#) and other [risks to collaboration](#) are discussed separately in two articles.)

Community partnerships

Some collaborations involve more than bridging countries and disciplines. We feature two projects in which communities work in close partnership with university researchers. One is between Jason Paliau, now at the Papua New Guinea University of Resources and Environment in Rabaul, and a senior-school student, Sammy. The pair worked together [to identify and count ants](#) in Papua New Guinea's lowland rainforest.



[Community-academic partnerships helped Flint through its water crisis](#)

The other is the initiative created in Flint. Lewis is a community activist and now principal investigator at the Flint Center for Health Equity Solutions. Sadler is a geographer at Michigan State University. They draw lessons from how researchers and members of the community worked together to identify where diseases were concentrated. It's a frank account that also flags the fact that some scientists discounted and overlooked ideas from communities, and raises the injustice of work that saves lives not necessarily meeting the 'excellence' criteria needed to progress in academic institutions.

These are clearly testing times for collaboration. The stories and data show that there is still some way to travel before all parts of the research enterprise recognize the true value of working across borders, cultures and disciplines.

Collaborations are essential — we need diverse teams to tackle global problems such as pandemics, and to help navigate social and geopolitical challenges. COVID-19 has provided a timely reminder that it can be done — and of the enormous rewards it can bring.

The metaphor ‘standing on the shoulders of giants’ has been much overused by scientists past and present. Today, such ‘giants’ are not only the investigators named on papers and project grants, but also every other participant in the research process. The future lies in standing on the shoulders of crowds.

Nature **594**, 301-302 (2021)

doi: <https://doi.org/10.1038/d41586-021-01581-z>

Related Articles

-  • [COVID has shown the power of science–industry collaboration](#)
-  • [How the COVID pandemic is changing global science collaborations](#)
-  • [Community–academic partnerships helped Flint through its water crisis](#)



- [A white-knuckle ride of open COVID drug discovery](#)



- [The authorship rows that sour scientific collaborations](#)



- [‘We need to talk’: ways to prevent collaborations breaking down](#)



- [Tapping local knowledge to save a Papua New Guinea forest](#)

Subjects

- [Research management](#)
- [Lab life](#)
- [Careers](#)
- [Publishing](#)
- [SARS-CoV-2](#)

[Jobs from Nature Careers](#)

- - - [All jobs](#)
 -

- **Post Doctoral Fellow Bioinformatics Modern and Ancient Infectious Diseases**

Faculty of Medicine, Dalhousie University

Multiple locations

JOB POST

- **Research Fellow - Molecular Pharmacology & Experimental Therapeutics**

Mayo Clinic Health System

Rochester, MN, United States

JOB POST

- **Research Fellow - Neurobiology**

Mayo Clinic Health System

Rochester, MN, United States

JOB POST

- **Scientist for PETRA III Beamline P07**

German Electron Synchrotron (DESY)

Hamburg, Germany

JOB POST

Download PDF

Related Articles



- [COVID has shown the power of science–industry collaboration](#)



- [How the COVID pandemic is changing global science collaborations](#)



- [Community–academic partnerships helped Flint through its water crisis](#)



- [A white-knuckle ride of open COVID drug discovery](#)



- [The authorship rows that sour scientific collaborations](#)



- [‘We need to talk’: ways to prevent collaborations breaking down](#)



- [Tapping local knowledge to save a Papua New Guinea forest](#)

Subjects

- [Research management](#)
- [Lab life](#)
- [Careers](#)
- [Publishing](#)
- [SARS-CoV-2](#)

This article was downloaded by **calibre** from <https://www.nature.com/articles/d41586-021-01581-z>

| [Section menu](#) | [Main menu](#) |

- EDITORIAL
- 16 June 2021

COVID has shown the power of science–industry collaboration

But a thriving relationship needs clearer rules around data ownership and intellectual property – and public trust in the process.





•

[Download PDF](#)



Credit: Cezary Kowalski/SOPA Images/Shutterstock

The pandemic has created a new kind of household name: AstraZeneca, BioNTech, Moderna and Pfizer are now as familiar as soap brands. But their life-saving vaccines would not have become a reality without remarkable and rapid collaboration with researchers at universities.

As part of this week's special issue on research collaborations, *Nature* spoke to industry scientists about their experiences of collaborating with academic colleagues on vaccine development. Collaboration between academia and industry is well established in many parts of the world. But the speed and scale of achievement during the pandemic — globally, 16 vaccines have been approved so far, with a further 9 in full phase III clinical trials — is rare, if not unprecedented, and interviewees praised the energy, enthusiasm and can-do attitude that they found in universities. Moreover, collaborating in the face of relentless media scrutiny as the world waited for a vaccine breakthrough has not been easy, interviewees added.



Research collaborations bring big rewards: the world needs more

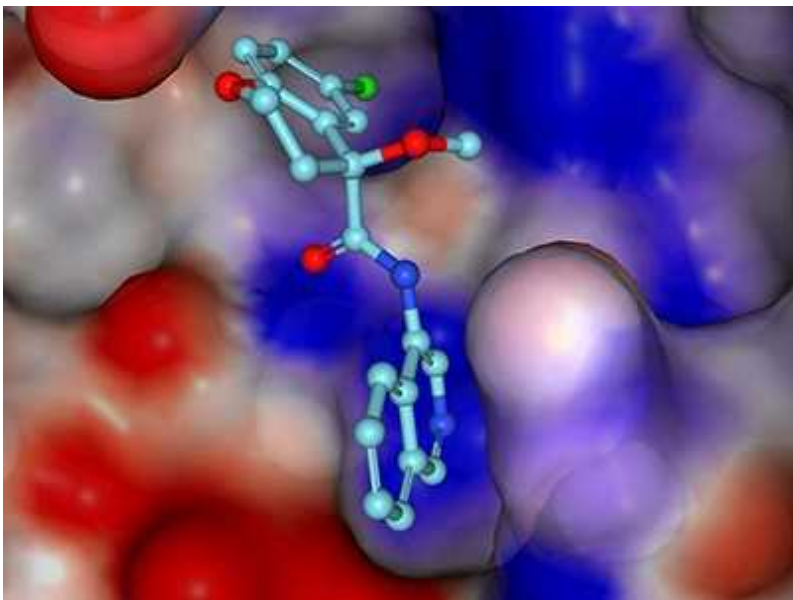
Unsurprisingly, respondents noted the limitations that virtual communication and lockdown restrictions have imposed on collaboration. They also urged more clarity on ownership of data and of intellectual property (IP) — areas where discussions with academic colleagues have been difficult.

This isn't new. Data ownership and intellectual property are sources of long-standing tensions in the academia–industry relationship. But there are ways these tensions can be eased.

The scientists *Nature* spoke to for this editorial say there have been robust exchanges with universities about how to apportion intellectual property when discussing collaborations. It's clear that some were not expecting that universities would also be thinking about monetizing their science; there remains a perception among some in industry that universities produce the science, and leave industry to commercialize it.

Universities do negotiate hard to maximize the returns on their science, effectively creating competition between universities and companies — something that did not exist in previous decades. And yet, there might be a silver lining. The campaign for time-limited IP relief on COVID-19 vaccines, backed by more than 100 countries, the World Health Organization and both China and, crucially, the United States, could help to reduce IP

disputes with universities, at least when it comes to collaboration on COVID-19 vaccines. Industry is against the campaign, but if it drops its opposition, more knowledge will become public, and at least some barriers to collaboration will disappear.



A white-knuckle ride of open COVID drug discovery

Access to data is another area where collaboration could be improved. For example, there need to be better mechanisms for researchers to access industry data in emergencies. These were discussed ahead of last week's meeting of the G7 group of some of the world's biggest economies in Cornwall, UK, and [might form part of a planned pandemic treaty](#). But solutions for data access also need to be found for collaborations to thrive outside of emergencies such as pandemics. Not all pharmaceutical-industry data that researchers can use is commercially sensitive. Other industries, such as finance and telecommunications, have similar challenges and experiences in data sharing, all of which need to be studied.

Dismantling barriers

Clearly, industry and academic colleagues have worked together at speed to deliver vaccines, underpinned by public and charitable investment; one analysis of the Oxford–AstraZeneca COVID-19 vaccine that has not yet

been peer reviewed showed that 98% of identified funding came from these sources ([S. Cross *et al.* Preprint at medRxiv https://doi.org/ghwh; 2021](https://doi.org/ghwh)).

Collaborations of this kind must continue beyond the pandemic. But, alongside goodwill, they will also require progress on ownership of data and IP.



How the COVID pandemic is changing global science collaborations

The pandemic has boosted public awareness of science–industry partnerships. It has also led to greater public understanding of research, manufacturing and quality-assurance processes. “People are hearing scientists talk. Taking them out of the labs is a new and now-accepted thing,” one industry representative told *Nature*.

Researchers need to study how this happened, in part to build on successes, and also to learn lessons for future pandemics, and to nurture the collaborations needed to tackle them. Researchers in academia and industry — and not only those who study infectious diseases — should now be looking to expand collaborations beyond the pandemic.

Success has also created expectations, in particular that academia and industry will deliver when called on. But future successes are not guaranteed, as both university- and industry-based researchers know. That is

why every lesson from this pandemic must be learnt, and barriers to collaboration must be dismantled as much as possible.

Nature **594**, 302 (2021)

doi: <https://doi.org/10.1038/d41586-021-01580-0>

Related Articles

-  [Research collaborations bring big rewards: the world needs more](#)
-  [How the COVID pandemic is changing global science collaborations](#)
-  [Community–academic partnerships helped Flint through its water crisis](#)
-  [A white-knuckle ride of open COVID drug discovery](#)
-  [The authorship rows that sour scientific collaborations](#)

-  ['We need to talk': ways to prevent collaborations breaking down](#)
-  [Tapping local knowledge to save a Papua New Guinea forest](#)

Subjects

- [SARS-CoV-2](#)
- [Infection](#)
- [Policy](#)

Jobs from Nature Careers

- - - [All jobs](#)
 - - [Post Doctoral Fellow Bioinformatics Modern and Ancient Infectious Diseases](#)

[Faculty of Medicine, Dalhousie University](#)

[Multiple locations](#)

[JOB POST](#)
- [Research Fellow - Molecular Pharmacology & Experimental Therapeutics](#)

[Mayo Clinic Health System](#)

[Rochester, MN, United States](#)

[JOB POST](#)

▪ [**Research Fellow - Neurobiology**](#)

[Mayo Clinic Health System](#)

[Rochester, MN, United States](#)

[JOB POST](#)

▪ [**Scientist for PETRA III Beamline P07**](#)

[German Electron Synchrotron \(DESY\)](#)

[Hamburg, Germany](#)

[JOB POST](#)

[Download PDF](#)

Related Articles



- [Research collaborations bring big rewards: the world needs more](#)



- [How the COVID pandemic is changing global science collaborations](#)

-  [Community-academic partnerships helped Flint through its water crisis](#)
-  [A white-knuckle ride of open COVID drug discovery](#)
-  [The authorship rows that sour scientific collaborations](#)
-  [‘We need to talk’: ways to prevent collaborations breaking down](#)
-  [Tapping local knowledge to save a Papua New Guinea forest](#)

Subjects

- [SARS-CoV-2](#)
- [Infection](#)
- [Policy](#)

| [Section menu](#) | [Main menu](#) |

- NEWS FEATURE
- 16 June 2021

How the COVID pandemic is changing global science collaborations

The pandemic and political tensions might slow the march towards more globalized science.

- [Brendan Maher](#) &
- [Richard Van Noorden](#)

1. Brendan Maher
[View author publications](#)

You can also search for this author in [PubMed](#) [Google Scholar](#)

2. Richard Van Noorden
[View author publications](#)

You can also search for this author in [PubMed](#) [Google Scholar](#)





•

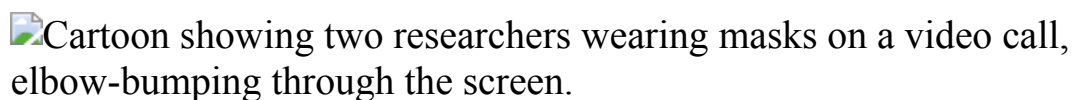


Illustration by Fabio Buonocore

[Download PDF](#)

In February 2020, as early COVID outbreaks were expanding in many countries, Nevan Krogan was grappling with a different kind of surge — in the size of his research collaboration. Krogan, a systems biologist, had been focused on tackling pressing issues in biology and health by forming interdisciplinary collaborations through the Quantitative Bioscience Institute

(QBI) at the University of California, San Francisco. His colleagues were eager to work on the new coronavirus — and they soon had lots of company.

What started as 10 scientists around a table jumped to 12 groups within a week, then to 42. When lockdowns started in March, the team's first Zoom call was exhilarating but chaotic. Hundreds of people joined, says Jacqueline Fabius, the QBI's chief operating officer.

Even though the institute specializes in bringing people together, the way everyone clicked into gear to work on COVID-19 was a surprise. "Different disciplines fit together much more seamlessly than I would have expected," says Krogan, who directs the QBI.

Within a few months, the collaboration had published research papers that map out protein interactions and other features of the SARS-CoV-2 virus that have helped to identify drug candidates now being tested against it.



[Research collaborations bring big rewards: the world needs more](#)

Those involved, including funders and industry partners, worked so openly and collegially, says Krogan, that he now wonders whether the rapid progress made on COVID-19 could be replicated for other diseases. "We should ask ourselves why it had to take such a gigantic human tragedy for us

to work together,” he and Fabius wrote in a commentary¹ about the experience.

The pandemic could leave its mark on research collaborations for years to come. Many scientists, like Krogan, strengthened existing connections and forged new ones. But the pandemic also interrupted projects and curtailed travel. And it might have intensified the challenges to international cooperation arising from long-standing political tensions, particularly between the United States and China. Analysis by *Nature* suggests that the growth in research collaborations involving the two countries might have started to slow before the pandemic.

There is also growing concern, heightened during the pandemic, about making collaborations equitable for — and beneficial to — all partners. That is still lacking, says Trudie Lang, a clinical-research scientist specializing in global health at the University of Oxford, UK. “The drivers and the rewards for team science just really aren’t there, yet.”

The rise of global collaboration

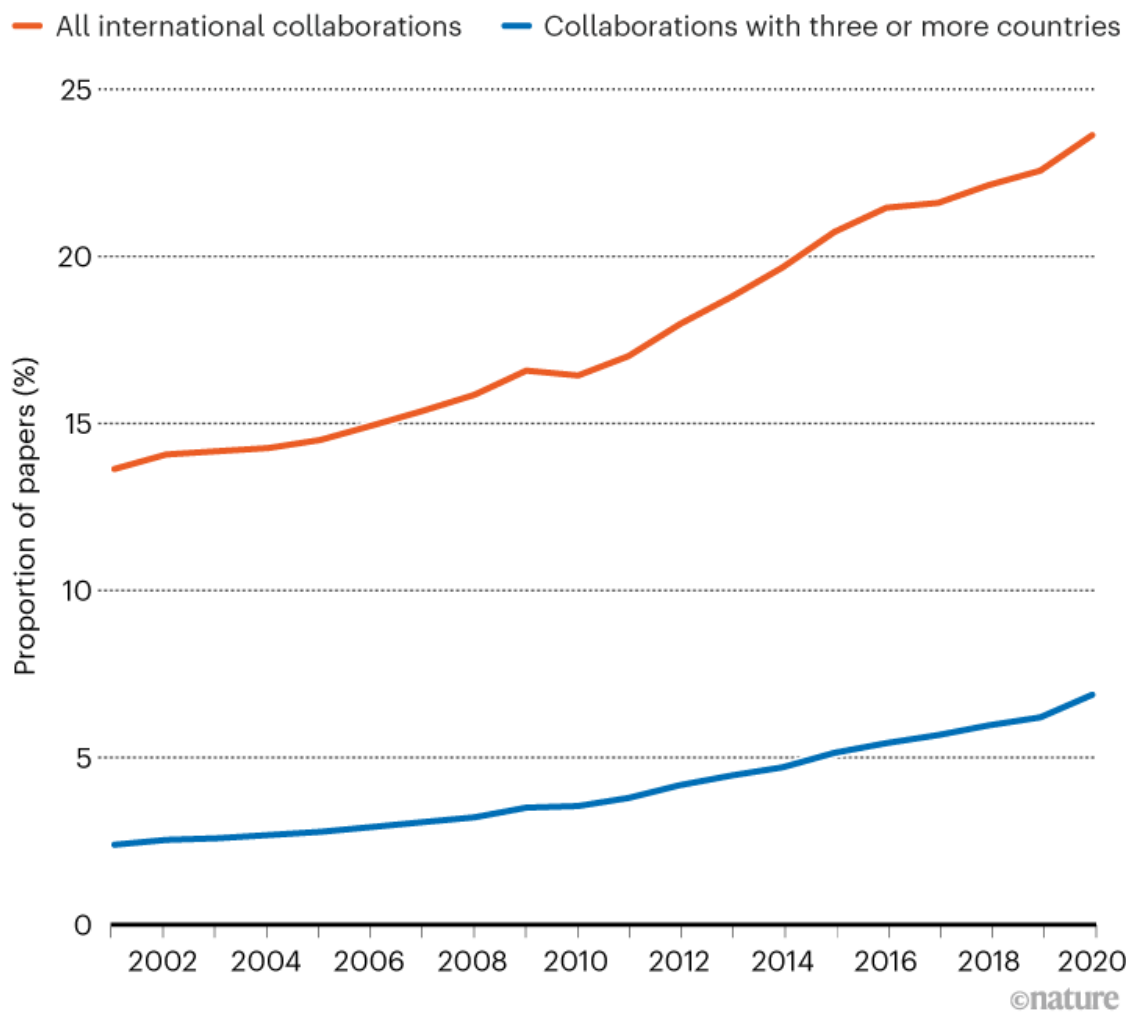
In the 1990s, the US Office of Science and Technology Policy — an agency that advises Congress on scientific matters — asked Caroline Wagner, then an analyst at the non-profit RAND Corporation, to help it understand the drivers of international collaboration. When she surveyed US scientists, Wagner found that about one-third of those who were collaborating internationally were originally from another country, and were connecting with colleagues there. Another third were collaborating with someone who had worked in one capacity or another in the United States. Scientists were maintaining connections that had been fostered locally, a trend that continues today. “As many as 90% of these international collaborations begin somehow face-to-face or side-by-side,” says Wagner, now a science-policy specialist at the Ohio State University in Columbus. And they do it because it helps the research.

The story of rising international collaboration, aided over decades by cheaper travel and better digital connectivity, is now familiar. Scientists can map this rise by looking at a proxy measure: co-authorship of research

papers (see ‘Collaborations on the rise’). In addition to the steady growth of international collaborations, one other trend has been clear for years: the papers that they produce tend to be cited more than domestically authored papers — a rough but useful measure of their relative impact on a field.

COLLABORATIONS ON THE RISE

The past few decades have seen a rapid rise in the fraction of papers with authors from more than one country.



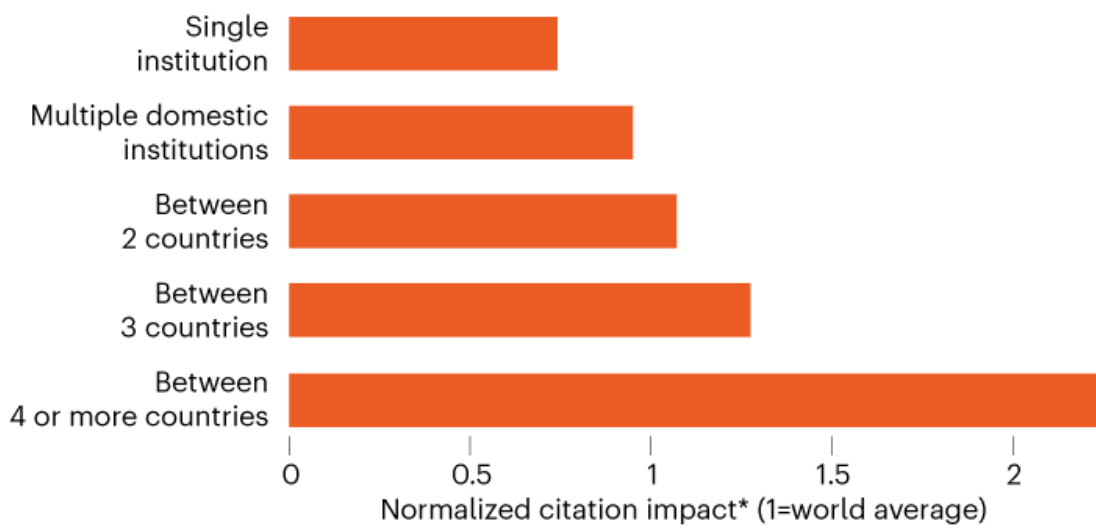
Source: *Nature* analysis of Dimensions database

A 2020 study², for example, showed that citation rates increase steadily with each additional country represented in an author list (see ‘Citation advantage’). The boost in impact is unsurprising, says Jonathan Adams, chief scientist at the analytics firm Clarivate in London, and an author of the

work. “People certainly don’t get involved in it unless there’s a very good reason for doing so.” Researchers have debated the connection between collaboration and quality, however. One study³ that examined subjective researcher assessments of biomedical papers suggested that, at least for a subset of the literature, international collaboration doesn’t correlate with better quality.

CITATION ADVANTAGE

Papers with multiple countries in their author affiliation lists gain more citations than those with only one or two.



*Each article's citation count divided by average citations for other articles in the same year and subject area.

©nature

Source: Ref. 2

One of the factors pushing the number of collaborations skywards is the rise of China as a research superpower. Although the majority of its papers are wholly domestically authored, its sheer publishing volume means that it has become the leading international partner for researchers in many other countries.

One trend that researchers have noticed is an increase in collaborations involving three or more nations. These now account for around 30% of international collaborations and 7% of all articles, according to a *Nature* analysis of Dimensions, a database owned by the analytics firm Digital Science in London. (Digital Science is operated by the Holtzbrinck Publishing Group, which also has a majority share in *Nature*'s publisher.)

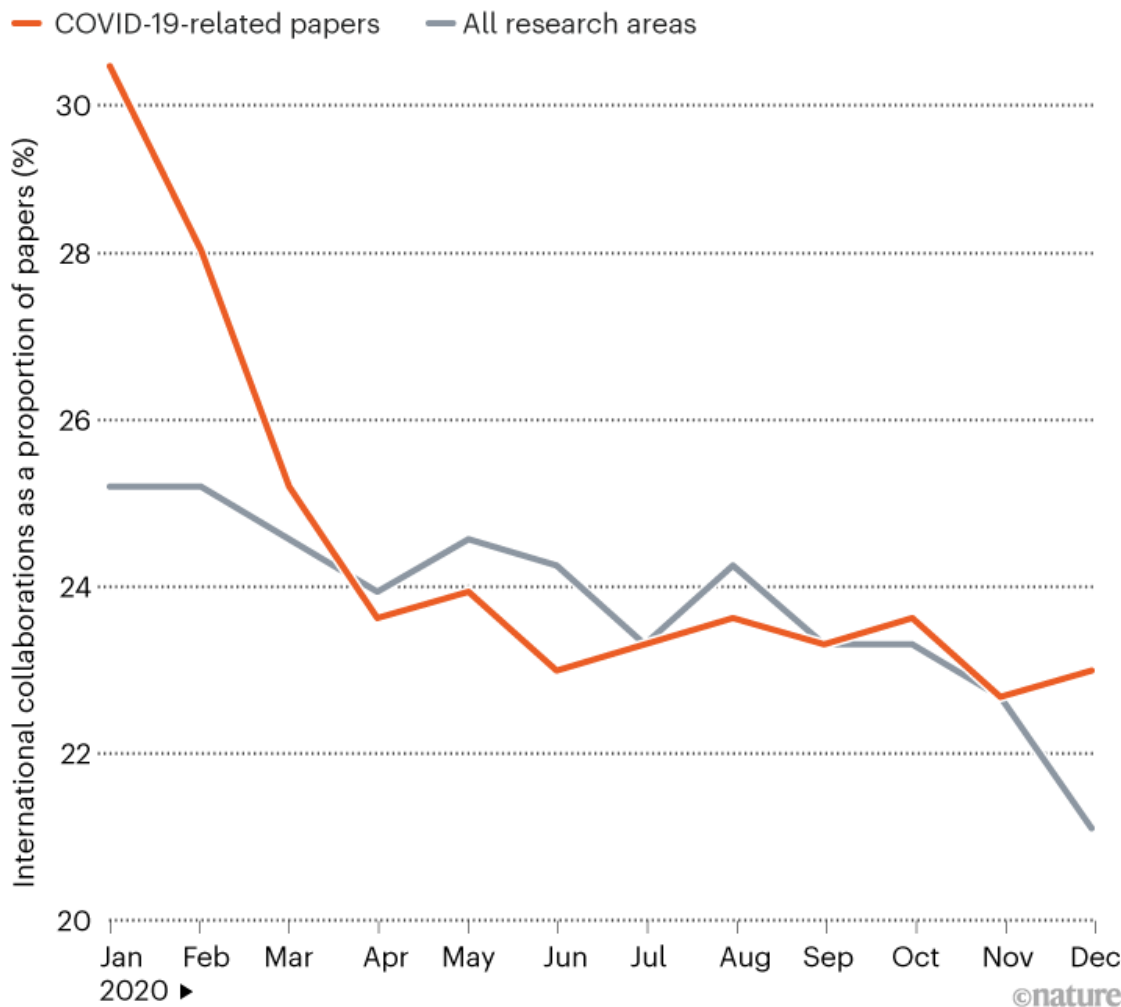
Some see the growth as a positive sign. “Generally, this is good news for those interested in knowledge being more global,” says Jenny Lee, who studies the geopolitics of higher education at the University of Arizona in Tucson.

COVID-19 and collaboration: boom and bust

Early in the COVID-19 pandemic, science leaders talked widely about leveraging global knowledge and working together. Their aspirations were only partly realized. According to multiple analyses of co-authorships of research studies^{4,5}, including *Nature*'s own for this article, the first few months of the pandemic probably did see more international collaboration on COVID-19-related papers than was typical for non-COVID-19 research. But collaboration was less common than for coronavirus research in previous years. As time wore on, the COVID-19 literature saw more domestically authored articles. And in 2020 as a whole, international collaboration rates for COVID-19 research ended up being similar to those for all research, *Nature*'s analysis suggests (see ‘COVID collaborations’).

COVID COLLABORATIONS

International collaboration on COVID-19-related papers was high in the first few months of 2020, similar to that of coronavirus research prior to the pandemic. But collaboration eventually dropped to levels typical of all types of research.



Source: *Nature* analysis of Dimensions database

There were some unusual wrinkles in collaboration patterns. In a preprint⁴, Ying Ding, an information scientist at the University of Texas, Austin, and her collaborators tracked a decline in international collaboration relative to previous coronavirus research, but also noted a 3% increase in collaborations involving individuals who had never worked together before. These “parachuting” collaborations, as the researchers called them, sometimes involved scientists from different disciplines, and showed signs of greater novelty, as measured by new combinations of biomedical terms;

the same signal of high novelty showed up in the international collaborations. The pandemic, Ding says, might have given birth to some creative partnerships (see also ‘*Finding that dream-team dynamic*’).

“Suddenly, everything’s paused, and you have to step out of your comfort zone and start thinking now about the common problem we all face.”

Finding that dream-team dynamic

Scientists who study collaboration are eager to explore how the diversity and structure of teams can influence the quality of research. And that means looking beyond the standard tools for judging research.

Viewing impact only through simple citation counts, for example, isn’t ideal, says James Evans, a sociologist and computational scientist at the University of Chicago, Illinois. He and his collaborators are trying to identify patterns that can provide clues to whether that work is new.

One potential indicator lies in how research is cited: “When people cite you, do they cite the things that you cite, or do they just cite you?” asks Evans. The latter, in his models, correlates with research that stakes out new areas for exploration. The former represents research that adds incrementally to previous work. In an analysis of 65 million papers¹¹, patents and software products, he found that large teams tended to produce research that builds on existing knowledge, whereas small teams’ research tended to be more disruptive.

Researchers also peer closely at team structure within papers. Because many journals now require scientists to detail their contributions to a given paper, Evans and other researchers are starting to look at whether team make-ups have a predictable influence on the nature of the work and its impact. The approach can be used to track career transitions from more hands-on ‘muscle’ roles to conceptual and creative ‘brain’ roles, Evans says, and it can identify what types of teams produce work that is more innovative, more disruptive or has unusual staying power.

Even factors such as the age of researchers in a group can be tracked, based on the amount of time they have been publishing on a particular topic. In unpublished work, Ying Ding, an information scientist at the University of

Texas, Austin, has found that teams with many years of experience — what she calls “team power” — tend to do well, in terms of citations, when there is not much difference in seniority among authors. Papers by lower-power teams do better when there is more of a hierarchy, she says; these teams need some people with more research experience. The worst performers are those with high power and lots of hierarchy, Ding says.

This is a universal pattern in science, she adds, “being proved by millions and millions of teams”. She and her collaborators are now looking at how team power is distributed in international collaborations. If a team has ten authors — five from the United States, three from China, two from Singapore — they can identify leadership not just from the last author on the paper, but also from the concentration of team power. “If the leader is the person from Singapore, then the leader is from the minority country. Are these kinds of teams more effective?” Ding asks.

Wagner and her colleagues looked at COVID-19 papers published up to the beginning of last October⁵. They found that coronavirus research teams shrank over this period, and involved fewer nations than was the case before the pandemic. But the teams that were international tended to involve more countries, particularly as the pandemic wore on, a trend that Wagner attributes to the need for diverse expertise.

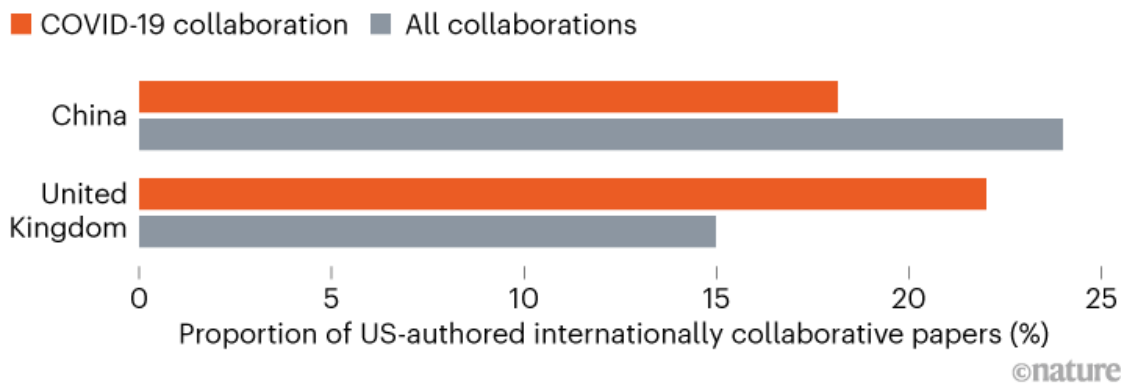
Researchers have paid particular attention to collaboration between the United States and China, the two nations with the biggest scientific output. In the first few months of the pandemic, these two countries collaborated on COVID-19 papers more than any other pair of nations, and at higher rates than they did for non-COVID-19 science, according to *Nature*'s analysis and work⁶ by Lee and John Haupt, an international-education specialist at the University of Arizona. That was in part because so many of the early papers on the pandemic had authors from China.

But as the pandemic wore on, the United States turned instead to collaborating on COVID-19 papers with other countries, such as the United Kingdom, *Nature*'s analysis and Wagner's work show⁵ (see ‘US COVID collaborations’). This corresponded with a decline in China's relative contribution to the literature, as case rates went down and as the government restricted the flow of information about COVID-19. Ding says she was

affected by these restrictions first-hand when she was working with researchers in Chinese universities to study the flow of misinformation about the new coronavirus. “Some of them said, ‘Sorry.’ They cannot work on COVID any more because that has to get approved,” Ding says.

US COVID COLLABORATIONS

For COVID-19-related papers in 2020, US-UK research collaborations were more common than US-China research collaborations: a reversal of the norm for papers across all subject areas.



Source: *Nature* analysis of Dimensions database

Krogan, too, says that building alliances with Chinese researchers has been particularly hard. The QBI was establishing connections in China before the pandemic, and things were going smoothly, says Krogan. But working on coronavirus presented extra challenges. “I know for a fact that over the last year it’s become harder,” he says. “The pandemic kind of triggered something, politically, I guess.” The QBI’s coronavirus research group currently has no official partners in China.

The data on collaboration during the pandemic are messy in part because of the massive publishing surge — the number of COVID-19 papers and preprints increased from about 5,000 in the first three months of the pandemic to 150,000 or more by the end of 2020. What’s more, preprints aren’t always included in the analyses, and comparing the massive infusion of coronavirus-related research with studies in other fields, many of which had to be put on hold owing to lockdowns, is difficult. The data also don’t typically capture industry collaborations and their impact.

In a few years' time, Adams says, one might be able to look back and see 'blips' in the research record due to work that stopped because people switched to working on coronavirus, reduced their international travel, or shut down their laboratories. [Some scientists have been stranded](#) or unable to hire people for key positions because of lockdowns, and the dearth of in-person meetings, symposiums and conferences has delayed networking opportunities that are especially important to junior researchers. Nevertheless, Adams thinks that COVID-19's impact on collaboration as a whole will be minor, particularly when compared with the impact on society more broadly.

But his is one of the more optimistic views. Others see the pandemic as potentially amplifying some of the forces that work against international collaboration.

Geopolitical tensions

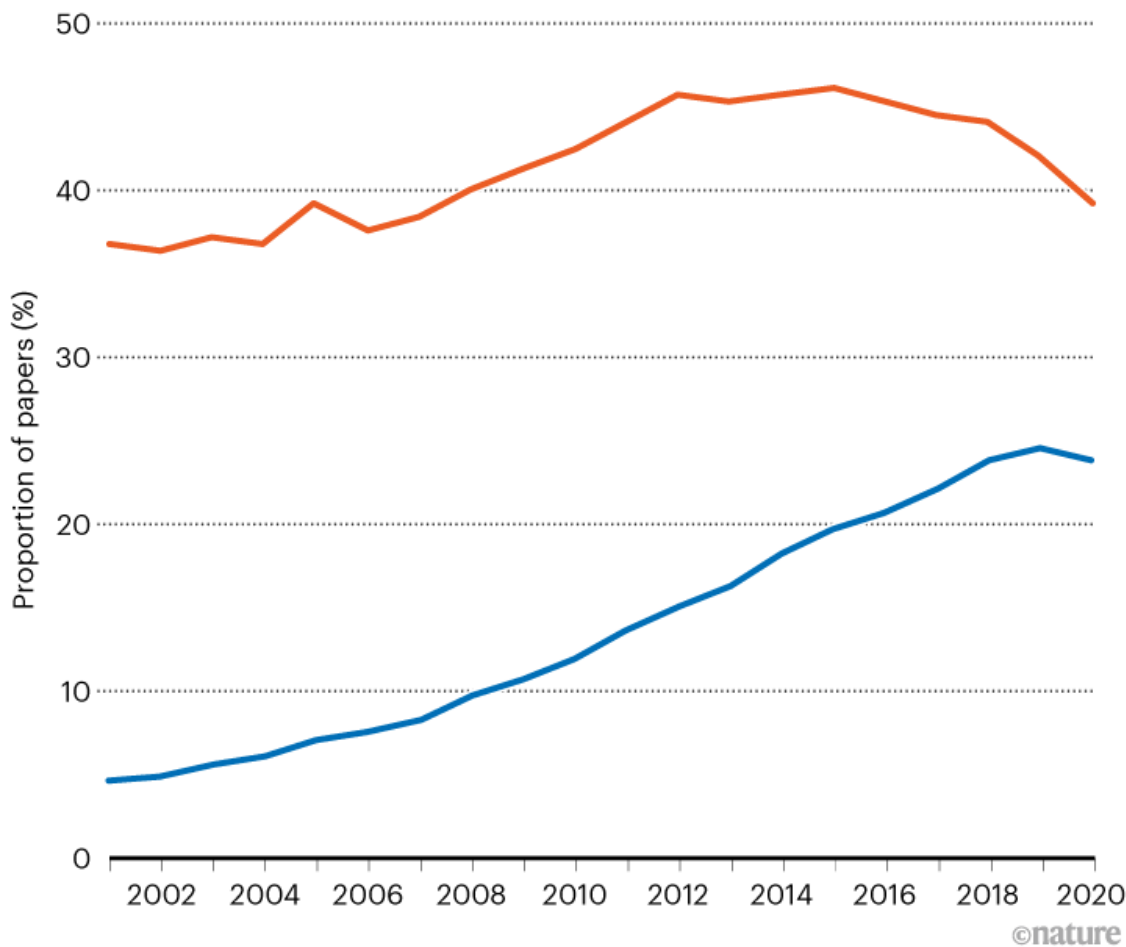
The drop in US–China collaborations on COVID-19 research that Wagner documented represents a small proportion of all the research the countries do together. But it might fit in with a broader slowdown in the growth of their collaboration.

Nature's analysis suggests that although the number of papers with both Chinese and US co-authors is still climbing, the fraction of China's international collaborations that involve US authors has been declining since 2017 — even as the share of papers co-authored with some other nations, such as the United Kingdom and Australia, is rising. Similarly, the fraction of US international collaborations that include China fell for the first time in 2020, after rising for two decades (see 'US–China collaborations').

US–CHINA COLLABORATIONS

The number of publications with US-based and China-based authors is rising. But starting in 2016, the fraction of China's international collaborations that include US co-authors began to fall. The share of US collaborations that have co-authors in China dipped more recently.

- Fraction of China's international papers with US co-authors
- Fraction of US international papers with Chinese co-authors

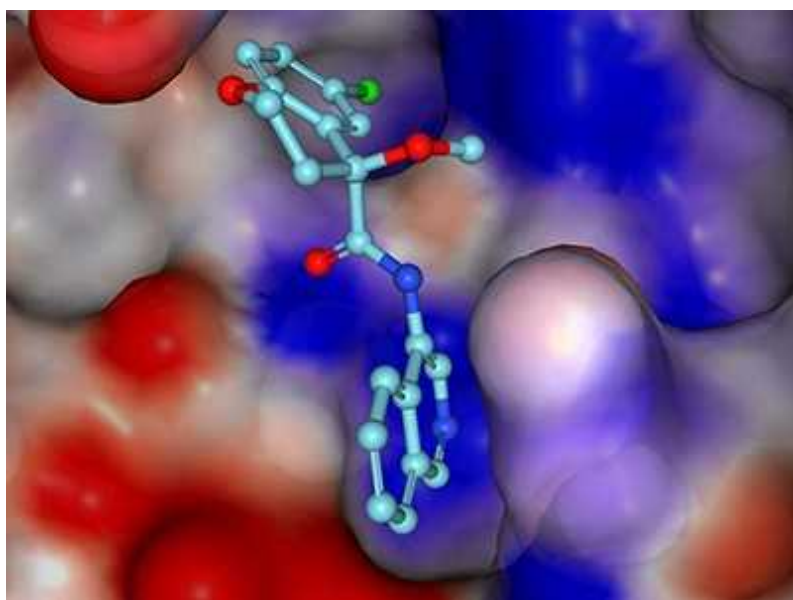


Source: *Nature* analysis of Dimensions database

And in May, analysts with the Nature Index, a database that tracks 82 well-known natural-sciences journals, reported seeing [zero growth in US–China papers](#) in these journals in 2020, after increases in previous years. (Nature Index is published by Springer Nature; *Nature*'s news team is editorially independent of its publisher.)

The reasons for the slowdown might relate to government interventions. Fuelled by fears of intellectual-property theft and espionage, the US government has been [scrutinizing scientists with ties to China](#); there have been arrests and sackings for failure to disclose funding from foreign entities and violations of peer review. The punitive measures have had a “chilling effect” on establishing new partnerships, says Cassidy Sugimoto, an information scientist at Georgia Tech in Atlanta. Perhaps more importantly, [visa restrictions](#) imposed by the administration of former US president Donald Trump last year might have reduced the number of visiting scholars and students training in the United States. “Any changes in policies or regulation around visas affects international collaboration,” Sugimoto says. And Chinese scientists already working in the United States might be less inclined to stay: [some report feeling less welcome](#) because of rising racial discrimination.

Migration patterns can take a long time to emerge in the data, but limitations were starting to show well before the pandemic. Li Tang, a science- and innovation-policy researcher at Fudan University in Shanghai, points to air-traffic data, for example. Since 2018, these have shown a 10% drop in the number of trips from China to US airports — specifically those near universities that typically host Chinese students⁷.



[A white-knuckle ride of open COVID drug discovery](#)

China's national policies could also be having an impact. In 2020, the government said that [Chinese researchers should be evaluated](#) less on the volume of their work in international-journal databases such as the Science Citations Index, and more on the quality of their papers — and that assessments should also consider research in journals published in China. As the number of Chinese-language journals expands, collaborations data could be harder to analyse. The policy could have a profound effect on international collaboration, says Lee.

Established collaborations shouldn't be strongly affected, but new work might be choked, according to researchers. "It'll undoubtedly have an effect when we're not even able to nurture the early seeds in collaboration," says Lee, who aims to explore the appetite for collaboration through interviews and surveys in the United States and China starting later this year.

But some researchers are more optimistic. Even if the rate of growth in US–China partnerships is dropping, the number of collaborative publications is still rising. James Wilsdon, a science-policy researcher at the Research on Research Institute in London, also warns against applying simplistic narratives to China. Despite the powerful levers that its government can pull to influence the way in which science is practised in the country, if researchers in China want to collaborate, they will find ways, he says.

Wilsdon is watching to see how nationalistic political narratives will affect collaboration in other countries. For instance, the United Kingdom's exit from the European Union, which took full effect this year, has raised barriers for some scientists who wish to migrate to the country. And [UK cuts to global health-research funding](#) in 2020 were "a destabilizing force", Wilsdon says. Now the UK government is busy smoothing visa requirements for science and technology professionals from overseas; it set up a new Office for Talent last year to attract researchers.

Scientific societies, meanwhile, have been compiling reports in support of international collaboration. The American Academy of Arts & Sciences, for example, in June released its second report⁸ in a series on large-scale international collaborations, detailing the scientific, economic and diplomatic benefits of participating in big international projects such as CERN, Europe's particle-physics laboratory near Geneva, Switzerland.

Another long-term trend that researchers are watching out for is the push for scientists to share their research data more openly. This was mandated by the biomedical funding charity, Wellcome, for research that it funded on COVID-19, although there have been instances of people circumventing the rules by making data available ‘upon request’.

In theory, the push for open data might lessen international collaboration if it is no longer necessary to establish personal relationships to access data.

Sugimoto says this could happen, but also wonders whether open data might help to link researchers from across the world by making their work more visible. “It could actually, in some ways, enhance and increase international collaboration rather than diminish it,” she says.

Unequal collaboration

The benefits of collaborative research are not always shared equally. And many scientists are looking for ways to better understand this unequal distribution — which ranges from credit on papers to downstream economic benefits. Lang points out that during the pandemic, most major international clinical trials have been led by wealthy nations and involved treatments and vaccines that could be administered in hospital settings. The cost, she has argued, is that it has taken a long time to make much progress on the kinds of testing and antiviral drugs that would benefit people in low- and middle-income countries.

“There’s really serious gaps that we would have got over if we’d have had much more collaborative effort. And that doesn’t mean just working together as a team but also means sharing what we’ve learnt between teams,” says Lang. Collaborative science, she notes, often follows an agenda that suits the bigger, richer partner. It could help to spur better, more independent research in low- and middle-income countries, but it’s not there yet, she says.

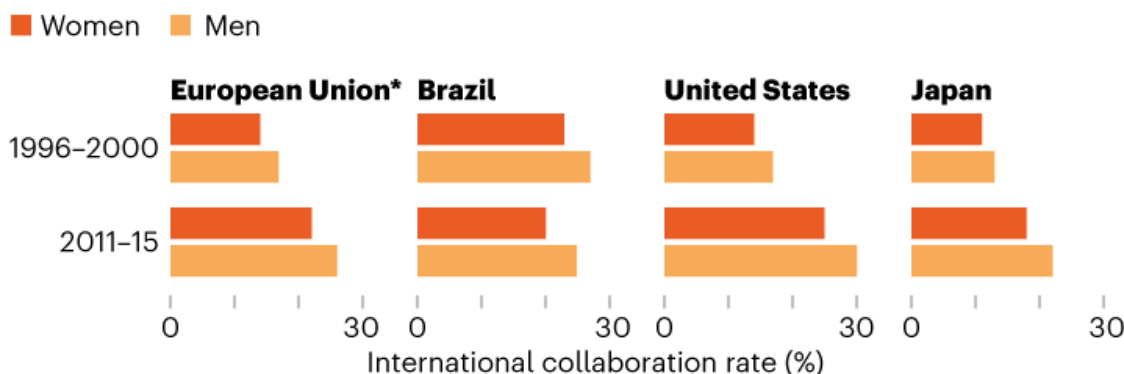
Science is still driven by rewards that are often given to individuals.

“Academics have it beaten into us to be very competitive,” says Lang, and that comes at a cost to team science, she says.

At the individual level, women face particular challenges as members of collaborations. Lesley Thompson, vice-president of academic and government relations at the science publisher Elsevier, says that the company's 2020 analysis⁹ of gender representation in science publications found that women typically have smaller networks of international collaborators than men do (see 'Male and female collaboration networks').

MALE AND FEMALE COLLABORATION NETWORKS

Women typically have fewer international collaborations than do men.



*Calculated for the 28 countries that made up the European Union from 2013-2020.

©nature

Source: Ref. 9

Several papers have [documented how the pandemic probably exacerbated disparities](#) that already existed between male and female researchers.

Sugimoto, for example, showed how women's names were falling out of primary authorship roles in preprints, and appearing deeper in the list of authors (see go.nature.com/2xhxqxr). They were also appearing less frequently in databases where scientists register studies, such as ClinicalTrials.gov, suggesting that they were less involved in initiating work. One contributing factor, according to surveys of thousands of female scientists, is that they are being asked to shoulder a great deal more of the childcare duties as a result of school and daycare closures during the pandemic¹⁰.

Leaders of the QBI coronavirus research group have considered these disparities. Fabius says that group organizers demanded equal representation for women at its symposium last June, for example, and it has made philanthropic funds available to the project's female scientists to use for

childcare costs or to hire extra help in the lab. “Investing money in that area is incredibly wise,” she says. “The infrastructure of the whole system needs to be more flexible with these issues.”

Krogan agrees. The pandemic exposed a lot of good things about how people work together, but also a lot of deficiencies, he says. “The onus is on us, as the dust settles, to fix these things.”

Nature **594**, 316–319 (2021)

doi: <https://doi.org/10.1038/d41586-021-01570-2>

References

1. 1.

Fabius, J. M. & Krogan, N. J. *Cell* **184**, 2271–2275 (2021).

[PubMed](#) [Article](#) [Google Scholar](#)

2. 2.

Potter, R. W. K., Szomszor, M. & Adams, J. *J. Informetr.* **14**, 101075 (2020).

[Article](#) [Google Scholar](#)

3. 3.

Bornmann, L. *J. Assoc. Inf. Sci. Technol.* **68**, 1036–1047 (2017).

[Article](#) [Google Scholar](#)

4. 4.

Liu, M. *et al.* Preprint at <https://arxiv.org/abs/2009.12500> (2021).

5. 5.

Cai, X., Fry, C. V. & Wagner, C. S. *Scientometrics* **126**, 3683–3692 (2021).

[Article](#) [Google Scholar](#)

6. 6.

Lee, J. J. & Haupt, J. P. *J. High. Educ.* **92**, 303–329 (2021).

[Article](#) [Google Scholar](#)

7. 7.

Wang, Z., Tang, L., Cao, C. & Zhou, Z. Available at <https://doi.org/10.2139/ssrn.3739306> (2020).

8. 8.

Challenges for International Scientific Partnerships Initiative. *Bold Ambition: International Large-Scale Science* (American Academy of Arts & Sciences, 2020). Available at <http://go.nature.com/3gdahja>.

9. 9.

Gender in the Global Research Landscape (Elsevier, 2020).

10. 10.

Myers, K. R. *et al. Nature Hum. Behav.* **4**, 880–883 (2020).

[PubMed](#) [Article](#) [Google Scholar](#)

11. 11.

Wu, L., Wang, D. & Evans, J. A. *Nature* **566**, 378–382 (2019).

[PubMed](#) [Article](#) [Google Scholar](#)

[Download references](#)

Related Articles

-  • [Research collaborations bring big rewards: the world needs more](#)
-  • [COVID has shown the power of science–industry collaboration](#)
-  • [Community–academic partnerships helped Flint through its water crisis](#)
-  • [A white-knuckle ride of open COVID drug discovery](#)
-  • [The authorship rows that sour scientific collaborations](#)
-  • [‘We need to talk’: ways to prevent collaborations breaking down](#)



- [Tapping local knowledge to save a Papua New Guinea forest](#)



- [Are women publishing less during the pandemic? Here's what the data say](#)



- [How COVID-19 has stomped on scientists' travel plans](#)



- [Protect precious scientific collaboration from geopolitics](#)

Subjects

- [Research management](#)
- [SARS-CoV-2](#)
- [Politics](#)
- [Government](#)

Jobs from Nature Careers

- - - [All jobs](#)
 -

- **Post Doctoral Fellow Bioinformatics Modern and Ancient Infectious Diseases**

Faculty of Medicine, Dalhousie University

Multiple locations

JOB POST

- **Research Fellow - Molecular Pharmacology & Experimental Therapeutics**

Mayo Clinic Health System

Rochester, MN, United States

JOB POST

- **Research Fellow - Neurobiology**

Mayo Clinic Health System

Rochester, MN, United States

JOB POST

- **Scientist for PETRA III Beamline P07**

German Electron Synchrotron (DESY)

Hamburg, Germany

JOB POST

Download PDF

Related Articles



- Research collaborations bring big rewards: the world needs more



- COVID has shown the power of science–industry collaboration



- Community–academic partnerships helped Flint through its water crisis



- A white-knuckle ride of open COVID drug discovery



- The authorship rows that sour scientific collaborations



- ‘We need to talk’: ways to prevent collaborations breaking down



- [Tapping local knowledge to save a Papua New Guinea forest](#)



- [Are women publishing less during the pandemic? Here's what the data say](#)



- [How COVID-19 has stomped on scientists' travel plans](#)



- [Protect precious scientific collaboration from geopolitics](#)

Subjects

- [Research management](#)
- [SARS-CoV-2](#)
- [Politics](#)
- [Government](#)

This article was downloaded by **calibre** from <https://www.nature.com/articles/d41586-021-01570-2>

- COMMENT
- 15 June 2021

Community–academic partnerships helped Flint through its water crisis

A city that faced a public-health emergency shows how collaborations with neighbourhood advocates can advance health equity.

- [E. Yvonne Lewis](#) ⁰ &
- [Richard C. Sadler](#) ¹

1. [E. Yvonne Lewis](#)

1. E. Yvonne Lewis is founder and chief executive of the National Center for African American Health Consciousness, Flint; co-community principal investigator at the Flint Center for Health Equity Solutions; co-director of the Healthy Flint Research Coordinating Center Community Core; and director of outreach, Genesee Health Plan, Flint, Michigan, USA.

[View author publications](#)

You can also search for this author in [PubMed](#) [Google Scholar](#)

2. [Richard C. Sadler](#)

1. Richard C. Sadler is associate professor of public health at Michigan State University, Flint, Michigan, USA.

[View author publications](#)

You can also search for this author in [PubMed](#) [Google Scholar](#)





•

[Download PDF](#)



Residents of Flint, Michigan, attended community blood-testing events in 2016 after lead contamination was found in the city's water supply. Credit: Brett Carlsen/Getty

Flint in Michigan is infamous for its water crisis. From 2014, the state government decided to divert the city's water supply through ageing pipes that contained lead, a neurotoxin, making many people unwell and leading to some deaths. Residents were left searching out water that was safe for drinking, washing and bathing. Nine public officials face criminal negligence charges around wilful neglect of duty and for allegedly concealing and misrepresenting data. A US\$640-million class-action lawsuit is moving its way through the courts.

But Flint should be known for more than its public-health tragedy. Accounts of the crisis often [cast pioneering scientists and physicians as lone heroes](#), assuming that those who documented the lead in the water and blood of Flint's residents were the ones who brought officials to account. That assumption erases the work of community activists who got academics to look for lead and its damaging health effects in the first place. Flint is a working example of how community members and academics can

collaborate on problems — such as how to collect data or develop robust models of health risks and injustices — and on finding solutions.



Research collaborations bring big rewards: the world needs more

Flint's water crisis came to light because of strong research partnerships between activists, academics and other specialists. These partnerships continue to advance work that matters to the community. Efforts include identifying neighbourhood conditions (including crime levels, asthma rates and access to healthy food) and assessing projects to improve them. It requires a commitment that research does not just end up in a thesis or paper, but becomes information that is useful to community members.

Here's one example. The Genesee Health Plan is a non-profit benefit programme that provides basic health-care coverage to uninsured residents of Genesee County, which includes Flint. It was established in 2001 and is supported by property taxes. One of us (E.Y.L.) helped to provide the other (R.C.S.) with data from a sample of Genesee Health Plan enrollees to produce maps of chronic conditions. One map showed the health plan's wide adoption in our community, and officials used it to advocate for voter support when the tax measure was renewed in 2018. This partnership was possible only because of the connections already formed between E.Y.L., who is a community organizer, and R.C.S., a geographer and public-health specialist at Michigan State University (MSU) in Flint.

Hear more about how community-research collaborations were made to work in Flint.

[Download MP3](#)

Long-standing efforts to ensure Flint community members have a voice in research have gained momentum. One tangible result was the creation of the Healthy Flint Research Coordinating Center in 2016. To form the centre, E.Y.L. and another Flint resident representing community organizations joined up with six researchers — two each at MSU, the University of Michigan in Ann Arbor and the University of Michigan–Flint. It works to minimize redundant research, maximize creation of new community–academic partnerships and ensure that research receives a community ethics review.

Also established in 2016 to support equitable community–academic partnerships was the Flint Center for Health Equity Solutions, funded by the US National Institutes of Health (NIH). E.Y.L. is the centre’s overall community principal investigator. Each of its four divisions and two research projects is co-directed by a community member and an academic. The divisions are: methodology (which R.C.S. directs); dissemination and implementation sciences; administrative; and consortium partners. A programme within the centre — in which people with substance-use disorders are coached by their peers — has expanded and is now supported by additional external funding.

Here, we distil how we’ve made community-based research work, and provide lessons others might use.

Distinct challenges

Each of us experienced different challenges before we formed our community partnership, which might offer some pointers for others considering such collaborations. To that end, here, we relate our stories individually.

R.C.S. writes: I grew up in Flint, and joined MSU as a faculty member in 2015. I knew that the kind of community-focused work I was most passionate about makes it harder to rack up the publications and citations required to progress in most academic institutions, which often treat these as a proxy for high-quality research.



A medical assistant checks for the presence of lead in blood samples as part of a community campaign in Flint, Michigan. Credit: Jim West/Alamy

I still worked to hit those markers, publishing more than 50 papers in 6 years. I secured several grants from agencies that fund research that has community value — including agencies in the NIH, the US Centers for Disease Control and Prevention (CDC) and the Michigan Department of Health and Human Services. My focus was on work that mattered to the community, and I didn't worry whether journals had high impact factors or huge name recognition.

The community-engaged philosophy of the College of Human Medicine at MSU — where I gained tenure this year — made it more open to alternative metrics, such as volunteering on local non-profit committees, conducting

community-based mapping and talking about research at local meetings. The key was to frame my academic output on a longer time scale than that of publications — long enough to see meaningful change.



Rethink how we plan research to shrink COVID health disparities

E.Y.L. writes: As an African American female community activist of decades' standing, I worried about being physically mistreated, emotionally abused and misrepresented by research institutions. On one occasion before I moved to Flint, I remarked that some physicians' descriptions of pregnant African American women as unconcerned with or unwilling to take care of their own needs did not reflect people in my community. I was asked about my academic credentials and then ignored for the rest of the conversation. I experienced this often during the water crisis: community members were touted as being great citizen scientists, until there was disagreement with the 'real scientists'. Then we were marginalized and told we lacked the necessary degrees to provide input.

As community members, we also see our ideas appropriated. For instance, during a discussion at one national meeting, I made a distinction — on the basis of my own experience — between projects that were faith-based (driven by religious principles) and those that were faith-placed (using spaces such as churches). The following year, a researcher presented data based on this model without acknowledging me as the inspiration. I felt

dishonoured, discouraged and demotivated. I now ask academic partners to give attribution for my ideas. Knowing the norms — and what credit to request — has helped me immeasurably.

Joint challenges

One of the biggest barriers to community participation is language. Words can have different meanings in different contexts — for instance, the phrase ‘those people’ can be highly offensive in many situations. When community members hear terms such as public engagement, they assume that ‘public’ refers to a broad, mixed group of individuals, such as those who might go to a public event. Yet academics often use the term to mean targeted outreach to specific groups of people — faith leaders, patient groups or policymakers, say. And to help navigate excessive jargon in the early stages of Flint’s partnerships, one group developed a glossary of acronyms such as NIH and CDC.



[The best research is produced when researchers and communities work together](#)

Importantly, everyone involved must take time to understand the culture and unique characteristics of the groups within communities. Not all Black communities are the same, for instance, and none is homogeneous. The

heterogeneity among people's levels of income, education and health insurance must be kept in mind in communications. Research materials written in English for a 'general audience' might not be appropriate — strong cultural dialects and a lack of access to information need to be considered.

Funding norms can also become a barrier to sustaining long-term relationships. Grants that last only one, two or five years are insufficient to address many community concerns. Too many communities have experienced projects for which funding ends and researchers move on, leaving unfinished work. Without sustained effort, the situation can revert to being the same or worse than it was before the project began. This is partly why community-engaged work is so important: researchers committed to the cause will continue as partners long after the funding is gone. And if grants from typical funders run out, academics will find other sources of support for community partners — such as by maintaining relationships with local philanthropies. (In Flint, such support has come from the C. S. Mott Foundation and Community Foundation of Greater Flint.)



A local church in Flint was set up as a water distribution centre because lead contamination had made the public supply unsafe.Credit: Tom Williams/CQ Roll Call

Researchers often come to communities with a prepared study design, seeking approval rather than input — even when input could improve a study. Researchers assessing campaigns to promote healthy eating might include a control group that receives nothing, whereas the treatment group receives a suite of services and vouchers. This creates a perception of unfairness that can warp a study and discourage participation. Too often, researchers treat community partners who point out such risks as a barrier to progress, rather than as a liaison to a robust study. That attitude undermines future interactions. Establishing realistic expectations is one way to mitigate this issue.

Researchers might also offer to provide training in work that is already under way. For example, Flint has a crime-reduction programme in which residents proactively assess whether street lights are working and maintain vacant properties. Proposals that disregard what is already in place are wasteful and cause resentment. At one point, a team of researchers approached us to implement a healthy-eating project, not realizing that the Flint community had helped to develop the recipe book on which it was based. The Healthy Flint Research Coordinating Center now maintains an index of projects to discourage redundant work (one of R.C.S.'s tasks).



Farmers transformed how we investigate climate

Before and especially during the water crisis, a string of ‘helicopter researchers’ from outside Flint came to study topics from environmental issues to violence. Community members were asked to fill out surveys, or learnt through informal chatter about researchers who wanted records about emergency hospitalizations. But data and insights were not brought back to the community. Many residents felt used and dismissed. The coordinating centre now works with researchers so their results can be applied to inform and improve the community where data were collected.

Interactions are generative: when academic researchers dismiss community ideas, take them without credit, bristle at valid input, ‘introduce’ programmes that are already in progress or focus more on producing papers than on helping communities, residents will expect the same of other researchers. Even those with the best of intentions can be rebuffed or face distrust, something R.C.S. was attuned to when he began his transition from Flint community member to academic.

Nurture relationships

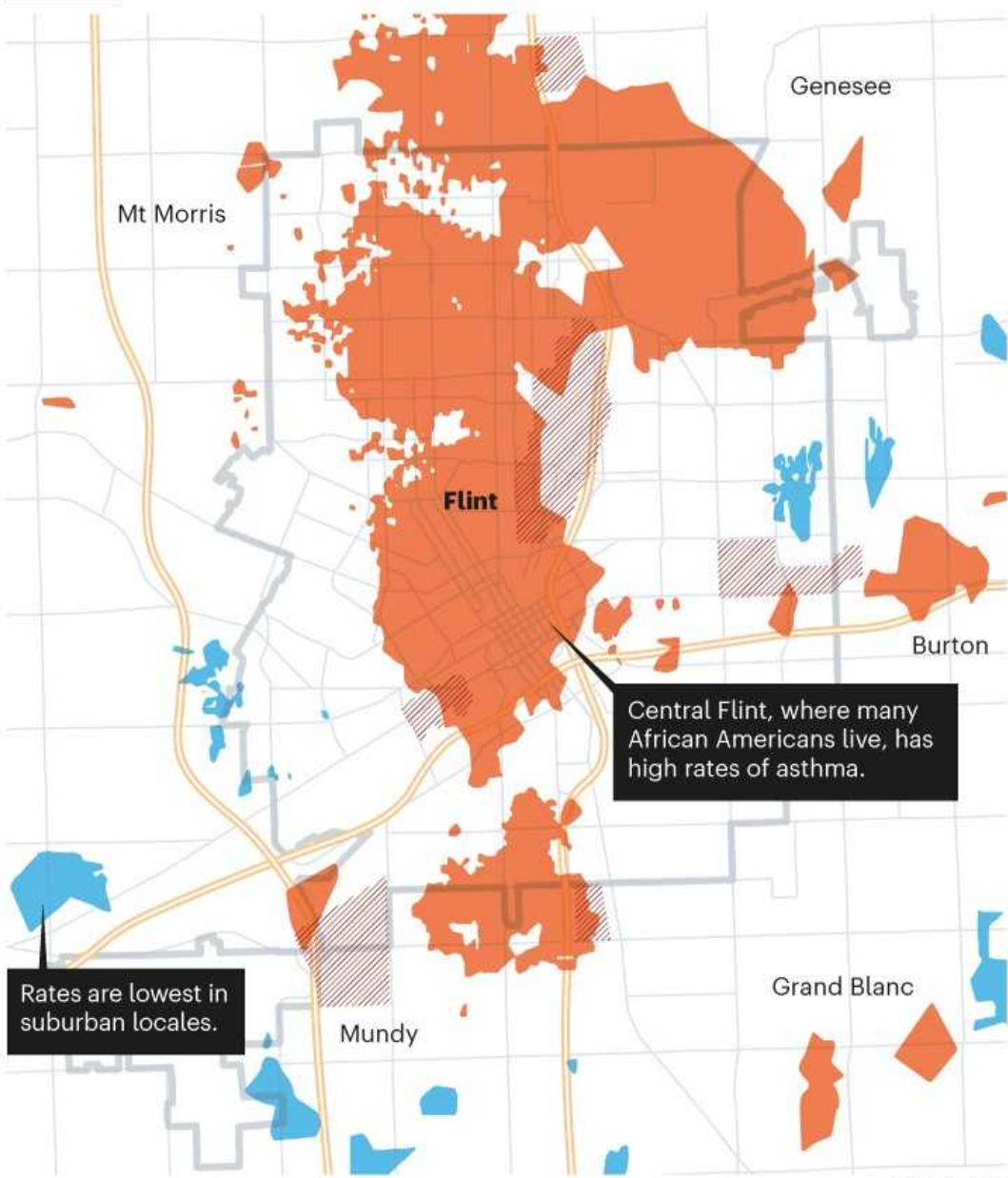
Ideally, interactions become constructive feedback loops. In 2018, E.Y.L. provided health-plan data to R.C.S.. The resulting analysis using a geographic information system (GIS) showed, for the first time, that the centre of Flint was an asthma hotspot (see ‘Asthma hotspots in Flint’). This pattern correlates with historical sites of car factories and lead contamination in the soil ([M. A. S. Laidlaw et al. Int. J. Environ. Res. Public Health 13, 358; 2016](#)). R.C.S. explored how best to show those patterns in ways that would be interpretable and helpful to community members. These results have informed targeted outreach activities, such as developing tailored materials based on local landmarks and identifying specific neighbourhoods, churches or community groups where the materials can be distributed.

ASTHMA HOTSPOTS IN FLINT

Community-academic partnerships strengthened during Flint's water crisis continue to bear fruit, such as revealing high rates of asthma in some areas. This helps to direct interventions such as mobile health units.

- Asthma most likely
- Asthma least likely
- City of Flint
- ▨ Current and former car factories
- Highways
- Major roads

1.6 kilometres



Source: E. Yvonne Lewis & Richard C. Sadler

None of this would have happened without the partnership and trust we had built. The university needed access to health-plan data. Health-plan officials had to trust researchers to answer relevant questions, honour patient confidentiality and provide insight to accomplish the plan's goal.

As the value of such analysis became clear, community members were eager for more. Most neighbourhood and community groups come together to solve a specific, immediate problem, not to form a self-sustaining, long-lasting organization, so they rarely consider mechanisms for collecting long-term data. Flint now sees community members approaching researchers; they seek to evaluate programmes that they've put into place. They want data to support the fact that they do good work and to show which efforts are most effective. A true partnership has been achieved.

The partnership represents many works in progress, far beyond what we describe here. There are still conflicts, miscommunication and lost opportunities. But we now know how to set ourselves up for success as projects emerge.

The most important ingredient in making collaborations work is commitment: to producing research that is relevant, and to understanding many angles and perspectives. This means spending less time and attention on conventional metrics, such as published papers, journal impact factors and procured grants, and much more on nurturing relationships. In true community-based partnerships, a paper is incomplete without a link back to the local community.

Although our experiences are specific to Flint, community–academic partnerships that focus on research that is relevant to policy are essential worldwide. Regions in the Rust Belt of North America, Eastern Europe and east Asia have all experienced population decline and economic problems. More will soon do so. Exploring solutions is of benefit both to researchers and to communities when they work together.

Nature **594**, 326-329 (2021)

doi: <https://doi.org/10.1038/d41586-021-01586-8>

Competing Interests

The authors declare no competing interests.

Related Articles

-  [Research collaborations bring big rewards: the world needs more](#)
-  [COVID has shown the power of science–industry collaboration](#)
-  [How the COVID pandemic is changing global science collaborations](#)
-  [A white-knuckle ride of open COVID drug discovery](#)
-  [The authorship rows that sour scientific collaborations](#)



- ['We need to talk': ways to prevent collaborations breaking down](#)



- [Tapping local knowledge to save a Papua New Guinea forest](#)



- [Rethink how we plan research to shrink COVID health disparities](#)



- [The best research is produced when researchers and communities work together](#)



- [Farmers transformed how we investigate climate](#)

Subjects

- [Society](#)
- [Water resources](#)
- [Environmental sciences](#)

[Jobs from Nature Careers](#)

- - - [All jobs](#)
 -
 - [Post Doctoral Fellow Bioinformatics Modern and Ancient Infectious Diseases](#)
 - [Faculty of Medicine, Dalhousie University](#)
 - [Multiple locations](#)
 - [JOB POST](#)
 - [Research Fellow - Molecular Pharmacology & Experimental Therapeutics](#)
 - [Mayo Clinic Health System](#)
 - [Rochester, MN, United States](#)
 - [JOB POST](#)
 - [Research Fellow - Neurobiology](#)
 - [Mayo Clinic Health System](#)
 - [Rochester, MN, United States](#)
 - [JOB POST](#)
 - [Scientist for PETRA III Beamline P07](#)
 - [German Electron Synchrotron \(DESY\)](#)
 - [Hamburg, Germany](#)
 - [JOB POST](#)

[Download PDF](#)

Related Articles

-  [Research collaborations bring big rewards: the world needs more](#)
-  [COVID has shown the power of science–industry collaboration](#)
-  [How the COVID pandemic is changing global science collaborations](#)
-  [A white-knuckle ride of open COVID drug discovery](#)
-  [The authorship rows that sour scientific collaborations](#)
-  [‘We need to talk’: ways to prevent collaborations breaking down](#)



- [Tapping local knowledge to save a Papua New Guinea forest](#)



- [Rethink how we plan research to shrink COVID health disparities](#)



- [The best research is produced when researchers and communities work together](#)



- [Farmers transformed how we investigate climate](#)

Subjects

- [Society](#)
- [Water resources](#)
- [Environmental sciences](#)

This article was downloaded by **calibre** from <https://www.nature.com/articles/d41586-021-01586-8>

- COMMENT
- 14 June 2021

A white-knuckle ride of open COVID drug discovery

In early 2020, a spontaneous global collaboration came together to design a new, urgent antiviral treatment. There are lessons in what happened next.

- [Frank von Delft](#)⁰,
- [Mark Calmiano](#)¹,
- [John Chodera](#)²,
- [Ed Griffen](#)³,
- [Alpha Lee](#)⁴,
- [Nir London](#)⁵,
- [Tatiana Matviuk](#)⁶,
- [Ben Perry](#)⁷,
- [Matt Robinson](#)⁸ &
- [Annette von Delft](#)⁹

1. [Frank von Delft](#)

1. Frank von Delft is professor of structural chemical biology at the University of Oxford, UK, and principal beamline scientist at Diamond Light Source, Didcot, UK.

[View author publications](#)

You can also search for this author in [PubMed](#) [Google Scholar](#)

2. Mark Calmiano

1. Mark Calmiano is a computational chemist at UCB Biopharma, Brussels, Belgium.

[View author publications](#)

You can also search for this author in [PubMed](#) [Google Scholar](#)

3. John Chodera

1. John Chodera is associate member at the Memorial Sloan Kettering Cancer Center, New York, USA.

[View author publications](#)

You can also search for this author in [PubMed](#) [Google Scholar](#)

4. Ed Griffen

1. Ed Griffen is technical director and co-founder of MedChemica, Ryecraft, UK.

[View author publications](#)

You can also search for this author in [PubMed](#) [Google Scholar](#)

5. Alpha Lee

1. Alpha Lee is group leader in the Department of Physics, University of Cambridge, UK, and chief scientific officer at PostEra, Boston, Massachusetts, USA.

[View author publications](#)

You can also search for this author in [PubMed](#) [Google Scholar](#)

6. Nir London

1. Nir London is assistant professor in the Department of Organic Chemistry at the Weizmann Institute of Science, Rehovot, Israel.

[View author publications](#)

You can also search for this author in [PubMed](#) [Google Scholar](#)

7. Tatiana Matviuk

1. Tatiana Matviuk is principal scientist at Enamine, Kiev, Ukraine.

[View author publications](#)

You can also search for this author in [PubMed](#) [Google Scholar](#)

8. Ben Perry

1. Ben Perry is discovery open innovation leader at the Drugs for Neglected Diseases initiative, Geneva, Switzerland.

[View author publications](#)

You can also search for this author in [PubMed](#) [Google Scholar](#)

9. Matt Robinson

1. Matt Robinson is chief technology officer of PostEra, Boston, Massachusetts, USA.

[View author publications](#)

You can also search for this author in [PubMed](#) [Google Scholar](#)

10. Annette von Delft

1. Annette von Delft is a translational scientist at the University of Oxford, UK.

[View author publications](#)

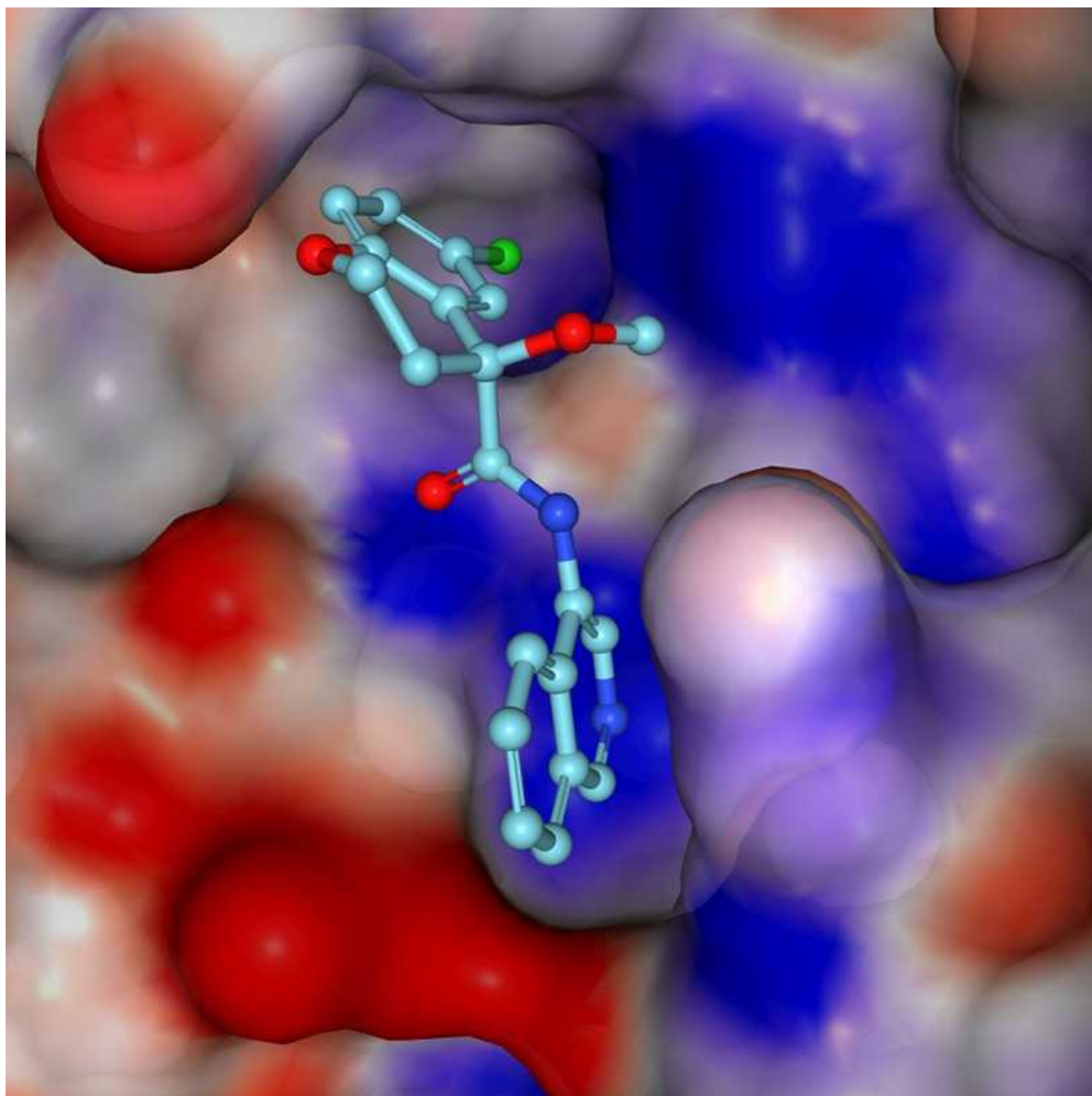
You can also search for this author in [PubMed](#) [Google Scholar](#)





•

[Download PDF](#)



Crystal structure of a COVID Moonshot advanced compound (turquoise) in the active site of the SARS-CoV-2 main protease. The molecular surface colours show electrostatic charge.Credit: fragalysis.diamond.ac.uk

Nearly 15 months ago, a large, fast-moving and unscheduled experiment began: probing a key protein of the coronavirus SARS-CoV-2 to find chemical starting points for drug discovery. The end point was to develop pills that people could take to treat COVID-19 and related diseases.

This experiment pulled together a spontaneous, open, global, Twitter-fuelled collaboration called the [COVID Moonshot](#). Urgency and a commitment to

working openly recruited more than 150 active participants, spanning a huge range of expertise and technology across academia, biotechnology, pharmaceuticals and more, all working without claiming intellectual property. Open drug-discovery efforts are invariably super slow — ours has been an express train on tracks we have laid down as we go. It is a way of working that none of us realized was possible.



[Research collaborations bring big rewards: the world needs more](#)

The intention for the original experiment was simply to help jump-start large drug-discovery initiatives that could draw directly on our data. In those first weeks, before the pandemic had taken hold in the United Kingdom or Israel (where the experiment started), we expected that some international effort was already in the works for countries and companies to collaborate on finding COVID-19 treatments, as was happening with vaccines.

Disappointingly, from the start of the COVID-19 fight, international funders decided to support only the development of repurposed small-molecule drugs and monoclonal antibodies to deliver treatments quickly, neglecting other approaches. The world seemed to give up on new antivirals before they even started, agreeing on a self-fulfilling prophecy that such drugs would take years to develop. Few seemed willing to contemplate such a timescale for this pandemic. Our first grant proposal was rejected, so we had to find a different way to press on.



The sprint to solve coronavirus protein structures — and disarm them with drugs

Amazing virtual collaborations sprang up around the pandemic in many fields: bioinformaticians and phylogeneticists [worked out ways to track new variants](#). Epidemiologists and computer modellers ran simulations. The World Health Organization activated a network of experts to [vet new publications and preprints](#). Military personnel transported medical equipment and vaccines, and set up community testing centres.

Our COVID Moonshot is different. Rather than engaging with patients while using personal protective equipment, we work in chemistry hoods and with spectrometers, X-rays, computer models and courier companies. It's driven by a conviction that conventional wisdom is wrong about *de novo* drug discovery being a job only for big pharma and peripheral to a fast-moving global outbreak: the pandemic is still here, and antiviral drugs against COVID-19 are not.

The screens

Drug-discovery efforts generally require a target, such as a protein that has an important role in disease. Promising drug compounds bind to the protein, affect its function and act safely in the body. Diamond Light Source near

Oxford is the UK national synchrotron — a particle accelerator essential for modern X-ray crystallography, the go-to technique for determining 3D structures of proteins. There, one of us (F.v.D.) leads the XChem facility that uses the technique to screen for very small compounds called fragments that bind to drug targets. Although these ‘fragment hits’ bind weakly and the throughput is low compared with other techniques (screening fewer than 1,000 compounds per experiment), the 3D structures show exactly how each fragment binds. This provides powerful clues about how to create bigger, more potent molecules.



Funders, now is the time to invest big in COVID drugs

By late January 2020, scientists in China had solved the first 3D crystal structures of the SARS-CoV-2 main protease (M^{pro}), an essential viral enzyme, and made them public. With their guidance, a group at Diamond led by Martin Walsh generated new, high-quality crystals by mid-February — lightning fast for such work. The group also shipped M^{pro} protein to the Weizmann Institute of Science in Rehovot, Israel, where N.L.’s group uses mass spectrometry to quickly identify covalent fragments that attach to proteins irreversibly. This is another way to find useful starting points for drugs.

Racing to exploit the two weeks before a scheduled shutdown of the synchrotron on 6 March last year, more than a dozen scientists from the

Walsh, F.v.D. and N.L. groups dropped everything to complete an XChem experiment four times the normal size¹. All the data were analysed within one month, and as soon as we had the first batch of results, we posted downloadable data and a short write-up on the Diamond web page, then [tweeted the link on 7 March](#).

The tweets

The response surprised us: almost 1,000 retweets in a week, and diverse offers for help. A.L. and M.R., two co-founders of the US–UK technology firm PostEra, got in touch to say that their machine-learning technology could propose synthetic routes to make new molecules inspired by the fragment hits. But first we needed drug-like molecules to be designed, and N.L. realized whom we could ask: medicinal chemists newly under lockdown restrictions, but full of expertise and desperate to help.

The next step was a tweet to crowdsource ideas for such molecules, declaring that we would make and test the best ones. A web page built by M.R. and his team in 48 hours enabled participants to submit machine-readable suggestions for compounds. The site made clear that contributions would have no strings attached, no intellectual property and no remuneration. We expected a few hundred submissions at most — in two weeks, we had more than 4,000, and had to work out how to test them.

The experiments

From March to May last year, we were on Zoom calls almost daily, lining up collaborators, logistics, expertise, funding, institutional support and permissions. All around us, the world was shutting down. We were trying to work out how to keep ourselves, our colleagues and our families sane, and our laboratories open.

We tapped an inexhaustible wellspring of goodwill. At the Ukrainian company Enamine, T.M. convinced management to commit to doing synthesis at cost, and to handle compound logistics. Its 650 chemists make molecules to order and have a renowned collection of building blocks for quick synthesis. By early May, new compounds were being shipped weekly

from Enamine to organizations in four countries, and that work continues. Two other contract research organizations, WuXi in China and Sai Life Sciences in India, pitched in with offers of chemists and discounts.



The race for antiviral drugs to beat COVID — and the next pandemic

Chris Schofield and his team at the University of Oxford, UK, together with Haim Barr and his colleagues at the Weizmann Institute, developed distinct biochemical assays that were key to cross-validating how well molecules inhibited the working M^{pro} enzyme. At the same time, for all compounds, the 3D mode of binding was assessed at Diamond in crystal structures. Half a dozen graduate students and postdocs suspended their own projects to coordinate, run and evaluate these assays, week after week. The work hasn't stopped since.

By mid-April 2020, a volunteer troop of industry-based medicinal chemists, chaired by E.G., were holding weekly meetings to scrutinize submissions, review results, discuss strategies, design molecules and coordinate with synthetic chemists at Enamine. This work continues, too.

Computational chemists assembled their own team through their own network, then met weekly to work out algorithms to rank submissions. J.C. developed new ways to use Folding@home, the world's largest crowdsourced supercomputer, which was already being used to generate

models of viral proteins. It crunched ‘free energy’ calculations to predict the best binders for up to 10,000 compounds a week: 100 times more than had been attempted before.

Pharmaceutical companies develop elaborate information systems to track, store and analyse compounds and their associated data; our global effort urgently needed this, too. The informatics web platform CDD Vault donated us cloud space in its infrastructure just hours after a phone call, also arranging training and support. Many other vendors provided licences for free, and XChem’s platform for sharing 3D data, the Fragalysis cloud, had fortunately just been released. M.R. built a back-end system that sent all data live on GitHub, which is more often used as a repository for programming code.

As the pandemic unfolded, on some calls, you could hear the ambulance sirens from half a world away. The first agenda item of every meeting was a list of participants’ latest constraints — lockdowns, lab closures and home-schooling. Children made regular Zoom appearances, and at least two of us came down with COVID-19 ourselves. People pulled their weight not for glory or reward, but because there was a job that needed doing, and it was one that they could do.

To cells and live virus

By June 2020, the Zoom-based collaboration had identified sets of molecules that clearly inhibited a crucial viral protein. The next step was to test antiviral activity in living cells. These are complex experiments, requiring level-three biosafety labs certified for airborne pathogens.



Six tips for data sharing in the age of the coronavirus

A.v.D., a translational clinician, coordinated a shifting coalition of groups. One virologist friend and colleague lived a 10-minute walk away, and they planned experiments on lockdown evening strolls. Other virology groups responded to our tweet for help, and offered a variety of assays. Compounds were shipped, early results trickled in and some compounds unambiguously stalled the virus. These initial successes were crucial, both scientifically and for morale.

Researchers at the Israel Institute for Biological Research near Rehovot agreed to run a single test plate once we had molecules that were sufficiently potent. When that test showed signs of drug-like activity, they worked out how to conduct regular measurements, filling a crucial gap in our testing cascade.

By September, we had reached a milestone with a chemical series that instilled confidence: the compounds inhibited enzymes at submicromolar concentrations, and blocked viral activity at single-digit micromolar concentrations.

The slog

Since then, for the past nine months, the project has entered familiar territory in medicinal chemistry: we have been tweaking and testing compound designs, and optimizing early lead molecules so that they behave like drugs — entering the blood and staying there without being toxic. Potency against the M^{pro} enzyme has improved 100-fold, as has antiviral activity, and we are honing compounds' solubility and rate of metabolism by the liver.

Above all, we can start predicting that these molecules will be straightforward to synthesize and will work as pills that are suitable for vaccine-hesitant or immunocompromised individuals, health-care workers and others in risky situations who could take them prophylactically. Furthermore, we expect them to work against vaccine-resistant variants: whereas vaccines target the spike protein on the virus capsule, our compounds target a conserved part of the virus machinery that works inside cells.



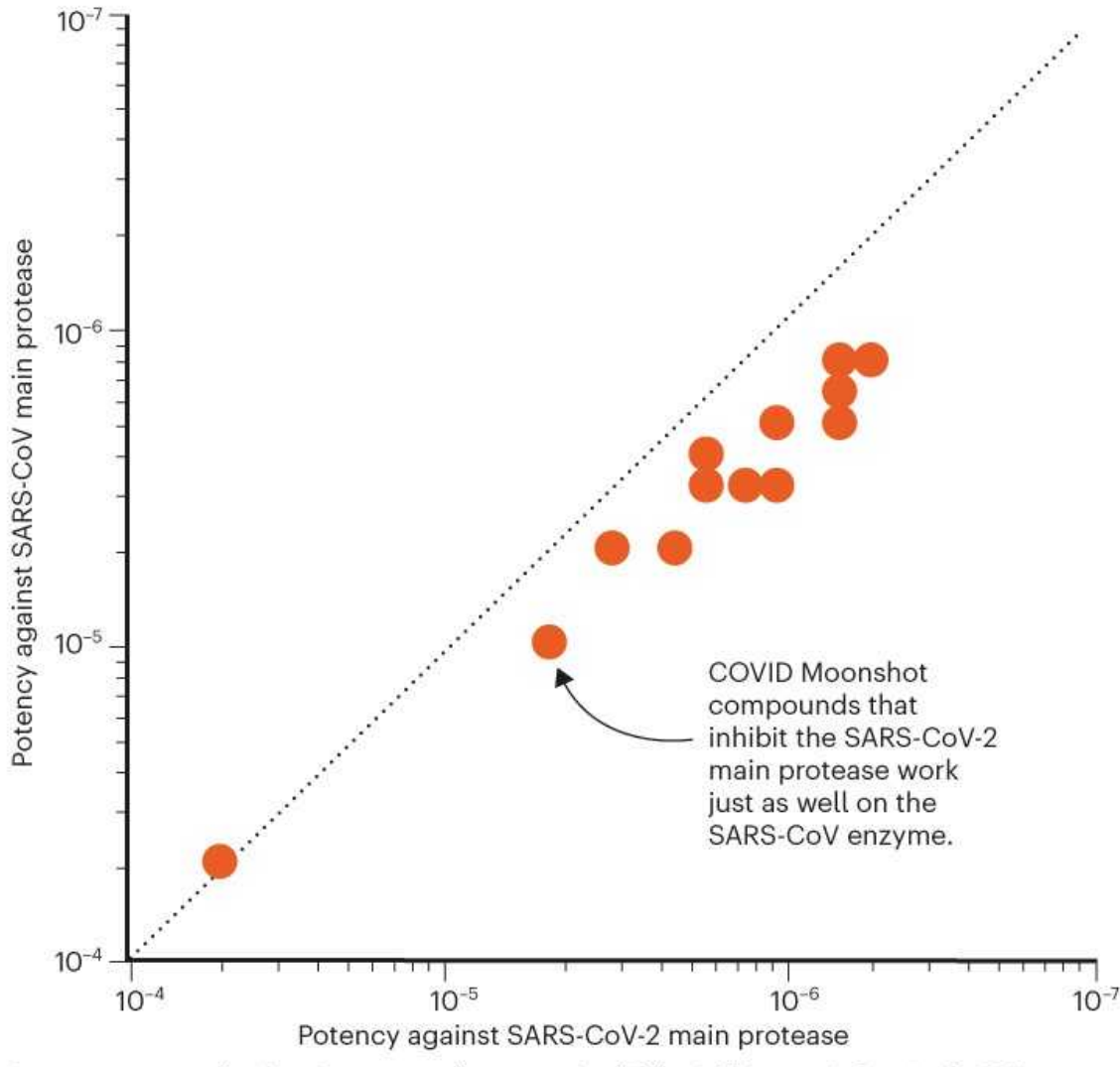
[COVID has shown the power of science–industry collaboration](#)

We've also had to deal with rejected grant proposals to advance antiviral drugs. Still, as vaccines have showed their dramatic successes, further variants have arrived and funders have begun calling urgently for antivirals and looking at how projects might be accelerated. In April this year, 16 months after the outbreak of SARS-CoV-2 in Wuhan, China, the United Kingdom finally launched a task force focusing on antivirals².

Pfizer's March announcement of early clinical trials for its antiviral pill is confirmation that an accelerated approach can work, and that we should persevere. Our molecules also inhibit proteins of the coronavirus that causes severe acute respiratory syndrome (SARS; see 'Missed opportunity'): had drug discovery persevered during the SARS epidemic in 2003, antiviral drugs would have been available when this pandemic hit. Above all, it has become much clearer how an antiviral would be most effective: the treatment must be readily available to everybody, long before they are hospitalized. Accordingly, we have been able to develop a clear plan for how to proceed, and the resources required.

MISSED OPPORTUNITY

Had direct-acting antivirals been developed for SARS, they would have worked for COVID-19.



©nature

Source: COVID Moonshot

We are approaching the capital-intensive, highly regulated phases of animal studies, producing kilograms of substance for clinical trials and, beyond that, worldwide manufacture and distribution of billions of pills. Our initial goal of delivering a drug straight from the discovery pipeline, free from patents and available for anyone to manufacture, cannot offer investors any conventional return on investment. Yet COVID-19 is not conventional, and vaccines have elevated the normally arcane question of intellectual property

into a major political concern. Perhaps the COVID Moonshot can also shape how open drug discovery reaches patients.

The moral

So, what has made our approach work? Presumably, the fact that the mission was clear, even if distant, and the ethos was unambiguous and clearly signposted^{3,4}. Initially, a few of us, fuelled by the urgency of the moment, acted on a conviction that our various combined technologies would accelerate drug discovery. We were soon joined by many people who did the hard work because they felt it was the right thing to do.

Also crucial was the existing large ecosystem of expertise and biopharma supply chains, coupled with new capabilities driven by long-term strategic investments in national infrastructure and research institutes. Tools for online collaboration have reached a critical mass, both general ones (such as Zoom or Google Docs) and those specific to drug discovery (in our case, CDD Vault). Serendipitously, for the segments of our project that had the most collaborators — such as submitting ideas for molecules — the requested contributions broke into discrete, doable tasks that easily accommodated each contributor's availability and know-how.

The project self-selected a team of reflexively collaborative people, with no big egos. So far, we have avoided bureaucracy — no one claims to be the head of the COVID Moonshot. We retained momentum with collective trust, combined with sufficiently diverse expertise and perspectives, which allowed us to rapidly reach and implement strategic decisions. Reassuringly, people seemed to leave the collaboration only once their part of the project had been completed.

Perhaps the most surprising asset was that we did not have time to plan much at all — if we had, we'd have been paralysed. It seems you just have to get started and set deadlines for when to move on. Even now, we are astonished at how quickly this infrastructure self-assembled, just by scientists unabashedly asking for help from colleagues, distant connections or vendors. With so clear a goal, so obvious a need and the complete absence of contracts, people across the world stepped up.

Nature **594**, 330-332 (2021)

doi: <https://doi.org/10.1038/d41586-021-01571-1>

References

1. 1.

Douangamath, A. *et al.* *Nature Commun.* **11**, 5047 (2020).

[PubMed](#) [Article](#) [Google Scholar](#)

2. 2.

Mahase, E. *Br. Med. J.* **373**, n1077 (2021).

[Article](#) [Google Scholar](#)

3. 3.

The COVID Moonshot Consortium *et al.* Preprint at bioRxiv
<https://doi.org/10.1101/2020.10.29.339317> (2020).

4. 4.

Chodera, J., Lee, A. A., London, N. & von Delft, F. *Nature Chem.* **12**, 581 (2020).

[PubMed](#) [Article](#) [Google Scholar](#)

[Download references](#)

Competing Interests

J.C. is a current member of the Scientific Advisory Board of OpenEye Scientific Software, Redesign Science, and Interline Therapeutics, and has equity interests in Redesign Science and Interline Therapeutics. His group receives or has received funding from multiple sources, including the

National Institutes of Health, the National Science Foundation, the Parker Institute for Cancer Immunotherapy, Relay Therapeutics, Entasis Therapeutics, Silicon Therapeutics, EMD Serono (Merck KGaA), AstraZeneca, Vir Biotechnology, Bayer, XtalPi, Foresite Laboratories, the Molecular Science. F.v.D.'s group receives and has received funding from the Structural Genomics Consortium and the SABS Centre for Doctoral Training, which are open science public-private partnerships that have collectively involved over 30 companies over the last 18 years. E.G. is a Director of MedChemica Ltd, MedChemica Consultancy Ltd and MedChemica Holdings Ltd; he is a shareholder in MedChemica Holdings Ltd and AstraZeneca plc. A.L. is the Chief Scientific Officer and a shareholder of PostEra Inc. His group at the University of Cambridge receives funding from multiple sources, including Pfizer, AstraZeneca, the Engineering and Physical Sciences Research Council, The Royal Society, and the Winton Programme for the Physics of Sustainability. N.L. is a member of the scientific advisory board of Monte Rosa Therapeutics, Totus Medicines and MetaboMed. His group lab has received funding from Pfizer, and Teva Pharmaceuticals. M.R. is the Chief Technology Officer and a shareholder of PostEra Inc.

F.v.D. and J.C. have been actively involved in, and vocal about, open science initiatives and partnerships for most of their research careers. E.G. undertakes software design and research and consultancy work in the pharmaceutical industry. In the anti-infective area, he consults for Bugworks Research Inc. which is focused on discovering new antibiotics for to treat resistant bacterial infections.

Related Articles

-  [Research collaborations bring big rewards: the world needs more](#)



- [COVID has shown the power of science–industry collaboration](#)



- [How the COVID pandemic is changing global science collaborations](#)



- [Community–academic partnerships helped Flint through its water crisis](#)



- [The authorship rows that sour scientific collaborations](#)



- [‘We need to talk’: ways to prevent collaborations breaking down](#)



- [Tapping local knowledge to save a Papua New Guinea forest](#)

-  [The race for antiviral drugs to beat COVID — and the next pandemic](#)
-  [Funders, now is the time to invest big in COVID drugs](#)
-  [Six tips for data sharing in the age of the coronavirus](#)
-  [The sprint to solve coronavirus protein structures — and disarm them with drugs](#)

Subjects

- [Drug discovery](#)
- [SARS-CoV-2](#)
- [Research management](#)
- [Medical research](#)

[Jobs from Nature Careers](#)

- - - [All jobs](#)
 -

- **Post Doctoral Fellow Bioinformatics Modern and Ancient Infectious Diseases**

Faculty of Medicine, Dalhousie University

Multiple locations

JOB POST

- **Research Fellow - Molecular Pharmacology & Experimental Therapeutics**

Mayo Clinic Health System

Rochester, MN, United States

JOB POST

- **Research Fellow - Neurobiology**

Mayo Clinic Health System

Rochester, MN, United States

JOB POST

- **Scientist for PETRA III Beamline P07**

German Electron Synchrotron (DESY)

Hamburg, Germany

JOB POST

Download PDF

Related Articles



- Research collaborations bring big rewards: the world needs more



- COVID has shown the power of science–industry collaboration



- How the COVID pandemic is changing global science collaborations



- Community–academic partnerships helped Flint through its water crisis



- The authorship rows that sour scientific collaborations



- ‘We need to talk’: ways to prevent collaborations breaking down



- [Tapping local knowledge to save a Papua New Guinea forest](#)



- [The race for antiviral drugs to beat COVID — and the next pandemic](#)



- [Funders, now is the time to invest big in COVID drugs](#)



- [Six tips for data sharing in the age of the coronavirus](#)



- [The sprint to solve coronavirus protein structures — and disarm them with drugs](#)

Subjects

- [Drug discovery](#)
 - [SARS-CoV-2](#)
 - [Research management](#)
 - [Medical research](#)
-

This article was downloaded by **calibre** from <https://www.nature.com/articles/d41586-021-01571-1>

| [Section menu](#) | [Main menu](#) |

- CAREER FEATURE
- 14 June 2021

The authorship rows that sour scientific collaborations

Team science suffers when junior researchers see their career-defining contributions to a paper downplayed. Here's how to tackle disputes.

- [Nic Fleming](#) 0

1. Nic Fleming

1. Nic Fleming is a science writer based in Bristol, UK.

[View author publications](#)

You can also search for this author in [PubMed](#) [Google Scholar](#)

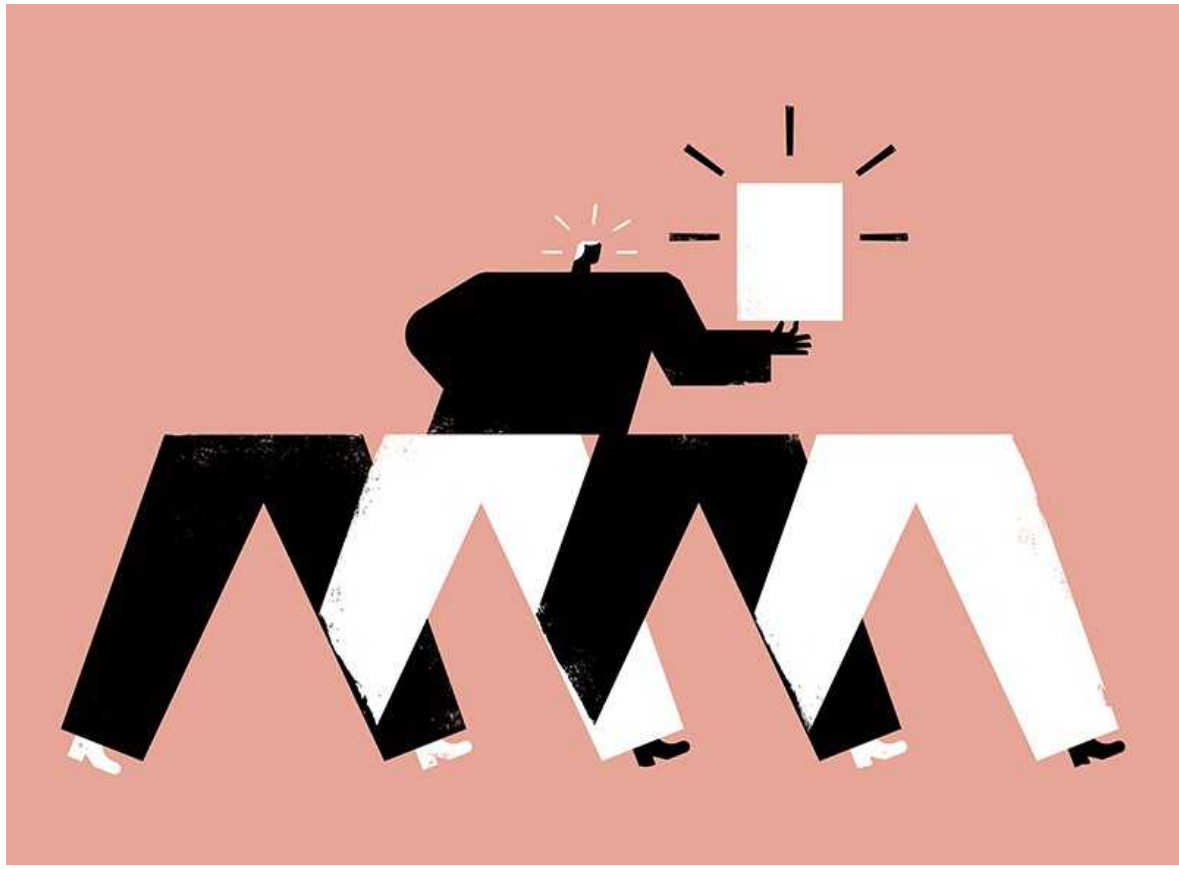




•

[Find a new job](#)

[Download PDF](#)



Credit: The Project Twins

“It felt like a slap in the face. It was as though the credit for half of my PhD was being handed to someone else. I burst into tears.” This is how one cell biologist reacted when her former supervisor made a fellow postdoctoral researcher a co-first author of a paper based on her PhD.

When she objected, he stood firm. Afraid of damaging important professional relationships at the end of her first collaboration, she swallowed her pride and relented, but wondered how it might affect her job prospects. “Research is all about teamwork, so if someone asks me in an interview why it looks as though I only have half a paper from my PhD, what am I supposed to say?” she says.



Research collaborations bring big rewards: the world needs more

Most in the scientific community have heard similar stories, often involving junior researchers who have given their all in collaborations only to then feel unfairly relegated down the author lists of resulting publications. Sometimes they do not make the list at all, becoming no more than 'ghost authors'.

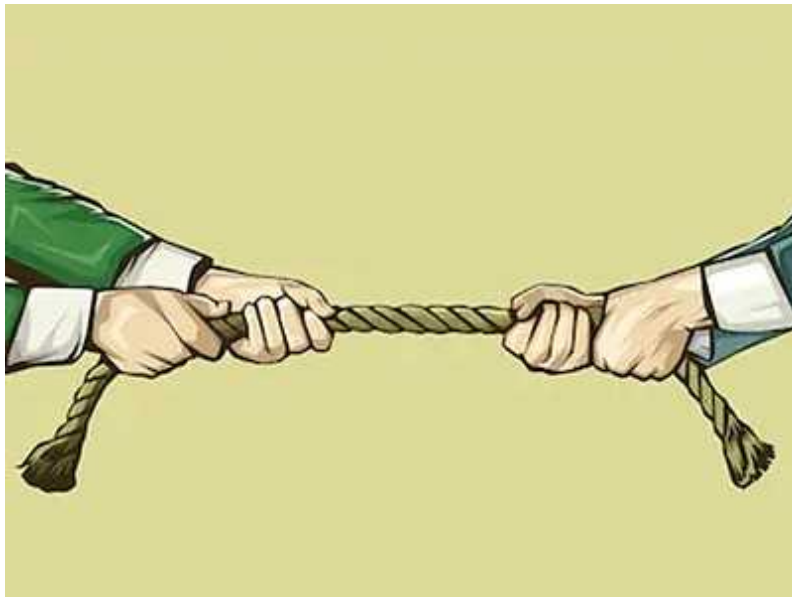
Internet forum posts reveal how upsetting it can be for those who think that their professional prospects will suffer as a result of their being cheated out of the credit they deserve.

Nature spoke to researchers about formative collaborations that descended into author disputes. We also heard from laboratory leaders, publishers and funders who are trying to devise a fairer system of recognizing individual contributions to academic papers. Here, they outline their efforts and describe steps that researchers can take to mitigate author disputes and other tensions that can arise in collaborations. One suggestion is to have a scientific 'pre-nup', or team charter, spelling out roles, responsibilities and processes for conflict resolution in advance. Some interviewees requested anonymity because of concerns that sharing their stories could harm their careers.

Authorship matters

“Researchers are still judged by what and where they publish,” says Liz Allen, director of strategic initiatives at F1000, an open-access science publisher. “It is pivotal to their careers, so if they don’t get the credit they deserve and visibility for their work, it’s a big problem for them.”

“While research is a collaborative endeavour, the job market is highly competitive,” adds Anna Hatch, who is the programme director at the San Francisco Declaration on Research Assessment (DORA), an initiative that campaigns to change how scientific research is evaluated. The incentive structure in science impedes progress, she says. “Things like collaboration, open science and reproducibility drive a field forward, but it is numbers of papers, positions in author lists and funding that advances academic careers.”



A three-step process for resolving paper disputes

Author lists are lengthening, which means that a smaller proportion of researchers are obtaining coveted first-author positions. One analysis of 30 million papers listed by the Pubmed archive and the MEDLINE database found that the average number of authors rose from 1.9 before 1975 to 5.9 during 2015–19 (see go.nature.com/3v64de). This trend was part of what led the UK’s Academy of Medical Sciences (AMS) to look into the impact of increased research collaboration on biomedical careers. In its 2016 report ‘Team Science’, an AMS working group concluded that a perceived lack of

recognition of their contributions is the chief deterrent to researchers' participation in multi-group research (see go.nature.com/355cep). Its authors stated: "Whilst team science is often recognised as important, there is little evidence that individuals' contributions will be valued in career-relevant decision-making, which is particularly concerning for PhD students and early career researchers."

Authorship disputes are rife. One 2011 survey¹ of the corresponding authors of more than 500 papers in 6 leading medical journals found that 17.6% admitted that their papers included 'honorary authors', individuals named as authors despite not meeting authorship criteria set out in guidelines issued by the International Committee of Medical Journal Editors, and 7.9% had ghost authors whose names were ultimately missing from the paper.

In another study², a group at the US National Institute of Environmental Health Sciences (NIEHS) in Research Triangle Park, North Carolina, carried out an online survey of almost 6,700 international researchers who had published papers that listed at least two authors. The results showed that 46.6% had experienced disagreements about author naming, and that 37.9% had had disputes about name order on author lists.



[How to manage a multi-author megapaper](#)

Female researchers were more likely than their male counterparts to have experienced authorship conflicts. In the NIEHS study, they were one-third more likely to have had disputes about inclusion on author lists and 20% more likely to have had disagreements about the order of author names. In another study³, papers with a male and a female co-first author were more likely to list the male researcher first.

“I don’t think I was only given co-first author because of my gender,” says the anonymous cell biologist, “but if it had been the other way around, I don’t think he would have accepted it. Is it easier to stand up to two men if you’re also a man? Yes, probably.”

During her PhD programme, she identified some previously unknown cell-signalling mechanisms. A journal accepted a paper reporting the findings subject to revisions. By then she was at another university, so researchers in her former supervisor’s lab did some additional experiments. She maintains that she did around 75% of the work that went into the paper.

It was shortly before the paper was due to be resubmitted that her former supervisor put the name of another team member alongside hers as co-first author. He listened sympathetically to her complaint but stuck to his original decision. The journal’s website said it did not get involved in authorship disputes, and publication went ahead. “It was annoying, but I needed the paper and didn’t want a big argument,” she says.

The NIEHS survey also found that disagreements about who to include as an author were 50% more common in the medical sciences than in the natural sciences, and disputes over name order were nearly 70% more common. Those involved in multidisciplinary teams were less likely to be involved in either type of conflict. Such variations in part reflect different practices across disciplines. In high-energy particle physics and economics, authors are generally listed alphabetically. In most other disciplines, order is determined by contribution level.

Where credit's due

Such conflicts can also affect more-senior scientists, although this is less common. One physicist and principal investigator at a UK university, who also asked not to be named, recruited a postdoctoral researcher to work on an advanced optical sensor needed for a fluid-dynamics project. It was agreed that this researcher would be first author on publications covering some of the work. However, he left the group before completing all his assigned tasks. A disagreement broke out when the postdoc was told that an undergraduate who was taking over from him would be first author on a final paper.



Genomicist Eleftheria Zeggini advises researchers to enquire about authorship at interviews. Credit: Jan Roeder

The principal investigator stresses that not every junior researcher who thinks they have been unfairly treated is right. “Part of the problem stems from a misunderstanding on the part of some junior researchers about how much of a project is done before they come along,” she says. “I’m not saying someone who does the major data collection should be bumped off the

author list, but those who build labs, come up with ideas, get funding, build experiments, train others and oversee data analysis and final papers deserve credit too.”

Some think that the key to reducing author disputes is to use more-detailed and transparent ways of acknowledging research contributions. Many journals now require the disclosure of author contributions when articles are submitted. Since its launch in 2014, hundreds of journals have adopted CRediT (Contributor Roles Taxonomy), a system that quantifies 14 roles (see ‘Counting credit’). *Nature*-branded journals have required authorship-contribution statements since 2009, and allow but does not mandate the use of CRediT. Springer Nature, the publisher of *Nature*, allows author-contribution statements, but does not demand them. (*Nature* is editorially independent of its publisher.)

Counting credit

Various organizations have attempted to outline what does and does not merit authorship credits.

The ICMJE’s guidelines

The International Committee of Medical Journal Editors (ICMJE) states that authors:

- should have made substantial contributions to the conception or design of the work, or to the acquisition, analysis or interpretation of data;
- should have drafted or revised it;
- should have approved the published version;
- should be accountable for that version.

The guidelines specify that those who would otherwise qualify should not be denied opportunities to help write, revise or approve the paper, in order to disqualify them from authorship.

The CRediT guidelines

Contributor Roles Taxonomy (CRediT) guidelines require researchers to quantify the involvement of all authors in 14 distinct roles:

- Conceptualization
- Data curation
- Analysis
- Funding acquisition
- Investigation
- Methodology
- Project administration
- Resources
- Software
- Supervision
- Validation
- Visualization
- Writing
- Reviewing and editing

Supporters say that the machine-readable platform used by the CRediT system not only provides more-detailed research contribution details, but also supports collaboration and peer-review identification, and reduces the chances of authorship disputes.

“CRediT provides more information and transparency about who has done what, who is making the impact, who is responsible and accountable for research,” says Allen, who co-founded the system. “It provides in more detail, and more accessibly, the information that was supposed to be described in an acknowledgement section, but never was.”

The AMS ‘Team Science’ report recommended that publishers work with initiatives such as CRediT to develop standardized ways of presenting contributor information. “We said ‘such as CRediT’ as we recognize not all journals would want to use those exact criteria,” says cell biologist Anne Ridley, head of the school of cellular and molecular medicine at the University of Bristol, UK, who chaired the AMS working group. “But we thought having 14 different criteria was a good, fair system for recognizing people’s contributions.”

Answers to authorship

Eleftheria Zeggini urges PhD and postdoctoral applicants to assess principal investigators’ attitudes to authorship during interviews, and, if possible, to contact and learn from current and previous team members. Zeggini, who leads the Institute of Translational Genomics at the Helmholtz Centre Munich in Germany, says: “It is important to learn about the team science culture and how good practice is applied within prospective professional homes.”

“Communicating about how credit and authorship are going to be handled, at the start of the process and during it, is really important,” adds Hatch. “It can involve uncomfortable conversations, but if there are disagreements, you can figure out next steps early on.” (See ‘Dispute tips’).

Dispute tips

Microbiologist Emily Fogarty, who now works at the University of Chicago, in Illinois, was eventually included in the acknowledgements section of a paper for which she’d been promised authorship during a previous position. These are her tips on how to avoid similar situations, and what to do if you get caught in one.

Past publications. Before deciding to work in a group, check whether and how the contributions of less-senior team members are recognized in previous publications.

Read the small print. Check out the authorship guidelines of journals that the lab frequently submits to.

Let's talk. Bring up authorship early on. Don't approach it as if it's an expectation, but if your work directly contributes to a manuscript, ask whether you will be a co-author.

Keep records. Senior colleagues might be too busy to remember contributions precisely. Keeping track yourself means that you can gently remind them, if necessary.

Get it in writing. If authorship is discussed in a meeting, follow up with an e-mail to ensure that everyone is on the same page.

Stay cool. If you find that you haven't been included as an author, explain politely, in a meeting or e-mail, why you think you should be. Getting angry won't help.

Appeal. You can appeal to your institution's research-ethics board, but bear in mind that it is likely to contact the other parties in your dispute if it decides to take the matter further.

Zeggini uses big data, genomics and other -omics approaches to study complex diseases. Those in her field usually work in large, multigroup collaborations, and so might be more aware of the need to establish systems that work for all involved. She uses simple spreadsheets to record assigned responsibilities and keep track of who is doing what, which greatly simplifies the later writing of detailed author-contribution sections for research papers. "It helps set expectations and can save a lot of time down the line," she says.

Neuroscientist Andrew Mickley found another way to set the ground rules in his laboratory at the Baldwin-Wallace University in Berea, Ohio, starting in the late 1990s. He gave his students a handbook detailing what he expected

of them, including requirements for authorship, such as showing initiative in experiment design and being able to explain the rationale for research.

“Authorship criteria sometimes describe making significant contributions to research conception or design, to data acquisition, analysis or interpretation,” says Mickley, who now teaches at Furman University in Greenville, South Carolina, and at Wofford College in Spartanburg, also in South Carolina. “We operationally defined what we considered ‘significant’ to mean, so there was no doubt about it.”



Neuroscientist Andrew Mickley gave his students a handbook of expectations.Credit: Greg Peters, Greenville, SC USA

Beyond ways to reduce the scope for disputes, there are specific things that researchers can do if they think that their contributions have not been sufficiently acknowledged. The anonymous cell biologist’s first move was to speak to trusted colleagues and mentors, including two co-authors of her paper and others who had nothing to do with her dispute.

After she expressed her unhappiness at having a co-first author, she says that her former supervisor made changes to the author-information section of the paper that better reflected her role. “I’m glad I said something,” she says. “Even if it didn’t change the author list as I would have liked, it did lead to changes that meant my concerns were at least acknowledged and taken seriously.”



[Collection: Careers toolkit](#)

Ridley says that those who think that their authorship concerns are not being addressed by their line managers should raise them elsewhere in their institutions. “I would be very concerned if I found out someone in my school was missing people off author lists,” she says. “My advice would be that they take this up within their department or school, with a mentor, postgraduate education director or a PhD second supervisor, perhaps.”

Those with authorship complaints about papers that have already been published should not let that put them off raising the issue. “It might seem too late if the paper is already out, but authors can still be added retrospectively,” adds Ridley.

Righting wrongs

The cell biologist who felt aggrieved at having a co-first author added to her PhD paper considered approaching the journal concerned. But its website, like those of many other journals, says it does not get involved in authorship disputes.

Corrections to authorship lists are made only occasionally — and usually after rulings by university ethics committees. The policy of journals published by Springer Nature, including *Nature*, is that editors do not get involved in investigating or adjudicating authorship disputes, and that these should be resolved by researchers or, failing that, their institutions.

Those who exhaust all avenues in their efforts to right perceived authorship wrongs should not despair. Zeggini says that those who think they have been unfairly missed off or relegated down an author list will often be able to describe their contributions in more detail in job and funding applications. “Those who find themselves in this situation should know that when they apply for new jobs, it is very important that they highlight their specific contributions to papers,” she says.

It is not possible to judge the merits of contentious cases with only partial sight of the facts. “A one-sided description may be correct, but until you have seen both sides of the story, you can’t make a judgement,” says the anonymous physicist. “I would advise people to speak up,” says the cell biologist. “If those affected don’t say anything, how are problems in academia like authorship disputes ever going to be solved?”

Nature **594**, 459-462 (2021)

doi: <https://doi.org/10.1038/d41586-021-01574-y>

References

1. 1.

Wislar, J. S. *Br. Med. J.* **343**, d6128 (2011).

[Article](#) [Google Scholar](#)

2. 2.

Smith, E. *et al. Sci. Eng. Ethics* **26**, 1967–1993 (2020).

[PubMed](#) [Article](#) [Google Scholar](#)

3. 3.

Broderick, N. A. & Casadevall, A. *eLife* **8**, e36399 (2019).

[PubMed](#) [Article](#) [Google Scholar](#)

[Download references](#)

Related Articles



- [Research collaborations bring big rewards: the world needs more](#)



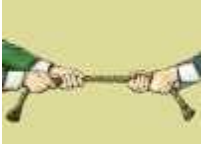
- [COVID has shown the power of science–industry collaboration](#)



- [How the COVID pandemic is changing global science collaborations](#)



- [Community–academic partnerships helped Flint through its water crisis](#)

-  [A white-knuckle ride of open COVID drug discovery](#)
-  ['We need to talk': ways to prevent collaborations breaking down](#)
-  [Tapping local knowledge to save a Papua New Guinea forest](#)
-  [Who gets credit? Survey digs into the thorny question of authorship](#)
-  [How to manage a multi-author megapaper](#)
-  [Collection: Careers toolkit](#)
-  [A three-step process for resolving paper disputes](#)



- [Careers Collection: Publishing](#)

Subjects

- [Careers](#)
- [Authorship](#)
- [Research management](#)

[Jobs from Nature Careers](#)

- - - [All jobs](#)
 - - [Post Doctoral Fellow Bioinformatics Modern and Ancient Infectious Diseases](#)
[Faculty of Medicine, Dalhousie University](#)
[Multiple locations](#)
[JOB POST](#)
 - [Research Fellow - Molecular Pharmacology & Experimental Therapeutics](#)
[Mayo Clinic Health System](#)
[Rochester, MN, United States](#)
[JOB POST](#)
 - [Research Fellow - Neurobiology](#)

[Mayo Clinic Health System](#)

[Rochester, MN, United States](#)

[JOB POST](#)

▪ [**Scientist for PETRA III Beamline P07**](#)

[German Electron Synchrotron \(DESY\)](#)

[Hamburg, Germany](#)

[JOB POST](#)

[Download PDF](#)

Related Articles



- [Research collaborations bring big rewards: the world needs more](#)



- [COVID has shown the power of science–industry collaboration](#)



- [How the COVID pandemic is changing global science collaborations](#)

-  [Community-academic partnerships helped Flint through its water crisis](#)
-  [A white-knuckle ride of open COVID drug discovery](#)
-  [‘We need to talk’: ways to prevent collaborations breaking down](#)
-  [Tapping local knowledge to save a Papua New Guinea forest](#)
-  [Who gets credit? Survey digs into the thorny question of authorship](#)
-  [How to manage a multi-author megapaper](#)
-  [Collection: Careers toolkit](#)

-  [A three-step process for resolving paper disputes](#)
-  [Careers Collection: Publishing](#)

Subjects

- [Careers](#)
- [Authorship](#)
- [Research management](#)

This article was downloaded by **calibre** from <https://www.nature.com/articles/d41586-021-01574-y>

| [Section menu](#) | [Main menu](#) |

- CAREER FEATURE
- 15 June 2021

‘We need to talk’: ways to prevent collaborations breaking down

Scientists who plan to partner on a research project should identify pressure points and consider a team charter at the outset.

- [Virginia Gewin](#) 0

1. Virginia Gewin

1. Virginia Gewin is a freelance writer in Portland, Oregon.

[View author publications](#)

You can also search for this author in [PubMed](#) [Google Scholar](#)

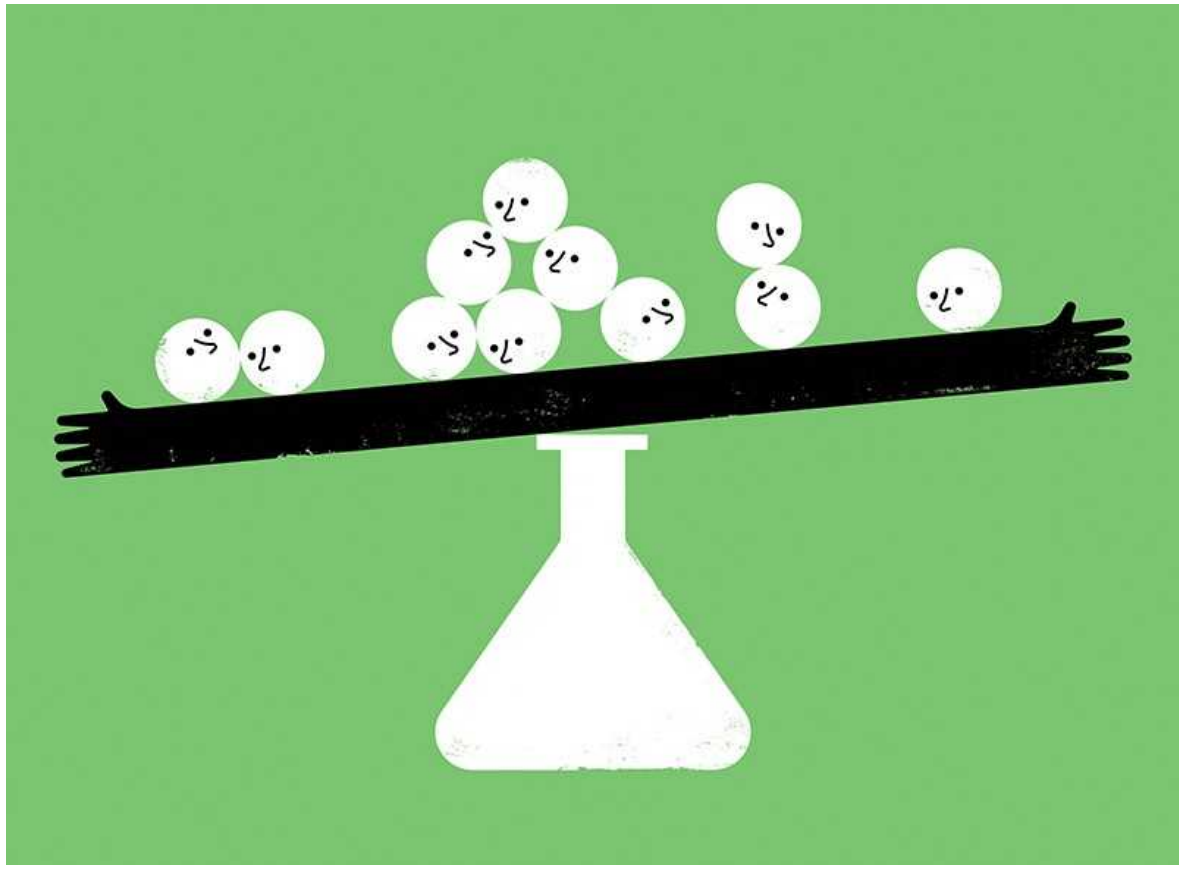




•

[Find a new job](#)

[Download PDF](#)



Credit: The Project Twins.

Research collaborations are the lifeblood of science. But it is often challenging to build an inclusive partnership that stays firm in the face of conflict.

Once collaborators lose trust in or respect for one another, it can be difficult, if not impossible, to salvage the team, says sociologist Martin Gargiulo, who studies social networks at the INSEAD business school in Singapore. Team members should identify potential pressure points in advance to avoid collaborations breaking down irretrievably, he says. Holding regular, open discussions to ensure that everyone is still on board is also extremely helpful.

Team charter

Some scholars back the idea of crafting a [scientific ‘prenup’ agreement](#), or team charter, to clearly lay out roles, responsibilities and author contributions, and to establish processes for navigating conflict resolution. Although a charter might not be that useful in a project’s early stages, when people haven’t yet worked together, its main advantage is encouraging team members to have that conversation, says researcher Inga Carboni, who studies organizational behaviour at the College of William & Mary in Williamsburg, Virginia. They can then model how they will make decisions, address conflict and listen to one another, sharing strengths, weaknesses and preferred methods of communication, she says.

The charter strategy is integral to the Human Cell Atlas, one of the largest collaborations that the UK biomedical funder Wellcome supports. A global effort to create a 3D map of how all cell types work together, the project involves more than 2,180 biologists, computational scientists and clinicians from 77 nations. In 2017, a year after the Human Cell Atlas was established, a committee for the consortium [crafted a white paper](#) that laid out policies and principles on data sharing and publishing; each consortium member must agree to abide by them.



[Research collaborations bring big rewards: the world needs more](#)

“We want to be assured a good research culture is embedded in the work we fund, but we try to be flexible,” says Katrina Gold, portfolio manager for

genetics and molecular sciences at Wellcome. “Instead of a one-size-fits-all approach, we ask applicants to detail how they’ll approach these concerns.”

Large grants involving multiple institutions and several principal investigators (PIs) are primed for conflict because parties are usually jockeying for money and prestige, says one anonymous established researcher at a small US West Coast university. The researcher says that, in their experience, funders tend to support senior scientists at prestigious institutions. Junior researchers at less-prestigious universities often lack enough administrative support to be the lead PI on a collaboration, even if they have a central role in the research. This lack of control often leaves them dependent on the PI, the researcher says. They recommend seeking advice from other junior researchers who have worked with those PIs.

Carla Figueira de Morisson Faria, a physicist at University College London, thinks that science isn’t always the main motivator of large international collaborations. “It’s not going to be the best scientists who push an agenda through; it’s those with political power and resources,” she says. She advises those launching a multi-institution partnership to secure their group’s resources as soon as possible. In some cases, funds have been delayed or withheld, she warns.

Authorship agony

After a colleague of Tanja Pyhäjärvi died unexpectedly, the forest geneticist took on some of the person’s PhD students as well as their collaborators. When the question of authorship order arose for a paper, “it ended up being a tricky situation because I didn’t know what had been agreed”, says Pyhäjärvi, at the University of Helsinki. She advises creating a written agreement on authorship slots in advance.



How the COVID pandemic is changing global science collaborations

Conflict around authorship is one of the biggest points of contention in collaborations, says Gargiulo. “We all believe we contribute more than what we actually contribute,” he says, adding that when he launches a new collaboration, he clarifies the order of authors from the outset. “That said, the order can be renegotiated” as work proceeds, he says. “But when you leave that order unclear, people might each use their own algorithm” — meaning that conflict is likely to arise if team members’ authorship calculations differ.

Although determining authorship can be as simple as noting who had the original idea, it’s often more complicated. “Ideas are not always so clear-cut,” Gargiulo says. “The original idea may be reshaped in so many ways during the process.” He and others recommend that collaborators regularly check in with one another about authorship during the process of writing a paper. Pyhäjärvi notes that, for junior researchers, knowing authorship in advance is crucial for prioritizing their time and energy.

Culture clashes

Conflict can also arise in a team when members have different backgrounds. Ecologist Danielle Ignace, an Indigenous researcher, recalls having

disappointing partnerships early in her career when she felt that she wasn't as integrated into the collaboration as she had anticipated. These experiences left her feeling forgotten or excluded, and suspicious that her participation had been sought for tokenistic reasons. As a result, Ignace, who on 1 July will assume a faculty position at the University of British Columbia in Vancouver, Canada, says that she prefers to work mostly with more-junior collaborators. In her experience, members of such partnerships are often more passionate about including and amplifying diverse voices than are senior colleagues. "I stay clear of the ones that don't do that," she says.

One anonymous junior geoscientist at a UK university, who is Black, recalls uncomfortable dynamics in collaborations that involved other junior Black researchers, some from developing nations, and senior colleagues who were white. He says that he experienced his senior teammates' behaviour as reflecting the sense that they were superior to the others. He now holds back in the early stages of a collaboration. "I give only 10% of my energy early on," he says. He prefers to gauge the situation, his collaborators and the project first, as well as whether he and his approach to research will be respected, before committing more deeply.



[Collection: The business of science](#)

Alongside formal research collaborations, some scientists embark on less-formal partnerships to discuss projects, journal papers or career issues, often

as friends. These can spawn their own set of problems. A female climate researcher at a US university remembers one such group with five other scientists who met regularly for these purposes. “We developed an informal social contract — we all agreed to act in good faith, and come to meetings because we were friends and enjoyed working together,” she says.

But when one of the collaborators left academia to launch a company, he sent junior colleagues to the meetings in his place. “I was like, ‘Wait, you signed on.’ There was no discussion of someone else coming in on a particular role,” she says. To avoid such missteps, the climate researcher recommends checking in with collaborators at regular intervals, at least once a year, to make sure everyone is still on board.

Frank discussions about sensitive topics are key to team success, says Katherine Sharkey, assistant dean for women in medicine and science at the Alpert Medical School of Brown University in Providence, Rhode Island. Ultimately, collaborators need to ensure that no issue, no matter how sticky, will be off limits. “When things go off the rails,” she says, “is when you wish you’d had these conversations.”

Nature **594**, 462-463 (2021)

doi: <https://doi.org/10.1038/d41586-021-01573-z>

Related Articles

-  [Research collaborations bring big rewards: the world needs more](#)
-  [COVID has shown the power of science–industry collaboration](#)



- [How the COVID pandemic is changing global science collaborations](#)



- [Community–academic partnerships helped Flint through its water crisis](#)



- [A white-knuckle ride of open COVID drug discovery](#)



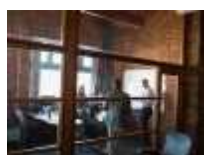
- [The authorship rows that sour scientific collaborations](#)



- [Tapping local knowledge to save a Papua New Guinea forest](#)



- [How to shape a productive scientist–artist collaboration](#)



- [Cluster hiring a ready-made collaboration](#)



- [Ways to promote and foster collaborative research in your lab](#)



- [Collection: The business of science](#)

Subjects

- [Careers](#)
- [Communication](#)
- [Publishing](#)

[Jobs from Nature Careers](#)

- - - [All jobs](#)
 -
 - [Post Doctoral Fellow Bioinformatics Modern and Ancient Infectious Diseases](#)
[Faculty of Medicine, Dalhousie University](#)
[Multiple locations](#)
[JOB POST](#)
- [Research Fellow - Molecular Pharmacology & Experimental Therapeutics](#)
[Mayo Clinic Health System](#)

[Rochester, MN, United States](#)

[JOB POST](#)

- [Research Fellow - Neurobiology](#)

[Mayo Clinic Health System](#)

[Rochester, MN, United States](#)

[JOB POST](#)

- [Scientist for PETRA III Beamline P07](#)

[German Electron Synchrotron \(DESY\)](#)

[Hamburg, Germany](#)

[JOB POST](#)

[Download PDF](#)

Related Articles



- [Research collaborations bring big rewards: the world needs more](#)



- [COVID has shown the power of science–industry collaboration](#)



- [How the COVID pandemic is changing global science collaborations](#)



- [Community-academic partnerships helped Flint through its water crisis](#)



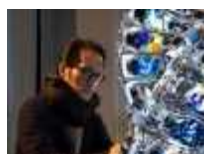
- [A white-knuckle ride of open COVID drug discovery](#)



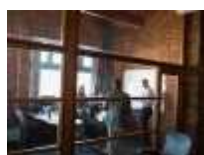
- [The authorship rows that sour scientific collaborations](#)



- [Tapping local knowledge to save a Papua New Guinea forest](#)



- [How to shape a productive scientist–artist collaboration](#)



- [Cluster hiring a ready-made collaboration](#)



- [Ways to promote and foster collaborative research in your lab](#)



- [Collection: The business of science](#)

Subjects

- [Careers](#)
- [Communication](#)
- [Publishing](#)

This article was downloaded by **calibre** from <https://www.nature.com/articles/d41586-021-01573-z>

| [Section menu](#) | [Main menu](#) |

- WHERE I WORK
- 14 June 2021

Tapping local knowledge to save a Papua New Guinea forest

Villagers who know the land help Jason Paliau to survey the region's insects.

- [Chris Woolston](#) ⁰

1. Chris Woolston

1. Chris Woolston is a freelance writer in Billings, Montana.

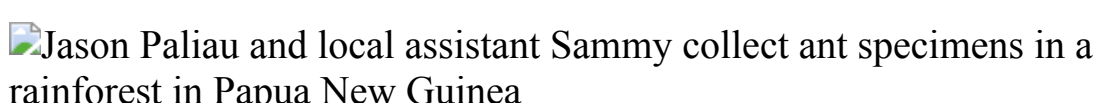
[View author publications](#)

You can also search for this author in [PubMed](#) [Google Scholar](#)





•



Jason Paliau is a lecturer at the Papua New Guinea University of Resources and Environment in Rabaul. Credit: UN-REDD Programme

[Download PDF](#)

It takes collaboration to get the full picture of a forest. Here, I'm teaming up with Sammy, a local senior-school student, to count and identify ants in a dense fragment of lowland rainforest. It's November 2019, when I was a research technician with the New Guinea Binatang Research Centre in

Madang, and we're near the village of Boredoa on the southern coast of Papua New Guinea.

I'm impressed by the locals' knowledge of the forest and its inhabitants. It's important to get more villagers involved in forest surveys and other conservation efforts so that they can work to protect them.



Research collaborations bring big rewards: the world needs more

Papua New Guinea — a country that makes up the eastern half of the island of New Guinea — is home to one of the world's largest and most biodiverse rainforests, but mining and timber companies are taking a terrible toll. The areas beyond these trees have been heavily logged, and we're checking to see how life in this remaining forest is faring, from the ants to the trees.

I grew up in the northern city of Lae, a place very different from this forest. I have formal training in forestry and entomology, but, unlike Sammy and other villagers, I don't have the experiences and insights that come from a lifetime of living on the land.

Our ant survey was part of the National Forest Inventory, a project of the United Nations Programme on Reducing Emissions from Deforestation and Forest Degradation. There are many places still waiting to be studied.

This forest is a hot, wet, challenging place to work. Villagers helped us to find relatively dry places to set up our tents. We had to wait for a break in the rain to set out our ant traps of tuna and fruit-flavoured drinks. In this particular sample, we identified six species, all native to the area. Introduced species such as fire ants and army ants have been taking over elsewhere in Papua New Guinea, but the local ants here have managed to hold on to their territory. For now.

Nature **594**, 466 (2021)

doi: <https://doi.org/10.1038/d41586-021-01587-7>

Related Articles



- [Research collaborations bring big rewards: the world needs more](#)



- [COVID has shown the power of science–industry collaboration](#)



- [How the COVID pandemic is changing global science collaborations](#)



- [Community–academic partnerships helped Flint through its water crisis](#)

-  [A white-knuckle ride of open COVID drug discovery](#)
-  [The authorship rows that sour scientific collaborations](#)
-  ['We need to talk': ways to prevent collaborations breaking down](#)
-  [Unpicking the rhythms of the Amazon rainforest](#)
-  [Catching a wave to study coral](#)
-  [Extreme research](#)

Subjects

- [Careers](#)
- [Conservation biology](#)
- [Ecology](#)

Jobs from Nature Careers

- - - [All jobs](#)
 - - [Post Doctoral Fellow Bioinformatics Modern and Ancient Infectious Diseases](#)

[Faculty of Medicine, Dalhousie University](#)

[Multiple locations](#)

[JOB POST](#)
 - [Research Fellow - Molecular Pharmacology & Experimental Therapeutics](#)

[Mayo Clinic Health System](#)

[Rochester, MN, United States](#)

[JOB POST](#)
 - [Research Fellow - Neurobiology](#)

[Mayo Clinic Health System](#)

[Rochester, MN, United States](#)

[JOB POST](#)
 - [Scientist for PETRA III Beamline P07](#)

[German Electron Synchrotron \(DESY\)](#)

Hamburg, Germany

JOB POST

Download PDF

Related Articles



- [Research collaborations bring big rewards: the world needs more](#)



- [COVID has shown the power of science–industry collaboration](#)



- [How the COVID pandemic is changing global science collaborations](#)



- [Community–academic partnerships helped Flint through its water crisis](#)



- [A white-knuckle ride of open COVID drug discovery](#)



- [The authorship rows that sour scientific collaborations](#)



- ['We need to talk': ways to prevent collaborations breaking down](#)



- [Unpicking the rhythms of the Amazon rainforest](#)



- [Catching a wave to study coral](#)



- [Extreme research](#)

Subjects

- [Careers](#)
- [Conservation biology](#)
- [Ecology](#)

This article was downloaded by **calibre** from <https://www.nature.com/articles/d41586-021-01587-7>

This Week

- [**How science-funding giant Wellcome is tackling racism**](#) [16 June 2021]
World View • A specialist in diversity and inclusion lays out the foundation's plan for promoting equity.
- [**Not just sorcery: scientists build an invisible portal**](#) [11 June 2021]
Research Highlight • 'Superscattering' material is used to construct a mini-doorway that is invisible in the microwave portion of the spectrum.
- [**Poor harvest: farmers earn a pitiful fraction of the money spent on food**](#) [08 June 2021]
Research Highlight • The bulk of consumer food spending around the world ends up in the coffers of distributors, processors and other parties beyond the farm gate.
- [**Menacing 'famine weed' grows more toxic as carbon levels soar**](#) [09 June 2021]
Research Highlight • A highly invasive weed might owe some of its success to easier access to carbon, a key component of the weed's toxin.
- [**A grey whale makes an epic swim into the record books**](#) [08 June 2021]
Research Highlight • A journey stretching around 20,000 kilometres might be the world's longest migration by ocean.
- [**Quantum keys dial up tamper-proof conference calls**](#) [09 June 2021]
Research Highlight • A new experiment efficiently distributes the highly secure keys to four parties instead of the typical two.
- [**Babies with mystery illnesses benefit from genome sequencing**](#) [04 June 2021]
Research Highlight • Rapid genomic sequencing on admission to hospital leads to more-precise care for sick infants.
- [**A small earthquake could pose a big risk to a US city**](#) [11 June 2021]
Research Highlight • The structure of faults beneath Salt Lake City, Utah, shows how the ground could liquefy during a shaking.

| [Next section](#) | [Main menu](#) | [Previous section](#) |

- WORLD VIEW
- 16 June 2021

How science-funding giant Wellcome is tackling racism



A specialist in diversity and inclusion lays out the foundation's plan for promoting equity.

- [Kalaiyashni Puwanendran](#) ✉

1. [Kalaiyashni Puwanendran](#)

1. Kalaiyashni Puwanendran is a diversity & inclusion project manager at Wellcome in London.

[View author publications](#)

You can also search for this author in [PubMed](#) [Google Scholar](#)





•

[Download PDF](#)

Two years ago, I was about to log off from my work at the research funder Wellcome when I got an e-mail from a senior leader. I remember tensing as I read it. I'd asked that Wellcome add its name to some general anti-racism commitments. The leader didn't refuse, but expressed doubts about timing and capacity. Anti-racism wasn't a priority.

I'd worked on diversity and inclusion at Wellcome and elsewhere for several years. I'd faced challenges as a woman of colour and was acutely aware of how structural racism had affected many working here or applying

for our funds. The hesitation stung, but speaking up was part of my job, so I persisted. After a couple of days' discussion, the leader agreed.

By mid-2020, people around the world were demanding drastic change after US police officer Derek Chauvin murdered George Floyd, a Black man, even as a pandemic further exposed structural racism — people from racially minoritized groups have lost lives and jobs at much higher rates than have white people. Wellcome, like many others, made a public statement supporting the Black Lives Matter movement. Seeing a post labelled 'Our commitment to tackling racism at Wellcome' on our website felt surreal. It was like the door I had been pushing had fallen open. Suddenly, I was allowed — encouraged! — to progress anti-racism work that I'd wanted to do for years. I am inspired by how millions of people protested for change, but it's horrifying that it took so much for organizations to get to this point.



Tackling systemic racism requires the system of science to change

By spending £1 billion (US\$1.4 billion) a year to support science that improves health, Wellcome holds power. We don't want to use it to uphold racial inequity. To help turn intentions into actions, I've spent the past year leading development of Wellcome's anti-racist principles, guidance and toolkit, co-created with staff and external experts and published this week (see go.nature.com/3vqqsqs). It's part of a broader anti-racism programme I

co-lead at Wellcome with Tunde Agbalaya that includes advising leaders, developing training and supporting colleagues. The framework boils down to five principles.

Prioritize anti-racism. Doing this work properly takes time. I stopped other work, and resisted requests to complete the project faster. Sure, we could have settled with the first draft or adapted work produced at other organizations, but that wouldn't have been as effective as something co-developed with staff and tailored to our organization. (That said, we are providing our handbook publicly, with a licence that allows others to adapt it as they find useful.) Our principles had to work across Wellcome's functions as a research funder, museum, library and more. After the protests of 2020, many were eager to participate. Collaborating across the organization kept staff and leaders enthusiastic. The co-creation process was crucial to the result.

Investigate racial inequity. Collecting data isn't enough; findings must be put to work. That could include identifying issues, tailoring actions or ensuring accountability. For instance, Wellcome funds very few Black researchers. Analysis showed that this wasn't because of a lack of applicants — the inequity was in our funding success rates. That has informed how Wellcome designs new funding schemes and practices. Our goal was not to prove that inequity is a problem — that's obvious — but to identify what to do about it.

Involve people of colour. Wellcome currently has an all-white executive leadership team. The lack of representation must not prevent people of colour being involved in decisions. For this programme, we wanted to include people across funding, research and Wellcome as an institution who had professional anti-racism expertise and lived experience of racism, without exploiting or harming them.



[Major physics society won't meet in cities with racist policing record](#)

We were careful about how we established a staff forum and an external expert group: we specified the budget and workload up front, so people knew what to expect. I took on much of the work on developing the principles so that the groups could focus on advising through multiple rounds of feedback, edits and discussion. The work is much stronger thanks to input from staff and experts. For example, we followed advice to tailor our principles to address leaders and funding committee chairs, because they have more power and accountability to make change.

Counteract racism. General diversity and inclusion initiatives rarely go far enough; targeted approaches speed up progress. For example, University College London designed its Research Opportunity Scholarships programme to support UK-resident Black, Pakistani and Bangladeshi postgraduate research students.

We prioritized on the basis of evidence of inequity. We also know that racism gets compounded by other forms of oppression, such as ableism, and so sought advice from the London-based charity Business Disability Forum.

Make measurable progress. Statements are only as good as the actions behind them. Holding leaders to account requires finding ways to measure progress. Outcomes, not intent, demonstrate whether actions are racist. In our most recent inclusion survey, 22% of staff from racially minoritized

groups reported experiencing offensive language, jokes or behaviours from colleagues. Our next survey will tell us if we're doing better. We'll continue to publish data on disparities in who we fund, and share anti-racism progress in our annual report.

There isn't a quick fix. For centuries, countless people have done hard, essential work to fight racism. Now it's our turn.

Nature **594**, 303 (2021)

doi: <https://doi.org/10.1038/d41586-021-01582-y>

Competing Interests

The author declares no competing interests.

Related Articles



- [Major physics society won't meet in cities with racist policing record](#)



- [Tackling systemic racism requires the system of science to change](#)

Subjects

- [Research management](#)
- [Funding](#)
- [Society](#)

[Jobs from Nature Careers](#)

- - - [All jobs](#)
 - - [**Post Doctoral Fellow Bioinformatics Modern and Ancient Infectious Diseases**](#)
[Faculty of Medicine, Dalhousie University](#)
[Multiple locations](#)
[JOB POST](#)
 - [**Research Fellow - Molecular Pharmacology & Experimental Therapeutics**](#)
[Mayo Clinic Health System](#)
[Rochester, MN, United States](#)
[JOB POST](#)
 - [**Research Fellow - Neurobiology**](#)
[Mayo Clinic Health System](#)
[Rochester, MN, United States](#)
[JOB POST](#)
 - [**Scientist for PETRA III Beamline P07**](#)
[German Electron Synchrotron \(DESY\)](#)
[Hamburg, Germany](#)

JOB POST

[Download PDF](#)

Related Articles



- [Major physics society won't meet in cities with racist policing record](#)



- [Tackling systemic racism requires the system of science to change](#)

Subjects

- [Research management](#)
- [Funding](#)
- [Society](#)

This article was downloaded by **calibre** from <https://www.nature.com/articles/d41586-021-01582-y>.



A portal can be rendered invisible with the help of an artificial material.
Credit: Getty

Optics and photonics

11 June 2021

Not just sorcery: scientists build an invisible portal

‘Superscattering’ material is used to construct a mini-doorway that is invisible in the microwave portion of the spectrum.





•

Invisible doorways have long been the stuff of fiction: Harry Potter, for example, entered a hidden portal to catch a train at King's Cross station in London. Now, a team has disguised a gateway in the real world.

The trick is to use a metamaterial — an artificial structure whose components collectively exhibit properties that the individual components do not. Metamaterials can be used to bend light in unusual ways and, with the right design, they can become ‘superscatterers’ that look larger than they really are.

Huanyang Chen of Xiamen University in China, Rui-Xin Wu at Nanjing University, also in China, and their colleagues built a superscattering

metamaterial from iron-rich ceramic rods arranged in parallel. They placed their metamaterial on one side of a 5-centimetre-wide gateway. When they shone microwave radiation at the opening, the metamaterial stopped the waves from moving through the gateway, rendering it ‘invisible’ at microwave wavelengths.

The team confirmed that changing patterns of electron density at the surface of the metamaterial are responsible for repelling the light.

[Phys. Rev. Lett. \(2021\)](#)

- [Optics and photonics](#)

This article was downloaded by **calibre** from <https://www.nature.com/articles/d41586-021-01561-3>

| [Section menu](#) | [Main menu](#) |



Workers harvest pineapples in Lingao County, China. Less than one-third of the money spent on food eaten at home reaches farmers. Credit: Yuan Chen/VCG/Getty

Economics

08 June 2021

Poor harvest: farmers earn a pitiful fraction of the money spent on food

The bulk of consumer food spending around the world ends up in the coffers of distributors, processors and other parties beyond the farm gate.





•

Farmers receive just one-quarter of the money that people in middle and high-income countries spend on food eaten at home and away.

Christopher Barrett at Cornell University in Ithaca, New York, and his colleagues studied private expenditure on food in 61 countries, representing 90% of the world economy. From 2005 to 2015, farmers received 27% of the money people spent on food consumed at home, and even less, on average, of the money spent on food while dining out.

In rich countries in particular, the largest share of individuals' food expenditure went to production, storage and distribution of processed

foodstuffs. More than 35% of at-home food expenditures in India went to farmers; in the United States, that share was less than 25%.

Convenience food that is extensively processed beyond farm gates and packaged in plastic is considered unfavourable for human health and bad for the environment. Understanding the segments of the food supply chain is essential for policies and incentives aimed at achieving sustainability goals, the authors say.

[Nature Food \(2021\)](#)

- [Economics](#)

This article was downloaded by **calibre** from <https://www.nature.com/articles/d41586-021-01536-4>

| [Section menu](#) | [Main menu](#) |



Rising levels of carbon dioxide in the atmosphere might have hastened the spread of famine weed, one of the most destructive invasive species on Earth. Credit: Shutterstock

Plant sciences

09 June 2021

Menacing ‘famine weed’ grows more toxic as carbon levels soar

A highly invasive weed might owe some of its success to easier access to carbon, a key component of the weed’s toxin.





•

Rising carbon-dioxide emissions have allowed a dangerous, invasive plant to become even more toxic, which might have helped it to push into new territory.

Famine weed (*Parthenium hysterophorus*), an herb native to the Americas, has infested regions across Africa, Asia and Australia for decades. The carbon-based toxin it secretes, called parthenin, suppresses the growth of nearby crops, contaminates the milk and meat of animals that ingest it, and causes dermatitis, hay fever and asthma in people.

Julie Wolf at the US Department of Agriculture in Beltsville, Maryland, and her colleagues conjectured that surging carbon-dioxide levels in the

atmosphere could have contributed to the weed's success by providing building blocks for the plant to ramp up its parthenin production.

The researchers grew two types of famine weed, one invasive and the other non-invasive, and exposed them to the atmospheric levels of carbon dioxide recorded in 1950 and 2020. In the invasive variety, parthenin concentrations peaked at the highest carbon levels. The results suggest that modern levels of carbon dioxide have contributed to the noxious weed's toxicity.

[Nature Plants \(2021\)](#)

- [Plant sciences](#)

This article was downloaded by **calibre** from <https://www.nature.com/articles/d41586-021-01539-1>

| [Section menu](#) | [Main menu](#) |



A young grey whale surfaces in a sheltered inlet off Mexico. The animals breed in the northern Pacific Ocean, but one has been spotted far afield, near Namibia. Credit: Claudio Contreras/Nature Picture Library

Animal behaviour

08 June 2021

A grey whale makes an epic swim into the record books

A journey stretching around 20,000 kilometres might be the world's longest migration by ocean.





•

Many sea creatures migrate thousands of kilometres every year, but a whale spotted off the coast of southern Africa might have broken travel records.

The male grey whale (*Eschrichtius robustus*) was sighted in Walvis Bay, Namibia — some 20,000 kilometres from the waters of the northern Pacific Ocean where its kind typically feed and breed. After sampling the animal's skin, Rus Hoelzel at Durham University, UK, and his colleagues compared its DNA with that of grey whales residing in the North Pacific.

The researchers found that the animal probably belongs to an endangered population that feeds near Sakhalin Island, Russia. To get to the shores of Namibia, the whale might have made a 27,000-kilometre journey by way of

the Northwest Passage, through the Canadian Arctic. It's also possible that the animal travelled a shorter route across the Indian Ocean or around South America's southern tip.

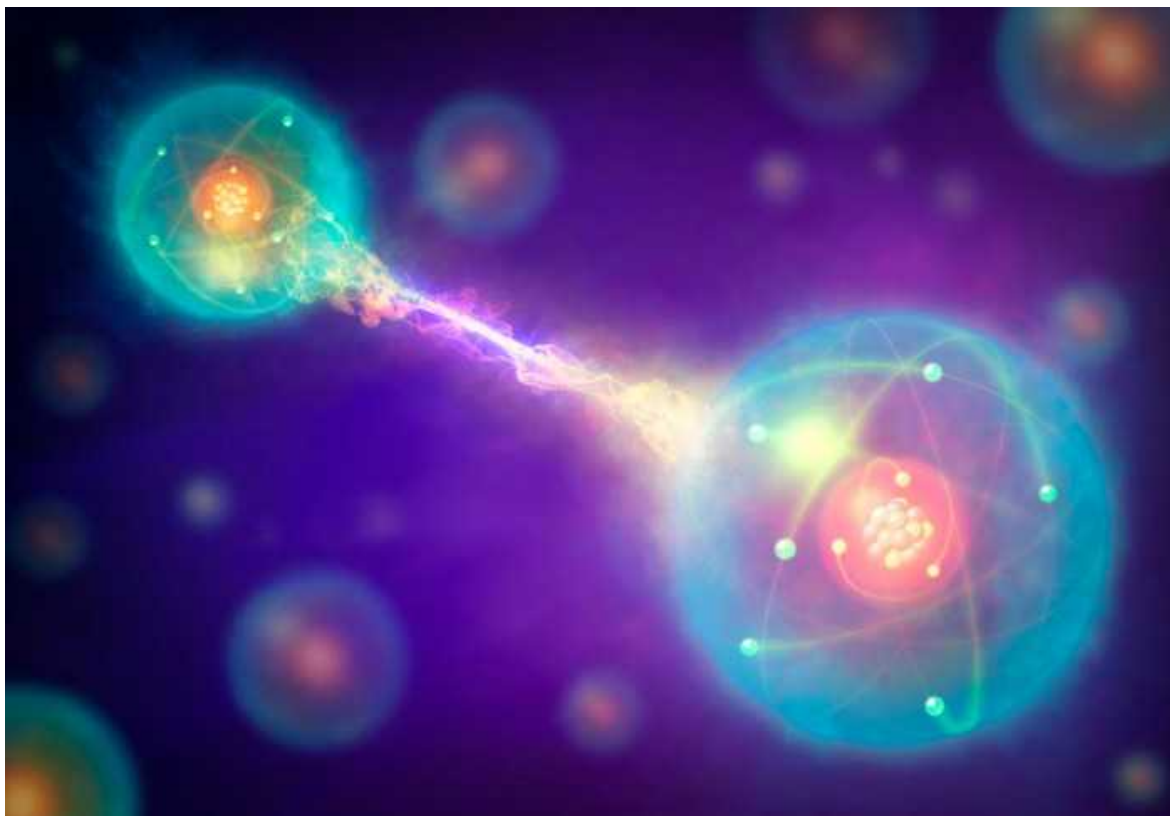
Other grey whales have been found over the past decade in the Atlantic Ocean. They might have accidentally strayed from home, or might have extended their foraging excursions as climate change enabled travel across the Arctic, the authors say.

Biol. Lett. (2021)

- [Animal behaviour](#)

This article was downloaded by **calibre** from <https://www.nature.com/articles/d41586-021-01535-5>

| [Section menu](#) | [Main menu](#) |



An artist's impression of 'entangled' particles, which share properties even at a distance. Entangled photons can be used to help secure a multi-party video meeting. Credit: Mark Garlick/Science Photo Library

Quantum information

09 June 2021

Quantum keys dial up tamper-proof conference calls

A new experiment efficiently distributes the highly secure keys to four parties instead of the typical two.





•

The ultra-secure ‘quantum internet’ hasn’t arrived yet, but when it does, it looks like we’ll have quantum video conferences.

One well-established quantum communication technique uses photons to create a string of data, or key, that can encrypt and decrypt messages. Eavesdroppers can be detected easily because observation disturbs the states of the photons. But these photon-based ‘quantum keys’ are typically distributed to only two parties.

Alessandro Fedrizzi at Heriot-Watt University in Edinburgh, UK, and his colleagues showed a way to pass out quantum keys efficiently to groups of three or more. For the demonstration, the team used lasers to produce sets of

four photons. Each of the four photons was ‘entangled’ with the others in its set: measuring it would affect the rest, making eavesdropping difficult.

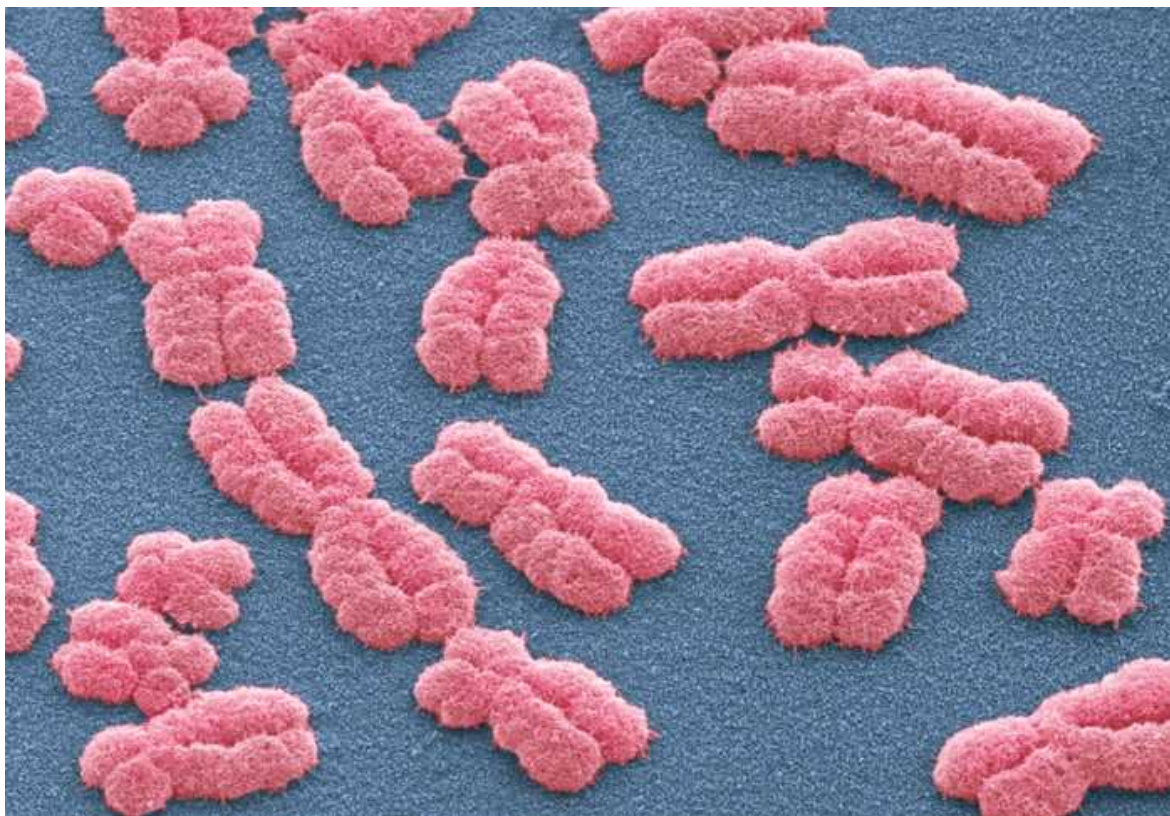
The researchers could distribute their entangled quartets over a network of fibre-optic cable with a combined length of as much as 50 kilometres. From the quartets of entangled photons, the team built a cryptographic key about one million bits long. The researchers used this to encrypt an illustration of Lewis Carroll’s Cheshire Cat and share it securely between four parties during a short conference call.

[Sci. Adv. \(2021\)](#)

- [Quantum information](#)

This article was downloaded by **calibre** from <https://www.nature.com/articles/d41586-021-01534-6>

| [Section menu](#) | [Main menu](#) |



Human chromosomes. A California scheme to sequence the entire genomes of babies with puzzling health problems led to diagnoses for many. Credit: Power and Syred/Science Photo Library

Genomics

04 June 2021

Babies with mystery illnesses benefit from genome sequencing

Rapid genomic sequencing on admission to hospital leads to more-precise care for sick infants.





•

In 2018, five hospitals in California launched an ambitious scheme: immediately provide rapid genomic sequencing for all babies admitted to the intensive care unit with an illness that had no obvious cause. Analysis now shows that the initiative allowed one-third of the babies to receive more targeted medical care.

David Dimmock at the Rady Children's Institute for Genomic Medicine in San Diego, California, and his colleagues sequenced the genomes of more than 180 hospitalized infants to flag any genetic reasons for the baby's illness. All the infants were under one year of age and received health care through a state programme.

Using the babies' genomic data, medics diagnosed the illnesses behind 40% of cases in an average of 3 days, and the results changed medical care for 32% of the infants. Most of the diagnoses were of very rare disorders that might not have come to light otherwise.

Although scientists know that rapid genome sequencing can improve medical care in research settings, the authors say these results show that it can be effective at scale and in a state's medical aid programme.

[Am. J. Hum. Genet. \(2021\)](#)

- [Genomics](#)

This article was downloaded by **calibre** from <https://www.nature.com/articles/d41586-021-01499-6>

| [Section menu](#) | [Main menu](#) |



Downtown Salt Lake City, Utah, could sustain serious damage in a relatively small earthquake. Credit: Aerial Archives/Alamy

Seismology

11 June 2021

A small earthquake could pose a big risk to a US city

The structure of faults beneath Salt Lake City, Utah, shows how the ground could liquefy during a shaking.





•

Geologists have long known that Salt Lake City, home to 200,000 people, lies atop a network of geological faults. Now, research shows that, during an earthquake, these faults could cause the ground beneath downtown buildings to flow like liquid.

The city, which is Utah's capital, lies between two large mountain ranges created by geological activity. Active faults snake near those mountains, along them and beneath Salt Lake City. But it has been unclear precisely how the faults linked underneath the city, and how much damage they might cause during a large earthquake.

Lee Liberty at Boise State University in Idaho and his colleagues probed the buried faults by repeatedly dropping a 200-kilogram weight along the city's streets. The scientists then analysed how seismic energy from the impact rippled through the ground.

They found that faults shoot through many rock layers that lie beneath the city. Even a relatively small earthquake, with a magnitude of less than 5, could cause the ground to liquefy in these areas. A 6.5-magnitude earthquake could damage buildings substantially.

[Seismic Rec. \(2021\)](#)

- [Seismology](#)

This article was downloaded by **calibre** from <https://www.nature.com/articles/d41586-021-01562-2>

| [Section menu](#) | [Main menu](#) |

News in Focus

- **China's vaccination surge, fast radio bursts and the dominant Alpha variant** [16 June 2021]
News Round-Up • The latest science news, in brief.
- **Landmark Alzheimer's drug approval confounds research community** [08 June 2021]
News • Many scientists say there is not enough evidence that Biogen's aducanumab is an effective therapy for the disease.
- **First science adviser in US president's cabinet talks COVID, spying and more** [04 June 2021]
News Q&A • Eric Lander spoke to Nature during his first day as the director of the White House Office of Science and Technology Policy.
- **Does vaccinating adults stop kids from spreading COVID too?** [10 June 2021]
News • Mass vaccination drives in several countries are providing new data on the extent to which adult vaccination protects children — but the conclusions are mixed.
- **The COVID lab-leak hypothesis: what scientists do and don't know** [08 June 2021]
News Explainer • Nature examines arguments that the coronavirus SARS-CoV-2 escaped from a lab in China, and the science behind them.
- **Forensic database challenged over ethics of DNA holdings** [15 June 2021]
News Feature • Geneticists say a global Y-chromosome database holds profiles from men who are unlikely to have given free informed consent.

- NEWS ROUND-UP
- 16 June 2021

China's vaccination surge, fast radio bursts and the dominant Alpha variant

The latest science news, in brief.





•

[Download PDF](#)



The CHIME radio telescope has detected 535 fast radio bursts in its first year of operation. Credit: Andre Renard/CHIME Collaboration

Fast radio bursts come in two types

A bumper crop of fast radio bursts shows that [the mysterious signals exist as two distinct types](#).

The Canadian Hydrogen Intensity Mapping Experiment (CHIME) radio telescope has detected 535 fast radio bursts — quadrupling the known tally of these powerful cosmic flashes, which flare for just milliseconds.

Most of the bursts are one-off events, but a minority repeat periodically and last at least ten times longer, on average, than do single bursts. The findings, announced during a virtual meeting of the American Astronomical Society on 9 June, suggest that fast radio bursts might originate from at least two distinct astrophysical phenomena.

Repeaters could occur when a highly magnetized neutron star circles around an ordinary star in an elongated orbit. As the neutron star periodically gets

closer to its companion, bursts could result from its magnetic field scattering the highly energetic stellar wind.

One-off bursts, by contrast, could be the result of cataclysmic events, such as collisions between neutron stars, or magnetic storms in young neutron stars called magnetars.

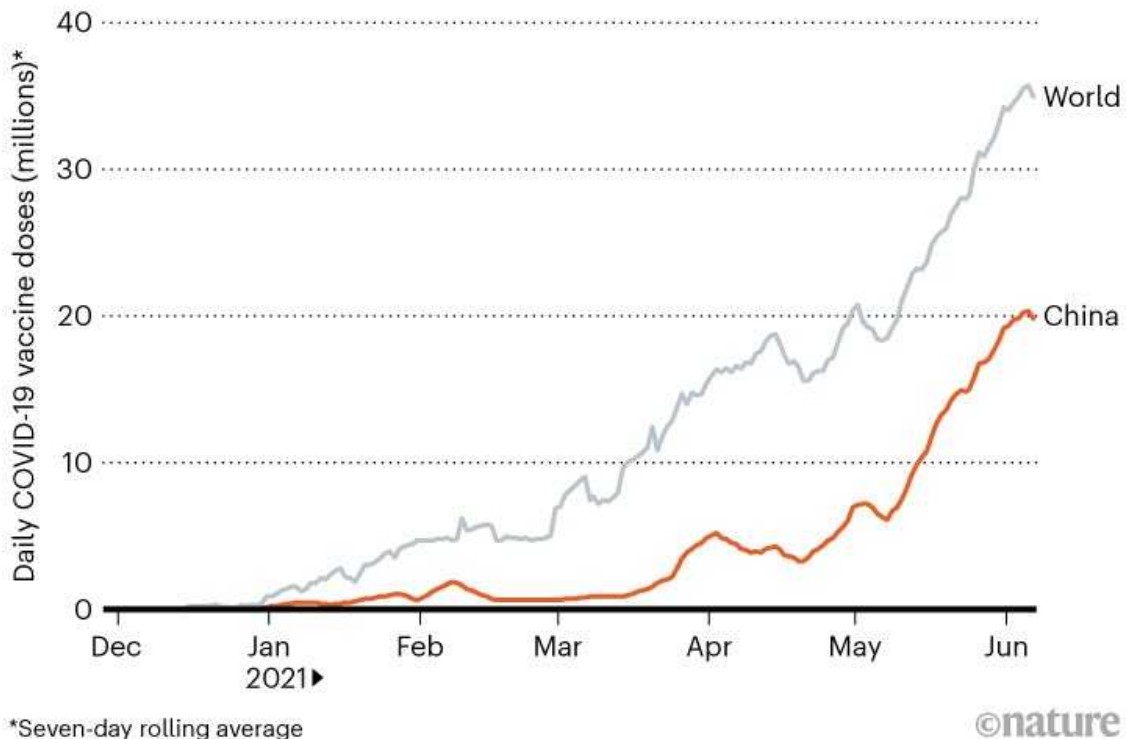
The CHIME team reported that the bursts' sources seemed to be evenly spread across the sky. Only a handful could be traced to any particular galaxy.

China is vaccinating 20 million people a day

For more than a week, [an average of about 20 million people have been vaccinated against COVID-19 every day in China](#). At this rate, the nation could have vaccinated the UK population in little more than six days. China accounts for more than half of the 35 million people globally getting a COVID-19 shot each day.

DAILY VACCINE DOSES ADMINISTERED

China is vaccinating so many people against COVID-19 each day that it accounts for nearly 60% of all doses given globally.



*Seven-day rolling average

©nature

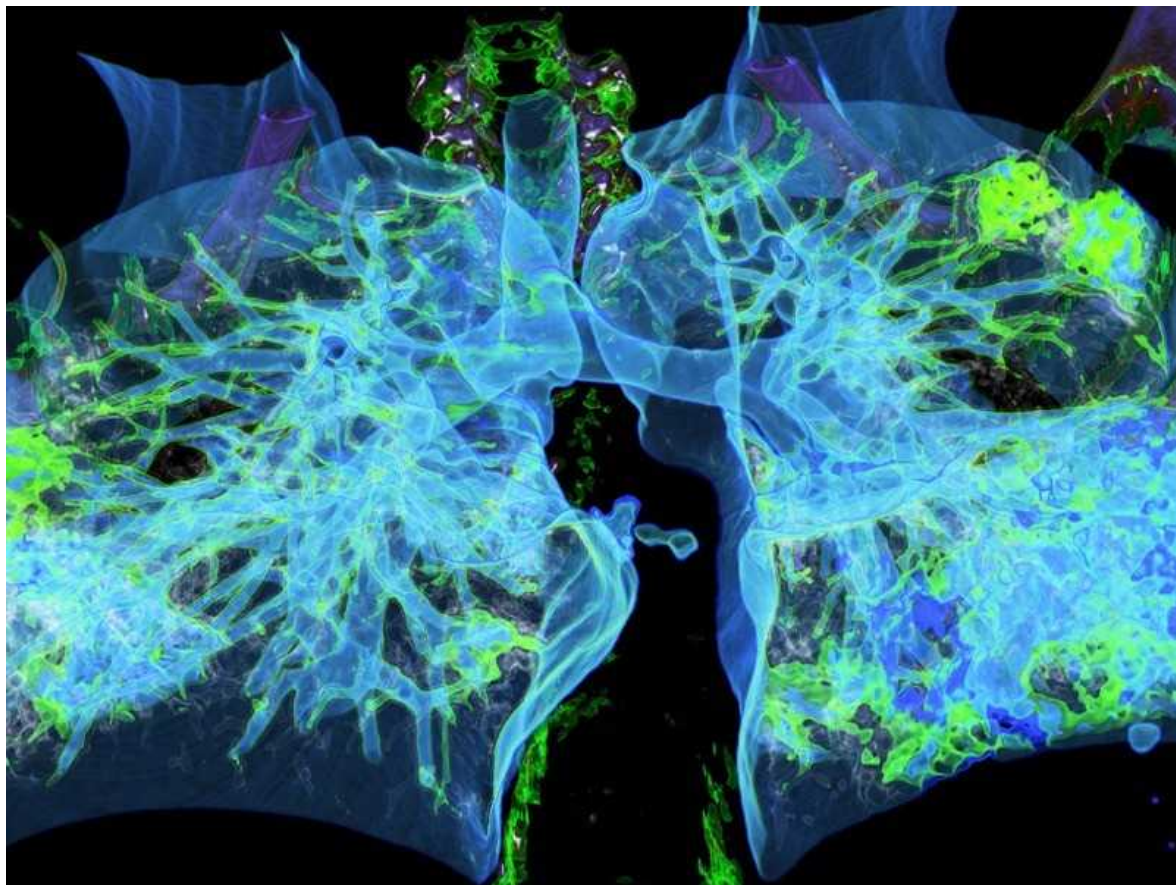
Source: Our World in Data

Zoltán Kis, a chemical engineer in the Future Vaccine Manufacturing Research Hub at Imperial College London, doesn't know of "anything even close to those production scales" for a vaccine. "The manufacturing efforts required", he says, "are tremendous."

Most of the doses given in China are of one of two vaccines, both approved for emergency use worldwide by the World Health Organization (WHO): CoronaVac, produced by Sinovac in Beijing, and another jab developed in Beijing by state-owned firm Sinopharm.

China's vaccine-production rate could make a significant dent in global demand, says Kis; that would be "a huge step in reducing the health-care and economic burden of the COVID-19 pandemic". China has supplied 350

million doses of the two vaccines to more than 75 nations, and WHO approval should trigger further distribution to low-income countries.



Widespread lung damage (green; artificially coloured computed tomography scan) indicates pneumonia in a person with COVID-19. Credit: Vsevolod Zviryk/SPL

Alpha variant blunts immune defences

A fast-spreading coronavirus variant [blunts the body's first line of defence](#), which could explain why it is more transmissible than previously circulating variants.

Since it was first detected in the United Kingdom late last year, B.1.1.7 — also called Alpha — has whizzed around the world to become the dominant form of SARS-CoV-2. Some studies suggest that Alpha's increased

transmissibility could stem from mutations in its spike protein that allow it to enter cells more efficiently.

But a preprint posted on 7 June suggests that Alpha also has tricks linked to mutations beyond the spike protein ([L. G. Thorne *et al. Preprint at bioRxiv https://doi.org/10.1101/2021.06.07.446545*](https://doi.org/10.1101/2021.06.07.446545)). These mutations probably mean that within hours of infecting a person, Alpha suppresses the body's rapid-response defences.

Researchers examined how cells from the human airway produced interferon, an immune protein that kick-starts the body's defences on the arrival of a pathogen. They found that cells infected with Alpha produce much less interferon than do cells infected with earlier variants. Alpha's suppression of interferon production helps the variant to stay in the body for longer.

Nature **594**, 307 (2021)

doi: <https://doi.org/10.1038/d41586-021-01583-x>

Subjects

- [Vaccines](#)
- [SARS-CoV-2](#)
- [Cosmology](#)

[Jobs from Nature Careers](#)

- - - [All jobs](#)
 -
 - [Post Doctoral Fellow Bioinformatics Modern and Ancient Infectious Diseases](#)
[Faculty of Medicine, Dalhousie University](#)

Multiple locations

JOB POST

- **Research Fellow - Molecular Pharmacology & Experimental Therapeutics**

Mayo Clinic Health System

Rochester, MN, United States

JOB POST

- **Research Fellow - Neurobiology**

Mayo Clinic Health System

Rochester, MN, United States

JOB POST

- **Scientist for PETRA III Beamline P07**

German Electron Synchrotron (DESY)

Hamburg, Germany

JOB POST

Download PDF

Subjects

- Vaccines
 - SARS-CoV-2
 - Cosmology
-

This article was downloaded by **calibre** from <https://www.nature.com/articles/d41586-021-01583-x>

| [Section menu](#) | [Main menu](#) |

- NEWS
- 08 June 2021

Landmark Alzheimer's drug approval confounds research community

Many scientists say there is not enough evidence that Biogen's aducanumab is an effective therapy for the disease.

- [Asher Mullard](#)

1. Asher Mullard

[View author publications](#)

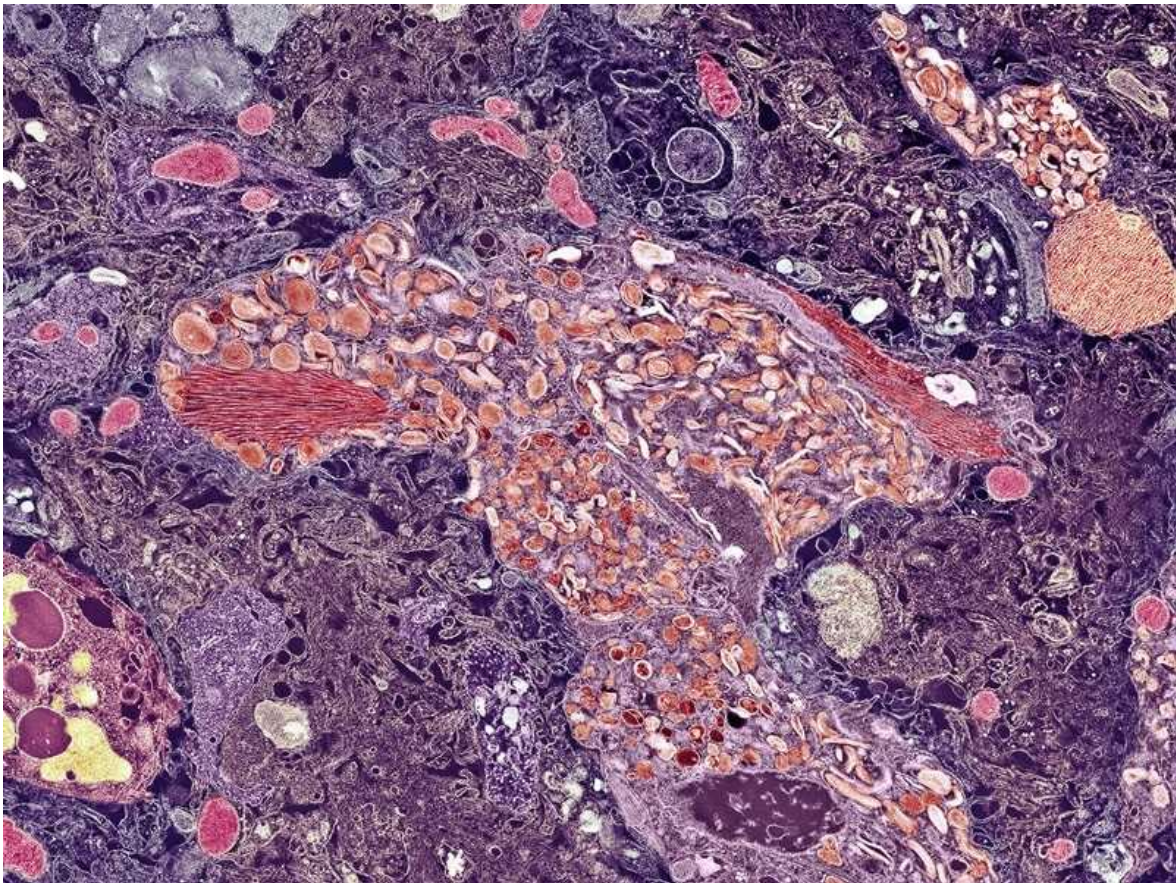
You can also search for this author in [PubMed](#) [Google Scholar](#)





•

[Download PDF](#)



Plaques of amyloid- β in the brain are one target of Alzheimer's disease treatments. Credit: Thomas Deerinck, NCMIR/SPL

The US Food and Drug Administration (FDA) approval yesterday of the first new drug for Alzheimer's disease in 18 years was welcomed by some people looking for hope against an intractable condition. But, for many researchers, it came as a surprise — and a disappointment.

Aducanumab — developed by biotechnology company Biogen in Cambridge, Massachusetts — is the first approved drug that attempts to treat a possible cause of the neurodegenerative disease, rather than just the symptoms. But the approval has sparked a contentious debate over whether the drug is effective. Many experts, including an independent panel of neurologists and biostatisticians, advised the FDA that clinical-trial data did not conclusively demonstrate that aducanumab could slow cognitive decline.

The FDA instead relied on an alternative measure of activity, which sets a dangerous precedent, some researchers warn.

Current Alzheimer's drugs address only disease symptoms, for instance by delaying memory loss by a few months. Aducanumab clears out clumps of a protein in the brain called amyloid- β , which some researchers think is the root cause of Alzheimer's. This theory is known as the amyloid hypothesis. The FDA approved the drug on the basis of its ability to reduce the levels of these plaques in the brain.

"This is a very slender reed upon which to hang an approval decision," says Jason Karlawish, a geriatrician and co-director of the Penn Memory Center in Philadelphia, Pennsylvania. Despite the dominance of the amyloid hypothesis over the past few decades, evidence that links reductions in plaque levels to improvements in cognition is "thin, at best", says Karlawish.

"Desperation should drive the funding of science, not drive the way we interpret the science," he says.

Desperate need

But some patient groups are desperate for anything that might offset the effects of the incurable, progressive disease. Estimates suggest that 35 million people worldwide have Alzheimer's.

"History has shown us that approvals of the first drug in a new category invigorate the field, increase investments in new treatments and encourage greater innovation," said Maria Carrillo, chief science officer for the patient-advocacy group Alzheimer's Association in Chicago, Illinois, in a statement. "We are hopeful, and this is the beginning — both for this drug and for better treatments for Alzheimer's."

Others worry that the approval will have the opposite effect — stymieing research efforts. Karlawish suspects that people with Alzheimer's might start dropping out of ongoing clinical trials to take aducanumab. Others worry that drug developers might abandon other targets. If demonstrating that amyloid-lowering activity is enough to win regulatory approval, it might discourage developers from focusing on treatments with the big cognitive benefits that patients need, say some scientists.

“This is going to set the research community back 10–20 years,” says George Perry, a neurobiologist at the University of Texas at San Antonio and a sceptic of the amyloid hypothesis.

‘Problematic data set’

Aducanumab, an intravenously infused antibody, is the latest in a long line of therapeutic candidates that aims to tackle amyloid plaques. Although every drug of this type has so far failed to improve cognition, questions have persisted about whether amyloid- β is the right drug target, as well as whether researchers are testing the optimal therapeutic candidates, the correct doses and the appropriate patients.

“The problem with most of the amyloid trials is that they didn’t disprove anything,” says Bart De Strooper, director of the UK Dementia Research Institute in London. “They just proved that a drug, in the way it was applied, didn’t work.”

Researchers’ concerns now centre on aducanumab’s tumultuous passage through clinical trials and the resulting data set, which is incomplete and unpublished.

The FDA’s approval is based on data from two phase III trials. In March 2019, researchers peeked at interim data while these trials — which were conducted in people with early-stage Alzheimer’s — were ongoing. They concluded that these were unlikely to succeed, and Biogen halted both trials early.

But months later, the biotech firm brought the antibody back from the brink, [after inspecting the data more closely](#). The slow of cognitive decline was statistically significant in the subset of participants who received the highest dose of aducanumab, Biogen’s re-analysis showed. Aducanumab did not have the same benefit when used at a lower dose in this trial, and it didn’t show a benefit at any dose in the other trial.

For Paul Aisen, director of the University of Southern California’s Alzheimer’s Therapeutic Research Institute in San Diego, the totality of the data supports approval. “My personal view is that aducanumab is an

effective therapy,” says Aisen, who consults for Biogen. “But this was a problematic data set. It was a very fraught situation,” he concedes.

These tensions were on display last November at an FDA meeting to discuss the trial data. An independent panel of experts advising the FDA evaluated the data and argued strongly against Biogen’s assertion that the partial positive trial results carried more weight than did the negative ones. Scott Emerson, a biostatistician at the University of Washington in Seattle, who was on the panel, called the approach akin to “firing a shotgun at a barn and then painting a target around the bullet holes”.

The data also showed that aducanumab has non-negligible side effects. Around 40% of treated participants in the two trials developed brain swelling. Most people wouldn’t have any symptoms related to the swelling, but they would need regular brain scans to avert dangerous complications — a burden for patients, neurologists and health-care systems.

At the November meeting, 10 out of 11 panellists ultimately voted that the presented data could not be considered as evidence of aducanumab’s effectiveness; the remaining panellist was uncertain. This week, the FDA reached the opposite conclusion.

Post-approval trial

As a condition of the FDA’s approval — which relied on the agency’s ‘accelerated approval’ programme — Biogen now must run a ‘post-marketing’ trial to confirm that the drug can improve cognition. It has yet to release details on when and how this trial will take place. Biogen has up to nine years to complete the trial.

This worries industry watchers. “Experience shows that relying on accelerated approval to gather timely, high-quality post-approval evidence is not necessarily a given,” says Aaron Kesselheim, who studies pharmacoconomics at Harvard Medical School in Boston, Massachusetts, and is a member of the FDA panel that discussed aducanumab.

The FDA’s choice to grant accelerated approval to aducanumab — after a rollercoaster of a clinical-trial programme — could have broader

implications, too. “This opens the door to drug companies seeking to use the accelerated approval programme as a way of getting drugs on the market based on extremely low-quality evidence or post-hoc data fishing,” says Kesselheim.

Ripple effects

Biogen is now in line for a major windfall with aducanumab; its share price jumped by 40% on the approval.

Some experts had expected the FDA to approve the antibody only for people with early-stage disease, but the regulator has not limited its use — anyone with Alzheimer’s can take it. Biogen will charge around US\$56,000 per year per person for the drug. If 5% of 6 million people with Alzheimer’s in the United States receive the treatment, the drug’s revenue would reach nearly \$17 billion per year. This would make it the second top-selling drug, by current revenues.

The Institute for Clinical and Economic Review, a non-profit organization in Boston, Massachusetts, estimates that a cost-effective price is \$2,500–8,300 per year.

The approval is also likely to shake up the development of future Alzheimer’s drugs, say researchers.

With a pathway to approval established, drug developers are likely to double down on anti-amyloid drugs. Drug companies Eli Lilly, Roche and Eisai already have anti-amyloid antibodies in phase III trials. They, too, might now be able to secure approvals with evidence of amyloid-lowering activity, regardless of the compounds’ effects on cognition.

Before the approval, the research community had started to shift towards other drug targets associated with Alzheimer’s disease. For instance, more than ten drug candidates now in clinical trials are designed to clear another toxic protein from the brain, called tau.

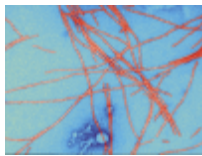
David Knopman, a neurologist at the Mayo Clinic in Rochester, Minnesota, hopes that these and earlier-stage efforts won’t falter as a result of

aducanumab's win, based on amyloid-lowering activity. "We need to look at other targets," he says.

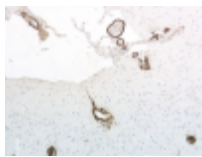
Nature **594**, 309-310 (2021)

doi: <https://doi.org/10.1038/d41586-021-01546-2>

Related Articles



- [The red-hot debate about transmissible Alzheimer's](#)



- [More evidence emerges for 'transmissible Alzheimer's' theory](#)

Subjects

- [Drug discovery](#)
- [Alzheimer's disease](#)

[Jobs from Nature Careers](#)

- - - [All jobs](#)
 -
 - [Post Doctoral Fellow Bioinformatics Modern and Ancient Infectious Diseases](#)

[Faculty of Medicine, Dalhousie University](#)

Multiple locations

JOB POST

- **Research Fellow - Molecular Pharmacology & Experimental Therapeutics**

Mayo Clinic Health System

Rochester, MN, United States

JOB POST

- **Research Fellow - Neurobiology**

Mayo Clinic Health System

Rochester, MN, United States

JOB POST

- **Scientist for PETRA III Beamline P07**

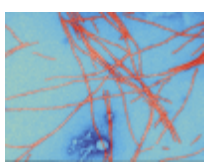
German Electron Synchrotron (DESY)

Hamburg, Germany

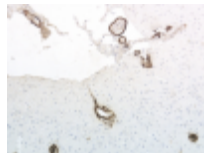
JOB POST

Download PDF

Related Articles



- **The red-hot debate about transmissible Alzheimer's**



- More evidence emerges for 'transmissible Alzheimer's' theory

Subjects

- Drug discovery
- Alzheimer's disease

This article was downloaded by **calibre** from <https://www.nature.com/articles/d41586-021-01546-2>

| [Section menu](#) | [Main menu](#) |

- NEWS Q&A
- 04 June 2021

First science adviser in US president's cabinet talks COVID, spying and more

Eric Lander spoke to *Nature* during his first day as the director of the White House Office of Science and Technology Policy.

- [Nidhi Subbaraman](#)

1. Nidhi Subbaraman
[View author publications](#)

You can also search for this author in [PubMed](#) [Google Scholar](#)





•

[Download PDF](#)



Eric Lander will be the first OSTP director to be a member of a US president's cabinet. Credit: Al Drago/Reuters

Expectations are high for geneticist Eric Lander, who was sworn in as director of the White House Office of Science and Technology Policy (OSTP) on 2 June, after a months-long confirmation process. In a first for any US president, Joe Biden [elevated the position of OSTP director](#) to his cabinet, potentially granting Lander more access and influence than any science adviser before him.



[Joe Biden names top geneticist Eric Lander as science adviser](#)

Lander has a decades-long reputation as a hard-charging and competitive leader. But he's also drawn criticism for some public moves: in 2016, he wrote a history of CRISPR gene-editing technology that [critics said diminished](#) the foundational contributions of two women — Jennifer Doudna at the University of California, Berkeley, and Emmanuelle Charpentier at the Max Planck Unit for the Science of Pathogens in Berlin — who would later [win a Nobel prize for their work](#). “I made a mistake, and when I make a mistake, I own it and try to do better,” Lander told lawmakers at an April hearing considering his nomination. At that hearing, lawmakers also scrutinized [two events he attended](#) at which sex offender and alleged sex trafficker Jeffrey Epstein was also a guest. Lander insisted that these were one-off donor events.

Nature spoke to Lander on his first day in office about his goals for the OSTP, criticisms of him, and some of the weighty priorities — such as addressing how to prepare for the next pandemic — that Biden has tasked him with.

Has President Biden asked for your advice yet?

Yes, but I don't want to elaborate, because the confidence of conversations with presidents is to be respected.

What does being part of the president's cabinet mean for you on a day-to-day basis?

Symbolically, I think it is a statement about the centrality of science and technology to many, many of the opportunities and challenges that are facing the United States. Being a member of the cabinet has already meant that there are direct discussions between myself and other members of the cabinet. There is a weekly Zoom call that involves cabinet members. We're getting to interact on a regular basis, so I've already had an opportunity to build relationships.



US Vice President Kamala Harris (far right) swears in Lander on 2 June.Credit: Erin Scott/Bloomberg/Getty

Staffing at the OSTP fell under former president Donald Trump to one-quarter of its previous level.

Where does it stand now?

I was sworn in this morning — I don't actually know the precise number. But what I can say is the OSTP is hiring right now, and growing.

What does the United States need to do to prevent the next pandemic?

We cannot be self-satisfied because we were able to produce a vaccine in under a year and get it approved. We should take one brief victory lap for doing that, and then we've got to say: we've got to do better next time. Can we have a solution for any of the 25 families of human viruses? Can we spin up even more rapid diagnostics? Can we spin up global surveillance, such as an early-warning system? There are a lot of discussions that will emerge in the coming weeks and months into a set of pretty bold goals for making sure we never again see infectious disease turn into a pandemic like this. And then we're going to have to hold our feet to the fire. The unforgivable thing would be to simply forget about this problem and move on, because there will be more infectious agents, more viruses with pandemic potential. It's not an if, it's a when.

The Trump administration gutted government science offices and eroded science policies. Can science recover?



[Biden has assembled a stellar science team — now they must pull together](#)

I think science is so essential to the future of the nation and the world that, no matter what, science not only has to be bouncing back, but also going much further than ever before.

Something that is core to science is dissent. I think a really important question is how to protect the ability for scientists who have a divergent point of view to be able to express that in a constructive way, including scientists who might have a divergent view from political appointees. I think we need to protect those sorts of things because it's the heart of the scientific method. It's about evidence, not authority.

The OSTP is holding meetings about how to protect scientific integrity. How's that going?

I just got sworn in this morning. But I have gotten reports that people are really fired up about the opportunity to think deeply about finding ways, over the long term, to really ingrain and protect scientific integrity. It's crucial to science being able to make a difference for policy.

Regarding your meetings with Jeffrey Epstein, did he fund or offer to fund your work?

Jeffrey Epstein is an abhorrent person. I had no relationship with him. I was at two Harvard donor events and met him briefly, that's it. Never saw him again. There were two events a decade ago, a few weeks apart. He never offered to fund my work or anything like that.

Your CRISPR essay and other actions have prompted worries that you're unfit for this office. How do you respond?

For 35 years, I have been doing a tremendous amount around the values of lifting up people and building institutions that are broadly inclusive. Those are where my values are, and that is really where my work is.

Democratic senator Maria Cantwell of Washington state says you've agreed that workforce diversity will be the 'first task' for the OSTP. What's the plan?



['Inspired choice': Biden appoints sociologist Alondra Nelson to top science post](#)

The only goal we should be aiming for is to have parity. We're not going to succeed unless we have everybody at the lab bench. One of the early things the OSTP will be doing is reaching out to many groups who have experience with different types of solutions. I think the first thing to do is talk to the people who are most knowledgeable, most affected — and bring together that conversation. I'm working with [Alondra Nelson](#), who is the first director ever of [the OSTP's] division of science and society. She and I have talked a lot about bringing people who are on the front lines of these issues together and then fashioning real solutions.

You've said that all Americans must be able to participate in and benefit from science. What's the biggest challenge to that?

Let's start with the fact that science has always been unwelcoming to women and people of colour. This is a major priority — to make sure that we really eliminate that. There are large parts of the country that really don't have a science high school or a science industry — where somebody who's really interested in science can't easily get involved. So there's unwelcoming and there's inaccessible. We've got to overcome both of those barriers.

In academia, we should even ask questions about the system of advising. It's a little bit of a medieval system, where you apprentice yourself to a single person. Maybe [more] welcoming communities have multiple mentors who are looking after people in different ways.

Scientists say that measures taken by the US government against research espionage have damaged scientific partnerships, especially with China. How will you address this?



[Biden pursues giant boost for science spending](#)

It's not acceptable if countries engage in industrial espionage to take intellectual property. I think we all agree on that. The question is, how do you manage that in a way that is effective — addresses the problem, but doesn't create huge burdens, doesn't create a sense of turning away international collaboration and doesn't promote racism and anti-Asian feelings? We have to balance two things: we have to get research security right, and we have to make sure we really take advantage of the full power of international scientific collaboration and the fact that so many great people want to come to the United States [to work and study]. We can get those things right with clear guidance about disclosure of information. And that's certainly going to be a role for this office — to look after both sides of that equation.

How will the OSTP coordinate research-security policies among US agencies, to ensure that scientists disclose foreign ties in their funding applications?

The OSTP is charged with making sure this is implemented in a way that's effective and non-burdensome. That's the next piece of work that's got to be done. What we don't want to do is produce a thicket of rules that everybody

has to go interpret in different ways. I very much agree with everybody who wants clarity, because, frankly, clarity is also what produces the best security. I think most people just want to do the right thing, and they want to have a simple path to do the right thing.

Nature **594**, 311 (2021)

doi: <https://doi.org/10.1038/d41586-021-01501-1>

This interview has been edited for length and clarity.

Related Articles



- [**Joe Biden names top geneticist Eric Lander as science adviser**](#)



- [**‘Inspired choice’: Biden appoints sociologist Alondra Nelson to top science post**](#)



- [**Biden has assembled a stellar science team — now they must pull together**](#)



- [**Biden pursues giant boost for science spending**](#)



- [Trump's science adviser on research ethics, immigration and presidential tweets](#)

Subjects

- [Scientific community](#)
- [SARS-CoV-2](#)
- [Politics](#)
- [Policy](#)
- [Government](#)

[Jobs from Nature Careers](#)

- - - [All jobs](#)
 - - [Post Doctoral Fellow Bioinformatics Modern and Ancient Infectious Diseases](#)
[Faculty of Medicine, Dalhousie University](#)
[Multiple locations](#)
[JOB POST](#)
 - [Research Fellow - Molecular Pharmacology & Experimental Therapeutics](#)
[Mayo Clinic Health System](#)
[Rochester, MN, United States](#)

JOB POST

- **Research Fellow - Neurobiology**

Mayo Clinic Health System

Rochester, MN, United States

JOB POST

- **Scientist for PETRA III Beamline P07**

German Electron Synchrotron (DESY)

Hamburg, Germany

JOB POST

Download PDF

Related Articles



- **Joe Biden names top geneticist Eric Lander as science adviser**



- **‘Inspired choice’: Biden appoints sociologist Alondra Nelson to top science post**



- **Biden has assembled a stellar science team — now they must pull together**



- [**Biden pursues giant boost for science spending**](#)



- [**Trump's science adviser on research ethics, immigration and presidential tweets**](#)

Subjects

- [Scientific community](#)
- [SARS-CoV-2](#)
- [Politics](#)
- [Policy](#)
- [Government](#)

This article was downloaded by **calibre** from <https://www.nature.com/articles/d41586-021-01501-1>

- NEWS
- 10 June 2021
- Correction [15 June 2021](#)

Does vaccinating adults stop kids from spreading COVID too?

Mass vaccination drives in several countries are providing new data on the extent to which adult vaccination protects children — but the conclusions are mixed.

- [Dyani Lewis](#)
 1. Dyani Lewis
[View author publications](#)

You can also search for this author in [PubMed](#) [Google Scholar](#)





•

[Download PDF](#)



Children in São Paulo city hold kits including sanitizing products and face masks for kids. Credit: Andre Penner/AP/Shutterstock

Unvaccinated children seem to be reaping the benefits of mass COVID-19 vaccination programmes in many parts of the world. Infections in children have fallen as adults get their shots. But experts disagree on whether this means that unvaccinated children are unlikely to become a ‘reservoir’ for infection — and a potential hotbed for the emergence of new variants.

The answer affects whether children in wealthy countries should be prioritized for vaccination — or whether their doses should go to poorer nations instead.

Compelling data on the impact of adult vaccination on children comes from the small town of Serrana in the Brazilian state of São Paulo, where 98% of adults have been vaccinated. The town was the site of a unique experiment — dubbed Project S — to measure the [real-world effectiveness of CoronaVac](#), developed by the pharmaceutical company Sinovac, based in Beijing.

Compared with other vaccines, Sinovac had been less successful at [preventing symptomatic infections](#) in some previous clinical trials, with efficacy rates as low as 50%.



[WHO approval of Chinese CoronaVac COVID vaccine will be crucial to curbing pandemic](#)

But last week, researchers at the Butantan Institute in São Paulo city detailed in a press conference a striking reduction in COVID-19 cases and deaths: symptomatic cases dropped by 80% and deaths by 95%. Only 62% of Serrana's 45,000 residents are adults, yet a similar drop in symptomatic infections occurred in unvaccinated children, according to Ricardo Palacios, the epidemiologist who led the study.

“This was one of our concerns — that if you vaccinate all the others, probably the disease will concentrate in the children and teenagers,” he says. “But we didn’t see that.”

Herd immunity?

Similar scenarios have played out in countries with high vaccination rates, such as Israel and the United States. In the latter, cases in children (generally those under the age of 18) fell by 84% between January and May. Just over half of the US population — predominantly adults — has received at least one vaccine dose.

“It just makes sense,” says Monica Gandhi, an infectious-diseases physician at the University of California, San Francisco. Vaccinating adults protects

others who are unvaccinated. “That is really what herd immunity means,” she says.



How kids' immune systems can evade COVID

Gandhi also points to evidence that children are [less likely than adults](#) to transmit the virus — another reason why they might not act as effective reservoirs for infection¹. The way in which the virus affects children is “just different”, she says, probably because children’s airways have fewer of the receptors that SARS-CoV-2 uses to gain entry into cells.

In Israel, infection rates have plummeted in those eligible for vaccination, from 559 cases per 100,000 people aged 16 years and over in mid-January to just 1.5 per 100,000 today. Most schools reopened by March, yet rates in unvaccinated children also dived, from 546 per 100,000 to 1.5 per 100,000 in those aged 11 or under, for example.

This suggests that children are most often infected by adults, says Eric Haas, a paediatric infectious-diseases physician and epidemiologist at the Israel Ministry of Health in Jerusalem. “Otherwise, you would expect that if children go back to school, they would just infect each other en masse.”



Children return to school in Jerusalem following a nationwide lockdown in Israel. Credit: Nir Alon/ZUMA Wire/Shutterstock

A mixed picture

But not everyone reads the data that way. Julian Tang, a virologist at the University of Leicester, UK, says that the speed of the vaccination roll-out in Israel might have contributed to it stamping out infections across all age groups. “By the time they finished the adult vaccination, there was no more source [of infection] from the adults to transmit to the children, to then go into schools,” he says.

And early data from the United Kingdom — where the vaccination rate is 60% — paint a more complicated picture when it comes to unvaccinated children and their potential to spread COVID-19.

By the end of May, cases in secondary-school children had fallen from a high of around 600 cases per 100,000 in January to less than 100 per 100,000. In younger school children, the numbers are now even lower.

But recent data also suggest that unvaccinated children might still be important spreaders of the virus. During May, almost 100 outbreaks — defined as two or more cases — occurred in primary and secondary schools in England.

That number is small, however, representing just a “tiny proportion” of England’s 25,000 schools, says Shamez Ladhani, a paediatric infectious-diseases physician with Public Health England. He also notes that overall infection rates in school-aged children changed little in the six weeks after schools reopened.

Circulating variants

Nonetheless, Tang says that [transmission in schools](#) shouldn’t be ignored. Britain’s vaccine roll-out has been slower than Israel’s, he argues, and school reopenings have coincided with the increased spread of B.1.617.2 — also known as the Delta variant — in UK communities. As a result, the virus might continue to circulate in children.

This is an important point, he says, because the longer the pandemic continues, the greater the chance that new variants with some resistance to vaccines will emerge.



[COVID vaccines and kids: five questions as trials begin](#)

The extent to which unvaccinated children act as spreaders has implications for whether they should be vaccinated once the adult population has been —

a question being hotly debated.

In the United States, the Food and Drug Administration approved the Pfizer vaccine for children aged 12–18 years on 10 May, and more than 7 million of these children have now received at least one dose. Agencies in Japan, the United Kingdom, the European Union and elsewhere have since done likewise.

But severe COVID-19 in children is rare². A May 2020 analysis across 26 countries estimated that just 0.14% of children infected by SARS-CoV-2 develop dangerous inflammation³. Other complications are also uncommon, says Ghandi.

Because of the lower risk, the World Health Organization argues that vaccinating children is not a high priority, given that global supplies are insufficient to immunize all adults.

‘Extremely worrying’

“You have countries basically vaccinating individuals that don’t really need it, when there are a lot of other countries who are desperate for the vaccine,” says Kim Mulholland, a paediatrician and vaccine researcher at the Murdoch Children’s Research Institute in Melbourne, Australia. “I find that to be extremely worrying.”



Why schools probably aren't COVID hotspots

But Haas would like to see vaccination in Israel extended to children aged 12 to 15. Although the risk of severe disease is lower for children, “it’s not ‘no risk’”, he says. Vaccinating adolescents would also ensure against further disruptions to schools and provide herd immunity to unvaccinated adults, he says.

Tang also sees vaccinating children as crucial to controlling the pandemic. It would remove them as a potential reservoir for asymptomatic infections and would guard against the emergence of new variants, he says.

In an ideal world, adds Tang, you would vaccinate all age groups, so that new variants would emerge neither in unvaccinated populations of adults, nor in children. Until vaccine production meets demand, it’s important to vaccinate not only adults in low-income nations, but also children in places that already have good vaccine coverage. “You can do a bit of both,” he says.

Nature **594**, 312 (2021)

doi: <https://doi.org/10.1038/d41586-021-01549-z>

Updates & Corrections

- **Correction 15 June 2021:** An earlier version of this story gave the wrong name for the US Food and Drug Administration.

References

1. 1.

McCartney, K. *et al. Lancet Child Adolesc. Health* **4**, 807–816 (2020).

[PubMed](#) [Article](#) [Google Scholar](#)

2. 2.

Graf, K. et al. *Pediatr. Infect. Dis. J.* **40**, e137–e145 (2021).

[PubMed](#) [Article](#) [Google Scholar](#)

3. 3.

Hoang, A. et al. *EClinicalMedicine* **24**, 100433 (2020).

[PubMed](#) [Article](#) [Google Scholar](#)

[Download references](#)

Related Articles

-  [**COVID vaccines and kids: five questions as trials begin**](#)
-  [**How kids' immune systems can evade COVID**](#)
-  [**Why schools probably aren't COVID hotspots**](#)

Subjects

- [SARS-CoV-2](#)
- [Vaccines](#)
- [Diseases](#)

[**Jobs from Nature Careers**](#)

- - - [All jobs](#)
 -
 - [Post Doctoral Fellow Bioinformatics Modern and Ancient Infectious Diseases](#)
 - [Faculty of Medicine, Dalhousie University](#)
 - [Multiple locations](#)
 - [JOB POST](#)
 - [Research Fellow - Molecular Pharmacology & Experimental Therapeutics](#)
 - [Mayo Clinic Health System](#)
 - [Rochester, MN, United States](#)
 - [JOB POST](#)
 - [Research Fellow - Neurobiology](#)
 - [Mayo Clinic Health System](#)
 - [Rochester, MN, United States](#)
 - [JOB POST](#)
 - [Scientist for PETRA III Beamline P07](#)
 - [German Electron Synchrotron \(DESY\)](#)
 - [Hamburg, Germany](#)
 - [JOB POST](#)

[Download PDF](#)

Related Articles

-  [COVID vaccines and kids: five questions as trials begin](#)
-  [How kids' immune systems can evade COVID](#)
-  [Why schools probably aren't COVID hotspots](#)

Subjects

- [SARS-CoV-2](#)
- [Vaccines](#)
- [Diseases](#)

This article was downloaded by **calibre** from <https://www.nature.com/articles/d41586-021-01549-z>

- NEWS EXPLAINER
- 08 June 2021

The COVID lab-leak hypothesis: what scientists do and don't know

Nature examines arguments that the coronavirus SARS-CoV-2 escaped from a lab in China, and the science behind them.

- [Amy Maxmen](#) &
- [Smriti Mallapaty](#)

1. Amy Maxmen
[View author publications](#)

You can also search for this author in [PubMed](#) [Google Scholar](#)

2. Smriti Mallapaty
[View author publications](#)

You can also search for this author in [PubMed](#) [Google Scholar](#)





•

[Download PDF](#)



The Wuhan Institute of Virology has carried out research on coronaviruses for years because these pathogens are endemic to the region where it's located. Credit: Kyodo News via Getty

Debate over the idea that the SARS-CoV-2 coronavirus emerged from a laboratory has escalated over the past few weeks, coinciding with the annual World Health Assembly, at which the World Health Organization (WHO) and officials from nearly 200 countries discussed the COVID-19 pandemic. After last year's assembly, the WHO agreed to sponsor the first phase of an investigation into the pandemic's origins, [which took place in China in early 2021.](#)

Most scientists say SARS-CoV-2 probably has a natural origin, and was transmitted from an animal to humans. However, a lab leak has not been ruled out, and many are calling for a deeper investigation into the hypothesis that the virus emerged from the Wuhan Institute of Virology (WIV), located in the Chinese city where the first COVID-19 cases were reported. On 26 May, US President Joe Biden tasked the US Intelligence Community to join efforts to find SARS-CoV-2's origins, whatever they might be, and report back in 90 days.



Divisive COVID ‘lab leak’ debate prompts dire warnings from researchers

Australia, the European Union and Japan have also called for a robust investigation into SARS-CoV-2’s origins in China. The WHO has yet to reveal the next phase of its investigation. But China has asked that the probe examine other countries. Such reticence, and the fact that China has withheld information in the past, has fuelled suspicions of a ‘lab leak’. For instance, Chinese government officials suppressed crucial public-health data at the start of the COVID-19 pandemic, and during the 2002–04 severe acute respiratory syndrome (SARS) epidemic, according to high-level reports^{1,2}.

At the assembly, Mike Ryan, director of health emergencies at the WHO, asked for less politicization of calls for an origin investigation, which have, in many ways, devolved into accusations. “Over the last number of days, we have seen more and more and more discourse in the media, with terribly little actual news, or evidence, or new material,” said Ryan. “This is disturbing.”

Nature looks at the key arguments that support a lab leak, and the extent to which research has answers.

There’s not yet any substantial evidence for a lab leak. Why are scientists still considering it?

Scientists don't have enough evidence about the origins of SARS-CoV-2 to rule out the lab-leak hypothesis, or to prove the alternative — that the virus has a natural origin. Many infectious-disease researchers agree that the most probable scenario is that the virus evolved naturally and spread from a bat either directly to a person or through an intermediate animal. Most emerging infectious diseases begin with a spillover from nature, as was seen with HIV, influenza epidemics, Ebola outbreaks and the coronaviruses that caused the SARS epidemic beginning in 2002 and the Middle East respiratory syndrome (MERS) outbreak beginning in 2012.



Scientists found SARS-CoV-2's closest known relative, RATG13, in a horseshoe bat.Credit: Shutterstock

Researchers have some leads that support a natural origin. Bats are known carriers of coronaviruses, and scientists have determined that the genome of SARS-CoV-2 is most similar to that of RATG13, a coronavirus that was first found in a horseshoe bat (*Rhinolophus affinis*) in the southern Chinese

province of Yunnan in 2013³. But RATG13's genome is only 96% identical to SARS-CoV-2's, suggesting that a closer relative of the virus — the one passed to humans — remains unknown.

Still, the possibility remains that SARS-CoV-2 escaped from a lab. Although lab leaks have never caused an epidemic, they have resulted in small outbreaks involving well-documented viruses. A relevant example happened in 2004, when two researchers were independently infected by the virus that causes SARS at a virology lab in Beijing that studied the disease. They [spread the infection to seven others](#) before the outbreak was contained.

What are the key arguments for a lab leak?

In theory, COVID-19 could have come from a lab in a few ways. Researchers might have collected SARS-CoV-2 from an animal and maintained it in their lab to study, or they might have created it by engineering coronavirus genomes. In these scenarios, a person in the lab might have then been accidentally or deliberately infected by the virus, and then spread it to others — sparking the pandemic. There is currently no clear evidence to back these scenarios, but they aren't impossible.

People have made a number of arguments for a lab origin for SARS-CoV-2 that are currently conjecture.



[The biggest mystery: what it will take to trace the coronavirus source](#)

One holds that it's suspicious that, almost a year and a half into the pandemic, SARS-CoV-2's closest relative still hasn't been found in an animal. Another suggests it is no coincidence that COVID-19 was first detected in Wuhan, where a top lab studying coronaviruses, the WIV, is located.

Some lab-leak proponents contend that the virus contains unusual features and genetic sequences signalling that it was engineered by humans. And some say that SARS-CoV-2 spreads among people so readily that it must have been created with that intention. Another argument suggests that SARS-CoV-2 might have derived from coronaviruses found in an unused mine where WIV researchers collected samples from bats between 2012 and 2015.

So what do infectious disease researchers and evolutionary biologists say about these arguments?

Is it suspicious that no animal has been identified as transmitting the virus to humans?

Outbreak-origin investigations often take years, and some culprits remain unknown. It took 14 years to nail down the origin of the SARS epidemic, which began with a virus in bats that spread to humans, [most likely through civets](#). To date, a complete Ebola virus has never been isolated from an animal in the region where the world's largest outbreak occurred between 2013 and 2016.

Origin investigations are complicated because outbreaks among animals that aren't the main hosts of a particular virus, such as civets in the case of SARS, are often sporadic. Researchers must find the right animal before it dies or clears the infection. And, even if the animal tests positive, viruses found in saliva, faeces or blood are often degraded, making it difficult to sequence the pathogen's whole genome.



[WHO report into COVID pandemic origins zeroes in on animal markets, not labs](#)

Scientists have made some progress since the pandemic began, however. For example, a report, posted to the preprint server bioRxiv on 27 May, suggests that RmYN02, a coronavirus in bats in southern China, might be more closely related to SARS-CoV-2 than RATG13 is⁴.

As for finding an intermediate host animal, researchers in China have tested more than 80,000 wild and domesticated animals; none have been positive for SARS-CoV-2. But this number is a tiny fraction of the animals in the country. To narrow the search down, researchers say, more strategic testing is needed to isolate animals that are most susceptible to infection and those that come in close contact with people. They also suggest using antibody tests to identify animals that have previously been infected with the virus.

Is it suspicious that the WIV is in Wuhan?

Virology labs tend to specialize in the viruses around them, says Vincent Munster, a virologist at the Rocky Mountain Laboratories, a division of the National Institutes of Health, in Hamilton, Montana. The WIV specializes in coronaviruses because many have been found in and around China. Munster names other labs that focus on endemic viral diseases: influenza labs in Asia, haemorrhagic fever labs in Africa and dengue-fever labs in Latin

America, for example. “Nine out of ten times, when there’s a new outbreak, you’ll find a lab that will be working on these kinds of viruses nearby,” says Munster.

Researchers note that a coronavirus outbreak in Wuhan isn’t surprising, because it’s a city of 11 million people in a broader region where coronaviruses have been found. It contains an airport, train stations and markets selling goods and wildlife transported there from around the region⁵ — meaning a virus could enter the city and spread rapidly.

Does the virus have features that suggest it was created in a lab?

Several researchers have looked into whether features of SARS-CoV-2 signal that it was bioengineered. One of the first teams to do so, led by Kristian Andersen, a virologist at Scripps Research in La Jolla, California, determined that this was “improbable” for a few reasons, including a lack of signatures of genetic manipulation⁶. Since then, others have asked whether the virus’s furin cleavage site — a feature that helps it to enter cells — is evidence of engineering, because SARS-CoV-2 has these sites but its closest relatives don’t. The furin cleavage site is important because it’s in the virus’s spike protein, and cleavage of the protein at that site is necessary for the virus to infect cells.



After the WHO report: what's next in the search for COVID's origins

But many other coronaviruses have furin cleavage sites, such as coronaviruses that cause colds⁷. Because viruses containing the site are scattered across the coronavirus family tree, rather than confined to a group of closely related viruses, Stephen Goldstein, a virologist at the University of Utah in Salt Lake City, says the site probably evolved multiple times because it provides an evolutionary advantage. Convergent evolution — the process by which organisms that aren't closely related independently evolve similar traits as a result of adapting to similar environments — is incredibly common.

Another feature of SARS-CoV-2 that has drawn attention is a combination of nucleotides that underlie a segment of the furin cleavage site: CGG (these encode the amino acid arginine). A *Medium* article that [speculates on a lab origin](#) for SARS-CoV-2 quotes David Baltimore, a Nobel laureate and professor emeritus at the California Institute of Technology in Pasadena, as saying that viruses don't usually have that particular code for arginine, but humans often do — a “smoking gun”, hinting that researchers might have tampered with SARS-CoV-2's genome.

Andersen says that Baltimore was incorrect about that detail, however. In SARS-CoV-2, [about 3% of the nucleotides](#) encoding arginine are CGG, he says. And he points out that around 5% of those encoding arginine in the virus that caused the original SARS epidemic are CGG, too. In an e-mail to *Nature*, Baltimore says Andersen could be correct that evolution produced SARS-CoV-2, but adds that “there are other possibilities and they need careful consideration, which is all I meant to be saying”.

Is it true that SARS-CoV-2 must have been engineered, because it's perfect for causing a pandemic?

Many scientists say no. Just because the virus spreads among humans doesn't mean it was designed to do so. It also flourishes among mink and infects [a host of carnivorous mammals](#). And it wasn't optimally

transmissible among humans for the better part of last year. Rather, new, more efficient variants have evolved around the world. To name one example, the highly transmissible variant of SARS-CoV-2 first reported in India (B.1.617.2, or Delta) has mutations in the nucleotides encoding its furin cleavage site that appear to make the virus better at infecting cells⁸.

“This was not some supremely adapted pathogen,” says Joel Wertheim, a molecular epidemiologist at the University of California San Diego.

Did researchers collect SARS-CoV-2 from a mine?

Researchers from the WIV collected hundreds of samples from bats roosting in a mine between 2012 and 2015, after several miners working there had gotten sick with an unknown respiratory disease. (Last year, researchers reported that blood samples taken from the miners tested negative for antibodies against SARS-CoV-2, meaning that the sickness was probably not COVID-19⁹.) Back at the lab, WIV researchers detected nearly 300 coronaviruses in the bat samples, but they were able to get whole or partial genomic sequences from fewer than a dozen, and none of those that were reported were SARS-CoV-2^{9,10}. During the WHO-led origins probe earlier this year, WIV researchers told investigators that they cultured only three coronaviruses at the lab, and none were closely related to SARS-CoV-2.



['Major stones unturned': COVID origin search must continue after WHO report, say scientists](#)

Although the investigators didn't sift through freezers at the WIV to confirm this information, the low number of genomes and cultures doesn't surprise virologists. Munster says it's exceedingly difficult to extract intact coronaviruses from bat samples. Virus levels tend to be low in the animals, and viruses are often degraded in faeces, saliva and droplets of blood. Additionally, when researchers want to study or genetically alter viruses, they need to keep them (or synthetic mimics of them) alive, by finding the appropriate live animal cells for the viruses to inhabit in the lab, which can be a challenge.

So, for SARS-CoV-2 to have come from this mine in China, WIV researchers would have had to overcome some serious technical challenges — and they would have kept the information secret for a number of years and misled investigators on the WHO-led mission, scientists point out. There's no evidence of this, but it can't be ruled out.

What's next for lab-leak investigations?

Biden asked the US Intelligence Community to report back to him in 90 days. Perhaps this investigation will shed light on undisclosed US intel [reported by The Wall Street Journal](#) suggesting that three staff members at the WIV were sick in November 2019, before the first cases of COVID-19 were reported in China. The article claims that US officials have different opinions on the quality of that intel. And researchers at the WIV [have maintained that](#) staff at the institute tested negative for antibodies that would indicate SARS-CoV-2 infection prior to January 2020.

Last week, Anthony Fauci, Biden's chief medical adviser, asked Chinese officials to release the hospital records of WIV staff members. Others have asked for blood samples from WIV staff members, and access to WIV bat and virus samples, laboratory notebooks and hard drives. But it's unclear what such asks will yield because China has not conceded to demands for a full lab investigation. A spokesperson for the Ministry of Foreign Affairs of the People's Republic of China, Zhao Lijian, [said](#) that US labs should instead

be investigated, and that some people in the United States “don’t care about facts or truth and have zero interest in a serious science-based study of origins”.

As Biden's investigation commences and the WHO considers the next phase in its origin study, pandemic experts are bracing themselves for a long road ahead. “We want an answer,” says Jason Kindrachuk, a virologist at the University of Manitoba in Winnipeg, Canada. “But we may have to keep piecing bits of evidence together as weeks and months and years move forward.”

Nature **594**, 313-315 (2021)

doi: <https://doi.org/10.1038/d41586-021-01529-3>

References

1. 1.

The Independent Panel for Pandemic Preparedness & Response
[COVID-19: Make it the Last Pandemic](#) (Independent Panel, 2021).

2. 2.

Huang, Y. in *Learning from SARS: Preparing for the Next Disease Outbreak: Workshop Summary* (eds Knobler, S. et al.) (National Academies Press, 2004).

[Google Scholar](#)

3. 3.

Zhou P. et al. *Nature* **579**, 270–273 (2020).

[PubMed Article](#) [Google Scholar](#)

4. 4.

Lytras, S. *et al.* Preprint at bioRxiv
<https://doi.org/10.1101/2021.01.22.427830> (2021).

5. 5.

Xiao, X. *et al.* *Sci. Rep.* **11**, 11898 (2021).

[PubMed](#) [Article](#) [Google Scholar](#)

6. 6.

Andersen, K. G. *et al.* *Nature Med.* **26**, 450–452 (2020).

[PubMed](#) [Article](#) [Google Scholar](#)

7. 7.

Wu, Y. & Zhao, S. *Stem Cell Res.* **50**, 102115 (2020).

[PubMed](#) [Article](#) [Google Scholar](#)

8. 8.

Peacock, T. P. *et al.* Preprint at bioRxiv
<https://doi.org/10.1101/2021.05.28.446163> (2021).

9. 9.

Zhou, P. *et al.* *Nature* **588**, E6 (2020).

[PubMed](#) [Article](#) [Google Scholar](#)

10. 10.

Guo, H. *et al.* Preprint at bioRxiv
<https://doi.org/10.1101/2021.05.21.445091> (2021).

[Download references](#)

Related Articles

-  [Divisive COVID ‘lab leak’ debate prompts dire warnings from researchers](#)
-  [WHO report into COVID pandemic origins zeroes in on animal markets, not labs](#)
-  [‘Major stones unturned’: COVID origin search must continue after WHO report, say scientists](#)
-  [After the WHO report: what’s next in the search for COVID’s origins](#)
-  [The biggest mystery: what it will take to trace the coronavirus source](#)

Subjects

- [Public health](#)
- [Epidemiology](#)
- [Diseases](#)
- [Politics](#)
- [SARS-CoV-2](#)

Jobs from Nature Careers

- - - [All jobs](#)
 - - [Post Doctoral Fellow Bioinformatics Modern and Ancient Infectious Diseases](#)
[Faculty of Medicine, Dalhousie University](#)
[Multiple locations](#)
[JOB POST](#)
 - [Research Fellow - Molecular Pharmacology & Experimental Therapeutics](#)
[Mayo Clinic Health System](#)
[Rochester, MN, United States](#)
[JOB POST](#)
 - [Research Fellow - Neurobiology](#)
[Mayo Clinic Health System](#)
[Rochester, MN, United States](#)
[JOB POST](#)
 - [Scientist for PETRA III Beamline P07](#)
[German Electron Synchrotron \(DESY\)](#)

Hamburg, Germany

JOB POST

Download PDF

Related Articles

-  [Divisive COVID ‘lab leak’ debate prompts dire warnings from researchers](#)
-  [WHO report into COVID pandemic origins zeroes in on animal markets, not labs](#)
-  [‘Major stones unturned’: COVID origin search must continue after WHO report, say scientists](#)
-  [After the WHO report: what’s next in the search for COVID’s origins](#)
-  [The biggest mystery: what it will take to trace the coronavirus source](#)

Subjects

- [Public health](#)
 - [Epidemiology](#)
 - [Diseases](#)
 - [Politics](#)
 - [SARS-CoV-2](#)
-

This article was downloaded by **calibre** from <https://www.nature.com/articles/d41586-021-01529-3>

| [Section menu](#) | [Main menu](#) |

- NEWS FEATURE
- 15 June 2021

Forensic database challenged over ethics of DNA holdings

Geneticists say a global Y-chromosome database holds profiles from men who are unlikely to have given free informed consent.

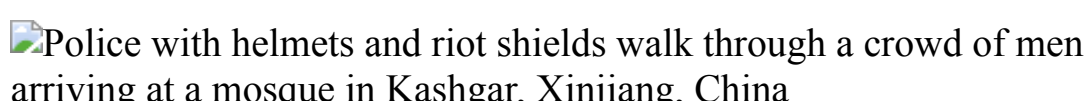
- [Quirin Schiermeier](#)
 1. Quirin Schiermeier
[View author publications](#)

You can also search for this author in [PubMed](#) [Google Scholar](#)





•



Police patrol Kashgar in China's Xinjiang region, where there are reports of systematic human-rights abuses against the Uyghur population. Credit: Johannes Eisele/AFP/Getty

[Download PDF](#)

In May 1999, a disturbing crime shocked the inhabitants of Kollum, a small village in the Netherlands. A local 16-year-old girl was found raped and murdered in a field nearby, and some people said that Iraqi or Afghan

residents at an asylum seekers' centre in the village could be to blame. Tensions rose: a fight broke out at a planning meeting about the centre. With the case unsolved, the public prosecutor turned to a newly launched research database containing Y-chromosome profiles from men across the world. When forensic scientists compared DNA from semen collected at the crime scene with profiles stored in this [Y-chromosome Haplotype Reference Database](#) (YHRD) and elsewhere, they found that the murderer was very probably of northwestern European descent, showing that the villagers' assumptions were unfounded. The discovery helped to calm social tensions — although the case was not solved for many years until, with the aid of more DNA work, a local farmer was found guilty.

The YHRD, which was first released online in 2000, is now widely used across the world to help solve sex crimes and settle paternity cases. Holding more than 300,000 anonymous Y-chromosome profiles, it shows how particular genetic markers are fingerprints of male lineages in more than 1,300 distinct global populations. It can point to the likely geographic origin of mystery males, as in the Kollum case, but is now more often relied on to calculate the weight of evidence against a male suspect whose Y-chromosome DNA profile matches traces found at a crime scene. Although the YHRD is a research database, scientists both from academia and crime laboratories have uploaded data to it, and it has become a key tool for prosecutors and defence lawyers.

“The YHRD is absolutely essential for suspects anywhere in the world to get a fair chance in court,” says Walther Parson, a forensic geneticist at Innsbruck Medical University in Austria, and the vice-president of the International Society for Forensic Genetics (ISFG).

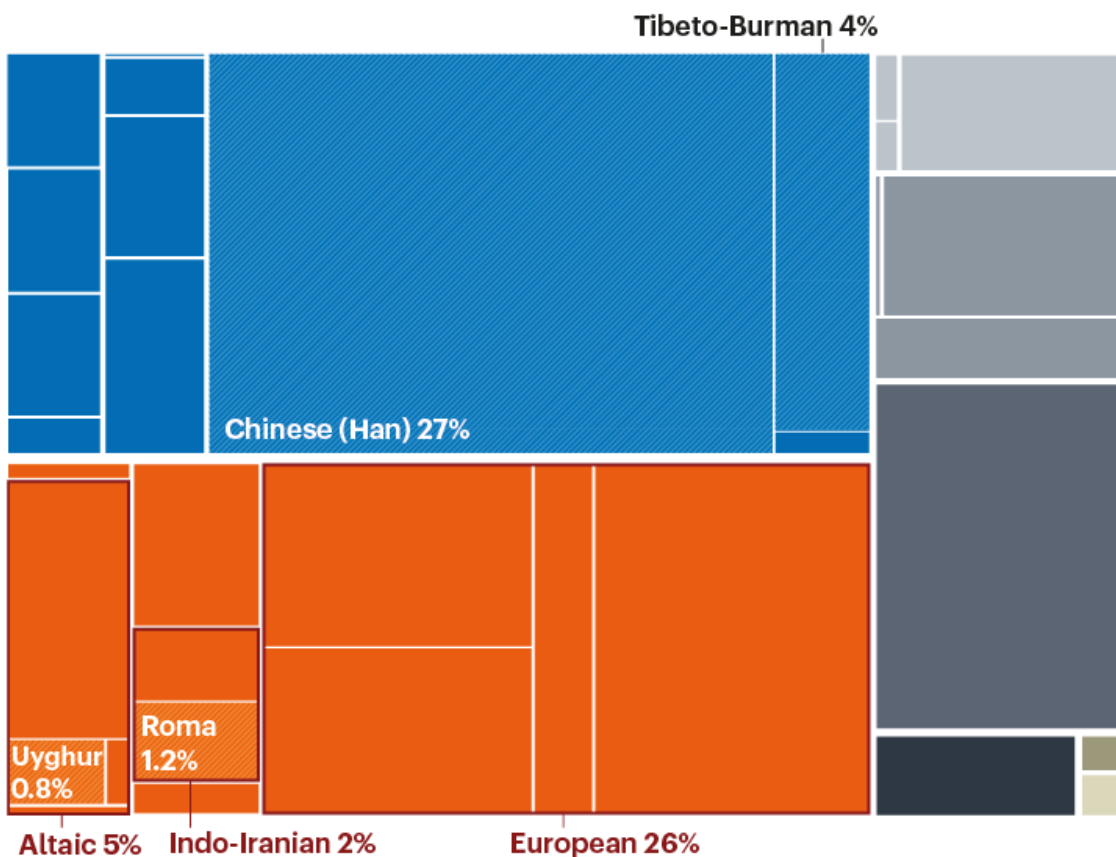
But some European geneticists say that the YHRD has an ethics problem. Thousands of the profiles it holds were obtained from men who are unlikely to have given free, informed consent, they say. These include data from minority ethnic populations such as the Uyghurs in China and the Roma in eastern Europe (see ‘Populations in a forensic database’).

POPULATIONS IN A FORENSIC DATABASE

The public Y-Chromosome Haplotype Reference Database (YHRD) holds information on signature markers in Y-chromosome profiles from men around the world. Some ethicists query whether Uyghur, Roma and other populations gave free, informed consent when providing data.

Share of YHRD profiles:

■ East Asian 41% ■ Eurasian 36% ■ Afro-Asiatic 4%
■ African 6% ■ Admixed 10% ■ Native American 2%
■ Eskimo Aleut 0.2% ■ Australian Aboriginal 0.2%



*Specific populations highlighted, using YHRD-defined meta-population names. Full breakdown at <https://yhrd.org/pages/resources/stats#metapopulations>. Data as of 9 May 2021.

©nature

Source: Y-chromosome Haplotype Reference Database

The criticisms raise questions about consent checks at the YHRD and other databases. They are also the latest strand of a wider campaign to draw attention to a ramping-up of DNA profiling across the world in the absence

of stringent ethical oversight. Some researchers are calling for geneticists to dissociate themselves from this by ensuring that such DNA studies are not given credence by being published in academic journals or databases.

Yves Moreau, a computational biologist at the Catholic University of Leuven in Belgium, has been leading calls for journals and the YHRD to investigate potentially unethical studies. He focuses on China, where the authorities have drawn international condemnation for mass detentions and human-rights abuses in the northwestern Xinjiang province. Journalists, human-rights groups and academics have collected testimonies from the Uyghurs, a predominantly Muslim population there, of abuses that include the forced collection of DNA. (The Chinese government says it is engaged in a re-education campaign in Xinjiang to quell a terrorist movement.)



[China's massive effort to collect its people's DNA concerns scientists](#)

“China is pursuing, and trying to export, an authoritarian political model based on surveillance technology, including genetic surveillance of minorities,” says Moreau, who also notes a controversial Chinese effort to build a domestic forensic database by [collecting DNA from millions of men across the country](#). “Researchers, database curators and science publishers should not be complicit in this model — absolutely in no way.”

In part because of Moreau's work, one set of DNA profiles has been removed from the YHRD, but many more have been questioned. *Nature* has learnt that the ISFG is now setting up an oversight board to examine cases in which consent is unclear. "Some might think that ethics is merely a lot of annoying bureaucracy," says Moreau. "But that's a false perception. Researchers must understand that they won't get recognition for unethical research."

Ethics concerns

Police forces in many nations collect DNA from suspected or convicted criminals, but usually keep this information privately for a limited time (defined by national law) and do not seek consent that would allow it to be shared publicly. By contrast, public, international DNA research databases that map human genetic diversity contain information acquired from across populations, and require that researchers who upload data have ethics-committee approval and informed consent from participants for their studies. These databases allow scientists to calculate the frequency with which particular inherited genetic clusters exist in populations, findings that are often useful for medical research.



[Science publishers review ethics of research on Chinese minority groups](#)

The YHRD is the largest database to focus on male lineages, and is unusual for its close connection to forensics and crime-solving. It is curated by two forensic geneticists, Sascha Willuweit and Lutz Roewer, who are both at Berlin's largest research hospital, the Charité. In common with other databases, it asks for, but doesn't verify, consent or ethical approval. Researchers who wish to upload data to it are encouraged to first publish an academic paper about their study — which puts the onus on a scientific journal to check for ethical compliance. In about 10% of cases, says Roewer, scientists have uploaded data without publishing a paper about their work.

In March 2019, Moreau began looking into studies of minority populations in China. He spotted a 2017 review¹ of almost 38,000 Y-chromosome profiles of men in China, held in the YHRD. It was co-authored by Willuweit and Roewer; other authors included researchers from Chinese public-security and police forces. “I realized that the YHRD was a problem,” says Moreau. The review stated that the profiles had been collected with informed consent — but Moreau argues that it’s hard to see how Uyghurs and other persecuted minority groups could have freely given it.

Moreau went on to find dozens of articles in leading international forensics journals, co-authored by members of the Chinese police, that described DNA profiling of Tibetans, Uyghurs and other minority groups. Most of these papers were not related to the YHRD. He contacted Springer Nature, which publishes some of the journals, and it began to investigate. (*Nature*'s news team is editorially independent of its publisher.) In December 2019, Moreau published his concerns in an opinion article², without mentioning the YHRD. Then, in January 2020, he asked the Charité to investigate. It declined, saying that it hosted but did not own or operate the database, a stance it has reiterated to *Nature*. Moreau began discussing his concerns with Roewer and Willuweit.

Roewer says he agrees with Moreau that researchers shouldn’t be using DNA taken without informed consent — but says that it is not the YHRD’s job to check or to initiate investigations. “We are not an ethical control body,” he says. (He also says that, because the 2017 study was a review of already-collated data, it didn’t need ethics approval.)



Crack down on genomic surveillance

Last year, Roewer removed profiles that had been uploaded by the authors of a paper describing DNA studies of Uyghur, Kazakh and Hui minority groups in China. He did so after Springer Nature investigated and [retracted that paper](#); the authors said that the study had been undertaken without the approval of an institutional ethics committee. Roewer says he'll remove related data if there are other retractions. Springer Nature has so far added editor's notes to 28 papers — including the 2017 review — stating that concerns have been raised about their ethics-approval and informed-consent procedures. It has also retracted a second paper. “We do expect to take further editorial action in at least some of these cases,” a spokesperson says. Moreau says he has identified at least nine other potentially problematic studies — involving co-authors from the Chinese police — for which data appear on the YHRD, but hasn't yet alerted journal editors or publishers to those concerns.

The YHRD contains eight data sets of Uyghur profiles that were uploaded directly. Roewer says that in these cases, too, it is not his responsibility to initiate investigations. “Anyone concerned about a particular data set would do better to contact the authors directly,” he says. (*Nature* e-mailed 15 researchers who'd uploaded Uyghur data; one, Yiping Hou, a forensic geneticist at Sichuan University in Chengdu, replied that the data were obtained with “valid informed consent”.)

In November 2020, the YHRD was criticized from a different angle when three researchers in Germany — science historian Veronika Liphhardt, sociologist Mihai Surdu, both at the University of Freiburg, and geneticist Gudrun Rappold at the University of Heidelberg — published preprints of their work on genetic studies about the Roma^{[3,4](#)}. The researchers noted that the YHRD holds profiles from population studies on eastern European Roma and, in some cases, that the uploaders' studies didn't make clear whether they obtained informed consent, or when the profiles were collected — and that they sometimes thanked police forces for collecting the DNA. "It is extremely doubtful that such studies were always done with people's fully informed consent," Liphhardt says, adding that there is a long history of discrimination against the Roma.



A Roma man walks in the remains of a house demolished by a bulldozer in a Roma suburb in the city of Plovdiv. Credit: Nikolay Doychinov/AFP/Getty

Liphhardt tried to follow up one such concern^{[4](#)}: in 2017, German police uploaded to the YHRD 74 profiles of male Romanians and Afghans living in Germany. Liphhardt asked the relevant criminal investigation authority — in the state of Baden-Württemberg — whether the data were described in a

paper, but was told that authorities considered the YHRD upload sufficient publication, and so no information was available on ethics procedures or consent. “Criminal investigators obviously have less stringent ethical standards than academic scientists when collecting and working with genetic information,” she says. Roewer says the criminal-investigation authority did talk to him about the issue, but it decided not to retract the data sets.

The field of forensic genetics was slow to catch up with ethical standards of biomedical genetics, Liphhardt says. It was only in 2010 that leading forensics journals introduced requirements for authors to mention informed consent or approval by ethics committees. Much of the data in forensic databases, including the YHRD, was collected before 2010, so even when data are connected to research papers, it is hard to find ethics statements.

The YHRD isn’t the only international database under scrutiny. In their preprint⁴, Liphhardt and Surdu note that a mitochondrial-DNA database called EMPOP also holds Roma data from journal studies that don’t explicitly state they have informed consent or ethical approval. (EMPOP is not a public database; its users must register.) Parson, who curates EMPOP, says that all profiles undergo “rigorous quality control” including ethical evaluation before they are uploaded, and adds that the Roma data were published in scientific journals with ethical requirements to which EMPOP adheres.

Peter Schneider, a forensic geneticist at the University of Cologne in Germany, says that because the YHRD and other databases hold information only on particular genetic markers, and not full DNA sequences, individual donors can’t be uniquely identified. He thinks that in such cases, keeping data accessible is more beneficial to society than harmful to an individual.

Roewer says that when there are concerns over consent procedures for uploaded DNA profiles that were never described in journals, an independent, objective board of experts should investigate them. The ISFG is going to set one up, he and Parson say: the society is currently deciding the panel’s remit.

Public outcry

The YHRD ethical discussion was bubbling behind the scenes, but spilled out online after Liphardt and her colleagues published their studies, which the newspaper [Süddeutsche Zeitung reported on](#). Then, in January 2021, the Charité decided to close the department for forensic genetics which maintains the YHRD — not for ethical reasons, but for economic ones. A court ruling had required German police authorities to allow competition to provide DNA analysis for criminal investigations, which meant that the department could lose much of a guaranteed income stream that it had relied on.

The decision, made public in February, caused a [huge outcry among geneticists and public prosecutors](#) fearing loss of forensic expertise, who also pointed out how useful the YHRD was. In March, the Wie-DNA initiative, a group of social scientists, geneticists and anthropologists who analyse how DNA is used, and which includes Liphardt, [issued a statement](#) saying it hoped the forensic institute could be saved, but also noting the ethical concerns around the YHRD's holdings.

In April, the Charité yielded to mounting political pressure and reversed its decision — but in May, the [Berliner Zeitung newspaper reported](#) that researchers in the Charité's forensic genetics institute would all be offered jobs direct with police authorities. (A Charité spokesperson told *Nature* that nothing had been decided, but that Roewer and Willuweit would preserve the YHRD in any eventuality.)

But the wider ethical debate continues. This January, Moreau and two other researchers writing on behalf of the European Society of Human Genetics published a commentary⁵ calling for academic institutions worldwide to stop collaborations with groups over which there are ethical concerns. “These problems extend beyond China,” the commentary stated, giving the example of the YHRD. “We would like to see an end to collaborations between academic and clinical institutions worldwide and institutions in countries carrying out widespread, unethical DNA collections and/or analysis.” The authors added that any study involving police or judicial authorities in authoritarian regimes should be considered “potentially ethically tainted”.

Parson says that, although he agrees that genetic profiles obtained without informed consent should be removed from databases, the YHRD must not be

curtailed more than necessary. Removing lineages of minority groups might distort analyses of the likelihood of a particular Y-chromosome profile coming from such a population. “Judges anywhere in the world rely on robust forensic data,” he says. “Excluding data from minority groups could bias statistical evaluations in forensic reports — to their disadvantage.”

Nature **594**, 320–322 (2021)

doi: <https://doi.org/10.1038/d41586-021-01584-w>

References

1. 1.

Nothnagel, M. *et al.* *Hum. Genet.* **136**, 485–497 (2017).

[PubMed](#) [Article](#) [Google Scholar](#)

2. 2.

Moreau, Y. *Nature* **576**, 36–38 (2019).

[PubMed](#) [Article](#) [Google Scholar](#)

3. 3.

Liphardt, V., Rappold, G. & Surdu, M. Preprint at ResearchGate
<https://doi.org/10.13140/RG.2.2.13286.04165> (2020).

4. 4.

Liphardt, V. & Surdu, M. Preprint at ResearchGate
<https://doi.org/10.13140/RG.2.2.16641.48484> (2020).

5. 5.

Forzano, F. *et al.* *Eur. J. Hum. Genet.* **29**, 894–896 (2021).

[PubMed](#) [Article](#) [Google Scholar](#)

[Download references](#)

Related Articles



- [China's massive effort to collect its people's DNA concerns scientists](#)



- [Science publishers review ethics of research on Chinese minority groups](#)



- [Crack down on genomic surveillance](#)

Subjects

- [Databases](#)
- [Genetics](#)
- [Ethics](#)
- [Law](#)

[Jobs from Nature Careers](#)

- - - [All jobs](#)
 -
 - [Post Doctoral Fellow Bioinformatics Modern and Ancient Infectious Diseases](#)

[Faculty of Medicine, Dalhousie University](#)

[Multiple locations](#)

[JOB POST](#)

- [Research Fellow - Molecular Pharmacology & Experimental Therapeutics](#)

[Mayo Clinic Health System](#)

[Rochester, MN, United States](#)

[JOB POST](#)

- [Research Fellow - Neurobiology](#)

[Mayo Clinic Health System](#)

[Rochester, MN, United States](#)

[JOB POST](#)

- [Scientist for PETRA III Beamline P07](#)

[German Electron Synchrotron \(DESY\)](#)

[Hamburg, Germany](#)

[JOB POST](#)

[Download PDF](#)

Related Articles

-  [China's massive effort to collect its people's DNA concerns scientists](#)
-  [Science publishers review ethics of research on Chinese minority groups](#)
-  [Crack down on genomic surveillance](#)

Subjects

- [Databases](#)
- [Genetics](#)
- [Ethics](#)
- [Law](#)

This article was downloaded by **calibre** from <https://www.nature.com/articles/d41586-021-01584-w>

Books & Arts

- **Katherine Johnson's memoir charts her bold trajectory to NASA and beyond** [14 June 2021]

Book Review • Mathematician overcame the gravitational pulls of gender and racial discrimination to play a key part in the space race.

- BOOK REVIEW
- 14 June 2021

Katherine Johnson's memoir charts her bold trajectory to NASA and beyond

Mathematician overcame the gravitational pulls of gender and racial discrimination to play a key part in the space race.

- [Ainissa Ramirez](#) ⁰

1. Ainissa Ramirez

1. Ainissa Ramirez (www.ainissaramirez.com) is a materials scientist and author of *The Alchemy of Us*. She has written a series of forthcoming children's picture books on Black inventors. Twitter: [@ainissaramirez](https://twitter.com/ainissaramirez)

[View author publications](#)

You can also search for this author in [PubMed](#) [Google Scholar](#)





•

[Download PDF](#)



Katherine Johnson performing calculations for space missions at NASA in 1966. Credit: NASA

My Remarkable Journey: A Memoir *Katherine Johnson, Joyelle Hylick & Katherine Moore, with Lisa Frazier Page Amistad (2021)*

When *Star Trek* first aired in the 1960s, communications officer Uhura (Nichelle Nichols) seemed to be the only Black woman affiliated with space travel. Little did society know that, as mathematicians, Black women such as Katherine Johnson actually made space flight possible. Johnson, who was highlighted in the 2016 blockbuster movie *Hidden Figures*, died last year, aged 101. She left readers a gift. *My Remarkable Journey* is a masterful memoir of a life well lived. Written with her daughters and an award-winning journalist, it captures Johnson's story against the backdrop of a dramatic century of US history.

It begins with exuberance, describing how public recognition changed her final years, from attending the Oscars in 2017 to being honoured with the Presidential Medal of Freedom in 2015 — and getting a kiss from president Barack Obama. After that, Johnson unfolds how a mathematics prodigy from White Sulphur Springs, West Virginia, became a 'human computer' for some of the most watched rocket launches in history. At NASA, she calculated trajectories and launch windows for the Project Mercury human space-flight programme. Meanwhile, she had to navigate her own path in an age when segregation and disenfranchisement were legal in the United States.



[Katherine Johnson \(1918–2020\)](#)

She entitles her chapters with life lessons — ‘Education Matters’, ‘Ask Brave Questions’, ‘Shoot for the Moon’. Johnson recognizes that she is a role model, and that few women and people of colour see their reflections in the sciences. I felt like I was sitting at the knee of a griot — a historian and storyteller — gaining years of insight into how to use idle times to prepare, to keep moving forwards when life hurts. Her down-home way of explaining science is enjoyable, too. Comparing orbital prediction with hunting, she writes: “You aim where you think the rabbit will be.”

Family support

Just as a rocket thrusts a space capsule upwards, Johnson benefited from the sacrifices of her parents. She and her three siblings moved 190 kilometres to Institute, West Virginia, to attend a school for Black pupils that went beyond primary grades. Her father, who had his own gift for numbers, taught her that she was “equal to anyone, no matter what the laws or traditions said”. This lesson stabilized her trajectory.

At 14, she entered West Virginia State College (now West Virginia State University) in Institute. There, her professor gave her a mission — to become a research mathematician. William Waldron Schieffelin Claytor was a gifted topologist whose own career was later stymied by academic racism. He prepared his protégé for her window of opportunity with one-on-one instruction in analytic geometry of space. Unknowingly, he furnished her with the boost she needed years later. Claytor exemplified the African American adage “lift as we climb”.



Katherine Johnson receiving the Presidential Medal of Freedom in 2015 from Barack Obama. Credit: Carlos Barria/Reuters/Alamy

Born in 1918, Johnson sat ringside to the Great Depression, the cold war and the US civil-rights movement, as well as the space race. Her life weaves through this greater tapestry, providing a deeper understanding of the past century. Johnson joined the precursor to NASA — the National Advisory Committee for Aeronautics — in the summer of 1953. Even before that, she shaped history. In 1939, she and two other Black students were selected by the president of West Virginia State College, a historically Black institution, to attend the previously all-white West Virginia University in Morgantown, desegregating it nearly two decades before the Little Rock Nine did the same for a high school in Arkansas in 1957. Johnson's path to NASA was as significant as the work she did there.

The pinnacle of the book is a story that appeared on the big screen — but Johnson's account is more gripping. She was indeed “the girl” on whom astronaut John Glenn called to hand-check the computer’s plan for his 1962 orbit of Earth, the first by an American. Hollywood embellished the scene; Johnson doesn’t need to. A depiction of performing calculations has never

been so engrossing. “I was the error checker, the last stop,” she writes. Although we know the outcome, there’s relief when the numbers agree. For one moment, a launch — and a nation — relied on Johnson’s mighty pencil.

Hidden stories

She also celebrates a world rarely seen in science-history books — that of working- to middle-class southern African Americans of the mid-twentieth century. Of course, Johnson did not live unscathed by the realities of the Jim Crow laws: she describes incidents such as her daughter being refused admission to a segregated hospital. And she experienced microaggressions intended to ‘keep her in her place’. When her white adviser at West Virginia University asks, “What are you going to do with this advanced degree?” he is enraged by what he considers an audacious comparison to himself when she says she will do the same thing as him. She recalls: “I hadn’t intended to insult him, but it did not bother me either.”



Hidden Figures: the movie

She created a full life of friends and family. She leant on her community during hardships, such as a house fire and her first husband’s death. She cultivated camaraderie with other educated Black women in her university sorority, Alpha Kappa Alpha. And she was nurtured by Black colleges.

Much achievement has been forged in these key institutions, as evidenced by US vice-president Kamala Harris, who studied at the historically Black Howard University in Washington DC. Johnson illuminates this inspiring world, long overlooked by dominant narratives. Yes, she writes about the space race — but she also writes about spaces where others enabled her to thrive, and about race.

My Remarkable Journey keenly shows how Johnson overcame the gravitational pulls of gender and racial discrimination. Decades ago, after she completed her calculations for the rendezvous between the lunar and command module for the eventual Apollo mission to the Moon, she said “my part was done”. With this final, beautiful opus, it is, indeed.

Nature **594**, 323-324 (2021)

doi: <https://doi.org/10.1038/d41586-021-01585-9>

Competing Interests

The author declares no competing interests.

Related Articles

-  [Katherine Johnson \(1918–2020\)](#)
-  [Hidden Figures: the movie](#)
-  [The Harvard computers](#)



- [How to get more women and people of colour into graduate school — and keep them there](#)



- [Three extraordinary women run the gauntlet of science — a documentary](#)

Subjects

- [History](#)
- [Astronomy and astrophysics](#)

Jobs from Nature Careers

- - - [All jobs](#)
 -
 - [Post Doctoral Fellow Bioinformatics Modern and Ancient Infectious Diseases](#)
 - [Faculty of Medicine, Dalhousie University](#)
 - [Multiple locations](#)
 - [JOB POST](#)
 - [Research Fellow - Molecular Pharmacology & Experimental Therapeutics](#)
 - [Mayo Clinic Health System](#)

[Rochester, MN, United States](#)

[JOB POST](#)

- [Research Fellow - Neurobiology](#)

[Mayo Clinic Health System](#)

[Rochester, MN, United States](#)

[JOB POST](#)

- [Scientist for PETRA III Beamline P07](#)

[German Electron Synchrotron \(DESY\)](#)

[Hamburg, Germany](#)

[JOB POST](#)

[Download PDF](#)

Related Articles



[Katherine Johnson \(1918–2020\)](#)



[Hidden Figures: the movie](#)



[The Harvard computers](#)



- [How to get more women and people of colour into graduate school — and keep them there](#)



- [Three extraordinary women run the gauntlet of science — a documentary](#)

Subjects

- [History](#)
- [Astronomy and astrophysics](#)

This article was downloaded by **calibre** from <https://www.nature.com/articles/d41586-021-01585-9>

| [Section menu](#) | [Main menu](#) |

Opinion

- **ISSCR guidelines fudge heritable human-genome editing** [15 June 2021]
Correspondence •
- **Don't abandon 14-day limit on embryo research, it makes sense** [15 June 2021]
Correspondence •
- **Concern over use of the term Z-DNA** [15 June 2021]
Correspondence •
- **Regulate waste recycling internationally** [15 June 2021]
Correspondence •

- CORRESPONDENCE
- 15 June 2021

ISSCR guidelines fudge heritable human-genome editing

- [Françoise Baylis](#) ORCID: <http://orcid.org/0000-0003-2961-5802> ✉

1. [Françoise Baylis](#)

1. Dalhousie University, Halifax, Nova Scotia, Canada. WHO Expert Advisory Committee on the Governance of Human Genome Editing.

[View author publications](#)

You can also search for this author in [PubMed](#) [Google Scholar](#)





•

[Download PDF](#)

I note troubling inconsistencies in the revised guidelines for stem-cell research and clinical translation, issued in May by the International Society for Stem Cell Research (ISSCR; see [Nature 594, 18–19; 2021](#)). These imply that, in time, research that involves making heritable changes to the human genome will be permitted.

On page 9, the guidelines divide research into review categories. Research that is “not allowed” is split into 3A (“currently unsafe”, with no mention of ethics) and 3B (“lacks compelling scientific rationale or is ethically

concerning”). Yet page 14 mentions ethics in both categories, and rebadges 3A as “currently not permitted” and 3B as “prohibited”.

Heritable human-genome editing is explicitly designated 3A. But, depending on one’s perspectives, and whether referring to page 9 or 14, it could just as legitimately be in 3B. There are sound arguments to support the view that research into heritable human-genome editing lacks a compelling scientific rationale and is ethically concerning. (See my 2019 book *Altered Inheritance*.)

Further, a survey last year found that 75 of 96 countries with policies on such research prohibit it; none of the 106 countries surveyed permits it ([E. Baylis et al. CRISPR J. 3, 365–377; 2020](#)). So why is reference to research that is “illegal in many jurisdictions” included in the 2016 guidelines and not in the 2021 guidelines?

Nature **594**, 333 (2021)

doi: <https://doi.org/10.1038/d41586-021-01618-3>

Competing Interests

The author declares no competing interests.

Related Articles

- [See more letters to the editor](#)

Subjects

- [Ethics](#)
- [Policy](#)
- [Developmental biology](#)

[Jobs from Nature Careers](#)

- - - [All jobs](#)
 - - [**Post Doctoral Fellow Bioinformatics Modern and Ancient Infectious Diseases**](#)
[Faculty of Medicine, Dalhousie University](#)
[Multiple locations](#)
[JOB POST](#)
 - [**Research Fellow - Molecular Pharmacology & Experimental Therapeutics**](#)
[Mayo Clinic Health System](#)
[Rochester, MN, United States](#)
[JOB POST](#)
 - [**Research Fellow - Neurobiology**](#)
[Mayo Clinic Health System](#)
[Rochester, MN, United States](#)
[JOB POST](#)
 - [**Scientist for PETRA III Beamline P07**](#)
[German Electron Synchrotron \(DESY\)](#)
[Hamburg, Germany](#)

JOB POST

[Download PDF](#)

Related Articles

- [See more letters to the editor](#)

Subjects

- [Ethics](#)
- [Policy](#)
- [Developmental biology](#)

This article was downloaded by **calibre** from <https://www.nature.com/articles/d41586-021-01618-3>

| [Section menu](#) | [Main menu](#) |

- CORRESPONDENCE
- 15 June 2021

Don't abandon 14-day limit on embryo research, it makes sense

- [Ronald M. Green](#) ORCID: <http://orcid.org/0000-0003-2844-6007>⁰,
- [Michael D. West](#) ORCID: <http://orcid.org/0000-0002-4842-5468>¹ &
- [Leonard Hayflick](#) ORCID: <http://orcid.org/0000-0003-1831-844X>²

1. [Ronald M. Green](#)

1. Dartmouth College, Hanover, New Hampshire, USA.

[View author publications](#)

You can also search for this author in [PubMed](#) [Google Scholar](#)

2. Michael D. West

1. AgeX Therapeutics, Alameda, California, USA.

[View author publications](#)

You can also search for this author in [PubMed](#) [Google Scholar](#)

3. Leonard Hayflick

1. University of California, San Francisco, USA.

[View author publications](#)

You can also search for this author in [PubMed](#) [Google Scholar](#)





•

[Download PDF](#)

As supporters of human-embryo research, we are troubled by the recommendations from the International Society for Stem Cell Research (ISSCR) to allow some *in vitro* studies of human embryo-like entities beyond the 14-day limit (see go.nature.com/3gfkw8 and *Nature* **593**, 479; 2021).

There are 4 compelling reasons for the 14-day limit. Its clarity leaves little room for misinterpretation. It corresponds to important biological events, including the beginning of ectoderm/neural progenitors. In marking the end

of the possibilities of twinning or chimaerism, it is the start of a unique biological identity. There is no later relevant nexus of events.

The guidelines recommend instead case-by-case approval for integrated embryos that are based on stem cells. This would permit research up to the “minimum time necessary” for scientific questions deemed “highly meritorious” through a “rigorous review process”.

We caution that these utilitarian objectives are limitless. Furthermore, the questions deemed “highly meritorious” can be addressed using *in vivo* murine or non-human primate models.

The ISSCR must offer more-compelling arguments for abandoning the 14-day limit.

Nature **594**, 333 (2021)

doi: <https://doi.org/10.1038/d41586-021-01619-2>

Competing Interests

The authors declare no competing interests.

Related Articles

- [See more letters to the editor](#)

Subjects

- [Stem cells](#)
- [Research management](#)
- [Policy](#)

[Jobs from Nature Careers](#)

-

- - [All jobs](#)
 - - **[Post Doctoral Fellow Bioinformatics Modern and Ancient Infectious Diseases](#)**
[Faculty of Medicine, Dalhousie University](#)
[Multiple locations](#)
[JOB POST](#)
 - **[Research Fellow - Molecular Pharmacology & Experimental Therapeutics](#)**
[Mayo Clinic Health System](#)
[Rochester, MN, United States](#)
[JOB POST](#)
 - **[Research Fellow - Neurobiology](#)**
[Mayo Clinic Health System](#)
[Rochester, MN, United States](#)
[JOB POST](#)
 - **[Scientist for PETRA III Beamline P07](#)**
[German Electron Synchrotron \(DESY\)](#)
[Hamburg, Germany](#)
[JOB POST](#)

[Download PDF](#)

Related Articles

- [See more letters to the editor](#)

Subjects

- [Stem cells](#)
- [Research management](#)
- [Policy](#)

This article was downloaded by **calibre** from <https://www.nature.com/articles/d41586-021-01619-2>

| [Section menu](#) | [Main menu](#) |

- CORRESPONDENCE
- 15 June 2021

Concern over use of the term Z-DNA

- [Alan Herbert](#) ORCID: <http://orcid.org/0000-0002-0093-1572>⁰,
- [Andrew H.-J. Wang](#) ORCID: <http://orcid.org/0000-0002-0016-5337>¹,
- [Thomas M. Jovin](#) ORCID: <http://orcid.org/0000-0001-7293-5081>²,
- [Edward S. Mocarski](#) ORCID: <http://orcid.org/0000-0002-8362-9490>³
- ,
- [Manolis Pasparakis](#) ORCID: <http://orcid.org/0000-0002-9870-0966>⁴
&
- [Karen M. Vasquez](#) ORCID: <http://orcid.org/0000-0002-6958-5073>⁵

1. [Alan Herbert](#)

1. InsideOutBio, Charlestown, Massachusetts, USA.

[View author publications](#)

You can also search for this author in [PubMed](#) [Google Scholar](#)

2. Andrew H.-J. Wang

1. Institute of Biological Chemistry, Academia Sinica, Nankang, Taipei, Taiwan.

[View author publications](#)

You can also search for this author in [PubMed](#) [Google Scholar](#)

3. Thomas M. Jovin

1. Max Planck Institute for Biophysical Chemistry, Göttingen, Germany.

[View author publications](#)

You can also search for this author in [PubMed](#) [Google Scholar](#)

4. Edward S. Mocarski

1. Emory University, Atlanta, Georgia, USA.

[View author publications](#)

You can also search for this author in [PubMed](#) [Google Scholar](#)

5. Manolis Pasparakis

1. University of Cologne, Germany.

[View author publications](#)

You can also search for this author in [PubMed](#) [Google Scholar](#)

6. Karen M. Vasquez

1. University of Texas at Austin, Texas, USA.

[View author publications](#)

You can also search for this author in [PubMed](#) [Google Scholar](#)





•

[Download PDF](#)

We are writing to express our concern over use of the term Z-DNA to describe a right-handed, double-stranded Watson–Crick helix that incorporates the modified base diaminopurine (also known as 2-aminoadenine; see [Nature 593, 181; 2021](#)). This use of Z-DNA is, we contend, confusing to scientists and the general public.

Z-DNA is the long-established nomenclature for a left-handed DNA structure first detailed at atomic resolution in 1979 ([A. H.-J. Wang et al. Nature 282, 680–686; 1979](#)). Z-DNA and Z-RNA have an essential role in

regulating type I interferon responses and programmed cell death by necroptosis. In other contexts, Z-DNA produces genomic instability, resulting in evolutionary adaptations and also in diseases such as cancer.

There are many examples of DNA structures that incorporate unusual or modified bases, but there is no precedent for renaming a structure because of this characteristic. In our view, a term other than Z-DNA should be used to characterize such findings.

Nature **594**, 333 (2021)

doi: <https://doi.org/10.1038/d41586-021-01595-7>

Competing Interests

The authors declare no competing interests.

Related Articles

- [See more letters to the editor](#)

Subjects

- [Genetics](#)
- [Structural biology](#)

[Jobs from Nature Careers](#)

- - - [All jobs](#)
 -
 - [Post Doctoral Fellow Bioinformatics Modern and Ancient Infectious Diseases](#)

[Faculty of Medicine, Dalhousie University](#)

[Multiple locations](#)

[JOB POST](#)

- [Research Fellow - Molecular Pharmacology & Experimental Therapeutics](#)

[Mayo Clinic Health System](#)

[Rochester, MN, United States](#)

[JOB POST](#)

- [Research Fellow - Neurobiology](#)

[Mayo Clinic Health System](#)

[Rochester, MN, United States](#)

[JOB POST](#)

- [Scientist for PETRA III Beamline P07](#)

[German Electron Synchrotron \(DESY\)](#)

[Hamburg, Germany](#)

[JOB POST](#)

[Download PDF](#)

Related Articles

- [See more letters to the editor](#)

Subjects

- [Genetics](#)
- [Structural biology](#)

This article was downloaded by **calibre** from <https://www.nature.com/articles/d41586-021-01595-7>

| [Section menu](#) | [Main menu](#) |

- CORRESPONDENCE
- 15 June 2021

Regulate waste recycling internationally

- [Zhe Liu](#) ✉

1. [Zhe Liu](#)

1. Xi'an Jiaotong University, Shaanxi Province, China.

[View author publications](#)

You can also search for this author in [PubMed](#) [Google Scholar](#)





•

[Download PDF](#)

China's 2017 ban on several types of waste import, and subsequent bans by countries in southeast Asia, stimulated a global trade in plastic waste. I call for improvements in the system to optimize the environmental benefits of waste reuse.

Recycling accords with the principles of a circular economy (see [Y. Geng et al. *Nature* 565, 153–155; 2019](#)). It can conserve resources, protect the environment and help to cut greenhouse-gas emissions ([Z. Liu et al. *J.*](#)

Environ. Mgmt **287**, 112283; 2021). But poor infrastructure for waste reuse turns some countries — Turkey, for instance — into a dumping ground.

To encourage more countries to recycle global waste, the process needs to be better organized and must conform to a set of international standards and regulations. Setting up an international database would help stakeholders to identify various categories of waste for reuse. Distribution chains from waste exporters to waste importers could become more efficient, environmentally friendly and cost-effective if backed by proper technical support at both ends.

Nature **594**, 333 (2021)

doi: <https://doi.org/10.1038/d41586-021-01620-9>

Competing Interests

The author declares no competing interests.

Related Articles

- [See more letters to the editor](#)

Subjects

- [Developing world](#)
- [Databases](#)
- [Economics](#)
- [Environmental sciences](#)

[Jobs from Nature Careers](#)

- - - [All jobs](#)

- **Post Doctoral Fellow Bioinformatics Modern and Ancient Infectious Diseases**

Faculty of Medicine, Dalhousie University

Multiple locations

JOB POST

- **Research Fellow - Molecular Pharmacology & Experimental Therapeutics**

Mayo Clinic Health System

Rochester, MN, United States

JOB POST

- **Research Fellow - Neurobiology**

Mayo Clinic Health System

Rochester, MN, United States

JOB POST

- **Scientist for PETRA III Beamline P07**

German Electron Synchrotron (DESY)

Hamburg, Germany

JOB POST

Download PDF

Related Articles

- [See more letters to the editor](#)

Subjects

- [Developing world](#)
- [Databases](#)
- [Economics](#)
- [Environmental sciences](#)

This article was downloaded by **calibre** from <https://www.nature.com/articles/d41586-021-01620-9>

| [Section menu](#) | [Main menu](#) |

Research

- **[Most rivers and streams run dry every year](#)** [16 June 2021]

News & Views • A model of the world's rivers and streams has been developed to predict which of these watercourses flow all year round and which go dry. The analysis shows that rivers and streams that run dry are ubiquitous throughout the world.

- **[Contact-tracing app curbed the spread of COVID in England and Wales](#)** [25 May 2021]

News & Views • Digital contact tracing has the potential to limit the spread of COVID-19. A contact-tracing smartphone app that has been readily adopted by people in England and Wales has shown efficacy in reducing disease spread.

- **[Glutamate receptor complexes open up and reveal their molecular dialect](#)** [02 June 2021]

News & Views • AMPA receptors are a class of protein complexes crucial for neuronal communication. Two complementary studies converge on structures of AMPA receptors found in a brain region called the hippocampus.

- **[Cancer stem cells in the gut have a bad influence on neighbouring cells](#)** [02 June 2021]

News & Views • Malignant stem cells in the gut secrete factors that promote the differentiation of neighbouring stem cells, thereby aiding the replacement of normal stem cells by those with cancer-promoting mutations.

- **[Attraction and repulsion cooperate during brain-circuit wiring](#)** [04 June 2021]

News & Views • Examination of the molecular interactions that govern the assembly of neural circuits in a brain region called the hippocampus reveals that neuronal projections are guided to their targets by both attractive and repulsive cues.

- **[Great Dimming of Betelgeuse explained](#)** [16 June 2021]

News & Views • Observations suggest that an unexpected dimming of the massive star Betelgeuse resulted from dust forming over a cold patch in the star's southern hemisphere. This finding improves our understanding of such massive stars.

- **[Peopling of the Americas as inferred from ancient genomics](#)** [16 June 2021]

Review Article • A review of the ancient human genomic record sheds light on the peopling processes of the Americas.

- [**The rise of intelligent matter**](#) [16 June 2021]
Perspective • Inanimate matter is beginning to show some signs of basic intelligence—the ability to sense, actuate and use memory, as controlled by an internal communication network in functional materials.
- [**A dusty veil shading Betelgeuse during its Great Dimming**](#) [16 June 2021]
Article • The southern hemisphere of Betelgeuse during its Great Dimming was an order of magnitude darker than usual, owing to a cool patch on the photosphere and associated dust formation.
- [**Correlated charge noise and relaxation errors in superconducting qubits**](#) [16 June 2021]
Article • Cosmic-ray particles and γ -rays striking superconducting circuits can generate qubit errors that are spatially correlated across several millimetres, hampering current error-correction approaches.
- [**Symmetry-enforced topological nodal planes at the Fermi surface of a chiral magnet**](#) [16 June 2021]
Article • Measurements on a chiral magnet show that non-symmorphic symmetries enforce topological crossings exactly at the Fermi level in certain materials; these crossings can be controlled by an applied magnetic field.
- [**Double-helical assembly of heterodimeric nanoclusters into supercrystals**](#) [16 June 2021]
Article • Ligand-protected gold nanoclusters are engineered to form complex arrangements of double and quadruple helices, which are based on the pairing of motifs on neighbouring enantiomers, akin to the base pairing seen in DNA double helices.
- [**Localization atomic force microscopy**](#) [16 June 2021]
Article • A localization algorithm is applied to datasets obtained with conventional and high-speed atomic force microscopy to increase image resolution beyond the limits set by the radius of the tip used.
- [**Global prevalence of non-perennial rivers and streams**](#) [16 June 2021]
Article • Non-perennial rivers and streams are mapped globally, showing that more than half of rivers worldwide experience no flow for at least one day per year.
- [**Interpreting type 1 diabetes risk with genetics and single-cell epigenomics**](#) [19 May 2021]
Article • A genome-wide association study combined with single-cell epigenomics identifies risk loci for type 1 diabetes.

- **Intercalated amygdala clusters orchestrate a switch in fear state** [26 May 2021]
Article • Distinct clusters of inhibitory neurons in the mouse amygdala perform opposing roles in fear extinction.
- **The epidemiological impact of the NHS COVID-19 app** [12 May 2021]
Article • Statistical analysis of COVID-19 transmission among users of a smartphone-based digital contact-tracing app suggests that such apps can be an effective measure for reducing disease spread.
- **Thymic development of gut-microbiota-specific T cells** [12 May 2021]
Article • In young mice, antigens from the gut microbiota are trafficked by CX3CR1+ dendritic cells from the gut to the thymus, where they induce the expansion of T cells that are specific to commensal microorganisms.
- **ARAF mutations confer resistance to the RAF inhibitor belvarafenib in melanoma** [05 May 2021]
Article • The development, characterization and phase I clinical testing of the RAF inhibitor belvarafenib in cancer and a new resistance mechanism mediated by ARAF mutations are described.
- **A phase-separated nuclear GBPL circuit controls immunity in plants** [26 May 2021]
Article • A family of plant guanylate-binding protein-like GTPases controls phase separation and assembly of condensates, thereby forming a circuit that regulates transcriptional responses to biotic stress.
- **NOTUM from Apc-mutant cells biases clonal competition to initiate cancer** [02 June 2021]
Article • NOTUM from Apc-mutant cells acts as a key mediator during the early stages of mutation fixation and drives the formation of intestinal adenomas.
- **Apc-mutant cells act as supercompetitors in intestinal tumour initiation** [02 June 2021]
Article • Using experiments in organoids and in vivo in mice, the authors show that Apc-mutant cells act as supercompetitors to initiate the formation of adenomas.
- **Tracing oncogene-driven remodelling of the intestinal stem cell niche** [02 June 2021]
Article • By inducing changes in surrounding tissue, mutant intestinal stem cells create an unfavourable niche environment that gives them a competitive advantage over non-mutant neighbours.

- **Hippocampal AMPA receptor assemblies and mechanism of allosteric inhibition** [12 May 2021]
Article • Analyses of hippocampal AMPA receptor–auxiliary subunit complexes provide insights into the predominant assemblies and organization of the AMPA receptor, TARP- γ 8 and CNIH2/SynDIG4 and explain the mechanism of inhibition of a clinically relevant, brain-region-specific allosteric inhibitor.
- **Gating and modulation of a hetero-octameric AMPA glutamate receptor** [02 June 2021]
Article • Analyses of AMPA receptor–auxiliary subunit complexes provide insights into the gating and modulation of the AMPA receptor by TARP- γ 8 and CNIH2.
- **Clusters of flowstone ages are not supported by statistical evidence** [16 June 2021]
Matters Arising •
- **Reply to: Clusters of flowstone ages are not supported by statistical evidence** [16 June 2021]
Matters Arising •

- NEWS AND VIEWS
- 16 June 2021

Most rivers and streams run dry every year

A model of the world's rivers and streams has been developed to predict which of these watercourses flow all year round and which go dry. The analysis shows that rivers and streams that run dry are ubiquitous throughout the world.

- [Kristin L. Jaeger](#) [ORCID: http://orcid.org/0000-0002-1209-8506](#) 0

1. [Kristin L. Jaeger](#)

1. Kristin L. Jaeger is at the Washington Water Science Center, US Geological Survey, Tacoma, Washington 98402, USA.

[View author publications](#)

You can also search for this author in [PubMed](#) [Google Scholar](#)



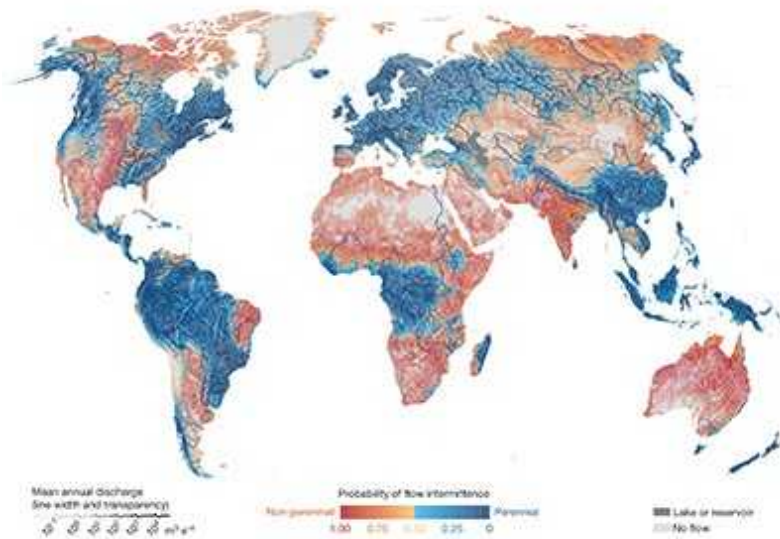


•

[Download PDF](#)

The flowing waters of surface rivers and streams efficiently transport sediment, organic material and nutrients, among other things, from hillsides and overland areas to downstream lakes, reservoirs and the ocean. Along the way, rivers and streams (hereafter referred to collectively as streams) provide important resources for our communities and support rich, complex ecosystems. Non-perennial streams, which do not flow year-round, are crucial in this context. However, because non-perennial streams are less reliable sources of surface water than perennial ones, they are less-well studied than their perennial counterparts. Writing in *Nature*, Messager *et al.*¹

provide a much-needed estimate of the total proportion of the world's stream network, by length, that is non-perennial — and find that most fall into this category.



[Read the paper: Global prevalence of non-perennial rivers and streams](#)

Messager and colleagues combined streamflow data from sites around the world with information describing the hydrology, climate, physical geography and land cover at those sites, to model the probability that water does not flow for at least one day per year. They then expanded their predictions to all stream segments recorded in a global stream-network database (RiverATLAS)².

The authors report that 51–60% of the world's streams do not flow for at least one day per year, and that 44–53% of global stream length is dry for at least one month (about 30 days) each year. Their modelling shows that non-perennial streams occur in all climates and biomes on every continent (see Fig. 1 of the paper¹). The model also shows that 95% of the stream network in hot, dry regions — which represent 10% of the global landmass — runs dry each year (Fig. 1). Astonishingly, even segments of major rivers, such as the Niger River in West Africa, are predicted to dry up in these arid regions. The vast prevalence of non-perennial streams in such locations highlights how even streams that do not flow continuously substantially affect water availability and water quality. The results emphasize the need for more-

detailed maps of perennial and non-perennial flows at regional and local scales, and for further studies of how non-perennial streams affect overall water availability and quality.



Figure 1 | The dried-up Darling River in New South Wales, Australia, February 2020. Messager and colleagues' analysis¹ shows that most rivers and streams run dry for at least one day per year, including sections of major rivers in arid regions. Credit: Mark Evans/Getty

Small headwater streams (those that have no tributaries) make up 70–80% of stream length worldwide³, similar to the way in which the collective length of one's fingers is much greater than the length of the palm of the hand. Messager and co-workers' model predicts that, even in the wettest regions, such as the Amazon River basin and portions of central Africa and southeast Asia, up to 35% of these headwater streams stop flowing at some point in the year. However, it should be noted that headwater streams are monitored by relatively few stream gauges, which tend to be located on larger,

perennial rivers downstream. The model might therefore provide highly uncertain estimates for the upstream regions of stream networks.

Lack of streamflow data is a common problem for the modelling of headwater streams, and so data-collection efforts are being implemented to fill this knowledge gap. For example, France has developed the Observatoire National des Étiages (ONDE) network, which complements the national stream-gauging network but focuses on headwater streams. However, these programmes are costly and require considerable investment of resources.



European rivers are fragmented by many more barriers than had been recorded

Stream gauges are also scarce for non-perennial streams more generally. In Messager and colleagues' analysis, for instance, there were no gauges in non-perennial streams in Argentina; just one in New Zealand; and 10 in the United States Pacific Northwest, out of a network of 250 gauges. To improve models that map perennial and non-perennial streams, low-cost field observations will be needed, coupled with the development of high-resolution remote-sensing technology that frequently detects — or at least predicts — surface flow in streams.

Messager and co-workers' analysis provides a robust, quantitative confirmation of the ubiquity of non-perennial rivers. Their results indicate

the need for a fundamental change in the fields of river and stream science and management, in which non-perennial streams have been largely overlooked⁴. In arid regions, the predominance of non-perennial streams might be a major driver of water availability and quality. And in areas where services developed by humans are not readily available, ecosystem services such as flowing water in streams are used to meet basic needs and will, in part, determine the well-being and prosperity of people in that area⁵. The new findings therefore shine a light on the need for global accounting of both perennial and non-perennial streams.

Moreover, changes in the distribution of streams can have far-reaching impacts on carbon and biogeochemical cycles at global and continental scales⁶, and on the survival of stream-dwelling organisms, including many endangered species⁷. A global benchmark of the prevalence of perennial and non-perennial streams is therefore crucial for evaluating the effects of future changes in their distribution associated with climate and land-use change. Finally, regional and local models of streams are needed, as well as better data for headwaters and non-perennial portions of the stream network, to further increase the value of global models.

Nature **594**, 335–336 (2021)

doi: <https://doi.org/10.1038/d41586-021-01528-4>

References

1. 1.

Messager, M. L. *et al.* *Nature* **594**, 391–397 (2021).

[Article](#) [Google Scholar](#)

2. 2.

Linke, S. *et al.* *Sci. Data* **6**, 283 (2019).

[PubMed](#) [Article](#) [Google Scholar](#)

3. 3.

Wohl, E. *Front. Earth Sci.* **11**, 447–456 (2017).

[Article](#) [Google Scholar](#)

4. 4.

Acuña, V. *et al.* *Science* **343**, 1080–1081 (2014).

[PubMed](#) [Article](#) [Google Scholar](#)

5. 5.

McClain, M. E. *Ambio* **42**, 549–565 (2013).

[PubMed](#) [Article](#) [Google Scholar](#)

6. 6.

Aufdenkampe, A. K. *et al.* *Front. Ecol. Environ.* **9**, 53–60 (2011).

[Article](#) [Google Scholar](#)

7. 7.

Magalhães, M. F., Beja, P., Schlosser, I. J. & Collares-Pereira, M. J. *Freshwat. Biol.* **52**, 1494–1510 (2007).

[Article](#) [Google Scholar](#)

[Download references](#)

Competing Interests

The author declares no competing interests.

Related Articles



- [Read the paper: Global prevalence of non-perennial rivers and streams](#)



- [European rivers are fragmented by many more barriers than had been recorded](#)



- [River conservation by an Indigenous community](#)
- [See all News & Views](#)

Subjects

- [Hydrology](#)
- [Environmental sciences](#)
- [Water resources](#)

[Jobs from Nature Careers](#)

- - - [All jobs](#)
 - - [Post Doctoral Fellow Bioinformatics Modern and Ancient Infectious Diseases](#)

[Faculty of Medicine, Dalhousie University](#)

Multiple locations

JOB POST

- **Research Fellow - Molecular Pharmacology & Experimental Therapeutics**

Mayo Clinic Health System

Rochester, MN, United States

JOB POST

- **Research Fellow - Neurobiology**

Mayo Clinic Health System

Rochester, MN, United States

JOB POST

- **Scientist for PETRA III Beamline P07**

German Electron Synchrotron (DESY)

Hamburg, Germany

JOB POST

Download PDF

Related Articles



- **Read the paper: Global prevalence of non-perennial rivers and streams**



- [European rivers are fragmented by many more barriers than had been recorded](#)



- [River conservation by an Indigenous community](#)
- [See all News & Views](#)

Subjects

- [Hydrology](#)
- [Environmental sciences](#)
- [Water resources](#)

This article was downloaded by **calibre** from <https://www.nature.com/articles/d41586-021-01528-4>

| [Section menu](#) | [Main menu](#) |

- NEWS AND VIEWS
- 25 May 2021

Contact-tracing app curbed the spread of COVID in England and Wales

Digital contact tracing has the potential to limit the spread of COVID-19. A contact-tracing smartphone app that has been readily adopted by people in England and Wales has shown efficacy in reducing disease spread.

- [C. Jason Wang](#) ⁰

1. [C. Jason Wang](#)

1. C. Jason Wang is in the Departments of Pediatrics and Medicine, and the Center for Policy, Outcomes and Prevention, Stanford University School of Medicine, Stanford, 94305 California, USA.

[View author publications](#)

You can also search for this author in [PubMed](#) [Google Scholar](#)

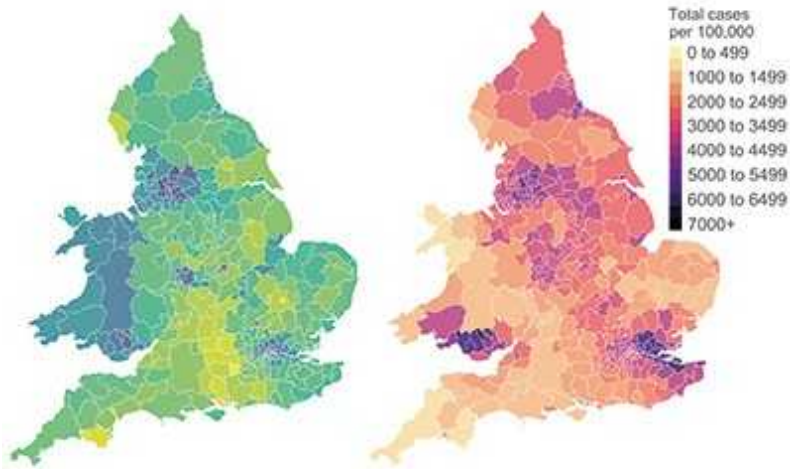




•

[Download PDF](#)

The idea behind digital contact tracing is that, when an individual tests positive for an infectious disease such as COVID-19, an app on their smartphone can send a notification to other smartphones that have been in close proximity, such as within 2 metres, for more than a certain period of time, say 15 minutes. However, such apps can be difficult for people living in a democracy to accept because of concerns about data privacy. Writing in *Nature*, Wymant *et al.*¹ demonstrate effective implementation of a digital contact-tracing app on a large scale in a democratic society: England and Wales in the United Kingdom.



[Read the paper: The epidemiological impact of the NHS COVID-19 App](#)

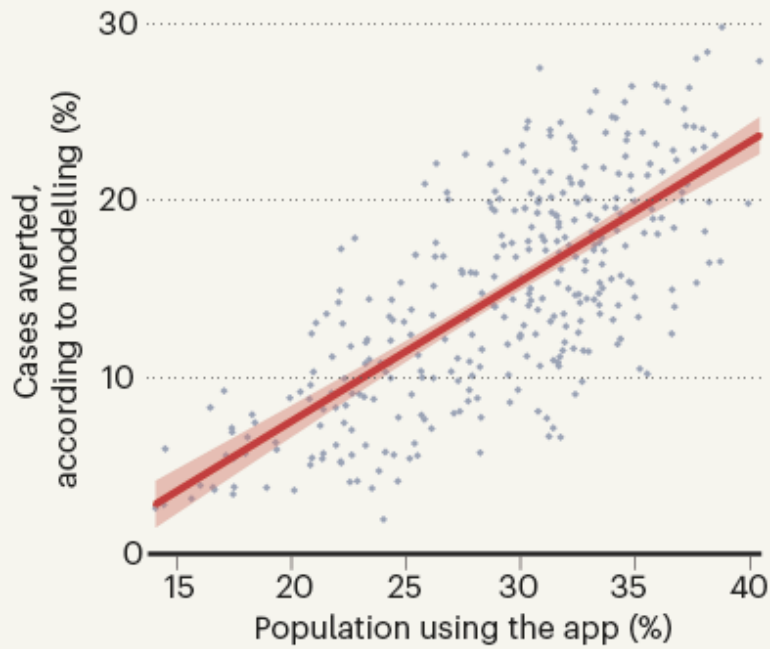
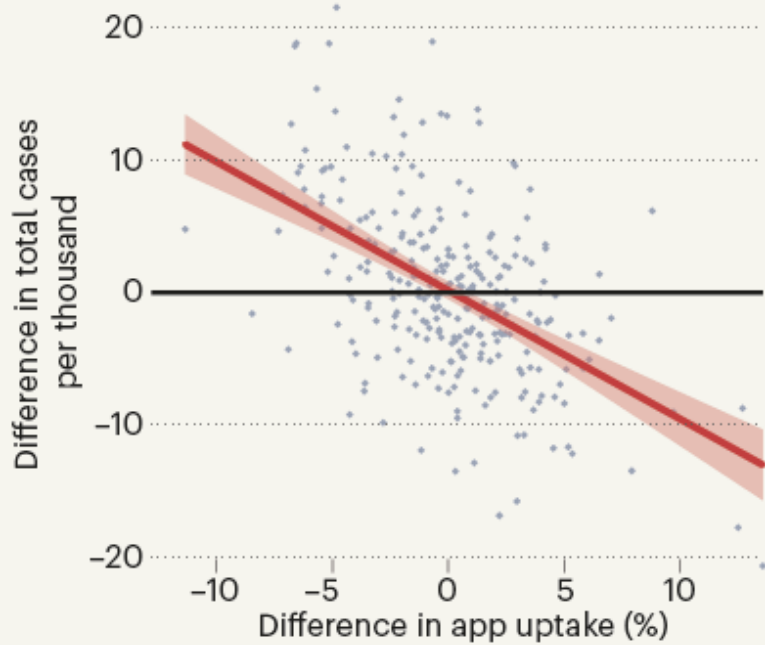
The technology used in the app, which was named the NHS COVID-19 app after Britain's National Health Service, is the Google Apple Exposure Notification (GAEN) system. This uses low-energy Bluetooth-enabled radio signals to send a randomly generated identification code from one phone to another that is in close proximity, creating a sort of 'handshake'; these codes change every 10–20 minutes. The codes of phones that have been in close physical contact over the previous 14 days are stored in the app on a user's phone. When a user tests positive for COVID-19, they can consent to have their codes sent anonymously to a central server. Other app users can sync with the central server for a match. Thus, the app can help to alert people who have potentially been exposed to COVID-19, so that they can then get tested, voluntarily place themselves in quarantine and inform their contacts that they should do the same.

A contact-tracing app will make a meaningful difference in the population only if a large enough proportion install and use it. The NHS COVID-19 app experience shows that there is enough participation in app use for it to be useful. An estimated 33.9 million people were eligible to download the app (that is, they were aged 16 or over, were located in England or Wales and had a compatible smartphone). Between its launch on 24 September 2020 and the end of 2020, the app was downloaded on 21 million separate devices and, between 1 November and 11 December 2020, it was regularly used by

an average of about 16.5 million users, which is about 49% of the eligible population, or 28% of the total population of England and Wales. Moreover, 72% of app-using ‘index’ cases (individuals who tested positive for COVID-19) consented to an app-based exposure notification being sent after testing positive.

Knowing that a randomized, controlled trial of a digital contact-tracing app is probably not feasible, Wymant *et al.* used two ways of estimating the impact of the app on the spread of COVID-19 from October to December 2020. First, using the number of observed notifications and the secondary attack rate — the proportion of contacts identified who ended up becoming infected — they modelled the number of cases averted as a result of app use. Second, they performed statistical comparisons of cumulative cases in neighbouring regions that had similar baseline infection rates but differing levels of app use, after adjusting for factors known to correlate with app uptake (such as areas being more rural, and having less poverty and a stronger local economy) and with infection rate.

The authors estimated that, for every 1% increase in app users, the number of cases could be reduced by 0.8% (from modelling), or by 2.3% (from statistical comparisons; Fig. 1). The authors also estimated the probability that someone who received a notification would test positive in the following 2 weeks to be 6%. Overall, approximately one new case was averted for each individual with confirmed COVID-19 who consented to their contacts being notified through the app.

a Modelling**b Statistical comparison**

©nature

Figure 1 | Estimated effects of a contact-tracing app on cases of COVID-19. Wymant *et al.*¹ used two approaches to examine the possible effect on

the spread of COVID-19 of a contact-tracing app deployed in England and Wales. **a**, First, they used modelling to estimate that the percentage of cases of COVID-19 averted in each local region (each region represented by a data point) increased by 0.8% for every percentage-point increase in app uptake. **b**, Second, the authors compared the numbers of COVID-19 cases per 1,000 people in similar, neighbouring regions that showed differences in app uptake. The comparison suggested that, for every 1% increase in app uptake, there was a 2.3% reduction in cases. The red-shaded areas represent 95% confidence intervals.

The estimated effect of the app on reducing spread of the disease is particularly remarkable given that COVID-19 testing was not mandatory, and self-isolation or quarantine was not strictly enforced for index cases or for those who were notified. In a series of UK surveys, among those who reported symptoms of COVID-19 in a 7-day period, only 20.2% reported having isolated fully, although around 70% intended to adhere to the rules if symptoms developed².

A common criticism of digital contact tracing is that it could create a lot of ‘noise’, by contacting a large number of individuals who have a low chance of having been infected, compared with the contacts identified by human (or ‘manual’) contact tracers, whose detailed interviews might be more likely to reach true close contacts. Wymant *et al.* showed that the secondary attack rate of 6% for the app is similar to the 6.9% rate achieved by manual contact tracing (see go.nature.com/2qxkkzf). They also found that the mean number of contacts reached was 4.4 for digital tracing, compared with 1.8 for manual tracing, with the app thought to have reached more contacts outside an individual’s household than did manual tracing. This strongly supports the idea that the app is as accurate as, and can be complementary to, manual contact tracing.



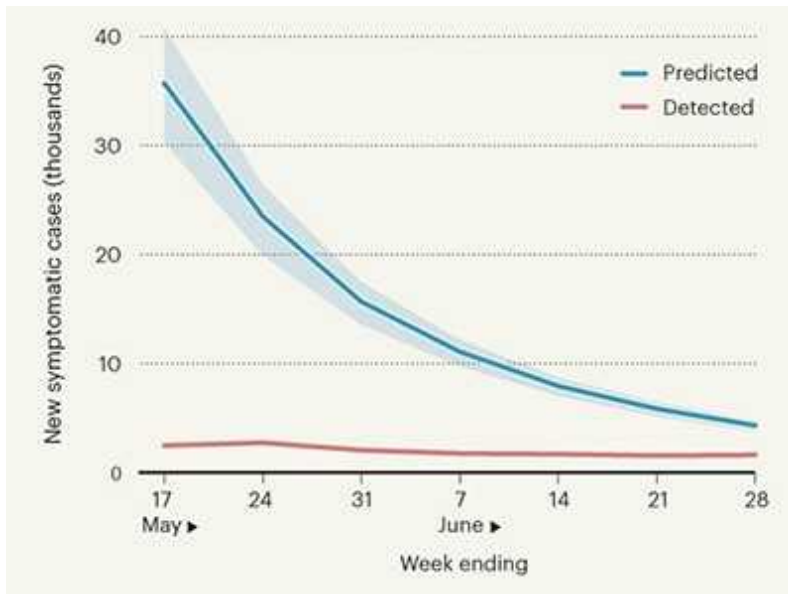
Big data and simple models used to track the spread of COVID-19 in cities

As mentioned above, digital contact tracing raises privacy concerns. Many citizens simply do not wish to be tracked for their health status, particularly when their freedom to travel might be compromised as a result³. However, the technology used in GAEN anonymizes the data and keeps them private in users' phones. Furthermore, an infected person must consent for the codes to be sent to the central server to allow contact matching. The identification codes cannot be used by someone at the central server to reveal the identity of the infected person or their contacts.

The main advantages of digital contact tracing are the speed and scalability it offers. This is particularly relevant to COVID-19, because individuals can transmit the SARS-CoV-2 virus for several days before developing symptoms, or can simply remain asymptomatic⁴. Contact-tracing apps might work more quickly and more reliably than manual approaches that involve interviewing infected people, many of whom do not keep track of their recent contacts and forget them. Another advantage of digital contact tracing is its ability to contact strangers; it is otherwise simply not possible to track down strangers who sat near an infected person on a bus.

The NHS COVID-19 app now has extra features. These include: the ability to 'check in' at a venue by scanning its QR code (a type of barcode) for later notification if the venue has positive cases; a symptom tracker that is linked

to a test-booking system; and the ability to order tests and receive results through the app.



An estimation of undetected COVID cases in France

To be maximally effective, digital contact tracing relies on the health system's ability to follow up on potential contacts and offer them testing, clinical care and social and material support during quarantine, as needed. The flow of data can also strongly affect the efficacy of digital contact tracing. For example, are positive test results self-reported to the app or directly obtained or auto-populated from the test laboratories? Will health-care providers and public-health officials be quickly informed about positive test results so that they can act quickly in contact tracing, advising quarantine and testing for close contacts, and providing support and care for infected individuals? All these elements can contribute to the effectiveness of both digital and manual contact-tracing efforts.

Although health officials in England and Wales are not made aware of the identities of infected individuals from the app, they can use data from the app to estimate infection rates in the postcode district (the first half of the postcode) that is entered by users during the app registration process. Given these restrictions and the focus on privacy and autonomy (that is, with users having the choice of whether or not to send a positive-test notification), it is remarkable that the contact-tracing app still showed impressive results in

mitigating the spread of COVID-19. The success of the NHS COVID-19 app offers hope that other digital contact-tracing apps might prove to be useful elsewhere, offering new capabilities in containing the spread of a rapidly spreading virus.

Nature **594**, 336-337 (2021)

doi: <https://doi.org/10.1038/d41586-021-01354-8>

References

1. 1.

Wymant, C. *et al.* *Nature* **594**, 408–412 (2021).

[Article](#) [Google Scholar](#)

2. 2.

Smith, L. E. *et al.* *Br. Med. J.* **372**, n608 (2021).

[Article](#) [Google Scholar](#)

3. 3.

Mello, M. M. & Wang, C. J. *Science* **368**, 951–954 (2020).

[PubMed](#) [Article](#) [Google Scholar](#)

4. 4.

Pollock, A. M. & Lancaster, J. *Br. Med. J.* **371**, m4851 (2020).

[Article](#) [Google Scholar](#)

[Download references](#)

Competing Interests

The author declares no competing interests.

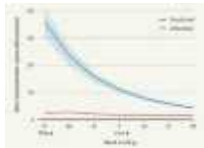
Related Articles



- [Read the paper: The epidemiological impact of the NHS COVID-19 App](#)



- [Big data and simple models used to track the spread of COVID-19 in cities](#)



- [An estimation of undetected COVID cases in France](#)
- [See all News & Views](#)

Subjects

- [Epidemiology](#)
- [Public health](#)

Jobs from Nature Careers

- - - [All jobs](#)
 - -

Post Doctoral Fellow Bioinformatics Modern and Ancient Infectious Diseases

[Faculty of Medicine, Dalhousie University](#)

[Multiple locations](#)

[JOB POST](#)

- **Research Fellow - Molecular Pharmacology & Experimental Therapeutics**

[Mayo Clinic Health System](#)

[Rochester, MN, United States](#)

[JOB POST](#)

- **Research Fellow - Neurobiology**

[Mayo Clinic Health System](#)

[Rochester, MN, United States](#)

[JOB POST](#)

- **Scientist for PETRA III Beamline P07**

[German Electron Synchrotron \(DESY\)](#)

[Hamburg, Germany](#)

[JOB POST](#)

[Download PDF](#)

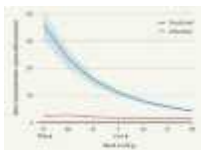
Related Articles



- [Read the paper: The epidemiological impact of the NHS COVID-19 App](#)



- [Big data and simple models used to track the spread of COVID-19 in cities](#)



- [An estimation of undetected COVID cases in France](#)
- [See all News & Views](#)

Subjects

- [Epidemiology](#)
- [Public health](#)

This article was downloaded by **calibre** from <https://www.nature.com/articles/d41586-021-01354-8>

- NEWS AND VIEWS
- 02 June 2021
- Correction [07 June 2021](#)

Glutamate receptor complexes open up and reveal their molecular dialect

AMPA receptors are a class of protein complexes crucial for neuronal communication. Two complementary studies converge on structures of AMPA receptors found in a brain region called the hippocampus.

- [Andrew J. R. Plested](#) 
1. [Andrew J. R. Plested](#)
 1. Andrew J. R. Plested is at the Humboldt University Berlin, the Leibniz Institute for Molecular Pharmacology and the NeuroCure Cluster of Excellence, Berlin, Germany.

[View author publications](#)

You can also search for this author in [PubMed](#) [Google Scholar](#)





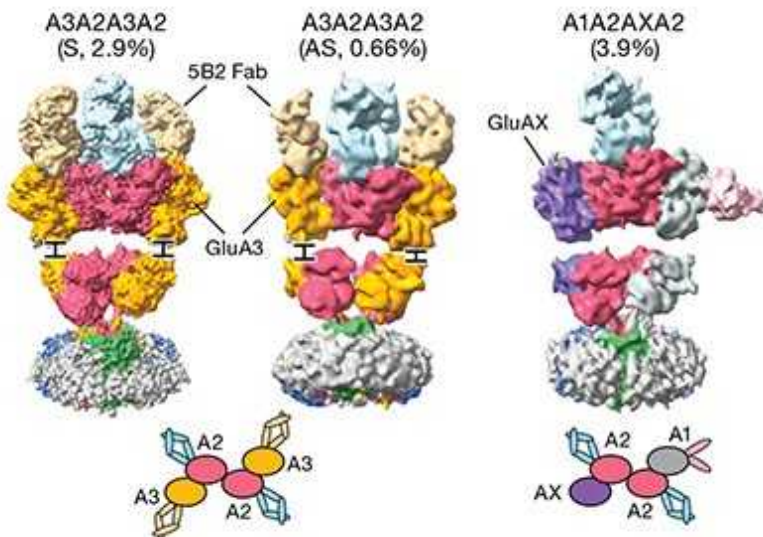
•

[Download PDF](#)

Dialects distinguish Berliners from Bavarians, and New Yorkers from New Englanders, reflecting differences not only in speakers' geographical location, but also in their culture and history. At first glance, it seems unlikely that such diversity would exist among AMPA receptors — a class of protein complexes activated by the neurotransmitter molecule glutamate during neuronal communication. These crucial receptors are found everywhere in the brain, but the protein subunits that form their central channel structure are encoded by just four genes, suggesting there might be little scope for them to have distinctive molecular 'accents' in different brain

regions. However, proteomic studies suggest that AMPA receptors could in fact be large complexes with many extra subunits, which have been challenging to isolate. Writing in *Nature*, [Yu et al.](#)¹ and [Zhang et al.](#)² provide complementary views of the structure of AMPA receptors from the hippocampus, a brain region central to memory, to show the molecular accents that colour their native ‘language’.

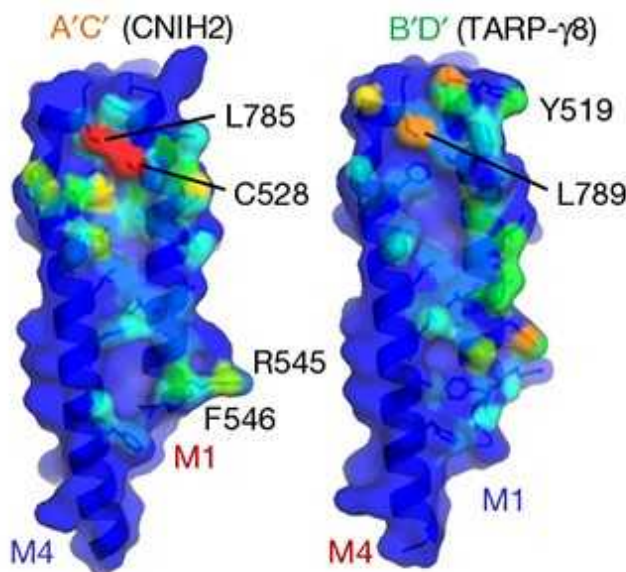
At an excitatory synaptic connection between two neurons, glutamate is released by the presynaptic neuron and binds to AMPA receptors in the cell membrane of the postsynaptic neuron. When AMPA receptors are activated, their channels open, allowing a rapid movement of ions into the cell that leads to electrical excitation. Newly assembled AMPA receptors are placed into the cell membrane and, once there, they can be pulled into the postsynaptic density (PSD) — a cluster of proteins in the postsynaptic neuron directly opposite the presynaptic sites from which glutamate is released. Scaffold proteins, such as PSD-95, draw in AMPA receptors depending on the level of the synapse’s activity. The strength of a synapse can be changed by adding or removing receptors. The processes that underlie synaptic plasticity (the ability of synapses to change in strength) are candidate cellular mechanisms for learning skills and retaining memories.



[Read the paper: Hippocampal AMPA receptor assemblies and mechanism of allosteric inhibition](#)

Pioneering work that measured the expression of the four AMPA receptor channel subunits, GluA1–4, in different cell types in the brains of rats³ explained some, but far from all, variations in the activation properties of AMPA receptors. Hippocampal AMPA receptors are fascinating because of their participation in synaptic plasticity, but what makes them special compared with AMPA receptors in other brain regions? AMPA receptors are decorated with members of an elusive class of more than 30 ‘auxiliary’ proteins⁴, which could provide AMPA receptors in different brain regions with a regional molecular accent.

Multiprotein complexes perform many tasks in biology, and characterizing assemblies sourced from native material (that is, derived from biological tissue) is important for understanding the true biological properties of these complexes. However, although previous work has resolved the structures, composition and activation properties of certain combinations of AMPA receptor subunits *in vitro*, native (or native-like) AMPA receptor complexes that contain more than a small number of subunits have largely defied similar classification.



[Read the paper: Gating and modulation of a hetero-octameric AMPA glutamate receptor](#)

Mining the impressive details of these receptor complexes relies on the ability of modern cryo-electron microscopy to sort and pool samples

consisting of a mixture of complexes with different subunit compositions. The two studies used different approaches to purify their complexes, albeit with each approach introducing some bias in the composition of the complexes obtained. Zhang *et al.*² fused together DNA sequences encoding the GluA2 subunit and the TARP γ 8 auxiliary protein, and expressed this construct and the GluA1 subunit in a cell line forced to co-express the auxiliary protein CNIH2. Yu *et al.*¹ extracted the scarce complexes directly from mouse hippocampi by trapping GluA2, the most prevalent subunit, and by promoting the extraction of complexes including TARP γ 8. They did this using a molecule called JNJ-55511118 that binds and blocks the activity of TARP γ 8-containing complexes. The authors were able to work out the combination of subunits in each complex using small antibody fragments that labelled specific subunits. In this way, Yu *et al.* were also able to resolve JNJ-55511118 in its binding site in structures of the native receptors, sandwiched between GluA1 and TARP γ 8.

The two studies' results are convergent, and each study provides independent support that their structural findings are representative of the composition of native complexes. Yu *et al.*¹ attached fluorescent dye molecules to the native receptors using selective antibodies. They found that the fluorescence of most of the dye molecules that were attached to TARP γ 8 subunits in each AMPA receptor complex could be photobleached (extinguished) in two steps, thus confirming that these complexes each contain two TARP γ 8 subunits. A complementary approach by Zhang and colleagues² showed that the activation properties of their octameric complexes containing two GluA1, GluA2, TARP γ 8 and CNIH2 subunits more closely mimicked those of receptors from the cell bodies of hippocampal pyramidal neurons than did those of lower-order combinations, for example with CNIH2 or TARP γ 8 alone.

A further structural analysis of the native complexes isolated by Yu and colleagues¹ signalled the presence of an unexpected α -helix at the periphery, between the GluA1 and CNIH2 subunits. Antibody labelling and photobleaching provided evidence that this helix belongs to the auxiliary protein SynDIG4 (Fig. 1). This unprecedented 10-subunit complex (the octamer plus two putative SynDIG4 subunits), is a thrilling find and a game-changer because it expands the number of possible ways in which the

function of AMPA receptors might be modulated by combinations of auxiliary proteins. With hindsight, the structure agrees surprisingly well with previous mass spectrometry data⁵ that suggested a peripheral location for this subunit. Curiously, SynDIG4 is predicted to have two membrane helices⁶; the fact that an expected part of this protein (the second membrane helix) is not visible in Yu and colleagues' structures suggests that there is more subunit diversity to be unveiled in AMPA receptors.

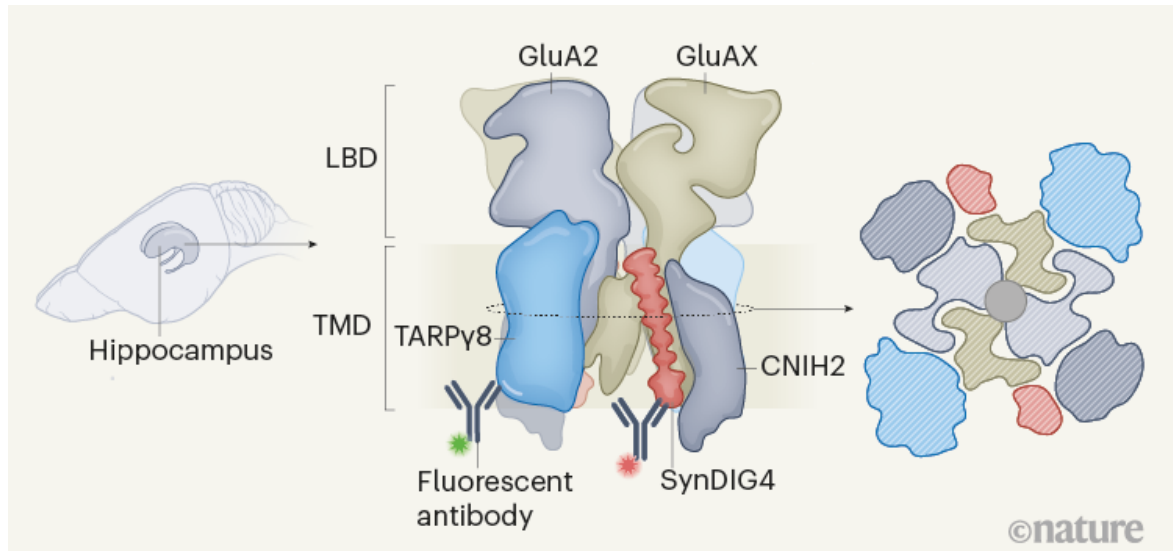


Figure 1 | The structure and composition of native AMPA receptor complexes. AMPA receptors are membrane-bound complexes of multiple different protein subunits, including channel-forming subunits (GluA1–GluA4) and auxiliary proteins such as TARPy8, CNIH2 and SynDIG4. Yu *et al.*¹ determined the composition of GluA2-containing AMPA receptors purified from a brain region called the hippocampus in mice. They used cryo-electron microscopy to resolve the structures of the complexes through labelling with small, subunit-selective antibody fragments; shown here are the ligand-binding domain (LBD) and transmembrane domain (TMD) of a complex containing two GluA2 channel subunits and two unspecified channel subunits (GluAX), along with three pairs of auxiliary subunits (membrane not shown). The authors also worked out the composition of complexes by labelling individual subunits with antibodies attached to fluorescent dye molecules.

The octameric complex generated by Zhang *et al.*² yields another gem: the structure of an activated state with an open ion-channel pore. From myriad structures of full-length glutamate receptors, this is only the third bona fide open structure^{7,8}. A comparison of the structures of resting and activated receptors shows that a gentle ‘flowering’ motion of the peripheral subunits accompanies activation (Fig. 2).

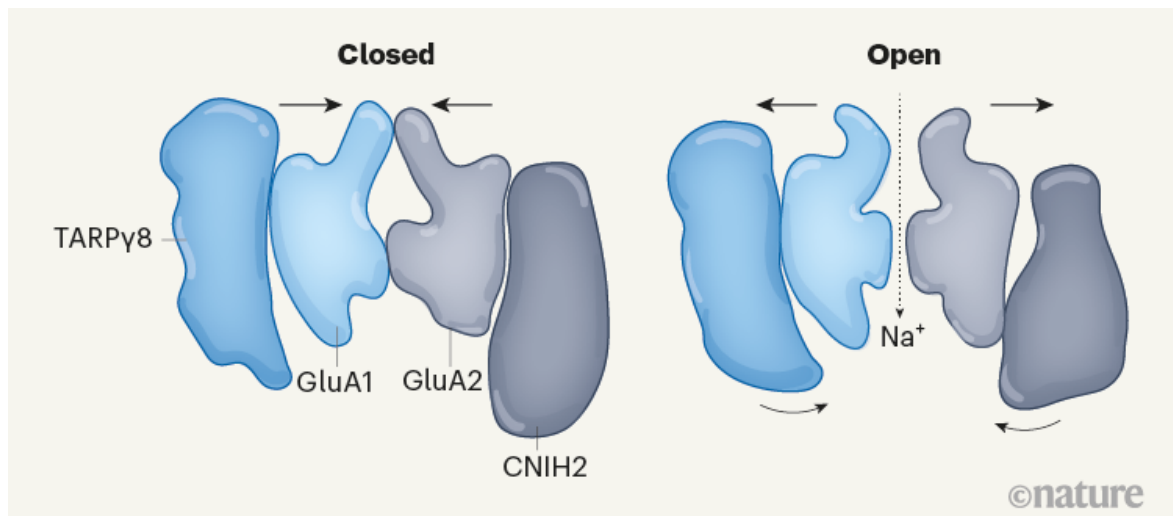


Figure 2 | The opening of the AMPA receptor complex. AMPA receptors include four central, channel-forming subunits (GluA1–GluA4), surrounded by auxiliary protein subunits such as CNIH2 and TARP γ 8 that can influence the activation properties of the complex. A cross section of one such receptor is shown here, with 4 out of the 8 subunits depicted. When the neurotransmitter molecule glutamate (not shown) binds to the AMPA receptor, the configuration of the receptor changes to open the channel, allowing ions such as sodium (Na^+) into the neuronal cell. Zhang *et al.*² used cryo-electron microscopy of AMPA receptor complexes to show that the activated receptor opens in an outwards ‘flowering’ motion (black arrows). The closed and open states of the cell-membrane-spanning part of a complex containing GluA1, GluA2, TARP γ 8 and CNIH2 subunits are depicted here (the cell membrane is not shown).

CNIH2 has been the subject of much controversy⁹, but is now without doubt a key player in AMPA receptor biology — it strongly stabilizes the open state, and the transition characterized by Zhang *et al.* gives two clues to how it does this. First, a triplet of phenylalanine amino-acid residues on the outer

face of CNIH2 controls assembly of the complex. Second, an extended helix of CNIH2 bears against the intracellular loops of the channel subunits, the movement of which with gating was previously detected by optical spectroscopy¹⁰.

A substantial fraction of neuronal AMPA receptors are stored inside the cell, or reside in the cell membrane outside synapses; thus, how representative the examined complexes¹² are of synaptic receptors is a pertinent question. The caveat that these are not synaptic receptors has regularly rung out in the 30 years since the cloning of these subunits¹¹. Yu *et al.*¹ found PSD-95 in their preparation, but whether this means that their receptors were synaptic is unclear, because PSD-95 is also found outside synapses¹². Unless methods can be developed to mark or capture synaptic receptors, and to work with the doubtless vanishingly small quantities that would be obtained, this gripe will persist.

That said, it would be a surprise, and a substantial waste, if the receptors resolved in these studies were not genuinely synaptic, because they have the requisite ‘hooks’ to get caught at PSDs. However, it is possible that they could instead be the raw materials from which synaptic receptors are made, perhaps following subunit exchange in the cell membrane. Synaptic receptors themselves might be harder to get at, anchored at their base to the PSD, and pinned by interactions between their extracellular domains and other molecules across the synapse.

Both studies introduce firm rules on how subunits participate in AMPA receptor complexes. However, other subunits, such as CKAMP44 and other TARP auxiliary proteins, should also be present in hippocampal AMPA receptor complexes, and how such complexes compare with those in other brain regions remains to be considered. Specialists will now eagerly await reports of other membrane protein complexes, and those from brain regions such as the cerebellum and cortex. Making sense of the interactions within such complexes requires functional and spectroscopic measurements, as done previously¹³. Time-resolved studies of the activation of native receptors, akin to those on the muscle nicotinic receptor from *Torpedo marmorata* electric ray fish¹⁴, should also now be possible.

Interpreters and expats often battle to follow baroque expressions and local vernacular. But, despite their thick accents, AMPA receptors now say loud and clear: “We have so much still to tell you.”

Nature **594**, 338–339 (2021)

doi: <https://doi.org/10.1038/d41586-021-01380-6>

Updates & Corrections

- **Correction 07 June 2021:** The original version of this article said that Yu *et al.* used nanobodies in their study, but they actually used antibody fragments.

References

1. 1.

Yu, J. *et al.* *Nature* **594**, 448–453 (2021)

[Article](#) [Google Scholar](#)

2. 2.

Zhang, D., Watson, J. F., Matthews, P. M., Cais, O. & Greger, I. H. *Nature* <https://doi.org/10.1038/s41586-021-03613-0> (2021)

[Article](#) [Google Scholar](#)

3. 3.

Geiger, J. R. P. *et al.* *Neuron* **15**, 193–204 (1995).

[PubMed](#) [Article](#) [Google Scholar](#)

4. 4.

Schwenk, J. *et al.* *Neuron* **74**, 621–633 (2012).

[PubMed](#) [Article](#) [Google Scholar](#)

5. 5.

Schwenk, J. *et al.* *Neuron* **84**, 41–54 (2014).

[PubMed](#) [Article](#) [Google Scholar](#)

6. 6.

Sällman Almén, M., Bringeland, N., Fredriksson, R. & Schiöth, H. B. *PLoS ONE* **7**, e31961 (2012).

[PubMed](#) [Article](#) [Google Scholar](#)

7. 7.

Twomey, E. C., Yelshanskaya, M. V., Grassucci, R. A., Frank, J. & Sobolevsky, A. I. *Nature* **549**, 60–65 (2017).

[PubMed](#) [Article](#) [Google Scholar](#)

8. 8.

Chen, S. *et al.* *Cell* **170**, 1234–1246 (2017).

[PubMed](#) [Article](#) [Google Scholar](#)

9. 9.

Brockie, P. J. & Maricq, A. V. *Neuron* **68**, 1017–1019 (2010).

[PubMed](#) [Article](#) [Google Scholar](#)

10. 10.

Zachariassen, L. G. *et al.* *Proc. Natl Acad. Sci. USA* **113**, E3950–E3959 (2016).

[PubMed](#) [Article](#) [Google Scholar](#)

11. 11.

Keinänen, K. *et al.* *Science* **249**, 556–560 (1990).

[PubMed](#) [Article](#) [Google Scholar](#)

12. 12.

Bresler, T. *et al.* *Mol. Cell Neurosci.* **18**, 149–167 (2001).

[PubMed](#) [Article](#) [Google Scholar](#)

13. 13.

Shaikh, S. A. *et al.* *Cell Rep.* **17**, 328–335 (2016).

[PubMed](#) [Article](#) [Google Scholar](#)

14. 14.

Unwin, N. & Fujiyoshi, Y. *J. Mol. Biol.* **422**, 617–634 (2012).

[PubMed](#) [Article](#) [Google Scholar](#)

[Download references](#)

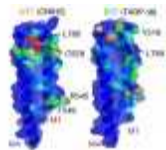
Competing Interests

The author declares no competing interests.

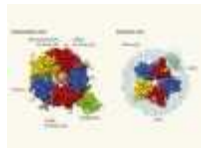
Related Articles



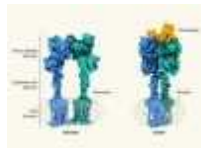
- [Read the paper: Hippocampal AMPA receptor assemblies and mechanism of allosteric inhibition](#)



- [Read the paper: Gating and modulation of a hetero-octameric AMPA glutamate receptor](#)



- [An in-depth structural view of a GABAA brain receptor](#)



- [How an activation signal is transmitted through an excitatory receptor](#)
- [See all News & Views](#)

Subjects

- [Structural biology](#)
- [Neuroscience](#)

[Jobs from Nature Careers](#)

- - - [All jobs](#)
 - - [Post Doctoral Fellow Bioinformatics Modern and Ancient Infectious Diseases](#)

[Faculty of Medicine, Dalhousie University](#)

Multiple locations

JOB POST

- **Research Fellow - Molecular Pharmacology & Experimental Therapeutics**

Mayo Clinic Health System

Rochester, MN, United States

JOB POST

- **Research Fellow - Neurobiology**

Mayo Clinic Health System

Rochester, MN, United States

JOB POST

- **Scientist for PETRA III Beamline P07**

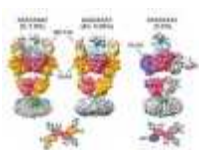
German Electron Synchrotron (DESY)

Hamburg, Germany

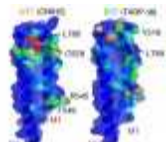
JOB POST

Download PDF

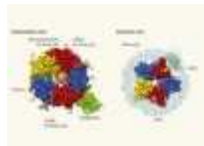
Related Articles



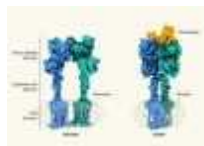
- **Read the paper: Hippocampal AMPA receptor assemblies and mechanism of allosteric inhibition**



- [Read the paper: Gating and modulation of a hetero-octameric AMPA glutamate receptor](#)



- [An in-depth structural view of a GABAA brain receptor](#)



- [How an activation signal is transmitted through an excitatory receptor](#)
- [See all News & Views](#)

Subjects

- [Structural biology](#)
- [Neuroscience](#)

This article was downloaded by **calibre** from <https://www.nature.com/articles/d41586-021-01380-6>

- NEWS AND VIEWS
- 02 June 2021

Cancer stem cells in the gut have a bad influence on neighbouring cells

Malignant stem cells in the gut secrete factors that promote the differentiation of neighbouring stem cells, thereby aiding the replacement of normal stem cells by those with cancer-promoting mutations.

- [Shi Biao Chia](#)⁰ &
- [James DeGregori](#)¹

1. Shi Biao Chia

1. Shi Biao Chia is in the Department of Biochemistry and Molecular Genetics, University of Colorado Anschutz Medical Campus, Aurora, Colorado 80045, USA.

[View author publications](#)

You can also search for this author in [PubMed](#) [Google Scholar](#)

2. [James DeGregori](#)

1. James DeGregori is in the Department of Biochemistry and Molecular Genetics, University of Colorado Anschutz Medical Campus, Aurora, Colorado 80045, USA.

[View author publications](#)

You can also search for this author in [PubMed](#) [Google Scholar](#)





•

[Download PDF](#)

Decades of research have revealed how mutations contribute to the evolution of malignant cells and to the ultimate characteristics of a given tumour. There is growing recognition that the surrounding tissue environment affects the natural selection of these mutation-driven characteristics. Less appreciated, however, have been the effects of interactions between malignant cells and their neighbouring wild-type cells — and how, through these interactions, malignant cells shape the surrounding environment to their advantage. Writing in *Nature*, [Yum et al.](#)¹, [Van Neerven et al.](#)² and

[Flanagan et al.³](#) provide crucial insights into the competitive dynamics of cancer cells and their neighbouring cells in the intestine.

To study interactions between cells with cancer-promoting mutations and neighbouring cells in their native environment, Yum *et al.*¹ developed a microscopy-based approach that uses a multicolour system to monitor cellular lineages (clones) in mice. This enabled the authors to track intestinal stem cells that express cancer-associated mutations in two key genes, *Kras* and *Pik3ca*, and also to assess their wild-type neighbouring cells. The authors report that the presence of intestinal stem cells harbouring these mutated genes increased the rate of differentiation of the surrounding wild-type cells. This outcome was driven by the mutant stem cells secreting specific factors — molecules that activate the BMP signalling pathway, and others that inhibit the WNT signalling pathway (Fig. 1).

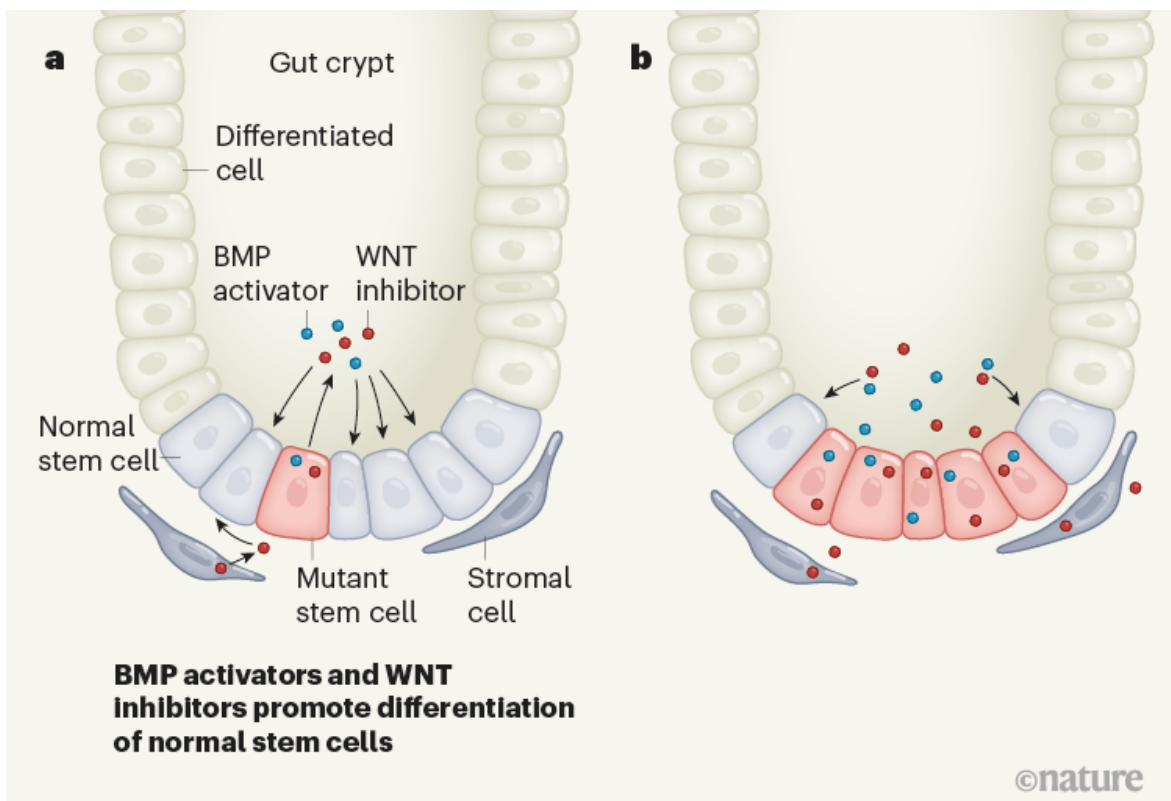
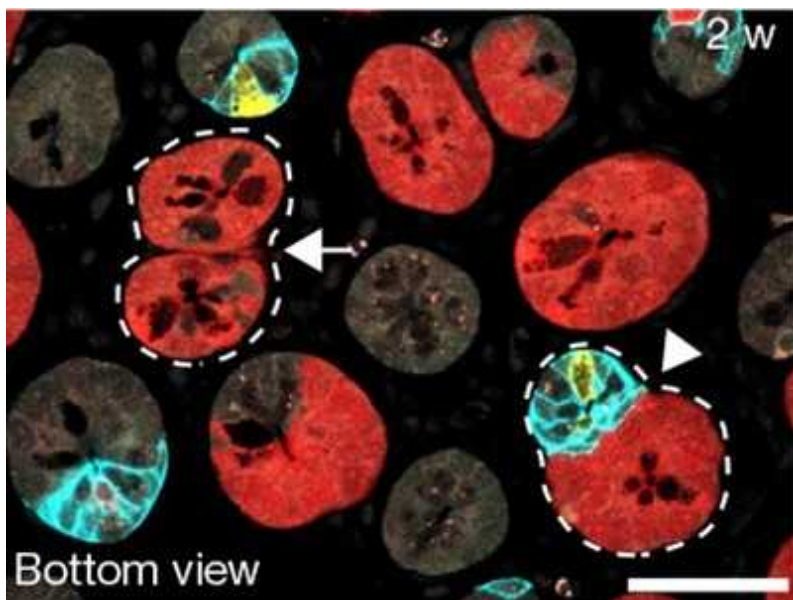


Figure 1 | Cellular competition in the mammalian gut that promotes tumour formation. Yum *et al.*¹, Van Neerven *et al.*² and Flanagan *et al.*³ present evidence that reveals how stem cells in the gut that carry cancer-promoting mutations can affect neighbouring normal stem cells in crypt

structures. **a**, Yum *et al.*¹ report that mutant stem cells secrete molecules that activate the BMP signalling pathway and inhibit the WNT signalling pathway. These molecules promote stem-cell differentiation and predominantly affect normal stem cells. Van Neerven *et al.*² and Flanagan *et al.*³ also report such secretion of WNT inhibitors. Moreover, Yum *et al.* found that mutant stem cells drive cells called stromal cells in their vicinity to secrete WNT inhibitors. **b**, After the normal stem cells differentiate, the mutant stem cells dominate the stem-cell pool.

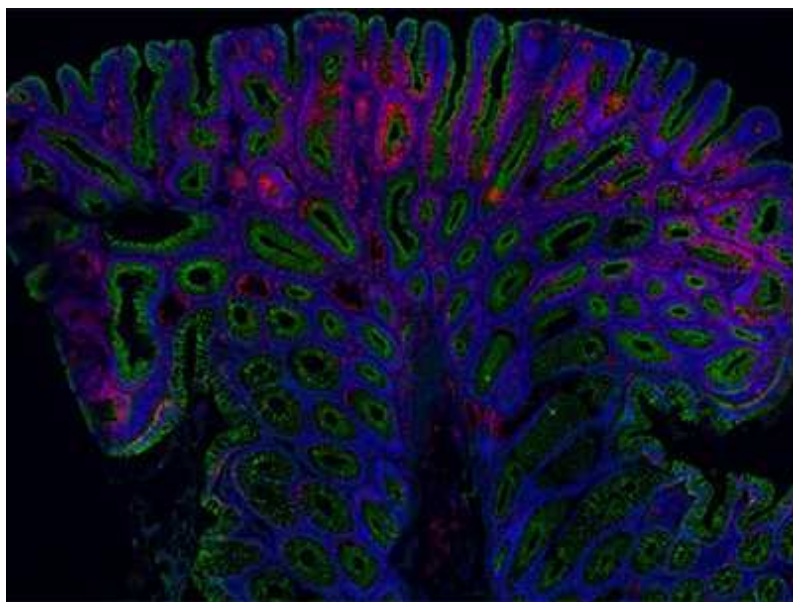
Moreover, Yum *et al.* found that structural cells (termed stromal cells) that surround stem cells — and that normally promote stem-cell maintenance — instead enhanced their secretion of pro-differentiation factors if mutant stem cells were present. This results in a less-supportive environment for the maintenance of intestinal stem cells. These secreted factors promote differentiation regardless of whether the stem cells have cancer-promoting mutations. Crucially, the cells with mutations are less affected than are those without, which gives the mutant stem cells a competitive edge. The intestinal regions (units called crypts) adjacent to the clones of cells produced through mutation showed a rise in cellular turnover, further promoting the establishment of the clones of mutant cells.



[Read the paper: Tracing oncogene-driven remodelling of the intestinal stem cell niche](#)

For a deep dive into mechanisms underlying the interactions between normal and malignant stem cells, Van Neerven *et al.*² and Flanagan *et al.*³ used mouse and human models of intestinal cancer mediated by inactivation of the *Apc* gene. Mutation of *Apc* initiates most colon cancers^{4,5}, and APC protein is a key negative regulator of the WNT signalling pathway. APC mediates the destruction of the protein b-catenin, a gene-expression regulator that helps to maintain the intestinal stem-cell state.

Van Neerven *et al.* and Flanagan *et al.* found that several genes associated with inhibition of the WNT pathway, particularly the gene *Notum*, showed higher expression in cells with an *Apc* mutation than in wild-type cells. The authors of these two papers used an *in vitro* system to culture cells together; in this system, individual stem cells developed into miniature intestine-like ‘organoid’ structures, providing a measure of stem-cell potential. Wild-type stem cells grown with cells that had mutant *Apc*, or exposed to liquid taken from the medium in which such cells had been grown, had a slower rate of organoid formation and growth than did wild-type stem cells that were exposed to other wild-type stem cells or their media. This result supports the hypothesis that cells with an *Apc* mutation adversely affect the potential of wild-type stem cells through the secretion of a diffusible factor. NOTUM protein, a secreted inhibitor of WNT signalling, was found by Van Neerven *et al.* and Flanagan *et al.* to be crucial for this inhibition of stem-cell potential.

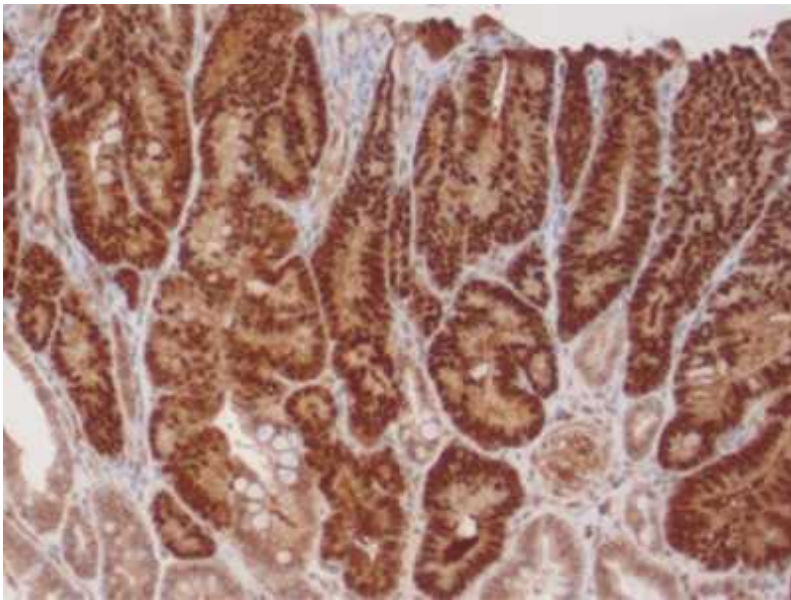


[Read the paper: Apc-mutant cells act as supercompetitors in intestinal tumour initiation](#)

In the fruit fly *Drosophila melanogaster*, cells with an *Apc* mutation can outcompete their surrounding wild-type cells by inducing the death of those cells⁶. By contrast, none of the three papers highlighted here reported an increase in cell death in wild-type cells adjacent to cells with *Apc*, *Kras* or *Pik3ca* mutations.

NOTUM-mediated inhibition of the WNT pathway was observed only in the wild-type cells examined by Van Neerven, Flanagan and their respective colleagues, not in the mutant cells. This is because the *Apc* mutation activates the WNT pathway downstream of the site of NOTUM action⁷ — NOTUM secretion by cells with an *Apc* mutation does not affect the mutant cells themselves, but has a negative effect on wild-type cells. Thus, cells with *Apc* mutations not only outcompete their neighbours by driving them to differentiate, but they are also shielded from NOTUM-mediated adverse effects. Activating the WNT pathway using molecules such as lithium chloride (as done by Van Neerven and colleagues) or a NOTUM inhibitor (used by Flanagan *et al.*), thus levelling the playing field between wild-type intestinal cells and those with mutant *Apc*, reduced cancer formation in the mouse intestine mediated by mutant *Apc*; this suggests a possible approach in developing innovative anticancer therapies.

Together, these three studies reveal how malignant intestinal stem cells can win competitive battles in the gut by promoting neighbouring stem cells to differentiate into specialized and less-proliferative cell types (Fig. 1). Other studies using models for the formation of leukaemia have similarly shown that malignant cells secrete factors, such as pro-inflammatory cytokine molecules, that impair the fitness of competing normal cells and boost the fitness of the malignant cells^{8,9}.



[Read the paper: NOTUM from Apc-mutant cells biases clonal competition to initiate cancer](#)

Although cell competition is a process that is clearly involved in the progression of malignancy, it also serves as a quality-control mechanism for maintaining tissue health. For example, during embryonic development, defective cells are eliminated to ensure healthy growth through a process that involves factors secreted from normal cells¹⁰; this phenomenon has echoes of the mechanism described in these three studies.

There are numerous other examples of cellular competition processes affecting health and disease. One study¹¹ reported that the expression of the protein COL17A1 regulates basal (stem) cell divisions in the skin. Damage to a cell results in the downregulation of COL17A1 expression, which drives the differentiation of these stem cells into mature cells of the outer skin layer. This results in healthy basal cells replacing damaged ones. Moreover, normal cells can ‘evict’ mutant cells; for example, normal epithelial cells force the extrusion of cells with a cancer-promoting mutation from the skin layer, thereby preventing cancer initiation¹². Beyond tumour-suppressive roles, the efficient recognition and elimination of ‘loser’ cells during cell competition is also crucial for the longevity of *D. melanogaster*¹³.

The incidence of colon cancer rises exponentially in old age, and the expression of NOTUM increases with ageing, too¹⁴. This raises the question of whether the processes reported in these studies might be some of the ways in which ageing creates an environment that promotes cancer initiation. Numerous studies over the past decade have described how cells with cancer-promoting mutations become increasingly abundant in our tissues as we age¹⁵. Given that the papers by Yum *et al.*, Van Neerven *et al.* and Flanagan *et al.* indicate that such cells can impair the maintenance of neighbouring stem cells, such pre-malignant clones could hypothetically contribute to both tissue ageing (by reducing tissue maintenance) and ageing-associated cancers (through selection for cancer-promoting mutations that might resist, and perhaps even reinforce, pro-differentiation forces).

Current developments in cancer therapeutics often focus on exploiting our own natural systems of defence against the disease. The focus so far has been on the promotion of defences mediated by the immune system. However, we are now gaining an appreciation of how stem cells and aspects of the tissue environment are important for tumour progression. Hence, interventions might be developed that promote stem cells and tissue contexts that are unfavourable to the evolution of malignancy. Given the ability of healthy tissues to eliminate dysfunctional or malignant cells¹², these three studies should further encourage the development of therapeutic strategies in which cancer is halted by counteracting the pro-differentiative influences of malignant cells, thus boosting the fitness of the competing normal cells.

Nature **594**, 340-341 (2021)

doi: <https://doi.org/10.1038/d41586-021-01379-z>

References

1. 1.

Yum, M. K. *et al.* *Nature* **594**, 442–447 (2021).

[Article](#) [Google Scholar](#)

2. 2.

van Neerven, S. M. *et al.* *Nature* **594**, 436–441 (2021).

[Article](#) [Google Scholar](#)

3. 3.

Flanagan, D. J. *et al.* *Nature* **594**, 430–435 (2021).

[Article](#) [Google Scholar](#)

4. 4.

Kinzler, K. W. & Vogelstein, B. *Cell* **87**, 159–170 (1996).

[PubMed](#) [Article](#) [Google Scholar](#)

5. 5.

Kwong, L. N. & Dove, W. F. *Adv. Exp. Med. Biol.* **656**, 85–106 (2009).

[PubMed](#) [Article](#) [Google Scholar](#)

6. 6.

Suijkerbuijk, S. J. E., Kolahgar, G., Kucinski, I. & Piddini, E. *Curr. Biol.* **26**, 428–438 (2016).

[PubMed](#) [Article](#) [Google Scholar](#)

7. 7.

Galluzzi, L., Spranger, S., Fuchs, E. & López-Soto, A. *Trends Cell Biol.* **29**, 44–65 (2019).

[PubMed](#) [Article](#) [Google Scholar](#)

8. 8.

Welner, R. S. *et al.* *Cancer Cell* **27**, 671–681 (2015).

[PubMed](#) [Article](#) [Google Scholar](#)

9. 9.

Reynaud, D. *et al.* *Cancer Cell* **20**, 661–673 (2011).

[PubMed](#) [Article](#) [Google Scholar](#)

10. 10.

Sancho, M. *et al.* *Dev. Cell* **26**, 19–30 (2013).

[PubMed](#) [Article](#) [Google Scholar](#)

11. 11.

Liu, N. *et al.* *Nature* **568**, 344–350 (2019).

[PubMed](#) [Article](#) [Google Scholar](#)

12. 12.

Tanimura, N. & Fujita, Y. *Semin. Cancer Biol.* **63**, 44–48 (2020).

[PubMed](#) [Article](#) [Google Scholar](#)

13. 13.

Merino, M. M. *et al.* *Cell* **160**, 461–476 (2015).

[PubMed](#) [Article](#) [Google Scholar](#)

14. 14.

Pentimikko, N. *et al.* *Nature* **571**, 398–402 (2019).

[PubMed](#) [Article](#) [Google Scholar](#)

15. 15.

Kakiuchi, N. & Ogawa, S. *Nature Rev. Cancer* **21**, 239–256 (2021).

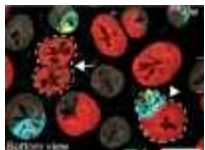
[PubMed](#) [Article](#) [Google Scholar](#)

[Download references](#)

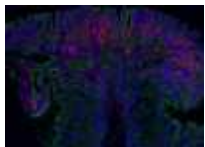
Competing Interests

The authors declare no competing interests.

Related Articles



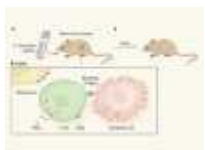
- [Read the paper: Tracing oncogene-driven remodelling of the intestinal stem cell niche](#)



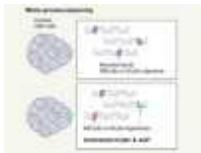
- [Read the paper: Apc-mutant cells act as supercompetitors in intestinal tumour initiation](#)



- [Read the paper: NOTUM from Apc-mutant cells biases clonal competition to initiate cancer](#)



- [A gut punch fights cancer and infection](#)



- [A mutational signature that can be made by a bacterium arises in human colon cancer](#)
- [See all News & Views](#)

Subjects

- [Cancer](#)
- [Stem cells](#)
- [Medical research](#)

Jobs from Nature Careers

- - - [All jobs](#)
 - - [Post Doctoral Fellow Bioinformatics Modern and Ancient Infectious Diseases](#)

[Faculty of Medicine, Dalhousie University](#)

[Multiple locations](#)

[JOB POST](#)

- [Research Fellow - Molecular Pharmacology & Experimental Therapeutics](#)

[Mayo Clinic Health System](#)

[Rochester, MN, United States](#)

JOB POST

- **Research Fellow - Neurobiology**

Mayo Clinic Health System

Rochester, MN, United States

JOB POST

- **Scientist for PETRA III Beamline P07**

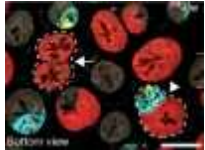
German Electron Synchrotron (DESY)

Hamburg, Germany

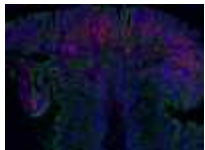
JOB POST

Download PDF

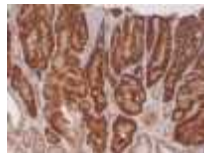
Related Articles



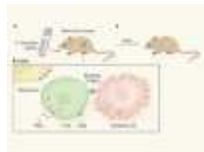
- **Read the paper: Tracing oncogene-driven remodelling of the intestinal stem cell niche**



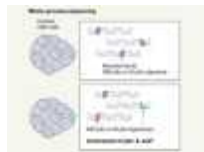
- **Read the paper: Apc-mutant cells act as supercompetitors in intestinal tumour initiation**



- [Read the paper: NOTUM from Apc-mutant cells biases clonal competition to initiate cancer](#)



- [A gut punch fights cancer and infection](#)



- [A mutational signature that can be made by a bacterium arises in human colon cancer](#)
- [See all News & Views](#)

Subjects

- [Cancer](#)
- [Stem cells](#)
- [Medical research](#)

This article was downloaded by **calibre** from <https://www.nature.com/articles/d41586-021-01379-z>

- NEWS AND VIEWS
- 04 June 2021

Attraction and repulsion cooperate during brain-circuit wiring

Examination of the molecular interactions that govern the assembly of neural circuits in a brain region called the hippocampus reveals that neuronal projections are guided to their targets by both attractive and repulsive cues.

- [Yajun Xie](#) ⁰ &
- [Corey Harwell](#) ¹

1. Yajun Xie

1. Yajun Xie is in the Department of Neurobiology, Harvard Medical School, Boston, Massachusetts 02115, USA.

[View author publications](#)

You can also search for this author in [PubMed](#) [Google Scholar](#)

2. [Corey Harwell](#)

1. Corey Harwell is in the Department of Neurobiology, Harvard Medical School, Boston, Massachusetts 02115, USA, and in the Department of Neurology, Eli and Edythe Broad Center of Regeneration Medicine, University of California, San Francisco, San Francisco, California 94143, USA, and in the Chan Zuckerberg Biohub, San Francisco.

[View author publications](#)

You can also search for this author in [PubMed](#) [Google Scholar](#)





•

[Download PDF](#)

Our ability to sense and navigate the world requires the precise assembly and function of neural circuits in the brain. During development, neuronal-cell projections called axons are guided by molecular cues to extend away from non-target regions of the brain and towards their target regions¹, where axons make synaptic connections with partner neurons. Over the past few decades, several candidate molecular cues have been identified²; however, questions remain as to whether distinct sets of cell-surface molecules mediate attraction to targets and avoidance of non-target regions. [Writing in Science](#), Pederick *et al.*³ show in mice that axon attraction and repulsion are

guided by the same cell-surface molecule during circuit assembly in the hippocampus, a brain region involved in spatial memory and navigation⁴.

The hippocampus contains the subfields CA1, CA2 and CA3, and neurons in the CA1 subfield project to a target region in an adjacent brain structure called the subiculum. CA1 projections to the subiculum are organized along a medial-to-lateral anatomical axis. In this way, in the medial part of the network, neurons in the proximal CA1 (located near the border with the CA2 region) project to the distal subiculum (the part farthest from the CA1 border), whereas, in the lateral part of the network, distal CA1 neurons project to the proximal subiculum (Fig. 1).

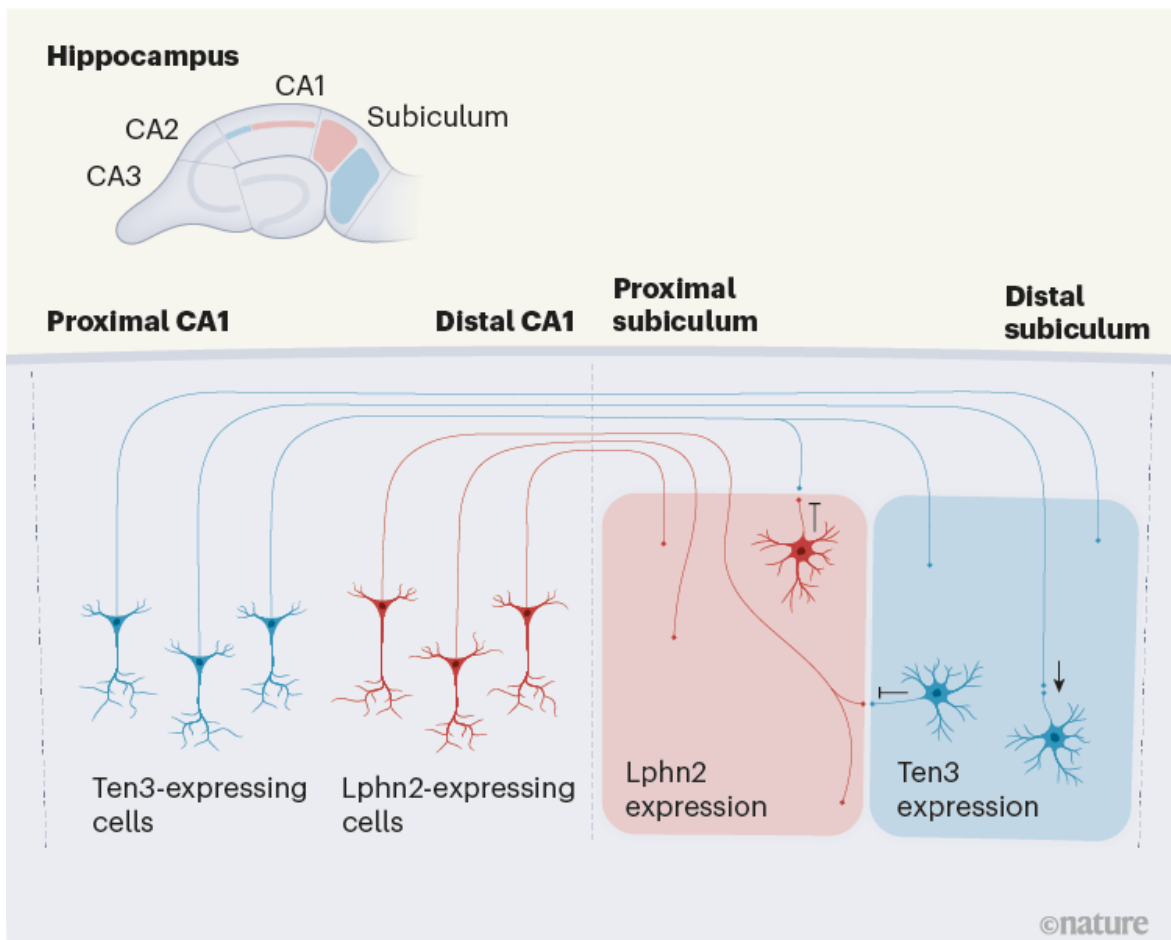
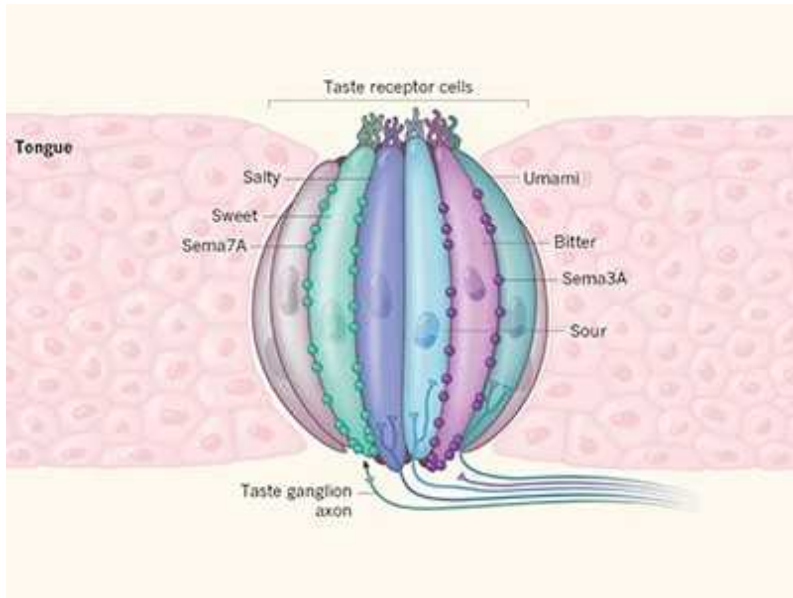


Figure 1 | Attractive and repulsive interactions mediate neuronal-circuit assembly. The hippocampus, a brain structure involved in memory, contains the CA1, CA2 and CA3 subfields. During development, neurons in the CA1 region extend projections called axons to another brain region, called the

subiculum, to form two networks. In the medial network, neurons in the proximal part of CA1 (proximal CA1) express the cell-surface molecule teneurin-3 (Ten3) and project to the distal subiculum, a region where other neurons express Ten3. In the lateral network, neurons in distal CA1 express latrophilin 2 (Lphn2) and project to the proximal subiculum, which also is rich in Lphn2. Previous work⁴ revealed that Ten3-expressing axons are attracted to Ten3-expressing regions (arrow). Pederick *et al.*³ manipulated Ten3 and Lphn2 expression in CA1 and the subiculum to reveal that Ten3-expressing axons of proximal CA1 are also repelled (blocking symbol) by Lphn2-expressing neurons in the proximal subiculum — and that, similarly, Lphn2-expressing axons from distal CA1 are repelled by Ten3-expressing cells in the distal subiculum.

A previous study by Pederick and colleagues' laboratory showed⁵ that a cell-surface molecule called teneurin-3 (Ten3) is expressed both by proximal CA1 neurons and by neurons in their target region, the distal subiculum. The study showed that molecules of Ten3 adhere to each other, and that this binding leads to attraction between neurons expressing this protein. Through this interaction, Ten3-expressing projections are attracted to target regions that express Ten3. Pederick *et al.* hypothesized that a similar mechanism — in which protein binding causes projections expressing that protein to be attracted to target regions expressing the same protein — might be involved in directing the formation of the lateral hippocampal network.

Using a technique called single-cell RNA sequencing to profile gene expression in individual cells from the developing mouse hippocampus, Pederick *et al.* found that the cell-surface protein latrophilin 2 (Lphn2) was expressed both in distal CA1 projections and in proximal-subiculum target neurons of the lateral hippocampal network. They initially investigated whether Lphn2–Lphn2 adhesion and attraction might, in a similar way to Ten3–Ten3 adhesion and attraction, direct the formation of hippocampal circuits. However, this was not the case: when the authors overexpressed Lphn2 in a non-adhesive cell line, the cells did not adhere to each other. By contrast, Lphn2-expressing cells readily formed aggregates with Ten3-expressing cells, consistent with previous reports of Lphn2–Ten3 binding⁶.



A bitter–sweet symphony

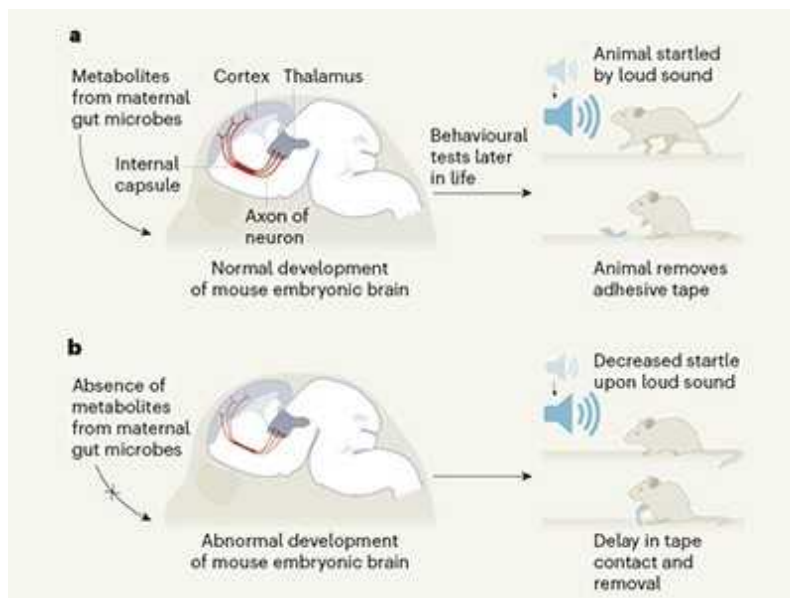
The binding of Lphn2 to Ten3 could potentially trigger the activation of signalling pathways inside an axon, resulting in it moving towards or away from the region in which the interaction takes place. Because the areas targeted by Ten3-expressing axons and Lphn2-expressing axons do not overlap, Pederick and colleagues reasoned that Ten3–Lphn2 interactions might result in repulsion. To test this, the authors used a clever approach that involved injecting engineered viruses into the hippocampus to manipulate the expression of Lphn2 and Ten3 by CA1 neurons, and by neurons in their subiculum target regions.

The authors injected a virus expressing Lphn2 into the distal part of the developing subiculum, where Lphn2 levels are normally low, to increase Lphn2 levels there. Once the hippocampus had developed fully, the authors injected a virus expressing a fluorescent protein into the proximal CA1, where Ten3 expression is high, to visualize the axons from that region that had innervated the subiculum. These axons avoided the regions where Lphn2 was artificially expressed. The authors then performed the converse experiment: reducing Lphn2 expression in the developing proximal subiculum, where expression of this protein is usually high. In this case, Ten3-expressing axons from the proximal CA1 region invaded the regions where Lphn2 expression was reduced. Together, these results suggest that

Lphn2–Ten3 interactions are necessary and sufficient for repulsive guidance of Ten3-expressing axons.

Crucially, the authors assessed the relative contributions of Ten3-mediated attraction and Lphn2-mediated repulsion of Ten3-expressing proximal CA1 axons, by reducing the expression of both Ten3 and Lphn2 across the entire subiculum. This manipulation led to an increase in axon projections in non-target regions and reduced innervation of the target region. Therefore, the precise targeting of Ten3-expressing proximal CA1 axons seems to require both Lphn2-mediated repulsion away from non-target regions and Ten3-mediated attraction.

How do Lphn2-expressing CA1 axons respond to target regions containing high levels of Ten3? Deletion of Ten3 expression from cells in the distal subiculum led to greater innervation of Lphn2-expressing axons from neurons in more-distal parts of CA1 into more-distal subiculum than was observed in hippocampi from control mice; this indicated that target-derived Ten3 repels Lphn2 axons.



Maternal microbes support fetal brain wiring

Cooperation between attraction and repulsion of axon projections is a familiar theme in the development of neural circuits². This study demonstrates that the connectivity between CA1 axons and subiculum

neurons in the hippocampal network tightly follows a ‘Ten3 axon to Ten3 target, Lphn2 axon to Lphn2 target’ rule, instructed by reciprocal repulsions between Ten3-expressing and Lphn2-expressing cells.

Pederick *et al.* beautifully demonstrate how the binding interactions between cell-surface molecules depend on cellular context: on CA1 projections, Ten3 acts as a receptor for both attractive (Ten3) and repulsive (Lphn2) target-derived cues, whereas in the subiculum, it serves to repel Lphn2-expressing axons (Fig. 1). The importance of developmental context for the mechanisms that guide circuit assembly is further indicated by another study⁷ showing that coincident binding of Lphn2, Ten3 and another cell-surface molecule, Flrt2, is required for the formation of neuronal synaptic connections between CA1 neurons and their partners upstream in the hippocampal circuit, rather than for axon guidance.

Further research is needed to identify the signalling cascades that are triggered by cell-surface molecules such as Ten3 and Lphn2, and that determine whether and how an axon is attracted to or repulsed by a given molecular cue. Also, if attraction and repulsion are both necessary for precise circuit assembly, what is the identity of the cell-surface molecule that mediates the attraction of Lphn2-expressing axons?

Given that the number of cell-surface molecules encoded by the genome is limited but the circuitry of the mammalian brain is highly complex, each cell-surface molecule that is involved in guiding axons to their appropriate targets probably serves multiple such functions in different circuits, depending on the cellular and developmental context. It will be crucial to account for each molecule’s context-dependent roles during the assembly of diverse neuronal circuits.

Nature **594**, 341-343 (2021)

doi: <https://doi.org/10.1038/d41586-021-01502-0>

References

1. 1.

Sperry, R. W. *Proc. Natl Acad. Sci. USA* **50**, 703–710 (1963).

[PubMed](#) [Article](#) [Google Scholar](#)

2. 2.

Sanes, J. R. & Zipursky, S. L. *Cell* **181**, 536–556 (2020).

[PubMed](#) [Article](#) [Google Scholar](#)

3. 3.

Pederick, D. T. *et al.* *Science* <https://doi.org/10.1126/science.abg1774> (2021).

[Article](#) [Google Scholar](#)

4. 4.

Igarashi, K. M., Ito, H. T., Moser, E. I. & Moser, M.-B. *FEBS Lett.* **588**, 2470–2476 (2014).

[PubMed](#) [Article](#) [Google Scholar](#)

5. 5.

Berns, D. S., DeNardo, L. A., Pederick, D. T. & Luo, L. *Nature* **554**, 328–333 (2018).

[PubMed](#) [Article](#) [Google Scholar](#)

6. 6.

Del Toro, D. *et al.* *Cell* **180**, 323–339e.19 (2020).

[PubMed](#) [Article](#) [Google Scholar](#)

7. 7.

Sando, R., Jiang, X. & Südhof, T. C. *Science* **363**, eaav7969 (2019).

[PubMed Article](#) [Google Scholar](#)

[Download references](#)

Competing Interests

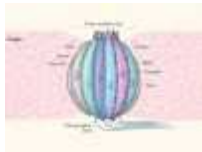
C.H. is in the process of transitioning from his appointment at Harvard Medical School to UCSF where he will also be a Chan Zuckerberg Biohub investigator. Stephen Quake is a co-author of the study referred to in this News & Views article and is currently co-president of the Chan Zuckerberg Biohub.

Related Articles

- [Reciprocal repulsions instruct the precise assembly of parallel hippocampal networks](#)



- [Maternal microbes support fetal brain wiring](#)



- [A bitter–sweet symphony](#)
- [See all News & Views](#)

Subjects

- [Neuroscience](#)
- [Brain](#)
- [Developmental biology](#)

Jobs from Nature Careers

- - - [All jobs](#)
 - - [Post Doctoral Fellow Bioinformatics Modern and Ancient Infectious Diseases](#)
[Faculty of Medicine, Dalhousie University](#)
[Multiple locations](#)
[JOB POST](#)
 - [Research Fellow - Molecular Pharmacology & Experimental Therapeutics](#)
[Mayo Clinic Health System](#)
[Rochester, MN, United States](#)
[JOB POST](#)
 - [Research Fellow - Neurobiology](#)
[Mayo Clinic Health System](#)
[Rochester, MN, United States](#)
[JOB POST](#)
 - [Scientist for PETRA III Beamline P07](#)
[German Electron Synchrotron \(DESY\)](#)

[Hamburg, Germany](#)

[JOB POST](#)

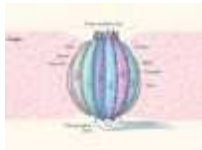
[Download PDF](#)

Related Articles

- [Reciprocal repulsions instruct the precise assembly of parallel hippocampal networks](#)



- [Maternal microbes support fetal brain wiring](#)



- [A bitter–sweet symphony](#)
- [See all News & Views](#)

Subjects

- [Neuroscience](#)
- [Brain](#)
- [Developmental biology](#)

This article was downloaded by **calibre** from <https://www.nature.com/articles/d41586-021-01502-0>

- NEWS AND VIEWS
- 16 June 2021

Great Dimming of Betelgeuse explained

Observations suggest that an unexpected dimming of the massive star Betelgeuse resulted from dust forming over a cold patch in the star's southern hemisphere. This finding improves our understanding of such massive stars.

- [Emily M. Levesque](#) 0

1. [Emily M. Levesque](#)

1. Emily M. Levesque is in the Department of Astronomy, University of Washington, Seattle, Washington 98195, USA.

[View author publications](#)

You can also search for this author in [PubMed](#) [Google Scholar](#)



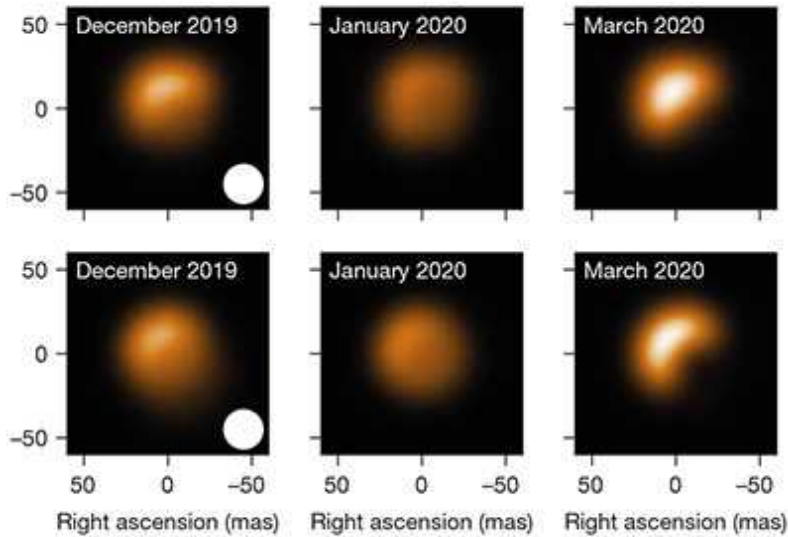


•

[Download PDF](#)

In December 2019, astronomers reported¹ a surprising change in the appearance of Betelgeuse. The bright red star in the shoulder of the Orion constellation had begun dimming dramatically during the preceding two months. In the following weeks, Betelgeuse's rapid and unprecedented dimming continued. By mid-February 2020, the star had plummeted to about 35% of its typical brightness² before swiftly recovering over the next few months. The event captivated professional and amateur stargazers alike because such rapid and visible changes in the night sky are rare. Now, a year after Betelgeuse's recovery from what has become known as its Great

Dimming, Montargès *et al.*³ [present a detailed picture](#) of and compelling explanation for this strange behaviour.



[Read the paper: A dusty veil shading Betelgeuse during its Great Dimming](#)

Betelgeuse was born with about 20 times the mass of the Sun⁴. Such massive stars evolve much faster than their lower-mass counterparts, with lifetimes of mere millions rather than billions of years. Betelgeuse is a red supergiant — a stage in the evolution of massive stars that begins when these stars transition from fusing hydrogen in their cores to fusing helium; this leads to the cooling and expansion of their outer layers. The cores then spend several million years fusing progressively heavier elements before collapsing. These dying stars produce the spectacular fireworks show of a supernova, leaving behind neutron stars or black holes, and enriching their surroundings as they hurl the elements made in their interiors into interstellar space.

Red supergiants represent an extreme stage of stellar evolution. They are the largest stars in the Universe — for instance, Betelgeuse has a radius 900 times that of the Sun⁴, and if it were placed at the centre of the Solar System, it would swallow all 4 inner planets and nearly reach the orbit of Jupiter. The huge cold outer layers of red supergiants pulsate, and host a handful of enormous convective cells (volumes of material that move as a result of

convection). Furthermore, these outer layers shed mass that can eventually form dust in the star's surrounding environment.

Modelling the outer layers of red supergiants is extremely challenging, because the mechanisms driving mass loss and dust production are complex, and the effects of these various quirks on the star's brightness, evolution and eventual death are far from clear. Nevertheless, efforts to better understand red supergiants are worth the trouble because these stars are key players in the cycle of stellar birth and death and in the chemical evolution of the cosmos.

Betelgeuse's Great Dimming was evident with the naked eye, but the observations presented by Montargès *et al.* reveal the full details of the star's sudden change in appearance. Betelgeuse's large size and close proximity to Earth (about 220 parsecs, or 724 light years⁵) make it one of only a few stars that can be seen as a spatially resolved disk rather than a single point. Using instruments on the European Southern Observatory's Very Large Telescope in Chile, Montargès and colleagues captured pictures of Betelgeuse both before and during the Great Dimming. A comparison of these images shows that the star hadn't simply shrunk or dimmed uniformly. Instead, the light loss was concentrated in the star's southern hemisphere (Fig. 1).

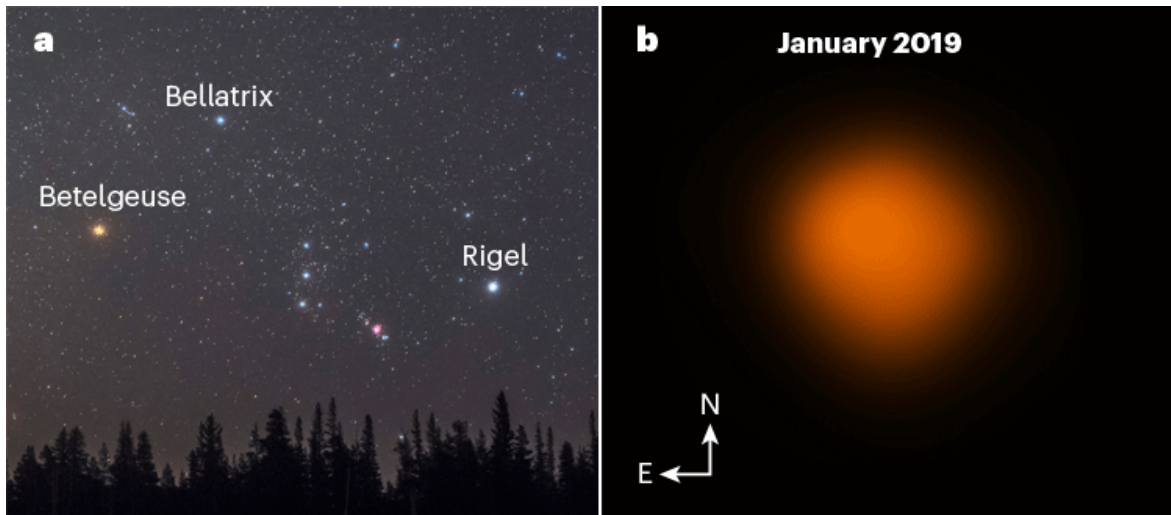
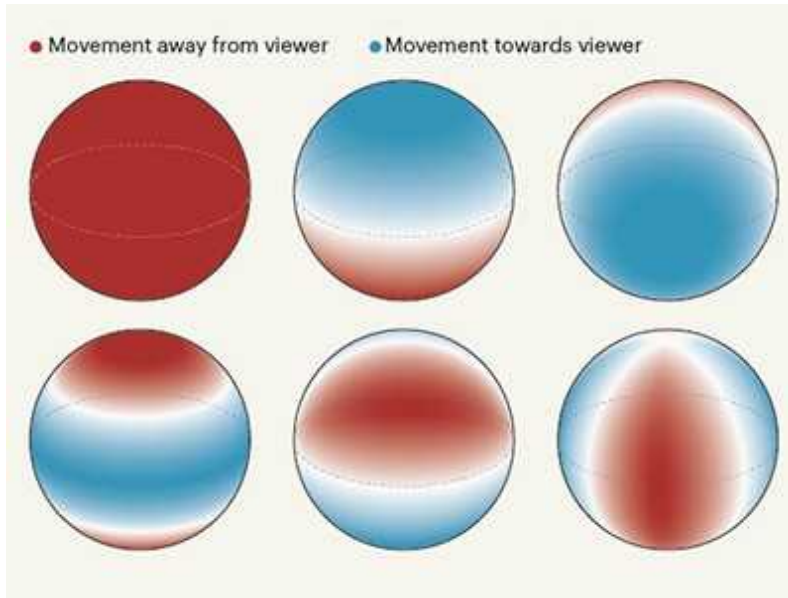


Figure 1 | Location and observations of Betelgeuse. **a**, Normally, Betelgeuse is the brightest star in the Orion constellation; Rigel is the second brightest and Bellatrix the third brightest. **b**, Montargès *et al.*³ observed Betelgeuse before (January 2019) and during (January 2020) a period known

as the Great Dimming, in which the star was comparable in brightness to Bellatrix. The observations show that the light loss was concentrated in Betelgeuse's southern hemisphere. A detailed analysis by the authors suggests that a southern dust cloud temporarily blocked much of the star's light.

Could the dimming be explained by a short-lived cold patch on Betelgeuse's southern surface, produced by the churn of enormous convective cells? Or might a clump of dust be blocking our view of the star, making it temporarily seem dimmer? Some early observations concluded that the dimming was probably caused by dust, and that this dust had been made by Betelgeuse itself^{6,7}. However, other work presented evidence of temperature changes in the star's atmosphere, and suggested that cooling might also have played a part in the dimming^{8,9}. Montargès *et al.* addressed this uncertainty by modelling both scenarios and comparing the models with their images. They conclude that, although dust was the ultimate culprit, the two scenarios are not at odds but are linked.

Observations show evidence of a mass-loss episode that began nearly a year before the Great Dimming^{7,10}, releasing a clump of gas. Montargès and colleagues suggest that, in late 2019, a combination of normal pulsation behaviour and a convection-driven cold patch in the star's southern hemisphere began to cool the local environment. The drop in temperature allowed the recently shed gas in that region to rapidly form dust. This process generated a dense southern dust cloud that temporarily blocked much of Betelgeuse's light, giving us what we saw as the Great Dimming.



A glimpse inside δ Scuti stars

What does this mean for Betelgeuse? Its behaviour in late 2019 made headlines, in part because of the tantalizing prospect that the dimming might be a sign of the star's imminent demise. Betelgeuse is an irresistible target on which to pin hopes of seeing a supernova happen in our own Galaxy. Such events are incredibly rare, with the most recent observation of a Milky Way supernova pre-dating the invention of the telescope. However, Montargès *et al.* make clear that the Great Dimming does not indicate any sign of an impending supernova. Importantly, they also note that Betelgeuse might not give us much warning — astronomers currently cannot predict, at least on any realistic human timescale, when a star will die.

The lack of an explosive conclusion might seem disappointing, but Montargès and colleagues' results go beyond explaining one brief wink of a nearby star. Could other red supergiants show signs of their own Great Dimmings? Next-generation facilities focused on monitoring stellar brightness over time, or on studying the signatures of dust in the infrared spectra of stars, could prove invaluable for expanding the lessons learnt here. This exquisitely detailed study of Betelgeuse's unexpected behaviour lays the groundwork for unravelling the properties of an entire population of stars.

doi: <https://doi.org/10.1038/d41586-021-01526-6>

References

1. 1.

Guinan, E. F., Wasatonic, R. J. & Calderwood, T. J. *Astron. Telegr.* 13341 (2019).

2. 2.

Guinan, E., Wasatonic, R., Calderwood, T. & Carona, D. *Astron. Telegr.* 13512 (2020).

3. 3.

Montargès, M. *et al.* *Nature* **594**, 365–368 (2021).

[Article](#) [Google Scholar](#)

4. 4.

Dolan, M. M. *et al.* *Astrophys. J.* **819**, 7 (2016).

[Article](#) [Google Scholar](#)

5. 5.

Harper, G. M. *et al.* *Astronom. J.* **154**, 11 (2017).

[Article](#) [Google Scholar](#)

6. 6.

Levesque, E. M. & Massey, P. *Astrophys. J.* **891**, L37 (2020).

[Article](#) [Google Scholar](#)

7. 7.

Dupree, A. K. *et al.* *Astrophys. J.* **899**, 68 (2020).

[Article](#) [Google Scholar](#)

8. 8.

Harper, G. M., Guinan, E. F., Wasatonic, R. & Ryde, N. *Astrophys. J.* **905**, 34 (2020).

[Article](#) [Google Scholar](#)

9. 9.

Dharmawardena, T. E. *et al.* *Astrophys. J.* **897**, L9 (2020).

[Article](#) [Google Scholar](#)

10. 10.

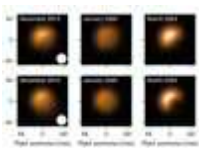
Kravchenko, K. *et al.* Preprint at <https://arxiv.org/abs/2104.08105> (2021).

[Download references](#)

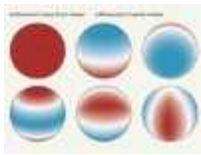
Competing Interests

The author declares no competing interests.

Related Articles



- [Read the paper: A dusty veil shading Betelgeuse during its Great Dimming](#)



- [A glimpse inside δ Scuti stars](#)



- [A turbulent stellar atmosphere in full view](#)
- [See all News & Views](#)

Subjects

- [Astronomy and astrophysics](#)

[Jobs from Nature Careers](#)

- - - [All jobs](#)
 -
 - [Post Doctoral Fellow Bioinformatics Modern and Ancient Infectious Diseases](#)
 - [Faculty of Medicine, Dalhousie University](#)
 - [Multiple locations](#)
 - [JOB POST](#)
 - [Research Fellow - Molecular Pharmacology & Experimental Therapeutics](#)
 - [Mayo Clinic Health System](#)

[Rochester, MN, United States](#)

[JOB POST](#)

▪ [**Research Fellow - Neurobiology**](#)

[Mayo Clinic Health System](#)

[Rochester, MN, United States](#)

[JOB POST](#)

▪ [**Scientist for PETRA III Beamline P07**](#)

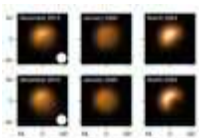
[German Electron Synchrotron \(DESY\)](#)

[Hamburg, Germany](#)

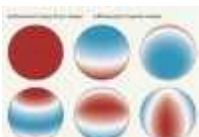
[JOB POST](#)

[Download PDF](#)

Related Articles



- [Read the paper: A dusty veil shading Betelgeuse during its Great Dimming](#)



- [A glimpse inside δ Scuti stars](#)



- [A turbulent stellar atmosphere in full view](#)

- [See all News & Views](#)

Subjects

- [Astronomy and astrophysics](#)

This article was downloaded by **calibre** from <https://www.nature.com/articles/d41586-021-01526-6>

| [Section menu](#) | [Main menu](#) |

- Review Article
- [Published: 16 June 2021](#)

Peopling of the Americas as inferred from ancient genomics

- [Eske Willerslev](#) ORCID: [orcid.org/0000-0002-7081-6748^{1,2,3 na1}](https://orcid.org/0000-0002-7081-6748) &
- [David J. Meltzer](#) ORCID: [orcid.org/0000-0001-8084-9802^{2,4 na1}](https://orcid.org/0000-0001-8084-9802)

Nature volume 594, pages 356–364 (2021) [Cite this article](#)

- 2405 Accesses
- 60 Altmetric
- [Metrics details](#)

Subjects

- [Genetics](#)
- [Population genetics](#)

Abstract

In less than a decade, analyses of ancient genomes have transformed our understanding of the Indigenous peopling and population history of the Americas. These studies have shown that this history, which began in the late Pleistocene epoch and continued episodically into the Holocene epoch, was far more complex than previously thought. It is now evident that the initial dispersal involved the movement from northeast Asia of distinct and previously unknown populations, including some for whom there are no currently known descendants. The first peoples, once south of the

continental ice sheets, spread widely, expanded rapidly and branched into multiple populations. Their descendants—over the next fifteen millennia—experienced varying degrees of isolation, admixture, continuity and replacement, and their genomes help to illuminate the relationships among major subgroups of Native American populations. Notably, all ancient individuals in the Americas, save for later-arriving Arctic peoples, are more closely related to contemporary Indigenous American individuals than to any other population elsewhere, which challenges the claim—which is based on anatomical evidence—that there was an early, non-Native American population in the Americas. Here we review the patterns revealed by ancient genomics that help to shed light on the past peoples who created the archaeological landscape, and together lead to deeper insights into the population and cultural history of the Americas.

Access options

Subscribe to Journal

Get full journal access for 1 year

\$199.00

only \$3.90 per issue

[Subscribe](#)

All prices are NET prices.

VAT will be added later in the checkout.

Tax calculation will be finalised during checkout.

Rent or Buy article

Get time limited or full article access on ReadCube.

from \$8.99

[Rent or Buy](#)

All prices are NET prices.

Additional access options:

- [Log in](#)
- [Access through your institution](#)
- [Learn about institutional subscriptions](#)

Fig. 1: Ancient whole-genomes and genome-wide SNP capture analyses from the Americas.

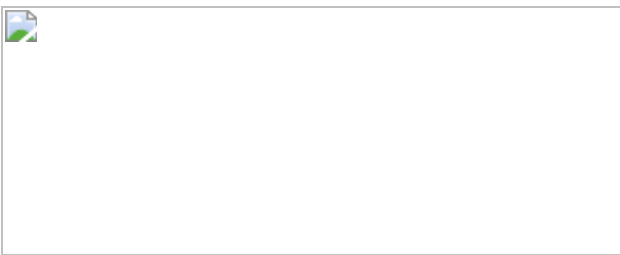


Fig. 2: Schematic of the processes of human dispersal and divergence into and within the Americas in the Pleistocene.

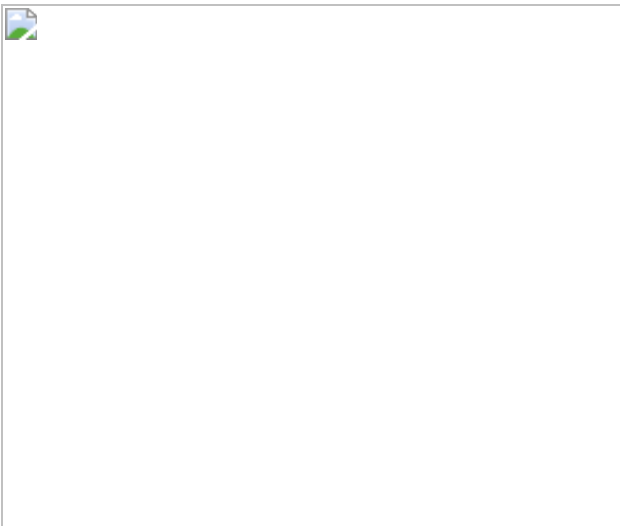
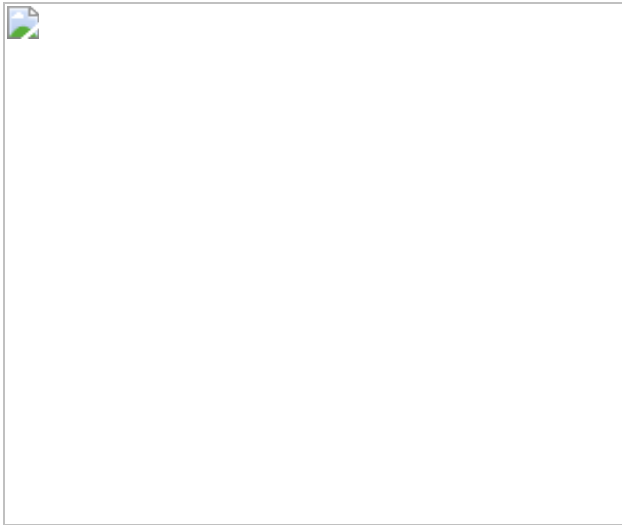


Fig. 3: Schematic of the processes of human dispersal and divergence into and within the Americas in the Holocene, and to the Caribbean Islands and Greenland in the late Holocene.



References

1. 1.

Achilli, A. et al. The phylogeny of the four pan-American mtDNA haplogroups: implications for evolutionary and disease studies. *PLoS ONE* **3**, e1764 (2008).

[ADS](#) [PubMed](#) [PubMed Central](#) [Google Scholar](#)

2. 2.

Achilli, A. et al. Reconciling migration models to the Americas with the variation of North American native mitogenomes. *Proc. Natl Acad. Sci. USA* **110**, 14308–14313 (2013).

[ADS](#) [CAS](#) [PubMed](#) [Google Scholar](#)

3. 3.

Fagundes, N. J. R. et al. Mitochondrial population genomics supports a single pre-Clovis origin with a coastal route for the peopling of the Americas. *Am. J. Hum. Genet.* **82**, 583–592 (2008).

[CAS](#) [PubMed](#) [PubMed Central](#) [Google Scholar](#)

4. 4.

Kashani, B. H. et al. Mitochondrial haplogroup C4c: a rare lineage entering America through the ice-free corridor? *Am. J. Phys. Anthropol.* **147**, 35–39 (2012).

[Google Scholar](#)

5. 5.

Malhi, R. S. et al. Brief communication: mitochondrial haplotype C4c confirmed as a founding genome in the Americas. *Am. J. Phys. Anthropol.* **141**, 494–497 (2009).

[Google Scholar](#)

6. 6.

Perego, U. A. et al. The initial peopling of the Americas: a growing number of founding mitochondrial genomes from Beringia. *Genome Res.* **20**, 1174–1179 (2010).

[CAS](#) [PubMed](#) [PubMed Central](#) [Google Scholar](#)

7. 7.

Volodko, N. V. et al. Mitochondrial genome diversity in arctic Siberians, with particular reference to the evolutionary history of Beringia and Pleistocene peopling of the Americas. *Am. J. Hum. Genet.* **82**, 1084–1100 (2008).

[CAS](#) [PubMed](#) [PubMed Central](#) [Google Scholar](#)

8. 8.

Battaglia, V. et al. The first peopling of South America: new evidence from Y-chromosome haplogroup Q. *PLoS ONE* **8**, e71390 (2013).

[ADS](#) [CAS](#) [PubMed](#) [PubMed Central](#) [Google Scholar](#)

9. 9.

Dulik, M. C. et al. Y-chromosome analysis reveals genetic divergence and new founding native lineages in Athapaskan- and Eskimoan-speaking populations. *Proc. Natl Acad. Sci. USA* **109**, 8471–8476 (2012).

[ADS](#) [CAS](#) [PubMed](#) [Google Scholar](#)

10. 10.

Malhi, R. S. et al. Distribution of Y chromosomes among native North Americans: a study of Athapaskan population history. *Am. J. Phys. Anthropol.* **137**, 412–424 (2008).

[PubMed](#) [PubMed Central](#) [Google Scholar](#)

11. 11.

Bolnick, D. A., Raff, J. A., Springs, L. C., Reynolds, A. W. & Miró-Herrans, A. T. Native American genomics and population histories. *Annu. Rev. Anthropol.* **45**, 319–340 (2016).

[Google Scholar](#)

12. 12.

Pickrell, J. K. & Reich, D. Toward a new history and geography of human genes informed by ancient DNA. *Trends Genet.* **30**, 377–389 (2014).

[CAS](#) [PubMed](#) [PubMed Central](#) [Google Scholar](#)

13. 13.

O'Fallon, B. D. & Fehren-Schmitz, L. Native Americans experienced a strong population bottleneck coincident with European contact. *Proc. Natl Acad. Sci. USA* **108**, 20444–20448 (2011).

[ADS](#) [PubMed](#) [Google Scholar](#)

14. 14.

Milner, G. R. in *Beyond Germs: Native Depopulation in North America* (eds Cameron, C. M. et al.) 50–73 (Univ. Arizona Press, 2015).

15. 15.

Reich, D. et al. Reconstructing Native American population history. *Nature* **488**, 370–374 (2012). **The first large-scale genome-wide SNP-array study of present-day Native American individuals.**

[ADS](#) [CAS](#) [PubMed](#) [PubMed Central](#) [Google Scholar](#)

16. 16.

Leonardi, M. et al. Evolutionary patterns and processes: lessons from ancient DNA. *Syst. Biol.* **66**, e1–e29 (2017).

[PubMed](#) [Google Scholar](#)

17. 17.

Stoneking, M. & Krause, J. Learning about human population history from ancient and modern genomes. *Nat. Rev. Genet.* **12**, 603–614 (2011).

[CAS](#) [PubMed](#) [Google Scholar](#)

18. 18.

Cappellini, E. et al. Ancient biomolecules and evolutionary inference. *Annu. Rev. Biochem.* **87**, 1029–1060 (2018).

[CAS](#) [PubMed](#) [Google Scholar](#)

19. 19.

Rasmussen, M. et al. The genome of a Late Pleistocene human from a Clovis burial site in western Montana. *Nature* **506**, 225–229 (2014).

The first ancient genome sequenced from the Americas, which revealed a deep basal split between North and South Native American populations, and continuity between Clovis and contemporary Native American populations.

[ADS](#) [CAS](#) [PubMed](#) [PubMed Central](#) [Google Scholar](#)

20. 20.

Meltzer, D. J. *First Peoples in a New World: Populating Ice Age America* 2nd edn (Cambridge Univ. Press, 2021).

21. 21.

Posth, C. et al. Reconstructing the deep population history of Central and South America. *Cell* **175**, 1185–1197.e22 (2018). **Genome-wide analyses of ancient Central and South American populations revealed the timing and patterns of population continuity and discontinuity over time.**

[CAS](#) [PubMed](#) [PubMed Central](#) [Google Scholar](#)

22. 22.

Pitulko, V. V. et al. The Yana RHS site: humans in the Arctic before the Last Glacial Maximum. *Science* **303**, 52–56 (2004).

[ADS](#) [CAS](#) [PubMed](#) [Google Scholar](#)

23. 23.

Pitulko, V., Pavlova, E. & Nikolskiy, P. Revising the archaeological record of the Upper Pleistocene Arctic Siberia: human dispersal and adaptations in MIS 3 and 2. *Quat. Sci. Rev.* **165**, 127–148 (2017).

[ADS](#) [Google Scholar](#)

24. 24.

Lambeck, K., Rouby, H., Purcell, A., Sun, Y. & Sambridge, M. Sea level and global ice volumes from the Last Glacial Maximum to the Holocene. *Proc. Natl Acad. Sci. USA* **111**, 15296–15303 (2014).

[ADS](#) [CAS](#) [PubMed](#) [Google Scholar](#)

25. 25.

Meiri, M. et al. Faunal record identifies Bering isthmus conditions as constraint to end-Pleistocene migration to the New World. *Proc. R. Soc. B* **281**, 20132167 (2014).

[PubMed](#) [Google Scholar](#)

26. 26.

Keigwin, L. D., Donnelly, J. P., Cook, M. S., Driscoll, N. W. & Brigham-Grette, J. Rapid sea-level rise and Holocene climate in the Chukchi Sea. *Geology* **34**, 861–864 (2006).

[ADS](#) [Google Scholar](#)

27. 27.

Pico, T., Mitrovica, J. X. & Mix, A. C. Sea level fingerprinting of the Bering Strait flooding history detects the source of the Younger Dryas climate event. *Sci. Adv.* **6**, eaay2935 (2020).

[ADS](#) [CAS](#) [PubMed](#) [PubMed Central](#) [Google Scholar](#)

28. 28.

Mann, D. H., Groves, P., Kunz, M. L., Reanier, R. E. & Gaglioti, B. V. Ice-age megafauna in Arctic Alaska: extinction, invasion, survival. *Quat. Sci. Rev.* **70**, 91–108 (2013).

[ADS](#) [Google Scholar](#)

29. 29.

Fitzhugh, B. in *Oxford Handbook of the Prehistoric Arctic* (eds Friesen, M. & Mason, O.) (Oxford Univ. Press, 2016).

30. 30.

Friesen, T. M. in *Oxford Handbook of the Prehistoric Arctic* (eds Friesen, M. & Mason, O.) (Oxford Univ. Press, 2016).

31. 31.

Goebel, T. & Potter, B. in *Oxford Handbook of the Prehistoric Arctic* (eds Friesen, M. & Mason, O.) (Oxford Univ. Press, 2016).

32. 32.

Graf, K. E. in *Paleoamerican Odyssey* (eds Graf, K. E. et al.) 65–80 (Texas A&M Press, 2014).

33. 33.

Kuzmin, Y. V. & Keates, S. G. Siberia and neighboring regions in the Last Glacial Maximum: did people occupy northern Eurasia at that time? *Archaeol. Anthropol. Sci.* **10**, 111–124 (2018).

[Google Scholar](#)

34. 34.

Holmes, C. E. Tanana River Valley archaeology circa 14,000 to 9000 B.P. *Arctic Anthropol.* **38**, 154–170 (2001).

[Google Scholar](#)

35. 35.

Dillehay, T. D. et al. Monte Verde: seaweed, food, medicine, and the peopling of South America. *Science* **320**, 784–786 (2008).

[ADS](#) [CAS](#) [PubMed](#) [Google Scholar](#)

36. 36.

Davis, L. G. et al. Late Upper Paleolithic occupation at Cooper's Ferry, Idaho, USA, ~16,000 years ago. *Science* **365**, 891–897 (2019).

[ADS](#) [CAS](#) [PubMed](#) [Google Scholar](#)

37. 37.

Jenkins, D. L. et al. Clovis age Western Stemmed projectile points and human coprolites at the Paisley Caves. *Science* **337**, 223–228 (2012).

[ADS](#) [CAS](#) [PubMed](#) [Google Scholar](#)

38. 38.

Waters, M. R. et al. Pre-Clovis projectile points at the Debra L. Friedkin site, Texas—implications for the Late Pleistocene peopling of the Americas. *Sci. Adv.* **4**, eaat4505 (2018).

[ADS](#) [CAS](#) [PubMed](#) [PubMed Central](#) [Google Scholar](#)

39. 39.

Ardelean, C. F. et al. Evidence of human occupation in Mexico around the Last Glacial Maximum. *Nature* **584**, 87–92 (2020).

[ADS](#) [CAS](#) [PubMed](#) [Google Scholar](#)

40. 40.

Dillehay, T. D. et al. New archaeological evidence for an early human presence at Monte Verde, Chile. *PLoS ONE* **10**, e0141923 (2015).

[PubMed](#) [PubMed Central](#) [Google Scholar](#)

41. 41.

Holen, S. R. et al. A 130,000-year-old archaeological site in southern California, USA. *Nature* **544**, 479–483 (2017).

[ADS](#) [CAS](#) [PubMed](#) [Google Scholar](#)

42. 42.

Braje, T. J. et al. Were hominins in California ~130,000 years ago? *PaleoAmerica* **3**, 200–202 (2017).

[Google Scholar](#)

43. 43.

Haynes, C. V. Jr. Fluted projectile points: their age and dispersion. *Science* **145**, 1408–1413 (1964).

[ADS](#) [PubMed](#) [Google Scholar](#)

44. 44.

Potter, B. A. et al. Current evidence allows multiple models for the peopling of the Americas. *Sci. Adv.* **4**, eaat5473 (2018).

[ADS](#) [PubMed](#) [PubMed Central](#) [Google Scholar](#)

45. 45.

Heintzman, P. D. et al. Bison phylogeography constrains dispersal and viability of the ice free corridor in western Canada. *Proc. Natl Acad. Sci. USA* **113**, 8057–8063 (2016).

[CAS](#) [PubMed](#) [Google Scholar](#)

46. 46.

Pedersen, M. W. et al. Postglacial viability and colonization in North America's ice-free corridor. *Nature* **537**, 45–49 (2016).

[ADS](#) [CAS](#) [PubMed](#) [Google Scholar](#)

47. 47.

Darvill, C. M., Menounos, B., Goehring, B. M., Lian, O. B. & Caffee, M. W. Retreat of the Western Cordilleran Ice Sheet margin during the last deglaciation. *Geophys. Res. Lett.* **45**, 9710–9720 (2018).

[ADS](#) [Google Scholar](#)

48. 48.

Lesnek, A. J., Briner, J. P., Lindqvist, C., Baichtal, J. F. & Heaton, T. H. Deglaciation of the Pacific coastal corridor directly preceded the human colonization of the Americas. *Sci. Adv.* **4**, eaar5040 (2018).

[ADS](#) [PubMed](#) [PubMed Central](#) [Google Scholar](#)

49. 49.

Menounos, B. et al. Cordilleran Ice Sheet mass loss preceded climate reversals near the Pleistocene Termination. *Science* **358**, 781–784 (2017).

[ADS](#) [CAS](#) [PubMed](#) [Google Scholar](#)

50. 50.

Smith, H. L. & Goebel, T. Origins and spread of fluted-point technology in the Canadian ice-free corridor and eastern Beringia. *Proc. Natl Acad. Sci. USA* **115**, 4116–4121 (2018).

[CAS](#) [PubMed](#) [Google Scholar](#)

51. 51.

Sikora, M. et al. The population history of northeastern Siberia since the Pleistocene. *Nature* **570**, 182–188 (2019).

[ADS](#) [CAS](#) [PubMed](#) [Google Scholar](#)

52. 52.

Raghavan, M. et al. Upper Palaeolithic Siberian genome reveals dual ancestry of Native Americans. *Nature* **505**, 87–91 (2014). **A Siberian Upper Paleolithic genome revealed a previously unsampled population that contributed to the ancestry of European, Siberian and Native American populations.**

[ADS](#) [PubMed](#) [Google Scholar](#)

53. 53.

Lipson, M. & Reich, D. A working model of the deep relationships of diverse modern human genetic lineages outside of Africa. *Mol. Biol. Evol.* **34**, 889–902 (2017).

[CAS](#) [PubMed](#) [PubMed Central](#) [Google Scholar](#)

54. 54.

Yu, H. et al. Paleolithic to Bronze Age Siberians reveal connections with First Americans and across Eurasia. *Cell* **181**, 1232–1245.e20 (2020).

[CAS](#) [PubMed](#) [Google Scholar](#)

55. 55.

Damgaard, P. D. B. et al. 137 ancient human genomes from across the Eurasian steppes. *Nature* **557**, 369–374 (2018).

[ADS](#) [CAS](#) [PubMed](#) [Google Scholar](#)

56. 56.

Raghavan, M. et al. Genomic evidence for the Pleistocene and recent population history of Native Americans. *Science* **349**, aab3884 (2015).

[PubMed](#) [PubMed Central](#) [Google Scholar](#)

57. 57.

Jakobson, R. The Paleosiberian languages. *Am. Anthropol.* **44**, 602–620 (1942).

[Google Scholar](#)

58. 58.

Moreno-Mayar, J. V. et al. Terminal Pleistocene Alaskan genome reveals first founding population of Native Americans. *Nature* **553**, 203–207 (2018). **An Alaskan genome dating to the Late Pleistocene/early Holocene showed the presence of a previously undiscovered population, Ancient Beringians, who diverged from the basal American branch before the formation of the Ancestral Native American population.**

[ADS](#) [CAS](#) [PubMed](#) [Google Scholar](#)

59. 59.

Moreno-Mayar, J. V. et al. Early human dispersals within the Americas. *Science* **362**, eaav2621 (2018). **This study demonstrated genetic affinities between distant early populations in North and South America, providing evidence of widespread, rapid dispersal of early group and evidence of later dispersals.**

[ADS](#) [PubMed](#) [Google Scholar](#)

60. 60.

Fu, Q. et al. The genetic history of Ice Age Europe. *Nature* **534**, 200–205 (2016).

[ADS](#) [CAS](#) [PubMed](#) [PubMed Central](#) [Google Scholar](#)

61. 61.

Skoglund, P. & Mathieson, I. Ancient genomics of modern humans: the first decade. *Annu. Rev. Genomics Hum. Genet.* **19**, 381–404 (2018).

[CAS](#) [PubMed](#) [Google Scholar](#)

62. 62.

Llamas, B. et al. Ancient mitochondrial DNA provides high-resolution time scale of the peopling of the Americas. *Sci. Adv.* **2**, e1501385 (2016).

[ADS](#) [PubMed](#) [PubMed Central](#) [Google Scholar](#)

63. 63.

Pinotti, T. et al. Y chromosome sequences reveal a short Beringian standstill, rapid expansion, and early population structure of Native American founders. *Curr. Biol.* **29**, 149–157.e3 (2019).

[CAS](#) [PubMed](#) [Google Scholar](#)

64. 64.

Tamm, E. et al. Beringian standstill and spread of Native American founders. *PLoS ONE* **2**, e829 (2007).

[ADS](#) [PubMed](#) [PubMed Central](#) [Google Scholar](#)

65. 65.

Kitchen, A., Miyamoto, M. M. & Mulligan, C. J. A three-stage colonization model for the peopling of the Americas. *PLoS ONE* **3**, e1596 (2008).

[ADS](#) [PubMed](#) [PubMed Central](#) [Google Scholar](#)

66. 66.

Lindo, J. et al. Ancient individuals from the North American Northwest Coast reveal 10,000 years of regional genetic continuity. *Proc. Natl Acad. Sci. USA* **114**, 4093–4098 (2017).

[CAS](#) [PubMed](#) [Google Scholar](#)

67. 67.

Lindo, J. et al. The genetic prehistory of the Andean highlands 7000 years BP through European contact. *Sci. Adv.* **4**, eaau4921 (2018).

[ADS](#) [CAS](#) [PubMed](#) [PubMed Central](#) [Google Scholar](#)

68. 68.

Scheib, C. L. et al. Ancient human parallel lineages within North America contributed to a coastal expansion. *Science* **360**, 1024–1027 (2018).

[ADS](#) [CAS](#) [PubMed](#) [Google Scholar](#)

69. 69.

Potter, B. A., Irish, J. D., Reuther, J. D. & McKinney, H. J. New insights into Eastern Beringian mortuary behavior: a terminal Pleistocene double infant burial at Upward Sun River. *Proc. Natl Acad. Sci. USA* **111**, 17060–17065 (2014).

[ADS](#) [CAS](#) [PubMed](#) [Google Scholar](#)

70. 70.

Johannsen, N. N., Larson, G., Meltzer, D. J. & Vander Linden, M. A composite window into human history. *Science* **356**, 1118–1120 (2017).

[CAS](#) [PubMed](#) [Google Scholar](#)

71. 71.

Skoglund, P. & Reich, D. A genomic view of the peopling of the Americas. *Curr. Opin. Genet. Dev.* **41**, 27–35 (2016).

[CAS](#) [PubMed](#) [PubMed Central](#) [Google Scholar](#)

72. 72.

Harris, D. N. et al. Evolutionary genomic dynamics of Peruvians before, during, and after the Inca Empire. *Proc. Natl Acad. Sci. USA* **115**, E6526–E6535 (2018).

[CAS](#) [PubMed](#) [Google Scholar](#)

73. 73.

Meltzer, D. J. Clocking the first Americans. *Annu. Rev. Anthropol.* **24**, 21–45 (1995).

[Google Scholar](#)

74. 74.

Nakatsuka, N. et al. Ancient genomes in South Patagonia reveal population movements associated with technological shifts and geography. *Nat. Commun.* **11**, 3868 (2020).

[ADS](#) [CAS](#) [PubMed](#) [PubMed Central](#) [Google Scholar](#)

75. 75.

Meltzer, D. J. in *The Settlement of the American Continents: a Multidisciplinary Approach to Human Biogeography* vol. 1 (eds Barton, C. M. et al.) 123–137 (Univ. Arizona Press, 2004).

76. 76.

Bergström, A. et al. Insights into human genetic variation and population history from 929 diverse genomes. *Science* **367**, eaay5012 (2020).

[PubMed](#) [PubMed Central](#) [Google Scholar](#)

77. 77.

Fagundes, N. J. R. et al. How strong was the bottleneck associated to the peopling of the Americas? New insights from multilocus sequence data. *Genet. Mol. Biol.* **41** (suppl 1), 206–214 (2018).

[PubMed](#) [PubMed Central](#) [Google Scholar](#)

78. 78.

Nakatsuka, N. et al. A paleogenomic reconstruction of the deep population history of the Andes. *Cell* **181**, 1131–1145.e21 (2020). **This genome-wide study showed the structure of and gene flow in Holocene Andean populations, and demonstrated that genetic continuity occurred even with the rise and fall of Andean Empires.**

[CAS](#) [PubMed](#) [PubMed Central](#) [Google Scholar](#)

79. 79.

Perri, A. R. et al. Dog domestication and the dual dispersal of people and dogs into the Americas. *Proc. Natl Acad. Sci. USA* **118**, e2010083118 (2021).

[PubMed](#) [Google Scholar](#)

80. 80.

Bradley, B. & Stanford, D. The North Atlantic ice-edge corridor: a possible Palaeolithic route to the New World. *World Archaeol.* **36**, 459–478 (2004).

[Google Scholar](#)

81. 81.

Raff, J. A. & Bolnick, D. A. Does mitochondrial haplogroup X indicate ancient trans-Atlantic migration to the Americas? A critical re-evaluation. *PaleoAmerica* **1**, 297–304 (2015).

[Google Scholar](#)

82. 82.

Brace, C. L. et al. Old World sources of the first New World human inhabitants: a comparative craniofacial view. *Proc. Natl Acad. Sci. USA* **98**, 10017–10022 (2001).

[CAS](#) [PubMed](#) [Google Scholar](#)

83. 83.

Neves, W. A. & Hubbe, M. Cranial morphology of early Americans from Lagoa Santa, Brazil: implications for the settlement of the New World. *Proc. Natl Acad. Sci. USA* **102**, 18309–18314 (2005).

[ADS](#) [CAS](#) [PubMed](#) [Google Scholar](#)

84. 84.

Owsley, D. W. & Jantz, R. L. in *Kennewick Man: The Scientific Investigation of an Ancient American Skeleton* (ed. Owsley, D. W.) 622–650 (Texas A&M Press, 2014).

85. 85.

Rasmussen, M. et al. The ancestry and affiliations of Kennewick Man. *Nature* **523**, 455–458 (2015).

[ADS](#) [PubMed](#) [PubMed Central](#) [Google Scholar](#)

86. 86.

Flegontov, P. et al. Palaeo-Eskimo genetic ancestry and the peopling of Chukotka and North America. *Nature* **570**, 236–240 (2019).

[ADS](#) [CAS](#) [PubMed](#) [PubMed Central](#) [Google Scholar](#)

87. 87.

Raghavan, M. et al. The genetic prehistory of the New World Arctic. *Science* **345**, 1255832 (2014).

[PubMed](#) [Google Scholar](#)

88. 88.

Rasmussen, M. et al. Ancient human genome sequence of an extinct Palaeo-Eskimo. *Nature* **463**, 757–762 (2010). **The first ancient human genome sequenced, revealing that American Paleo-Inuit were from a dispersal independent of Native Americans and Inuit.**

[ADS](#) [CAS](#) [PubMed](#) [PubMed Central](#) [Google Scholar](#)

89. 89.

Flegontov, P. et al. Genomic study of the Ket: a Paleo-Eskimo-related ethnic group with significant ancient North Eurasian ancestry. *Sci. Rep.* **6**, 20768 (2016).

[ADS](#) [CAS](#) [PubMed](#) [PubMed Central](#) [Google Scholar](#)

90. 90.

Vajda, E. Dene–Yeniseian: progress and unanswered questions. *Diachronica* **35**, 277–295 (2018).

[Google Scholar](#)

91. 91.

Campbell, L. The Dene–Yeniseian connection. *Int. J. Am. Linguist.* **77**, 445–451 (2011).

[Google Scholar](#)

92. 92.

Campbell, L. Do languages and genes correlate? *Lang. Dyn. Chang.* **5**, 202–226 (2015).

[Google Scholar](#)

93. 93.

Duggan, A. T. et al. Genetic discontinuity between the Maritime Archaic and Beothuk populations in Newfoundland, Canada. *Curr. Biol.* **27**, 3149–3156.e11 (2017).

[CAS](#) [PubMed](#) [Google Scholar](#)

94. 94.

Friesen, T. M. Radiocarbon evidence for fourteenth-century Dorset occupation in the eastern North American Arctic. *Am. Antiq.* **85**, 222–240 (2020).

[Google Scholar](#)

95. 95.

Ameen, C. et al. Specialized sledge dogs accompanied Inuit dispersal across the North American Arctic. *Proc. R. Soc. B* **286**, 20191929 (2019).

[CAS](#) [PubMed](#) [Google Scholar](#)

96. 96.

Sinding, M. S. et al. Arctic-adapted dogs emerged at the Pleistocene-Holocene transition. *Science* **368**, 1495–1499 (2020).

[ADS](#) [CAS](#) [PubMed](#) [PubMed Central](#) [Google Scholar](#)

97. 97.

Barrett, J. H. *Contact, Continuity, and Collapse: The Norse Colonization of the North Atlantic* vol. 5 (Brepols, 2003).

98. 98.

Margaryan, A. et al. Population genomics of the Viking world. *Nature* **585**, 390–396 (2020).

[ADS](#) [CAS](#) [PubMed](#) [Google Scholar](#)

99. 99.

Napolitano, M. F. et al. Reevaluating human colonization of the Caribbean using chronometric hygiene and Bayesian modeling. *Sci. Adv.* **5**, eaar7806 (2019).

[CAS](#) [PubMed](#) [PubMed Central](#) [Google Scholar](#)

100. 100.

Nägele, K. et al. Genomic insights into the early peopling of the Caribbean. *Science* **369**, 456–460 (2020).

[ADS](#) [PubMed](#) [Google Scholar](#)

101. 101.

Schroeder, H. et al. Origins and genetic legacies of the Caribbean Taino. *Proc. Natl Acad. Sci. USA* **115**, 2341–2346 (2018).

[CAS](#) [PubMed](#) [Google Scholar](#)

102. 102.

Fernandes, D. M. et al. A genetic history of the pre-contact Caribbean. *Nature* **590**, 103–110 (2021).

[ADS](#) [CAS](#) [PubMed](#) [Google Scholar](#)

103. 103.

Racimo, F., Sikora, M., Vander Linden, M., Schroeder, H. & Lalueza-Fox, C. Beyond broad strokes: sociocultural insights from the study of ancient genomes. *Nat. Rev. Genet.* **21**, 355–366 (2020).

[CAS](#) [PubMed](#) [Google Scholar](#)

104. 104.

Moreno-Mayar, J. V. et al. Genome-wide ancestry patterns in Rapanui suggest pre-European admixture with Native Americans. *Curr. Biol.* **24**, 2518–2525 (2014).

[CAS](#) [PubMed](#) [Google Scholar](#)

105. 105.

Fehren-Schmitz, L. et al. Genetic ancestry of Rapanui before and after European Contact. *Curr. Biol.* **27**, 3209–3215.e6 (2017).

[CAS](#) [PubMed](#) [Google Scholar](#)

106. 106.

Ioannidis, A. G. et al. Native American gene flow into Polynesia predating Easter Island settlement. *Nature* **583**, 572–577 (2020).

[ADS](#) [CAS](#) [PubMed](#) [Google Scholar](#)

107. 107.

Grayson, D. K. *The Great Basin: a Natural Prehistory* (Univ. California Press, 2011).

108. 108.

Prohaska, A. et al. Human disease variation in the light of population genomics. *Cell* **177**, 115–131 (2019).

[CAS](#) [PubMed](#) [Google Scholar](#)

109. 109.

Meltzer, D. J. Why don't we know when the first people came to North America? *Am. Antiq.* **54**, 471–490 (1989).

[Google Scholar](#)

110. 110.

Gómez-Carballa, A. et al. The peopling of South America and the trans-Andean gene flow of the first settlers. *Genome Res.* **28**, 767–779 (2018).

[PubMed](#) [PubMed Central](#) [Google Scholar](#)

111. 111.

Moreno-Estrada, A. et al. The genetics of Mexico recapitulates Native American substructure and affects biomedical traits. *Science* **344**, 1280–1285 (2014).

[ADS](#) [CAS](#) [PubMed](#) [PubMed Central](#) [Google Scholar](#)

112. 112.

Ringbauer, H., Steinrücken, M., Fehren-Schmitz, L. & Reich, D. Increased rate of close-kin unions in the central Andes in the half millennium before European contact. *Curr. Biol.* **30**, R980–R981 (2020).

[CAS](#) [PubMed](#) [Google Scholar](#)

113. 113.

Bos, K. I. et al. Pre-Columbian mycobacterial genomes reveal seals as a source of New World human tuberculosis. *Nature* **514**, 494–497 (2014).

[ADS](#) [CAS](#) [PubMed](#) [PubMed Central](#) [Google Scholar](#)

114. 114.

Jones, E. E. Spatiotemporal analysis of Old World diseases in North America, A.D. 1519–1807. *Am. Antiq.* **79**, 487–506 (2014).

[Google Scholar](#)

115. 115.

Dillehay, T. D. *The First Americans: Search and Research* (eds Dillehay, T. D. & Meltzer, D. J.) 231–264 (CRC, 1991).

116. 116.

Lindo, J. et al. A time transect of exomes from a Native American population before and after European contact. *Nat. Commun.* **7**, 13175 (2016). **One of the first studies to show evidence of positive selection and changing frequencies in HLA alleles before and after European contact.**

[ADS](#) [CAS](#) [PubMed](#) [PubMed Central](#) [Google Scholar](#)

117. 117.

Reynolds, A. W. et al. Comparing signals of natural selection between three Indigenous North American populations. *Proc. Natl Acad. Sci. USA* **116**, 9312–9317 (2019).

[CAS](#) [PubMed](#) [Google Scholar](#)

118. 118.

Wagner, J. K. et al. Fostering responsible research on ancient DNA. *Am. J. Hum. Genet.* **107**, 183–195 (2020).

[CAS](#) [PubMed](#) [PubMed Central](#) [Google Scholar](#)

119. 119.

Bardill, J. et al. Advancing the ethics of paleogenomics. *Science* **360**, 384–385 (2018).

[ADS](#) [CAS](#) [PubMed](#) [PubMed Central](#) [Google Scholar](#)

120. 120.

Garrison, N. A. Genetic ancestry testing with tribes: ethics, identity & health implications. *Daedalus* **147**, 60–69 (2018).

[Google Scholar](#)

121. 121.

Colwell, C. Collaborative archaeologies and descendant communities. *Annu. Rev. Anthropol.* **45**, 113–127 (2016).

[Google Scholar](#)

122. 122.

Claw, K. G. et al. A framework for enhancing ethical genomic research with Indigenous communities. *Nat. Commun.* **9**, 2957 (2018).

[ADS](#) [PubMed](#) [PubMed Central](#) [Google Scholar](#)

123. 123.

Garrison, N. A. et al. Genomic research through an Indigenous lens: understanding the expectations. *Annu. Rev. Genomics Hum. Genet.* **20**, 495–517 (2019).

[CAS](#) [PubMed](#) [Google Scholar](#)

124. 124.

Fox, K. & Hawks, J. Use ancient remains more wisely. *Nature* **572**, 581–583 (2019).

[ADS](#) [CAS](#) [PubMed](#) [Google Scholar](#)

125. 125.

Willerslev, E. et al. Diverse plant and animal genetic records from Holocene and Pleistocene sediments. *Science* **300**, 791–795 (2003).

[ADS](#) [CAS](#) [PubMed](#) [Google Scholar](#)

126. 126.

Pedersen, M. W. et al. Ancient and modern environmental DNA. *Phil. Trans. R. Soc. Lond. B* **370**, 20130383 (2015).

[Google Scholar](#)

127. 127.

Slon, V. et al. Neandertal and Denisovan DNA from Pleistocene sediments. *Science* **356**, 605–608 (2017).

[ADS](#) [CAS](#) [PubMed](#) [Google Scholar](#)

128. 128.

Skoglund, P. et al. Genetic evidence for two founding populations of the Americas. *Nature* **525**, 104–108 (2015).

[ADS](#) [CAS](#) [PubMed](#) [PubMed Central](#) [Google Scholar](#)

129. 129.

McColl, H. et al. The prehistoric peopling of Southeast Asia. *Science* **361**, 88–92 (2018).

[ADS](#) [CAS](#) [PubMed](#) [Google Scholar](#)

130. 130.

Araújo Castro e Silva, M., Ferraz, T., Cátira Bortolini, M., Comas, D. & Hünemeier, T. Deep genetic affinity between coastal Pacific and Amazonian natives evidenced by Australasian ancestry. *Proc. Natl Acad. Sci. USA* **118**, e2025739118 (2021).

[Google Scholar](#)

[Download references](#)

Acknowledgements

We thank M. Adler, R. Kelly, D. Mann, V. Moreno-Mayar, T. Pinotti, M. Raghavan, H. Schroeder, M. Sikora and M. Vander Linden for providing comments and advice on this paper, and V. Moreno-Mayar and K. Kjær for help with the figures; M. Avila-Arcos, T. Dillehay, C. Lalueza-Fox and B. Llamas for their detailed and constructive comments; and St John's College, Cambridge University, where E.W. is a Fellow and D.J.M. was a Beaufort Visiting Scholar, for providing a stimulating environment in which the idea and much of the work on this manuscript took place. E.W. thanks Illumina for collaboration. E.W. is financially supported by the Wellcome Trust, the Lundbeck Foundation, the Carlsberg Foundation and the Novo Nordic Foundation. D.J.M.'s research is supported by the Quest Archaeological Research Fund and the Potts & Sibley Foundation.

Author information

Author notes

1. These authors contributed equally: Eske Willerslev, David J. Meltzer

Affiliations

1. GeoGenetics Group, Department of Zoology, University of Cambridge, Cambridge, UK

Eske Willerslev

2. Lundbeck Foundation GeoGenetics Centre, GLOBE Institute,
University of Copenhagen, Copenhagen, Denmark

Eske Willerslev & David J. Meltzer

3. Wellcome Trust Sanger Institute, Cambridge, UK

Eske Willerslev

4. Department of Anthropology, Southern Methodist University, Dallas,
TX, USA

David J. Meltzer

Authors

1. Eske Willerslev

[View author publications](#)

You can also search for this author in [PubMed](#) [Google Scholar](#)

2. David J. Meltzer

[View author publications](#)

You can also search for this author in [PubMed](#) [Google Scholar](#)

Contributions

E.W. and D.J.M. conceived and wrote the manuscript. The authors contributed equally to this work.

Corresponding authors

Correspondence to [Eske Willerslev](#) or [David J. Meltzer](#).

Ethics declarations

Competing interests

The authors declare no competing interests.

Additional information

Peer review information *Nature* thanks Maria Avila-Arcos, Tom Dillehay, Carles Lalueza-Fox and Bastien Llamas for their contribution to the peer review of this work.

Publisher's note Springer Nature remains neutral with regard to jurisdictional claims in published maps and institutional affiliations.

Rights and permissions

[Reprints and Permissions](#)

About this article



Check for
updates

Cite this article

Willerslev, E., Meltzer, D.J. Peopling of the Americas as inferred from ancient genomics. *Nature* **594**, 356–364 (2021).
<https://doi.org/10.1038/s41586-021-03499-y>

[Download citation](#)

- Received: 09 November 2020
- Accepted: 26 March 2021

- Published: 16 June 2021
- Issue Date: 17 June 2021
- DOI: <https://doi.org/10.1038/s41586-021-03499-y>

Comments

By submitting a comment you agree to abide by our [Terms](#) and [Community Guidelines](#). If you find something abusive or that does not comply with our terms or guidelines please flag it as inappropriate.

[Access through your institution](#)

[Change institution](#)

[Buy or subscribe](#)

Advertisement

This article was downloaded by **calibre** from <https://www.nature.com/articles/s41586-021-03499-y>.

| [Section menu](#) | [Main menu](#) |

- Perspective
- [Published: 16 June 2021](#)

The rise of intelligent matter

- [C. Kaspar](#) ORCID: [orcid.org/0000-0002-1788-6966¹](https://orcid.org/0000-0002-1788-6966),
- [B. J. Ravoo](#) ORCID: [orcid.org/0000-0003-2202-7485^{2,3}](https://orcid.org/0000-0003-2202-7485),
- [W. G. van der Wiel](#) ORCID: [orcid.org/0000-0002-3479-8853^{1,4}](https://orcid.org/0000-0002-3479-8853),
- [S. V. Wegner](#) ORCID: [orcid.org/0000-0002-9072-0858⁵](https://orcid.org/0000-0002-9072-0858) &
- [W. H. P. Pernice](#) ORCID: [orcid.org/0000-0003-4569-4213^{1,3}](https://orcid.org/0000-0003-4569-4213)

Nature volume 594, pages 345–355 (2021) [Cite this article](#)

- 2801 Accesses
- 55 Altmetric
- [Metrics details](#)

Subjects

- [Composites](#)
- [Molecular self-assembly](#)
- [Nanoscale biophysics](#)

Abstract

Artificial intelligence (AI) is accelerating the development of unconventional computing paradigms inspired by the abilities and energy efficiency of the brain. The human brain excels especially in computationally intensive cognitive tasks, such as pattern recognition and classification. A long-term goal is de-centralized neuromorphic computing, relying on a network of distributed cores to mimic the massive parallelism

of the brain, thus rigorously following a nature-inspired approach for information processing. Through the gradual transformation of interconnected computing blocks into continuous computing tissue, the development of advanced forms of matter exhibiting basic features of intelligence can be envisioned, able to learn and process information in a delocalized manner. Such intelligent matter would interact with the environment by receiving and responding to external stimuli, while internally adapting its structure to enable the distribution and storage (as memory) of information. We review progress towards implementations of intelligent matter using molecular systems, soft materials or solid-state materials, with respect to applications in soft robotics, the development of adaptive artificial skins and distributed neuromorphic computing.

Access options

Subscribe to Journal

Get full journal access for 1 year

\$199.00

only \$3.90 per issue

[Subscribe](#)

All prices are NET prices.

VAT will be added later in the checkout.

Tax calculation will be finalised during checkout.

Rent or Buy article

Get time limited or full article access on ReadCube.

from \$8.99

[Rent or Buy](#)

All prices are NET prices.

Additional access options:

- [Log in](#)
- [Access through your institution](#)
- [Learn about institutional subscriptions](#)

Fig. 1: Conceptual transition from structural to intelligent matter with increasing functionality and complexity, and corresponding examples.



Fig. 2: Adaptive swarm behaviour of autonomous robots and clusters of colloids.



Fig. 3: Responsive soft matter and soft matter with embedded memory functionality.

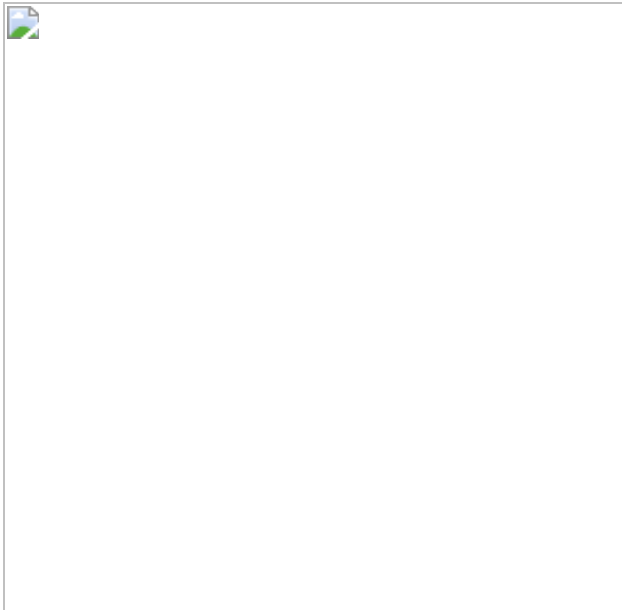


Fig. 4: Adaptive soft materials with homeostatic properties and enzyme-powered motility.

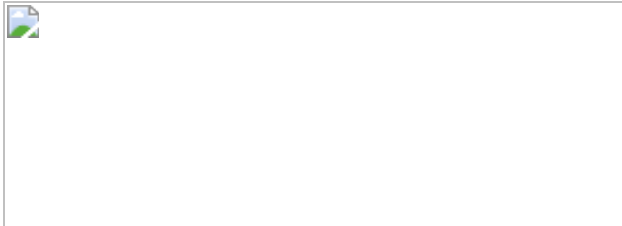
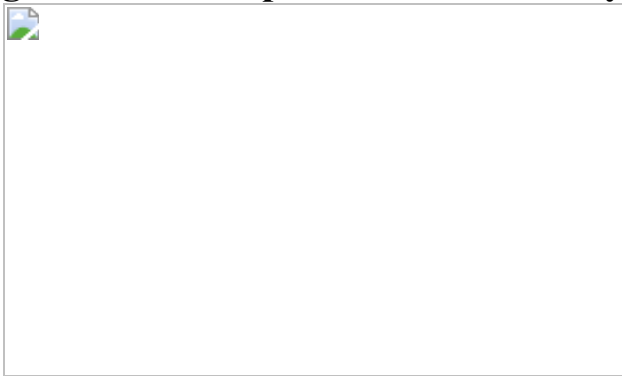


Fig. 5: Neuromorphic materials and systems.



References

1. 1.

Sternberg, R. J. *Handbook of Intelligence* (Cambridge Univ. Press, 2000).

2. 2.

Sternberg, R. J. Theories of intelligence. In *APA Handbook of Giftedness and Talent* (eds Pfeiffer, S. I. et al.) 145–161 (American Psychological Association, 2018).

3. 3.

Legg, S. & Hutter, M. Universal intelligence: a definition of machine intelligence. *Minds Mach.* **17**, 391–444 (2007).

[Google Scholar](#)

4. 4.

Amato, F. et al. Artificial neural networks in medical diagnosis. *J. Appl. Biomed.* **11**, 47–58 (2013).

[CAS Google Scholar](#)

5. 5.

Lane, N. D., Bhattacharya, S., Mathur, A., Forlivesi, C. & Kawsar, F. Squeezing deep learning into mobile and embedded devices. *IEEE Pervasive Comput.* **16**, 82–88 (2017).

[Google Scholar](#)

6. 6.

Hecht, J. Lidar for self-driving cars. *Opt. Photonics News* **29**, 26–33 (2018).

[ADS Google Scholar](#)

7. 7.

Kanao, K. et al. Highly selective flexible tactile strain and temperature sensors against substrate bending for an artificial skin. *RSC Adv.* **5**,

30170–30174 (2015).

[ADS](#) [Google Scholar](#)

8. 8.

Kim, J. et al. Stretchable silicon nanoribbon electronics for skin prosthesis. *Nat. Commun.* **5**, 5747 (2014).

[CAS](#) [PubMed](#) [ADS](#) [Google Scholar](#)

9. 9.

Fernández-Caramés, T. M. & Fraga-Lamas, P. Towards the internet-of-smart-clothing: a review on IoT wearables and garments for creating intelligent connected E-textiles. *Electronics* **7**, 405 (2018).

[Google Scholar](#)

10. 10.

Whitesides, G. M. Soft robotics. *Angew. Chem. Int. Ed.* **57**, 4258–4273 (2018).

[CAS](#) [Google Scholar](#)

11. 11.

Majidi, C. Soft robotics: a perspective—current trends and prospects for the future. *Soft Robot.* **1**, 5–11 (2014).

[Google Scholar](#)

12. 12.

Hamdioui, S. et al. Applications of computation-in-memory architectures based on memristive devices. In *Proc. 2019 Design, Automation and Test in Europe Conference and Exhibition* 486–491, <https://doi.org/10.23919/DATE.2019.8715020> (2019).

13. 13.

Ielmini, D. & Wong, H. S. P. In-memory computing with resistive switching devices. *Nat. Electron.* **1**, 333–343 (2018).

[Google Scholar](#)

14. 14.

Sebastian, A., Le Gallo, M., Khaddam-Aljameh, R. & Eleftheriou, E. Memory devices and applications for in-memory computing. *Nat. Nanotechnol.* **15**, 529–544 (2020).

[CAS](#) [PubMed](#) [ADS](#) [Google Scholar](#)

15. 15.

Wegst, U. G. K., Bai, H., Saiz, E., Tomsia, A. P. & Ritchie, R. O. Bioinspired structural materials. *Nat. Mater.* **14**, 23–36 (2015).

[CAS](#) [PubMed](#) [ADS](#) [Google Scholar](#)

16. 16.

Isaacoff, B. P. & Brown, K. A. Progress in top-down control of bottom-up assembly. *Nano Lett.* **17**, 6508–6510 (2017).

[CAS](#) [PubMed](#) [ADS](#) [Google Scholar](#)

17. 17.

McEvoy, M. A. & Correll, N. Materials that couple sensing, actuation, computation, and communication. *Science* **347**, 1261689 (2015).

[CAS](#) [PubMed](#) [Google Scholar](#)

18. 18.

Walther, A. Viewpoint: from responsive to adaptive and interactive materials and materials systems: a roadmap. *Adv. Mater.* **32**, 1905111 (2020).

[CAS](#) [Google Scholar](#)

19. 19.

Merindol, R. & Walther, A. Materials learning from life: concepts for active, adaptive and autonomous molecular systems. *Chem. Soc. Rev.* **46**, 5588–5619 (2017).

[CAS](#) [PubMed](#) [Google Scholar](#)

20. 20.

Urban, M. W. *Handbook of Stimuli-Responsive Materials* (Wiley, 2011).

21. 21.

He, X. et al. Synthetic homeostatic materials with chemo-mechano-chemical self-regulation. *Nature* **487**, 214–218 (2012). **An intriguing example of an autonomous, homeostatic material system based on chemo-mechanical feedback loops.**

[CAS](#) [PubMed](#) [ADS](#) [Google Scholar](#)

22. 22.

Anderson, C., Theraulaz, G. & Deneubourg, J. L. Self-assemblages in insect societies. *Insectes Soc.* **49**, 99–110 (2002).

[Google Scholar](#)

23. 23.

Lopez, U., Gautrais, J., Couzin, I. D. & Theraulaz, G. From behavioural analyses to models of collective motion in fish schools.

Interface Focus **2**, 693–707 (2012).

[PubMed](#) [PubMed Central](#) [Google Scholar](#)

24. 24.

Bajec, I. L. & Heppner, F. H. Organized flight in birds. *Anim. Behav.* **78**, 777–789 (2009).

[Google Scholar](#)

25. 25.

Hinchey, M. G., Sterritt, R. & Rouff, C. Swarms and swarm intelligence. *Computer* **40**, 111–113 (2007).

[Google Scholar](#)

26. 26.

Rubenstein, M., Cornejo, A. & Nagpal, R. Programmable self-assembly in a thousand-robot swarm. *Science* **345**, 795–799 (2014).

[CAS](#) [PubMed](#) [ADS](#) [Google Scholar](#)

27. 27.

Yu, J., Wang, B., Du, X., Wang, Q. & Zhang, L. Ultra-extensible ribbon-like magnetic microswarm. *Nat. Commun.* **9**, 3260 (2018). **This article demonstrates how paramagnetic nanoparticles self-organize in a microswarm that can pass obstacles and how its locomotion can be controlled by applying oscillating magnetic fields.**

[PubMed](#) [PubMed Central](#) [ADS](#) [Google Scholar](#)

28. 28.

Palacci, J., Sacanna, S., Steinberg, A. P., Pine, D. J. & Chaikin, P. M. Living crystals of light-activated colloidal surfers. *Science* **339**, 936–940 (2013).

[CAS](#) [PubMed](#) [ADS](#) [Google Scholar](#)

29. 29.

Yan, J., Bloom, M., Bae, S. C., Luijten, E. & Granick, S. Linking synchronization to self-assembly using magnetic Janus colloids. *Nature* **491**, 578–581 (2012).

[CAS](#) [PubMed](#) [ADS](#) [Google Scholar](#)

30. 30.

Liang, X. et al. Hierarchical microswarms with leader–follower-like structures: electrohydrodynamic self-organization and multimode collective photoresponses. *Adv. Funct. Mater.* **30**, 1908602 (2020).

[CAS](#) [Google Scholar](#)

31. 31.

Mou, F. et al. Phototactic flocking of photochemical micromotors. *iScience* **19**, 415–424 (2019). **This study shows flocking behaviour of synthesized spherical microparticles, which can execute transporting tasks along predefined pathways or bypass obstacles.**

[PubMed](#) [PubMed Central](#) [ADS](#) [Google Scholar](#)

32. 32.

Dai, B. et al. Programmable artificial phototactic microswimmer. *Nat. Nanotechnol.* **11**, 1087–1092 (2016).

[CAS](#) [PubMed](#) [ADS](#) [Google Scholar](#)

33. 33.

Tagliazucchi, M., Weiss, E. A. & Szleifer, I. Dissipative self-assembly of particles interacting through time-oscillatory potentials. *Proc. Natl Acad. Sci. USA* **111**, 9751–9756 (2014).

[CAS](#) [PubMed](#) [ADS](#) [Google Scholar](#)

34. 34.

Carnall, J. M. A. et al. Mechanosensitive self-replication driven by self-organization. *Science* **327**, 1502–1506 (2010).

[CAS](#) [PubMed](#) [ADS](#) [Google Scholar](#)

35. 35.

Sadownik, J. W., Mattia, E., Nowak, P. & Otto, S. Diversification of self-replicating molecules. *Nat. Chem.* **8**, 264–269 (2016).

[CAS](#) [PubMed](#) [Google Scholar](#)

36. 36.

Monreal Santiago, G., Liu, K., Browne, W. R. & Otto, S. Emergence of light-driven protometabolism upon recruitment of a photocatalytic cofactor by a self-replicator. *Nat. Chem.* **12**, 603–607 (2020).

[CAS](#) [PubMed](#) [Google Scholar](#)

37. 37.

Rus, D. & Tolley, M. T. Design, fabrication and control of soft robots. *Nature* **521**, 467–475 (2015).

[CAS](#) [PubMed](#) [ADS](#) [Google Scholar](#)

38. 38.

Zhu, B. et al. Skin-inspired haptic memory arrays with an electrically reconfigurable architecture. *Adv. Mater.* **28**, 1559–1566 (2016).

[CAS](#) [PubMed](#) [Google Scholar](#)

39. 39.

Son, D. et al. Multifunctional wearable devices for diagnosis and therapy of movement disorders. *Nat. Nanotechnol.* **9**, 397–404 (2014).

[CAS](#) [PubMed](#) [ADS](#) [Google Scholar](#)

40. 40.

Miriyev, A., Stack, K. & Lipson, H. Soft material for soft actuators. *Nat. Commun.* **8**, 596 (2017).

[PubMed](#) [PubMed Central](#) [ADS](#) [Google Scholar](#)

41. 41.

Zhao, Z., Wang, C., Yan, H. & Liu, Y. Soft robotics programmed with double crosslinking DNA hydrogels. *Adv. Funct. Mater.* **29**, 1905911 (2019). **This article shows impressively how to translate nanometre-scale DNA self-assembly into macroscopic movements of soft materials, an encouraging achievement for soft robotics.**

[CAS](#) [Google Scholar](#)

42. 42.

Yang, H. et al. 3D printed photoresponsive devices based on shape memory composites. *Adv. Mater.* **29**, 1701627 (2017).

[Google Scholar](#)

43. 43.

Lai, Y. C. et al. Actively perceiving and responsive soft robots enabled by self-powered, highly extensible, and highly sensitive triboelectric proximity- and pressure-sensing skins. *Adv. Mater.* **30**, 1801114 (2018). **This work presents soft robots driven by self-generated**

electricity via the triboelectric effect, which can sense and embrace close objects.

[Google Scholar](#)

44. 44.

Schroeder, T. B. H. et al. An electric-eel-inspired soft power source from stacked hydrogels. *Nature* **552**, 214–218 (2017).

[CAS](#) [PubMed](#) [PubMed Central](#) [ADS](#) [Google Scholar](#)

45. 45.

Liu, Y. et al. Stretchable motion memory devices based on mechanical hybrid materials. *Adv. Mater.* **29**, 1701780 (2017).

[Google Scholar](#)

46. 46.

Oh, J. Y. et al. Intrinsically stretchable and healable semiconducting polymer for organic transistors. *Nature* **539**, 411–415 (2016).

[CAS](#) [PubMed](#) [ADS](#) [Google Scholar](#)

47. 47.

Urban, M. W. et al. Key-and-lock commodity self-healing copolymers. *Science* **225**, 220–225 (2018). **A remarkable example for an advanced soft material with self-healing capabilities.**

[ADS](#) [Google Scholar](#)

48. 48.

Chen, Y., Kushner, A. M., Williams, G. A. & Guan, Z. Multiphase design of autonomic self-healing thermoplastic elastomers. *Nat. Chem.* **4**, 467–472 (2012).

[CAS](#) [PubMed](#) [Google Scholar](#)

49. 49.

Li, C. H. et al. A highly stretchable autonomous self-healing elastomer. *Nat. Chem.* **8**, 618–624 (2016).

[CAS](#) [PubMed](#) [Google Scholar](#)

50. 50.

Beyer, H. M. et al. Synthetic biology makes polymer materials count. *Adv. Mater.* **30**, 1800472 (2018).

[Google Scholar](#)

51. 51.

Nakajima, K., Hauser, H., Li, T. & Pfeifer, R. Information processing via physical soft body. *Sci. Rep.* **5**, 10487 (2015).

[PubMed](#) [PubMed Central](#) [ADS](#) [Google Scholar](#)

52. 52.

Zhang, H., Zeng, H., Priimagi, A. & Ikkala, O. Programmable responsive hydrogels inspired by classical conditioning algorithm. *Nat. Commun.* **10**, 3267 (2019).

[PubMed](#) [PubMed Central](#) [ADS](#) [Google Scholar](#)

53. 53.

Zeng, H., Zhang, H., Ikkala, O. & Priimagi, A. Associative learning by classical conditioning in liquid crystal network actuators. *Matter* **2**, 194–206 (2020). **Associative learning is realized in a liquid crystal network material via a conditioning process, where an initially neutral light stimulus is associated with heating.**

[PubMed](#) [PubMed Central](#) [Google Scholar](#)

54. 54.

Kumar, B. V. V. S. P., Patil, A. J. & Mann, S. Enzyme-powered motility in buoyant organoclay/DNA protocells. *Nat. Chem.* **10**, 1154–1163 (2018).

[CAS](#) [PubMed](#) [Google Scholar](#)

55. 55.

Garrad, M., Soter, G., Conn, A. T., Hauser, H. & Rossiter, J. A soft matter computer for soft robots. *Sci. Robot.* **4**, eaaw6060 (2019). **The authors propose a computational system integrated into a soft material, which, inspired by biological systems, transfers information via a fluid perfusing through the system.**

[PubMed](#) [Google Scholar](#)

56. 56.

Miller, J. F. & Downing, K. Evolution in materio: looking beyond the silicon box. In *Proc. NASA/DoD Conference on Evolvable Hardware* 167–176, <https://doi.org/10.1109/EH.2002.1029882> (2002).

57. 57.

Feynman, R. P. *The Character of Physical Law* (MIT Press, 1967).

58. 58.

Yoshihito, A. Information processing using intelligent materials - information-processing architectures for material processors. *J. Intell. Mater. Syst. Struct.* **5**, 418–423 (1994).

[Google Scholar](#)

59. 59.

Merolla, P. A. et al. A million spiking-neuron integrated circuit with a scalable communication network and interface. *Science* **345**, 668–673 (2014).

[CAS](#) [ADS](#) [Google Scholar](#)

60. 60.

Metz, C. Google built its very own chips to power its AI bots. *Wired* <https://www.wired.com/2016/05/google-tpu-custom-chips/> (accessed 10 July 2020).

61. 61.

Zhang, W., Mazzarello, R., Wuttig, M. & Ma, E. Designing crystallization in phase-change materials for universal memory and neuro-inspired computing. *Nat. Rev. Mater.* **4**, 150–168 (2019).

[CAS](#) [ADS](#) [Google Scholar](#)

62. 62.

Sebastian, A. et al. Tutorial: brain-inspired computing using phase-change memory devices. *J. Appl. Phys.* **124**, 111101 (2018).

[ADS](#) [Google Scholar](#)

63. 63.

Boybat, I. et al. Neuromorphic computing with multi-memristive synapses. *Nat. Commun.* **9**, 2514 (2018).

[PubMed](#) [PubMed Central](#) [ADS](#) [Google Scholar](#)

64. 64.

Feldmann, J., Youngblood, N., Wright, C. D., Bhaskaran, H. & Pernice, W. H. P. All-optical spiking neurosynaptic networks with self-learning capabilities. *Nature* **569**, 208–214 (2019).

[CAS](#) [PubMed](#) [PubMed Central](#) [ADS](#) [Google Scholar](#)

65. 65.

Ríos, C. et al. Integrated all-photonic non-volatile multi-level memory. *Nat. Photon.* **9**, 725–732 (2015).

[ADS](#) [Google Scholar](#)

66. 66.

Cheng, Z., Ríos, C., Pernice, W. H. P., David Wright, C. & Bhaskaran, H. On-chip photonic synapse. *Sci. Adv.* **3**, e1700160 (2017). **This article shows an artificial synapse consisting of a photonic waveguide and a phase-change material, which paves the way for on-chip neuromorphic computing.**

[PubMed](#) [PubMed Central](#) [ADS](#) [Google Scholar](#)

67. 67.

Gupta, A., Sakthivel, T. & Seal, S. Recent development in 2D materials beyond graphene. *Prog. Mater. Sci.* **73**, 44–126 (2015).

[CAS](#) [Google Scholar](#)

68. 68.

Novoselov, K. S., Mishchenko, A., Carvalho, A. & Castro Neto, A. H. 2D materials and van der Waals heterostructures. *Science* **353**, aac9439 (2016).

[CAS](#) [PubMed](#) [Google Scholar](#)

69. 69.

Geim, A. K. & Grigorieva, I. V. Van der Waals heterostructures. *Nature* **499**, 419–425 (2013).

[CAS](#) [Google Scholar](#)

70. 70.

Mak, K. F., Lee, C., Hone, J., Shan, J. & Heinz, T. F. Atomically thin MoS₂: a new direct-gap semiconductor. *Phys. Rev. Lett.* **105**, 136805 (2010).

[PubMed](#) [ADS](#) [Google Scholar](#)

71. 71.

Splendiani, A. et al. Emerging photoluminescence in monolayer MoS₂. *Nano Lett.* **10**, 1271–1275 (2010).

[CAS](#) [PubMed](#) [ADS](#) [Google Scholar](#)

72. 72.

Wan, J. et al. Tuning two-dimensional nanomaterials by intercalation: materials, properties and applications. *Chem. Soc. Rev.* **45**, 6742–6765 (2016).

[CAS](#) [PubMed](#) [Google Scholar](#)

73. 73.

Zeng, M. et al. Bandgap tuning of two-dimensional materials by sphere diameter engineering. *Nat. Mater.* **19**, 528–533 (2020).

[CAS](#) [PubMed](#) [ADS](#) [Google Scholar](#)

74. 74.

Choi, C. et al. Human eye-inspired soft optoelectronic device using high-density MoS₂-graphene curved image sensor array. *Nat. Commun.* **8**, 1664 (2017).

[PubMed](#) [PubMed Central](#) [ADS](#) [Google Scholar](#)

75. 75.

Shi, Y. et al. Electronic synapses made of layered two-dimensional materials. *Nat. Electron.* **1**, 458–465 (2018).

[Google Scholar](#)

76. 76.

He, C. et al. Artificial synapse based on van der Waals heterostructures with tunable synaptic functions for neuromorphic computing. *ACS Appl. Mater. Interfaces* **12**, 11945–11954 (2020).

[CAS](#) [PubMed](#) [Google Scholar](#)

77. 77.

Park, H., Mastro, M. A., Tadjer, M. J. & Kim, J. Programmable multilevel memtransistors based on van der Waals heterostructures. *Adv. Electron. Mater.* **5**, 1900333 (2019).

[CAS](#) [Google Scholar](#)

78. 78.

Liu, C. et al. A semi-floating gate memory based on van der Waals heterostructures for quasi-non-volatile applications. *Nat. Nanotechnol.* **13**, 404–410 (2018).

[CAS](#) [PubMed](#) [ADS](#) [Google Scholar](#)

79. 79.

Mennel, L. et al. Ultrafast machine vision with 2D material neural network image sensors. *Nature* **579**, 62–66 (2020). **The presented image sensor based on a 2D material constitutes at the same time an artificial neural network.**

[CAS](#) [PubMed](#) [ADS](#) [Google Scholar](#)

80. 80.

Bose, S. K. et al. Evolution of a designless nanoparticle network into reconfigurable Boolean logic. *Nat. Nanotechnol.* **10**, 1048–1052 (2015). **Computational functionality is experimentally realized in a disordered nanomaterial network consisting of arbitrarily interconnected, functionalized nanoparticles.**

[CAS](#) [PubMed](#) [ADS](#) [Google Scholar](#)

81. 81.

Chen, T. et al. Classification with a disordered dopant-atom network in silicon. *Nature* **577**, 341–345 (2020).

[CAS](#) [PubMed](#) [ADS](#) [Google Scholar](#)

82. 82.

Ruiz Euler, H.-C. et al. A deep-learning approach to realising functionality in nanoelectronic devices. *Nat. Nanotechnol.* **15**, 992–998 (2020).

[PubMed](#) [ADS](#) [Google Scholar](#)

83. 83.

Ruiz Euler, H.-C. et al. Dopant network processing units: towards efficient neural-network emulators with high-capacity nanoelectronic nodes. Preprint at <http://arxiv.org/abs/2007.12371> (2020).

84. 84.

Lin, X. et al. All-optical machine learning using diffractive deep neural networks. *Science* **361**, 1004–1008 (2018).

[MathSciNet](#) [CAS](#) [PubMed](#) [MATH](#) [ADS](#) [Google Scholar](#)

85. 85.

Estakhri, N. M., Edwards, B. & Engheta, N. Inverse-designed metastructures that solve equations. *Science* **363**, 1333–1338 (2019).

[MathSciNet](#) [MATH](#) [ADS](#) [Google Scholar](#)

86. 86.

Hirano, Y., Segawa, Y., Kuroda-Sowa, T., Kawai, T. & Matsumoto, T. Conductance with stochastic resonance in Mn₁₂ redox network without tuning. *Appl. Phys. Lett.* **104**, 233104 (2014).

[ADS](#) [Google Scholar](#)

87. 87.

Hopfield, J. J. Neural networks and physical systems with emergent collective computational abilities. *Proc. Natl Acad. Sci. USA* **79**, 2554–2558 (1982).

[MathSciNet](#) [CAS](#) [PubMed](#) [MATH](#) [ADS](#) [Google Scholar](#)

88. 88.

Lukoševičius, M. & Jaeger, H. Reservoir computing approaches to recurrent neural network training. *Comput. Sci. Rev.* **3**, 127–149 (2009).

[MATH](#) [Google Scholar](#)

89. 89.

Jaeger, H. *The “Echo State” Approach to Analysing and Training Recurrent Neural Networks*. GMD Report 148
<http://www.faculty.jacobs-university.de/hjaeger/pubs/EchoStatesTechRep.pdf> (German National Research Institute for Computer Science, 2001).

90. 90.

Maass, W., Natschläger, T. & Markram, H. Real-time computing without stable states: a new framework for neural computation based on perturbations. *Neural Comput.* **14**, 2531–2560 (2002).

[PubMed](#) [MATH](#) [Google Scholar](#)

91. 91.

Steil, J. J. Backpropagation-decorrelation: online recurrent learning with O(N) complexity. In *IEEE Int. Conf. on Neural Networks* **2**, 843–848 (IEEE, 2004).

92. 92.

Schürmann, F., Meier, K. & Schemmel, J. Edge of chaos computation in mixed-mode VLSI—a hard liquid. In *Advances in Neural Information Processing Systems* **17**, 1201–1208 (2004).

93. 93.

Schrauwen, B., D’Haene, M., Verstraeten, D. & Van Campenhout, J. Compact hardware liquid state machines on FPGA for real-time speech recognition. *Neural Netw.* **21**, 511–523 (2008).

[PubMed](#) [Google Scholar](#)

94. 94.

Fernando, C. & Sojakka, S. Pattern recognition in a bucket. In *Proc. ECAL* 588–597 (2003).

95. 95.

Jones, B., Stekel, D., Rowe, J. & Fernando, C. Is there a liquid state machine in the bacterium *Escherichia coli*? In *Proc. 2007 IEEE Symp. Artif. Life (CI-ALife 2007)* 187–191, <https://doi.org/10.1109/ALIFE.2007.367795> (2007).

96. 96.

Dai, X. in *Advances in Neural Networks* Vol. 3174 (eds Yin, F. L. et al.) 519–524 (Springer, 2004).

97. 97.

Goudarzi, A., Lakin, M. R. & Stefanovic, D. DNA reservoir computing: a novel molecular computing approach. In *DNA Computing and Molecular Programming* (eds Soloveichik D. & Yurke, B.) Vol. 8141, 76–89 (Springer, 2013).

98. 98.

Nikolić, D., Haeusler, S., Singer, W. & Maass, W. Temporal dynamics of information content carried by neurons in the primary visual cortex. In *Advances in Neural Information Processing Systems* 1041–1048, <https://doi.org/10.7551/mitpress/7503.003.0135> (2007).

99. 99.

Duport, F., Smerieri, A., Akroud, A., Haelterman, M. & Massar, S. Fully analogue photonic reservoir computer. *Sci. Rep.* **6**, 22381 (2016).

[CAS](#) [PubMed](#) [PubMed Central](#) [ADS](#) [Google Scholar](#)

100. 100.

Larger, L. et al. Photonic information processing beyond Turing: an optoelectronic implementation of reservoir computing. *Opt. Express* **20**, 3241 (2012).

[CAS](#) [PubMed](#) [ADS](#) [Google Scholar](#)

101. 101.

Vandoorne, K. et al. Experimental demonstration of reservoir computing on a silicon photonics chip. *Nat. Commun.* **5**, 3541 (2014).

[PubMed](#) [ADS](#) [Google Scholar](#)

102. 102.

Larger, L. et al. High-speed photonic reservoir computing using a time-delay-based architecture: million words per second classification. *Phys. Rev. X* **7**, 011015 (2017).

[Google Scholar](#)

103. 103.

Appeltant, L. et al. Information processing using a single dynamical node as complex system. *Nat. Commun.* **2**, 468 (2011).

[CAS](#) [PubMed](#) [PubMed Central](#) [ADS](#) [Google Scholar](#)

104. 104.

Kulkarni, M. S. Memristor-based reservoir computing. In *2012 IEEE/ACM Int. Symp. on Nanoscale* 226–232,
<https://doi.org/10.1145/2765491.2765531> (IEEE/ACM, 2012).

105. 105.

Bürger, J. & Teuscher, C. Variation-tolerant computing with memristive reservoirs. In *2013 IEEE/ACM Int. Symp. on Nanoscale Architectures (NANOARCH)* 1–6,
<https://doi.org/10.1109/NanoArch.2013.6623028> (IEEE/ACM, 2013).

106. 106.

Merkel, C., Saleh, Q., Donahue, C. & Kudithipudi, D. Memristive reservoir computing architecture for epileptic seizure detection. *Proc. Comput. Sci.* **41**, 249–254 (2014).

[Google Scholar](#)

107. 107.

Hassan, A. M., Li, H. H. & Chen, Y. Hardware implementation of echo state networks using memristor double crossbar arrays. In *2017 Int. Joint Conf. on Neural Networks (IJCNN)* 2171–2177, <https://doi.org/10.1109/IJCNN.2017.7966118> (IEEE, 2017).

108. 108.

Soures, N., Hays, L. & Kudithipudi, D. Robustness of a memristor based liquid state machine. In *2017 Int. Joint Conf. on Neural Networks (IJCNN)* 2414–2420, <https://doi.org/10.1109/IJCNN.2017.7966149> (IEEE, 2017).

109. 109.

Du, C. et al. Reservoir computing using dynamic memristors for temporal information processing. *Nat. Commun.* **8**, 2204 (2017).

[PubMed](#) [PubMed Central](#) [ADS](#) [Google Scholar](#)

110. 110.

Moon, J. et al. Temporal data classification and forecasting using a memristor-based reservoir computing system. *Nat. Electron.* **2**, 480–487 (2019).

[Google Scholar](#)

111. 111.

Sillin, H. O. et al. A theoretical and experimental study of neuromorphic atomic switch networks for reservoir computing. *Nanotechnology* **24**, 384004 (2013).

[Google Scholar](#)

112. 112.

Demis, E. C. et al. Atomic switch networks—nanoarchitectonic design of a complex system for natural computing. *Nanotechnology* **26**,

204003 (2015).

[CAS](#) [PubMed](#) [ADS](#) [Google Scholar](#)

113. 113.

Demis, E. C. et al. Nanoarchitectonic atomic switch networks for unconventional computing. *Jpn. J. Appl. Phys.* **55**, 1102B2 (2016).

[Google Scholar](#)

114. 114.

Dale, M., Stepney, S., Miller, J. F. & Trefzer, M. Reservoir computing in materio: an evaluation of configuration through evolution. In *2016 IEEE Symp. Ser. Comput. Intell. SSCI 2016* <https://doi.org/10.1109/SSCI.2016.7850170> (IEEE, 2016).

115. 115.

Dale, M., Miller, J. F. & Stepney, S. Reservoir computing as a model for in-materio computing. In *Advances in Unconventional Computing* (ed. Adamatzky, A.) 533–571 (Springer, 2017).

116. 116.

Tanaka, H. et al. A molecular neuromorphic network device consisting of single-walled carbon nanotubes complexed with polyoxometalate. *Nat. Commun.* **9**, 2693 (2018).

[PubMed](#) [PubMed Central](#) [ADS](#) [Google Scholar](#)

117. 117.

Appeltant, L., Van Der Sande, G., Danckaert, J. & Fischer, I. Constructing optimized binary masks for reservoir computing with delay systems. *Sci. Rep.* **4**, 3629 (2015).

[Google Scholar](#)

118. 118.

Dale, M., Miller, J. F., Stepney, S. & Trefzer, M. A. Evolving Carbon nanotube reservoir computers. In *Unconventional Computation and Natural Computation* (eds Amos, M. & Condon, A.) 49–61 (Springer, 2016). **This study demonstrates how physical media can be exploited as a reservoir for machine-learning capabilities.**

119. 119.

Tanaka, G. et al. Recent advances in physical reservoir computing: a review. *Neural Netw.* **115**, 100–123 (2019).

[PubMed](#) [Google Scholar](#)

[Download references](#)

Acknowledgements

This research was supported by the Volkswagen Foundation through the Momentum program (grant A126874). This work was further funded by the Deutsche Forschungsgemeinschaft (DFG, German Research Foundation) through project 433682494 – SFB 1459. The project has further received funding from the European Union’s Horizon 2020 research and innovation programme under grant agreement number 101017237.

Author information

Affiliations

1. Institute of Physics, University of Münster, Münster, Germany

C. Kaspar, W. G. van der Wiel & W. H. P. Pernice

2. Organic Chemistry Institute, University of Münster, Münster, Germany

B. J. Ravoo

3. Center for Soft Nanoscience, University of Münster, Münster, Germany

B. J. Ravoo & W. H. Pernice

4. NanoElectronics Group, MESA+ Institute for Nanotechnology and BRAINS Center for Brain-Inspired Nano Systems, University of Twente, Enschede, The Netherlands

W. G. van der Wiel

5. Institute of Physiological Chemistry and Pathobiochemistry, University of Münster, Münster, Germany

S. V. Wegner

Authors

1. C. Kaspar

[View author publications](#)

You can also search for this author in [PubMed](#) [Google Scholar](#)

2. B. J. Ravoo

[View author publications](#)

You can also search for this author in [PubMed](#) [Google Scholar](#)

3. W. G. van der Wiel

[View author publications](#)

You can also search for this author in [PubMed](#) [Google Scholar](#)

4. S. V. Wegner

[View author publications](#)

You can also search for this author in [PubMed](#) [Google Scholar](#)

5. W. H. Pernice

[View author publications](#)

You can also search for this author in [PubMed](#) [Google Scholar](#)

Contributions

All authors discussed the topic and wrote the manuscript together.

Corresponding author

Correspondence to [W. H. P. Pernice](#).

Ethics declarations

Competing interests

The authors declare no competing interests.

Additional information

Peer review information *Nature* thanks the anonymous reviewer(s) for their contribution to the peer review of this work.

Publisher's note Springer Nature remains neutral with regard to jurisdictional claims in published maps and institutional affiliations.

Rights and permissions

[Reprints and Permissions](#)

About this article



Check for
updates

Cite this article

Kaspar, C., Ravoo, B.J., van der Wiel, W.G. *et al.* The rise of intelligent matter. *Nature* **594**, 345–355 (2021). <https://doi.org/10.1038/s41586-021-03453-y>

[Download citation](#)

- Received: 07 August 2020
- Accepted: 14 March 2021
- Published: 16 June 2021
- Issue Date: 17 June 2021
- DOI: <https://doi.org/10.1038/s41586-021-03453-y>

Comments

By submitting a comment you agree to abide by our [Terms](#) and [Community Guidelines](#). If you find something abusive or that does not comply with our terms or guidelines please flag it as inappropriate.

[Access through your institution](#)

[Change institution](#)

[Buy or subscribe](#)

Advertisement

| [Section menu](#) | [Main menu](#) |

- Article
- [Published: 16 June 2021](#)

A dusty veil shading Betelgeuse during its Great Dimming

- [M. Montargès](#) ORCID: [orcid.org/0000-0002-7540-999X^{1,2}](https://orcid.org/0000-0002-7540-999X),
- [E. Cannon²](#),
- [E. Lagadec³](#),
- [A. de Koter^{2,4}](#),
- [P. Kervella](#) ORCID: [orcid.org/0000-0003-0626-1749¹](https://orcid.org/0000-0003-0626-1749),
- [J. Sanchez-Bermudez](#) ORCID: [orcid.org/0000-0002-9723-0421^{5,6}](https://orcid.org/0000-0002-9723-0421),
- [C. Paladini](#) ORCID: [orcid.org/0000-0003-4974-7239⁷](https://orcid.org/0000-0003-4974-7239),
- [F. Cantaloube](#) ORCID: [orcid.org/0000-0002-3968-3780⁵](https://orcid.org/0000-0002-3968-3780),
- [L. Decin](#) ORCID: [orcid.org/0000-0002-5342-8612^{2,8}](https://orcid.org/0000-0002-5342-8612),
- [P. Scicluna](#) ORCID: [orcid.org/0000-0002-1161-3756⁷](https://orcid.org/0000-0002-1161-3756),
- [K. Kravchenko](#) ORCID: [orcid.org/0000-0003-4484-9295⁹](https://orcid.org/0000-0003-4484-9295),
- [A. K. Dupree¹⁰](#),
- [S. Ridgway¹¹](#),
- [M. Wittkowski](#) ORCID: [orcid.org/0000-0002-7952-9550¹²](https://orcid.org/0000-0002-7952-9550),
- [N. Anugu](#) ORCID: [orcid.org/0000-0002-2208-6541^{13,14}](https://orcid.org/0000-0002-2208-6541),
- [R. Norris¹⁵](#),
- [G. Rau](#) ORCID: [orcid.org/0000-0002-3042-4539^{16,17}](https://orcid.org/0000-0002-3042-4539),
- [G. Perrin¹](#),
- [A. Chiavassa³](#),
- [S. Kraus¹⁴](#),
- [J. D. Monnier¹⁸](#),
- [F. Millour³](#),
- [J.-B. Le Bouquin^{18,19}](#),
- [X. Haubois](#) ORCID: [orcid.org/0000-0001-7878-7278⁷](https://orcid.org/0000-0001-7878-7278),

- [B. Lopez³](#),
- [P. Stee ORCID: orcid.org/0000-0001-8220-0636³](#) &
- [W. Danchi¹⁶](#)

[*Nature* volume 594](#), pages 365–368 (2021) [Cite this article](#)

- 1443 Accesses
- 1 Citations
- 1016 Altmetric
- [Metrics details](#)

Subjects

- [Stars](#)
- [Stellar evolution](#)
- [Time-domain astronomy](#)
- [Transient astrophysical phenomena](#)

Abstract

Red supergiants are the most common final evolutionary stage of stars that have initial masses between 8 and 35 times that of the Sun¹. During this stage, which lasts roughly 100,000 years¹, red supergiants experience substantial mass loss. However, the mechanism for this mass loss is unknown². Mass loss may affect the evolutionary path, collapse and future supernova light curve³ of a red supergiant, and its ultimate fate as either a neutron star or a black hole⁴. From November 2019 to March 2020, Betelgeuse—the second-closest red supergiant to Earth (roughly 220 parsecs, or 724 light years, away)^{5,6}—experienced a historic dimming of its visible brightness. Usually having an apparent magnitude between 0.1 and 1.0, its visual brightness decreased to 1.614 ± 0.008 magnitudes around 7–13 February 2020⁷—an event referred to as Betelgeuse’s Great Dimming. Here we report high-angular-resolution observations showing that the

southern hemisphere of Betelgeuse was ten times darker than usual in the visible spectrum during its Great Dimming. Observations and modelling support a scenario in which a dust clump formed recently in the vicinity of the star, owing to a local temperature decrease in a cool patch that appeared on the photosphere. The directly imaged brightness variations of Betelgeuse evolved on a timescale of weeks. Our findings suggest that a component of mass loss from red supergiants⁸ is inhomogeneous, linked to a very contrasted and rapidly changing photosphere.

Access options

Subscribe to Journal

Get full journal access for 1 year

\$199.00

only \$3.90 per issue

[Subscribe](#)

All prices are NET prices.

VAT will be added later in the checkout.

Tax calculation will be finalised during checkout.

Rent or Buy article

Get time limited or full article access on ReadCube.

from \$8.99

[Rent or Buy](#)

All prices are NET prices.

Additional access options:

- [Log in](#)

- [Access through your institution](#)
- [Learn about institutional subscriptions](#)

Fig. 1: Light curve of Betelgeuse over the past six years.



Fig. 2: VLT/SPHERE–ZIMPOL observations of Betelgeuse after deconvolution in the Cnt_H α filter.



Fig. 3: Best model images obtained in the Cnt_H α filter.



Data availability

Raw data were generated at the ESO under programs 0102.D-0240(A), 0102.D-0240(D), 104.20UZ and 104.20V6.004. Derived data that support the findings of this study are available at the Centre de Données Astronomiques de Strasbourg (CDS) via anonymous ftp to cdsarc.u-strasbg.fr (130.79.128.5) or via <http://cdsarc.u-strasbg.fr/viz-bin/qcat?J/other/Nat> (for the VLT/SPHERE–ZIMPOL images) and at the Optical Interferometry Database (OiDB; for the VLTI/GRAVITY and VLT/SPHERE–IRDIS SAM observations). [Source data](#) are provided with this paper.

Code availability

The SPHERE and GRAVITY pipelines are available on the ESO website (<http://www.eso.org/sci/software/pipelines/index.html>). The PyRAF implementation of the Richardson–Lucy deconvolution algorithm is publicly available at <https://astroconda.readthedocs.io/en/latest/>. The RADMC3D code is publicly available at <https://github.com/dullemond/radmc3d-2.0>.

References

1. 1.

Ekström, S. et al. Grids of stellar models with rotation. I. Models from 0.8 to $120 M_{\odot}$ at solar metallicity ($Z = 0.014$). *Astron. Astrophys.* **537**, A146 (2012).

[Google Scholar](#)

2. 2.

Arroyo-Torres, B. et al. What causes the large extensions of red supergiant atmospheres? Comparisons of interferometric observations with 1D hydrostatic, 3D convection, and 1D pulsating model atmospheres. *Astron. Astrophys.* **575**, A50 (2015).

[Google Scholar](#)

3. 3.

Moriya, T. J., Förster, F., Yoon, S.-C., Gräfener, G. & Blinnikov, S. I. Type IIP supernova light curves affected by the acceleration of red supergiant winds. *Mon. Not. R. Astron. Soc.* **476**, 2840–2851 (2018).

[ADS](#) [CAS](#) [Google Scholar](#)

4. 4.

Meynet, G. et al. Impact of mass-loss on the evolution and pre-supernova properties of red supergiants. *Astron. Astrophys.* **575**, A60 (2015).

[Google Scholar](#)

5. 5.

Harper, G. M. et al. An updated 2017 astrometric solution for Betelgeuse. *Astron. J.* **154**, 11 (2017).

[ADS](#) [Google Scholar](#)

6. 6.

Joyce, M. et al. Standing on the shoulders of giants: new mass and distance estimates for Betelgeuse through combined evolutionary, asteroseismic, and hydrodynamic simulations with MESA. *Astrophys. J.* **902**, 63 (2020).

[ADS](#) [CAS](#) [Google Scholar](#)

7. 7.

Guinan, E., Wasatonic, R., Calderwood, T. & Carona, D. The fall and rise in brightness of Betelgeuse. *Astron. Telegr.* 13512 (2020).

8. 8.

Kervella, P. et al. The close circumstellar environment of Betelgeuse. II. Diffraction-limited spectro-imaging from 7.76 to 19.50 μ m with VLT/VISIR. *Astron. Astrophys.* **531**, A117 (2011).

[Google Scholar](#)

9. 9.

Kervella, P. et al. The close circumstellar environment of Betelgeuse. III. SPHERE/ZIMPOL imaging polarimetry in the visible. *Astron. Astrophys.* **585**, A28 (2016).

[Google Scholar](#)

10. 10.

Ohnaka, K. et al. Imaging the dynamical atmosphere of the red supergiant Betelgeuse in the CO first overtone lines with VLTI/AMBER. *Astron. Astrophys.* **529**, A163 (2011).

[Google Scholar](#)

11. 11.

Levesque, E. M. & Massey, P. Betelgeuse just is not that cool: effective temperature alone cannot explain the recent dimming of Betelgeuse. *Astrophys. J.* **891**, L37 (2020).

[ADS](#) [CAS](#) [Google Scholar](#)

12. 12.

Harper, G. M., Guinan, E. F., Wasatonic, R. & Ryde, N. The photospheric temperatures of Betelgeuse during the Great Dimming of 2019/2020: no new dust required. *Astrophys. J.* **905**, 34 (2020).

[ADS](#) [CAS](#) [Google Scholar](#)

13. 13.

Dharmawardena, T. E. et al. Betelgeuse fainter in the submillimeter too: an analysis of JCMT and APEX monitoring during the recent optical minimum. *Astrophys. J.* **897**, L9 (2020).

[ADS](#) [Google Scholar](#)

14. 14.

Kravchenko, K. et al. Atmosphere of Betelgeuse before and during the great dimming revealed by tomography. *Astron. Astrophys.* <https://doi.org/10.1051/0004-6361/202039801> (in the press).

15. 15.

López Ariste, A. et al. Convective cells in Betelgeuse: imaging through spectropolarimetry. *Astron. Astrophys.* **620**, A199 (2018).

[Google Scholar](#)

16. 16.

Freytag, B., Steffen, M. & Dorch, B. Spots on the surface of Betelgeuse – results from new 3D stellar convection models. *Astron. Nachr.* **323**, 213–219 (2002).

[ADS](#) [CAS](#) [Google Scholar](#)

17. 17.

Freytag, B. et al. Simulations of stellar convection with CO5BOLD. *J. Comput. Phys.* **231**, 919–959 (2012).

[ADS](#) [MATH](#) [Google Scholar](#)

18. 18.

Chiavassa, A., Freytag, B., Masseron, T. & Plez, B. Radiative hydrodynamics simulations of red supergiant stars. IV. Gray versus non-gray opacities. *Astron. Astrophys.* **535**, A22 (2011).

[ADS](#) [Google Scholar](#)

19. 19.

Freytag, B., Liljegren, S. & Höfner, S. Global 3D radiation-hydrodynamics models of AGB stars. Effects of convection and radial pulsations on atmospheric structures. *Astron. Astrophys.* **600**, A137 (2017).

[ADS](#) [Google Scholar](#)

20. 20.

Lançon, A., Hauschildt, P. H., Ladjal, D. & Mouhcine, M. Near-IR spectra of red supergiants and giants. I. Models with solar and with mixing-induced surface abundance ratios. *Astron. Astrophys.* **468**, 205–220 (2007).

[ADS](#) [Google Scholar](#)

21. 21.

Dullemond, C. P. et al. RADMC-3D: a multi-purpose radiative transfer tool. *Astrophysics Source Code Library* <http://ascl.net/1202.015> (2012).

[Google Scholar](#)

22. 22.

Mauron, N. & Josselin, E. The mass-loss rates of red supergiants and the de Jager prescription. *Astron. Astrophys.* **526**, A156 (2011).

[ADS](#) [Google Scholar](#)

23. 23.

De Beck, E. et al. Probing the mass-loss history of AGB and red supergiant stars from CO rotational line profiles. II. CO line survey of

evolved stars: derivation of mass-loss rate formulae. *Astron. Astrophys.* **523**, A18 (2010).

[Google Scholar](#)

24. 24.

Dolan, M. M. et al. Evolutionary tracks for Betelgeuse. *Astrophys. J.* **819**, 7 (2016).

[ADS](#) [Google Scholar](#)

25. 25.

Cotton, D. V., Bailey, J., Horta, A. D., Norris, B. R. M. & Lomax, J. R. Multi-band aperture polarimetry of Betelgeuse during the 2019–20 dimming. *Res. Notes Am. Astron. Soc.* **4**, 39 (2020); erratum **4**, 47 (2020).

[ADS](#) [Google Scholar](#)

26. 26.

Safonov, B. et al. Differential speckle polarimetry of Betelgeuse in 2019–2020: the rise is different from the fall. Preprint at <https://arXiv.org/abs/2005.05215> (2020).

27. 27.

Stothers, R. B. Giant convection cell turnover as an explanation of the long secondary periods in semiregular red variable stars. *Astrophys. J.* **725**, 1170–1174 (2010).

[ADS](#) [Google Scholar](#)

28. 28.

Dupree, A. K. et al. Spatially resolved ultraviolet spectroscopy of the Great Dimming of Betelgeuse. *Astrophys. J.* **899**, 68 (2020).

[ADS](#) [CAS](#) [Google Scholar](#)

29. 29.

Höfner, S. & Freytag, B. Exploring the origin of clumpy dust clouds around cool giants. A global 3D RHD model of a dust-forming M-type AGB star. *Astron. Astrophys.* **623**, A158 (2019).

[ADS](#) [Google Scholar](#)

30. 30.

Boulangier, J., Gobrecht, D., Decin, L., de Koter, A. & Yates, J. Developing a self-consistent AGB wind model – II. Non-classical, non-equilibrium polymer nucleation in a chemical mixture. *Mon. Not. R. Astron. Soc.* **489**, 4890–4911 (2019).

[ADS](#) [Google Scholar](#)

31. 31.

Fadeyev, I. A. Carbon dust formation in R Coronae Borealis stars. *Mon. Not. R. Astron. Soc.* **233**, 65–78 (1988).

[ADS](#) [CAS](#) [Google Scholar](#)

32. 32.

Ohnaka, K. Imaging the outward motions of clumpy dust clouds around the red supergiant Antares with VLT/VISIR. *Astron. Astrophys.* **568**, A17 (2014).

[ADS](#) [Google Scholar](#)

33. 33.

Scicluna, P. et al. Large dust grains in the wind of VY Canis Majoris. *Astron. Astrophys.* **584**, L10 (2015).

[ADS](#) [Google Scholar](#)

34. 34.

Kervella, P. et al. The close circumstellar environment of Betelgeuse. Adaptive optics spectro-imaging in the near-IR with VLT/NACO. *Astron. Astrophys.* **504**, 115–125 (2009).

[ADS](#) [Google Scholar](#)

35. 35.

O’Gorman, E. et al. CARMA CO($J = 2 - 1$) Observations of the Circumstellar Envelope of Betelgeuse. *Astron. J.* **144**, 36 (2012).

[ADS](#) [Google Scholar](#)

36. 36.

Decin, L. et al. The enigmatic nature of the circumstellar envelope and bow shock surrounding Betelgeuse as revealed by Herschel. I. Evidence of clumps, multiple arcs, and a linear bar-like structure. *Astron. Astrophys.* **548**, A113 (2012).

[Google Scholar](#)

37. 37.

Kervella, P. et al. The close circumstellar environment of Betelgeuse. V. Rotation velocity and molecular envelope properties from ALMA. *Astron. Astrophys.* **609**, A67 (2018).

[Google Scholar](#)

38. 38.

Humphreys, R. M., Helton, L. A. & Jones, T. J. The three-dimensional morphology of VY Canis Majoris. I. The kinematics of the ejecta. *Astron. J.* **133**, 2716–2729 (2007).

[ADS](#) [Google Scholar](#)

39. 39.

Smith, N., Hinkle, K. H. & Ryde, N. Red supergiants as potential type IIn supernova progenitors: spatially resolved 4.6 μm CO emission around VY CMa and Betelgeuse. *Astron. J.* **137**, 3558–3573 (2009).

[ADS](#) [CAS](#) [Google Scholar](#)

40. 40.

Dupree, A., Guinan, E., Thompson, W. T. & STEREO/SECCHI/HI Consortium. Photometry of Betelgeuse with the STEREO mission while in the glare of the Sun from Earth. *Astron. Telegr.* 13901 (2020).

41. 41.

Sigismondi, C. et al. Second dust cloud on Betelgeuse. *Astron. Telegr.* 13982 (2020).

42. 42.

Fuller, J. Pre-supernova outbursts via wave heating in massive stars – I. Red supergiants. *Mon. Not. R. Astron. Soc.* **470**, 1642–1656 (2017).

[ADS](#) [CAS](#) [Google Scholar](#)

43. 43.

Smith, N. et al. Endurance of SN 2005ip after a decade: X-rays, radio and H α like SN 1988Z require long-lived pre-supernova mass-loss. *Mon. Not. R. Astron. Soc.* **466**, 3021–3034 (2017).

[ADS](#) [CAS](#) [Google Scholar](#)

44. 44.

Smith, N. & Arnett, W. D. Preparing for an explosion: hydrodynamic instabilities and turbulence in presupernovae. *Astrophys. J.* **785**, 82 (2014).

[ADS](#) [Google Scholar](#)

45. 45.

Woosley, S. E. & Heger, A. The remarkable deaths of 9–11 solar mass stars. *Astrophys. J.* **810**, 34 (2015).

[ADS](#) [Google Scholar](#)

46. 46.

Quataert, E. & Shiode, J. Wave-driven mass loss in the last year of stellar evolution: setting the stage for the most luminous core-collapse supernovae. *Mon. Not. R. Astron. Soc.* **423**, L92–L96 (2012).

[ADS](#) [Google Scholar](#)

47. 47.

Yaron, O. et al. Confined dense circumstellar material surrounding a regular type II supernova. *Nat. Phys.* **13**, 510–517 (2017).

[CAS](#) [Google Scholar](#)

48. 48.

Andrews, J. E. et al. SN 2007od: a type IIP supernova with circumstellar interaction. *Astrophys. J.* **715**, 541–549 (2010).

[ADS](#) [CAS](#) [Google Scholar](#)

49. 49.

Johnson, S. A., Kochanek, C. S. & Adams, S. M. The quiescent progenitors of four type II-P/L supernovae. *Mon. Not. R. Astron. Soc.*

480, 1696–1704 (2018).

[ADS](#) [CAS](#) [Google Scholar](#)

50. 50.

Beuzit, J. L. et al. SPHERE: the exoplanet imager for the Very Large Telescope. *Astron. Astrophys.* **631**, A155 (2019).

[CAS](#) [Google Scholar](#)

51. 51.

Roelfsema, R. et al. The ZIMPOL high contrast imaging polarimeter for SPHERE: system test results. *Proc. SPIE* **9147**, 91473W (2014).

[Google Scholar](#)

52. 52.

Chesneau, O. et al. Time, spatial, and spectral resolution of the H α line-formation region of Deneb and Rigel with the VEGA/CHARA interferometer. *Astron. Astrophys.* **521**, A5 (2010).

[Google Scholar](#)

53. 53.

Kervella, P. et al. The dust disk and companion of the nearby AGB star L₂ Puppis. SPHERE/ZIMPOL polarimetric imaging at visible wavelengths. *Astron. Astrophys.* **578**, A77 (2015).

[Google Scholar](#)

54. 54.

Cheetham, A. C. et al. Sparse aperture masking with SPHERE. *Proc. SPIE* **9907**, 99072T (2016).

[Google Scholar](#)

55. 55.

Dohlen, K. et al. The infra-red dual imaging and spectrograph for SPHERE: design and performance. *Proc. SPIE* **7014**, 70143L (2008).

[Google Scholar](#)

56. 56.

Delorme, P. et al. The SPHERE data center: a reference for high contrast imaging processing. In *Proc. Annual Meeting of the French Society of Astronomy and Astrophysics* (eds Reylé, C. et al.) 347–361 (2017).

57. 57.

Pavlov, A. et al. SPHERE data reduction and handling system: overview, project status, and development. *Proc. SPIE* **7019**, 701939 (2008).

[Google Scholar](#)

58. 58.

Lacour, S. et al. Sparse aperture masking at the VLT. I. Faint companion detection limits for the two debris disk stars HD 92945 and HD 141569. *Astron. Astrophys.* **532**, A72 (2011).

[Google Scholar](#)

59. 59.

Greenbaum, A. Z., Pueyo, L., Sivaramakrishnan, A. & Lacour, S. An image-plane algorithm for JWST’s non-redundant aperture mask data. *Astrophys. J.* **798**, 68 (2015).

[ADS](#) [Google Scholar](#)

60. 60.

Gravity Collaboration. First light for GRAVITY: phase referencing optical interferometry for the Very Large Telescope Interferometer. *Astron. Astrophys.* **602**, A94 (2017).

[Google Scholar](#)

61. 61.

Duvert, G. JMDC: JMMC measured stellar diameters catalogue. *VizieR Online Data Catalog* II/345 (2016).

62. 62.

Ohnaka, K., Hadjara, M. & Maluenda Berna, M. Y. L. Spatially resolving the atmosphere of the non-Mira-type AGB star SW Vir in near-infrared molecular and atomic lines with VLTI/AMBER. *Astron. Astrophys.* **621**, A6 (2019).

[ADS](#) [CAS](#) [Google Scholar](#)

63. 63.

Verhoelst, T. et al. The dust condensation sequence in red supergiant stars. *Astron. Astrophys.* **498**, 127–138 (2009).

[ADS](#) [CAS](#) [Google Scholar](#)

64. 64.

Cardelli, J. A., Clayton, G. C. & Mathis, J. S. The relationship between infrared, optical, and ultraviolet extinction. *Astrophys. J.* **345**, 245–256 (1989).

[ADS](#) [CAS](#) [Google Scholar](#)

65. 65.

Arentsen, A. et al. Stellar atmospheric parameters for 754 spectra from the X-shooter spectral library. *Astron. Astrophys.* **627**, A138 (2019).

[ADS](#) [CAS](#) [Google Scholar](#)

66. 66.

Massey, P. et al. The reddening of red supergiants: when smoke gets in your eyes. *Astrophys. J.* **634**, 1286–1292 (2005).

[ADS](#) [CAS](#) [Google Scholar](#)

67. 67.

Jaeger, C., Mutschke, H., Begemann, B., Dorschner, J. & Henning, T. Steps toward interstellar silicate mineralogy. I: Laboratory results of a silicate glass of mean cosmic composition. *Astron. Astrophys.* **292**, 641–655 (1994).

[ADS](#) [CAS](#) [Google Scholar](#)

68. 68.

Dorschner, J., Begemann, B., Henning, T., Jaeger, C. & Mutschke, H. Steps toward interstellar silicate mineralogy. II. Study of Mg-Fe-silicate glasses of variable composition. *Astron. Astrophys.* **300**, 503 (1995).

[ADS](#) [CAS](#) [Google Scholar](#)

69. 69.

Tange, O. *GNU Parallel 2018* (Ole Tange, 2018).

70. 70.

Pérez, F. & Granger, B. E. IPython: a system for interactive scientific computing. *Comput. Sci. Eng.* **9**, 21–29 (2007).

[Google Scholar](#)

71. 71.

van der Walt, S., Colbert, S. C. & Varoquaux, G. The NumPy array: a structure for efficient numerical computation. *Comput. Sci. Eng.* **13**, 22–30 (2011).

[Google Scholar](#)

72. 72.

Hunter, J. D. Matplotlib: a 2D graphics environment. *Comput. Sci. Eng.* **9**, 90–95 (2007).

[Google Scholar](#)

73. 73.

Virtanen, P. et al. SciPy 1.0: fundamental algorithms for scientific computing in Python. *Nat. Methods* **17**, 261–272 (2020); author correction **17**, 352 (2020).

[CAS](#) [PubMed](#) [PubMed Central](#) [Google Scholar](#)

74. 74.

McKinney, W. Data structures for statistical computing in Python. In *Proc. 9th Python in Science Conference* (eds van der Walt, S. & Millman, J) 56–61 (2010).

75. 75.

The Astropy Collaboration. Astropy: a community Python package for astronomy. *Astron. Astrophys.* **558**, A33 (2013).

[Google Scholar](#)

[Download references](#)

Acknowledgements

This research used variable star observations from the AAVSO International Database contributed by observers worldwide. This project received funding from the European Union’s Horizon 2020 research and innovation programme under Marie Skłodowska-Curie grant agreement number 665501 with the research Foundation Flanders (FWO; [PEGASUS]² Marie Curie fellowship 12U2717N awarded to M.M.). E.C. acknowledges funding from KU Leuven C1 grant MAESTRO C16/17/007. L.D. and M.M. acknowledge support from ERC consolidator grant 646758 AEROSOL. J.S.B. acknowledges the support received from the UNAM PAPIIT project IA 101220. S.K. acknowledges support from ERC starting grant 639889 ImagePlanetFormDiscs. The material is based on work supported by NASA under award number 80GSFC17M0002. We thank the ESO staff for their fast response in accepting the DDT proposal and carrying out the observations. We are grateful that Betelgeuse underwent this peculiar event more than 700 years ago in the appropriate solid angle. This work made use of the SPHERE data center, jointly operated by OSUG/IPAG (Grenoble), PYTHEAS/LAM/CeSAM (Marseille), OCA/Lagrange (Nice) and Observatoire de Paris/LESIA (Paris). This research made use of the Jean-Marie Mariotti Center Aspro and SearchCal services (<http://www.jmmc.fr>). We used the SIMBAD and VIZIER databases at CDS, Strasbourg (France; <http://cdsweb.u-strasbg.fr/>), and NASA’s Astrophysics Data System Bibliographic Services. This research made use of GNU Parallel⁶⁹, IPython⁷⁰, Numpy⁷¹, Matplotlib⁷², SciPy⁷³, Pandas⁷⁴ (<https://github.com/pandas-dev/pandas>), Astropy⁷⁵ (<http://www.astropy.org/>) and Uncertainties (<http://pythonhosted.org/uncertainties/>).

Author information

Affiliations

1. LESIA, Observatoire de Paris, Université PSL, CNRS, Sorbonne Université, Université de Paris, Meudon, France

M. Montargès, P. Kervella & G. Perrin

2. Institute of Astronomy, KU Leuven, Leuven, Belgium

M. Montargès, E. Cannon, A. de Koter & L. Decin

3. Université Côte d'Azur, Observatoire de la Côte d'Azur, CNRS,
Laboratoire Lagrange, France

E. Lagadec, A. Chiavassa, F. Millour, B. Lopez & P. Stee

4. Anton Pannenkoek Institute for Astronomy, University of Amsterdam,
Amsterdam, The Netherlands

A. de Koter

5. Max Planck Institute for Astronomy, Heidelberg, Germany

J. Sanchez-Bermudez & F. Cantaloube

6. Instituto de Astronomía, Universidad Nacional Autónoma de México,
Ciudad de México, Mexico

J. Sanchez-Bermudez

7. European Southern Observatory, Santiago, Chile

C. Paladini, P. Scicluna & X. Haubois

8. School of Chemistry, University of Leeds, Leeds, UK

L. Decin

9. Max Planck Institute for Extraterrestrial Physics, Garching, Germany

K. Kravchenko

10. Center for Astrophysics | Harvard and Smithsonian, Cambridge, MA,
USA

A. K. Dupree

11. NSF's National Optical-Infrared Astronomy Research Laboratory,
Tucson, AZ, USA

S. Ridgway

12. European Southern Observatory, Garching bei München, Germany

M. Wittkowski

13. Steward Observatory, University of Arizona, Tucson, AZ, USA

N. Anugu

14. School of Physics and Astronomy, University of Exeter, Exeter, UK

N. Anugu & S. Kraus

15. Physics Department, New Mexico Institute of Mining and Technology,
Socorro, NM, USA

R. Norris

16. Exoplanets and Stellar Astrophysics Laboratory, NASA Goddard
Space Flight Center, Greenbelt, MD, USA

G. Rau & W. Danchi

17. Department of Physics, Catholic University of America, Washington,
DC, USA

G. Rau

18. Department of Astronomy, University of Michigan, Ann Arbor, MI,
USA

J. D. Monnier & J.-B. Le Bouquin

19. IPAG, Université Grenoble Alpes, CNRS, Grenoble, France

J.-B. Le Bouquin

Authors

1. M. Montargès

[View author publications](#)

You can also search for this author in [PubMed](#) [Google Scholar](#)

2. E. Cannon

[View author publications](#)

You can also search for this author in [PubMed](#) [Google Scholar](#)

3. E. Lagadec

[View author publications](#)

You can also search for this author in [PubMed](#) [Google Scholar](#)

4. A. de Koter

[View author publications](#)

You can also search for this author in [PubMed](#) [Google Scholar](#)

5. P. Kervella

[View author publications](#)

You can also search for this author in [PubMed](#) [Google Scholar](#)

6. J. Sanchez-Bermudez

[View author publications](#)

You can also search for this author in [PubMed](#) [Google Scholar](#)

7. C. Paladini

[View author publications](#)

You can also search for this author in [PubMed](#) [Google Scholar](#)

8. F. Cantalloube

[View author publications](#)

You can also search for this author in [PubMed](#) [Google Scholar](#)

9. L. Decin

[View author publications](#)

You can also search for this author in [PubMed](#) [Google Scholar](#)

10. P. Scicluna

[View author publications](#)

You can also search for this author in [PubMed](#) [Google Scholar](#)

11. K. Kravchenko

[View author publications](#)

You can also search for this author in [PubMed](#) [Google Scholar](#)

12. A. K. Dupree

[View author publications](#)

You can also search for this author in [PubMed](#) [Google Scholar](#)

13. S. Ridgway

[View author publications](#)

You can also search for this author in [PubMed](#) [Google Scholar](#)

14. M. Wittkowski

[View author publications](#)

You can also search for this author in [PubMed](#) [Google Scholar](#)

15. N. Anugu

[View author publications](#)

You can also search for this author in [PubMed](#) [Google Scholar](#)

16. R. Norris

[View author publications](#)

You can also search for this author in [PubMed](#) [Google Scholar](#)

17. G. Rau

[View author publications](#)

You can also search for this author in [PubMed](#) [Google Scholar](#)

18. G. Perrin

[View author publications](#)

You can also search for this author in [PubMed](#) [Google Scholar](#)

19. A. Chiavassa

[View author publications](#)

You can also search for this author in [PubMed](#) [Google Scholar](#)

20. S. Kraus

[View author publications](#)

You can also search for this author in [PubMed](#) [Google Scholar](#)

21. J. D. Monnier

[View author publications](#)

You can also search for this author in [PubMed](#) [Google Scholar](#)

22. F. Millour

[View author publications](#)

You can also search for this author in [PubMed](#) [Google Scholar](#)

23. J.-B. Le Bouquin

[View author publications](#)

You can also search for this author in [PubMed](#) [Google Scholar](#)

24. X. Haubois

[View author publications](#)

You can also search for this author in [PubMed](#) [Google Scholar](#)

25. B. Lopez

[View author publications](#)

You can also search for this author in [PubMed](#) [Google Scholar](#)

26. P. Stee

[View author publications](#)

You can also search for this author in [PubMed](#) [Google Scholar](#)

27. W. Danchi

[View author publications](#)

You can also search for this author in [PubMed](#) [Google Scholar](#)

Contributions

M.M. wrote the observing proposals, prepared all the observations, reduced and calibrated the ZIMPOL and GRAVITY data, ran the PHOENIX and RADMC3D simulations, made all the figures and is the main contributor to the text. E.C. cross-checked the RADMC3D modelling. E.L., J.S.-B. and F.C. reduced the SPHERE–IRDIS data. A.d.K. and L.D. wrote the discussion and conclusion. All authors contributed substantially to discussion, writing and revisions of the article.

Corresponding author

Correspondence to [M. Montargès](#).

Ethics declarations

Competing interests

The authors declare no competing interests.

Additional information

Peer review information *Nature* thanks Manfred Cuntz, Edward Guinan and the other, anonymous, reviewer(s) for their contribution to the peer review of this work. Peer reviewer reports are available.

Publisher's note Springer Nature remains neutral with regard to jurisdictional claims in published maps and institutional affiliations.

Extended data figures and tables

[Extended Data Fig. 1 Spectral energy distributions for the various epochs.](#)

a–d, Photometry from the ZIMPOL filters (black circles) and from the AAVSO measurements (grey triangles) is compared to a 3,700-K PHOENIX model (light orange), the best-matching composite PHOENIX model with a cool spot (blue) and best-matching RADMC3D dust clump model (violet). The flux error bars correspond to 1 s.d. The wavelength error bars correspond to the width of the ZIMPOL filters. The AAVSO error bars have been re-estimated from 0.01 mag mostly to 0.1 mag to take into account the uncertainty on the magnitudes of the calibrator star.

[Source data](#)

[Extended Data Fig. 2 Visual light curve of Betelgeuse.](#)

The data are taken from the AAVSO database over the past century.

[Source data](#)

Extended Data Fig. 3 Deconvolved intensity images of Betelgeuse for the various filters observed with ZIMPOL.

The spatial scale is indicated in the bottom left image. North is up; east is left. Each row corresponds to a single filter. Each column corresponds to a single epoch. The colour scales are linear.

Extended Data Fig. 4 Fit of the GRAVITY and IRDIS continuum data by a uniform-disk model.

The black points correspond to the data and the solid red curve to the model. The grey points correspond to excluded photospheric lines. The error bars correspond to 1 s.d. **a**, Squared visibilities for January 2019. **b**, Corresponding closure phases. **c**, Squared visibilities for February 2020. **d**, Corresponding closure phases.

[Source data](#)

Extended Data Fig. 5 Best-matching composite PHOENIX model.

The spatial scale is indicated in the bottom right image. North is up; east is left. Each row corresponds to a single filter. Each column corresponds to a single epoch. The colour scales are linear.

Extended Data Fig. 6 Identification of the RADMC3D model.

Dec, declination; RA, right ascension; R_* , stellar radius; d , distance of the star to Earth. The clump parameters are defined in Methods.

Extended Data Fig. 7 Best-matching RADMC3D dusty-clump models.

The spatial scale is indicated in the bottom right image. North is up; east is left. Each row corresponds to a single filter. Each column corresponds to a single epoch. The colour scales are linear.

Extended Data Table 1 Log of the VLT/SPHERE observations

[Full size table](#)

Extended Data Table 2 Log of the VLTI/GRAVITY observations on the A0–B2–D0–C1 quadruplet

[Full size table](#)

Extended Data Table 3 Modelling results

[Full size table](#)

Supplementary information

[Peer Review File](#)

Source data

[Source Data Fig. 1](#)

[Source Data Extended Data Fig. 1](#)

[Source Data Extended Data Fig. 2](#)

[Source Data Extended Data Fig. 4](#)

Rights and permissions

[Reprints and Permissions](#)

About this article



Check for
updates

Cite this article

Montargès, M., Cannon, E., Lagadec, E. *et al.* A dusty veil shading Betelgeuse during its Great Dimming. *Nature* **594**, 365–368 (2021). <https://doi.org/10.1038/s41586-021-03546-8>

[Download citation](#)

- Received: 06 November 2020
- Accepted: 13 April 2021
- Published: 16 June 2021
- Issue Date: 17 June 2021
- DOI: <https://doi.org/10.1038/s41586-021-03546-8>

Further reading

- [Why the supergiant star Betelgeuse went mysteriously dim last year](#)
 - Davide Castelvecchi

Nature (2021)

Comments

By submitting a comment you agree to abide by our [Terms](#) and [Community Guidelines](#). If you find something abusive or that does not comply with our terms or guidelines please flag it as inappropriate.

[Access through your institution](#)

[Change institution](#)

[Buy or subscribe](#)

Associated Content

Great Dimming of Betelgeuse explained

- Emily M. Levesque

Advertisement

This article was downloaded by **calibre** from <https://www.nature.com/articles/s41586-021-03546-8>

| [Section menu](#) | [Main menu](#) |

- Article
- [Published: 16 June 2021](#)

Correlated charge noise and relaxation errors in superconducting qubits

- [C. D. Wilen](#) [ORCID: orcid.org/0000-0002-7091-8007¹](#),
- [S. Abdullah¹](#),
- [N. A. Kurinsky](#) [ORCID: orcid.org/0000-0002-5872-519X^{2,3}](#),
- [C. Stanford⁴](#),
- [L. Cardani⁵](#),
- [G. D'Imperio](#) [ORCID: orcid.org/0000-0002-2945-0983⁵](#),
- [C. Tomei⁵](#),
- [L. Faoro^{1,6}](#),
- [L. B. Ioffe⁷](#),
- [C. H. Liu¹](#),
- [A. Opremcak¹](#),
- [B. G. Christensen¹](#),
- [J. L. DuBois⁸](#) &
- [R. McDermott¹](#)

[Nature](#) volume **594**, pages 369–373 (2021) [Cite this article](#)

- 1355 Accesses
- 72 Altmetric
- [Metrics details](#)

Subjects

- [Quantum information](#)
- [Qubits](#)

Abstract

The central challenge in building a quantum computer is error correction. Unlike classical bits, which are susceptible to only one type of error, quantum bits (qubits) are susceptible to two types of error, corresponding to flips of the qubit state about the X and Z directions. Although the Heisenberg uncertainty principle precludes simultaneous monitoring of X - and Z -flips on a single qubit, it is possible to encode quantum information in large arrays of entangled qubits that enable accurate monitoring of all errors in the system, provided that the error rate is low¹. Another crucial requirement is that errors cannot be correlated. Here we characterize a superconducting multiqubit circuit and find that charge noise in the chip is highly correlated on a length scale over 600 micrometres; moreover, discrete charge jumps are accompanied by a strong transient reduction of qubit energy relaxation time across the millimetre-scale chip. The resulting correlated errors are explained in terms of the charging event and phonon-mediated quasiparticle generation associated with absorption of γ -rays and cosmic-ray muons in the qubit substrate. Robust quantum error correction will require the development of mitigation strategies to protect multiqubit arrays from correlated errors due to particle impacts.

Access options

Subscribe to Journal

Get full journal access for 1 year

\$199.00

only \$3.90 per issue

[Subscribe](#)

All prices are NET prices.
VAT will be added later in the checkout.
Tax calculation will be finalised during checkout.

Rent or Buy article

Get time limited or full article access on ReadCube.

from \$8.99

[Rent or Buy](#)

All prices are NET prices.

Additional access options:

- [Log in](#)
- [Access through your institution](#)
- [Learn about institutional subscriptions](#)

Fig. 1: Chip layout and charge response.

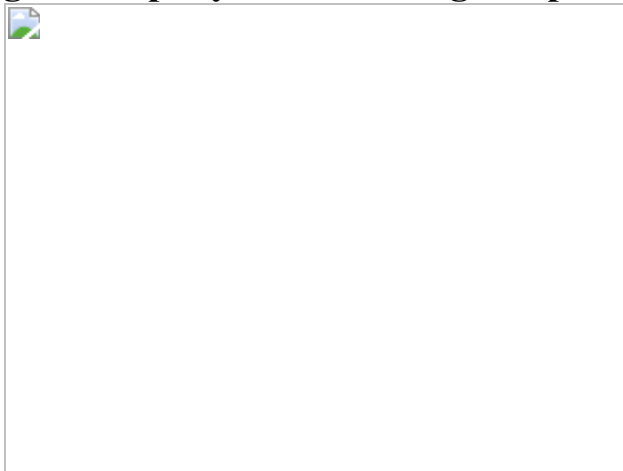


Fig. 2: Characterization of correlated charge fluctuations.

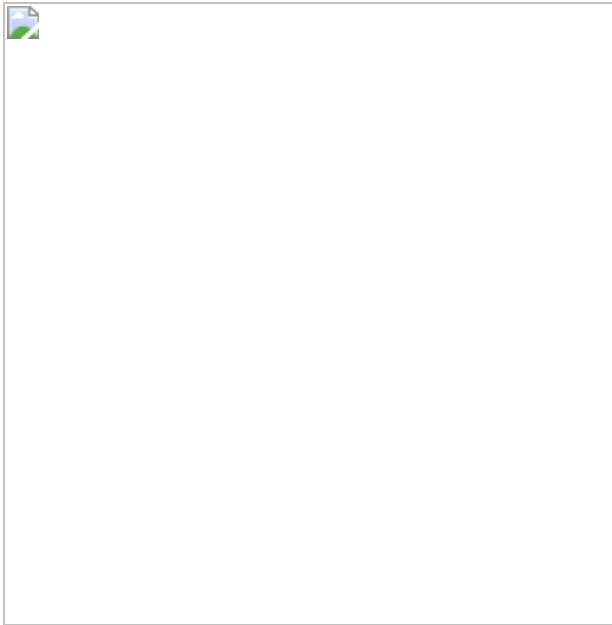


Fig. 3: Modelling of muon and γ -ray impacts.

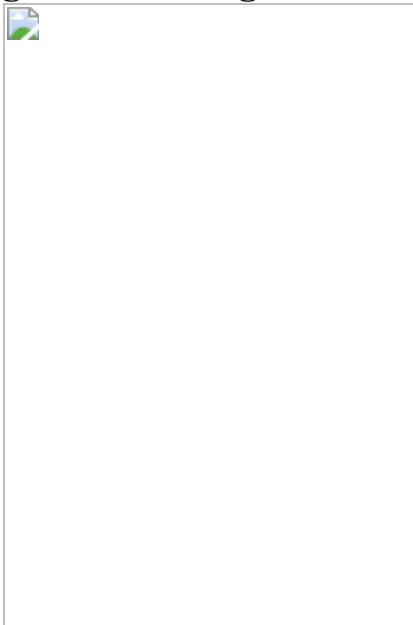
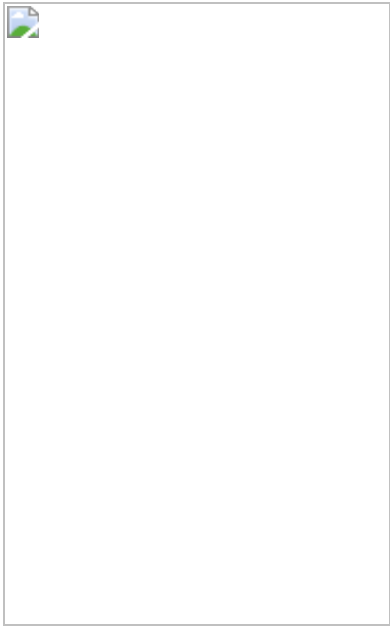


Fig. 4: Characterization of correlated relaxation errors.



Data availability

The data shown in this paper are available upon request.

References

1. 1.

Fowler, A. G., Mariantoni, M., Martinis, J. M. & Cleland, A. N.
Surface codes: towards practical large-scale quantum computation.
Phys. Rev. A **86**, 032324 (2012).

[ADS](#) [Article](#) [Google Scholar](#)

2. 2.

Barends, R. et al. Superconducting quantum circuits at the surface code threshold for fault tolerance. *Nature* **508**, 500–503 (2014).

[ADS](#) [CAS](#) [Article](#) [Google Scholar](#)

3. 3.

Sheldon, S. et al. Characterizing errors on qubit operations via iterative randomized benchmarking. *Phys. Rev. A* **93**, 012301 (2016).

[ADS](#) [Article](#) [Google Scholar](#)

4. 4.

Jeffrey, E. et al. Fast accurate state measurement with superconducting qubits. *Phys. Rev. Lett.* **112**, 190504 (2014).

[ADS](#) [Article](#) [Google Scholar](#)

5. 5.

Walter, T. et al. Rapid high-fidelity single-shot dispersive readout of superconducting qubits. *Phys. Rev. Appl.* **7**, 054020 (2017).

[ADS](#) [Article](#) [Google Scholar](#)

6. 6.

Opremcak, A. et al. High-fidelity measurement of a superconducting qubit using an on-chip microwave photon counter. *Phys. Rev. X* **11**, 011027 (2021).

[CAS](#) [Google Scholar](#)

7. 7.

Christensen, B. G. et al. Anomalous charge noise in superconducting qubits. *Phys. Rev. B* **100**, 140503 (2019).

[ADS](#) [CAS](#) [Article](#) [Google Scholar](#)

8. 8.

Vepsäläinen, A. P. et al. Impact of ionizing radiation on superconducting qubit coherence. *Nature* **584**, 551–556 (2020).

[ADS](#) [Article](#) [Google Scholar](#)

9. 9.

Agostinelli, S. et al. GEANT4—a simulation toolkit. *Nucl. Instrum. Methods Phys. Res. A* **506**, 250–303 (2003).

[ADS](#) [CAS](#) [Article](#) [Google Scholar](#)

10. 10.

Allison, J. et al. GEANT4 developments and applications. *IEEE Trans. Nucl. Sci.* **53**, 270–278 (2006).

[ADS](#) [Article](#) [Google Scholar](#)

11. 11.

Allison, J. et al. Recent developments in GEANT4. *Nucl. Instrum. Methods Phys. Res. A* **835**, 186–225 (2016).

[ADS](#) [CAS](#) [Article](#) [Google Scholar](#)

12. 12.

Shukla, P. & Sankrith, S. Energy and angular distributions of atmospheric muons at the Earth. Preprint at <https://arxiv.org/abs/1606.06907> (2018).

13. 13.

Ramanathan, K. & Kurinsky, N. Ionization yield in silicon for eV-scale electron-recoil processes. *Phys. Rev. D* **102**, 063026 (2020).

[ADS](#) [CAS](#) [Article](#) [Google Scholar](#)

14. 14.

Brandt, D. et al. Semiconductor phonon and charge transport Monte Carlo simulation using GEANT4. Preprint at
<https://arxiv.org/abs/1403.4984> (2014).

15. 15.

Kelsey, M., Agnese, R., Brandt, D. & Redl, P. G4CMP: GEANT4 add-on framework for phonon and charge-carrier physics.
<https://github.com/kelseymh/G4CMP> (2020).

16. 16.

Moffatt, R. A. et al. Spatial imaging of charge transport in silicon at low temperature. *Appl. Phys. Lett.* **114**, 032104 (2019).

[ADS](#) [Article](#) [Google Scholar](#)

17. 17.

Martinis, J. M., Ansmann, M. & Aumentado, J. Energy decay in superconducting Josephson-junction qubits from nonequilibrium quasiparticle excitations. *Phys. Rev. Lett.* **103**, 097002 (2009).

[ADS](#) [Article](#) [Google Scholar](#)

18. 18.

Lenander, M. et al. Measurement of energy decay in superconducting qubits from nonequilibrium quasiparticles. *Phys. Rev. B* **84**, 024501 (2011).

[ADS](#) [Article](#) [Google Scholar](#)

19. 19.

Wenner, J. et al. Excitation of superconducting qubits from hot nonequilibrium quasiparticles. *Phys. Rev. Lett.* **110**, 150502 (2013).

[ADS](#) [CAS](#) [Article](#) [Google Scholar](#)

20. 20.

Wang, C. et al. Measurement and control of quasiparticle dynamics in a superconducting qubit. *Nat. Commun.* **5**, 5836 (2014).

[ADS](#) [CAS](#) [Article](#) [Google Scholar](#)

21. 21.

Serniak, K. et al. Hot nonequilibrium quasiparticles in transmon qubits. *Phys. Rev. Lett.* **121**, 157701 (2018).

[ADS](#) [CAS](#) [Article](#) [Google Scholar](#)

22. 22.

Ristè, D. et al. Millisecond charge-parity fluctuations and induced decoherence in a superconducting transmon qubit. *Nat. Commun.* **4**, 1913 (2013).

[ADS](#) [Article](#) [Google Scholar](#)

23. 23.

Catelani, G., Schoelkopf, R. J., Devoret, M. H. & Glazman, L. I. Relaxation and frequency shifts induced by quasiparticles in superconducting qubits. *Phys. Rev. B* **84**, 064517 (2011).

[ADS](#) [Article](#) [Google Scholar](#)

24. 24.

Dell’Oro, S., Marcocci, S., Viel, M. & Vissani, F. Neutrinoless double beta decay: 2015 review. *Adv. High Energy Phys.* **2016**, 1–37 (2016).

[Article](#) [Google Scholar](#)

25. 25.

Poda, D. & Giuliani, A. Low background techniques in bolometers for double-beta decay search. *Int. J. Mod. Phys. A* **32**, 1743012 (2017).

[ADS](#) [CAS](#) [Article](#) [Google Scholar](#)

26. 26.

Baudis, L. The search for dark matter. *Eur. Rev.* **26**, 70–81 (2018).

[Article](#) [Google Scholar](#)

27. 27.

Pirro, S. & Mauskopf, P. Advances in bolometer technology for fundamental physics. *Annu. Rev. Nucl. Part. Sci.* **67**, 161–181 (2017).

[ADS](#) [CAS](#) [Article](#) [Google Scholar](#)

28. 28.

Szücs, T. et al. Background in γ -ray detectors and carbon beam tests in the Felsenkeller shallow-underground accelerator laboratory. *Eur. Phys. J. A* **55**, 174 (2019).

[ADS](#) [Article](#) [Google Scholar](#)

29. 29.

Aglietta, M. et al. Muon ‘depth–intensity’ relation measured by the lvd underground experiment and cosmic-ray muon spectrum at sea level. *Phys. Rev. D* **58**, 092005 (1998).

[ADS](#) [Article](#) [Google Scholar](#)

30. 30.

Jillings, C. The SNOLAB science program. *J. Phys. Conf. Ser.* **718**, 062028 (2016).

[Article](#) [Google Scholar](#)

31. 31.

Alessandria, F. et al. Validation of techniques to mitigate copper surface contamination in CUORE. *Astropart. Phys.* **45**, 13–22 (2013).

[ADS](#) [Article](#) [Google Scholar](#)

32. 32.

Aprile, E. et al. Material screening and selection for XENON100. *Astropart. Phys.* **35**, 43–49 (2011).

[ADS](#) [Article](#) [Google Scholar](#)

33. 33.

Busto, J., Gonin, Y., Hubert, F., Hubert, P. & Vuilleumier, J.-M. Radioactivity measurements of a large number of adhesives. *Nucl. Instrum. Methods Phys. Res. A* **492**, 35–42 (2002).

[ADS](#) [CAS](#) [Article](#) [Google Scholar](#)

34. 34.

ILIAS Database. <http://radiopurity.in2p3.fr> (accessed November 2020).

35. 35.

Cardani, L. et al. Reducing the impact of radioactivity on quantum circuits in a deep-underground facility. Preprint at <https://arxiv.org/abs/2005.02286> (2020).

36. 36.

Aumentado, J., Keller, M. W., Martinis, J. M. & Devoret, M. H. Nonequilibrium quasiparticles and $2e$ periodicity in single-Cooper-pair

transistors. *Phys. Rev. Lett.* **92**, 066802 (2004).

[ADS](#) [CAS](#) [Article](#) [Google Scholar](#)

37. 37.

Patel, U., Pechenezhskiy, I. V., Plourde, B. L. T., Vavilov, M. G. & McDermott, R. Phonon-mediated quasiparticle poisoning of superconducting microwave resonators. *Phys. Rev. B* **96**, 220501(R) (2017).

[ADS](#) [Article](#) [Google Scholar](#)

38. 38.

Martinis, J. M. Saving superconducting quantum processors from qubit decay and correlated errors generated by gamma and cosmic rays. Preprint at <https://arxiv.org/abs/2012.06137> (2020).

39. 39.

Beckman, S. M. et al. Development of cosmic ray mitigation techniques for the LiteBIRD space mission. *Proc. SPIE* **10708**, <https://doi.org/10.1117/12.2314288> (2018).

[Download references](#)

Acknowledgements

We acknowledge stimulating discussions with R. Barends, I. M. Pop and J. M. Martinis. We thank S. Pirro for discussions and for sharing the results of his measurements of environmental radioactivity, J. W. Engle for assistance with the calibration of the NaI scintillation detector used to characterize background radioactivity in the laboratory in Madison, and A. Riswadkar for support with device fabrication. Work at UW-Madison was supported by the US Department of Energy (DOE), Office of Science, Basic Energy Sciences under award no. DE-SC0020313. Parts of this document were prepared using the resources of the Fermi National

Accelerator Laboratory (Fermilab), a US DOE, Office of Science, HEP User Facility. Fermilab is managed by Fermi Research Alliance, LLC (FRA), acting under contract no. DE-AC02-07CH11359. Contributions from J.L.D. were performed under the auspices of the US DOE by Lawrence Livermore National Laboratory under contract DE-AC52-07NA27344. Parts of this work were supported by the DEMETRA start-up grant from INFN. The authors acknowledge use of facilities and instrumentation at the UW-Madison Wisconsin Centers for Nanoscale Technology, partially supported by the US National Science Foundation through the University of Wisconsin Materials Research Science and Engineering Center (DMR-1720415). We acknowledge the US Intelligence Advanced Research Projects Activity (IARPA) and Lincoln Laboratory for providing the travelling-wave parametric amplifier used in some of these experiments.

Author information

Affiliations

1. Department of Physics, University of Wisconsin-Madison, Madison, WI, USA

C. D. Wilen, S. Abdullah, L. Faoro, C. H. Liu, A. Opremcak, B. G. Christensen & R. McDermott

2. Fermi National Accelerator Laboratory, Center for Particle Astrophysics, Batavia, IL, USA

N. A. Kurinsky

3. Kavli Institute for Cosmological Physics, University of Chicago, Chicago, IL, USA

N. A. Kurinsky

4. Department of Physics, Stanford University, Stanford, CA, USA

C. Stanford

5. INFN Sezione di Roma, Rome, Italy

L. Cardani, G. D'Imperio & C. Tomei

6. Sorbonne Université, Laboratoire de Physique Théorique et Hautes Energies, Paris, France

L. Faoro

7. Google Inc, Venice, CA, USA

L. B. Ioffe

8. Physics Division, Lawrence Livermore National Laboratory, Livermore, CA, USA

J. L. DuBois

Authors

1. C. D. Wilen

[View author publications](#)

You can also search for this author in [PubMed](#) [Google Scholar](#)

2. S. Abdullah

[View author publications](#)

You can also search for this author in [PubMed](#) [Google Scholar](#)

3. N. A. Kurinsky

[View author publications](#)

You can also search for this author in [PubMed](#) [Google Scholar](#)

4. C. Stanford

[View author publications](#)

You can also search for this author in [PubMed](#) [Google Scholar](#)

5. L. Cardani

[View author publications](#)

You can also search for this author in [PubMed](#) [Google Scholar](#)

6. G. D'Imperio

[View author publications](#)

You can also search for this author in [PubMed](#) [Google Scholar](#)

7. C. Tomei

[View author publications](#)

You can also search for this author in [PubMed](#) [Google Scholar](#)

8. L. Faoro

[View author publications](#)

You can also search for this author in [PubMed](#) [Google Scholar](#)

9. L. B. Ioffe

[View author publications](#)

You can also search for this author in [PubMed](#) [Google Scholar](#)

10. C. H. Liu

[View author publications](#)

You can also search for this author in [PubMed](#) [Google Scholar](#)

11. A. Opremcak

[View author publications](#)

You can also search for this author in [PubMed](#) [Google Scholar](#)

12. B. G. Christensen

[View author publications](#)

You can also search for this author in [PubMed](#) [Google Scholar](#)

13. J. L. DuBois

[View author publications](#)

You can also search for this author in [PubMed](#) [Google Scholar](#)

14. R. McDermott

[View author publications](#)

You can also search for this author in [PubMed](#) [Google Scholar](#)

Contributions

C.D.W. and S.A. took and analysed the data. N.A.K. and C.S. simulated charge transport in the silicon substrate. L.C., G.D. and C.T. performed the GEANT4 simulations. L.F., L.B.I. and J.L.D. provided theoretical insights and support. C.H.L., A.O. and B.G.C. helped to develop the measurement and fabrication infrastructure. R.M. designed the experiment and directed data-taking and analysis. C.D.W., R.M., N.A.K. and L.C. co-wrote the manuscript.

Corresponding authors

Correspondence to [C. D. Wilen](#) or [R. McDermott](#).

Ethics declarations

Competing interests

The authors declare no competing interests.

Additional information

Peer review information *Nature* thanks Joseph Formaggio, Kevin Osborn and the other, anonymous, reviewer(s) for their contribution to the peer

review of this work. Peer reviewer reports are available.

Publisher's note Springer Nature remains neutral with regard to jurisdictional claims in published maps and institutional affiliations.

Supplementary information

Supplementary Information

This file includes supplementary text, figures s1–s10, supplementary tables, supplementary equations 1–20 and supplementary references.

Peer Review File

Rights and permissions

Reprints and Permissions

About this article



Check for
updates

Cite this article

Wilen, C.D., Abdullah, S., Kurinsky, N.A. *et al.* Correlated charge noise and relaxation errors in superconducting qubits. *Nature* **594**, 369–373 (2021). <https://doi.org/10.1038/s41586-021-03557-5>

Download citation

- Received: 14 December 2020
- Accepted: 15 April 2021

- Published: 16 June 2021
- Issue Date: 17 June 2021
- DOI: <https://doi.org/10.1038/s41586-021-03557-5>

Comments

By submitting a comment you agree to abide by our [Terms](#) and [Community Guidelines](#). If you find something abusive or that does not comply with our terms or guidelines please flag it as inappropriate.

[Access through your institution](#)

[Change institution](#)

[Buy or subscribe](#)

Advertisement

This article was downloaded by **calibre** from <https://www.nature.com/articles/s41586-021-03557-5>

| [Section menu](#) | [Main menu](#) |

Symmetry-enforced topological nodal planes at the Fermi surface of a chiral magnet
[Download PDF](#)

- Article
- Open Access
- [Published: 16 June 2021](#)

Symmetry-enforced topological nodal planes at the Fermi surface of a chiral magnet

- [Marc A. Wilde](#) ^{1,2},
- [Matthias Dödenhöft](#)¹,
- [Arthur Niedermayr](#) [ORCID: orcid.org/0000-0002-7915-1201](#)¹,
- [Andreas Bauer](#)^{1,2},
- [Moritz M. Hirschmann](#) [ORCID: orcid.org/0000-0003-0610-4612](#)³,
- [Kirill Alpin](#) [ORCID: orcid.org/0000-0001-7658-1911](#)³,
- [Andreas P. Schnyder](#) [ORCID: orcid.org/0000-0002-1029-815X](#)³ &
- [Christian Pfleiderer](#) [ORCID: orcid.org/0000-0001-7749-7965](#)^{1,2,4}

[Nature](#) volume **594**, pages 374–379 (2021) [Cite this article](#)

- 2006 Accesses
- 11 Altmetric
- [Metrics details](#)

Subjects

- [Electronic properties and materials](#)
- [Topological insulators](#)

Abstract

Despite recent efforts to advance spintronics devices and quantum information technology using materials with non-trivial topological properties, three key

challenges are still unresolved^{1,2,3,4,5,6,7,8,9}. First, the identification of topological band degeneracies that are generically rather than accidentally located at the Fermi level. Second, the ability to easily control such topological degeneracies. And third, the identification of generic topological degeneracies in large, multisheeted Fermi surfaces. By combining de Haas–van Alphen spectroscopy with density functional theory and band-topology calculations, here we show that the non-symmorphic symmetries^{10,11,12,13,14,15,16,17} in chiral, ferromagnetic manganese silicide (MnSi) generate nodal planes (NPs)^{11,12}, which enforce topological protectorates (TPs) with substantial Berry curvatures at the intersection of the NPs with the Fermi surface (FS) regardless of the complexity of the FS. We predict that these TPs will be accompanied by sizeable Fermi arcs subject to the direction of the magnetization. Deriving the symmetry conditions underlying topological NPs, we show that the 1,651 magnetic space groups comprise 7 grey groups and 26 black-and-white groups with topological NPs, including the space group of ferromagnetic MnSi. Thus, the identification of symmetry-enforced TPs, which can be controlled with a magnetic field, on the FS of MnSi suggests the existence of similar properties—amenable for technological exploitation—in a large number of materials.

[Download PDF](#)

Main

Nearly a century ago Wigner, von Neumann and Herring^{1,2} addressed the conditions under which Bloch states form degenerate band crossings, but their topological character and technological relevance has been recognized only recently^{3,4,5}. To be useful^{4,5,6,7,8,9}, tiny changes of a control parameter must generate a large response, underscoring the lack of control over the band filling as the unresolved key challenge in materials with band crossings known so far. This raises the question whether topological band crossings exist that are (1) generically located at the Fermi level, (2) separated sufficiently in the Brillouin zone (BZ) and (3) easy to control.

Natural candidates are systems with non-symmorphic symmetries—for example, screw rotations—that generate positions in reciprocal space at which band-crossings are symmetry-enforced. The associated key characteristics include^{10,11,12,13,14,15,16,17}: (1) the crossings are due to symmetry alone, that is, they occur on all bands independent of details such as chemical composition; (2) pairs of band crossings with opposite chirality are separated in k -space by about half a reciprocal lattice vector; (3) the band crossings may be enforced on entire planes^{11,12}, forming so-called nodal planes (NPs) with non-zero topological charge; and (4) their existence may be controlled by means of symmetry breaking. Thus, if in a material the Fermi surfaces (FSs) cross such topological NPs, they enforce pairwise FS degeneracies with large

Berry curvatures. The topology of these FS degeneracies, which we refer to as topological protectorates (TPs), will be independent of material-specific details and, moreover, may be controlled by symmetry breaking. The putative existence of topological NPs has been studied in phononic metamaterials^{18,19,20}, and mentioned in a study of non-magnetic chiral systems focusing on Kramers–Weyl fermions²¹.

To demonstrate the formation of symmetry-enforced TPs at the intersection of NPs with the FS, we decided to study the ferromagnetic state of manganese silicide (MnSi), which has attracted great interest for its itinerant-electron magnetism²², helimagnetism, skyrmion lattice²³ and quantum phase transition²⁴. Crystallizing in space group (SG) 198, MnSi is a magnetic sibling of non-magnetic RhSi (ref. ²⁵), CoSi (ref. ²⁶) and PdGa (ref. ²⁷), in which sizeable Fermi arcs and multifold fermions were recently inferred from angle-resolved photoemission spectroscopy. MnSi is ideally suited for our study, as magnetic fields exceeding around 0.7 T stabilize ferromagnetism with magnetic screw-rotation symmetries enforcing NPs.

Initial assessment

A first theoretical assessment establishes that a ferromagnetic spin polarization along a high-symmetry direction, for example, [010], reduces the symmetries from SG 198 ($P2_13$) of paramagnetic MnSi to the magnetic SG 19.27 ($P2_12'_12'_1$) (Supplementary Note 1, Extended Data Fig. 1). This SG contains two magnetic screw rotations $\langle\langle \theta_{\tilde{C}}(2)^x \rangle\rangle$ and $\langle\langle \theta_{\tilde{C}}(2)^z \rangle\rangle$ (Fig. 1a), that is, 180° screw rotations around the x and z axes combined with time-reversal symmetry θ . These rotations act like mirror symmetries, as they relate Bloch wave functions at (k_x, k_y, k_z) to those at $(-k_x, k_y, k_z)$ and $(k_x, k_y, -k_z)$, respectively, leaving the planes $k_x = 0$ and $k_z = 0$ and the BZ boundaries $k_x = \pm\pi$ and $k_z = \pm\pi$ invariant. Squaring $\langle\langle \theta_{\tilde{C}}(2)^x \rangle\rangle$ and $\langle\langle \theta_{\tilde{C}}(2)^z \rangle\rangle$ and letting them operate on the Bloch state $|\psi(\mathbf{k})\rangle$, one finds that $\langle\langle \theta_{\tilde{C}}(2)^x \rangle\rangle^2 |\psi(\mathbf{k})\rangle = \langle\langle \rm{e}^{\rm{i}k_x} \rangle\rangle |\psi(\mathbf{k})\rangle$ and $\langle\langle \theta_{\tilde{C}}(2)^z \rangle\rangle^2 |\psi(\mathbf{k})\rangle = \langle\langle \rm{e}^{\rm{i}k_z} \rangle\rangle |\psi(\mathbf{k})\rangle$. Hence, by Kramers theorem²⁸, all Bloch states on planes with $k_x = \pm\pi$ or $k_z = \pm\pi$ are two-fold degenerate. Moving away from these BZ boundaries, the symmetries are lowered such that the Bloch states become non-degenerate. Therefore, all bands in ferromagnetic MnSi are forced to cross at $k_x = \pm\pi$ and $k_z = \pm\pi$, representing a duo of NPs.

Fig. 1: Symmetries, band topology, Fermi surface protectorates and band structure of ferromagnetic MnSi.

 **figure1**

a, Action of the magnetic screw rotations and time-reversal symmetry (TRS) on the k -points in the BZ. **b**, Pairs of energy bands $E(k)$ close to the Fermi energy E_F forming a topological NP (red line) on the BZ boundary that is perpendicular to the screw-rotation axis. This NP is the topological partner of a single Weyl point (WP) in the

bulk (blue dot) of opposite topological charge. **c**, High-symmetry paths in the cubic primitive BZ. Special k -points are denoted by the orthorhombic primitive notation with subscripts for easier identification. **d**, Generic tight-binding band structure illustrating the generic band degeneracies of ferromagnetic MnSi with its magnetic space group, SG 19.27, namely Weyl points, four-fold degenerate points (FPs), NPs and TPs. **e**, Band structure of ferromagnetic MnSi for magnetization along [010] as calculated using DFT. Ten bands cross the Fermi level, as distinguished by different colours corresponding to the FS sheets numbered in **f**. **f**, Calculated FS sheets adapted to match the experimental data under magnetic field along [010], as discussed in Methods. Note the presence of NPs on the BZ boundaries, $k_x = \pm\pi$ and $k_z = \pm\pi$, as well as TPs marked in red. a.u., arbitrary units.

[Full size image](#)

The topological charge v of this duo of NPs (Fig. 1b) may be determined with the fermion doubling theorem²⁹, which states that v summed over all band crossings must be zero. We note that besides the NPs, there is an odd number of symmetry-enforced band crossings on the Y_1 – Γ – Y and R_1 – U – R lines forming Weyl points ($v = \pm 1$) and four-fold points ($v = \pm 2$), respectively (Fig. 1c,d, Extended Data Fig. 2, Supplementary Note 1). Moreover, due to the effective mirror symmetries, accidental Weyl points away from these high-symmetry lines must form pairs or quadruplets with the same v . As the sum over v of all of these Weyl and four-fold points is odd, the duo of NPs must carry a non-zero topological charge to satisfy the fermion doubling theorem. Hence, the duo of NPs at the BZ boundary is the topological partner of a single Weyl point on the Y_1 – Γ – Y line (Fig. 1b). This is a counter-example to Weyl semimetals, in which Weyl points occur always in pairs.

Shown in Fig. 1d is the band structure of a generic tight-binding model satisfying SG 19.27 (Supplementary Note 2), where pairs of bands form NPs on the BZ boundaries $k_x = \pm\pi$ and $k_z = \pm\pi$, whereas on the Y_1 – Γ – Y and R_1 – U – R lines there are Weyl and four-fold points, respectively. Explicit calculation of the Chern numbers shows that all of these band crossings, including those at the NPs, exhibit non-zero topological charges as predicted above. In turn, all of the FSs carry substantial Berry curvatures. The numerical analysis shows that these Berry curvatures become extremal at the NPs and close to the four-fold and Weyl points (Extended Data Fig. 3). By the bulk–boundary correspondence^{3,4}, the non-trivial topology of these band crossings generates large Fermi arcs on the surface, which extend over half of the BZ of the surface (Extended Data Fig. 4). These arguments may be extended to 254 of the 1,651 magnetic SGs, of which 33 have NPs whose topological charges are enforced to be non-zero by symmetry alone (Supplementary Note 3).

Calculated electronic structure

Figure 1e shows the density functional theory (DFT) band structure of MnSi, taking into account spin–orbit coupling, for the experimental moment of 0.41 Bohr magnetons (μ_B) per Mn atom along the [010] direction (Methods, Extended Data Fig. 5). Ten bands are found to cross the Fermi level (Fig. 1e). In agreement with our symmetry analysis and the tight-binding model (Fig. 1d), we find the same generic band crossings, namely: (1) NPs on the BZ boundaries $k_x = \pm\pi$ and $k_z = \pm\pi$; (2) an odd number of Weyl points along $Y_1-\Gamma-Y$; and (3) an odd number of four-fold points along R_1-U-R .

The calculated FSs as matched to experiment are shown in Fig. 1f, highlighting the NPs at the BZ boundaries at $k_x = \pm\pi$ and $k_z = \pm\pi$ (see Extended Data Table 1 for key parameters and Extended Data Fig. 5). Eight FS sheets centred at Γ comprise two small isolated hole pockets (sheets 1 and 2), two intersecting hole pockets with avoided crossings and magnetic breakdown due to spin–orbit coupling (sheets 3 and 4) and two pairs of jungle-gym-type sheets (sheets 5 and 6, and sheets 7 and 8). Sheets 9 and 10 are centred at R , comprising eight three-fingered electron pockets around the [111] axes and a tiny electron pocket, respectively. The sheet pairs (5, 6), (7, 8) and (9, 10) extend beyond the BZ boundaries with pairwise sticking at the NPs. They represent TPs (marked in red) with extremal Berry curvatures protected by the magnetic screw rotations $\langle\langle\theta_{\tilde{C}}(2x)\rangle\rangle$ and $\langle\langle\theta_{\tilde{C}}(2z)\rangle\rangle$. In contrast, sheets 5 to 10 do not form TPs at the BZ boundary $k_y = \pm\pi$, because the moment pointing along [010] breaks $\langle\langle\theta_{\tilde{C}}(2y)\rangle\rangle$.

Rotating the direction of the magnetization away from [010] distorts the FS sheets, where TPs exist only on those BZ boundaries parallel to the magnetization (Supplementary Videos 1 and 2). For instance, rotating the moments within the $x-y$ plane away from [010] breaks the magnetic screw rotation $\langle\langle\theta_{\tilde{C}}(2x)\rangle\rangle$, but keeps $\langle\langle\theta_{\tilde{C}}(2z)\rangle\rangle$ intact. In turn, the TPs gap out on the $k_y = \pm\pi$ and $k_x = \pm\pi$ planes, whereas they remain degenerate at the $k_z = \pm\pi$ planes (Extended Data Fig. 1, Supplementary Note 1).

Experimental results

To experimentally prove the mechanism causing generic TPs at the intersection of the FS with symmetry-enforced NPs and their dependence on the direction of the magnetization, we mapped out the FS by means of the de Haas–van Alphen (dHvA) effect using capacitive cantilever magnetometry (Methods, Extended Data Fig. 5,

Supplementary Note 4). In the following, we focus on magnetic field rotations in the (001) plane, where φ denotes the angle of the field with respect to [100]. This plane proves to be sufficient to infer the main FS features. Complementary data for the (001) and ($\overline{1}\overline{1}0$) planes are presented in Extended Data Fig. 5. Typical torque data at different temperatures for $\varphi = 82.5^\circ$ (Fig. 2a,b) show pronounced dHvA oscillations for magnetic fields exceeding $B \approx 0.7$ T. The hysteretic behaviour below about 0.7 T (Fig. 2a, inset) originates from the well understood helimagnetic and conical phases³⁰. Figure 2b shows the oscillatory high-field part of the torque $\tau(1/B)$ at temperature $T = 35$ mK with the low-frequency components removed for clarity. To extract the dHvA frequencies, a fast Fourier transform (FFT) analysis of $\tau(1/B)$ was carried out, where the effects of demagnetizing fields and the unsaturated magnetization were taken into account (Methods). The FFT frequencies correspond to extremal FS cross-sections in low effective fields of about 0.7–1.9 T (Methods).

Fig. 2: Typical dHvA data of ferromagnetic MnSi.

 figure2

a, dHvA oscillations detected in the magnetic torque τ as a function of magnetic field for a fixed field direction $\varphi = 82.5^\circ$. Different colours represent different temperatures within the range 0.035 K to 5 K. The inset shows the hysteretic behaviour in the regime of the helical and conical phases at low fields. **b**, High-field part of the magnetic torque $\tau(1/B)$ at $T = 35$ mK with low-frequency components removed. **c**, FFT spectra of $\tau(1/B)$ for the same field angle and temperature range as in **a**. The spectra naturally group into five regimes (labelled by I–V), each of which exhibits a number of pronounced dHvA frequencies (Greek letters). **d**, Normalized FFT amplitudes of six selected dHvA frequencies as a function of temperature. The lines represent fits to the Lifshitz–Kosevich formula, from which we obtain the effective masses m^* for the corresponding extremal FS orbits.

[Full size image](#)

Typical dHvA frequencies and FFT amplitudes, shown for $\varphi = 82.5^\circ$ in Fig. 2c, show five different regimes of dHvA frequencies labelled I to V. They comprise over 40 dHvA frequencies corresponding to different extremal FS orbits, as denoted by Greek letters (Fig. 2c, Extended Data Table 2). In our data analysis, we delineated artefacts due to the finite FFT window, such as the side lobes between κ_2 and $2\kappa_1$, or $3\kappa_2$ and ξ_1 (Methods). Fitting the temperature dependence of the FFT amplitudes within Lifshitz–Kosevich theory³¹, the effective masses for each of the orbits were deduced ranging from $m^* = 0.4m_e$ to $m^* = 17m_e$, where m_e is the bare electron mass (Fig. 2d).

To relate the dHvA frequencies to the calculated FS orbits, the torque amplitude was inferred from the DFT band structure by means of the Lifshitz–Kosevich formalism, using small rigid band shifts of the order of 10 meV to improve the matching following convention (Methods, Extended Data Table 1). The assignment to experiment was based on the consistency between dHvA frequency, angular dispersion, strength of torque signal, field dependence of the dHvA frequencies, effective masses and presence of magnetic breakdown, as explained in Methods, Extended Data Table 2, Extended Data Figs. 6, 7, Supplementary Note 5.

Figure 3a shows an intensity map of the experimental data of the (001) plane as a function of φ , where the theoretical dHvA branches are depicted by coloured lines (colours correspond to the FS sheets in Fig. 1). For comparison, Figure 3b shows an intensity map of the calculated dHvA spectra, where the experimental frequencies are marked by grey crosses.

Fig. 3: Experimental and theoretical dHvA spectra in the (001) plane as a function of field angle φ .

 figure3

a, FFT amplitudes of the experimentally observed dHvA spectra at $T = 280$ mK as a function of frequency f and field angle φ . The thin coloured lines represent the theoretical dHvA branches, calculated from the ab initio band structure, where the colour and number indicates the FS sheet (Fig. 1f) from which the dHvA branch

originates. The first harmonic (1st) of the branches originating from sheet 2 is also labelled for clarity. A line cut of this colour map for fixed field angle $\varphi = 82.5^\circ$ is shown in Fig. 2c. More than 40 dHvA branches were observed as listed in Extended Data Table 2. b, Torque amplitudes of the dHvA spectra inferred from the ab initio band structure (Methods), as a function of f and φ , with the experimental frequencies of the dHvA branches indicated by crosses. To obtain a quantitative matching between theoretical and experimental dHvA branches, small rigid energy shifts to the ab initio bands were applied, as summarized in Extended Data Table 1, Supplementary Note 4. The detailed procedure how the experimental and theoretical dHvA branches were matched is described in the main text and in Supplementary Note 5.

[Full size image](#)

For regimes I to IV, featuring contributions of the large FS sheets (5, 6) and (7, 8), all frequencies may be assigned unambiguously (Extended Data Figs. 6, 7, Supplementary Note 5). Namely, regime I contains the loop orbits around U associated with pair (5, 6) (blue and orange) and the neck orbit of sheet 8 (yellow). Regime II exhibits the dHvA branches originating from neck orbits around Γ -Y- Γ on sheet 7 (purple). The neck orbits of sheet 8 (yellow), which evades detection because of the large slope of the dispersion, its high mass and the suppression of the magnetic torque near the [010] high-symmetry direction, is consistent with an anomalous frequency splitting at the expected crossing with the loop orbits of pair (5, 6) (blue and orange) around 6.5 kT (Supplementary Note 5). Regime III arises from both pairs (5, 6) and (7, 8), that is, neck orbits around Γ -Y- Γ of (5, 6) and loop orbits around U of (7, 8). The remaining cascade of frequencies in regime III reflects breakdown orbits (translucent yellow) arising from avoided crossings between sheets 3 and 4 (red and green). Regime IV is, finally, dominated by sheet 2 of the isolated hole pocket and the first harmonic of sheet 2.

As the magnetic torque generically vanishes at high-symmetry directions, which corresponds to the $\langle 100 \rangle$ axes in regimes I to IV, the associated FS sheets are centred at the Γ point. Likewise, the lowest frequency in regime V corresponds to a Γ -centred FS sheet, which can be assigned to the small hole pocket of sheet 1. In stark contrast, for regime V above about 0.05 kT, the high-symmetry directions correspond to the $\langle 111 \rangle$ axes, whereas the torque for the $\langle 100 \rangle$ axes is finite (see also Fig. 3b, Extended Data Fig. 5g). Hence, regime V is related to FS pockets in the vicinity of the R point that may be assigned to FS sheets (9, 10). This allows for a basic estimate of the size and the effective mass of FS sheets (9, 10) without the need for a detailed account of their shape, completing the assignment. The calculations demonstrate the presence of symmetry-enforced crossings of sheets (9, 10) if they intersect the NPs (Fig. 1).

To confirm that we observed the entire FS, we calculated the Sommerfeld coefficient of the specific heat from the density of states at the Fermi level as rescaled by the

measured mass enhancements (Extended Data Table 1). Excellent agreement is observed within a few percent of experiment³², $\gamma \approx 28 \text{ mJ mol}^{-1} \text{ K}^{-2}$ at $B = 12 \text{ T}$. This analysis reveals, that sheets (5, 6), (7, 8) and (9, 10), which form TPs, contribute 86% to the total density of states at the Fermi level.

Topological NPs

Spectroscopic evidence of the symmetry-enforced topological band degeneracies at the BZ boundaries may be inferred from FS sheets (5, 6). Identical characteristics are observed for FS sheets (7, 8) (Extended Data Fig. 7, Supplementary Note 5). We note that the dHvA cyclotron orbits are perpendicular to the NPs for fundamental reasons, piercing through them at specific points of the TPs. As shown in Fig. 4a, a magnetic field parallel to [010] leads to extremal cross-sections for FS sheets (5, 6), supporting cyclotron orbits in the vicinity of the U and the Y_1 points on planes depicted by blue and green shading, respectively. Centred with respect to the U point are possible cyclotron orbits comprising different segments of FS sheets 5 and 6, which interact at TP1 to TP4 with the BZ boundaries at $k_x = \pm\pi$ and $k_z = \pm\pi$. In the absence of the non-symmorphic symmetries, these intersections would exhibit anticrossing and magnetic breakdown, leading to several orbits with different cross-sections and hence several dHvA frequencies. Instead, the behaviour is distinctly different to magnetic breakdown or Klein tunnelling^{33,34}.

Fig. 4: Extremal orbits and spectroscopic signatures of NPs and TPs.

 figure4

Identical features presented here for sheet pair (5, 6) are also observed for FS sheet pair (7, 8) (Extended Data Fig. 7, Supplementary Note 5). **a**, FS sheet pair (5, 6) for a field (**B**) along the [010] direction (for an alternative colour shading see Extended Data Fig. 6d1). Planes illustrating loop- and neck-type orbits around the U point and

the Γ – Y_1 – Γ line are indicated by blue and green shading, respectively. Loop orbits with respect to the U point intersect at TP1 to TP4 with the NPs on the $k_x = \pi$ and $k_z = \pi$ BZ boundaries. The NPs enforce degeneracies at TP1 to TP4, where the wave functions are orthogonal. **b**, Instead of anticrossing and magnetic breakdown, topological orbits stabilize. Top: cross-sectional areas under field along [010] at $\varphi = 90^\circ$. Bottom: schematic cross-sectional areas under rotated field for $\varphi = 80^\circ$. **c**, Intensity map of dHvA spectra in the regime of loop- and neck-type orbits around the U point (Fig. 3). The spectra are in excellent agreement with the topological orbits. No evidence for independent orbits of FS sheets 5 and 6 are observed. **d**, Top left: symmetrical positions of extremal orbits 1 and 2 in a plot of the FS cross-sectional area a along Γ – X – Γ with respect to the NP at the X point. The orbits give rise to identical dHvA frequencies. Note that these orbits are not accessible experimentally. Bottom left: asymmetrical position of extremal FS cross-sections along Γ – Y_1 – Γ with respect to the BZ boundary at $k_y = \pm\pi$. Top right: the associated orbits give rise to different dHvA frequencies. **e**, Intensity map of dHvA spectra in the regime of neck-type orbits around the Y_1 point (Fig. 3). Spectra are in excellent agreement with two orbits as shown in **d** (bottom left and top right), that is, no NP at the BZ boundary at $k_y = \pm\pi$ containing Y_1 .

[Full size image](#)

As the BZ boundaries at $k_x = \pm\pi$ and $k_z = \pm\pi$ represent symmetry-enforced NPs, the crossing points of sheets 5 and 6 at TP1 to TP4 are, hence, protected band degeneracies at which the wavefunctions are orthogonal, that is, TP1 to TP4 are part of the TPs that suppress transitions between orbits (we call orbits containing at least one TP ‘topological orbits’). In turn, two independent topological orbits (topological orbits 1 and 2) with identical areas and hence the same dHvA frequencies are expected (Fig. 4b, top). This is in excellent agreement with experiment, which shows a single dHvA frequency for field parallel [010] ($\varphi = 90^\circ$ in Fig. 4c). Rotating the direction of the magnetic field within the x – y plane away from [010], the NP at $k_x = \pm\pi$ gaps out, whereas the NP at $k_z = \pm\pi$ remains protected. Thus, the associated loop orbits around U (Fig. 4b, bottom) continue to include two points on the FS at $k_z = \pm\pi$ (TP3 and TP4), leading to two additional topological orbits (topological orbits 3 and 4) of identical cross-section with the same dHvA frequency, in perfect agreement with the observed spectra (Fig. 4c).

Comparing the extremal cross-sections of the neck orbits around Γ – Y_1 – Γ with those around Γ – X – Γ , the latter crosses an NP whereas the former does not. With respect to Γ – X – Γ , there would be two extremal cross-sections with identical areas, positioned symmetrically with respect to X (Fig. 4d, top left), whereas for the cross-sections with

respect to Γ – Y_1 – Γ there are two extremal orbits with different areas positioned asymmetrically with respect to Y_1 (Fig. 4d, bottom left). Thus, within our symmetry analysis and our DFT calculations, we expect a single dHvA branch for neck orbits parallel to a NP compared with two dHvA branches for neck orbits that are not parallel to a NP (Fig. 4d, top right). Keeping in mind that only neck orbits around Y_1 are accessible experimentally, we clearly observe two branches, giving strong evidence that there are no NPs on the $k_y = \pm\pi$ BZ boundary (Fig. 4e).

Concluding remarks

The symmetry-enforced NPs and TPs that are generically located at the Fermi level, which support large Berry curvatures, may account for various properties, such as anomalous Hall currents³⁵ or the nonlinear optical responses³⁶. Indeed, large anomalous contributions to the Hall response are in excellent quantitative agreement with ab initio calculations, where the calculated FS and Berry curvatures were essentially identical to the FS we report here³⁷. Our calculations imply also sizeable Fermi arcs at the surface of MnSi and related magnetic compounds such as FeGe and $Fe_{1-x}Co_xSi$, connecting the topological charge of the NPs directly with a Weyl point (Extended Data Fig. 4). These Fermi arcs reflect the presence of duos of NPs. Analogous Fermi arcs will not exist in non-magnetic materials with SG 198^{25,26,27}, which support trios of NPs (Supplementary Note 1).

In systems with symmetry-enforced NPs and TPs, tiny changes of the direction of the magnetization will control the topological band crossing in the bulk and the Fermi arcs, causing massive changes of Berry curvature that may be exploited technologically. The formation of TPs irrespective of the complexity of the FS raises the question of whether they affect the transport properties³⁸ and enable exotic states of matter³⁹. Extending the analysis presented here to all 1,651 magnetic SGs, we find that there is a large number of candidate materials, such as $CoNb_3S_6$ (ref. 40) or Nd_5Si_3 (ref. 41) with similar TPs (Extended Data Table 3, Supplementary Note 3), which await to be explored from a fundamental point of view and harnessed for future technologies.

Methods

Sample preparation

For our study, two MnSi samples were prepared from a high-quality single crystalline ingot obtained by optical float-zoning⁴². The samples were oriented by X-ray Laue

diffraction and cut into $1 \times 1 \times 1$ mm³ cubes with faces perpendicular to [100], [110], and [110] and [110], and [111] and [112] cubic equivalent directions, respectively. Both samples exhibited a residual resistivity ratio close to 300.

Experimental methods

Quantum oscillations of the magnetization, that is, the dHvA effect, was measured by means of cantilever magnetometry measuring the magnetic torque $\tau = \mathbf{m} \times \mathbf{B}$. The double-beam type cantilevers sketched in Extended Data Fig. 5e were obtained from CuBe foil by standard optical lithography and wet-chemical etching. The cantilever position was read out in terms of the capacitance between the cantilever and a fixed counter electrode using an Andeen-Hagerling AH2700A capacitance bridge, similar to the design described in refs. 43,44.

Angular rotation studies were performed in a ³He insert with a manual rotation stage at a base temperature $T = 280$ mK under magnetic fields up to 15 T. In addition, the effective charge carrier mass was determined using a dilution refrigerator insert with fixed sample stage under magnetic fields up to 14 T (16 T using a Lambda stage) at temperatures down to 35 mK.

We discuss partial rotations in the (001) and ($(\overline{1}\backslash\overline{1}0)$) crystallographic planes. The angle φ is measured from [100] in the (001) plane and the angle θ is measured from [001] in the ($(\overline{1}\backslash\overline{1}0)$) plane.

Corresponding data are shown in Fig. 3a and Extended Data Fig. 5g. Owing to the topology of the FS and the simple cubic BZ, the (001) plane rotation shows most of the extremal orbits and is already sufficient for an assignment to the FS sheets. For this reason, the discussion of the dHvA data in the main text focuses on the rotation in the (001) plane.

The response of the cantilever was calibrated by means of the electrostatic displacement, taking into account the cantilever bending line obtained from an Euler–Bernoulli approach⁴⁵. Applying a d.c. voltage, U , to the capacitance $C_0 = \varepsilon_0 A / d_0$, defined by the area A , the plate distance d_0 and the vacuum permittivity ε_0 , leads to an electrostatic force $F = C_0 U^2 / 2d_0$. This force is equivalent to a torque $\tau = \beta F L$, where L is the effective beam length and $\beta = 0.78$ is a geometry-dependent prefactor accounting for the different mechanical response of a bending beam to a torque and force, respectively. From this, the calibration constant $K(C) = \tau / \Delta C$ quantifying the capacitance change ΔC in response to the torque was obtained for different values of C . Changes in $K(C)$ up to 10% were recorded during magnetic field sweeps. The torque was calculated using

$$\$ \tau(C) = \int_{C_0}^{C} K(C') \frac{\partial C'}{\partial d} d C' . \$$$

(1)

Evaluation of the dHvA signal

The dependence of the capacitance, $C(B_{\text{ext}})$, was converted into torque and corrected as described below, where B_{ext} is the applied magnetic field. An exemplary torque curve obtained at $T = 280$ mK and $\varphi = 82.5^\circ$ is shown in Fig. 2a. In the regime below $B \approx 0.7$ T the transitions from helical to conical and field-polarized state generated a strongly hysteretic behaviour. At higher fields, magnetic quantum oscillations on different amplitude and frequency scales could be readily resolved. The first low-frequency components appeared at magnetic fields as low as $B \approx 4$ T, whereas several high-frequency components, corresponding to larger extremal cross-sections, could only be resolved in high fields (Fig. 2b). Consequently, the data acquisition and evaluation was optimized by treating low- and high-frequency components separately.

To eliminate the non-oscillatory component of the signal, low-order polynomial fits or curves obtained by adjacent averaging over suitable field intervals were subtracted from the data, producing consistent results. FFTs of $\tau(1/B)$ were used to determine the frequency components contained in the signal. Field sweeps were performed from 0 T to 15 T at $0.03\text{--}0.04$ T min $^{-1}$ and from 15 T to 10 T at 0.008 T min $^{-1}$. FFTs over the range 4 T to 15 T (10 T to 15 T) were performed to evaluate frequency components below (above) $f = 350$ T for measurements in the ^3He insert and from 10 T to 14 T (11 T to 16 T with Lambda stage) in the dilution refrigerator. The values correspond to the applied field before taking into account demagnetization. Rectangular FFT windows were chosen to maximize the ability to resolve closely spaced frequency peaks. See Supplementary Note 4 for details.

Internal magnetic field and dHvA frequency $f(B)$ in a weak itinerant magnet

MnSi is a weak ferromagnet with an unsaturated magnetization up to the largest magnetic fields studied. This results in two different peculiarities concerning the observed dHvA frequencies. (1) The field governing the quantum oscillations is the internal field³¹ $\mathbf{B}_{\text{int}} = \mu_0 \mathbf{H}_{\text{ext}} + \mu_0(1 - N_d)\mathbf{M}$, where μ_0 is the vacuum permeability, \mathbf{H}_{ext} is the applied magnetic field and \mathbf{M} is the magnetization. Taking into account the demagnetization factor⁴⁶ $N_d = 1/3$ for a cubic sample to first order yields a field correction $\Delta B = \frac{2}{3} \frac{\mu_0}{M_{\text{exp}}} M_{\text{exp}} \approx 0.131 \sqrt{T}$, where M_{exp} is the low-field value of the magnetization in the field-polarized phase determined experimentally. The applied field was corrected by this value. The field dependence of the magnetic moment yields only a minor correction of the internal

field that may be neglected. (2) The effect of the unsaturated magnetization on the Fermi surface is more prominent and may be described in a good approximation as a rigid Stoner exchange splitting that scales with the magnitude of the magnetization. Consequently, FS cross-sectional areas are enlarged with increasing B for the majority electron orbits and minority hole orbits. Cross-sectional areas shift downwards for majority hole and minority electron orbits.

This change in cross-sectional area is not directly proportional to the change in the observed dHvA frequencies f , that is, the dHvA frequencies deviate from the field-dependent frequency $\langle f \rangle_{\{B\}}(B) = \frac{\hbar}{2\pi e} A_k(B)$ obeying the Onsager relation (here A_k is the extremal cross-sectional area in k -space, \hbar is the reduced Planck constant and e is the electron charge). The frequency f observed may be inferred⁴⁷ from the derivative of the dHvA phase factor $(2\pi)^{\left(\frac{f}{B} - \gamma\right)} \pm \frac{1}{4}$ with respect to $1/B$:

$$\begin{aligned} f(B) &= \frac{\partial}{\partial B} \left[\ln \left(\frac{f}{B} - \gamma \right) \right] \\ &= \frac{1}{B} - \frac{\gamma}{B^2} \end{aligned} \quad (2)$$

Thus, a linear relation $f_B(B)$ results in a constant $f(B)$. This may be understood intuitively, because a linear term in $f_B(B)$ leads only to a phase shift since the oscillations are periodic in $1/B$. Equation (2) shows that $f(B)$ is the zero-field intercept of the tangent to $f_B(B)$.

In the Stoner picture of rigidly split bands, $f_B(B)$ may be related to the magnetization^{47,48} using

$$f_B(B) = \frac{I_s m_b}{4\mu B} M(B) \quad (3)$$

where I is the Stoner exchange parameter, m_b is the band mass, the \pm is for electron and hole orbits, respectively, $s = \pm 1$ is the spin index and f_0 is the hypothetical frequency without exchange splitting. Note, that this model is only meaningful in the field-polarized regime $B \gtrsim 0.7$ T. Using the experimental $M(B)$ curve of MnSi³², we estimate that the frequencies $f(B)$ in the windows used for $f > 350$ T defined above with centre fields $B_{\text{average}} = 2B_{\text{high}}B_{\text{low}}/(B_{\text{low}} + B_{\text{high}})$ ranging from 11.8 T to 13.2 T correspond to the extremal cross-sections at $B \approx 1.7$ –1.9 T (Extended Data Fig. 5f). For the window used for frequencies $f < 350$ T, it is $B_{\text{average}} = 6.5$ T and $f(B)$

corresponds to the extremal cross-sections at $B \approx 0.7$ T. Thus, even under large magnetic fields, the experimental frequency values correspond to a field-polarized state in a low field.

Quantum oscillatory torque and Lifshitz–Kosevich equation

Evaluation and interpretation of the quantum oscillatory torque magnetization was performed using the Lifshitz–Kosevich formalism³¹. The components of \mathbf{M} parallel (\parallel) and perpendicular (\perp) to the field are given by:

$$\begin{aligned} \text{\$}\{ M \}_{\parallel} = & -\left(\frac{e}{\hbar} \right)^{3/2} \frac{f}{B} V m^* \pi^{1/2} \sum_{p=1}^{\infty} \frac{R_T}{R} \frac{p^{3/2}}{4} \sin(2\pi p(\frac{f}{B} - \gamma)) \end{aligned} \quad (4)$$

and

$$\begin{aligned} \text{\$}\{ M \}_{\perp} = & -\frac{1}{f} \frac{\partial f}{\partial \phi} \end{aligned} \quad (5)$$

where V is the sample volume, p is the harmonic index, A'' is the curvature of the cross-sectional area parallel to \mathbf{B} , and f is the dHvA frequency observed (see comments above). The phase $\gamma = 1/2$ corresponds to a parabolic band. In general, the phase includes also contributions due to Berry phases when the orbit encloses topologically non-trivial structures in k -space. The \pm holds for maximal and minimal cross-sections, respectively. The torque amplitude is given by $\tau_{\text{osc}} = M_{\text{osc},\perp} B$. The torque thus vanishes in high-symmetry directions where $f(\phi)$ is stationary. This feature of τ may be used to infer additional information about the symmetry properties of a dHvA branch. R_T describes the temperature dependence of the oscillations

$$\begin{aligned} R_T = & \frac{\sinh(X)}{X} \frac{w_i t}{\hbar B} \end{aligned} \quad (6)$$

from which the effective mass m^* including renormalization effects can be extracted, where, k_B is the Boltzmann constant. Equation (6) was fitted to the temperature dependence of the FFT peaks using the average fields B_{average} defined above. No systematic changes in the mass values were observed within the standard deviation of

the fits when different window sizes were chosen. See Supplementary Note 4 for details. The Dingle factor

$$\text{R} = \exp \left(-\frac{\pi p_m^*}{eB\tau} \right) = \exp \left(-\frac{\pi p \omega_c}{eB\tau} \right) \quad (7)$$

describes the influence of a finite scattering time τ . Here, $\omega_c = eB/m^*$ is the cyclotron frequency.

DFT calculations

The band structure and FS sheets of MnSi in the field-polarized phase were calculated using DFT. The calculations included the effect of spin–orbit coupling. In all calculations, the magnetic part of the exchange-correlation terms was scaled⁴⁹ to match the experimental magnetic moment of $0.41\mu_B$ per Mn atom at low fields. As input for the DFT calculations, the experimental crystal structure of MnSi was used, that is, space group $P2_13$ (198) with an experimental lattice constant $a = 4.558 \text{ \AA}$. Both Mn and Si occupy Wyckoff positions $4a$ with coordinates (u, u, u) , $(-u + 1/2, -u, u + 1/2)$, $(-u, u + 1/2, -u + 1/2)$, $(u + 1/2, -u + 1/2, -u)$ where $u_{\text{Mn}} = 0.137$ and $u_{\text{Si}} = 0.845$ (Extended Data Fig. 5a).

Calculations were carried out using WIEN2k⁵⁰, ELK⁵¹ and VASP^{52,53} using different versions of the local spin density approximation. The results are consistent within the expected reproducibility of current DFT codes⁵⁴. The remaining uncertainties motivate a comprehensive experimental FS determination as reported in this study. In the main text, we focus on the results obtained with WIEN2k, using the local spin density approximation parametrization of Perdew and Wang⁵⁵ and a sampling of the full BZ with a $23 \times 23 \times 23$ Γ -centred grid. The results of Extended Data Figs. 1, 2, 4 were obtained using VASP with the PBE functional⁵⁶ and a BZ sampling with a $15 \times 15 \times 15$ k -mesh centred around Γ .

Bands used for the determination of the Fermi surface were calculated with WIEN2k on a $50 \times 50 \times 50$ k -mesh. Owing to the presence of spin–orbit coupling, but the absence of both inversion and time-reversal symmetry, band structure data had to be calculated for different directions of the spin quantization axis. For a given experimental plane of rotation, calculations were performed in angular steps of 10° . The bands were then interpolated k -point-wise using third-order splines to obtain band structure information in 1° steps.

For the prediction of the dHvA branches from the DFT results, the Supercell k -space Extremal Area Finder (SKEAF)⁵⁷ was used on interpolated data corresponding to

$150 \times 150 \times 150$ k -points in the full BZ. The theoretical torque amplitudes shown in Fig. 3b were calculated directly from the prefactors in equations (4) and (5) convoluted with a suitable distribution function.

To compute the surface states of MnSi in the field-polarized phase (Extended Data Fig. 4), we first constructed a DFT-derived tight-binding model using the maximally localized Wannier function method as implemented in Wannier90⁵⁸. Using this tight-binding model, we computed the momentum-resolved surface density of states by means of an iterative Green's function method, using WannierTools⁵⁹. The symmetry eigenvalues of the DFT bands were computed from expectation values using VASP pseudo wavefunctions, as described in ref. 60.

Magnetic breakdown

The probabilities for magnetic breakdown at a junction i is given by $\langle\{ p \}_i \rangle = \{\{ \text{rm} \{ e \} \}^{\wedge} \{-\text{frac}\{ \{ B \}_0 \} \{ B \} \} \}$. The probability for no breakdown to occur is thus $q_i = 1 - p_i$. The breakdown fields B_0 were calculated from Chamber's formula

$$\$ \$ \{ B \}_0 = \text{frac}\{ \{ \text{rm} \{ \pi \} \} \{ \hbar \} \{ 2e \} \{ \sqrt{\text{frac}\{ \{ k \}_g \}^{\wedge} \{ 3 \}} \{ a+b \} } \}, \$ \$ (8)$$

where k_g is the gap in k -space and a and b are the curvatures of the trajectories at the breakdown junction³¹. In our study of MnSi, we observed magnetic breakdown in particular between sheets 3 and 4, which exhibit up to eight junctions depending on the magnetic field direction and between FS sheet pairs touching the BZ surfaces on which the NP degeneracy is lifted. Only breakdown orbits that are closed after one cycle are considered in the analysis. Further details can be found in the Supplementary Note 5.

Assignment of dHvA orbits and rigid band shifts

The assignment of the experimental dHvA branches to the corresponding extremal FS cross-sections was based on the following criteria: (1) dHvA frequency—determining sheet size in terms of the cross-sectional area; (2) angular dispersion—relating to sheet shape, topology and symmetry; (3) torque signal strength—relating to sheet shape and symmetry; (4) direction of $f(B)$ shift—relating to spin orientation and charge carrier type; (5) effective mass—relating to the temperature dependence; (6) magnetic breakdown behaviour—relating to proximity of neighbouring sheets.

The majority of the observed dHvA branches could be related directly to the FS as calculated. In addition, we used the well-established procedure of small rigid band shifts to optimize the matching. While this procedure is, in general, neither charge nor

spin conserving, it results in a very clear picture of the experimental FS. One has to bear in mind, however, that the deviations between the true FS and the calculated FS are not due to a rigid band shift (this might be justified, for example, in case of unintentional doping, which we rule out here). Rather, it may be attributed to differences in the band dispersions that originate in limitations of our DFT calculations (for example, neglecting electronic correlations and the coupling to the spin fluctuation spectrum).

The dHvA orbits, the assignments to a specific extremal cross-section, the observed and predicted frequencies, the observed and predicted masses and mass enhancements are listed in Extended Data Table 2. Extended Data Table 1 summarizes the resulting characteristic properties of the FS sheets including their contribution to the density of states at the Fermi level.

Symmetry analysis

The symmetry-enforced band crossings and the band topology follow from the non-trivial winding of the symmetry eigenvalues through the BZ. This winding of the eigenvalues is derived in Supplementary Note 1, both for the paramagnetic and ferromagnetic phases of MnSi. Supplementary Note 1 also contains the derivation of the topological charges of the NPs, Weyl points and four-fold points, which are obtained from generalizations of the Nielsen–Ninomiya theorem²⁹. To illustrate the band topology for ferromagnets in SG 19.27 and SG 4.9, two tight-binding models are derived in Supplementary Note 2, which includes also a discussion of the Berry curvature and the surface states. The classification of NPs in magnetic materials is given in Supplementary Note 3. It is found that among the 1,651 magnetic SGs, 254 exhibit symmetry-enforced NPs. We find that (at least) 33 of these have NPs whose topological charge is guaranteed to be non-zero due to symmetry alone.

Data availability

Materials and additional data related to this paper are available from the corresponding authors upon reasonable request.

References

1. 1.

von Neumann, J. & Wigner, E. Über das Verhalten von Eigenwerten bei adiabatischen Prozessen. *Z. Phys.* **30**, 467–470 (1929).

[MATH](#) [Google Scholar](#)

2. 2.

Herring, C. Accidental degeneracy in the energy bands of crystals. *Phys. Rev.* **52**, 365–373 (1937).

[ADS](#) [CAS](#) [Google Scholar](#)

3. 3.

Chiu, C.-K., Teo, J. C. Y., Schnyder, A. P. & Ryu, S. Classification of topological quantum matter with symmetries. *Rev. Mod. Phys.* **88**, 035005 (2016).

[ADS](#) [Google Scholar](#)

4. 4.

Armitage, N. P., Mele, E. J. & Vishwanath, A. Weyl and Dirac semimetals in three-dimensional solids. *Rev. Mod. Phys.* **90**, 015001 (2018).

[ADS](#) [MathSciNet](#) [CAS](#) [Google Scholar](#)

5. 5.

Burkov, A. Weyl metals. *Annu. Rev. Condens. Matter Phys.* **9**, 359–378 (2018).

[ADS](#) [CAS](#) [Google Scholar](#)

6. 6.

Wang, Q. et al. Large intrinsic anomalous Hall effect in half-metallic ferromagnet $\text{Co}_3\text{Sn}_2\text{S}_2$ with magnetic Weyl fermions. *Nat. Commun.* **9**, 3681 (2018); correction **9**, 4212 (2018).

[ADS](#) [PubMed](#) [PubMed Central](#) [Google Scholar](#)

7. 7.

Huang, X. et al. Observation of the chiral-anomaly-induced negative magnetoresistance in 3D Weyl semimetal TaAs. *Phys. Rev. X* **5**, 031023 (2015).

[Google Scholar](#)

8. 8.

Liang, S. et al. Experimental tests of the chiral anomaly magnetoresistance in the Dirac–Weyl semimetals Na_3Bi and GdPtBi . *Phys. Rev. X* **8**, 031002 (2018).

[CAS](#) [Google Scholar](#)

9. 9.

Huang, S.-M. et al. A Weyl fermion semimetal with surface Fermi arcs in the transition metal monopnictide TaAs class. *Nat. Commun.* **6**, 7373 (2015).

[ADS](#) [CAS](#) [PubMed](#) [PubMed Central](#) [Google Scholar](#)

10. 10.

Michel, L. & Zak, J. Elementary energy bands in crystals are connected. *Phys. Rep.* **341**, 377–395 (2001).

[ADS](#) [MathSciNet](#) [CAS](#) [MATH](#) [Google Scholar](#)

11. 11.

Young, S. M. et al. Dirac semimetal in three dimensions. *Phys. Rev. Lett.* **108**, 140405 (2012).

[ADS](#) [CAS](#) [PubMed](#) [Google Scholar](#)

12. 12.

Furusaki, A. Weyl points and Dirac lines protected by multiple screw rotations. *Sci. Bull.* **62**, 788–794 (2017).

[Google Scholar](#)

13. 13.

Zhao, Y. X. & Schnyder, A. P. Nonsymmorphic symmetry-required band crossings in topological semimetals. *Phys. Rev. B* **94**, 195109 (2016).

[ADS](#) [Google Scholar](#)

14. 14.

Zhang, J. et al. Topological band crossings in hexagonal materials. *Phys. Rev. Mater.* **2**, 074201 (2018).

[CAS](#) [Google Scholar](#)

15. 15.

Yu, Z.-M., Wu, W., Zhao, Y. X. & Yang, S. A. Circumventing the no-go theorem: a single Weyl point without surface Fermi arcs. *Phys. Rev. B* **100**, 041118 (2019).

[ADS](#) [CAS](#) [Google Scholar](#)

16. 16.

Wu, W. et al. Nodal surface semimetals: theory and material realization. *Phys. Rev. B* **97**, 115125 (2018).

[ADS](#) [CAS](#) [Google Scholar](#)

17. 17.

Türker, O. & Moroz, S. Weyl nodal surfaces. *Phys. Rev. B* **97**, 075120 (2018).

[ADS](#) [Google Scholar](#)

18. 18.

Xiao, M. & Fan, S. Topologically charged nodal surface. Preprint at <https://arxiv.org/abs/1709.02363> (2017).

19. 19.

Yang, Y. et al. Observation of a topological nodal surface and its surface-state arcs in an artificial acoustic crystal. *Nat. Commun.* **10**, 5185 (2019).

[ADS](#) [PubMed](#) [PubMed Central](#) [Google Scholar](#)

20. 20.

Xiao, M. et al. Experimental demonstration of acoustic semimetal with topologically charged nodal surface. *Sci. Adv.* **6**, eaav2360 (2020).

[ADS](#) [PubMed](#) [PubMed Central](#) [Google Scholar](#)

21. 21.

Chang, G. et al. Topological quantum properties of chiral crystals. *Nat. Mater.* **17**, 978–985 (2018).

[ADS](#) [CAS](#) [PubMed](#) [Google Scholar](#)

22. 22.

Lonzarich, G. G. Magnetic oscillations and the quasiparticle bands of heavy electron systems. *J. Magn. Magn. Mater.* **76–77**, 1–10 (1988).

[ADS](#) [Google Scholar](#)

23. 23.

Mühlbauer, S. et al. Skyrmion lattice in a chiral magnet. *Science* **323**, 915–919 (2009).

[ADS](#) [PubMed](#) [Google Scholar](#)

24. 24.

Pfleiderer, C., McMullan, G. J., Julian, S. R. & Lonzarich, G. G. Magnetic quantum phase transition in MnSi under hydrostatic pressure. *Phys. Rev. B* **55**, 8330–8338 (1997).

[ADS](#) [CAS](#) [Google Scholar](#)

25. 25.

Sanchez, D. S. et al. Topological chiral crystals with helicoid-arc quantum states. *Nature* **567**, 500–505 (2019).

[ADS](#) [CAS](#) [PubMed](#) [Google Scholar](#)

26. 26.

Rao, Z. et al. Observation of unconventional chiral fermions with long Fermi arcs in CoSi. *Nature* **567**, 496–499 (2019).

[ADS](#) [CAS](#) [PubMed](#) [Google Scholar](#)

27. 27.

Schröter, N. B. M. et al. Observation and control of maximal Chern numbers in a chiral topological semimetal. *Science* **369**, 179–183 (2020).

[ADS](#) [PubMed](#) [Google Scholar](#)

28. 28.

Kramers, H. A. Théorie générale de la rotation paramagnétique dans les cristaux. *Proc. Amsterdam Acad.* **33**, 959–972 (1930).

[CAS](#) [MATH](#) [Google Scholar](#)

29. 29.

Nielsen, H. & Ninomiya, M. A no-go theorem for regularizing chiral fermions. *Phys. Lett. B* **105**, 219–223 (1981).

[ADS](#) [Google Scholar](#)

30. 30.

Bauer, A. et al. Symmetry breaking, slow relaxation dynamics, and topological defects at the field-induced helix reorientation in MnSi. *Phys. Rev. B* **95**, 024429 (2017).

[ADS](#) [Google Scholar](#)

31. 31.

Shoenberg, D. *Magnetic Oscillations in Metals* (Cambridge Univ. Press, 1984).

32. 32.

Bauer, A. et al. Quantum phase transitions in single-crystal $\text{Mn}_{1-x}\text{Fe}_x\text{Si}$ and $\text{Mn}_{1-x}\text{Co}_x\text{Si}$: crystal growth, magnetization, ac susceptibility, and specific heat. *Phys. Rev. B* **82**, 064404 (2010).

[ADS](#) [Google Scholar](#)

33. 33.

Alexandradinata, A. & Glazman, L. Geometric phase and orbital moment in quantization rules for magnetic breakdown. *Phys. Rev. Lett.* **119**, 256601 (2017).

[ADS](#) [CAS](#) [PubMed](#) [Google Scholar](#)

34. 34.

van Delft, M. R. et al. Electron–hole tunneling revealed by quantum oscillations in the nodal-line semimetal HfSiS. *Phys. Rev. Lett.* **121**, 256602 (2018).

[ADS](#) [PubMed](#) [Google Scholar](#)

35. 35.

Xiao, D., Chang, M.-C. & Niu, Q. Berry phase effects on electronic properties. *Rev. Mod. Phys.* **82**, 1959–2007 (2010).

[ADS](#) [MathSciNet](#) [CAS](#) [MATH](#) [Google Scholar](#)

36. 36.

Morimoto, T. & Nagaosa, N. Topological nature of nonlinear optical effects in solids. *Sci. Adv.* **2**, e1501524 (2016).

[ADS](#) [PubMed](#) [PubMed Central](#) [Google Scholar](#)

37. 37.

Franz, C. et al. Real-space and reciprocal-space Berry phases in the Hall effect of $\text{Mn}_{1-x}\text{Fe}_x\text{Si}$. *Phys. Rev. Lett.* **112**, 186601 (2014).

[ADS](#) [CAS](#) [PubMed](#) [Google Scholar](#)

38. 38.

Smith, M. F. Small-angle interband scattering as the origin of the $T^{3/2}$ resistivity in MnSi. *Phys. Rev. B* **74**, 172403 (2006).

[ADS](#) [Google Scholar](#)

39. 39.

Grover, T. & Fisher, M. P. A. Quantum disentangled liquids. *J. Stat. Mech.* **1014**, P10010 (2014).

[MathSciNet](#) [MATH](#) [Google Scholar](#)

40. 40.

Tenasini, G. et al. Giant anomalous Hall effect in quasi-two-dimensional layered antiferromagnet $\text{Co}_{1/3}\text{NbS}_2$. *Phys. Rev. Res.* **2**, 023051 (2020).

[CAS](#) [Google Scholar](#)

41. 41.

Boulet, P., Weizer, F., Hiebl, K. & Noël, H. Structural chemistry, magnetism and electrical properties of binary Nd silicides. *J. Alloys Compd.* **315**, 75–81 (2001).

[CAS](#) [Google Scholar](#)

42. 42.

Neubauer, A. et al. Ultra-high vacuum compatible image furnace. *Rev. Sci. Instrum.* **82**, 013902 (2011).

[ADS](#) [CAS](#) [PubMed](#) [Google Scholar](#)

43. 43.

Wilde, M. A. et al. Magnetometry on quantum Hall systems: thermodynamic energy gaps and the density of states distribution. *Phys. Status Solidi B* **245**, 344–355 (2008).

[ADS](#) [CAS](#) [Google Scholar](#)

44. 44.

Wilde, M., Heitmann, D. & Grundler, D. *Magnetization of Interacting Electrons in Low-Dimensional Systems* Ch. 10, 245 (Springer Nanoscience and Technology, 2010).

45. 45.

Wilde, M. *Magnetization Measurements on Low-Dimensional Electron Systems in High-Mobility GaAs and SiGe Heterostructures*. PhD thesis, Universität Hamburg (2004).

46. 46.

Aharoni, A. Demagnetizing factors for rectangular ferromagnetic prisms. *J. Appl. Phys.* **83**, 3432–3434 (1998).

[ADS](#) [CAS](#) [Google Scholar](#)

47. 47.

van Ruitenbeek, J. M. et al. A de Haas–van Alphen study of the field dependence of the Fermi surface in ZrZn₂. *J. Phys. F* **12**, 2919–2928 (1982).

[ADS](#) [Google Scholar](#)

48. 48.

Kimura, N. et al. de Haas–van Alphen effect in ZrZn₂ under pressure: crossover between two magnetic states. *Phys. Rev. Lett.* **92**, 197002 (2004).

[ADS](#) [CAS](#) [PubMed](#) [Google Scholar](#)

49. 49.

Hoshino, T., Zeller, R., Dederichs, P. H. & Weinert, M. Magnetic energy anomalies of 3d systems. *Europhys. Lett.* **24**, 495–500 (1993).

[ADS](#) [CAS](#) [Google Scholar](#)

50. 50.

Blaha, P. et al. Wien2k: an apw+lo program for calculating the properties of solids. *J. Chem. Phys.* **152**, 074101 (2020).

[CAS](#) [PubMed](#) [Google Scholar](#)

51. 51.

The Elk Code (GNU General Public License, 2021); <https://elk.sourceforge.io/>

52. 52.

Kresse, G. & Furthmüller, J. Efficiency of ab-initio total energy calculations for metals and semiconductors using a plane-wave basis set. *Comput. Mater. Sci.* **6**, 15–50 (1996).

[CAS](#) [Google Scholar](#)

53. 53.

Kresse, G. & Furthmüller, J. Efficient iterative schemes for ab initio total-energy calculations using a plane-wave basis set. *Phys. Rev. B* **54**, 11169–11186 (1996).

[ADS](#) [CAS](#) [Google Scholar](#)

54. 54.

Lejaeghere, K. A. Reproducibility in density functional theory calculations of solids. *Science* **351**, aad3000 (2016).

[PubMed](#) [Google Scholar](#)

55. 55.

Perdew, J. P. & Wang, Y. Accurate and simple analytic representation of the electron-gas correlation energy. *Phys. Rev. B* **45**, 13244–13249 (1992).

[ADS](#) [CAS](#) [Google Scholar](#)

56. 56.

Perdew, J. P., Burke, K. & Ernzerhof, M. Generalized gradient approximation made simple. *Phys. Rev. Lett.* **77**, 3865–3868 (1996).

[ADS](#) [CAS](#) [PubMed](#) [Google Scholar](#)

57. 57.

Rourke, P. & Julian, S. Numerical extraction of de Haas–van Alphen frequencies from calculated band energies. *Comput. Phys. Commun.* **183**, 324–332 (2012).

[ADS](#) [CAS](#) [Google Scholar](#)

58. 58.

Mostofi, A. A. et al. Wannier90: a tool for obtaining maximally-localised Wannier functions. *Comput. Phys. Commun.* **178**, 685–699 (2008).

[ADS](#) [CAS](#) [MATH](#) [Google Scholar](#)

59. 59.

Wu, Q., Zhang, S., Song, H.-F., Troyer, M. & Soluyanov, A. A. Wanniertools: an open-source software package for novel topological materials. *Comput. Phys. Commun.* **224**, 405–416 (2018).

[ADS](#) [CAS](#) [Google Scholar](#)

60. 60.

Gao, J., Wu, Q., Persson, C. & Wang, Z. Irvsp: to obtain irreducible representations of electronic states in the VASP. *Comput. Phys. Commun.* **261**, 107760 (2021).

[MathSciNet](#) [CAS](#) [Google Scholar](#)

[Download references](#)

Acknowledgements

We thank D. Grundler, F. Rucker, A. Leonhardt, A. Rosch, T. Rapp, S. G. Albert and S. M. Sauther for support and discussions. Preliminary band structure calculations for a limited number of field orientations using FLEUR and JuDFT KKR-GGA were carried out in collaboration with F. Freimuth, B. Zimmermann and Y. Mokrousov in the very early stages of this study. M.A.W., A.B. and C.P. were supported through DFG TRR80 (project-id 107745057, project E1 and E3), DFG SPP 2137 (Skyrmionics) under grant number PF393/19 (project-id 403191981), DFG GACR Projekt WI 3320/3-1, ERC Advanced Grants number 291079 (TOPFIT) and number 788031 (ExQuiSid), and Germany's excellence strategy EXC-2111 390814868.

Funding

Open access funding provided by Max Planck Society.

Author information

Affiliations

1. Physik Department, Technische Universität München, Garching, Germany

Marc A. Wilde, Matthias Dodenhöft, Arthur Niedermayr, Andreas Bauer & Christian Pfleiderer

2. Centre for QuantumEngineering (ZQE), Technische Universität München, Garching, Germany

Marc A. Wilde, Andreas Bauer & Christian Pfleiderer

3. Max-Planck-Institute for Solid State Research, Stuttgart, Germany

Moritz M. Hirschmann, Kirill Alpin & Andreas P. Schnyder

4. MCQST, Technische Universität München, Garching, Germany

Christian Pfleiderer

Authors

1. Marc A. Wilde

[View author publications](#)

You can also search for this author in [PubMed](#) [Google Scholar](#)

2. Matthias Dodenhöft

[View author publications](#)

You can also search for this author in [PubMed](#) [Google Scholar](#)

3. Arthur Niedermayr

[View author publications](#)

You can also search for this author in [PubMed](#) [Google Scholar](#)

4. Andreas Bauer

[View author publications](#)

You can also search for this author in [PubMed](#) [Google Scholar](#)

5. Moritz M. Hirschmann

[View author publications](#)

You can also search for this author in [PubMed](#) [Google Scholar](#)

6. Kirill Alpin

[View author publications](#)

You can also search for this author in [PubMed](#) [Google Scholar](#)

7. Andreas P. Schnyder

[View author publications](#)

You can also search for this author in [PubMed](#) [Google Scholar](#)

8. Christian Pfleiderer

[View author publications](#)

You can also search for this author in [PubMed](#) [Google Scholar](#)

Contributions

M.A.W. and C.P. conceived the experiment and devised its interpretation together with A.P.S. A.B. prepared and characterized the samples. M.D. and M.A.W. conducted the measurements and analysed the data. M.A.W., A.N. and K.A. performed comprehensive band structure calculations. M.A.W. connected the experimental data with the calculated band structure. M.M.H., K.A. and A.P.S. performed the symmetry analysis and identified the topological properties of the band structure. M.M.H. and K.A. calculated the surface states and the Berry curvatures. M.A.W., A.P.S. and

C.P. wrote the manuscript with contributions from M.M.H. and K.A. All authors discussed the data and commented on the manuscript.

Corresponding authors

Correspondence to [Marc A. Wilde](#) or [Andreas P. Schnyder](#) or [Christian Pfleiderer](#).

Ethics declarations

Competing interests

The authors declare no competing interests.

Additional information

Peer review information *Nature* thanks Zhiqiang Mao, Gang Xu and the other, anonymous, reviewer(s) for their contribution to the peer review of this work. Peer reviewer reports are available.

Publisher's note Springer Nature remains neutral with regard to jurisdictional claims in published maps and institutional affiliations.

Extended data figures and tables

[Extended Data Fig. 1 Magnetic space groups and electronic band structures for different directions of the magnetization.](#)

a, Magnetic subgroups of space group 198 ($P2_13$) and their group–subgroup relations. The magnetic space groups describing the symmetries for magnetizations along [010] and within the x – y plane are highlighted in green and blue, respectively. **b**, Orthorhombic BZ for ferromagnetic MnSi (left) and magnetization directions used for the ab initio calculations in **c–f** (right). **c–f**, Ab initio electronic band structure of ferromagnetic MnSi along the four high-symmetry paths indicated in **b**: Y_1 – Γ – Y (**c**), X_1 – Γ – X (**d**), R_1 –

$\text{U}-\text{R}$ (**e**) and $\text{R}_2-\text{S}-\text{R}$ (**f**). In the first, second and third rows, the magnetization is oriented along [010], 10° rotated into the $x-y$ plane and along [110], respectively. Some of the Weyl points and four-fold degenerate points at (or near) the high-symmetry lines are highlighted by violet and brown circles.

Extended Data Fig. 2 Momentum dependence of the screw-rotation eigenvalues.

a, Schematic band connectivity diagrams for a minimal set of bands along the $\text{Y}_1-\Gamma-\text{Y}$ line (**a1**), the $\text{R}_1-\text{U}-\text{R}$ line (**a2**) and the $\text{S}_1-\text{X}-\text{S}$ (**a3**) line, respectively. The eigenvalues of the screw-rotation symmetry $\langle \tilde{C}^2_y \rangle$ are indicated by colour. **b**, Ab initio electronic band structure of MnSi in the [010] FM phase with the $\langle \tilde{C}^2_y \rangle$ eigenvalues indicated by colour. The crossings of bands with different colour on the $\text{Y}_1-\Gamma-\text{Y}$ line (**b1**) and on the $\text{R}_1-\text{U}-\text{R}$ line (**b2**) are Weyl points and four-fold degenerate points, respectively.

Extended Data Fig. 3 Berry curvature on the Fermi surface.

a, Berry curvature $\Omega_\mu(\mathbf{k})$ on one of the Fermi surfaces of a tight-binding model in SG 19.27, corresponding to ferromagnetic MnSi with the magnetization pointing along [010]. **a1** shows the three components of Ω_μ as a function of k_x , along the direction indicated by the green arrow in **a2**. The absolute value of the Berry curvature $|\Omega(\mathbf{k})|$ is indicated in **a2** by a logarithmic colour code. **b**, Same as **a** but for a tight-binding model in SG 4.9, corresponding to ferromagnetic MnSi with the magnetization rotated into the $x-y$ plane.

Extended Data Fig. 4 Topological surface states.

a–c, Density of states (DOS) at the (010) surface of the tight-binding model with SG 19.27 (**a, b**) and ferromagnetic MnSi with the magnetization aligned along [010] (**c**). The first and second rows display the DOS at the top and bottom surfaces, respectively. In **a**, the surface DOS is shown at an

energy $E = -1.2$ of the single Weyl point (WP) on the $\text{Y}_1\text{--}\Gamma\text{--}\text{Y}$ line. A single Fermi arc emanates from the projected Weyl point and connects to the $k_z = \pi$ NP. In **b**, the surface DOS is shown at the energy $E = +1.4$ of the four-fold point (FP) on the $\text{R}_1\text{--U--R}$ line, whose chirality $v = -2$ is compensated by two accidental Weyl points in the bulk. Two Fermi arcs emanate from the projected four-fold point and connect to the accidental Weyl points in the bulk. In **c**, the DFT-derived surface DOS of ferromagnetic MnSi is shown at the Fermi level $E = E_F$. Fermi arcs emanate from the projected Weyl points on the $\text{Y}_1\text{--}\Gamma\text{--}\text{Y}$ line and connect with the bulk bands forming NPs on the BZ boundaries.

Extended Data Fig. 5 Crystal structure, calculated Fermi surfaces, experimental methods, and dHvA spectra in the (001) and ($(\overline{1}\overline{1}0)$) planes.

a, Crystal structure of MnSi. **b**, Fermi surface as calculated within local spin density approximation without rigid band shifts. **c**, Calculated Fermi surface neglecting spin–orbit coupling. **d**, Calculated Fermi surface neglecting spin–orbit coupling and highlighting majority and minority spin. **e**, Sketch of the cantilever magnetometer chip with capacitive readout. **f**, Magnetic field dependence of the frequency $f_B(B)$ tracking the magnetic-field dependence of the unsaturated magnetization in the field-polarized phase. The frequency $f(B)$ observed corresponds to the zero-field intercept of the tangent to $f_B(B)$. **g**, Experimental dHvA frequency branches (crosses) for rotation in the (001) and ($(\overline{1}\overline{1}0)$) planes together with the theory (lines) matched to the experiment. See Supplementary Note 5 for details.

Extended Data Fig. 6 Details of the assignment of experimental dHvA orbits to FS sheets 1 to 6.

a1, Experimental signature of sheet 2. Colour scale corresponds to experimental FFT amplitude and crosses show positions of maxima. **a2**, Torque signal predicted from DFT as calculated. Lines show theoretical branches, crosses show experimental positions. **a3**, FS sheet 2 as calculated.

Three extremal orbits 2Γ and $2\Gamma Y(1,2)$ are present for \mathbf{B} close to [010], which are assigned to $\kappa_{1,2,3}$. **a4**, Calculated dHvA branch including a small upward band shift of 20 meV, yielding a good match with experiment (crosses). **a5**, Comparison of as-calculated (inner) and matched (outer) FS sheet 2. **b1**, Dispersions of bands 1, 2 and 3 in the k_x - k_z plane without (transparent) and with spin-orbit coupling (solid), showing a spin-1 excitation-like three-fold degeneracy that is lifted by spin-orbit coupling. Since band 2 (cyan) crosses the Fermi level, the α branch must originate from band 1 and not band 3. The Fermi level matching the experimental frequency is shown in black. **b2**, FS sheet 1 as calculated (outer) and matched to experiment (inner). The α branch is assigned to orbit 1Γ . **c1**, FS sheets 3 and 4 exhibit extremal orbits with 8 breakdown junctions j_1 to j_8 for \mathbf{B} close to [010] as shown in **c2**. The inset shows the two extremal orbits that arise when spin-orbit coupling is neglected. **c3**, 256 breakdown orbit branches originating from sheets 3 and 4. Symbol size reflects orbit probability. The torque amplitude is not considered in this graph. The breakdown orbits group into five sets labelled in red. The branches ρ and H are assigned to the inner and outer orbits 3Γ and 4Γ , respectively. **d1**, FS sheets 5 and 6 as in Fig. [4a](#) with two neck orbits $5\Gamma Y$ and $6\Gamma Y$ and the loop orbits $5U6U$ assigned to (ξ_1, ξ_2) , π and M_1 , respectively. **d2**, Top: neck cross-sectional areas of sheet 5 (blue) and 6 (orange) versus k_{\parallel} neglecting (dashed) and including (solid) spin-orbit coupling for $\varphi = 90^\circ$ and $\varphi = 180^\circ$. Middle: cross-sectional area a of sheet 5 versus k_{\parallel} for field directions 70° – 90° and 160° – 180° . Dashed line: position of single extremal area around $\varphi = 90^\circ$. Shaded grey area: neck being on the verge of developing a second minimum close to 180° but not around 90° that could give rise to ξ_2 . Bottom: derivative da/dk_{\parallel} , where zero-crossings correspond to extremal orbits. **d3**, FFT amplitude of the loop orbits around $\varphi = 90^\circ$ and $\varphi = 180^\circ$. Left: a distinct splitting of the M_1 branch into M_1 and M_2 is observed close to $\varphi = 180^\circ$ but not around $\varphi = 90^\circ$. Right: the FFT amplitude of the M_1 branch shows unexpected secondary minima (shaded areas) close to $\varphi = 90^\circ$ on both sides. Both effects may be connected to either the quasi-degeneracy of the $U5U6$ orbits shown in Fig. [4b3](#), [b4](#) or to a crossing with the $8\Gamma Y$ branch.

Extended Data Fig. 7 Assignment of experimental dHvA orbits to FS sheets 7 to 10.

a1, Along Γ –Y₁– Γ three neck orbits on sheet 7 (purple), one neck orbit on sheet 8 (yellow), and two loop orbits around U are predicted for $\mathbf{B} \parallel [010]$. **a2**, Loop orbits are shared between the sheets at TP1 to TP4 in analogy to the sheet pair (5, 6). **a3**, For $B \parallel [010]$, the upper two lens-shaped orbits exist, while for \mathbf{B} in the (001) plane away from [010] the lower two heart-shaped orbits are allowed in addition. **b**, Sheet 9 neglecting spin–orbit coupling in perspective (**b1**), top (**b2**) and back (**b3**) views for $\varphi = 83^\circ$, that is, \mathbf{B} slightly off the [010] direction. Bands 9 and 10 are shifted upward by 10 meV for an optimal match to the low frequencies as shown in **b4**, where grey lines correspond to the calculations. In total, 15 orbits are predicted for this specific field direction alone. Without spin–orbit coupling, band 10 does not cross the Fermi level for this shift. **c1–c3**, Sheets 9 and 10 and predicted dHvA orbits including spin–orbit coupling for $\varphi = 83^\circ$ and a shift of 11 meV yielding a good match as shown in **c4**. Sheet 10 resides inside sheet 9 as highlighted by black arrows. It occurs only for field directions where two or more ‘banana bunches’ cross the BZ surface and connect. In the situation depicted here, (001) is an NP, thereby connecting parts of sheets 9 and 10 in such a way that extremal orbits cross from one sheet to the other.

Extended Data Table 1 Key properties of the FS sheets

[Full size table](#)

Extended Data Table 2 Assignment of observed dHvA branches to orbits on the calculated FS

[Full size table](#)

Extended Data Table 3 Catalogue of space groups with symmetry-enforced NPs

[Full size table](#)

Supplementary information

[Supplementary Information](#)

This Supplementary Information file provides comprehensive information on the theoretical framework, theoretical analysis, and magnetic space groups featuring topological nodal planes, as well as the analysis of the experimental data. It is organized in terms of the following five sections: (S1) Band Topology of MnSi; (S2) Tight-binding models, Berry curvature, and surface states; (S3) Catalogue of space groups with symmetry-enforced nodal planes; (S4) Technical aspects of the analysis; and (S5) Comprehensive Fermi surface determination.

Peer Review File

Supplementary Video 1

This video highlights the evolution of a cut-away view of the Fermi surface akin Fig.1(f) as a function of the direction of the magnetization (blue arrow) following an applied magnetic field. Note the emergence of the topological degeneracies of Fermi surface pairs (5,6), (7,8) and (9,10) perpendicular to the direction of the magnetization.

Supplementary Video 2

This video highlights the evolution of a cut-away view of the Fermi surface akin Fig.1(f) as a function of the direction of the magnetization (blue arrow) following an applied magnetic field. Note the emergence of the topological degeneracies of Fermi surface sheet pairs (5,6), (7,8) and (9,10) perpendicular to the direction of the magnetization.

Rights and permissions

Open Access This article is licensed under a Creative Commons Attribution 4.0 International License, which permits use, sharing, adaptation, distribution and reproduction in any medium or format, as long as you give appropriate credit to the original author(s) and the source, provide a link to the Creative Commons license, and indicate if changes were made. The images or other third party material in this article are included in the article's Creative Commons license, unless indicated

otherwise in a credit line to the material. If material is not included in the article's Creative Commons license and your intended use is not permitted by statutory regulation or exceeds the permitted use, you will need to obtain permission directly from the copyright holder. To view a copy of this license, visit <http://creativecommons.org/licenses/by/4.0/>.

[Reprints and Permissions](#)

About this article



Check for
updates

Cite this article

Wilde, M.A., Dodenhöft, M., Niedermayr, A. *et al.* Symmetry-enforced topological nodal planes at the Fermi surface of a chiral magnet. *Nature* **594**, 374–379 (2021). <https://doi.org/10.1038/s41586-021-03543-x>

[Download citation](#)

- Received: 08 October 2020
- Accepted: 09 April 2021
- Published: 16 June 2021
- Issue Date: 17 June 2021
- DOI: <https://doi.org/10.1038/s41586-021-03543-x>

Comments

By submitting a comment you agree to abide by our [Terms](#) and [Community Guidelines](#). If you find something abusive or that does not comply with our

terms or guidelines please flag it as inappropriate.

[Download PDF](#)

Advertisement

This article was downloaded by **calibre** from <https://www.nature.com/articles/s41586-021-03543-x>

| [Section menu](#) | [Main menu](#) |

- Article
- [Published: 16 June 2021](#)

Double-helical assembly of heterodimeric nanoclusters into supercrystals

- [Yingwei Li](#) ORCID: orcid.org/0000-0002-4813-6009^{1 na1},
- [Meng Zhou](#) ORCID: orcid.org/0000-0001-5187-9084^{2 na1},
- [Yongbo Song](#) ORCID: orcid.org/0000-0001-5353-8072^{3 na1},
- [Tatsuya Higaki](#) ORCID: orcid.org/0000-0002-6759-9009¹,
- [He Wang](#) ORCID: orcid.org/0000-0003-1365-0304² &
- [Rongchao Jin](#) ORCID: orcid.org/0000-0002-2525-8345¹

Nature volume **594**, pages 380–384 (2021) [Cite this article](#)

- 1794 Accesses
- 19 Altmetric
- [Metrics details](#)

Subjects

- [Nanoscale materials](#)
- [Physical chemistry](#)

Abstract

DNA has long been used as a template for the construction of helical assemblies of inorganic nanoparticles^{1,2,3,4,5}. For example, gold

nanoparticles decorated with DNA (or with peptides) can create helical assemblies^{6,7,8,9}. But without such biological ligands, helices are difficult to achieve and their mechanism of formation is challenging to understand^{10,11}. Atomically precise nanoclusters that are protected by ligands such as thiolate^{12,13} have demonstrated hierarchical structural complexity in their assembly at the interparticle and intraparticle levels, similar to biomolecules and their assemblies¹⁴. Furthermore, carrier dynamics can be controlled by engineering the structure of the nanoclusters¹⁵. But these nanoclusters usually have isotropic structures^{16,17} and often assemble into commonly found supercrystals¹⁸. Here we report the synthesis of homodimeric and heterodimeric gold nanoclusters and their self-assembly into superstructures. While the homodimeric nanoclusters form layer-by-layer superstructures, the heterodimeric nanoclusters self-assemble into double- and quadruple-helical superstructures. These complex arrangements are the result of two different motif pairs, one pair per monomer, where each motif bonds with its paired motif on a neighbouring heterodimer. This motif pairing is reminiscent of the paired interactions of nucleobases in DNA helices. Meanwhile, the surrounding ligands on the clusters show doubly or triply paired steric interactions. The helical assembly is driven by van der Waals interactions through particle rotation and conformational matching. Furthermore, the heterodimeric clusters have a carrier lifetime that is roughly 65 times longer than that of the homodimeric clusters. Our findings suggest new approaches for increasing complexity in the structural design and engineering of precision in supercrystals.

Access options

Subscribe to Journal

Get full journal access for 1 year

\$199.00

only \$3.90 per issue

[Subscribe](#)

All prices are NET prices.
VAT will be added later in the checkout.
Tax calculation will be finalised during checkout.

Rent or Buy article

Get time limited or full article access on ReadCube.

from \$8.99

[Rent or Buy](#)

All prices are NET prices.

Additional access options:

- [Log in](#)
- [Access through your institution](#)
- [Learn about institutional subscriptions](#)

Fig. 1: Characterization of $\text{Au}_{29}(\text{SAdm})_{19}$ and $\text{Au}_{30}(\text{SAdm})_{18}$ nanoclusters.

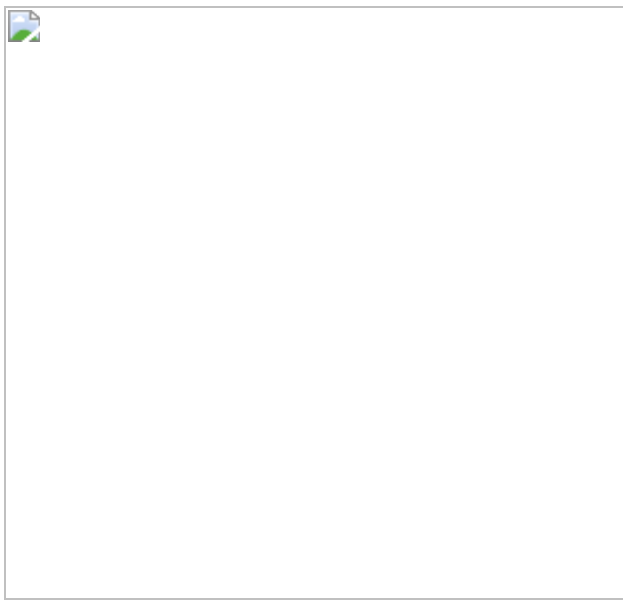


Fig. 2: Double-helical assembly of $\text{Au}_{29}(\text{SAdm})_{19}$ nanoclusters in supercrystals.

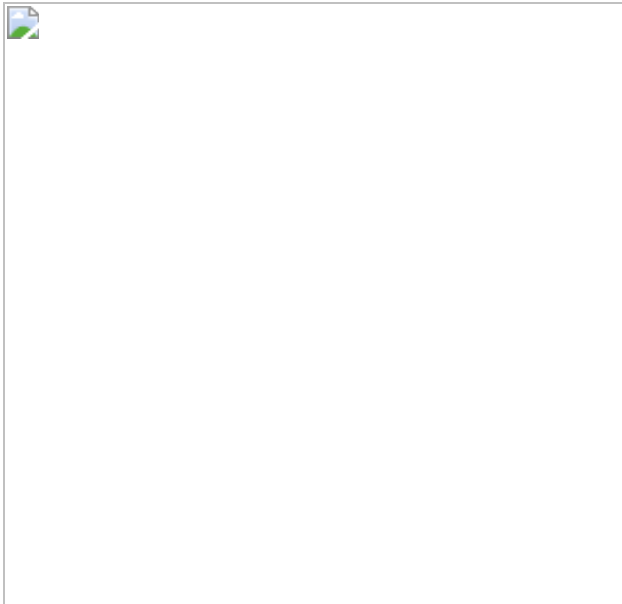


Fig. 3: Quadruple-helical assembly of $\text{Au}_{29}(\text{SAdm})_{19}$ nanoclusters in supercrystals.

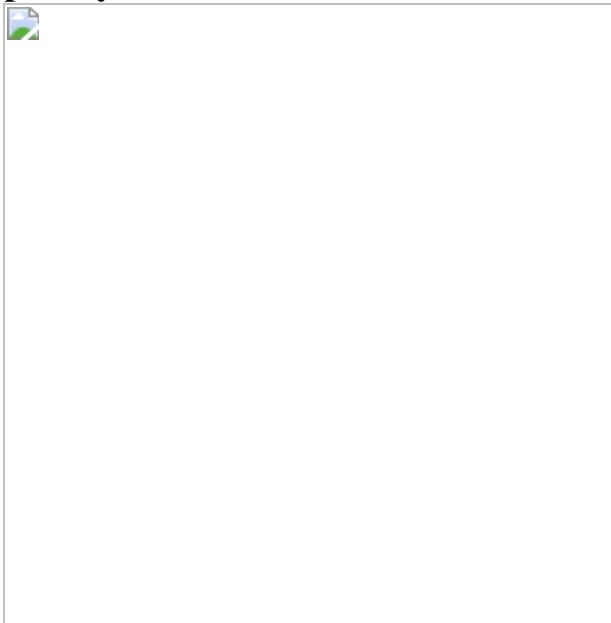


Fig. 4: Comparisons of transient absorption data and carrier dynamics for $\text{Au}_{29}(\text{SAdm})_{19}$ and $\text{Au}_{30}(\text{SAdm})_{18}$ nanoclusters.



Data availability

The cif files for the crystal structures of $\text{Au}_{29}(\text{SAdm})_{19}$ and $\text{Au}_{30}(\text{SAdm})_{18}$, and videos to show the double or quadruple helices in the $\text{Au}_{29}(\text{SAdm})_{19}$ supercrystal, are provided as Supplementary Information with this paper. The cif files can be found at the Cambridge Crystallographic Data Centre (CCDC; <https://www.ccdc.cam.ac.uk>) under accession numbers 2072909 for $\text{Au}_{29}(\text{SAdm})_{19}$ and 2072908 for $\text{Au}_{30}(\text{SAdm})_{18}$.

References

1. 1.

Srivastava, S. et al. Light-controlled self-assembly of semiconductor nanoparticles into twisted ribbons. *Science* **327**, 1355–1359 (2010).

[ADS](#) [CAS](#) [Article](#) [Google Scholar](#)

2. 2.

Singh, G. et al. Self-assembly of magnetite nanocubes into helical superstructures. *Science* **345**, 1149–1153 (2014).

[ADS](#) [CAS](#) [Article](#) [Google Scholar](#)

3. 3.

Shenhar, R. & Rotello, V. M. Nanoparticles: scaffolds and building blocks. *Acc. Chem. Res.* **36**, 549–561 (2003).

[CAS](#) [Article](#) [Google Scholar](#)

4. 4.

Gao, Y. & Tang, Z. Design and application of inorganic nanoparticle superstructures: current status and future challenges. *Small* **7**, 2133–2146 (2011).

[CAS](#) [Article](#) [Google Scholar](#)

5. 5.

Saleh, L. M. A., Dziedzic, R. & Spokoyny, A. M. An inorganic twist in nanomaterials: making an atomically precise double helix. *ACS Cent. Sci.* **2**, 685–686 (2016).

[CAS](#) [Article](#) [Google Scholar](#)

6. 6.

Sharma, J. et al. Control of self-assembly of DNA tubules through integration of gold nanoparticles. *Science* **323**, 112–116 (2009).

[ADS](#) [CAS](#) [Article](#) [Google Scholar](#)

7. 7.

Kuzyk, A. et al. DNA-based self-assembly of chiral plasmonic nanostructures with tailored optical response. *Nature* **483**, 311–314 (2012).

[ADS](#) [CAS](#) [Article](#) [Google Scholar](#)

8. 8.

Chen, C.-L., Zhang, P. & Rosi, N. L. A new peptide-based method for the design and synthesis of nanoparticle superstructures: construction of highly ordered gold nanoparticle double helices. *J. Am. Chem. Soc.* **130**, 13555–13557 (2008).

[CAS](#) [Article](#) [Google Scholar](#)

9. 9.

Shen, X. et al. Rolling up gold nanoparticle-dressed DNA origami into three-dimensional plasmonic chiral nanostructures. *J. Am. Chem. Soc.* **134**, 146–149 (2012).

[CAS](#) [Article](#) [Google Scholar](#)

10. 10.

Berl, V., Huc, I., Khoury, R. G., Krische, M. J. & Lehn, J.-M. Interconversion of single and double helices formed from synthetic molecular strands. *Nature* **407**, 720–723 (2000).

[ADS](#) [CAS](#) [Article](#) [Google Scholar](#)

11. 11.

Engelkamp, H. & Middelbeek, S. & Nolte, R. J. M. Self-assembly of disk-shaped molecules to coiled-coil aggregates with tunable helicity. *Science* **284**, 785–788 (1999).

[ADS](#) [CAS](#) [Article](#) [Google Scholar](#)

12. 12.

Jin, R., Zeng, C., Zhou, M. & Chen, Y. Atomically precise colloidal metal nanoclusters and nanoparticles: fundamentals and opportunities. *Chem. Rev.* **116**, 10346–10413 (2016).

[CAS](#) [Article](#) [Google Scholar](#)

13. 13.

Li, Y., Higaki, T., Du, X. & Jin, R. Chirality and surface bonding correlation in atomically precise metal nanoclusters. *Adv. Mater.* **32**, 1905488 (2020).

[CAS](#) [Article](#) [Google Scholar](#)

14. 14.

Zeng, C., Chen, Y., Kirschbaum, K., Lambright, K. J. & Jin, R. Emergence of hierarchical structural complexities in nanoparticles and their assembly. *Science* **354**, 1580–1584 (2016).

[ADS](#) [CAS](#) [Article](#) [Google Scholar](#)

15. 15.

Zhou, M. et al. Three-orders-of-magnitude variation of carrier lifetimes with crystal phase of gold nanoclusters. *Science* **364**, 279–282 (2019).

[ADS](#) [CAS](#) [Article](#) [Google Scholar](#)

16. 16.

Zhu, M., Aikens, C. M., Hollander, F. J., Schatz, G. C. & Jin, R. Correlating the crystal structure of a thiol-protected Au_{25} cluster and optical properties. *J. Am. Chem. Soc.* **130**, 5883–5885 (2008).

[CAS](#) [Article](#) [Google Scholar](#)

17. 17.

Desireddy, A. et al. Ultrastable silver nanoparticles. *Nature* **501**, 399–402 (2013).

[ADS](#) [CAS](#) [Article](#) [Google Scholar](#)

18. 18.

Macfarlane, R. J. et al. Nanoparticle superlattice engineering with DNA. *Science* **334**, 204–208 (2011).

[ADS](#) [CAS](#) [Article](#) [Google Scholar](#)

19. 19.

Li, Y. & Jin, R. Seeing ligands on nanoclusters and in their assemblies by X-ray crystallography: atomically precise nanochemistry and beyond. *J. Am. Chem. Soc.* **142**, 13627–13644 (2020).

[CAS](#) [Article](#) [Google Scholar](#)

20. 20.

Gan, Z. et al. The fourth crystallographic closest packing unveiled in the gold nanocluster crystal. *Nat. Commun.* **8**, 14739 (2017).

[ADS](#) [CAS](#) [Article](#) [Google Scholar](#)

21. 21.

Gu, H., Zheng, R., Zhang, X. & Xu, B. Facile one-pot synthesis of bifunctional heterodimers of nanoparticles: a conjugate of quantum dot and magnetic nanoparticles. *J. Am. Chem. Soc.* **126**, 5664–5665 (2004).

[CAS](#) [Article](#) [Google Scholar](#)

22. 22.

Choi, J. et al. Biocompatible heterostructured nanoparticles for multimodal biological detection. *J. Am. Chem. Soc.* **128**, 15982–15983 (2006).

[CAS](#) [Article](#) [Google Scholar](#)

23. 23.

Brown, L. V., Sobhani, H., Lassiter, J. B., Nordlander, P. & Halas, N. J. Heterodimers: plasmonic properties of mismatched nanoparticle pairs. *ACS Nano* **4**, 819–832 (2010).

[CAS](#) [Article](#) [Google Scholar](#)

24. 24.

Buck, M. R., Bondi, J. F. & Schaak, R. E. A total-synthesis framework for the construction of high-order colloidal hybrid nanoparticles. *Nat. Chem.* **4**, 37–44 (2012).

[CAS](#) [Article](#) [Google Scholar](#)

25. 25.

Zhu, H. et al. Self-assembly of quantum dot–gold heterodimer nanocrystals with orientational order. *Nano Lett.* **18**, 5049–5056 (2018).

[ADS](#) [CAS](#) [Article](#) [Google Scholar](#)

26. 26.

Xiong, L., Peng, B., Ma, Z., Wang, P. & Pei, Y. A ten-electron (10e) thiolate-protected $\text{Au}_{29}(\text{SR})_{19}$ cluster: structure prediction and a ‘gold-atom insertion, thiolate-group elimination’ mechanism. *Nanoscale* **9**, 2895–2902 (2017).

[CAS](#) [Article](#) [Google Scholar](#)

27. 27.

Chen, Y. et al. Isomerism in $\text{Au}_{28}(\text{SR})_{20}$ nanocluster and stable structures. *J. Am. Chem. Soc.* **138**, 1482–1485 (2016).

[CAS](#) [Article](#) [Google Scholar](#)

28. 28.

Li, Y. et al. A correlated series of Au/Ag nanoclusters revealing the evolutionary patterns of asymmetric Ag doping. *J. Am. Chem. Soc.* **140**, 14235–14243 (2018).

[CAS](#) [Article](#) [Google Scholar](#)

29. 29.

Higaki, T. et al. Controlling the atomic structure of Au_{30} nanoclusters by a ligand-based strategy. *Angew. Chem. Int. Edn* **55**, 6694–6697 (2016).

[CAS](#) [Article](#) [Google Scholar](#)

30. 30.

Zhou, M. et al. Three-stage evolution from nonscalable to scalable optical properties of thiolate-protected gold nanoclusters. *J. Am. Chem. Soc.* **141**, 19754–19764 (2019).

[CAS](#) [Article](#) [Google Scholar](#)

31. 31.

Dolomanov, O. V., Bourhis, L. J., Gildea, R. J., Howard, J. A. K. & Puschmann, H. *OLEX2*: a complete structure solution, refinement and analysis program. *J. Appl. Cryst.* **42**, 339–341 (2009).

[CAS](#) [Article](#) [Google Scholar](#)

32. 32.

Bourhis, L. J., Dolomanov, O. V., Gildea, R. J., Howard, J. A. K. & Puschmann, H. The anatomy of a comprehensive constrained,

restrained refinement program for the modern computing environment —*Olex2* dissected. *Acta Crystallogr. A* **71**, 59–75 (2015).

[MathSciNet](#) [CAS](#) [Article](#) [Google Scholar](#)

33. 33.

Sheldrick, G. M. *SHELXT*—integrated space-group and crystal-structure determination. *Acta Crystallogr. A* **71**, 3–8 (2015).

[Article](#) [Google Scholar](#)

[Download references](#)

Acknowledgements

Y.L. and R.J. thank T.-Y. Luo for help in analysing crystal data. R.J. acknowledges financial support from the US National Science Foundation (NSF; grant DMR-1808675). H.W. acknowledges financial support from US Air Force Office of Scientific Research (AFOSR) award FA9550-17-1-0099. Y.S. acknowledges the startup.

Author information

Author notes

1. These authors contributed equally: Yingwei Li, Meng Zhou, Yongbo Song

Affiliations

1. Department of Chemistry, Carnegie Mellon University, Pittsburgh, PA, USA

Yingwei Li, Tatsuya Higaki & Rongchao Jin

2. Department of Physics, University of Miami, Coral Gables, FL, USA

Meng Zhou & He Wang

3. School of Biomedical Engineering, Research and Engineering Center of Biomedical Materials, Anhui Medical University, Hefei, Anhui, China

Yongbo Song

Authors

1. Yingwei Li

[View author publications](#)

You can also search for this author in [PubMed](#) [Google Scholar](#)

2. Meng Zhou

[View author publications](#)

You can also search for this author in [PubMed](#) [Google Scholar](#)

3. Yongbo Song

[View author publications](#)

You can also search for this author in [PubMed](#) [Google Scholar](#)

4. Tatsuya Higaki

[View author publications](#)

You can also search for this author in [PubMed](#) [Google Scholar](#)

5. He Wang

[View author publications](#)

You can also search for this author in [PubMed](#) [Google Scholar](#)

6. Rongchao Jin

[View author publications](#)

You can also search for this author in [PubMed](#) [Google Scholar](#)

Contributions

Y.L. carried out the preparation and crystallization of nanoclusters. M.Z. carried out the transient absorption measurements and analysed these data with H.W. Y.S. solved the crystal structures and measured photoluminescence. Y.L., M.Z. and R.J. wrote the manuscript, with T.H. providing suggestions.

Corresponding author

Correspondence to [Rongchao Jin](#).

Ethics declarations

Competing interests

The authors declare no competing interests.

Additional information

Peer review information *Nature* thanks the anonymous reviewer(s) for their contribution to the peer review of this work.

Publisher's note Springer Nature remains neutral with regard to jurisdictional claims in published maps and institutional affiliations.

Extended data figures and tables

[Extended Data Fig. 1 Separation by TLC and characterization of Au₂₉\(SAdm\)₁₉ and Au₃₀\(SAdm\)₁₈ nanoclusters.](#)

a, Separation of multiple Au-SAdm nanoclusters by TLC. **b**, Absorption spectra of heterodimeric Au₂₉(SAdm)₁₉ and homodimeric Au₃₀(SAdm)₁₈ nanoclusters on a photon energy scale. The bandgaps are determined to be 1.45 eV and 1.25 eV, respectively. **c**, Isotope peaks corresponding to

$[\text{Au}_{30}(\text{SAdm})_{18}]^{2+}$ and $[\text{Au}_{30}(\text{SAdm})_{18}]^+$ (red lines), $[\text{Au}_{29}(\text{SAdm})_{19}]^{2+}$, $[\text{Au}_{29}(\text{SAdm})_{19}]^+$, $[\text{Au}_{29}(\text{SAdm})_{19}\text{Ag}]^{2+}$ and $[\text{Au}_{29}(\text{SAdm})_{19}\text{Ag}]^+$ (blue lines). The experimental isotopic patterns match well with the calculated ones (black lines). Note that the 2+ and 1+ charges are due to the ionization in ESI, and are not the native charge states of the nanoclusters. In addition, an Ag cation can be picked up by $\text{Au}_{29}(\text{SAdm})_{19}$ during ESI-MS analysis owing to the existence of Ag^+ in the ion source.

Extended Data Fig. 2 Anatomy of the structure of gold nanoclusters.

a, $\text{Au}_{30}(\text{SR})_{18}$; **b** $\text{Au}_{28}(\text{SR})_{20}$; **c**, $\text{Au}_{29}(\text{SR})_{19}$.

Extended Data Fig. 3 Ligand interactions between two neighbouring $\text{Au}_{29}(\text{SAdm})_{19}$ enantiomers.

a, The triply paired ligands associated with the matching motif pairs on two neighbouring enantiomers—that is, E1C1–E2C3 and E1C3–E2C1—with interacting ligands' carbons marked in orange (for C1) and red (for C3). **b**, The doubly paired ligands associated with the matching motif pairs on two neighbouring enantiomers—E1L3–E2L1 and E1L1–E2L3—with interacting ligands' carbons marked in light blue (for L1) and green (for L3). In other colours: blue/cyan, Au in different enantiomers; yellow, S; grey, C; white, H.

Extended Data Fig. 4 Supercrystal of $\text{Au}_{30}(\text{SAdm})_{18}$ nanoclusters.

a, Self-assembly of $\text{Au}_{30}(\text{SAdm})_{18}$ nanoclusters in the superlattice. **b**, The neighbouring enantiomers approach each other by matching their L3 staple motifs, with doubly paired and triply paired ligand interactions between the two enantiomers.

Extended Data Fig. 5 Supercrystal of Au₂₁(SAdm)₁₅ nanoclusters.

a, Self-assembly of Au₂₁(SAdm)₁₅ nanoclusters in the superlattice. **b**, Ligand interactions between two enantiomers. We made this figure using crystal data from ref. [28](#).

Extended Data Fig. 6 Supercrystal of Au₂₀Ag₁(SAdm)₁₅ nanoclusters.

a, Self-assembly of Au₂₀Ag₁(SAdm)₁₅ nanoclusters in the superlattice. **b**, Ligand interactions between two enantiomers. We made this figure using crystal data from ref. [28](#).

Extended Data Fig. 7 Supercrystal of Au₁₉Ag₄(SAdm)₁₅ nanoclusters.

a, Self-assembly of Au₁₉Ag₄(SAdm)₁₅ nanoclusters in the superlattice. **b**, Ligand interactions between two enantiomers. We made this figure using crystal data from ref. [28](#).

Extended Data Fig. 8 Supercrystal of Au_{23-x}Ag_x(SAdm)₁₅ nanoclusters (where x is approximately 7).

a, Self-assembly of Au_{23-x}Ag_x(SAdm)₁₅ nanoclusters (x is approximately 7) in the superlattice. **b**, Ligand interactions between two enantiomers. We made this figure using crystal data from ref. [28](#).

Extended Data Fig. 9 Maps of picosecond transient absorption data and kinetic traces of Au₂₉(SAdm)₁₉ and Au₃₀(SAdm)₁₈ nanoclusters, with NIR photoluminescence of Au₂₉(SAdm)₁₉.

a–c, $\text{Au}_{29}(\text{SAdm})_{19}$ (kinetic traces probed at 500 nm (blue), 630 nm (red) and 700 nm (green)). **d–f**, $\text{Au}_{30}(\text{SAdm})_{18}$ (kinetic traces probed at 600 nm (blue), 700 nm (red) and 540 nm (green)). Both nanoclusters were excited at 400 nm. **g**, Emission spectra ($\lambda_{\text{ex}} = 430 \text{ nm}$) for a solution (red; toluene solvent), film (blue; drop casting from a concentrated solution) and supercrystals (brown) of $\text{Au}_{29}(\text{SAdm})_{19}$. Inset, photograph of $\text{Au}_{29}(\text{SAdm})_{19}$ supercrystals under optical microscopy.

Extended Data Table 1 Crystal data and structure refinement of $\text{Au}_{29}(\text{SC}_{10}\text{H}_{15})_{19}$ and $\text{Au}_{30}(\text{SC}_{10}\text{H}_{15})_{18}$ nanoclusters

[Full size table](#)

Supplementary information

[Supplementary Information](#)

CheckCif1 report for the crystal structure of $\text{Au}_{29}(\text{SAdm})_{19}$.

[Supplementary Information](#)

CheckCif2 report for the crystal structure of $\text{Au}_{30}(\text{SAdm})_{18}$.

[Video 1](#)

The double helix of $\text{Au}_{29}(\text{SAdm})_{19}$ NCs in right-handed rotation.

[Video 2](#)

The double helix of $\text{Au}_{29}(\text{SAdm})_{19}$ NCs in left-handed rotation.

[Video 3](#)

The quadruple helix of $\text{Au}_{29}(\text{SAdm})_{19}$ NCs in right-handed rotation.

Video 4

The quadruple helix of Au₂₉(SAdm)₁₉ NCs in left-handed rotation.

Rights and permissions

Reprints and Permissions

About this article



Check for
updates

Cite this article

Li, Y., Zhou, M., Song, Y. *et al.* Double-helical assembly of heterodimeric nanoclusters into supercrystals. *Nature* **594**, 380–384 (2021).
<https://doi.org/10.1038/s41586-021-03564-6>

Download citation

- Received: 31 August 2020
- Accepted: 19 April 2021
- Published: 16 June 2021
- Issue Date: 17 June 2021
- DOI: <https://doi.org/10.1038/s41586-021-03564-6>

Comments

By submitting a comment you agree to abide by our [Terms](#) and [Community Guidelines](#). If you find something abusive or that does not comply with our terms or guidelines please flag it as inappropriate.

[Access through your institution](#)

[Change institution](#)

[Buy or subscribe](#)

Advertisement

This article was downloaded by **calibre** from <https://www.nature.com/articles/s41586-021-03564-6>

| [Section menu](#) | [Main menu](#) |

Localization atomic force microscopy

[Download PDF](#)

- Article
- [Published: 16 June 2021](#)

Localization atomic force microscopy

- [George R. Heath](#) [ORCID: orcid.org/0000-0001-6431-2191](#)¹ nAff4,
- [Ekaterina Kots](#) [ORCID: orcid.org/0000-0002-7139-7098](#)²,
- [Janice L. Robertson](#) [ORCID: orcid.org/0000-0002-5499-9943](#)³,
- [Shifra Lansky](#)¹,
- [George Khelashvili](#) [ORCID: orcid.org/0000-0001-7235-8579](#)²,
- [Harel Weinstein](#) [ORCID: orcid.org/0000-0003-3473-9818](#)² &
- [Simon Scheuring](#) [ORCID: orcid.org/0000-0003-3534-069X](#)^{1,2}

Nature volume **594**, pages 385–390 (2021) [Cite this article](#)

- 8490 Accesses
- 442 Altmetric
- [Metrics details](#)

Subjects

- [Atomic force microscopy](#)
- [Imaging techniques](#)
- [Nanoscale biophysics](#)
- [Single-molecule biophysics](#)

Abstract

Understanding structural dynamics of biomolecules at the single-molecule level is vital to advancing our knowledge of molecular mechanisms. Currently, there are few techniques that can capture dynamics at the sub-nanometre scale and in physiologically relevant conditions. Atomic force microscopy (AFM)¹ has the advantage of analysing unlabelled single molecules in physiological buffer and at ambient temperature and pressure, but its resolution limits the assessment of

conformational details of biomolecules². Here we present localization AFM (LAFM), a technique developed to overcome current resolution limitations. By applying localization image reconstruction algorithms³ to peak positions in high-speed AFM and conventional AFM data, we increase the resolution beyond the limits set by the tip radius, and resolve single amino acid residues on soft protein surfaces in native and dynamic conditions. LAFM enables the calculation of high-resolution maps from either images of many molecules or many images of a single molecule acquired over time, facilitating single-molecule structural analysis. LAFM is a post-acquisition image reconstruction method that can be applied to any biomolecular AFM dataset.

[Download PDF](#)

Main

Observing the native structure and behaviour of biomolecules is challenging owing to their architectural complexity and dynamic nature. Additionally, biomolecules can adopt multiple interchanging conformational states. Protein structure determination is progressing rapidly thanks to recent advances in cryo electron microscopy (cryo-EM) and X-ray crystallography. However, these structures represent static snapshots of averaged ensembles acquired from molecules incorporated into crystals and/or imaged at cryogenic temperature, whereas individual molecules at physiological temperature are highly dynamic. In contrast to cryo-EM, which provides three-dimensional (3D) volume data, AFM is restricted to surface analysis. Nevertheless, AFM images molecules in a native-like environment: (i) at ambient temperature, (ii) at ambient pressure, (iii) in physiological buffer and (iv) in membranes (in the case of membrane proteins). Furthermore, the AFM measurement mechanism and the openness of the fluid cell allow for (v) buffer exchanges, (vi), temperature changes and (vii) force changes during image acquisition^{2,4}.

High-speed AFM (HS-AFM)⁵ has an additional advantage in that it yields real-time nanometre topographical information of single biomolecules at unprecedented spatiotemporal resolutions^{6,7,8,9,10,11,12,13}, through the integration of short cantilevers¹⁴ and the development of faster scanners¹⁵ and feedback operation¹⁶. Although this is proving powerful in revealing conformational changes of proteins^{4,17}, it is often not possible to resolve sub-molecular structural features on protein surfaces, primarily owing to the finite size of the AFM tip. For probes typically used to image biological samples, the resolution in the z direction (topography) is about 1 Å, whereas the lateral resolution in the x, y directions is about 1 nm, fundamentally limited by the probe geometry and the probe–sample interaction forces. The lateral resolution is further reduced when imaging softer samples, owing to an increased contact area between the tip and flexible protein structures¹⁸. Because of these limitations, sub-nanometre

lateral resolution of biological samples has only been reported for two-dimensional (2D) crystals^{19,20}, and was evidenced to be an overestimation due to periodic tip convolution effects²¹. In an attempt to circumvent such limitations, tip deconvolution algorithms were proposed^{22,23}, which produced sharpened images but could introduce artefacts.

Localization microscopy methods, also known as super-resolution fluorescence microscopies, such as stochastic optical reconstruction microscopy (STORM)²⁴ and photoactivated localization microscopy (PALM)³, have provided insights into the architecture and macromolecular assemblies of cells. By isolating and pinpointing the source of excited fluorescence signals with high spatial precision in many images, high-lateral-resolution maps can be reconstructed, taking the ~400 nm resolution limit set by the diffraction limit of light down to about 20 nm (refs. [25,26](#)).

Here, inspired by these fluorescence localization microscopy methods (Extended Data Fig. [1a–d](#)), we develop LAFM, whereby localization algorithms are applied to the spatial fluctuations of topographic features in AFM and HS-AFM images (Extended Data Fig. [1e–h](#)). Comparisons with X-ray structures and molecular dynamics (MD) simulations show that this approach can reveal angstrom-range high-resolution details on protein surfaces.

Breaking the resolution limit

Under specific conditions; that is, with an atomically sharp tip and rapidly decaying tip–sample interaction forces, atomic resolution is attainable on flat incompressible materials such as mica by conventional AFM imaging¹⁸. Achieving and maintaining such conditions on biological samples, which are not only soft and dynamic, but also immersed in liquid at room temperature, is not possible. Typically, the tip geometry from the apex up to the height of the objects being imaged is much larger than the separation distance between the features of interest (Fig. [1a, b](#), surface). The finite tip radius results in convoluted lateral dimensions. The signal is further obstructed by noise in the z direction and stochastic fluctuations of flexible protein surface features (Supplementary Video 1) in the x , y and z directions (Fig. [1b](#), AFM traces). Averaging several of these traces removes noise and results in a noise-free topography trace but the tip convolution remains a limiting factor (Fig. [1b](#), average AFM). By applying localization algorithms that detect the local maxima in the same series of traces (Fig. [1b](#), AFM traces, crosses), extracting the location-specific heights (Fig. [1b](#), LAFM height) and merging the individual detections in a peaking-probability map (Fig. [1b](#), LAFM probability), the surface structures are reconstructed with greater lateral resolution in an LAFM map (Fig. [1b](#), LAFM). Local peak-search algorithms to identify and accumulate local maxima in AFM data have previously been used to

create probability density maps, from which energy landscapes were calculated to sample the conformational space of protein moieties²⁷ and to derive stiffness maps⁷. Here we build on this concept and extend the approach, leveraging the methodological knowledge generated by the development of super-resolution fluorescence localization microscopies^{3,24}. Localization-based fluorescence microscopy methods taught us that a resolution superior to the physical limitations can be achieved when the localization of isolated signals is determined with high spatial precision in many images, which are later merged in a compiled map³, which has higher lateral resolution than the initial data. Advantage is taken of the fact that the peak position of signals with wide intensity distributions can be determined with astonishing precision. Here, we adapt this transformative rationale to AFM data (Extended Data Fig. [1e–h](#)). First, the pixel-and/or AFM-restricted low-lateral-resolution data are oversampled to allow peak positions to be determined with increased spatial localization resolution. Peak positions are measured and localization data are then merged to give a reconstructed map with higher lateral resolution than the initial pixel sampling and/or technique allowed (Fig. [1b](#); compare LAFM with average AFM).

Fig. 1: Principle of LAFM.



a, Schematic of an AFM tip scanning a high topography with high-resolution features. Dashed line, theoretical contour. Coloured lines, three representative simulated topography traces. Open symbols and lines, vertical and lateral positions of detected local maxima. **b**, Simulations ($n = 1,000$) of the LAFM method on surfaces with one (top), two (middle) and many (bottom) height-modulated surface features. Surface: representation of idealized surface features (grey). AFM traces: nine representative simulated topography traces (coloured lines), with detected local maxima (crosses). Average AFM: average topography ($n = 1,000$). LAFM height: average height of detected local maxima. LAFM probability: peaking probability distribution of detected local maxima. LAFM: LAFM map merging real-space height with peaking

probability. Insets: false-colour scales represent height, probability and height/probability. **c**, High-spatial-resolution topography local maxima detection. (i), (iv), Two representative sequential ($t = 0$ s, $t = 1$ s) raw data images of an A5 trimer. (ii), (v), Magnified views of raw data (4 Å per pixel). Blue squares, local maxima pixels. Local maxima labelled ‘1’, ‘2’ and ‘3’ are detected at identical pixel locations in both images. (iii), (vi), Same image regions after image expansion (0.5 Å per pixel). Red squares, local maxima pixels.

[Full size image](#)

The LAFM map reconstruction is best illustrated in the simulation, where several features of varying height are contoured next to each other (Fig. 1b, bottom row). Simulations show that the LAFM algorithm detects features that are hidden to theoretical and average topographies (Fig. 1b, Extended Data Fig. 3). However, the detection probability performs best on flat samples, and is nonlinear with the protrusion height if there are closely neighbouring higher features (Extended Data Fig. 2). Each pixel in these maps contains both height and probability information (Fig. 1b, bottom right). Further simulations with varying tip radius and shape on simple (Extended Data Fig. 4, Supplementary Video 2) and more complex (Extended Data Fig. 5) model 3D surfaces showed that the LAFM algorithm outperformed averaging methods within 10–100 images, showing the greatest improvement in resolution (about 1/5) for tip radii greater than the separation of structural features. These analyses corroborate that the quality of the LAFM map increases with increasing number of observations until it plateaus, at around 50 (for a sharp tip) and around 500 (for a blunt tip) particles are analysed.

On real AFM data, detection of local height maxima is performed after image expansion (Fig. 1c). Image expansion using bicubic interpolation (see [Methods](#)) does not increase the lateral resolution of the topography but allows the detection of local maxima with far greater spatial precision (Fig. 1c; compare panels (ii) and (v) with (iii) and (vi)). Merging the high-precision local maxima from several particles results in resolving structural features with separation distances shorter than the initial pixel sampling. To retain the topographic structural information, the topography height value from each peak location is carried into the LAFM reconstruction, where height and peaking probability are encoded by a 2D false-colour scale in which the green/red ratio scales linearly with height h and probability P from white at $P = 1$ to black at $P = 0$ (Extended Data Fig. 1i,j). Furthermore, each peaking detection, originating from an atomic tip–sample interaction, is assigned a 2D Gaussian density function decaying from 1 to 0 over 1.4 Å to approximate atomic solvent-accessible surface areas. A reconstructed LAFM map thus compiles, from many particles, the average topography height refined by the peaking probability (Fig. 1b, right), where each pixel carries the full information about topography and its likelihood of being detected at this location. In merging many particles, randomly distributed apparatus noise does not

merge into consistent height/probability data. Conversely, peaking detections that emerge from protein surface fluctuations will merge into strong localized signals in high-resolution reconstructed LAFM maps.

Single amino acids on protein surfaces

To illustrate the power of the LAFM approach, we first applied it to a former conventional AFM dataset²⁰. After extraction and alignment of aquaporin-Z (AqpZ) tetrameric channels, the LAFM map revealed details comparable to the surface of the X-ray structure (Fig. 2a, Supplementary Video 3), resolving single amino-acids on surface protruding loops (Fig. 2b). Line profile analysis and image comparison between the average AFM topography, previous peak probability mapping methods²⁷ and LAFM probability maps of independent dataset half-maps show the ability of LAFM to detect previously hidden structural features (separated by 2.6 Å) well beyond the details resolved by previous averaging and peak probability methods (11 Å) and the Nyquist frequency of the raw data (1/(6.6 Å)) (Extended Data Fig. 6a–i). Interestingly, among the AqpZ X-ray structures, E31 in the central a-loop is in different orientations, and the LAFM map indicates that in physiological buffer the E31 rotamer configuration, as found in PDB 2ABM, is preferred (Extended Data Fig. 6j). We also applied the LAFM approach to annexin-V (A5) trimers extracted from HS-AFM videos^{5,9,28} (Fig. 2d, Supplementary Video 4) and found that the LAFM map resolved fine structural details (whereas the average resolved only the protein envelope) along the backbone of the molecule (Fig. 2b).

Fig. 2: LAFM of AqpZ and A5.



figure2

a–c, AqpZ; **d–f**, A5. **a, d**, Left, average AFM maps; middle, LAFM maps; and right, surface representations of X-ray structures. **b, e**, Detail views of LAFM maps and X-ray structures, with recognizable residues labelled. **c, f**, FRC analyses of LAFM half-

maps. AqpZ data acquisition: AqpZ reconstituted in DMPC/POPC (1/1) membranes imaged by conventional AFM in contact mode; scan speed, 6.8 lines per second; scan area, 169 nm; image size, 512 pixels; pixel sampling, 3.3 Å per pixel²⁰. A5 data acquisition: A5 on a DOPC/DOPS (8/2) bilayer imaged by HS-AFM in amplitude modulation mode; scan speed, 1 frame per second; scan area, 80 nm; image size, 200 pixels; pixel sampling, 4.0 Å per pixel. LAFM map pixel sampling, 0.5 Å per pixel; AqpZ: $n = 128$, A5: $n = 698$, filtered to 5 Å. X-ray structures: AqpZ, PDB 2ABM, A5, PDB 1HVD.

[Full size image](#)

To quantitatively assess the resolution of the LAFM maps, we applied the Fourier ring correlation (FRC) method, developed for electron microscopy²⁹ and more recently adapted for super-resolution fluorescence microscopy²⁶. The FRC method splits the datasets into halves and assesses their statistical resemblance as a function of the resolution range. This analysis resulted in a resolution of 4.0 Å for AqpZ, 5.1 Å for A5 and 4.5 Å for A5 P13W-G14W (Fig. 2c,f, Extended Data Fig. 7a,b,h). The FRC curve of AqpZ has, in addition to the signal power up to about 4.0 Å, a second information-containing range in the 2-Å regime. Thus, both the real-space (Extended Data Fig. 6h,i) and the statistical analysis of AqpZ LAFM half-maps report resolution at distances shorter than the Nyquist frequency of the raw data. Accordingly, LAFM maps of both AqpZ and A5 resolve details down to the amino acid size range (around 5 Å to 4 Å), and some signal power on the quasi-atomic scale (around 2 Å) in the case of AqpZ (Fig. 2b,c, Extended Data Fig. 6). We also capitalized on the serendipitous co-existence of two differently oriented A5 trimers in the A5 lattice. LAFM of the two trimer datasets, independent from each other and acquired through different relative AFM scan-directions, agree in great detail (Extended Data Fig. 7c-e). Finally, we cloned, expressed and purified a mutant A5, replacing two amino acids in the N terminus with tryptophans (P13W, G14W), and imaged the A5-mutant by HS-AFM (Extended Data Fig. 7f-h). LAFM maps of the A5 mutant show overall rearrangements of the N terminus with increased height and peaking probability at the mutation site.

Localization AFM of CLC antiporters

The AFM data of A5 and AqpZ were acquired on 2D lattices, however, a considerable advantage of LAFM is that the biomolecules do not need to be confined in a crystal for analysis, but can be sparsely populating a native-like environment. Furthermore, the buffer conditions inside the fluid cell can be changed to assess structural changes in response to environmental changes. Therefore, we studied CLC-ec1 (a Cl⁻/H⁺ antiporter from *E. coli*)^{30,31}, which, to our knowledge, has not been observed by AFM,

and whose transport mechanism remains unresolved. Mutations in human CLC family homologues have been associated with diseases³².

HS-AFM of CLC-ec1 in membranes formed through proteo-liposome fusion showed a dispersed population of proteins protruding 1.2 nm from the membrane (Fig. 3a–c, Supplementary Video 5). CLC-ec1 was predominantly dimeric, with small populations of monomers and higher-order oligomers assembled from multiple dimers (Fig. 3b). The topography and lateral dimensions of the dimers (Fig. 3c) were consistent with the 5.5 nm × 9.6 nm dimensions of the extracellular face of CLC-ec1 (Extended Data Fig. 8a–e)^{33,34}. Because the dimers were not confined, they exhibited translational and rotational freedom (Fig. 3c, Supplementary Video 5), which led us to establish a generalized LAFM workflow (Fig. 3d; see Methods): (1) a HS-AFM video is acquired and (2) low-pass-filtered, so that (3) particles can automatically be detected. Particles are thus (4) tracked throughout the HS-AFM observation and (5) selected and extracted in a gallery. (6) Bicubic image expansion allows for (7) precise particle centring and (8) rotational alignment to an arbitrary molecule reference. A second cycle of (9.1) lateral and (9.2) rotational alignment, this time with respect to an ensemble average, prepares particles for (10) application of the LAFM method (Supplementary Video 6). As described in Fig. 1,(10.1) local maxima peaks are detected and (10.2) the height at these locations is extracted with a 1.4-Å-wide probability radius. Finally, all detections are merged in a height–probability LAFM map (Fig. 3e). The particle gallery (step 5) can be assembled from many molecule observations in one or several frames. Alternatively, an LAFM map can be reconstructed from one molecule observed over time, which gives this method unique possibilities to access high-resolution information of individual molecules.

Fig. 3: HS-AFM imaging and LAFM workflow of CLC-ec1.



a–c, HS-AFM images of CLC-ec1 in a POPE:POPG (2:1 w-w) membrane at 400 nm (300 pixels) (**a**), 120 nm (300 pixels) (**b**) and 40 nm (300 pixels) (**c**) image (frame) size of predominantly dimeric CLC-ec1 at low density in a membrane. **d**, LAFM method workflow steps: (1) HS-AFM video acquisition; (2) image Gaussian filtering; (3) molecule detection; (4) 2D tracking to separate single molecules (molecules highlighted blue or red can be treated individually); (5) molecule selection; (6) bicubic expansion (original pixel sampling, 1.33 Å per pixel; expanded pixel sampling, 0.5 Å per pixel); (7) molecule centring (first round) by centre of mass; (8) rotational alignment (first round) of molecules through rotational cross-correlation with a reference frame, ref(#1); (9) translational and rotational alignment (second round) through cross-correlation with the average molecule, ref(ave), from step 8 (inset histograms, rotation angle distributions for all particles in steps 8 and 9); (10) LAFM method; insets: aligned HS-AFM images ($n = 200$); (10.1) LAFM peak detection of local maxima; (10.2) height extraction at each peak position and application of a 1.4-Å localization probability distribution; (11) LAFM map reconstruction through merging of all LAFM detections.

[Full size image](#)

Conformational changes in CLC-ec1

The exchange pathway in the CLC-ec1 Cl^-/H^+ -antiporter has been proposed to have two separate entrances/exits for H^+ and Cl^- on the intracellular face, converging to a central binding region from which both ions follow the same path to the extracellular side. However, there is debate about whether the gating mechanism requires only localized side-chain motions in the Cl^- pathway based on X-ray structures, or if greater movements occur, as evidenced by nuclear magnetic resonance (NMR)^{35,36}, computational³⁷ and helix-crosslinking studies³⁸. Findings by these non-crystallographic methods^{35,36,37,38,39} have led to suggestions that confinement of CLC in 3D lattices inhibit large conformational movements (Extended Data Table 1, Extended Data Fig. 8f), similar to other transporters^{40,41,42,43}. Cl^- transport by CLC-ec1 is maximal at acidic pH and stalled at neutral and basic pH (owing to pH-dependent activation and lack of H^+ as substrate)⁴⁴. A more recent structure of a protonation-mimicking triple mutant also indicates conformational rearrangements⁴⁵. Therefore, we performed HS-AFM of transporters sparsely packed in lipid membranes and in physiological buffer. Subsequent LAFM of the pH 7.6 (inactive state) and pH 4.5 (active state) observations should inform on whether large-scale conformational changes occur.

On the basis of the X-ray structure surface (Fig. 4a), we assigned the protruding residues expected to give signals in AFM: Asp73 in loop B-C, Glu235, Asp240 and Lys243 in the long loop I-J, Asn327 in loop L-M, and Gln381 and His383 in loop N-O. To refine the interpretation of LAFM reconstructions, we used MD simulations to convert the static X-ray structure into a dynamic molecular system fluctuating at room temperature and at pH 7 (Supplementary Video 1). Similar to the LAFM method, we plotted a population density map of the distribution of the z-coordinate local maxima on the CLC-ec1 extracellular face from MD trajectories, which reflected side-chain motions of membrane-protruding residues (Fig. 4b, Extended Data Fig. 8g, h). The MD trajectories show how structural fluctuations that are probed (in AFM) and merged (in LAFM) allow extraction of high-resolution information of amino acid residues on protein surfaces.

Fig. 4: Conformational changes in CLC-ec1 at neutral and acidic pH.



a, Extracellular surface of CLC-ec1 at pH 9.5 (PDB 1OTS³¹); membrane-protruding residues in four major protrusions (1–4) are labelled. **b**, Logarithmic-scale population density map of the positions of atoms with the highest z coordinates on the extracellular surface of CLC-ec1 from 5.6- μ s MD simulations at pH 7 (simulated from PDB 1OTS). Major protrusions (1–4) are labelled. Major contributions to each population peak: (1) D73 (97%), A72 (2.7%); (2) N237 (91%), D240 (2.2%); (3) Q381 (42.3%), H383 (54.7%); (4) K243 (52%), D240 (21.7%), S245 (3.4%). **c, d**, LAFM reconstructions of CLC-ec1 at pH 7.6 (**c**) and pH 4.5 (**d**). The ion pathway entry is labelled with an asterisk. The four major protrusions (1–4) are highlighted for comparison with the X-ray structure and the MD population density map. **e**, Detection probability difference map between CLC-ec1 LAFM reconstructions at pH 7.6 (**c**) and pH 4.5 (**d**). The difference map highlights the conformational changes of the four major protrusions, notably a ~6- \AA movement of peak 1 towards the dimer axis.

[Full size image](#)

The CLC-ec1 LAFM reconstructions at pH 7.6 and pH 4.5 display the same set of structural features as the X-ray structure and the MD population map, but in distinctly different configurations (Fig. [4c, d](#)). Peaks 2, 3 and 4, which form a triangle close to the dimer interface, pack more loosely at pH 4.5, and peak 3 moves towards a more lateral position on the dimer, while the most remarkable conformational change is a ~6- \AA movement of peak 1 towards the dimer interface at acidic pH. The extracellular Cl⁻/H⁺ ion pathway lies between Asp73, Asn327 and Glu235 (Fig. [4c](#), asterisk); thus, under the premise that these displacements are related to movements in the underlying helices, these structural changes might alter accessibility to the extracellular gate. In summary, LAFM reports large pH-dependent conformational changes (Fig. [4e](#), Supplementary Video [7](#)).

By recording 3D topographic images and videos, AFM and HS-AFM offer rich data, captured through many atomic interactions between tip and sample in liquid and at ambient conditions. By pinpointing peak interaction locations with high spatial precision in oversampled topographies, LAFM produces quasi-atomic resolution maps of protein surfaces from such data. We demonstrate the ability of LAFM to detect amino acid side chains on the surfaces of AqpZ, A5 and CLC-ec1, mutation-related differences in A5, and conformational changes in the angstrom range in CLC-ec1. Our LAFM maps, calculated from CLC-ec1 imaged at physiological and acidic pH, identified substantial differences in the central region, where helices N and O are located, and at the peripheral end of helix B, which moves towards the dimer centre, giving the entire molecule a ~1.2-nm shortened appearance (Fig. [4d, e](#)).

HS-AFM⁵ operates in amplitude modulation mode using short cantilevers that oscillate at resonance at around 660 kHz (oscillation cycle of around 1.5 μ s). The tip

touches the surface only during ~10% of an oscillation cycle⁴, thus about 150 ns. Even though this is a short period in the life of a protein, side-chain fluctuations occur in such time regimes, thus blurring the signal. Hence, LAFM will provide improved data when the next generation of faster HS-AFM systems arrive. Today, amplitude detectors oversample the cantilever^{5,46}, but feedback operation and the z-piezo are limiting (about 100 kHz) factors and need improvement.

The LAFM method can be used in two different ways: LAFM maps can be reconstructed (i) from many molecules recorded in one or several frames or (ii) from a single molecule over time. The first approach allows us to resolve time- or environment-dependent conformational changes. About 50 particles are needed to reconstruct an LAFM map (Extended Data Fig. 5); therefore, the temporal resolution of LAFM is decreased to the time required to accumulate these 50 observations. Faster HS-AFM operation will of course improve time-resolved studies of single molecules. Alternatively, imaging densely packed proteins (with around 50 particles in each frame^{8,47}) would allow LAFM map reconstruction of the conformation of the proteins in each frame, giving high-resolution structural changes as a function of time. The second approach gives the method the unique capability to provide high-resolution information of single molecules or of non-ordered supramolecular assemblies. Altogether, we envisage that LAFM will become the standard method applied to AFM imaging, allowing the extraction of high-resolution information beyond the tip-radius resolution limit in the study of single biomolecules in native-like environments.

Methods

HS-AFM

HS-AFM measurements (annexin-V, CLC-ec1) were taken with an amplitude modulation mode HS-AFM (RIBM), as previously described in ref. 28. In brief, we used short cantilevers (USC-F1.2-k0.15, NanoWorld) with a spring constant of 0.15 N m^{-1} , a resonance frequency of ~0.66 MHz and a quality factor of ~1.5 in buffer.

AFM

AFM data (aquaporin-Z) were taken by contact-mode AFM using a Nanoscope-III AFM (Digital Instruments) equipped with a 120-μm scanner (J-scanner) and oxide-sharpened Si_3N_4 cantilevers with a length of 120 μm and spring constant of 0.1 N m^{-1} (Olympus Ltd), as detailed in ref. 20.

Cloning, expression and purification of annexin-V-P13W-G14W

The P13W-G14W site-directed mutagenesis was performed on an untagged human annexin pET28a expression vector using the Q5 site-directed mutagenesis kit (New England BioLabs) and the following mutagenic primers (mutated nucleotides are in bold): 5'-GACCGATTTCGGTGGTTGATGAACGTGCTGATGCC-3' and 5'-ACGGTACCA CGCAGCACTG-3'.

The mutated genes were sequenced to confirm that only the desired mutations were inserted into the plasmid. The annexin-V-P13W-G14W plasmid was then transformed into BL21 (DE3) pLysE chemically competent *E. coli* cells (Invitrogen), and grown overnight at 37 °C for small-scale culture. The overnight culture (50 ml) was inoculated into 2 l fresh Luria–Bertani broth media at 37 °C, and once an optical density (A₆₀₀) of 0.6–0.8 was achieved, the cells were induced by addition of 0.4 mM isopropyl β-D-1-thiogalactopyranoside. After induction for 4 h, the cells were separated from the culture medium by centrifugation (5,000 g; 20 min) and resuspended in ice-cold calcium buffer (50 mM Tris pH 7.5, 10 mM CaCl₂). The suspension was three times tip-sonicated on ice for 5 min (one pulse every 9 s), and centrifuged (23,000 g; 45 min). The supernatant was discarded, and the pellet was resuspended in ice-cold EGTA buffer (50 mM Tris pH 7.5, 60 mM EGTA). After gentle shaking for 30 min, the cell debris were removed by centrifugation (23,000 g; 45 min), and the supernatant containing the soluble Annexin-V-P13W-G14W was dialysed overnight against buffer A (20 mM Tris pH 7.5, 20 mM NaCl). The solution was applied to a HiTrap DEAE FF sepharose column (5 ml) ÄKTA Avant (GE Healthcare Life Sciences), and eluted with a linear gradient of 0–1 M NaCl. Fractions containing annexin-V-P13W-G14W (based on SDS–PAGE analysis) were concentrated to ~1 mg ml⁻¹ using 10 kDa centrifugal filters (Amicon, Millipore), and subjected to a final purification step with a Superdex 200 Increase 10/300 gel filtration column (equilibrated with 20 mM Tris pH 7.5, 100 mM NaCl buffer), reaching a final purity of >95% according to SDS–PAGE analysis.

CLC-ec1 expression and purification

Expression and purification of CLC-ec1 were carried out as previously described⁴⁸. BL21-AI *E. coli* competent cells (Thermo Fisher Scientific) were transformed with the plasmid and then 2 l Terrific Broth supplemented with ampicillin was inoculated and grown at 37 °C. Protein expression was induced with anhydro-tetracycline at OD₆₀₀ = 1.0. After 3 h of induction, cells were harvested, then lysed by sonication in buffer supplemented with 5 mM reducing agent TCEP (Tris(2-carboxyethyl)phosphine; Soltec Bioscience) and pH adjusted to 7.5. Protein extraction was carried out with 2% *n*-decyl-β-D-maltopyranoside (DM; Anatrace) for 2 h at room temperature. Cell debris was pelleted down, and the supernatant was run on a 2 ml column volume (CV) TALON cobalt affinity resin (Clontech Laboratories) equilibrated in cobalt column wash buffer (CoWB)/TCEP: 100 mM NaCl, 20 mM

Tris, 1 mM TCEP, pH 7.5 with NaOH, 5 mM DM. After binding, the column was washed with 15 CVs of CoWB/TCEP followed by a low-imidazole wash of CoWB/TCEP containing 20 mM imidazole (Sigma-Aldrich). CLC-ec1 was eluted with CoWB/TCEP containing 400 mM imidazole, then concentrated in 30-kDa nominal molecular weight limit (NMWL) centrifugal filters (Amicon, EMD Millipore) to ~500 µl and injected on a Superdex 200 10/30 GL size exclusion column (GE Healthcare) equilibrated in size exclusion buffer (SEB): 150 mM NaCl, 20 mM MOPS pH7.5, 5 mM analytical-grade DM, attached to a medium-pressure chromatography system (NGC, Bio-Rad).

CLC-ec1 reconstitution and bilayer formation

Lipids were resuspended in 300 mM KCl, 20 mM citrate pH 4.5 with NaOH. CHAPS (35 mM) solubilized lipids were combined with protein at 100 µg CLC-ec1 per 1 mg of lipids, corresponding to a protein/lipid mole fraction of 7.6×10^{-4} (assuming a 50% incorporation yield)⁴⁸. The protein–lipid–detergent mixture was dialysed in cassettes (NMWL 10 kDa; ThermoFisher Scientific) at 4 °C against 4 l of buffer for 48 h with buffer changes every 8–12 h. After completion of dialysis, the proteo-liposomes were harvested from the cassettes, freeze/thawed and then extruded using an Avanti Polar Lipids Mini Extruder (Alabaster) through a 400-nm membrane. 1.5 µl of the SUV solution with a total lipid concentration of 0.1 mg ml⁻¹ was deposited onto freshly cleaved mica to form supported lipid bilayers (SLBs) through vesicle fusion. The excess lipids, after SLB formation, were rinsed first with deionized water, followed by buffer. For experiments at pH 7.6 the sample was rinsed with 25 mM Tris, 300 mM KCl pH 7.6.

Image expansion

AFM topography images were expanded using bicubic interpolation (Catmull–Rom interpolation; implemented in imageJ, scripted using the method of Burger and Burge)⁴⁹. The method considers values over a 16-pixel surface (4×4 pixels) to calculate the new intermediate surface, $p(x, y)$, created by expansion across the central 2×2 area. The interpolated values are approximated by 3rd-order polynomials in both the x and y directions:

$$\$\$ p(x,y)=\mathop{\sum}\limits_{i=0}^3\mathop{\sum}\limits_{j=0}^3 a_{ij}x^i y^j, \$\$$$

where i and j are the order of the polynomial for x and y , respectively, and a_{ij} are 16 possible corresponding coefficients. The resulting polynomial can be calculated using the values at the four corners of the central 2×2 grid ($f(x, y)$), the gradients at each of those positions in the x and y directions ($f_x(x, y), f_y(x, y)$) and the cross-derivatives

$(f_{xy}(x, y))$ requiring the 4×4 pixel grid, with the derivatives being calculated numerically. The interpolated surface, $p(x, y)$, between four corner pixels can be described by:

$$\begin{aligned} \$\$ p(x,y) = & [1, x, \{x\}^2, \{x\}^3], \left[\begin{array}{cccc} a_{00} & a_{01} & a_{02} & a_{03} \\ a_{10} & a_{11} & a_{12} & a_{13} \\ a_{20} & a_{21} & a_{22} & a_{23} \\ a_{30} & a_{31} & a_{32} & a_{33} \end{array} \right] \left[\begin{array}{c} 1 \\ y \\ y^2 \\ y^3 \end{array} \right] \end{aligned}$$

where the 16 coefficients can be calculated using the values and derivatives at the four corners:

$$\begin{aligned} \$\$ \left[\begin{array}{cccc} c_{00} & c_{01} & c_{02} & c_{03} \\ c_{10} & c_{11} & c_{12} & c_{13} \\ c_{20} & c_{21} & c_{22} & c_{23} \\ c_{30} & c_{31} & c_{32} & c_{33} \end{array} \right] = & \left[\begin{array}{cccc} f(0,0) & f(0,1) & f(1,0) & f(1,1) \\ f_y(0,0) & f_y(0,1) & f_y(1,0) & f_y(1,1) \\ f_{xx}(0,0) & f_{xx}(0,1) & f_{xx}(1,0) & f_{xx}(1,1) \\ f_{xy}(0,0) & f_{xy}(0,1) & f_{xy}(1,0) & f_{xy}(1,1) \end{array} \right] \end{aligned}$$

Using this method, all our datasets were resampled to 0.5 \AA per pixel, as indicated in the figure captions. The reason for expanding to 0.5 \AA per pixel is based on approximating the picked maxima features to the solvent-accessible surface of atoms with Gaussian profiling, as detailed in the Methods section ‘Detection probability’. By constructing the interpolant value from continuous piecewise polynomials, the result is always continuous. This works particularly well for interpolation of smooth areas, as in the case of tip-radius-limited imaging, and therefore considerably improves local maxima localization, but does not increase image resolution.

Detection of local maxima

A local maximum position (Fig. 1c) is defined if a given pixel is higher than all the surrounding eight pixels in a 3×3 pixel grid (Figs. 1c, 3d). This 3×3 pixel grid is ‘scanned’ pixel by pixel over the image, and thus all pixels (with the exception of those at the image borders) in each particle image are checked for maxima. To reduce the selection of maxima due to noise in certain datasets, a noise tolerance algorithm that selects maxima based on their prominence above surrounding maxima was implemented. The prominence of each maximum, p_i , is calculated by the following

steps: (i) search for the closest neighbouring maximum h_n with higher height than the current maximum h_i or closest image boundary; (ii) find the minimum height along the profile between h_i and h_n or between h_i and the image boundary; and (iii) define the peak prominence as:

$$\$ \$ \{ p \} \{ i \} = \{ h \} \{ i \} - \{ h \} \{ \min \{ \{ h \} \{ i \} \{ \text{to} \{ h \} \{ n \} \} \} \} . \$ \$$$

In our method, for a local maximum to be selected, its prominence must be greater than the noise tolerance (typically 1–2 Å). In our plugin, the noise tolerance is defined by the user from 0 to 100%, where the noise tolerance parameter corresponds to the range of height values from lowest to highest in the image. These maxima selection criteria are based on the noise level of the AFM imaging and the typical root-mean-square fluctuations at protein surfaces (Extended Data Fig. 8g, h). An alternative method is to apply a Gaussian filter to the image to reduce noise and use 0% noise tolerance. The repulsive interaction forces between the farthest exposed atoms of the tip and the atoms in protein moieties that protrude most have very steep separation distance dependence. Very strong short-range interactions occur, including Pauli repulsion and van der Waals, hydration, steric and ionic forces, which depend on the surface properties of both the AFM tip and the protein⁵⁰. As a result, the most exposed atoms dominate local topographic detection and high-resolution information can be obtained through merging many tip–sample atomic interactions at different localizations and time points or on different molecules of the same kind.

Detection probability

The peaking probability at a given localization in an LAFM map, is the cumulative probability that a pixel (in the expanded image) is detected within all particles analysed. It is the sum of: picking events (n), multiplied by the power of the 2D Gaussian, $g(0 < P < 1)$ on each pixel, divided by the total number of particles merged (N).

$$\$ \$ \{ P \} \{ x, y \} = \frac{\sum_{i=1}^N \{ n \} \{ x_i, y_i \} \{ g \} \{ x, y \}}{N} . \$ \$$$

The 2D Gaussian in all our datasets was set to 1.4 Å width to approximate the solvent-accessible surface of the underlaying atoms (the solvent-accessible surface area is defined as the surface traced out by the centre of a water sphere rolled over the protein atoms)⁵¹ while imparting a continuous probability density to each discreetly selected maximum. The application of larger Gaussian radii to approximate the atomic origin of the tip–sample interactions or pre-filtering the data before peaking leads to loss of resolution or loss of peaking detection of lower features, respectively (Extended Data Fig. 9). Because AFM can reproducibly image atoms on solid surfaces, for example,

on mica, the piezo-elements that mediate the scanning of the AFM sample stage have sub-atomic x - y position precision.

Height extraction

The real-space topographic height is extracted at each detection to produce a set of N matrices containing height values for each value of n . This matrix is then false-coloured to allow distinction between height and probability information.

Merging height and detection probability

The false-coloured extracted height values in each image are then multiplied by the greyscale probability values in each image, and then averaged for the whole image set to reconstruct an LAFM map.

LAFM workflow

The HS-AFM videos were 1st-order flattened to compensate for sample stage tilt, drift-corrected and contrast-adjusted by laboratory-built image analysis software in ImageJ and MATLAB (Mathworks). The workflow used to calculate an LAFM map from molecular HS-AFM raw data is outlined in Fig. 3. The key steps in the preparation for the LAFM method are: extraction of molecular observations from images (Fig. 3d, steps 1–5), image expansion (Fig. 3d, step 6; see [Methods](#) section ‘Image expansion’) and creation of a particle gallery with laterally and rotationally well aligned particles (Fig. 3d, steps 7–9). Several image processing packages used for electron microscopy (for example, ref. [52](#)) allow particle extraction and alignment, and could be used for convenience. The particle gallery of pixel-expanded (0.5 Å per pixel) molecular observations is the entry for the LAFM algorithm, which comprises detection of local maxima, height extraction and merging of height and peaking probabilities (Fig. 3d, steps 10–11; Methods sections ‘Detection of local maxima’, ‘Detection probability’, ‘Height extraction’ and ‘Merging height and detection probability’) in the final LAFM map. The LAFM method is available as code in the form of an appendix and as an ImageJ plugin (Supplementary Information).

LAFM simulations

2D and 3D LAFM simulations were performed using MATLAB. In 2D simulations (x , z), various model surfaces were created with different features depending on the simulation (Fig. 1b; simulation parameters: tip radius, 20 pixels; feature height, 3 pixels; feature width and separation, 2 pixels; scanning noise, 0.05 (standard deviation, σ), feature fluctuation, 0.3 (σ); the Gaussian surface topography (bottom row) has $\sigma = 20$; varying parameters are used in Extended Data Figs. 2, 3, given in the figure

captions). Each topographic feature was given a height higher than the surrounding baseline surface (set at zero). Normally distributed random numbers with set standard deviation were then generated and added to each x position containing a topographic feature, increasing or decreasing the height. These random fluctuations were added independently of neighbouring x positions. A semicircular tip of defined radius was calculated numerically and then scanned across the simulated 2D surface to create a tip-convoluted topography. To simulate the AFM instrument noise, normally distributed random noise was then added in the z direction to the tip-convoluted topography at all positions. Many randomly generated topographies were then analysed using the LAFM algorithm to produce peaking probability and peaking height traces. 3D simulations were run using a similar methodology, however a hemispherical tip was scanned across 3D model surfaces (Extended Data Figs. 4, 5, Supplementary Video 2).

Simulation data are compared to a theoretical resolution limit (Extended Data Fig. 3) on the basis of geometric considerations, assuming a rigid pair of spikes separated by a distance (d) and a height difference (Δh), contacted by a tip radius (R) without noise or fluctuations. The resolution limit is defined as being resolved if the probe is able to reach a minimum (Δz) below the height of the smallest spike⁵³:

$$d = \sqrt{2R} \sqrt{\varDelta z + \sqrt{\varDelta z + \varDelta h}}$$

The absolute resolution limit under these considerations occurs when maxima can be detected at both spikes when $\Delta z = 0$.

MD simulations of CLC

Construct for MD simulations

The molecular model of the CLC-ec1 dimer used in all MD simulations described in this work was based on the X-ray structure PDB 1OTS³¹. The protonation states of the titratable residues at pH 7 were determined from constant-pH calculations with the neMD/MC (non-equilibrium MD/Monte Carlo) approach⁵⁴. The spatial arrangement of the CLC-ec1 dimer in the bilayer was optimized using the Orientations of Proteins in Membranes (OPM) database⁵⁵ and input to the Membrane Builder module on the CHARMM-GUI web server⁵⁶ to assemble the protein–membrane system. The CLC-ec1 dimer was embedded in a 629-lipid membrane bilayer containing a ~70:30 mixture of POPE (1-palmitoyl-2-oleoyl-sn-glycero-3-phosphoethanolamine) and POPG (1-palmitoyl-2-oleoyl-sn-glycero-3-phospho-(1'-rac-glycerol)), solvated in 150 mM KCl explicit water to achieve electroneutrality.

MD simulation procedures

The assembled molecular system was subjected to an initial equilibration phase using NAMD⁵⁷ (version 2.13) following two protocols. The first used the standard six-step equilibration protocol provided by CHARMM-GUI. The other used a laboratory-built multi-step equilibration, in which the backbone of the protein was first fixed⁵⁸. Backbone constraints were gradually released in three 300-ps steps of force constant change (1 to 0.5 and to 0.1 kcal per mol⁻¹ Å⁻²). The final structures from the equilibration phases were subjected to short (46 ns and 48 ns) unbiased MD with NAMD (2-fs time steps, vdwForceSwitching option, and PME for electrostatic interactions)⁵⁹. The runs were in the NPT ensemble under semi-isotropic pressure coupling at 24 °C. The Nose–Hoover–Langevin piston algorithm⁶⁰ was used to control the target $P = 1$ atm pressure with LangevinPistonPeriod = 50 fs and LangevinPistonDecay = 25 fs. Van der Waals interactions had a cutoff distance of 12 Å. The first phase of production runs (Production 1) was initiated by all-atom velocity resetting and continued with simulations of the system in 50 independent replicates of ~150 ns each (that is, 100 replicates overall for a cumulative 15 μs) using ACEMD⁶¹. At the conclusion of Production 1, the trajectories were analysed to assess the stability of the bound Cl⁻ ions, and replicates with the most stably bound Cl⁻ ions were identified. The final snapshots from 48 replicates were selected as starting points for the next phase, Production 2, in which the systems were simulated using NAMD with the parameters described above for ~120 ns (cumulative 5.76 μs). Run parameters: timestep 4 fs, vdwforceswitching on, switching on, switchdist 7.5, cutoff 9, fullelectfrequency 2, langevindamping 0.1, pme on, and pmegridspacing 1.0. All the simulations used the latest CHARMM36 force-field parameters for proteins, lipids and ions.

Population density maps from the MD trajectories

To analyse the height of protein atoms with respect to the membrane plane during the MD simulations, the symmetry axis of the CLC-ec1 dimer was set perpendicular to the X – Y plane. In analogy to the LAFM method, the highest z -coordinate values on the CLC extracellular surface were selected for each frame to plot the position distribution map. Maps were constructed by taking the 8, 10 and 16 highest points in each frame, leading to the conclusion that detection of more than 8 points resulted in sampling the neighbouring atoms of residues already included in the 8-point set. Thus, the distribution maps were obtained by pooling the 8 highest- z -coordinate peaks from each frame. Analysis performed separately on Production 1 and Production 2 trajectories did not show notable differences, and in the main text we show the results from the analysis of 5.6 μs with 20-ps time strides of Production 2 trajectories. Because both protomers of CLC-ec1 were considered identical, we symmetrized the data by aligning trajectories of each protomer onto another one.

MD simulation of annexin-V P13W-G14W

MD simulations of the mutant annexin-V-P13W-G14W were conducted with Gromacs2019.1⁶², using the Amber03 force field⁶³. The initial molecular model of annexin-V-P13W-G14W was generated using the X-ray structure PDB 1HVD, and the double mutation introduced using the program Coot⁶⁴. This model was then solvated with ~40,000 water molecules in accordance with the Tip3P water model⁶⁵, and neutralized with Na⁺ and Cl⁻ ions to a concentration of 150 mM. The system was placed in a dodecahedron box, with a minimal distance of 1.0 nm between protein and box wall. Van der Waals interactions were implemented with a cutoff at 1.0 nm, and long-range electrostatic effects were treated with the particle mesh Ewald method. The protein–solvent model was then put through four rounds of geometry optimization and energy minimization, followed by a 50-ps protein position-restrained equilibration and an additional 50 ps of unrestrained equilibration. The system was then heated to 300 K using a velocity-rescaling thermostat⁶⁶ (50 ps), and equilibrated to a constant pressure of 1 bar using a Parrinello–Rahman barostat (50 ps). Following these equilibration procedures, a time trajectory of 100 ns was simulated at constant temperature and pressure, using time steps of 2 fs and the same thermostat and barostat. The data were then symmetrized along the threefold axis by aligning trajectories of each protomer one onto the other. To build an annexin-V-P13W-G14W mutant structural model that represents the rotamer conformations of the mutated Trp residues, clustering analysis of the simulation trajectories was performed with Gromacs (g_cluster, gromos algorithm)⁶², with a root-mean-square deviation cut-off of 0.2 with respect to the mutated Trp residues in positions 13–14. Out of the 10 resulting clusters, the most representative structure was extracted from the centre of the most populated cluster (containing ~50% of total protein structures).

Data availability

The datasets generated and/or analysed during the current study are available from the corresponding author on reasonable request.

Code availability

The custom-written script implemented in ImageJ to create LAFM maps from a stack of aligned and expanded images is available in Supplementary Information. MATLAB codes used in 2D and 3D LAFM simulations are also available in Supplementary Information.

References

1. 1.

Binnig, G., Quate, C. F. & Gerber, C. Atomic force microscope. *Phys. Rev. Lett.* **56**, 930–933 (1986).

[ADS](#) [CAS](#) [PubMed](#) [Google Scholar](#)

2. 2.

Heath, G. R. & Scheuring, S. Advances in high-speed atomic force microscopy (HS-AFM) reveal dynamics of transmembrane channels and transporters. *Curr. Opin. Struct. Biol.* **57**, 93–102 (2019).

[CAS](#) [PubMed](#) [PubMed Central](#) [Google Scholar](#)

3. 3.

Betzig, E. et al. Imaging intracellular fluorescent proteins at nanometer resolution. *Science* **313**, 1642–1645 (2006).

[ADS](#) [CAS](#) [PubMed](#) [Google Scholar](#)

4. 4.

Lin, Y. C. et al. Force-induced conformational changes in PIEZO1. *Nature* **573**, 230–234 (2019).

[ADS](#) [CAS](#) [PubMed](#) [PubMed Central](#) [Google Scholar](#)

5. 5.

Ando, T. et al. A high-speed atomic force microscope for studying biological macromolecules. *Proc. Natl Acad. Sci. USA* **98**, 12468–12472 (2001).

[ADS](#) [CAS](#) [PubMed](#) [Google Scholar](#)

6. 6.

Kodera, N., Yamamoto, D., Ishikawa, R. & Ando, T. Video imaging of walking myosin V by high-speed atomic force microscopy. *Nature* **468**, 72–76 (2010).

[ADS](#) [CAS](#) [PubMed](#) [Google Scholar](#)

7. 7.

Preiner, J. et al. High-speed AFM images of thermal motion provide stiffness map of interfacial membrane protein moieties. *Nano Lett.* **15**, 759–763 (2015).

[ADS](#) [CAS](#) [PubMed](#) [Google Scholar](#)

8. 8.

Ruan, Y. et al. Structural titration of receptor ion channel GLIC gating by HS-AFM. *Proc. Natl Acad. Sci. USA* **115**, 10333–10338 (2018).

[CAS](#) [PubMed](#) [Google Scholar](#)

9. 9.

Heath, G. R. & Scheuring, S. High-speed AFM height spectroscopy reveals μ s-dynamics of unlabeled biomolecules. *Nat. Commun.* **9**, 4983 (2018).

[ADS](#) [PubMed](#) [PubMed Central](#) [Google Scholar](#)

10. 10.

Nievergelt, A. P., Banterle, N., Andany, S. H., Gönczy, P. & Fantner, G. E. High-speed photothermal off-resonance atomic force microscopy reveals assembly routes of centriolar scaffold protein SAS-6. *Nat. Nanotechnol.* **13**, 696–701 (2018).

[ADS](#) [CAS](#) [PubMed](#) [Google Scholar](#)

11. 11.

Eeftens, J. M. et al. Condensin Smc2-Smc4 dimers are flexible and dynamic. *Cell Rep.* **14**, 1813–1818 (2016).

[CAS](#) [PubMed](#) [PubMed Central](#) [Google Scholar](#)

12. 12.

Shibata, M. et al. Oligomeric states of microbial rhodopsins determined by high-speed atomic force microscopy and circular dichroic spectroscopy. *Sci. Rep.* **8**, 8262 (2018).

[ADS](#) [PubMed](#) [PubMed Central](#) [Google Scholar](#)

13. 13.

Nasrallah, H. et al. Imaging artificial membranes using high-speed atomic force microscopy. *Methods Mol. Biol.* **1886**, 45–59 (2019).

[CAS](#) [PubMed](#) [Google Scholar](#)

14. 14.

Viani, M. B. et al. Fast imaging and fast force spectroscopy of single biopolymers with a new atomic force microscope designed for small cantilevers. *Rev. Sci. Instrum.* **70**, 4300–4303 (1999).

[ADS](#) [CAS](#) [Google Scholar](#)

15. 15.

Kodera, N., Yamashita, H. & Ando, T. Active damping of the scanner for high-speed atomic force microscopy. *Rev. Sci. Instrum.* **76**, 053708 (2005).

[ADS](#) [Google Scholar](#)

16. 16.

Kodera, N., Sakashita, M. & Ando, T. Dynamic proportional-integral-differential controller for high-speed atomic force microscopy. *Rev. Sci. Instrum.* **77**, 083704 (2006).

[ADS](#) [Google Scholar](#)

17. 17.

Shibata, M. et al. Real-space and real-time dynamics of CRISPR-Cas9 visualized by high-speed atomic force microscopy. *Nat. Commun.* **8**, 1430 (2017).

[ADS](#) [PubMed](#) [PubMed Central](#) [Google Scholar](#)

18. 18.

Gan, Y. Atomic and subnanometer resolution in ambient conditions by atomic force microscopy. *Surf. Sci. Rep.* **64**, 99–121 (2009).

[ADS](#) [CAS](#) [Google Scholar](#)

19. 19.

Müller, D. J., Schabert, F. A., Büldt, G. & Engel, A. Imaging purple membranes in aqueous solutions at sub-nanometer resolution by atomic force microscopy. *Biophys. J.* **68**, 1681–1686 (1995).

[ADS](#) [PubMed](#) [PubMed Central](#) [Google Scholar](#)

20. 20.

Scheuring, S. et al. High resolution AFM topographs of the *Escherichia coli* water channel aquaporin Z. *EMBO J.* **18**, 4981–4987 (1999).

[CAS](#) [PubMed](#) [PubMed Central](#) [Google Scholar](#)

21. 21.

Fechner, P. et al. Structural information, resolution, and noise in high-resolution atomic force microscopy topographs. *Biophys. J.* **96**, 3822–3831 (2009).

[ADS](#) [CAS](#) [PubMed](#) [PubMed Central](#) [Google Scholar](#)

22. 22.

Markiewicz, P. & Goh, M. C. Atomic force microscopy probe tip visualization and improvement of images using a simple deconvolution procedure. *Langmuir* **10**, 5–7 (1994).

[CAS](#) [Google Scholar](#)

23. 23.

Bukharaev, A. A., Bukharaev, A. A., Berdunov, N. V., Ovchinnikov, D. V. & Salikhov, K. M. Three-dimensional probe and surface reconstruction for atomic force microscopy using a deconvolution algorithm. *eCM J.* **12**, 225 (1998).

[Google Scholar](#)

24. 24.

Rust, M. J., Bates, M. & Zhuang, X. Sub-diffraction-limit imaging by stochastic optical reconstruction microscopy (STORM). *Nat. Methods* **3**, 793–796 (2006).

[CAS](#) [PubMed](#) [PubMed Central](#) [Google Scholar](#)

25. 25.

Small, A. & Stahlheber, S. Fluorophore localization algorithms for super-resolution microscopy. *Nat. Methods* **11**, 267–279 (2014); corrigendum **11**, 971 (2014).

[CAS](#) [PubMed](#) [Google Scholar](#)

26. 26.

Nieuwenhuizen, R. P. J. et al. Measuring image resolution in optical nanoscopy. *Nat. Methods* **10**, 557–562 (2013).

[CAS](#) [PubMed](#) [PubMed Central](#) [Google Scholar](#)

27. 27.

Scheuring, S., Müller, D., Stahlberg, H., Engel, H.-A. & Engel, A. Sampling the conformational space of membrane protein surfaces with the AFM. *Eur. Biophys. J.* **31**, 172–178 (2002).

[CAS](#) [PubMed](#) [Google Scholar](#)

28. 28.

Miyagi, A., Chipot, C., Rangl, M. & Scheuring, S. High-speed atomic force microscopy shows that annexin V stabilizes membranes on the second timescale. *Nat. Nanotechnol.* **11**, 783–790 (2016).

[ADS](#) [CAS](#) [PubMed](#) [Google Scholar](#)

29. 29.

Saxton, W. O. & Baumeister, W. The correlation averaging of a regularly arranged bacterial cell envelope protein. *J. Microsc.* **127**, 127–138 (1982).

[CAS](#) [PubMed](#) [Google Scholar](#)

30. 30.

Accardi, A. & Miller, C. Secondary active transport mediated by a prokaryotic homologue of ClC Cl⁻ channels. *Nature* **427**, 803–807 (2004).

[ADS](#) [CAS](#) [PubMed](#) [Google Scholar](#)

31. 31.

Dutzler, R., Campbell, E. B. & MacKinnon, R. Gating the selectivity filter in ClC chloride channels. *Science* **300**, 108–112 (2003).

[ADS](#) [CAS](#) [PubMed](#) [Google Scholar](#)

32. 32.

Jentsch, T. J. & Pusch, M. CLC chloride channels and transporters: structure, function, physiology, and disease. *Physiol. Rev.* **98**, 1493–1590 (2018).

[CAS](#) [PubMed](#) [Google Scholar](#)

33. 33.

Accardi, A. et al. Separate ion pathways in a Cl^-/H^+ exchanger. *J. Gen. Physiol.* **126**, 563–570 (2005).

[CAS](#) [PubMed](#) [PubMed Central](#) [Google Scholar](#)

34. 34.

Dutzler, R., Campbell, E. B., Cadene, M., Chait, B. T. & MacKinnon, R. X-ray structure of a ClC chloride channel at 3.0 Å reveals the molecular basis of anion selectivity. *Nature* **415**, 287–294 (2002).

[ADS](#) [CAS](#) [PubMed](#) [Google Scholar](#)

35. 35.

Abraham, S. J. et al. ^{13}C NMR detects conformational change in the 100-kD membrane transporter ClC-ec1. *J. Biomol. NMR* **61**, 209–226 (2015).

[CAS](#) [PubMed](#) [PubMed Central](#) [Google Scholar](#)

36. 36.

Khantwal, C. M. et al. Revealing an outward-facing open conformational state in a CLC Cl^-/H^+ exchange transporter. *eLife* **5**, e11189 (2016).

[PubMed](#) [PubMed Central](#) [Google Scholar](#)

37. 37.

Miloshevsky, G. V., Hassanein, A. & Jordan, P. C. Antiport mechanism for Cl⁻/H⁺ in CLC-ec1 from normal-mode analysis. *Biophys. J.* **98**, 999–1008 (2010).

[ADS](#) [CAS](#) [PubMed](#) [PubMed Central](#) [Google Scholar](#)

38. 38.

Basilio, D., Noack, K., Picollo, A. & Accardi, A. Conformational changes required for H⁺/Cl⁻ exchange mediated by a CLC transporter. *Nat. Struct. Mol. Biol.* **21**, 456–463 (2014).

[CAS](#) [PubMed](#) [PubMed Central](#) [Google Scholar](#)

39. 39.

Osteen, J. D. & Mindell, J. A. Insights into the CLC-4 transport mechanism from studies of Zn²⁺ inhibition. *Biophys. J.* **95**, 4668–4675 (2008).

[ADS](#) [CAS](#) [PubMed](#) [PubMed Central](#) [Google Scholar](#)

40. 40.

Reyes, N., Ginter, C. & Boudker, O. Transport mechanism of a bacterial homologue of glutamate transporters. *Nature* **462**, 880–885 (2009).

[ADS](#) [CAS](#) [PubMed](#) [PubMed Central](#) [Google Scholar](#)

41. 41.

Ruan, Y. et al. Direct visualization of glutamate transporter elevator mechanism by high-speed AFM. *Proc. Natl Acad. Sci. USA* **114**, 1584–1588 (2017).

[CAS](#) [PubMed](#) [Google Scholar](#)

42. 42.

Krishnamurthy, H. & Gouaux, E. X-ray structures of LeuT in substrate-free outward-open and apo inward-open states. *Nature* **481**, 469–474 (2012).

[ADS](#) [CAS](#) [PubMed](#) [PubMed Central](#) [Google Scholar](#)

43. 43.

Hofmann, S. et al. Conformation space of a heterodimeric ABC exporter under turnover conditions. *Nature* **571**, 580–583 (2019).

[CAS](#) [PubMed](#) [Google Scholar](#)

44. 44.

Accardi, A., Kolmakova-Partensky, L., Williams, C. & Miller, C. Ionic currents mediated by a prokaryotic homologue of CLC Cl⁻ channels. *J. Gen. Physiol.* **123**, 109–119 (2004).

[CAS](#) [PubMed](#) [PubMed Central](#) [Google Scholar](#)

45. 45.

Chavan, T. S. et al. A CLC-ec1 mutant reveals global conformational change and suggests a unifying mechanism for the Cl⁻/H⁺ transport cycle. *eLife* **9**, e53479 (2020).

[PubMed](#) [PubMed Central](#) [Google Scholar](#)

46. 46.

Miyagi, A. & Scheuring, S. A novel phase-shift-based amplitude detector for a high-speed atomic force microscope. *Rev. Sci. Instrum.* **89**, 083704 (2018).

[ADS](#) [PubMed](#) [Google Scholar](#)

47. 47.

Marchesi, A. et al. An iris diaphragm mechanism to gate a cyclic nucleotide-gated ion channel. *Nat. Commun.* **9**, 3978 (2018).

[ADS](#) [PubMed](#) [PubMed Central](#) [Google Scholar](#)

48. 48.

Chadda, R. et al. The dimerization equilibrium of a ClC Cl⁻/H⁺ antiporter in lipid bilayers. *eLife* **5**, e17438 (2016).

[PubMed](#) [PubMed Central](#) [Google Scholar](#)

49. 49.

Burger, W. & Burge, M. J. *Digital Image Processing: An Algorithmic Introduction Using Java* (Springer, 2016).

50. 50.

Fukuma, T. & Garcia, R. Atomic- and molecular-resolution mapping of solid–liquid interfaces by 3D atomic force microscopy. *ACS Nano* **12**, 11785–11797 (2018).

[CAS](#) [PubMed](#) [Google Scholar](#)

51. 51.

Lee, B. & Richards, F. M. The interpretation of protein structures: estimation of static accessibility. *J. Mol. Biol.* **55**, 379–400 (1971).

[CAS](#) [PubMed](#) [Google Scholar](#)

52. 52.

Scheres, S. H. W. Semi-automated selection of cryo-EM particles in RELION-1.3. *J. Struct. Biol.* **189**, 114–122 (2015).

[ADS](#) [CAS](#) [PubMed](#) [PubMed Central](#) [Google Scholar](#)

53. 53.

Bustamante, C. & Keller, D. Scanning force microscopy in biology. *Phys. Today* **48**, 32–38 (1995).

[ADS](#) [Google Scholar](#)

54. 54.

Olsson, M. H. M., Sondergaard, C. R., Rostkowski, M. & Jensen, J. H. PROPKA3: consistent treatment of internal and surface residues in empirical pKa predictions. *J. Chem. Theory Comput.* **7**, 525–537 (2011).

[CAS](#) [PubMed](#) [Google Scholar](#)

55. 55.

Lomize, M. A., Lomize, A. L., Pogozheva, I. D. & Mosberg, H. I. OPM: orientations of proteins in membranes database. *Bioinformatics* **22**, 623–625

(2006).

[CAS](#) [PubMed](#) [Google Scholar](#)

56. 56.

Jo, S., Lim, J. B., Klauda, J. B. & Im, W. CHARMM-GUI membrane builder for mixed bilayers and its application to yeast membranes. *Biophys. J.* **97**, 50–58 (2009).

[ADS](#) [CAS](#) [PubMed](#) [PubMed Central](#) [Google Scholar](#)

57. 57.

Phillips, J. C. et al. Scalable molecular dynamics with NAMD. *J. Comput. Chem.* **26**, 1781–1802 (2005).

[CAS](#) [PubMed](#) [PubMed Central](#) [Google Scholar](#)

58. 58.

Khelashvili, G. et al. Spontaneous inward opening of the dopamine transporter is triggered by pip-regulated dynamics of the N-terminus. *ACS Chem. Neurosci.* **6**, 1825–1837 (2015).

[CAS](#) [PubMed](#) [PubMed Central](#) [Google Scholar](#)

59. 59.

Essmann, U. et al. A smooth particle mesh Ewald method. *J. Chem. Phys.* **103**, 8577–8593 (1995).

[ADS](#) [CAS](#) [Google Scholar](#)

60. 60.

Evans, D. J. & Holian, B. L. The Nose–Hoover thermostat. *J. Chem. Phys.* **83**, 4069–4074 (1985).

[ADS](#) [CAS](#) [Google Scholar](#)

61. 61.

Harvey, M., Giupponi, G. & De Fabritiis, G. ACEMD: accelerated molecular dynamics simulations in the microseconds timescale. *J. Chem. Theory Comput.* **5**,

1632–1639 (2009).

[CAS](#) [PubMed](#) [Google Scholar](#)

62. 62.

Van Der Spoel, D. et al. GROMACS: fast, flexible, and free. *J. Comput. Chem.* **26**, 1701–1718 (2005).

[Google Scholar](#)

63. 63.

Duan, Y. et al. A point-charge force field for molecular mechanics simulations of proteins based on condensed-phase quantum mechanical calculations. *J. Comput. Chem.* **24**, 1999–2012 (2003).

[CAS](#) [PubMed](#) [Google Scholar](#)

64. 64.

Emsley, P. & Cowtan, K. Coot: model-building tools for molecular graphics. *Acta Crystallogr. D* **60**, 2126–2132 (2004).

[PubMed](#) [Google Scholar](#)

65. 65.

Jorgensen, W. L., Chandrasekhar, J., Madura, J. D., Impey, R. W. & Klein, M. L. Comparison of simple potential functions for simulating liquid water. *J. Chem. Phys.* **79**, 926–935 (1983).

[ADS](#) [CAS](#) [Google Scholar](#)

66. 66.

Bussi, G., Donadio, D. & Parrinello, M. Canonical sampling through velocity rescaling. *J. Chem. Phys.* **126**, 014101 (2007).

[ADS](#) [PubMed](#) [Google Scholar](#)

[Download references](#)

Acknowledgements

This work was supported by grants from the National Institute of Health, NIH, DP1AT010874 (to S.S.) and R01GM120260 (to J.L.R.). We thank A. Razavi for help with the initial stages of the MD simulation analysis and for discussions. The computational work was performed using resources of the Oak Ridge Leadership Computing Facility (allocation BIP109 and Director's Discretionary) at the Oak Ridge National Laboratory, which is a DOE Office of Science User Facility supported under contract DE-AC05-00OR22725; resources and support provided at the RPI Artificial Intelligence Multiprocessing Optimized System (AiMOS) system, accessed through an award from the COVID-19 HPC Consortium (<https://covid19-hpc-consortium.org/>); and the computational resources of the David A. Cofrin Center for Biomedical Information in Institute for Computational Biomedicine at Weill Cornell Medical College. Support from the 1923 Fund is gratefully acknowledged.

Author information

Author notes

1. George R. Heath

Present address: School of Physics and Astronomy, University of Leeds, Leeds, UK

Affiliations

1. Department of Anesthesiology, Weill Cornell Medicine, New York, NY, USA

George R. Heath, Shifra Lansky & Simon Scheuring

2. Department of Physiology and Biophysics, Weill Cornell Medicine, New York, NY, USA

Ekaterina Kots, George Khelashvili, Harel Weinstein & Simon Scheuring

3. Department of Biochemistry and Molecular Biophysics, Washington University, St. Louis, MO, USA

Janice L. Robertson

Authors

1. George R. Heath

[View author publications](#)

You can also search for this author in [PubMed](#) [Google Scholar](#)

2. Ekaterina Kots

[View author publications](#)

You can also search for this author in [PubMed](#) [Google Scholar](#)

3. Janice L. Robertson

[View author publications](#)

You can also search for this author in [PubMed](#) [Google Scholar](#)

4. Shifra Lansky

[View author publications](#)

You can also search for this author in [PubMed](#) [Google Scholar](#)

5. George Khelashvili

[View author publications](#)

You can also search for this author in [PubMed](#) [Google Scholar](#)

6. Harel Weinstein

[View author publications](#)

You can also search for this author in [PubMed](#) [Google Scholar](#)

7. Simon Scheuring

[View author publications](#)

You can also search for this author in [PubMed](#) [Google Scholar](#)

Contributions

G.R.H. and S.S. designed the study and developed the LAFM algorithm; J.L.R. purified and reconstituted the CLC-ec1. G.R.H. and S.L. performed HS-AFM experiments. E.K. and G.K. performed CLC MD simulations. S.L. performed A5 P13W-G14W cloning, expression, purification and MD simulations. G.R.H., E.K., G.K., H.W. and S.S. analysed the data. G.R.H., E.K., J.L.R, G.K., H.W. and S.S. wrote the paper.

Corresponding author

Correspondence to [Simon Scheuring](#).

Ethics declarations

Competing interests

The authors declare no competing interests.

Additional information

Peer review information *Nature* thanks Franz J. Giessibl, Victor Shahin and the other, anonymous, reviewer(s) for their contribution to the peer review of this work.

Publisher's note Springer Nature remains neutral with regard to jurisdictional claims in published maps and institutional affiliations.

Extended data figures and tables

[Extended Data Fig. 1 Localization principles in PALM and LAFM.](#)

a, A diffraction-limited image/profile of two fluorescent molecules located at a separation distance smaller than the diffraction limit. **b–d**, Spatially resolved positions of the fluorophores after application of optical localization methods such as PALM or STORM. The position of each fluorophore can be spatially localized with high precision if the emitted signal can be isolated from neighbouring fluorophores, permitted by stochastic activation of the right (**c**) or left (**d**) fluorophore. **e**, A tip-convoluted AFM image of two structural features located at a separation distance smaller than the sharpness of the AFM tip. **f–h**, Spatially resolved positions of structural features after application of LAFM. Stochastic height fluctuations allow the position of each feature to be localized by the protruding height signal of the right (**g**) or left (**h**) feature peaking over the neighbouring features. In **a–h**, top panels show 2D intensity/topography

images and bottom panels show intensity/height profiles across the central x line of the top panels. **i**, **j**, LAFM false-colour scale used to encode topography and localization peaking probability information. **i**, The LAFM map is encoded by a false-colour scale in which red (R), green (G) and blue (B) values follow the relations: $R(h) = -h^2/255 + 2h - 2$; $G(h) = Rh/255$; $B(h) = h\{\sin[0.036(h + 127)] + 1\}/2$, where h is the topography scale and RGB values range between 0 and 255 (minimum to maximum). The ratio of green to red (G/R) increases linearly with height (dashed line), whereas the blue value increases and oscillates to produce a visually informative false-colour scale. **j**, To incorporate the probability, each picked location is given a Gaussian probability density function that peaks at value 1. To generate the final LAFM map, the peaks of all molecules are merged, and thus an average topography height and related peaking probability (grey scale; bottom) at any location is calculated, resulting in a 2D false-colour table in which each pixel carries the full information about topography and the likeliness of a topography to be detected at this location.

Extended Data Fig. 2 Simulations of varying cleft height and cleft width, and detection of features in varying topographic superstructures by the LAFM algorithm.

a, Example average surface topography (top) and peaking probability (bottom) for 24, 8 and 2 pixels cleft width and cleft heights of 0, 90 and 100%. At a separation of 2 pixels (cleft width), averaging is unable to detect any topography change as the cleft height is changed, because the tip never probes into the cleft. In contrast, the LAFM method reports lower peaking probabilities in this region separating the two features. The detection probability in the cleft areas depends on the tip radius, feature separation and height fluctuation, and is therefore not linear. The height detection in the cleft areas is the same as the topography (see Fig. 1b). **b**, Surface plot showing the peaking probability in the cleft region relative to the pillar positions for varying cleft heights and widths. In the simulations the tip radius is 20 pixels and each surface feature pixel has feature fluctuation standard deviation of 0.3, and fluctuations are independent of neighbouring pixels. **c**, Peak detection of surface features on Gaussian curved surfaces. Features are 2 pixels wide interspersed by 2 pixels multiplied by Gaussian functions with $\sigma = 10, 20, 40$ and a flat surface, respectively, scanned by a

tip with a radius of 20 pixels (noise, 0.3). **d, e**, Surface plots of the height of the model surface (**d**) and the relative peaking probability compared to the probability at the central peak (**e**) for each Gaussian surface topography up to a distance of 8 peaks from the central peak. The probability of peak detection is affected by neighbouring peaks and tip radius, leading to a correct representation of the height, but a nonlinear relation between surface height and peaking probability. There is little to no lateral error of localization position detection on peaks of different local height.

Extended Data Fig. 3 Simulations of feature detection with varying topographic height by the LAFM algorithm.

a, Schematic of two sharp features in which the feature separation, d , and height difference, Δh , are varied by changing the position/height of the secondary feature. Feature fluctuations are then simulated by adding or subtracting a randomly generated height (normally distributed), f , with a set standard deviation, f_{sd} , before being scanned by a model AFM tip of radius R . **b**, Example simulations of topographies with $d = 4$, $\Delta h = 1$ (top) and $d = 10$, $\Delta h = 3$ (bottom), scanned by a tip with a radius $R = 20$, for varying amounts of feature fluctuation from left to right ($f_{\text{sd}} = 0, 0.1, 0.3$ and 0.6). Coloured lines are three representative simulated topography traces and thick grey lines show the average scanned topography ($n = 2,000$). Panels above each topography plot give the LAFM peaking probability at each position in the topography. **c**, Matrix of simulations plotted as an image in which each pixel represents the LAFM peaking probability of the secondary feature for a different height difference–separation distance combination. The black pixels indicate zero probability and therefore no peak detection. Also plotted are the theoretical resolution limits according to geometrical arguments allowing the apex of the tip to contact the feature (see [Methods](#) section ‘LAFM simulations’) and the average AFM maximum resolution, according to whether a local maximum can be detected for the secondary feature in the average topography. **d**, Lateral position of peaking probability for the different height difference–separation distance combinations. Each coloured line represents a different lateral separation and error bars show the peak width ($\pm \text{s.d.}$). **e**, Matrix of simulations plotted as an image in which each pixel represents the difference between the detected LAFM

average height and the model height for each height difference–separation distance combination. In **c–e**, each row from top to bottom represents a different feature fluctuation standard deviation of 0, 0.1, 0.3 and 0.6. For each fluctuation level, 286 Δh – d combinations were each simulated 2,000 times.

Extended Data Fig. 4 Simulations to assess the ability to resolve two spatial features in LAFM maps.

a–e, A tip with varying tip radius r (here 100 pixels) is scanned over two different simulation surfaces featuring topographic lines (**b**) or topographic points (**c**). These lines and points have a size of 1 pixel in the x , y and z directions, and are interspaced by 1, 2, 3, 4 and 5 pixels. This procedure, including sample fluctuations and contouring noise, results in individual simulated topography images for the line topography (**d**) and the point topography (**e**) that are either averaged or analysed using the LAFM algorithm (average AFM and LAFM maps result from merging 2,000 simulated topographies). **f**, Surface plot of the simulated LAFM map resolution determined by FRC as a function of the number of merged images and simulation tip radius, showing that when \sim 100 particles are analysed, features of size \sim 1/40 (for a blunt tip) to \sim 1/5 (for a sharp tip) of the tip radius can be resolved.

Extended Data Fig. 5 Influence of tip radius and number of merged particles for the calculation of LAFM maps.

First column: simulation experiments in which the surface topography (S) with a ring diameter of 35 pixels (top) is probed by five different tips, four spherical tips with increasing radius (1–4, $R = 10, 100, 300, 600$) and an irregular tip with a ‘double-tip’ protrusion ($R = 40$, peak to peak = 12 pixels). Second column: simulated individual raw data images (comprising random noise) of the topography (S) contoured by the various tips. Third column: average image of 500 simulated images. Fourth column: LAFM map derived from the same 500 simulated images. The numbers in the top right corner of each image are the normalized cross-correlation values (CCV [0,1]) between the image and the surface model. The graphs

show the dependence of the CCV between average or LAFM maps with the topography as a function of the number of merged particles. In the case of the sharpest tip (top row), the LAFM map CCV plateaus after merging \sim 50 molecules. Right: analysis of localization map image quality and CCV for the largest tip (4) when merging up to 10,000 particles. In the case of the bluntest tip, the LAFM map CCV plateaus after merging \sim 500 particles.

Extended Data Fig. 6 Resolution comparison between averaging, peak probability and LAFM methods applied to AFM images of AqpZ.

a, b, Average AFM images at the original pixel sampling of 3.3 Å per pixel (**a**) and after bicubic interpolation to 0.5 Å per pixel (**b**). **c, d**, Peak probability maps²⁰ calculated at the original pixel sampling of 3.3 Å per pixel (**c**) and after bicubic interpolation to 0.5 Å per pixel (**d**) ($n = 128$ for average height and probability maps). **e–g**, LAFM probability maps calculated at 0.5 Å per pixel with 1.4-Å Gaussian peaking probability distribution using 128 AqpZ particles with highest correlation to the average map (**e**) or using two randomly generated independent 128-particle sets from a set of 256 to create two independent half-maps (**f, g**). **h, i**, Line profiles along arrow 1 (**h**) and arrow 2 (**i**) in **b** and **g**, measuring height (for average AFM images) and probability across structural features in the average AFM, probability and LAFM probability maps. The features in the two line profiles are consistently resolved near and below the highest theoretical resolution based on the discrete sampling of a single image (raw data Nyquist frequency is $1/(6.6 \text{ \AA})$). **j**, Left: alignment of the nine available AqpZ X-ray structures. The structures can be grouped with respect to the side-chain orientation of E31 in the a-loop. Middle: surface representation overlay of 1RC2 and 2ABM, highlighting how the different E31 rotamers alter the surface structure. Right: representative structures (top) and surface representations (bottom) of 1RC2 and 2ABM. The 2ABM structure features an E31 conformation that fits closely the reconstructed LAFM map (**g** and Fig. 2a, b), suggesting that in the membrane, physiological buffer and room-temperature E31 is in a conformation similar to the 2ABM structure.

Extended Data Fig. 7 LAFM map resolution and quality assessment.

a, b, AFM image frames of AqpZ (**a**) and A5 (**b**) are alternately extracted into two separate image sets (Set A and Set B). The LAFM algorithm is then applied to each image set to produce two independent LAFM half-maps of AqpZ (left) and A5 (right). FRC analysis of the LAFM half-maps is then used for quantification of the power as a function of the spatial resolution in the AqpZ dataset (left) and A5 (right). Dashed and dotted lines show the 1/2-bit and 3σ criteria, respectively. **c**, Image from an HS-AFM video of A5 in a *p*6 lattice (centre), showing that the A5 lattice contains trimers of two fixed orientations labelled U and D. The two A5 trimer types U and D are scanned with different relative orientation with respect to the HS-AFM fast-scan axis. Extracted images of the trimers in each of the two orientations are shown on either side for set U (up; left) and set D (down; right). **d**, Average AFM and LAFM maps filtered to 5 Å of A5 trimers in the U ($n = 700$) and D ($n = 697$) orientations. **e**, Structural comparison between LAFM maps obtained from the independent differently orientated A5 and the probability difference map (image U has been rotated 180° to allow direct comparison). **f**, Analysis of A5 P13W-G14W mutant (data acquisition: A5 P13W-G14W on a DOPC/DOPS (1/1) bilayer imaged by HS-AFM in amplitude modulation mode; scan speed, 1 frame per second; scan area, 120 nm; image size, 300 pixels; pixel sampling, 4.0 Å per pixel). Average AFM map (left), LAFM map (middle; pixel sampling, 0.5 Å per pixel; number of particles $n = 300$, filtered to 4.5 Å) and surface representations of an A5 P13W-G14W structural model. **g**, Detail views of the LAFM maps (top) and structures (bottom; MD-refined structural model of A5 P13W-G14W and X-ray structure of A5). The mutations appear to induce conformational rearrangements in the N-terminal region (residues 1 to 15), with an increased height and peaking probability at positions 13–14 in the LAFM map. **h**, FRC analysis of the A5 P13W-G14W LAFM map.

Extended Data Fig. 8 Extracellular sidedness assignment of CLC-ec1.

a, b, HS-AFM video frames of CLC-ec1 in a POPE:POPG (ratio of 2:1 w-w) bilayer: molecules protruding just a little and S-shaped molecules protruding farther from the membrane were detected. **c**, Section analysis of the two molecules shown in **b**: one molecular species protrudes only ~4 Å from the bilayer, whereas the S-shaped representation of the CLC-ec1 protrudes ~11 Å from the membrane surface. **d, e**, Surface representations of the intracellular (**d**) and extracellular (**e**) faces of the X-ray structure (PDB 1OTS). Based on the structural comparison, we assigned the S-shaped CLC-ec1 HS-AFM topography to the extracellular face. Only the S-shaped extracellular-face molecules were integrated into the LAFM analysis. **f**, Alignment of CLC-ec1 X-ray structures (PDB: 1OTS, 2FEE, 2H2P, 3DET, 2HTK, 4KKB) exhibiting essentially identical conformations, leading to the suggestion that the transport mechanism implicates only minor side-chain motion. NMR, computational and biochemical studies have suggested larger-scale movements of helices N³⁹, O³⁸ and B³⁷ in transport. Protruding residues detectable by LAFM are shown in sticks and are labelled. **g**, Root-mean-square fluctuations (RMSF) of the backbone (left) and the side-chain (right) atoms of membrane-protruding extracellular CLC-ec1 residues from the analysis of MD trajectories at pH 7. The coloured blocks demarcate the groups of residues attributed to the four major LAFM and MD population map peaks, and the key residues are labelled. **h**, Key residues contributing to the peak observations in LAFM maps in the PDB 1OTS structure (middle and top right panels). The black shadowed plane illustrates the average position of the lipid phosphate atoms throughout the MD trajectories and thus represents the membrane level. Surrounding images (labelled 1 to 4) show representative snapshots from MD simulations highlighting re-orientations/fluctuations of the side chains of the residues contributing to the LAFM-detected peaks.

[Extended Data Fig. 9 Analysis of the influence of the 2D Gaussian radius to the peaking events and data pre-filtering on LAFM map reconstruction.](#)

Horizontal panels show reconstructed AqpZ LAFM maps of peaking detections with varying 2D Gaussian radii of 0.7 Å, 1.4 Å, 2.8 Å, 4.2 Å and 5.6 Å (without any pre-processing Gaussian filtering). The vertical panels show reconstructed AqpZ LAFM maps of images pre-processed with

varying Gaussian filters of 0 Å, 1 Å, 2 Å, 3 Å and 4 Å while varying the peaking detection 2D Gaussian radius. The comparison shows that applying a filter to the data before applying the LAFM method results in a loss of information, particularly from features that are smaller or of lower height. Whereas increasing the 2D Gaussian radius applied to each localization during the LAFM method results in a loss of lateral resolution in the reconstructed LAFM map. Highlighted in red is our standard method for constructing LAFM maps, using no pre-filtering and a peaking detection 2D Gaussian of 1.4 Å, approximating the solvent-accessible surface of atoms.

Extended Data Table 1 Set of available PDB structures of CLC-ec1 at various conditions

[Full size table](#)

Supplementary information

Supplementary Information

This file contains the localization atomic force microscopy ImageJ code, LAFM LUT colour scale and MATLAB code to simulate topography fluctuations.

Supplementary Video 1

MD simulation video of CLC-ec1 fluctuation trajectories. The video shows CLC-ec1 viewed in the plane of the membrane at pH 7. Protruding extracellular residues attributed to the four major LAFM and MD population map peaks are colored in blue (His73), orange (Asn327), magenta (Asp240, Lys243, Ser 245) and yellow (Gln381, His383).

Supplementary Video 2

Example simulated AFM videos of single pixel lines and single point functions for a tip radius of 100.

Supplementary Video 3

Aligned contact mode AFM video of AqpZ (left) with corresponding LAFM picked heights (middle left), symmetrized cumulative LAFM map (middle right), and X-ray structure surface (right). AFM image parameters: frame size: 10 nm, image capture: 3 pixels/nm, scan speed: 6.8 lines/s.

Supplementary Video 4

HS-AFM video of annexin A5 trimers (left) with corresponding LAFM picked heights (middle left), symmetrized cumulative LAFM map (middle right) and X-ray structure surface (right). HS-AFM video parameters: frame size: 19 nm, image capture: 4 pixels/nm, scan speed: 1 frame/s.

Supplementary Video 5

HS-AFM videos of CLC-ec1 in a POPE:POPG bilayer at 400nm. From left to right: Video 1 parameters: frame size: 400 nm, image capture: 0.75 pixels/nm, scan speed: 1 frame/s. Video 2 parameters: frame size: 240 nm, image capture: 1.25 pixels/nm, scan speed: 1 frame/s. Video 3 parameters: frame size: 120 nm, image capture: 1.67 pixels/nm, scan speed: 1 frame/s. Monomers, dimers and tetramers (dimers-of-dimers) are observed. Video 4 parameters: frame size: 40 nm, image capture: 7.5 pixels/nm, scan speed: 1 frame/s. Structural features and rotational dynamics are observed.

Supplementary Video 6

HS-AFM video of CLC-ec1(left), with corresponding LAFM picked heights (middle left) and symmetrized cumulative LAFM map (middle right) and X-ray structure surface (right). HS-AFM video parameters: frame size: 30 nm, image capture: 10 pixels/nm, scan speed: 5.56 frame/s.

Supplementary Video 7

‘Difference morphing’ between the CLC-ec1 pH 7.6 (red) and pH 4.5 (blue) LAFM maps.

Rights and permissions

[Reprints and Permissions](#)

About this article



Check for
updates

Cite this article

Heath, G.R., Kots, E., Robertson, J.L. *et al.* Localization atomic force microscopy. *Nature* **594**, 385–390 (2021). <https://doi.org/10.1038/s41586-021-03551-x>

[Download citation](#)

- Received: 20 December 2019
- Accepted: 13 April 2021
- Published: 16 June 2021
- Issue Date: 17 June 2021
- DOI: <https://doi.org/10.1038/s41586-021-03551-x>

Comments

By submitting a comment you agree to abide by our [Terms](#) and [Community Guidelines](#). If you find something abusive or that does not comply with our terms or guidelines please flag it as inappropriate.

[Download PDF](#)

Advertisement

This article was downloaded by **calibre** from <https://www.nature.com/articles/s41586-021-03551-x>

| [Section menu](#) | [Main menu](#) |

- Article
- [Published: 16 June 2021](#)

Global prevalence of non-perennial rivers and streams

- [Mathis Loïc Messager](#) [ORCID: orcid.org/0000-0002-3051-8068](#)^{1,2},
- [Bernhard Lehner](#) [ORCID: orcid.org/0000-0003-3712-2581](#)¹,
- [Charlotte Cockburn](#) [ORCID: orcid.org/0000-0001-8608-0192](#)¹ nAff7,
- [Nicolas Lamouroux](#) [ORCID: orcid.org/0000-0002-9184-2558](#)²,
- [Hervé Pella](#) [ORCID: orcid.org/0000-0003-2715-0677](#)²,
- [Ton Snelder](#) [ORCID: orcid.org/0000-0002-2330-4563](#)³,
- [Klement Tockner](#)^{4,5},
- [Tim Trautmann](#)⁶,
- [Caitlin Watt](#) [ORCID: orcid.org/0000-0002-8439-9463](#)¹ nAff8 &
- [Thibault Datry](#) [ORCID: orcid.org/0000-0003-1390-6736](#)²

[Nature](#) volume 594, pages 391–397 (2021) [Cite this article](#)

- 2405 Accesses
- 499 Altmetric
- [Metrics details](#)

Subjects

- [Geography](#)
- [Hydrology](#)
- [Limnology](#)
- [Water resources](#)

Abstract

Flowing waters have a unique role in supporting global biodiversity, biogeochemical cycles and human societies^{1,2,3,4,5}. Although the importance of permanent watercourses is well recognized, the prevalence, value and fate of non-perennial rivers and streams that periodically cease to flow tend to be overlooked, if not ignored^{6,7,8}. This oversight contributes to the degradation of the main source of water and livelihood for millions of people⁵. Here we predict that water ceases to flow for at least one day per year along 51–60 per cent of the world’s rivers by length, demonstrating that non-perennial rivers and streams are the rule rather than the exception on Earth. Leveraging global information on the hydrology, climate, geology and surrounding land cover of the Earth’s river network, we show that non-perennial rivers occur within all climates and biomes, and on every continent. Our findings challenge the assumptions underpinning foundational river concepts across scientific disciplines⁹. To understand and adequately manage the world’s flowing waters, their biodiversity and functional integrity, a paradigm shift is needed towards a new conceptual model of rivers that includes flow intermittence. By mapping the distribution of non-perennial rivers and streams, we provide a stepping-stone towards addressing this grand challenge in freshwater science.

Access options

Subscribe to Journal

Get full journal access for 1 year

\$199.00

only \$3.90 per issue

[Subscribe](#)

All prices are NET prices.
VAT will be added later in the checkout.

Tax calculation will be finalised during checkout.

Rent or Buy article

Get time limited or full article access on ReadCube.

from \$8.99

[Rent or Buy](#)

All prices are NET prices.

Additional access options:

- [Log in](#)
- [Access through your institution](#)
- [Learn about institutional subscriptions](#)

Fig. 1: Global distribution of non-perennial rivers and streams.

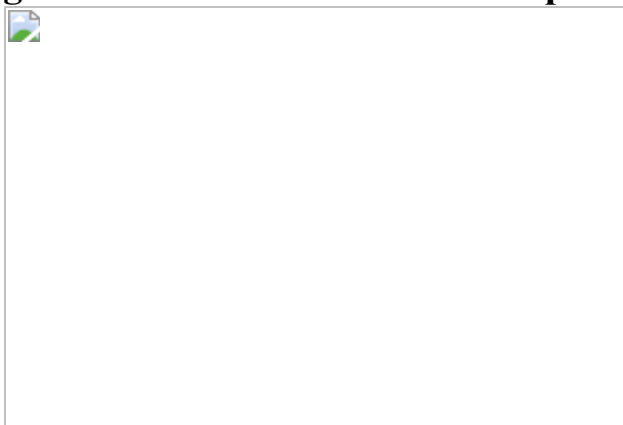


Fig. 2: Climate-induced aridity and hydrologic variables are the main predictors of global flow intermittence.

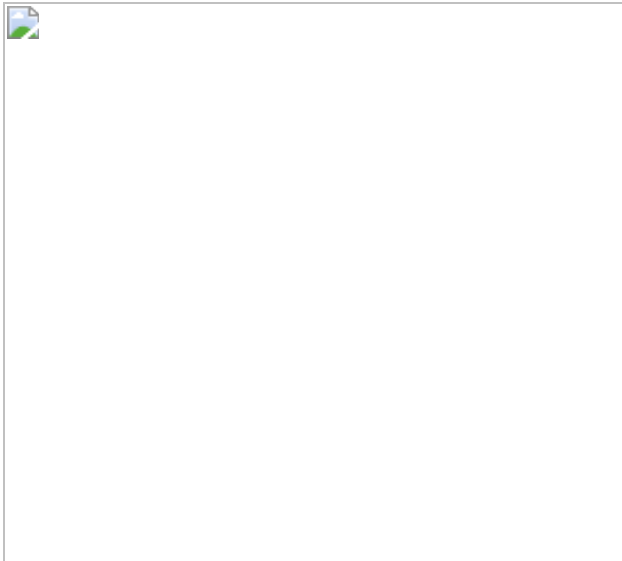
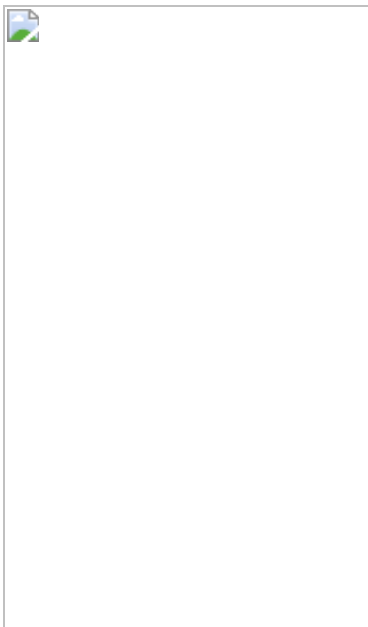


Fig. 3: Flow intermittence classification accuracy decreases and prediction bias increases in river basins with fewer streamflow gauging stations.



Data availability

The global river network dataset and the associated attribute information for every river reach—that is, the hydro-environmental attributes, predicted probability of intermittence and associated binary class—as well as the main results of the study are available at

<https://doi.org/10.6084/m9.figshare.14633022>. The dataset can be used

together with the published source code (see ‘Code availability’) to recalculate the main study results with updated data and parameters. The streamflow time series from the Global Runoff Data Centre are available in summarized format. The daily records are not available in the data repository owing to licensing issues but are freely available upon written request through

https://www.bafg.de/GRDC/EN/Home/homepage_node.html. Original data that supported the study are freely available and their sources are summarized in Extended Data Fig. 7b. [Source data](#) are provided with this paper.

Code availability

The source code and results of this research are available under the GNU General Public License v3.0 at <https://messamat.github.io/globalIRmap/>.

References

1. 1.

Larned, S. T., Datry, T., Arscott, D. B. & Tockner, K. Emerging concepts in temporary-river ecology. *Freshw. Biol.* **55**, 717–738 (2010).

[Google Scholar](#)

2. 2.

Leigh, C. & Datry, T. Drying as a primary hydrological determinant of biodiversity in river systems: a broad-scale analysis. *Ecography* **40**, 487–499 (2017).

[Google Scholar](#)

3. 3.

Datry, T. et al. A global analysis of terrestrial plant litter dynamics in non-perennial waterways. *Nat. Geosci.* **11**, 497–503 (2018).

[ADS](#) [CAS](#) [Google Scholar](#)

4. 4.

Marcé, R. et al. Emissions from dry inland waters are a blind spot in the global carbon cycle. *Earth Sci. Rev.* **188**, 240–248 (2019).

[ADS](#) [Google Scholar](#)

5. 5.

Steward, A. L., von Schiller, D., Tockner, K., Marshall, J. C. & Bunn, S. E. When the river runs dry: human and ecological values of dry riverbeds. *Front. Ecol. Environ.* **10**, 202–209 (2012).

[Google Scholar](#)

6. 6.

Acuña, V. et al. Why should we care about temporary waterways? *Science* **343**, 1080–1081 (2014).

[ADS](#) [PubMed](#) [PubMed Central](#) [Google Scholar](#)

7. 7.

Fritz, K., Cid, N. & Autrey, B. Governance, legislation, and protection of intermittent rivers and ephemeral streams. In *Intermittent Rivers and Ephemeral Streams: Ecology and Management* 477–507 (Academic Press, 2017); <https://doi.org/10.1016/B978-0-12-803835-2.00019-X>.

8. 8.

Sullivan, S. M. P., Rains, M. C., Rodewald, A. D., Buzbee, W. W. & Rosemond, A. D. Distorting science, putting water at risk. *Science*

369, 766–768 (2020).

[ADS](#) [CAS](#) [PubMed](#) [PubMed Central](#) [Google Scholar](#)

9. 9.

Allen, D. C. et al. River ecosystem conceptual models and non-perennial rivers: a critical review. *Wiley Interdiscip. Rev. Water* **7**, e1473 (2020).

[Google Scholar](#)

10. 10.

Datry, T., Larned, S. T. & Tockner, K. Intermittent rivers: a challenge for freshwater ecology. *Bioscience* **64**, 229–235 (2014).

[Google Scholar](#)

11. 11.

Ficklin, D. L., Abatzoglou, J. T., Robeson, S. M., Null, S. E. & Knouft, J. H. Natural and managed watersheds show similar responses to recent climate change. *Proc. Natl Acad. Sci. USA* **115**, 8553–8557 (2018).

[ADS](#) [CAS](#) [PubMed](#) [PubMed Central](#) [Google Scholar](#)

12. 12.

Jaeger, K. L., Olden, J. D. & Pelland, N. A. Climate change poised to threaten hydrologic connectivity and endemic fishes in dryland streams. *Proc. Natl Acad. Sci. USA* **111**, 13894–13899 (2014).

[ADS](#) [CAS](#) [PubMed](#) [PubMed Central](#) [Google Scholar](#)

13. 13.

Pumo, D., Caracciolo, D., Viola, F. & Noto, L. V. Climate change effects on the hydrological regime of small non-perennial river basins. *Sci. Total Environ.* **542**, 76–92 (2016).

[ADS](#) [CAS](#) [PubMed](#) [PubMed Central](#) [Google Scholar](#)

14. 14.

Stubbington, R. et al. Biomonitoring of intermittent rivers and ephemeral streams in Europe: current practice and priorities to enhance ecological status assessments. *Sci. Total Environ.* **618**, 1096–1113 (2018).

[ADS](#) [CAS](#) [PubMed](#) [PubMed Central](#) [Google Scholar](#)

15. 15.

Acuña, V. et al. Accounting for flow intermittency in environmental flows design. *J. Appl. Ecol.* **57**, 742–753 (2020).

[Google Scholar](#)

16. 16.

Arthington, A. H. et al. The Brisbane Declaration and Global Action Agenda on Environmental Flows (2018). *Front. Environ. Sci.* **6**, 45 (2018).

[Google Scholar](#)

17. 17.

Zimmer, M. A. et al. Zero or not? Causes and consequences of zero-flow stream gage readings. *Wiley Interdiscip. Rev. Water* **7**, e1436 (2020).

[Google Scholar](#)

18. 18.

Beaufort, A., Lamouroux, N., Pella, H., Datry, T. & Sauquet, E. Extrapolating regional probability of drying of headwater streams using discrete observations and gauging networks. *Hydrol. Earth Syst. Sci.* **22**, 3033–3051 (2018).

[ADS](#) [Google Scholar](#)

19. 19.

Jaeger, K. L. & Olden, J. D. Electrical resistance sensor arrays as a means to quantify longitudinal connectivity of rivers. *River Res. Appl.* **28**, 1843–1852 (2012).

[Google Scholar](#)

20. 20.

Yu, S. et al. Evaluating a landscape-scale daily water balance model to support spatially continuous representation of flow intermittency throughout stream networks. *Hydrol. Earth Syst. Sci.* **24**, 5279–5295 (2020).

[ADS](#) [CAS](#) [Google Scholar](#)

21. 21.

Snelder, T. H. et al. Regionalization of patterns of flow intermittence from gauging station records. *Hydrol. Earth Syst. Sci.* **17**, 2685–2699 (2013).

[ADS](#) [Google Scholar](#)

22. 22.

Jaeger, K. L. et al. Probability of Streamflow Permanence Model (PROSPER): a spatially continuous model of annual streamflow permanence throughout the Pacific Northwest. *J. Hydrol. X* **2**, 100005 (2019).

[Google Scholar](#)

23. 23.

Yu, S., Bond, N. R., Bunn, S. E. & Kennard, M. J. Development and application of predictive models of surface water extent to identify aquatic refuges in eastern Australian temporary stream networks. *Water Resour. Res.* **55**, 9639–9655 (2019).

[ADS](#) [Google Scholar](#)

24. 24.

Kennard, M. J. et al. Classification of natural flow regimes in Australia to support environmental flow management. *Freshw. Biol.* **55**, 171–193 (2010).

[Google Scholar](#)

25. 25.

Lane, B. A., Dahlke, H. E., Pasternack, G. B. & Sandoval-Solis, S. Revealing the diversity of natural hydrologic regimes in California with relevance for environmental flows applications. *J. Am. Water Resour. Assoc.* **53**, 411–430 (2017).

[ADS](#) [Google Scholar](#)

26. 26.

Müller Schmied, H. et al. Sensitivity of simulated global-scale freshwater fluxes and storages to input data, hydrological model structure, human water use and calibration. *Hydrol. Earth Syst. Sci.* **18**, 3511–3538 (2014).

[ADS](#) [Google Scholar](#)

27. 27.

Linke, S. et al. Global hydro-environmental sub-basin and river reach characteristics at high spatial resolution. *Sci. Data* **6**, 283 (2019).

[PubMed](#) [PubMed Central](#) [Google Scholar](#)

28. 28.

Tooth, S. Process, form and change in dryland rivers: a review of recent research. *Earth Sci. Rev.* **51**, 67–107 (2000).

[ADS](#) [Google Scholar](#)

29. 29.

Costigan, K. H., Jaeger, K. L., Goss, C. W., Fritz, K. M. & Goebel, P. C. Understanding controls on flow permanence in intermittent rivers to aid ecological research: integrating meteorology, geology and land cover. *Ecohydrology* **9**, 1141–1153 (2016).

[Google Scholar](#)

30. 30.

Benstead, J. P. & Leigh, D. S. An expanded role for river networks. *Nat. Geosci.* **5**, 678–679 (2012).

[ADS](#) [CAS](#) [Google Scholar](#)

31. 31.

Godsey, S. E. & Kirchner, J. W. Dynamic, discontinuous stream networks: hydrologically driven variations in active drainage density, flowing channels and stream order. *Hydrol. Processes* **28**, 5791–5803 (2014).

[ADS](#) [Google Scholar](#)

32. 32.

Metzger, M. J. et al. A high-resolution bioclimate map of the world: a unifying framework for global biodiversity research and monitoring. *Glob. Ecol. Biogeogr.* **22**, 630–638 (2013).

[Google Scholar](#)

33. 33.

Tolonen, K. E. et al. Parallels and contrasts between intermittently freezing and drying streams: From individual adaptations to biodiversity variation. *Freshw. Biol.* **64**, 1679–1691 (2019).

[Google Scholar](#)

34. 34.

Prancevic, J. P. & Kirchner, J. W. Topographic controls on the extension and retraction of flowing streams. *Geophys. Res. Lett.* **46**, 2084–2092 (2019).

[ADS](#) [Google Scholar](#)

35. 35.

FAO. *AQUAMAPS: Global Spatial Database on Water and Agriculture* (Food and Agriculture Organization of the United Nations, accessed 15 October 2020); <https://data.apps.fao.org/aquamaps/>

36. 36.

Schneider, A. et al. Global-scale river network extraction based on high-resolution topography and constrained by lithology, climate, slope, and observed drainage density. *Geophys. Res. Lett.* **44**, 2773–2781 (2017).

[ADS](#) [Google Scholar](#)

37. 37.

Raymond, P. A. et al. Global carbon dioxide emissions from inland waters. *Nature* **503**, 355–359 (2013); erratum **507**, 387 (2014).

[ADS](#) [CAS](#) [PubMed](#) [PubMed Central](#) [Google Scholar](#)

38. 38.

Tramblay, Y. et al. Trends in flow intermittence for European rivers. *Hydrol. Sci. J.* **66**, 37–49 (2021).

[Google Scholar](#)

39. 39.

Döll, P., Douville, H., Güntner, A., Müller Schmied, H. & Wada, Y. Modelling freshwater resources at the global scale: challenges and prospects. *Surv. Geophys.* **37**, 195–221 (2016).

[ADS](#) [Google Scholar](#)

40. 40.

Hammond, J. C. et al. Spatial patterns and drivers of nonperennial flow regimes in the contiguous United States. *Geophys. Res. Lett.* **48**, e2020GL090794 (2021).

[ADS](#) [Google Scholar](#)

41. 41.

Döll, P. & Schmied, H. M. How is the impact of climate change on river flow regimes related to the impact on mean annual runoff? A global-scale analysis. *Environ. Res. Lett.* **7**, 014037 (2012).

[ADS](#) [Google Scholar](#)

42. 42.

Gleeson, T. et al. The water planetary boundary: interrogation and revision. *One Earth* **2**, 223–234 (2020).

[Google Scholar](#)

43. 43.

Dickens, C. et al. *Incorporating Environmental Flows into “Water Stress” Indicator 6.4.2: Guidelines for a Minimum Standard Method for Global Reporting* (FAO, 2019);
<http://www.fao.org/documents/card/en/ca3097en/>

44. 44.

Sood, A. et al. *Global Environmental Flow Information for the Sustainable Development Goals*. IWMI Research Report 168 (International Water Management Institute, 2017);
<https://doi.org/10.5337/2017.201>

45. 45.

Vannote, R. L., Minshall, G. W., Cummins, K. W., Sedell, J. R. & Cushing, C. E. The River Continuum Concept. *Can. J. Fish. Aquat. Sci.* **37**, 130–137 (1980).

[Google Scholar](#)

46. 46.

Grill, G. et al. Mapping the world’s free-flowing rivers. *Nature* **569**, 215–221 (2019); correction **572**, E9 (2019).

[ADS](#) [CAS](#) [PubMed](#) [PubMed Central](#) [Google Scholar](#)

47. 47.

Stanley, E. H., Fisher, S. G. & Grimm, N. B. Ecosystem expansion and contraction in streams: desert streams vary in both space and time and fluctuate dramatically in size. *Bioscience* **47**, 427–435 (1997).

[Google Scholar](#)

48. 48.

Datry, T. et al. Flow intermittence and ecosystem services in rivers of the Anthropocene. *J. Appl. Ecol.* **55**, 353–364 (2018).

[PubMed](#) [PubMed Central](#) [Google Scholar](#)

49. 49.

Nembrini, S., König, I. R. & Wright, M. N. The revival of the Gini importance? *Bioinformatics* **34**, 3711–3718 (2018).

[CAS](#) [PubMed](#) [PubMed Central](#) [Google Scholar](#)

50. 50.

Lehner, B. & Grill, G. Global river hydrography and network routing: baseline data and new approaches to study the world's large river systems. *Hydrol. Processes* **27**, 2171–2186 (2013).

[ADS](#) [Google Scholar](#)

51. 51.

Lehner, B., Verdin, K. & Jarvis, A. New global hydrography derived from spaceborne elevation data. *Eos* **89**, 93–94 (2008).

[ADS](#) [Google Scholar](#)

52. 52.

Messager, M. L., Lehner, B., Grill, G., Nedeva, I. & Schmitt, O. Estimating the volume and age of water stored in global lakes using a geo-statistical approach. *Nat. Commun.* **7**, 13603 (2016).

[ADS](#) [CAS](#) [PubMed](#) [PubMed Central](#) [Google Scholar](#)

53. 53.

Global Runoff Data Centre. *In-situ river discharge data* (World Meteorological Organization, accessed 15 May 2015);
<https://portal.grdc.bafg.de/applications/public.html?publicuser=PublicUser#dataDownload/Home>

54. 54.

Do, H. X., Gudmundsson, L., Leonard, M. & Westra, S. The Global Streamflow Indices and Metadata Archive (GSIM) – Part 1: The production of a daily streamflow archive and metadata. *Earth Syst. Sci. Data* **10**, 765–785 (2018).

[ADS](#) [Google Scholar](#)

55. 55.

Gudmundsson, L., Do, H. X., Leonard, M. & Westra, S. The Global Streamflow Indices and Metadata Archive (GSIM) – Part 2: Quality control, time-series indices and homogeneity assessment. *Earth Syst. Sci. Data* **10**, 787–804 (2018).

[ADS](#) [Google Scholar](#)

56. 56.

Lehner, B. et al. High-resolution mapping of the world's reservoirs and dams for sustainable river-flow management. *Front. Ecol. Environ.* **9**, 494–502 (2011).

[Google Scholar](#)

57. 57.

Mackay, S. J., Arthington, A. H. & James, C. S. Classification and comparison of natural and altered flow regimes to support an Australian trial of the Ecological Limits of Hydrologic Alteration framework. *Ecohydrology* **7**, 1485–1507 (2014).

[Google Scholar](#)

58. 58.

Zhang, Y., Zhai, X., Shao, Q. & Yan, Z. Assessing temporal and spatial alterations of flow regimes in the regulated Huai River Basin, China. *J. Hydrol.* **529**, 384–397 (2015).

[ADS](#) [Google Scholar](#)

59. 59.

Reynolds, L. V., Shafroth, P. B. & LeRoy Poff, N. Modeled intermittency risk for small streams in the Upper Colorado River Basin under climate change. *J. Hydrol.* **523**, 768–780 (2015).

[ADS](#) [Google Scholar](#)

60. 60.

Costigan, K. H. et al. Flow regimes in intermittent rivers and ephemeral streams. In *Intermittent Rivers and Ephemeral Streams: Ecology and Management* 51–78 (Academic Press, 2017);
<https://doi.org/10.1016/B978-0-12-803835-2.00003-6>

61. 61.

Pickens, A. H. et al. Mapping and sampling to characterize global inland water dynamics from 1999 to 2018 with full Landsat time-series. *Remote Sens. Environ.* **243**, 111792 (2020).

[ADS](#) [Google Scholar](#)

62. 62.

Hengl, T. et al. SoilGrids250m: Global gridded soil information based on machine learning. *PLoS ONE* **12**, e0169748 (2017).

[PubMed](#) [PubMed Central](#) [Google Scholar](#)

63. 63.

Fick, S. E. & Hijmans, R. J. WorldClim 2: new 1-km spatial resolution climate surfaces for global land areas. *Int. J. Climatol.* **37**, 4302–4315 (2017).

[Google Scholar](#)

64. 64.

Trabucco, A. & Zomer, R. Global Aridity Index and Potential Evapotranspiration (ET0) Climate Database v2. figshare <https://doi.org/10.6084/m9.figshare.7504448.v3> (2018).

65. 65.

Bond, N. R. & Kennard, M. J. Prediction of hydrologic characteristics for ungauged catchments to support hydroecological modeling. *Water Resour. Res.* **53**, 8781–8794 (2017).

[ADS](#) [Google Scholar](#)

66. 66.

Kotsiantis, S. B., Zaharakis, I. D. & Pintelas, P. E. Machine learning: a review of classification and combining techniques. *Artif. Intell. Rev.* **26**, 159–190 (2006).

[Google Scholar](#)

67. 67.

Wainer, J. Comparison of 14 different families of classification algorithms on 115 binary datasets. Preprint at <https://arxiv.org/abs/1606.00930> (2016).

68. 68.

Malley, J. D., Kruppa, J., Dasgupta, A., Malley, K. G. & Ziegler, A. Probability machines. *Methods Inf. Med.* **51**, 74–81 (2012).

[CAS](#) [PubMed](#) [PubMed Central](#) [Google Scholar](#)

69. 69.

Wright, M. N. & Ziegler, A. ranger: a fast implementation of random forests for high dimensional data in C++ and R. *J. Stat. Softw.* **77**, <https://doi.org/10.18637/jss.v077.i01> (2017).

70. 70.

Lang, M. et al. mlr3: a modern object-oriented machine learning framework in R. *J. Open Source Softw.* **4**, 1903 (2019).

[ADS](#) [Google Scholar](#)

71. 71.

Landau, W. M. The drake R package: a pipeline toolkit for reproducibility and high-performance computing. *J. Open Source Softw.* **3**, 550 (2018).

[ADS](#) [Google Scholar](#)

72. 72.

Hothorn, T., Hornik, K. & Zeileis, A. Unbiased recursive partitioning: a conditional inference framework. *J. Comput. Graph. Stat.* **15**, 651–674 (2006).

[MathSciNet](#) [Google Scholar](#)

73. 73.

Hothorn, T. & Zeileis, A. Partykit: a modular toolkit for recursive partytioning in R. *J. Mach. Learn. Res.* **16**, 3905–3909 (2015).

[MathSciNet](#) [MATH](#) [Google Scholar](#)

74. 74.

Wright, M. N., Dankowski, T. & Ziegler, A. Unbiased split variable selection for random survival forests using maximally selected rank statistics. *Stat. Med.* **36**, 1272–1284 (2017).

[MathSciNet](#) [PubMed](#) [PubMed Central](#) [Google Scholar](#)

75. 75.

Zhang, G. & Lu, Y. Bias-corrected random forests in regression. *J. Appl. Stat.* **39**, 151–160 (2012).

[MathSciNet](#) [MATH](#) [Google Scholar](#)

76. 76.

Japkowicz, N. & Stephen, S. The class imbalance problem: a systematic study. *Intell. Data Anal.* **6**, 429–449 (2002).

[MATH](#) [Google Scholar](#)

77. 77.

Bischl, B., Mersmann, O., Trautmann, H. & Weihs, C. Resampling methods for meta-model validation with recommendations for evolutionary computation. *Evol. Comput.* **20**, 249–275 (2012).

[CAS](#) [PubMed](#) [PubMed Central](#) [Google Scholar](#)

78. 78.

Probst, P., Wright, M. N. & Boulesteix, A. L. Hyperparameters and tuning strategies for random forest. *Wiley Interdiscip. Rev. Data Min. Knowl. Discov.* **9**, e1301 (2019).

[Google Scholar](#)

79. 79.

Probst, P. & Boulesteix, A. L. To tune or not to tune the number of trees in random forest. *J. Mach. Learn. Res.* **18**, 1–8 (2018).

[MathSciNet](#) [MATH](#) [Google Scholar](#)

80. 80.

Schratz, P., Muenchow, J., Iturritxa, E., Richter, J. & Brenning, A. Hyperparameter tuning and performance assessment of statistical and machine-learning algorithms using spatial data. *Ecol. Modell.* **406**, 109–120 (2019).

[Google Scholar](#)

81. 81.

Brenning, A. Spatial cross-validation and bootstrap for the assessment of prediction rules in remote sensing: the R package sperrorest. In *2012 IEEE Int. Geoscience and Remote Sensing Symp. (IGARSS)* 5372–5375 (2012); <https://doi.org/10.1109/IGARSS.2012.6352393>

82. 82.

Meyer, H., Reudenbach, C., Hengl, T., Katurji, M. & Nauss, T. Improving performance of spatio-temporal machine learning models using forward feature selection and target-oriented validation. *Environ. Model. Softw.* **101**, 1–9 (2018).

[Google Scholar](#)

83. 83.

Meyer, H., Reudenbach, C., Wöllauer, S. & Nauss, T. Importance of spatial predictor variable selection in machine learning applications – moving from data reproduction to spatial prediction. *Ecol. Modell.* **411**, 108815 (2019).

[Google Scholar](#)

84. 84.

Brodersen, K. H., Ong, C. S., Stephan, K. E. & Buhmann, J. M. The balanced accuracy and its posterior distribution. In *Proc. Int. Conf. Pattern Recognition* 3121–3124 (2010);
<https://doi.org/10.1109/ICPR.2010.764>

85. 85.

Altmann, A., Tološi, L., Sander, O. & Lengauer, T. Permutation importance: a corrected feature importance measure. *Bioinformatics* **26**, 1340–1347 (2010).

[CAS](#) [PubMed](#) [PubMed Central](#) [Google Scholar](#)

86. 86.

Amaratunga, D., Cabrera, J. & Lee, Y.-S. Enriched random forests. *Bioinformatics* **24**, 2010–2014 (2008).

[CAS](#) [PubMed](#) [PubMed Central](#) [Google Scholar](#)

87. 87.

Evans, J. S., Murphy, M. A., Holden, Z. A. & Cushman, S. A. Modeling species distribution and change using random forest. In *Predictive Species and Habitat Modeling in Landscape Ecology: Concepts and Applications* 139–159 (Springer, 2011);
https://doi.org/10.1007/978-1-4419-7390-0_8

88. 88.

Jones, Z. M. & Linder, F. J. edarf: Exploratory Data Analysis using Random Forests. *J. Open Source Softw.* **1**, 92 (2016).

[ADS](#) [Google Scholar](#)

89. 89.

Friedman, J. H. Greedy function approximation: a gradient boosting machine. *Ann. Stat.* **29**, 1189–1232 (2001).

[MathSciNet](#) [MATH](#) [Google Scholar](#)

90. 90.

Bondarenko, M., Kerr, D., Sorichetta, A. & Tatem, A. J. *Census/projection-disaggregated gridded population datasets for 189 countries in 2020 using Built-Settlement Growth Model (BSGM) outputs* (WorldPop, University of Southampton, accessed 26 November 2020); <https://doi.org/10.5258/SOTON/WP00684>

91. 91.

Colvin, S. A. R. et al. Headwater streams and wetlands are critical for sustaining fish, fisheries, and ecosystem services. *Fisheries* **44**, 73–91 (2019).

[Google Scholar](#)

92. 92.

Hastie, T., Tibshirani, R. & Friedman, J. *The Elements of Statistical Learning: Data Mining, Inference, and Prediction* (Springer Science & Business Media, 2009).

93. 93.

Clauset, A., Shalizi, C. R. & Newman, M. E. J. Power-law distributions in empirical data. *SIAM Rev.* **51**, 661–703 (2009).

[ADS](#) [MathSciNet](#) [MATH](#) [Google Scholar](#)

94. 94.

Fritz, K. M. et al. Comparing the extent and permanence of headwater streams from two field surveys to values from hydrographic databases and maps. *J. Am. Water Resour. Assoc.* **49**, 867–882 (2013).

[ADS](#) [Google Scholar](#)

95. 95.

Stoddard, J. L. et al. *Environmental Monitoring and Assessment Program (EMAP): Western Streams and Rivers Statistical Summary*. Report no. EPA/620/R-05/006 (NTIS PB2007-102088) (US Environmental Protection Agency, 2005).

96. 96.

Hafen, K. C., Blasch, K. W., Rea, A., Sando, R. & Gessler, P. E. The influence of climate variability on the accuracy of NHD perennial and nonperennial stream classifications. *J. Am. Water Resour. Assoc.* **56**, 903–916 (2020).

[ADS](#) [Google Scholar](#)

97. 97.

Colson, T., Gregory, J., Dorney, J. & Russell, P. Topographic and soil maps do not accurately depict headwater stream networks. *Natl Wetlands Newsl.* **30**, 25–28 (2008).

[Google Scholar](#)

98. 98.

Allen, D. C. et al. Citizen scientists document long-term streamflow declines in intermittent rivers of the desert southwest, USA. *Freshw. Sci.* **38**, 244–256 (2019).

[Google Scholar](#)

99. 99.

Datry, T., Pella, H., Leigh, C., Bonada, N. & Hugueny, B. A landscape approach to advance intermittent river ecology. *Freshw. Biol.* **61**, 1200–1213 (2016).

[Google Scholar](#)

100. 100.

McShane, R. R., Sando, R. & Hockman-Wert, D. P. Streamflow observation points in the Pacific Northwest, 1977–2016. U.S. Geological Survey data release <https://doi.org/10.5066/F7BV7FSP> (2017).

101. 101.

Observatoire National des étiages (ONDE) (French Office for Biodiversity (OFC), accessed 21 June 2020);
<https://onde.eaufrance.fr/content/t%C3%A9l%C3%A9charger-les-donn%C3%A9es-des-campagnes-par-ann%C3%A9e>

102. 102.

Aguas Continentales de Argentina (Argentinian National Geographic Institute (IGN), accessed 11 June 2020);
<https://www.ign.gob.ar/NuestrasActividades/InformacionGeoespacial/CapasSIG>

103. 103.

Australian Hydrological Geospatial Fabric (Geofabric, v. 3.2) (Australian Bureau of Meteorology (BOM), accessed 11 June 2020);
ftp://ftp.bom.gov.au/anon/home/geofabric/Geofabric_Metadata_GDB_V3_2.zip

104. 104.

Base Cartográfica Continua do Brasil (BC250, 2019 version) (Brazilian Institute of Geography and Statistics (IBGE); accessed 11 June 2020);

https://geoftp.ibge.gov.br/cartas_e_mapas/bases_cartograficas_continuas/bc250/versao2019/

105. 105.

National Hydrography Dataset Plus (NHDPlus, medium resolution, v.2) (US Geological Survey, accessed 11 June 2020);
<https://www.epa.gov/waterdata/get-nhdplus-national-hydrography-dataset-plus-data>

106. 106.

Busch, M. H. et al. What's in a name? Patterns, trends, and suggestions for defining non-perennial rivers and streams. *Water* **12**, 1980 (2020).

[PubMed](#) [PubMed Central](#) [Google Scholar](#)

107. 107.

Datry, T. et al. Science and management of intermittent rivers and ephemeral streams (SMIRES). *Res. Ideas Outcomes* **3**, e21774 (2017).

[Google Scholar](#)

108. 108.

Trabucco, A. & Zomer, R. J. Global high-resolution soil–water balance. <https://doi.org/10.6084/m9.figshare.7707605.v3> (2010).

109. 109.

Hall, D. K. & Riggs, G. A. *MODIS/Aqua Snow Cover Daily L3 Global 500m SIN Grid, Version 6. [2002–2015]* (NASA National Snow and Ice Data Center Distributed Active Archive Center, accessed 15 February 2017); <https://doi.org/10.5067/MODIS/MYD10A1.006>

110. 110.

Fan, Y., Li, H. & Miguez-Macho, G. Global patterns of groundwater table depth. *Science* **339**, 940–943 (2013).

[ADS](#) [CAS](#) [PubMed](#) [PubMed Central](#) [Google Scholar](#)

111. 111.

Fluet-Chouinard, E., Lehner, B., Rebelo, L.-M., Papa, F. & Hamilton, S. K. Development of a global inundation map at high spatial resolution from topographic downscaling of coarse-scale remote sensing data. *Remote Sens. Environ.* **158**, 348–361 (2015).

[ADS](#) [Google Scholar](#)

112. 112.

Döll, P., Kaspar, F. & Lehner, B. A global hydrological model for deriving water availability indicators: model tuning and validation. *J. Hydrol.* **270**, 105–134 (2003).

[ADS](#) [Google Scholar](#)

113. 113.

Bartholomé, E. & Belward, A. S. GLC2000: a new approach to global land cover mapping from Earth observation data. *Int. J. Remote Sens.* **26**, 1959–1977 (2005).

[ADS](#) [Google Scholar](#)

114. 114.

GLIMS and National Snow and Ice Data Center. *GLIMS Glacier Database V1* (2012); <https://doi.org/10.7265/N5V98602>

115. 115.

Gruber, S. Derivation and analysis of a high-resolution estimate of global permafrost zonation. *Cryosphere* **6**, 221–233 (2012).

[ADS](#) [Google Scholar](#)

116. 116.

Ramankutty, N. & Foley, J. A. Estimating historical changes in global land cover: croplands from 1700 to 1992. *Glob. Biogeochem. Cycles* **13**, 997–1027 (1999).

[ADS](#) [CAS](#) [Google Scholar](#)

117. 117.

Lehner, B. & Döll, P. Development and validation of a global database of lakes, reservoirs and wetlands. *J. Hydrol.* **296**, 1–22 (2004).

[ADS](#) [Google Scholar](#)

118. 118.

Robinson, N., Regetz, J. & Guralnick, R. P. EarthEnv-DEM90: a nearly-global, void-free, multi-scale smoothed, 90m digital elevation model from fused ASTER and SRTM data. *ISPRS J. Photogramm. Remote Sens.* **87**, 57–67 (2014).

[ADS](#) [Google Scholar](#)

119. 119.

Williams, P. W. & Ford, D. C. Global distribution of carbonate rocks. *Z. Geomorphol. Suppl.* **147**, 1–2 (2006).

[Google Scholar](#)

120. 120.

Hartmann, J. & Moosdorf, N. The new global lithological map database GLiM: a representation of rock properties at the Earth surface. *Geochem. Geophys. Geosyst.* **13**, Q12004 (2012).

[ADS](#) [Google Scholar](#)

[Download references](#)

Acknowledgements

We thank T. Elrick and the Geographic Information Centre at McGill University for providing us with high-performance computing resources, and the Global Runoff Data Centre (GRDC) for providing us with global streamflow gauging data. Funding for this study was provided in part by the Natural Sciences and Engineering Research Council of Canada (B.L., C.C., C.W., M.L.M., NSERC Discovery grants RGPIN/341992-2013 and RGPIN/04541-2019); McGill University (M.L.M., Tomlinson Fellowship), Montreal, Quebec, Canada; H₂O'Lyon Doctoral School (M.L.M., Doctoral Fellowship, ANR-17-EURE-0018), Lyon, France; T.D., N.L., H.P. and T.T. were supported by the DRYvER project (<http://www.dryver.eu/>), which has received funding from the European Union's Horizon 2020 research and innovation programme under grant agreement no. 869226.

Author information

Author notes

1. Charlotte Cockburn

Present address: Department of Earth Science, Dartmouth College, Hanover, NH, USA

2. Caitlin Watt

Present address: Lethbridge Research and Development Centre, Agriculture and Agri-Food Canada, Lethbridge, Alberta, Canada

Affiliations

1. Department of Geography, McGill University, Montreal, Quebec, Canada

Mathis Loïc Messager, Bernhard Lehner, Charlotte Cockburn & Caitlin Watt

2. RiverLY Research Unit, National Research Institute for Agriculture, Food and Environment (INRAE), Villeurbanne, France

Mathis Loïc Messager, Nicolas Lamouroux, Hervé Pella & Thibault Datry

3. LWP Ltd, Christchurch, New Zealand

Ton Snelder

4. Senckenberg Society for Nature Research, Frankfurt am Main, Germany

Klement Tockner

5. Faculty of Biological Sciences, Goethe University Frankfurt, Frankfurt am Main, Germany

Klement Tockner

6. Institute of Physical Geography, Goethe University Frankfurt, Frankfurt am Main, Germany

Tim Trautmann

Authors

1. Mathis Loïc Messager
[View author publications](#)

You can also search for this author in [PubMed](#) [Google Scholar](#)

2. Bernhard Lehner

[View author publications](#)

You can also search for this author in [PubMed](#) [Google Scholar](#)

3. Charlotte Cockburn

[View author publications](#)

You can also search for this author in [PubMed](#) [Google Scholar](#)

4. Nicolas Lamouroux

[View author publications](#)

You can also search for this author in [PubMed](#) [Google Scholar](#)

5. Hervé Pella

[View author publications](#)

You can also search for this author in [PubMed](#) [Google Scholar](#)

6. Ton Snelder

[View author publications](#)

You can also search for this author in [PubMed](#) [Google Scholar](#)

7. Klement Tockner

[View author publications](#)

You can also search for this author in [PubMed](#) [Google Scholar](#)

8. Tim Trautmann

[View author publications](#)

You can also search for this author in [PubMed](#) [Google Scholar](#)

9. Caitlin Watt

[View author publications](#)

You can also search for this author in [PubMed](#) [Google Scholar](#)

10. Thibault Datry

[View author publications](#)

You can also search for this author in [PubMed](#) [Google Scholar](#)

Contributions

CRediT (Contributor Roles Taxonomy): conceptualization—T.D., B.L., K.T., M.L.M.; methodology—M.L.M., B.L., T.S., C.C., N.L.; data curation—M.L.M., B.L., C.C., C.W., T.S., H.P.; software, validation, visualization—M.L.M.; formal analysis—M.L.M., C.C.; writing original draft—M.L.M., T.D., B.L.; writing, review and editing—all authors; project administration and supervision—M.L.M., B.L., T.D.; funding acquisition—B.L., T.D., M.L.M.

Corresponding authors

Correspondence to [Mathis Loïc Messager](#) or [Bernhard Lehner](#) or [Thibault Datry](#).

Ethics declarations

Competing interests

The authors declare no competing interests.

Additional information

Peer review information *Nature* thanks Kristin Jaeger, Georgia Papacharalampous and the other, anonymous, reviewer(s) for their contribution to the peer review of this work. Peer reviewer reports are available.

Publisher's note Springer Nature remains neutral with regard to jurisdictional claims in published maps and institutional affiliations.

Extended data figures and tables

Extended Data Fig. 1 Global prevalence of IRES with at least one zero-flow month per year on average.

a, Distribution of global climate zones used in this study. Data provided by Global Environmental Stratification (GENS)³². **b**, Predicted probability of river flow intermittence, defined as at least one zero-flow month (30 days) per year on average, across the global river and stream network²⁷. The median probability threshold of 0.5 was used to determine the binary flow intermittence class for each reach. **c**, Global prevalence of IRES with at least one zero-flow month (30 days) per year on average, across climate zones and streamflow size classes (based on long-term average naturalized discharge). Note that in regions with sparse training data, the model results can differ substantially from the results shown in Table 1, as the underlying random forest and extrapolation models were developed independently. No stations were available in climate zones Arctic 1 and Arctic 2, and few stations were available in ‘Extremely cold and wet’ (1 and 2) and in ‘Extremely hot and arid’ climates (together representing 3% of global river and stream length). Rows are sorted in the same order as in Table 1, and the same footnotes as in Table 1 apply. Mapping software: ArcMap (ESRI).

Extended Data Fig. 2 Distribution of cross-validation results.

a, Maps of spatially cross-validated predictive accuracy of flow intermittence for streamflow gauging stations. See Supplementary Fig. 3 for the distribution of spatial cross-validation folds and details on the cross-validation procedure. The classification errors shown here are not necessarily present in the final predictions but illustrate the ability of the model to predict the flow intermittence class for each region if that region was excluded from the training set. For instance, it shows that the model would be unable to predict the presence of IRES in western France and northern Spain (inset ii, dark red dots), or in western India (inset iii) without training stations in these regions. **b–e**, Intermittence prediction residuals versus gauging station characteristics and environmental variables. The mean intermittence prediction residual (IPR) is the difference between the

average predicted probability of flow intermittence (across three cross-validation folds and two repetitions) and the observed flow intermittence of the gauging station (1 = non-perennial, 0 = perennial). Overall, prediction errors and uncertainties decrease with an increase in the number of recorded years by gauging stations as well as the drainage area and the degree of flow intermittence (average annual number of zero-flow days and flow cessation events) of the corresponding reaches. Mapping software: ArcMap (ESRI).

Extended Data Fig. 3 Comparing global predictions to national maps of IRES in the USA and Australia.

Comparison of **a**, the US National Hydrography Dataset (NHDPlus, medium resolution) and **d**, the Australian hydrological geospatial fabric, with our model predictions based on two thresholds of flow intermittence, either ≥ 1 zero-flow day per year (**b**, **e**), or ≥ 1 zero-flow month (30 days) per year (**c**, **f**), on average. Only rivers and streams with $MAF \geq 0.1 \text{ m}^3 \text{ s}^{-1}$ are shown for the USA (**a–c**) and with drainage area $\geq 10 \text{ km}^2$ for Australia (**d–f**). The US reference dataset portrays 19–22% of the length of rivers and streams as non-perennial, depending on whether reaches without flow intermittence status are assumed to be perennial or removed; our estimates range from 51% (≥ 1 zero-flow day per year) to 36% (≥ 1 zero-flow month per year). We hypothesize that the remaining gap in IRES prevalence is attributable to a tendency of our model to overpredict intermittence across the eastern USA and an under-accounting of intermittence in medium to large rivers by the national dataset. The Australian reference dataset portrays 91% of the length of rivers and streams as non-perennial; our estimates range from 95% (≥ 1 zero-flow day per year) to 92% (≥ 1 zero-flow month per year). See Extended Data Fig. [7b](#) for data sources. Mapping software: ArcMap (ESRI).

Extended Data Fig. 4 Comparing global predictions to national maps of IRES in Brazil, Argentina, and France.

Comparison of **a**, the continuous cartographic base of Brazil (BC250), **d**, the Argentinian hydrographic network, and **g**, model predictions for France

from Snelder et al.²¹, with our model predictions based on two thresholds of flow intermittence, either ≥ 1 zero-flow day per year (**b**, **e**, **h**) or ≥ 1 zero-flow month (30 days) per year (**c**, **f**), on average. In **a** and **d**, only first-order streams (determined through network analysis) are visually differentiated (finer, semi-transparent lines), owing to the lack of a watercourse-size attribute in the Brazilian and Argentinian datasets. In **b**, **c**, **e–h**, only rivers and streams with $MAF \geq 0.1 \text{ m}^3 \text{ s}^{-1}$ are shown. Snelder et al.²¹ predict that 17% of the length of rivers and streams in France are non-perennial. We predict that 14% are non-perennial. This slight divergence may be partly driven by the difference in definition of flow intermittence: Snelder et al.²¹ classified stations with ≥ 1 zero-flow day in the streamflow record as IRES whereas we used a threshold of 1 zero-flow day per year across the streamflow record. See Extended Data Fig. [7b](#) for data sources. Mapping software: ArcMap (ESRI).

[Extended Data Fig. 5 Quantitative comparison between the predicted prevalence of flow intermittence and national estimates.](#)

a–f, Comparisons were conducted for France (**a**, **b**), the USA (**c**, **d**), and Australia (**e**, **f**), on the basis of two thresholds of flow intermittence, either ≥ 1 zero-flow day per year (**a**, **c**, **e**) or ≥ 1 zero-flow month (30 days) per year (**b**, **d**, **f**), on average. Bars for mapped rivers and streams with $MAF < 0.1 \text{ m}^3 \text{ s}^{-1}$ (for France and the USA) are greyed out as they were not included in the calculation of summary statistics. Inset graphs in **b**, **d**, **f** show comparisons of total river network length (log-transformed *y* axis), which in case of discrepancies can explain some of the differences in the predicted prevalence of intermittence.

[Extended Data Fig. 6 Comparing global predictions to on-the-ground observations of flow cessation.](#)

a, b, Maps show individual RiverATLAS reaches and their predictive accuracy for France (**a**), and the US Pacific Northwest (**b**). Maps are drawn at identical cartographic scales. France ($n = 2,297$): balanced accuracy = 0.59, classification accuracy = 51%, sensitivity = 24%,

specificity = 94%. US Pacific Northwest ($n = 3,725$): balanced accuracy = 0.47, classification accuracy = 80%, sensitivity = 10%, specificity = 83%. See Extended Data Fig. 7b for data sources. Mapping software: ArcMap (ESRI).

Extended Data Fig. 7 Overview of study design and main data sources.

a, Diagram of modelling workflow. **b**, Main data sources used in model development, predictions, diagnostics and comparisons. Data sources: Global Runoff Data Centre⁵³, Do et al.⁵⁴, Gudmundsson et al.⁵⁵, Linke et al.²⁷, Snelder et al.²¹, McShane et al.¹⁰⁰, ONDE eau 2012–2019¹⁰¹, National Hydrographic Data^{102,103,104,105}, WorldPop⁹⁰.

Extended Data Fig. 8 Spatial and environmental distribution of streamflow gauging stations used in model training and cross-validation.

a, b, Gauging stations ($n = 5,615$) were deemed perennial (**a**) if their streamflow record included less than one zero-flow day per year, on average, across their record, or non-perennial (**b**) if they included at least one zero-flow day per year, on average, and at least one zero-flow day in every 20-year moving window across their record. Stations fulfilling neither condition **a** nor **b** were excluded. Darker points symbolize longer streamflow records. Only gauging stations with streamflow time series spanning at least 10 years were included in this analysis, excluding years with more than 20 missing days. **c–p**, Distribution of values for 14 hydro-environmental variables across the streamflow gauging stations used for model training/testing (purple, $n = 5,615$) and across all reaches of the global river network (blue, $n = 6.2 \times 10^6$). The distribution plots show empirical probability density functions (that is, the area under each density function is equal to one) for all variables, aside from climate zones (**g**) for which the relative frequency distribution is shown. All variables were averaged across the total drainage area upstream of the reach pour point associated with each gauging station or river reach, respectively. See Extended Data Table 2 for a description of the variables and Extended Data

Fig. 1a for a description of the climate zones. No stations were available for climate zones Arctic 1 and Arctic 2. Mapping software: R statistical software (R Core Team).

Extended Data Table 1 Definitions of commonly used terms for non-perennial rivers and streams

[Full size table](#)

Extended Data Table 2 Hydro-environmental characteristics used as candidate predictor variables in the split random forest model

[Full size table](#)

Extended Data Table 3 Performance summary of binary flow intermittence class predictions

[Full size table](#)

Supplementary information

Supplementary Information

This file contains Supplementary Information Sections I-VI, Supplementary Tables S1-S3, Supplementary Figures S1-S8, and Supplementary References. Sections include: a comparison between model predictions and previous estimates of the global prevalence of intermittent rivers and ephemeral streams (Section I), additional information on the pre-processing and validation of input data (gauging stations and discharge data in Section II, national hydrographic datasets and local on-the-ground visual observations of flow intermittence in Section VI), and technical documentation on model development and diagnostics (Sections III-V).

Peer Review File

Supplementary Table 1

Predicted global prevalence of intermittent rivers and ephemeral streams across streamflow size classes by climate zone, terrestrial biome, freshwater major habitat type, and country.

Source data

[Source Data Fig. 2](#)

Rights and permissions

[Reprints and Permissions](#)

About this article



Check for
updates

Cite this article

Messager, M.L., Lehner, B., Cockburn, C. *et al.* Global prevalence of non-perennial rivers and streams. *Nature* **594**, 391–397 (2021).
<https://doi.org/10.1038/s41586-021-03565-5>

[Download citation](#)

- Received: 12 November 2020
- Accepted: 19 April 2021
- Published: 16 June 2021
- Issue Date: 17 June 2021
- DOI: <https://doi.org/10.1038/s41586-021-03565-5>

Comments

By submitting a comment you agree to abide by our [Terms](#) and [Community Guidelines](#). If you find something abusive or that does not comply with our terms or guidelines please flag it as inappropriate.

[Access through your institution](#)

[Change institution](#)

[Buy or subscribe](#)

Associated Content

[Most rivers and streams run dry every year](#)

- Kristin L. Jaeger

Advertisement

This article was downloaded by **calibre** from <https://www.nature.com/articles/s41586-021-03565-5>

| [Section menu](#) | [Main menu](#) |

Interpreting type 1 diabetes risk with genetics and single-cell epigenomics

[Download PDF](#)

- Article
- [Published: 19 May 2021](#)

Interpreting type 1 diabetes risk with genetics and single-cell epigenomics

- [Joshua Chiou](#) [ORCID: orcid.org/0000-0002-4618-0647](#)^{1 nAff7},
- [Ryan J. Geusz](#)¹,
- [Mei-Lin Okino](#)²,
- [Jee Yun Han](#)³,
- [Michael Miller](#)³,
- [Rebecca Melton](#)¹,
- [Elisha Beebe](#)²,
- [Paola Benaglio](#)²,
- [Serina Huang](#)²,
- [Katha Korgaonkar](#)²,
- [Sandra Heller](#) [ORCID: orcid.org/0000-0002-8704-2646](#)⁴,
- [Alexander Kleger](#) [ORCID: orcid.org/0000-0003-0592-5232](#)⁴,
- [Sebastian Preissl](#)³,
- [David U. Gorkin](#)^{3 nAff8},
- [Maike Sander](#)^{2,5,6} &
- [Kyle J. Gaulton](#) [ORCID: orcid.org/0000-0003-1318-7161](#)^{2,6}

[Nature](#) volume 594, pages 398–402 (2021) [Cite this article](#)

- 6891 Accesses
- 175 Altmetric
- [Metrics details](#)

Subjects

- [Epigenomics](#)
- [Gene regulation](#)

- [Genome-wide association studies](#)
- [Type 1 diabetes](#)

Abstract

Genetic risk variants that have been identified in genome-wide association studies of complex diseases are primarily non-coding¹. Translating these risk variants into mechanistic insights requires detailed maps of gene regulation in disease-relevant cell types². Here we combined two approaches: a genome-wide association study of type 1 diabetes (T1D) using 520,580 samples, and the identification of candidate *cis*-regulatory elements (cCREs) in pancreas and peripheral blood mononuclear cells using single-nucleus assay for transposase-accessible chromatin with sequencing (snATAC-seq) of 131,554 nuclei. Risk variants for T1D were enriched in cCREs that were active in T cells and other cell types, including acinar and ductal cells of the exocrine pancreas. Risk variants at multiple T1D signals overlapped with exocrine-specific cCREs that were linked to genes with exocrine-specific expression. At the *CFTR* locus, the T1D risk variant rs7795896 mapped to a ductal-specific cCRE that regulated *CFTR*; the risk allele reduced transcription factor binding, enhancer activity and *CFTR* expression in ductal cells. These findings support a role for the exocrine pancreas in the pathogenesis of T1D and highlight the power of large-scale genome-wide association studies and single-cell epigenomics for understanding the cellular origins of complex disease.

[Download PDF](#)

Main

Type 1 diabetes is a complex autoimmune disease that is characterized by the loss of insulin-producing pancreatic beta cells³, but the triggers of autoimmunity and disease onset remain poorly understood. T1D has a strong genetic component, most prominently at the major histocompatibility complex (MHC) locus, but including 59 additional risk loci^{4,5,6}. Risk variants for T1D are largely non-coding, and intersection of risk variants with epigenomic data has shown that these variants are enriched within lymphoid enhancers⁴. However, owing to limited sample sizes, incomplete variant coverage, and limited cell-type resolution of existing epigenomic maps, the causal variants and cellular mechanisms of action of T1D risk loci are largely unresolved.

Discovery and fine mapping of T1D loci

We performed a genome-wide association study (GWAS) of 18,942 patients with T1D and 501,638 control participants of European ancestry from 9 cohorts (Supplementary Table 1). After applying uniform quality control (Supplementary Fig. 1), we imputed genotypes into the TOPMed reference panel and tested for association with T1D⁷. Through meta-analysis, we combined the association results for 61,947,369 variants and identified 81 loci that reached genome-wide significance ($P < 5 \times 10^{-8}$), including 48 of 59 known loci and 33 loci that were previously unreported, to our knowledge (Fig. 1a, Supplementary Fig. 2, Supplementary Table 2). At 92 total loci (59 known and 33 novel), we identified 44 independent signals, of which 36 were previously unreported (Fig. 1b, Supplementary Fig. 3). Nearly a third of loci (32%; 29 of 92) contained more than one signal; for example, the *PTPN2* and *BCL11A* loci had three signals each (Extended Data Fig. 1).

Fig. 1: Genome-wide association and fine mapping identify T1D risk signals.



figure1

a, Genome-wide T1D association (two-sided $-\log_{10}$ -transformed P values from meta-analysis of $n = 520,580$ samples, unadjusted for multiple comparisons). Previously unidentified loci are coloured red (± 250 kb of the index variant) and labelled with the nearest gene. Dotted line indicates genome-wide significance ($P = 5 \times 10^{-8}$). **b**, Breakdown of 136 T1D risk signals, including 92 main signals (59 known and 33 novel) and 44 independent signals (38 at known and 6 at novel loci). **c**, Number of signals per locus (top), 99% credible set variants from fine mapping (middle), and variants with posterior probability of association (PPA) at various thresholds (bottom).

[Full size image](#)

We fine-mapped causal variants for 136 T1D signals (92 main and 44 independent signals; Fig. 1b). We obtained the posterior probability of association (PPA) for tested variants and defined 99% credible sets for each signal (Supplementary Table 3, Supplementary Data 1). Compared to a previous study⁸, fine-mapping resolution was improved on the basis of credible set size and maximum posterior probability (Supplementary Fig. 4). The median credible set size was 31 variants, where nearly a quarter (24%; 32 of 136) contained 5 or fewer variants, and 28% (38 of 136) contained a single variant with a PPA of less than 0.50 (Fig. 1c). Credible sets at 15% of signals (21 of 136) contained a nonsynonymous variant with $PPA > 0.01$, including the novel loci *AIRE* p.Arg471Cys (PPA = 0.99), *BATF3* p.Val11Ile (PPA = 0.078), *PRF1* p.Ala91Val (PPA = 0.28), and *INPP5B* p.Gly250Cys (PPA = 0.055) (Supplementary Table 4).

The TOPMed reference panel enables more accurate imputation of rare variants. We identified four novel variants with a minor allele frequency (MAF) of below 0.005 and large effects on T1D (Extended Data Fig. 2a). Among these, rs541856133 (MAF = 0.0015, odds ratio (OR) = 3.01, 95% confidence interval (CI) = 2.33–3.89) mapped directly upstream of *CEL*, a gene that has been implicated in maturity-onset diabetes of the young type 8 (MODY8)⁹. We also identified a novel protein-coding protective variant at *IFIH1* (p.Asn160Asp, rs75671397, MAF = 0.002, OR = 0.35, 95% CI = 0.22–0.55) independent of known signals in this gene. Two additional non-coding risk variants mapped to *SH2B3* (rs570074821, MAF = 0.0019, OR = 1.89, 95% CI = 1.37–2.61) and *CAMK4* (rs72663304, MAF = 0.0013, OR = 2.54, 95% CI = 1.72–3.76) (Extended Data Fig. 2b).

We characterized genetic correlations (r_g) between T1D and other complex traits and diseases. Consistent with previous reports^{4,10}, T1D had significant (false discovery rate (FDR) < 0.10) positive correlations with autoimmune diseases such as rheumatoid arthritis ($r_g = 0.44$, FDR = 7.52×10^{-5}) and systemic lupus erythematosus ($r_g = 0.35$, FDR = 5.05×10^{-7}), and a negative correlation with ulcerative colitis ($r_g = -0.18$,

$\text{FDR} = 1.95 \times 10^{-3}$) (Extended Data Fig. 3). We also observed positive correlations with metabolic traits such as fasting insulin level ($r_g = 0.18$, $\text{FDR} = 4.04 \times 10^{-3}$), coronary artery disease ($r_g = 0.12$, $\text{FDR} = 1.23 \times 10^{-2}$), and type 2 diabetes (T2D; $r_g = 0.10$, $\text{FDR} = 1.95 \times 10^{-3}$), and with pancreatic diseases such as pancreatic cancer ($r_g = 0.25$, $\text{FDR} = 1.11 \times 10^{-1}$), although the latter was just above significance. These results demonstrate relationships between genetic effects on T1D and autoimmune, metabolic and pancreatic disease.

Pancreas and immune cell gene regulation

The majority of T1D risk is likely to affect gene regulation⁴. To annotate T1D risk variants, we generated an accessible chromatin reference map using snATAC-seq of peripheral blood and pancreas from donors without diabetes (Supplementary Table 5). We grouped chromatin accessibility profiles from 131,554 cells into 28 clusters (Fig. 2a, Supplementary Fig. 5a–c) and assigned cell-type identities using chromatin accessibility at marker genes (Supplementary Table 6). For example, chromatin accessibility at *C1QB* marked pancreas tissue-resident macrophages, *REGIA* marked acinar cells, and *CFTR* marked ductal cells (Extended Data Fig. 4a). We also observed patterns of chromatin accessibility at marker genes for cell subtypes, such as *FOXP3* for regulatory T cells (Extended Data Fig. 4a). To relate cell-type-resolved accessible chromatin to gene expression, we created a single-cell RNA sequencing (scRNA-seq) reference map of peripheral blood and pancreas. We assigned cell-type identities for 90,495 cells to 29 clusters, which identified similar cell types and proportions to snATAC-seq (Extended Data Fig. 5a–c).

Fig. 2: Reference map of single-cell chromatin accessibility from T1D-relevant tissues.

 **figure2**

a, Leiden clustering of single-cell accessible chromatin profiles from $n = 131,554$ cells. Cells are plotted on the first two uniform manifold approximation and projection (UMAP) components, clusters are grouped into categories of cell types, and the number of cells per cluster is shown to the right of each list. **b**, Relative accessibility

(row-normalized) for the 25,436 cCREs that were most specific to each cluster (left), and enriched gene ontology terms for cCREs that were specific to pancreatic macrophages, ductal cells and acinar cells (right). MΦ, macrophage; DC, dendritic cell; NK, natural killer.

[Full size image](#)

To characterize *cis*-regulatory programs, we aggregated reads from cells within each snATAC-seq cluster and identified accessible chromatin peaks that represented cCREs. There were 448,142 cCREs across all 28 clusters and an average of 77,812 cCREs per cluster (Supplementary Data 2). We also aggregated reads from cells within each scRNA-seq cluster to derive normalized expression (Supplementary Data 3). To delineate regulatory programs that specified each cell type, we identified 25,436 cCREs with accessibility patterns that were most specific to each cluster (Fig. 2b, Supplementary Data 4). Genes within 100 kb of cCREs specific to a cell type had more specific expression for that cell type than genes that were close to cCREs specific to other cell types (Supplementary Fig. 6). Cell-type-specific cCREs were also enriched for gene ontology (GO) terms that represent highly specialized cellular processes (Fig. 2b, Supplementary Table 7).

We defined transcriptional regulators of cCRE activity by assessing transcription factor (TF) motif enrichment (Supplementary Data 5). Enriched TF motifs included those with lineage, cell-type, and cell-state specificity (Extended Data Fig. 4b). As TFs within subfamilies often have similar motifs, we grouped TFs into subfamilies to identify TFs with matching expression and motif enrichment patterns (Supplementary Table 8). For example, the FOXA subfamily TF genes *FOXA2* and *FOXA3* were specifically expressed in pancreatic endocrine and exocrine cells, the HNF1 subfamily TF gene *HNF1B* was specifically expressed in ductal cells, and the ROR subfamily TF gene *RORC* was specifically expressed in memory CD8⁺ T cells (Extended Data Fig. 4b, Supplementary Table 8).

As the target genes of cCRE activity are largely unknown, we identified cell-type-resolved co-accessibility links between distal (non-promoter) cCREs and putative target gene promoters. Across all cell types, we observed 1,028,428 links (with co-accessibility more than 0.05) between distal cCREs and gene promoters (Supplementary Data 6). Co-accessible links were often cell-type-specific; for example, distal cCREs were co-accessible with the *AQPI* promoter in ductal cells and the *CEL* promoter in acinar cells (Extended Data Fig. 4c). In nearly every cell type, target genes that were co-accessible with distal cCREs were more likely than matched genes to be expressed in that cell type (Supplementary Fig. 7).

Cell-type annotation of T1D risk variants

We measured the enrichment of variants associated with T1D and other complex traits and diseases for cell-type cCREs. For T1D, the most significant enrichment was in T cell cCREs (naive T cell, Z -score (Z) = 5.57, FDR = 2.26×10^{-5} ; memory CD8 $^{+}$ T cell, Z = 4.80, FDR = 4.67×10^{-4} ; activated CD4 $^{+}$ T cell, Z = 4.62, FDR = 6.74×10^{-4} ; cytotoxic CD8 $^{+}$ T cell, Z = 4.49, FDR = 1.09×10^{-3} ; regulatory T cell, Z = 3.26, FDR = 7.23×10^{-3}) and adaptive natural killer cells (Z = 3.50, FDR = 9.93×10^{-3} ; Extended Data Fig. 6). Notably, we did not observe enrichment in pancreas-resident immune cells (CD8 $^{+}$ T cell, Z = 0.65, FDR = 1.0; macrophage, Z = -0.56, FDR = 1.0). For other immune-related diseases, variants were primarily enriched within lymphocyte cCREs, whereas those associated with T2D and glycaemic traits were enriched in pancreatic endocrine, acinar, and ductal cCREs (Extended Data Fig. 6). These results show that T1D variants are broadly enriched for T cell cCREs and highlight other traits that are enriched for pancreatic and immune cell cCREs.

Despite the strong enrichment of T1D-associated variants in T cells, many T1D signals did not overlap a T cell cCRE, which suggests that additional cell types contribute to T1D risk. To identify additional disease-relevant cell types, we used an orthogonal approach to test for enrichment of T1D variants within the subset of cell-type-specific cCREs. As expected, T1D-associated variants were enriched in cCREs specific to T cells and beta cells (activated CD4 $^{+}$ T cell, $\ln(\text{enrich})$ = 4.25, 95% CI = 1.11–5.43; cytotoxic CD8 $^{+}$ T cell, $\ln(\text{enrich})$ = 4.04, 95% CI = 0.20–5.20; INS^{high} beta cell, $\ln(\text{enrich})$ = 3.58, 95% CI = 0.95–4.84) (Fig. 3a). Notably, T1D variants were also enriched in cCREs specific to plasmacytoid dendritic cells (pDC) ($\ln(\text{enrich})$ = 4.00, 95% CI = 1.96–5.10), classical monocytes ($\ln(\text{enrich})$ = 3.78, 95% CI = 2.23–4.74), acinar cells ($\ln(\text{enrich})$ = 3.35, 95% CI = 1.59–4.46) and ductal cells ($\ln(\text{enrich})$ = 3.28, 95% CI = 0.18–4.69) (Fig. 3a).

Fig. 3: Cell-type-specific enrichment and mechanisms of T1D risk variants.

 figure3

a, T1D $\ln(\text{enrichment})$ within cell-type-specific cCREs. Labelled cell types have positive enrichment and 95% CI lower bound above 0. Data are $\ln(\text{enrichment}) \pm 95\%$ CI from fgwas. **b**, T1D signals with highest cPPA in cCREs for disease-enriched cell types (more than 0.20 cPPA for T cells and monocytes, more than 0.10 cPPA for other

groups), and more than 0.01 cPPA away from the next closest group (top). Column-normalized expression for genes with transcripts per million (TPM) above 1 in the highlighted cell type(s) and within ± 500 kb of the index variant. Genes that are co-accessible with cCREs that contain risk variants are annotated in rectangles (bottom). Mono., monocyte. Index variants shown in parentheses.

[Full size image](#)

Given insight into key T1D-relevant cell types, we next annotated T1D signals in cCREs for these cell types. More than 75% of T1D signals (103 of 136) contained at least one variant ($PPA > 0.01$) that overlapped with a cCRE, and at 65% of these signals (67 of 103) the cCRE was co-accessible with a gene promoter (Supplementary Table 9). Variants with high probabilities ($PPA > 0.50$) were significantly more likely than other credible set variants to map in a cCRE ($OR = 3.9$, 95% CI = 1.9–7.8, $P = 1.9 \times 10^{-4}$), and these cCREs were more likely to be co-accessible with a promoter ($OR = 6.1$, 95% CI = 1.3–55.9, $P = 7.1 \times 10^{-3}$). For each signal, we calculated the cumulative posterior probability (cPPA) of credible set variants overlapping distal cCREs in each disease-enriched cell type. Numerous T1D signals had high cPPA in T cell cCREs and not in other disease-relevant cell types (Fig. 3b). We also found T1D signals that had high cPPA in acinar and ductal (exocrine) cell, beta cell, monocyte and pDC cCREs, several of which were highly cell-type-specific (Fig. 3b). For each signal, we further annotated genes within 1 Mb that were expressed in the same cell type and co-accessible with cCREs (Fig. 3b, Supplementary Table 9).

Multiple T1D signals had high cPPA specifically in pancreatic exocrine cells and were linked to genes with exocrine-specific expression. At the *GP2* locus, three variants accounted for 0.951 PPA and mapped in an acinar-specific cCRE that was co-accessible with the promoter of *GP2*, which had acinar-specific expression (Fig. 3b, Extended Data Fig. 7a). Similarly, rs72802342 at the *BCARI* locus ($PPA = 0.30$) mapped in an acinar-specific cCRE that was co-accessible with the promoters of *CTRB1* and *CTRB2*, both of which had acinar-specific expression (Fig. 3b, Extended Data Fig. 7b). Other signals such as *CEL* had similar exocrine-specific profiles (Supplementary Fig. 8a–c). Exocrine cCREs at T1D loci were also largely specific relative to accessible chromatin in stimulated immune and islet cells (Supplementary Table 10).

T1D variant affects *CFTR* in ductal cells

The *CFTR* locus contained the fine-mapped variant rs7795896 ($PPA = 0.63$) in a distal cCRE that is specific to ductal cells and co-accessible with the *CFTR* promoter, in addition to other genes (Fig. 4a). Recessive mutations in *CFTR* cause cystic fibrosis, which is often comorbid with exocrine pancreas insufficiency and cystic fibrosis-

related diabetes (CFRD)¹¹. Furthermore, carriers of *CFTR* mutations often develop chronic pancreatitis¹². As *CFTR* has not been implicated in T1D, we sought to validate the mechanism of this locus. The T1D risk allele of rs7795896 significantly reduced enhancer activity (594-bp sequence two-sided ANOVA, $P = 1.15 \times 10^{-2}$, Extended Data Fig. 8a; 180-bp sequence two-sided *t*-test, $P = 3.35 \times 10^{-2}$, Extended Data Fig. 8b) and reduced protein binding (bound fraction rs7795896 C allele = 0.007, T allele = 0.081; Extended Data Fig. 8c, Supplementary Fig. 9) in Capan-1 cells. The variant mapped in a sequence motif for HNF1B, albeit in a position predicted to minimally affect binding, and overlapped a HNF1B chromatin immunoprecipitation with sequencing (ChIP-seq) site that was previously identified in ductal cells¹³ (Extended Data Fig. 8d).

Fig. 4: Fine-mapped T1D variant regulates *CFTR* in pancreatic ductal cells.

 **figure4**

a, Variant rs7795896 at the *CFTR* locus mapped in a cCRE that is co-accessible with *CFTR* and other genes. Zoomed-in view (top) shows that the cCRE is ductal cell-specific. **b**, Expression of genes that are co-accessible with the distal cCRE in Capan-1 cells with CRISPR-inactivated enhancer (Enh; $n = 9$, 3 single-guide RNAs)

(sgRNAs) \times 3 biological replicates) compared to non-targeting control sgRNA ($n = 3$ biological replicates). Data are mean \pm 95% CI. P values by two-sided ANOVA; NS, not significant.

[Source data](#)

[Full size image](#)

To determine whether the enhancer that contains rs7795896 regulates *CFTR* in ductal cells, we used CRISPR interference (CRISPRi) to inactivate enhancer activity (*CFTR*^{Enh}) in Capan-1 cells (Supplementary Table 11). As positive and negative controls, we inactivated the *CFTR* promoter (*CFTR*^{Prom}) and used a non-targeting guide RNA, respectively. Quantitative PCR (qPCR) showed that there was a significant reduction in *CFTR* expression after enhancer inactivation (two-sided ANOVA, $P = 1.77 \times 10^{-4}$), whereas expression of other genes at the locus was unchanged (Fig. 4b, Extended Data Fig. 8e). We tested whether risk variants affected *CFTR* expression using pancreas expression quantitative trait locus (eQTL) data from the GTEx Consortium¹⁴. Out of 13 tested genes, only *CFTR* had evidence for an eQTL ($P = 4.31 \times 10^{-4}$), which was colocalized with the T1D signal (shared posterior probability (PP_{shared}) = 91.8%) (Extended Data Fig. 9a). Among candidate variants for which eCAVIAR provided evidence for driving the shared signal (colocalization posterior probability ($CLPP$) > 0.01), only rs7795896 mapped in a cCRE. The T1D risk allele of rs7795896 was associated with decreased *CFTR* expression, consistent with its effects on enhancer activity and TF binding. We recalculated the eQTL association to include estimated pancreas cell-type proportion as an interaction term, and only ductal cells showed a significant association ($P = 2.37 \times 10^{-4}$) (Extended Data Fig. 9b–d).

As *CFTR* has been implicated in pancreatic cancer¹⁵ and pancreatitis¹⁶, we investigated whether rs7795896 was associated with these phenotypes in the UK Biobank and FinnGen. The T1D risk allele was associated with increased risk of pancreatitis (chronic pancreatitis OR = 1.15, $P = 3.18 \times 10^{-3}$; acute pancreatitis OR = 1.07, $P = 1.15 \times 10^{-2}$) and other pancreatic diseases (OR = 1.13, $P = 4.72 \times 10^{-5}$) (Extended Data Fig. 10a). By contrast, rs7795896 was not associated with other autoimmune diseases (all $P > 0.05$). T1D signals that were associated with increased risk of pancreatic disease had significantly higher cPPA in exocrine cCREs compared to other signals (two-sided Student's *t*-test, $P = 0.027$) and showed no difference in T cell cCREs ($P = 0.36$). Together, our findings support a model in which variants that regulate *CFTR* and other genes in the exocrine pancreas increase the risk of T1D and pancreatic diseases (Extended Data Fig. 10b).

High-resolution mapping of both genetic variants that influence T1D risk and cell-type-specific *cis*-regulatory programs in T1D-relevant tissues enabled us to gain insight into disease mechanisms. Risk variants at multiple loci mapped to genes with specialized functions in exocrine cells. Although our results support the idea that variants in exocrine cCREs mediate T1D risk, fine mapping has not resolved a single variant at most loci. Risk variants in exocrine-specific cCREs may also function in other cell types in the context of development, environmental changes, or disease progression. Continued fine mapping in trans-ethnic cohorts with systematic evaluation of variant function in relevant cell types will further clarify risk mechanisms. Furthermore, as co-accessible links represent correlations that require both sites to vary in their accessibility, future studies will benefit from linking changes in chromatin to gene expression directly through single-cell multi-omics.

Observational studies have reported exocrine pancreas abnormalities at the onset of T1D¹⁷, but it was unknown whether this caused the disease¹⁸. Genomic studies have also identified changes in exocrine cells in patients with T1D^{19,20}. Abnormalities in the exocrine pancreas have been considered secondary to other disease processes in T1D, such as beta cell loss causing reduced insulinotropic effects on exocrine cells or viral infection leading to exocrine inflammation. By contrast, our findings provide evidence that exocrine cells intrinsically contribute to T1D. Reduced *CFTR* leads to CFRD via intra-islet inflammation and immune infiltration, and immune infiltration in the exocrine pancreas has been suggested to contribute to T1D^{21,22,23}. Other implicated genes encode proteins that are secreted from acinar cells and have been linked to risk of pancreatic disease^{24,25,26}, and may contribute to an inflammatory state. We therefore hypothesize that gene regulation in the exocrine pancreas has a causal role in T1D, which may provide new avenues for therapeutic discovery.

Methods

No statistical methods were used to predetermine sample size. The experiments were not randomized and investigators were not blinded to allocation during experiments and outcome assessment.

Genotype quality control and imputation

We compiled individual-level genotype data and summary statistics from 18,942 individuals with T1D and 501,638 control individuals of European ancestry from public sources (Supplementary Table 1), where T1D case cohorts were matched to population control cohorts on the basis of genotyping array (Affymetrix, Illumina Infinium, Illumina Omni, and Immunochip) and country of origin where possible (USA, UK, and Ireland). For the GENIE-UK cohort, because we were unable to find a

matched country of origin control cohort, we used individuals of British ancestry (defined by individuals within 1.5 interquartile range of CEU/GBR subpopulations on the first four principal components (PCs) from principal component analysis (PCA) with European 1000 Genomes Project samples) from the University of Michigan Health and Retirement study (HRS). For non-UK Biobank cohorts, we first applied individual and variant exclusion lists (where available) to remove low-quality, duplicate, or non-European ancestry samples and failed genotype calls for each cohort. For control cohorts, we also used phenotype files (where available) to remove individuals with T2D or autoimmune diseases.

We then applied the HRC imputation preparation program (version 4.2.9) and used PLINK²⁷ (version 1.90b6.7) to remove variants based on (i) low frequency (MAF < 1%), (ii) missing genotypes (missing >5%), (iii) violation of Hardy–Weinberg equilibrium (HWE $P < 1 \times 10^{-5}$ in control cohorts and HWE $P < 1 \times 10^{-10}$ in case cohorts), (iv) difference in allele frequency >0.2 compared to the Haplotype Reference Consortium r1.1 reference panel²⁸, and (v) allele ambiguity defined as AT/GC variants with MAF >40%²⁹. We further removed individuals for (i) missing genotypes (missing >5%), (ii) sex mismatch with phenotype records ($\text{hom}_{\text{chrX}} > 0.2$ for females and $\text{hom}_{\text{chrX}} < 0.8$ for males), (iii) cryptic relatedness through identity-by-descent (IBD >0.2), and (iv) non-European ancestry through PCA with 1000 Genomes Project³⁰ (>3 interquartile range from 25th and 75th percentiles of European 1KGP samples on the first four PCs) (Supplementary Fig. 1). Lists of independent variants for IBD and PCA calculations were generated using PLINK ('--indep 50 5 2'). For the affected sib-pair (ASP) cohort genotyped on the Immunochip, we retained only one T1D sample from each family selected at random. For the GRID case and 1958 birth control cohorts genotyped on the Immunochip, a portion of the cases overlapped the T1DGC or 1958 birth cohorts genotyped on a genome-wide array. We thus used sample IDs from the phenotype files to remove these samples from the GRID and 1958 birth cohorts and verified that no samples were duplicated between the Immunochip and genome-wide array data sets by checking IBD. We combined data for matched case and control cohorts based on genotyping array and country of origin for imputation. We used the TOPMed Imputation Server³¹ to impute genotypes into the TOPMed r2 panel⁷ and removed variants based on low imputation quality ($R^2 < 0.3$). Following imputation, we implemented post-imputation filters to remove variants based on potential genotyping or imputation artefacts based on empirical R^2 (genotyped variants with empirical $R^2 < 0.5$ and all imputed variants in at least low linkage disequilibrium; LD, $r^2 > 0.3$).

For the UK Biobank cohort, we downloaded imputed genotype data from the UK Biobank v3 release that were imputed using a combination of the HRC and UK10K + 1000 Genomes reference panels. We removed data for individuals who had withdrawn

participation from the UK Biobank. We used phenotype data to remove individuals of non-European descent. To resolve duplicate samples represented in both the UK Biobank and other cohorts on different genotyping arrays, we calculated IBD between samples in the UK Biobank and cohorts of UK origin, removing duplicated samples from the UK Biobank ($\text{IBD} > 0.9$). Following these filters, we then used a combination of ICD10 (International Classification of Diseases 10th Revision) codes to define 1,445 T1D cases (T1D diagnosis, insulin treatment within a year of diagnosis, no T2D diagnosis). We defined controls as 362,050 individuals without diabetes (no T1D, T2D, or gestational diabetes diagnosis) or other autoimmune diseases (systemic lupus erythematosus, rheumatoid arthritis, juvenile arthritis, Sjögren syndrome, alopecia areata, multiple sclerosis, autoimmune thyroiditis, vitiligo, coeliac disease, primary biliary cirrhosis, psoriasis, or ulcerative colitis). We removed variants with low imputation quality ($R^2 < 0.3$).

For the FinnGen cohort, we downloaded GWAS summary statistics for T1D (T1D_STRICT) from FinnGen freeze 3 (<http://r3.finngen.fi/>). This phenotype definition excluded individuals with T2D from both cases and controls.

Association testing and meta-analysis

We tested variants with $\text{MAF} > 1 \times 10^{-5}$ for association to T1D with Firth bias reduced logistic regression using EPACTS (<https://genome.sph.umich.edu/wiki/EPACTS>) for non-UK Biobank cohorts or SAIGE³² (version 0.38) for the UK Biobank, using genotype dosages adjusted for sex and the first four ancestry PCs. For the UK Biobank we used SAIGE as it is designed to run on biobank-scale cohorts and with highly imbalanced ratios of cases to controls. For FinnGen, we used association results from the freeze 3 release that were generated using SAIGE. Before meta-analysis, we used liftOver (<https://genome.ucsc.edu/cgi-bin/hgLiftOver>) to convert GRCh37/hg19 into GRCh38/hg38 coordinates for the UK Biobank. We then combined association results across matched cohorts through inverse-variance weighted meta-analysis. We used liftOver to convert GRCh38/hg38 back into GRCh37/hg19 coordinates for the meta-analysis. We removed variants that could not be converted, were duplicated after coordinate conversion, or were located on different chromosomes after conversion. In total, our association data contained summary statistics for 61,947,369 variants. To evaluate the extent to which genomic inflation was driven by the polygenic nature of T1D or population stratification, we used LD score regression³³ to compare the LDSC intercept to lambda genomic control (GC). We observed an intercept of 1.07 (s.e. = 0.03) compared to a lambda GC of 1.20, suggesting that the majority of the observed inflation was driven by polygenicity rather than population stratification.

Stochastic search and fine mapping of independent signals

We identified 59 loci (excluding the MHC locus) with T1D risk variants that had been reported in previous genetic studies of T1D^{4,5,6,34}, and considered a locus in our study known if the most associated variant mapped within 500 kb of a previously reported T1D variant. We defined 33 novel loci where a variant reached genome-wide significance ($P < 5 \times 10^{-8}$), and both mapped at least 500 kb away and was not in LD ($r^2 < 0.01$) with a previously reported T1D variant. At 92 (59 known and 33 novel) loci, we defined the ‘index’ variant as the variant with strongest T1D association at the locus.

For all 92 loci, we used a 1-Mb window around the index variant as the region for fine mapping using FINEMAP³⁵ (version 1.4). For each region, we first filtered for variants with MAF > 0.0005 and constructed pairwise LD matrices with PLINK²⁷ (‘--r --square --keep-allele-order’) using the TOPMed2-imputed cohorts with genome-wide coverage (DCCT-EDIC, GENIE-ROI, GENIE-UK, GoKinD, T1DGC, WTCCC1-T1D and their respective control cohorts). We then applied FINEMAP using these matrices to conduct shotgun stochastic search and Bayesian fine mapping using the default prior (‘--sss --n-causal-snps 10 --prob-cred-set 0.99 --prior-std 0.05’). We selected the number of independent signals (causal variants) for each region based on the configuration with the highest FINEMAP posterior probability and used 99% credible sets from the FINEMAP output for the resulting signals. We calculated the effective sample size for all credible set variants, and no credible set variant with PPA > 0.01 had <50% of the maximum effective sample size. We compared fine-mapping results to a previous fine-mapping dataset⁸. At 56 signals in common to both studies, we calculated the number of variants in the 99% credible set and the probability of the most likely causal variant.

GWAS correlation analyses

We used LD score regression^{29,33} (version 1.0.1) to estimate genome-wide genetic correlations between T1D and immune diseases^{36,37,38,39,40,41,42,43,44}, other diseases^{45,46,47,48,49,50,51,52,53,54,55}, and non-disease traits^{56,57,58,59,60,61,62,63,64,65,66,67,68,69,70,71,72,73,74}, using European subsets of GWAS where applicable. For acute pancreatitis, chronic pancreatitis, and pancreatic cancer, we used inverse variance weighted meta-analysis to combine SAIGE analysis results from the UK Biobank³² (PheCodes 577.1, 577.2, and 157) and FinnGen r3 (K11_ACUTPANC, K11_CHRONPANC, C3_PANCREAS_EXALLC). We used pre-computed European 1000 Genomes LD scores to calculate correlation estimates (r_g) and standard errors. We then corrected P values for multiple tests using FDR correction and considered FDR < 0.1 as significant. We also performed genetic correlation analyses using a version of the T1D meta-analysis excluding the Immunochip cohorts and observed highly similar results.

Generation of snATAC-seq libraries

Combinatorial indexing single-cell ATAC-seq (snATAC-seq)

We performed snATAC-seq as described previously^{75,76,77} with several modifications as described below. For the islet samples, approximately 3,000 islet equivalents (IEQ, roughly 1,000 cells each) were resuspended in 1 ml nuclei permeabilization buffer (10 mM Tris-HCl (pH 7.5), 10 mM NaCl, 3 mM MgCl₂, 0.1% Tween-20 (Sigma), 0.1% IGEPAL-CA630 (Sigma) and 0.01% Digitonin (Promega) in water) and homogenized using a 1-ml glass dounce homogenizer with a tight-fitting pestle for 15 strokes. Homogenized islets were incubated for 10 min at 4 °C and filtered with a 30-µm filter (CellTrics). For the pancreas samples, frozen tissue was pulverized with a mortar and pestle while frozen and immersed in liquid nitrogen. Approximately 22 mg of pulverized tissue was then transferred to an Eppendorf tube and resuspended in 1 ml cold permeabilization buffer for 10 min on a rotator at 4 °C. Permeabilized sample was filtered with a 30-µm filter (CellTrics), and the filter was washed with 300 µl permeabilization buffer to increase nucleus recovery.

Once permeabilized and filtered, nuclei were pelleted with a swinging bucket centrifuge (500g, 5 min, 4 °C; 5920R, Eppendorf) and resuspended in 500 µl high-salt tagmentation buffer (36.3 mM Tris acetate (pH 7.8), 72.6 mM potassium acetate, 11 mM Mg acetate, 17.6% DMF) and counted using a haemocytometer. Concentration was adjusted to 4,500 nuclei per 9 µl, and 4,500 nuclei were dispensed into each well of a 96-well plate. Glycerol was added to the leftover nucleus suspension for a final concentration of 25% and nuclei were stored at -80 °C. For tagmentation, 1 µl barcoded Tn5 transposomes were added using a BenchSmart 96 (Mettler Toledo), mixed five times and incubated for 60 min at 37 °C with shaking (500 rpm). To inhibit the Tn5 reaction, 10 µl of 40 mM EDTA was added to each well with a BenchSmart 96 (Mettler Toledo) and the plate was incubated at 37 °C for 15 min with shaking (500 rpm). Next, 20 µl 2 × sort buffer (2% BSA, 2 mM EDTA in PBS) was added using a BenchSmart 96 (Mettler Toledo). All wells were combined into a FACS tube and stained with 3 µM Draq7 (Cell Signaling). Using an SH800 (Sony), 20 nuclei were sorted per well into eight 96-well plates (total of 768 wells) containing 10.5 µl EB (25 pmol primer i7, 25 pmol primer i5, 200 ng BSA (Sigma)). Preparation of sort plates and all downstream pipetting steps were performed on a Biomek i7 Automated Workstation (Beckman Coulter). After addition of 1 µl 0.2% SDS, samples were incubated at 55 °C for 7 min with shaking (500 rpm). We added 1 µl 12.5% Triton-X to each well to quench the SDS and 12.5 µl NEBNext High-Fidelity 2 × PCR Master Mix (NEB). Samples were PCR-amplified (72 °C 5 min, 98 °C 30 s, (98 °C 10 s, 63 °C 30 s, 72 °C 60 s) × 12 cycles, held at 12 °C). After PCR, all wells were combined. Libraries were purified according to the MinElute PCR Purification Kit manual (Qiagen) using a vacuum manifold (QIAvac 24 plus, Qiagen) and size selection was performed with

SPRI Beads (Beckmann Coulter, 0.55 \times and 1.5 \times). Libraries were purified one more time with SPRI Beads (Beckmann Coulter, 1.5 \times). Libraries were quantified using a Qubit fluorimeter (Life technologies) and the nucleosomal pattern was verified using a TapeStation (High Sensitivity D1000, Agilent). The library was sequenced on a HiSeq2500 sequencer (Illumina) using custom sequencing primers, 25% spike-in library and the following read lengths: 50 + 43 + 40 + 50 (Read1 + Index1 + Index2 + Read2).

Droplet-based 10x single-cell ATAC-seq (snATAC-seq)

The 10x single-cell ATAC-seq protocol from 10x Genomics was followed: Chromium SingleCell ATAC ReagentKits UserGuide (CG000209, Rev A). Cryopreserved PBMC samples were thawed in a 37 °C water bath for 2 min according to the ‘PBMC thawing protocol’ in the UserGuide. After cells were thawed, the pellets were resuspended in 1 ml chilled PBS (with 0.04% PBS) and filtered with 50 μ m CellTrics (04-0042-2317, Sysmex). The cells were centrifuged (300g, 5 min, 4 °C) and permeabilized with 100 μ l chilled lysis buffer (10 mM Tris-HCl pH 7.4, 10 mM NaCl, 3 mM MgCl₂, 0.1% Tween-20, 0.1% IGEPAL-CA630, 0.01% digitonin and 1% BSA). The samples were incubated on ice for 3 min and resuspended with 1 ml chilled wash buffer (10 mM Tris-HCl pH 7.4, 10 mM NaCl, 3 mM MgCl₂, 0.1% Tween-20 and 1% BSA). After centrifugation (500g, 5 min, 4 °C), the pellets were resuspended in 100 μ l chilled Nuclei buffer (2000153, 10x Genomics). The nucleus concentration was adjusted to between 3,000 and 7,000 per μ l and 15,300 nuclei (which targets 10,000 nuclei) were used for the experiment. For pancreas tissue (pulverized as described above), approximately 31.7 mg of pulverized tissue was transferred to a LoBind tube (Eppendorf) and resuspended in 1 ml cold permeabilization buffer (10 mM Tris-HCL (pH 7.5), 10 mM NaCl, 3 mM MgCl₂, 0.1% Tween-20 (Sigma), 0.1% IGEPAL-CA630 (Sigma), 0.01% Digitonin (Promega) and 1% BSA (Proliant 7500804) in water) for 10 min on a rotator at 4 °C. Permeabilized nuclei were filtered with a 30- μ m filter (CellTrics). Filtered nuclei were pelleted with a swinging bucket centrifuge (500g, 5 min, 4 °C; 5920R, Eppendorf) and resuspended in 1 ml wash buffer (10 mM Tris-HCL (pH 7.5), 10 mM NaCl, 3 mM MgCl₂, 0.1% Tween-20, and 1% BSA (Proliant 7500804) in molecular biology-grade water). The nucleus wash was repeated once. Next, washed nuclei were resuspended in 30 μ l 1 \times nuclei buffer (10x Genomics). Nuclei were counted using a haemocytometer, and finally the nucleus concentration was adjusted to 3,000 nuclei per μ l. We used 15,360 nuclei as input for tagmentation.

Nuclei were diluted to 5 μ l with 1 \times nuclei buffer (10x Genomics) and mixed with ATAC buffer (10x Genomics) and ATAC enzyme (10x Genomics) for tagmentation (60 min, 37 °C). Single-cell ATAC-seq libraries were generated using the Chromium Chip E Single Cell ATAC kit (10x Genomics, 1000086) and indexes (Chromium i7

Multiplex Kit N, Set A, 10x Genomics, 1000084) following the manufacturer's instructions. Final libraries were quantified using a Qubit fluorimeter (Life Technologies) and the nucleosomal pattern was verified using a TapeStation (High Sensitivity D1000, Agilent). Libraries were sequenced on a NextSeq 500 and HiSeq 4000 sequencer (Illumina) with the following read lengths: 50 + 8 + 16 + 50 (Read1 + Index1 + Index2 + Read2).

Single-cell chromatin accessibility data processing

Before read alignment, we used trim_galore (version 0.4.4) to remove adaptor sequences from reads using default parameters. For combinatorial barcoding data, we aligned reads to the hg19 reference genome using bwa mem⁷⁸ (version 0.7.17-r1188; ‘-M -C’) and removed low mapping quality (MAPQ < 30), secondary, unmapped, and mitochondrial reads using samtools⁷⁹ (version 1.10). To remove duplicate sequences on a per-barcode level, we used the MarkDuplicates tool from picard (‘BARCODE_TAG’). For droplet-based 10x data, we used Cell Ranger ATAC (version 1.1.0) to process, align, and remove duplicate reads. For each tissue and snATAC-seq technology, we used log-transformed read depth distributions from each experiment to determine a threshold separating real cell barcodes from background noise. We used >500 total reads for combinatorial barcoding snATAC-seq and >2,300–4,000 total reads, as well as >0.3 fraction of reads in peaks, for 10x snATAC-seq experiments (Supplementary Fig. 7a).

Single-cell chromatin accessibility clustering

We identified snATAC-seq clusters using a previously described pipeline with a few modifications⁷⁵. For each experiment, we first constructed a counts matrix consisting of read counts in 5-kb windows for each cell. Using scanpy⁸⁰ (version 1.4.4.post1), we normalized cells to a uniform read depth and log-transformed counts. We extracted highly variable (hv) windows (‘min_mean = 0.01, min_disp = 0.25’) and regressed out the total log-transformed read depth within hv windows (usable counts). We then merged datasets from the same tissue and performed PCA to extract the top 50 PCs. We used Harmony⁸¹ (version 1.0) to correct the PCs for batch effects across experiments, using categorical covariates including donor-of-origin, biological sex, and snATAC-seq assay technology. We used the corrected components to construct a 30 nearest neighbour graph using the cosine metric, which we used for UMAP dimensionality reduction (‘min_dist = 0.3’) and clustering with the Leiden algorithm⁸² (‘resolution = 1.5’).

Before combining cells across all tissues, we performed iterative clustering to identify and remove cells with low fraction of reads in peaks (using preliminary peaks called from data in bulk) or low usable counts (islets: 948, pancreas: 2,588, PBMCs: 5,268

cells removed in total). Next, after removing low-quality cells and repeating the previous clustering steps, we sub-clustered the resulting main clusters at high resolution ('resolution = 3.0') to identify sub-clusters containing potential doublets (islets: 886, pancreas: 4,495, PBMCs: 5,844 cells removed in total). We noted that these sub-clusters tended to have higher average usable counts, promoter usage, and accessibility at more than one marker gene promoter. After removing 20,029 low-quality or potential doublet cells, we performed a final round of clustering using experiments from all tissues, including tissue-of-origin as another covariate. We further removed 672 cells that mapped to improbable cluster assignments (islet or pancreatic cells in PBMC clusters or vice versa). After all filters, we ended up with 131,554 cells mapping to 28 distinct clusters with consistent representation across samples from the same tissue (Supplementary Fig. 7b). We catalogued known marker genes for each cell type using a combination of literature search and PanglaoDB⁸³ (Supplementary Table 6) and assessed gene accessibility (sum of read counts across each gene body) to assign labels to each cluster.

Single-cell gene expression clustering

We compiled publicly available scRNA-seq data sets of peripheral blood (10x Genomics; v1 Chemistry: 3k, 6k, and 33k; v2 Chemistry: 4k and 8k; v3 Chemistry: 5k and 10k; v3.1 Chemistry: 5k, 10k single indexed, and 10k dual indexed) and pancreatic islets⁸⁴. We re-processed each dataset using Cell Ranger RNA (version 4.0.0) with the GRCh37 reference genome and removed cells with <500 genes expressed (non-zero counts). We extracted hv genes for PBMCs and pancreatic islets separately and merged both lists to obtain a single set of hv genes. For each sample, we used count matrices as input for scanpy⁸⁰ (version 1.4.4.post1), normalized counts for each cell to uniform read depth, log-transformed the normalized counts, and regressed out the log total counts for hv genes. We then merged all datasets and extracted the top 100 PCs using PCA. We used Harmony⁸¹ (version 1.0) to correct PCs for covariates including the experiment, donor, tissue, and biological sex. We constructed a 30 nearest neighbour graph using the cosine metric, performed UMAP dimensionality reduction ('min_dist = 0.3'), and clustered with the Leiden algorithm⁸² ('resolution = 1.25'). We performed iterative clustering to remove 10,014 low quality and 5,286 potential doublet cells, leaving 90,495 cells for the cell-type-resolved expression reference map. We used a combination of literature search and PanglaoDB⁸³ (Supplementary Table 6) to assign labels to each cluster. For each cell type, we normalized aggregated reads from individual cells to derive TPM for each gene.

Cataloguing cell-type-resolved cCREs

We identified chromatin accessibility peaks with MACS2⁸⁵ (version 2.1.2) by calling peaks on aggregated reads from each cluster. In brief, we extracted reads from all cells within a given cluster, shifted reads aligned to the positive strand by +4 bp and reads aligned to the negative strand by -5 bp, and centred the reads. We then used MACS2 to call peaks (' --nomodel --keep-dup-all') and removed peaks that overlapped ENCODE blacklisted regions^{2,86}. We then merged peaks from all 28 clusters with bedtools⁸⁷

(version 2.26.0) to create a consistent set of 448,142 cCREs for subsequent analyses.

To compare accessible chromatin profiles from snATAC-seq to those from bulk ATAC-seq on FACS-purified cell types, we reprocessed published ATAC-seq data from sorted pancreatic⁸⁸ and unstimulated immune cells⁸⁹. We created pseudobulk profiles from the snATAC-seq data for each donor and cluster, retaining those that contained information from >50 cells. We then extracted read counts in the 448,142 cCREs for all sorted and pseudobulk profiles. We used PCA to extract the top 20 principal components and used UMAP for dimensionality reduction and visualization ('min_dist = 0.5, n_neighbours = 80').

Defining cell-type-specific cCREs

To identify cCREs with accessibility levels most specific to each cluster, we used logistic regression models for each cCRE treating each cell as an individual data point. We performed separate regressions for each cluster, with binary cluster assignment and the covariates donor-of-origin and the log usable count as predictors and binary accessibility of the peak as the outcome, to calculate chromatin accessibility (CA) *t*-statistics. For a given cluster, we defined cCREs with activity most specific to that cluster by taking the top 1,000 cCREs with the highest CA *t*-statistics, after first filtering out cCREs that also had high CA *t*-statistics for other clusters (cCRE cell type CA *t*-statistics >90th percentile in >2 other cell types). The cCREs were all significant after Bonferroni correction for the number of peaks ($P < 1.1 \times 10^{-7}$) except for pancreatic CD8⁺ T cells ($n = 428$ after correction), regulatory T cells ($n = 347$) and memory CD8⁺ T cells ($n = 175$). We then used GREAT⁹⁰ (version 3) to annotate gene ontology terms that were enriched in each set of cell-type-specific cCREs compared to a background of all cCREs.

To assess whether cell-type-specific cCREs tended to be close in proximity to genes with cell-type-specific expression, we defined 100-kb windows around the midpoint of each cell-type-specific cCRE and annotated genes with overlapping TSSs. For each cell type that had a corresponding cluster in scRNA-seq, we compared whether genes around cell-type-specific

cCREs for that cell type had higher gene expression specificity scores than the rest of the cell type-specific cCREs using two-sided Welch's *t*-tests. We collapsed cell-type-specific cCREs for cell types with more than one state in snATAC-seq but only one state in scRNA-seq.

Comparing single-cell chromatin accessibility and gene expression clusters

To compare cell types from snATAC-seq and scRNA-seq, we first derived gene expression *t*-statistics for each gene using linear regression models separately for each cluster of log-transformed read count as a function of binary cluster assignment, donor-of-origin, and log sequencing depth, treating cells as individual data points. For each gene, we also used chromatin accessibility *t*-statistics for promoter cCREs (see 'Defining cell-type-specific cCREs'). For each scRNA-seq cluster, we extracted the top 100 most specific genes based on the gene expression *t*-statistic. Using a merged list of the most specific genes across all clusters, we compared gene expression and promoter accessibility *t*-statistics using Pearson correlation.

Single-cell motif enrichment

We estimated TF motif enrichment *z*-scores for each cell using chromVAR⁹¹ (version 1.5.0) by following the steps outlined in the user manual. First, we constructed a sparse binary matrix encoding read overlap with merged peaks for each cell. For each merged peak, we estimated the GC content bias to obtain a set of matched background peaks. To ensure a motif enrichment value for each cell, we did not apply any additional filters based on total reads or the fraction of reads in peaks. Next, using 580 TF motifs within the JASPAR 2018 CORE vertebrate (non-redundant) set⁹², we computed GC bias-corrected enrichment *z*-scores (chromVAR deviation scores) for each cell. For each cell type, we considered a TF motif enriched if the average *z*-score across cells was greater than 2. We used the TFClass database⁹³ (<http://tfclass.bioinf.med.uni-goettingen.de/>) to group enriched TF motifs into structural sub-families. We determined the expression of all TFs within the subfamily in each cell type identified in scRNA-seq and considered TFs expressed in a cell type with TPM > 1.

Single-cell co-accessibility

We used Cicero⁹⁴ (version 1.3.3) to calculate co-accessibility scores between pairs of peaks for each cluster. As in the single-cell motif enrichment analysis, we started from a sparse binary matrix. For each cluster, we only retained merged peaks that overlapped peaks from the cluster. Within each cluster, we aggregated cells based on the 50 nearest neighbours and used Cicero to calculate co-accessibility scores, using a 1-Mb window size and a distance constraint of 500 kb. We then defined promoters as ± 500 bp from the TSS of protein-coding transcripts from GENCODE v19⁹⁵ to annotate co-accessibility links between gene promoters and distal cCREs (non-promoter cCREs).

To assess whether genes with co-accessible links between the promoter and distal cCREs (co-accessible genes; co-accessibility score >0.05) were expressed more often than non-co-accessible genes (co-accessibility score <0) within each cell type, we separated co-accessible links into bins based on the distance between the gene promoter and distal cCRE. Within each bin, we then compared the fraction of genes expressed in the cell type (TPM > 1 from scRNA-seq) between co-accessible and non-co-accessible genes using two-sided Fisher's exact tests. We collapsed co-accessible links for cell types with more than one state in snATAC-seq but only one state in scRNA-seq (alpha, beta, and delta cells). No comparison was made for pancreatic CD8⁺ T cells, which did not have a corresponding cluster in scRNA-seq.

GWAS enrichment analyses

We used stratified LD score regression^{33,96,97} (version 1.0.1) to calculate genome-wide enrichment z-scores for 32 diseases and traits including T1D. We obtained GWAS summary statistics for autoimmune and inflammatory diseases (immune-related)^{36,37,38,39,40,41,42,43,44}, other diseases^{45,46,47,48,49,50,51,52,53}, and quantitative endophenotypes^{56,57,58,59,60,61,62,63,64,65}, and where necessary, we filled in variant IDs and alleles. Using 'munge_sumstats.py', we converted summary statistics to the LD score regression standard format. For each cluster, we

considered overlap with chromatin accessibility peaks as a binary annotation for variants. Then, we computed annotation-specific LD scores by following the instructions for creating partitioned LD scores. We estimated enrichment coefficient z -scores for each annotation relative to the background annotations in the baseline-LD model (version 2.2). Using the enrichment z -scores, we computed two-sided P values to assess significance and corrected for multiple tests using the Benjamini–Hochberg procedure. We also calculated GWAS enrichment z -scores for T1D using a version of the meta-analysis excluding the Immunochip cohorts and observed highly similar enrichment results.

From the full GWAS summary statistics, we first extracted variants with $\text{MAF} > 0.05$ and calculated approximate Bayes factors⁹⁸ for each variant, assuming prior variance in allelic effects = 0.04. We then used fgwas⁹⁹ (version 0.3.6) to estimate T1D enrichment for common variants ($\text{MAF} > 0.05$) within cell-type-specific cCREs using an average window size of 1 Mb and also including annotations for coding exons, 3'/5'UTR regions and 1 kb upstream of the TSS from GENCODE in each model. We considered cell-type annotations enriched where $\ln(95\% \text{ CI lower bound}) > 0$ and depleted where $\ln(95\% \text{ CI upper bound}) < 0$.

Annotating cell-type mechanisms of variants at fine mapped signals

We compared the proportion of credible set variants with $\text{PPA} > 0.50$ that overlapped a cCRE compared to other credible set variants using a two-sided Fisher's exact test. Among credible set variants in cCREs, we further compared the proportion of credible set variants with $\text{PPA} > 0.50$ in a cCRE that was co-accessible with a gene promoter compared to other credible set variants using a two-sided Fisher's exact test.

For each T1D signal, we calculated the cumulative posterior probability of all credible set variants that overlapped cCREs that were active in T cells, monocytes, plasmacytoid dendritic cells, beta cells, acinar cells and ductal cells. For each signal that overlapped cCREs, we annotated genes within 1 Mb of the index variant that were (i) expressed in the same cell type(s)

(TPM >1 from scRNA-seq) and (ii) co-accessible with a cCRE harbouring a credible set variant with PPA > 0.01.

Luciferase reporter assays

We tested for allelic differences in enhancer activity at rs7795896 using multiple constructs. First, we cloned a 180-bp sequence of human DNA (Coriell) containing the reference or alternate allele into the luciferase reporter vector pGL4.23 (Promega) in the forward direction using the restriction enzymes SacI and KpnI. Second, we cloned a larger 594-bp sequence of human DNA (Coriell) containing the rs7795896 reference allele that corresponded to the coordinates of the ductal-specific cCRE into pGL4.23 in the forward direction using the restriction enzymes SacI and KpnI. We introduced the alternate allele via SDM using the NEB Q5 Site Directed Mutagenesis kit (New England Biolabs) on 1 ng plasmid containing the reference allele and primers designed using the NEBaseChanger v.1.2.8 software. Sequence identity for all plasmids was confirmed with Sanger sequencing using the RV3 primer. Cloning primers were designed using Primer3 version 0.4.0. Primer sequences for cloning and SDM are listed in Supplementary Table [11](#).

We obtained Capan-1 cells from ATCC, and cells were authenticated by ATCC using karyotyping, morphology and PCR-based approaches. Cells tested negative for mycoplasma contamination. We grew Capan-1 cells, a model for ductal cells [100](#), to approximately 70% confluence according to ATCC culture recommendations in 6-well or 24-well plates and fed complete growth medium the day before transfection. For the 180-bp construct, 2,500 ng experimental or empty (pGL4.23) vector was co-transfected with 50 ng pRL-SV40 per sample using Lipofectamine 3000 (Invitrogen) into Capan-1 cells grown in a 6-well plate. For the 594-bp construct, 500 ng experimental or empty vector was co-transfected with 10 ng pRL-TK per sample using Lipofectamine 3000 (Invitrogen) into Capan-1 cells grown in a 24-well plate. The experiment was also repeated using 50 ng pRL-TK per sample. For all experiments, samples were assayed 48 h after transfection using the Dual-Glo Luciferase Assay System (Promega). We normalized Firefly:Renilla ratios with respect to the empty vector and

used either two-sided, two-way ANOVA or two-sided Student's *t*-test to compare luciferase activity between the two alleles.

Electrophoretic mobility shift assay

We ordered double-stranded 5' biotinylated and corresponding unlabelled (cold) oligonucleotides of 16 bp centred on rs7795896 with the reference and alternate alleles from Integrated DNA Technologies. Oligo sequences are listed in Supplementary Table 11. We performed EMSA using the LightShift Chemiluminescent EMSA kit (Thermo Fisher) according to the manufacturer's instructions with the following adjustments: 100 fmol of biotinylated duplex probe per reaction, and 20 pmol of the same-allele non-biotinylated duplex 'cold' probe in competition reactions ($200 \times$ molar excess of the biotin probe). We used the NE-PER Nuclear Protein and Cytoplasmic Extraction Reagents (Thermo Fisher) kit to extract nuclear protein from Capan-1 cells and used 2 μ l nuclear extract per binding reaction, corresponding to approximately 5–15 μ g nuclear protein per reaction. We quantified bound and free probe (unbound) band intensity using ImageJ (v.1.53) and calculated the ratio of bound to unbound intensity. We then averaged bound ratios for replicates of each allele and compared ratios between alleles.

CRISPR inactivation of enhancer element

We obtained HEK293T cells from ATCC, and cells were authenticated by ATCC using karyotyping, morphology and PCR-based approaches. Cells tested negative for mycoplasma contamination. We maintained HEK293T cells in DMEM containing 100 units/ml penicillin and 100 mg/ml streptomycin sulfate supplemented with 10% fetal bovine serum. To generate CRISPRi lentiviral expression vectors, we designed guide RNA sequences to target the enhancer containing rs7795896 or the *CFTR* promoter. These guide RNAs, as well as a non-targeting control guide RNA, were placed downstream of the human U6 promoter in the pLV hU6-sgRNA hUbC-dCas9-KRAB-T2a-Puro backbone (Addgene, plasmid #71236). Targeting guide RNAs were designed using Benchling and selected to maximize both on-target binding¹⁰¹ and guide specificity¹⁰². The non-targeting control guide RNA was selected from a previously validated

genome-wide library¹⁰³. Guide RNA sequences and targeted regions are listed in Supplementary Table 11. Higher scores indicate greater on-target binding and specificity.

We generated high-titre lentiviral supernatants by co-transfection of the resulting plasmid and lentiviral packaging constructs into HEK293T cells. Specifically, we co-transfected CRISPRi vectors with the pCMV-R8.74 (Addgene, #22036) and pMD2.G (Addgene, #12259) expression plasmids into HEK293T cells using a 1 mg/ml PEI solution (Polysciences). We collected lentiviral supernatants at 48 and 72 h after transfection and concentrated lentiviruses by ultracentrifugation for 120 min at 19,500 rpm using a Beckman SW28 ultracentrifuge rotor at 4 °C. Lentiviral titres were subsequently determined using a qPCR Lentivirus Titer Kit (Abm Bio), and aliquots were stored at –80 °C.

We obtained Capan-1 pancreatic ductal adenocarcinoma cell lines from ATCC and cultured them using Iscove's modified Dulbecco's medium with 20% fetal bovine serum, 100 units/ml penicillin, and 100 mg/ml streptomycin sulfate. Twenty-four hours before transduction, we passaged cells into a 12-well plate at a density of 100,000 cells per well. The following day, we added fresh medium containing 8 µg/ml polybrene and concentrated CRISPRi lentivirus at an MOI of 40 to each well. For each condition (1 non-targeting guide RNA, 3 enhancer-targeting guide RNAs, and 1 promoter-targeting guide RNA) we transduced 3 wells for a total of 15 wells. We additionally included 3 wells of mock-transduced cells without lentivirus. We incubated the cells at 37 °C for 30 min and then spun them in a centrifuge for 1 h at 30 °C at 950g. Six hours later, we replaced viral medium with fresh base culture medium for cell recovery. After 48 h, we replaced medium daily with the addition of 1 µg/ml puromycin for an additional 72 h, at which point all mock-transduced cells were killed. We reduced the concentration of puromycin to 0.5 µg/ml and cultured cells with daily medium changes for an additional week before passaging each cell line into a 48-well plate at a density of approximately 100,000 cells per well. The following morning, we harvested cells from each condition and isolated RNA using the RNeasy Micro Kit (Qiagen) according to the manufacturer's instructions.

For qRT–PCR, we performed cDNA synthesis using the iScript cDNA Synthesis Kit (Bio-Rad) and 250 ng of isolated RNA per reaction. We performed qRT–PCR reactions in triplicate with 5 ng of template cDNA per reaction using a CFX96 Real-Time PCR Detection System and the iQ SYBR Green Supermix (Bio-Rad). We used PCR of the TATA binding protein (TBP) coding sequence as an internal control, quantified relative expression via double delta CT analysis, and compared relative expression using two-sided ANOVA (enhancer inactivation versus non-targeting control) or a two-sided Student’s *t*-test (promoter inactivation versus non-targeting control). Genes with C_t values greater than 34 were considered as not expressed. We also evaluated changes in expression of the puromycin resistance gene and the dCAS9 gene as additional controls. For eukaryotic genes, each primer pair was designed to span an exon–exon junction. Primers used for qPCR are listed in Supplementary Table 11.

Colocalization and deconvolution of the pancreas *CFTR* eQTL

We obtained GTEx v7¹⁴ eQTL summary statistics for pancreas tissue from 220 samples and used effect size (beta) and standard error estimates from the regression model for *CFTR* expression to calculate approximate Bayes factors⁹⁸ for each variant, assuming prior variance in allelic effects = 0.04. We considered all variants in a 500-kb window around the T1D index variant at *CFTR* (rs7795896) tested in both the GWAS and eQTL data sets and used coloc¹⁰⁴ (version 4.0.4) to calculate the probability that the variants driving T1D and eQTL signals were shared, using prior probabilities $PP_{T1D} = 1 \times 10^{-4}$, $PP_{eQTL} = 1 \times 10^{-4}$, and $PP_{shared} = 1 \times 10^{-5}$. We considered the T1D and *CFTR* eQTL signals to be colocalized on the basis that the probability that they were shared (PP_{shared}) > 0.9. We applied eCAVIAR¹⁰⁵ (version 2.2) using variants in a 500-kb window that were tested for both T1D and eQTL association using LD calculated from EUR samples in 1000 Genomes³⁰ and considered variants with CLPP > 0.01 to be candidate causal variants for a shared signal.

We used MuSiC¹⁰⁶ (version 0.1.1) to estimate the proportions of major pancreatic cell types (acinar, duct, stellate, alpha, beta, delta, gamma) in each GTEx v7 pancreas sample. As input, we used raw count matrices from

scRNA-seq of pancreatic cell types with labels from the gene expression reference map and GTEx v7 pancreas samples. For each cell type, we used the proportion as an interaction term and constructed linear models of TMM-normalized *CFTR* expression as a function of the interaction between genotype dosage and cell-type proportion, accounting for covariates used by GTEx including sex, sequencing platform, 3 genotype PCs, and 28 inferred PCs from the expression data. From the original 30 inferred PCs, we excluded inferred PCs 2 and 3 because they were highly correlated with acinar cell proportion (Spearman's $\rho > 0.7$). No remaining PCs were highly correlated (Spearman's $\rho < 0.3$) with the proportions of other cell types.

Phenotype associations at T1D signals

We tested association of the T1D index variant at *CFTR* (rs7795896) for pancreatic and autoimmune disease phenotypes. For acute pancreatitis, chronic pancreatitis, and pancreatic cancer, we used inverse variance weighted meta-analysis to combine SAIGE analysis results from the UK Biobank³² (PheCodes 577.1, 577.2, and 157) and FinnGen (K11_ACUTPANC, K11_CHRONPANC, C3_PANCREAS_EXALLC). As mutations that cause cystic fibrosis (CF), which are risk factors for pancreatitis and pancreatic cancer, map to this locus, we determined the impact of the most common CF mutation F508del/rs199826652 on the association results for rs7795896. For T1D, we tested for association of rs7795896 conditional on F508del/rs199826652 in all cohorts except for FinnGen and observed no evidence for a difference in T1D association. For pancreatitis and pancreatic cancer, we identified F508del/rs199826652 carriers in the UK Biobank and repeated the association analysis for these phenotypes in UK Biobank data after removing these individuals and observed no evidence of a change in the effect of rs7795896.

We identified T1D signals where the risk allele had at least nominal association ($P < 0.05$) with increased risk of acute pancreatitis, chronic pancreatitis, or pancreatic cancer. We then tested whether these T1D signals had a difference in cPPA in exocrine cell cCREs or T cell cCREs compared to other T1D signals using a two-sided Student's *t*-test.

Human participant ethics

Genotype data obtained from dbGAP, WTCCC, and the UK Biobank were used in accordance with approved research plans for these data as obtained from the respective data repositories. Tissue samples for pancreas and peripheral blood were obtained from external biorepositories nPOD and Hemacare, and all individuals gave consent for the use of tissue samples. All genotype data and tissue samples were de-identified before being obtained and all studies were approved by the Institutional Review Board of UCSD.

Reporting summary

Further information on research design is available in the [Nature Research Reporting Summary](#) linked to this paper.

Data availability

Full summary statistics for the T1D GWAS have been deposited into the NHGRI-EBI GWAS catalogue with accession number GCST90014023 and can be downloaded from

http://ftp.ebi.ac.uk/pub/databases/gwas/summary_statistics/GCST90014001-GCST90015000/GCST90014023/. Sequencing data for snATAC-seq have been deposited into the NCBI Gene Expression Omnibus (GEO) with accession number [GSE163160](#). Data obtained from the TFClass database are available at <http://tfclass.bioinf.med.uni-goettingen.de/> and from the PanglaoDB database at <https://panglaodb.se/>. Source data are provided with this paper.

Code availability

Code used for processing snATAC-seq data sets and clustering cells is available at

https://github.com/kjgaulton/pipelines/tree/master/T1D_snATAC_pipeline.

References

1. 1.

Claussnitzer, M. et al. A brief history of human disease genetics. *Nature* **577**, 179–189 (2020).

[ADS](#) [CAS](#) [PubMed](#) [PubMed Central](#) [Google Scholar](#)

2. 2.

ENCODE Project Consortium. An integrated encyclopedia of DNA elements in the human genome. *Nature* **489**, 57–74 (2012).

[ADS](#) [Google Scholar](#)

3. 3.

Katsarou, A. et al. Type 1 diabetes mellitus. *Nat. Rev. Dis. Primers* **3**, 17016 (2017).

[PubMed](#) [Google Scholar](#)

4. 4.

Onengut-Gumuscu, S. et al. Fine mapping of type 1 diabetes susceptibility loci and evidence for colocalization of causal variants with lymphoid gene enhancers. *Nat. Genet.* **47**, 381–386 (2015).

[CAS](#) [PubMed](#) [PubMed Central](#) [Google Scholar](#)

5. 5.

Barrett, J. C. et al. Genome-wide association study and meta-analysis find that over 40 loci affect risk of type 1 diabetes. *Nat. Genet.* **41**, 703–707 (2009).

[CAS](#) [PubMed](#) [PubMed Central](#) [Google Scholar](#)

6. 6.

Bradfield, J. P. et al. A genome-wide meta-analysis of six type 1 diabetes cohorts identifies multiple associated loci. *PLoS Genet.* **7**, e1002293 (2011).

[CAS](#) [PubMed](#) [PubMed Central](#) [Google Scholar](#)

7. 7.

Taliun, D. et al. Sequencing of 53,831 diverse genomes from the NHLBI TOPMed Program. *Nature* **590**, 290–299 (2021).

[ADS](#) [CAS](#) [PubMed](#) [PubMed Central](#) [Google Scholar](#)

8. 8.

Aylward, A., Chiou, J., Okino, M.-L., Kadakia, N. & Gaulton, K. J. Shared genetic risk contributes to type 1 and type 2 diabetes etiology. *Hum. Mol. Genet.* ddy314 (2018).

9. 9.

Raeder, H. et al. Mutations in the CEL VNTR cause a syndrome of diabetes and pancreatic exocrine dysfunction. *Nat. Genet.* **38**, 54–62 (2006).

[CAS](#) [PubMed](#) [Google Scholar](#)

10. 10.

Ramos, P. S. et al. A comprehensive analysis of shared loci between systemic lupus erythematosus (SLE) and sixteen autoimmune diseases reveals limited genetic overlap. *PLoS Genet.* **7**, e1002406 (2011).

[CAS](#) [PubMed](#) [PubMed Central](#) [Google Scholar](#)

11. 11.

Gibson-Corley, K. N., Meyerholz, D. K. & Engelhardt, J. F. Pancreatic pathophysiology in cystic fibrosis. *J. Pathol.* **238**, 311–320 (2016).

[PubMed](#) [Google Scholar](#)

12. 12.

Sharer, N. et al. Mutations of the cystic fibrosis gene in patients with chronic pancreatitis. *N. Engl. J. Med.* **339**, 645–652 (1998).

[CAS](#) [PubMed](#) [Google Scholar](#)

13. 13.

Diaferia, G. R. et al. Dissection of transcriptional and cis-regulatory control of differentiation in human pancreatic cancer. *EMBO J.* **35**, 595–617 (2016).

[CAS](#) [PubMed](#) [PubMed Central](#) [Google Scholar](#)

14. 14.

GTEX Consortium. Genetic effects on gene expression across human tissues. *Nature* **550**, 204–213 (2017).

15. 15.

McWilliams, R. R. et al. Cystic fibrosis transmembrane conductance regulator (CFTR) gene mutations and risk for pancreatic adenocarcinoma. *Cancer* **116**, 203–209 (2010).

[CAS](#) [PubMed](#) [PubMed Central](#) [Google Scholar](#)

16. 16.

Noone, P. G. et al. Cystic fibrosis gene mutations and pancreatitis risk: relation to epithelial ion transport and trypsin inhibitor gene mutations. *Gastroenterology* **121**, 1310–1319 (2001).

[CAS](#) [PubMed](#) [Google Scholar](#)

17. 17.

Virostko, J. et al. Pancreas volume declines during the first year after diagnosis of type 1 diabetes and exhibits altered diffusion at disease onset. *Diabetes Care* **42**, 248–257 (2019).

[CAS](#) [PubMed](#) [Google Scholar](#)

18. 18.

Campbell-Thompson, M., Rodriguez-Calvo, T. & Battaglia, M. Abnormalities of the exocrine pancreas in type 1 diabetes. *Curr. Diab. Rep.* **15**, 79 (2015).

[PubMed](#) [PubMed Central](#) [Google Scholar](#)

19. 19.

Camunas-Soler, J. et al. Patch-seq links single-cell transcriptomes to human islet dysfunction in diabetes. *Cell Metab.* **31**, 1017–1031 (2020).

[CAS](#) [PubMed](#) [PubMed Central](#) [Google Scholar](#)

20. 20.

Fasolino, M. et al. Multiomics single-cell analysis of human pancreatic islets reveals novel cellular states in health and type 1 diabetes. Preprint at <https://doi.org/10.1101/2021.01.28.428598> (2021).

21. 21.

Hart, N. J. et al. Cystic fibrosis-related diabetes is caused by islet loss and inflammation. *JCI Insight* **3**, e98240 (2018).

[PubMed Central](#) [Google Scholar](#)

22. 22.

Valle, A. et al. Reduction of circulating neutrophils precedes and accompanies type 1 diabetes. *Diabetes* **62**, 2072–2077 (2013).

[CAS](#) [PubMed](#) [PubMed Central](#) [Google Scholar](#)

23. 23.

Navis, A. & Bagnat, M. Loss of *cftr* function leads to pancreatic destruction in larval zebrafish. *Dev. Biol.* **399**, 237–248 (2015).

[CAS](#) [PubMed](#) [PubMed Central](#) [Google Scholar](#)

24. 24.

Lin, Y. et al. Genome-wide association meta-analysis identifies GP2 gene risk variants for pancreatic cancer. *Nat. Commun.* **11**, 3175 (2020).

[ADS](#) [CAS](#) [PubMed](#) [PubMed Central](#) [Google Scholar](#)

25. 25.

Wolpin, B. M. et al. Genome-wide association study identifies multiple susceptibility loci for pancreatic cancer. *Nat. Genet.* **46**, 994–1000 (2014).

[CAS](#) [PubMed](#) [PubMed Central](#) [Google Scholar](#)

26. 26.

Johansson, B. B. et al. The role of the carboxyl ester lipase (CEL) gene in pancreatic disease. *Pancreatology* **18**, 12–19 (2018).

[CAS](#) [PubMed](#) [Google Scholar](#)

27. 27.

Purcell, S. et al. PLINK: a tool set for whole-genome association and population-based linkage analyses. *Am. J. Hum. Genet.* **81**, 559–575 (2007).

[CAS](#) [PubMed](#) [PubMed Central](#) [Google Scholar](#)

28. 28.

McCarthy, S. et al. A reference panel of 64,976 haplotypes for genotype imputation. *Nat. Genet.* **48**, 1279–1283 (2016).

[CAS](#) [PubMed](#) [PubMed Central](#) [Google Scholar](#)

29. 29.

Bulik-Sullivan, B. et al. An atlas of genetic correlations across human diseases and traits. *Nat. Genet.* **47**, 1236–1241 (2015).

[CAS](#) [PubMed](#) [PubMed Central](#) [Google Scholar](#)

30. 30.

1000 Genomes Project Consortium A global reference for human genetic variation. *Nature* **526**, 68–74 (2015).

31. 31.

Das, S. et al. Next-generation genotype imputation service and methods. *Nat. Genet.* **48**, 1284–1287 (2016).

[CAS](#) [PubMed](#) [PubMed Central](#) [Google Scholar](#)

32. 32.

Zhou, W. et al. Efficiently controlling for case-control imbalance and sample relatedness in large-scale genetic association studies. *Nat. Genet.* **50**, 1335–1341 (2018).

[CAS](#) [PubMed](#) [PubMed Central](#) [Google Scholar](#)

33. 33.

Bulik-Sullivan, B. K. et al. LD score regression distinguishes confounding from polygenicity in genome-wide association studies. *Nat. Genet.* **47**, 291–295 (2015).

[CAS](#) [PubMed](#) [PubMed Central](#) [Google Scholar](#)

34. 34.

Evangelou, M. et al. A method for gene-based pathway analysis using genomewide association study summary statistics reveals nine new type 1 diabetes associations. *Genet. Epidemiol.* **38**, 661–670 (2014).

[PubMed](#) [PubMed Central](#) [Google Scholar](#)

35. 35.

Benner, C. et al. FINEMAP: efficient variable selection using summary data from genome-wide association studies. *Bioinformatics* **32**, 1493–1501 (2016).

[CAS](#) [PubMed](#) [PubMed Central](#) [Google Scholar](#)

36. 36.

Ji, S.-G. et al. Genome-wide association study of primary sclerosing cholangitis identifies new risk loci and quantifies the genetic relationship with inflammatory bowel disease. *Nat. Genet.* **49**, 269–273 (2017).

[MathSciNet](#) [CAS](#) [PubMed](#) [Google Scholar](#)

37. 37.

Bentham, J. et al. Genetic association analyses implicate aberrant regulation of innate and adaptive immunity genes in the pathogenesis of systemic lupus erythematosus. *Nat. Genet.* **47**, 1457–1464 (2015).

[CAS](#) [PubMed](#) [PubMed Central](#) [Google Scholar](#)

38. 38.

Cordell, H. J. et al. International genome-wide meta-analysis identifies new primary biliary cirrhosis risk loci and targetable pathogenic

pathways. *Nat. Commun.* **6**, 8019 (2015).

[CAS](#) [PubMed](#) [PubMed Central](#) [Google Scholar](#)

39. 39.

Okada, Y. et al. Genetics of rheumatoid arthritis contributes to biology and drug discovery. *Nature* **506**, 376–381 (2014).

[ADS](#) [CAS](#) [PubMed](#) [Google Scholar](#)

40. 40.

de Lange, K. M. et al. Genome-wide association study implicates immune activation of multiple integrin genes in inflammatory bowel disease. *Nat. Genet.* **49**, 256–261 (2017).

[PubMed](#) [PubMed Central](#) [Google Scholar](#)

41. 41.

Dubois, P. C. A. et al. Multiple common variants for celiac disease influencing immune gene expression. *Nat. Genet.* **42**, 295–302 (2010).

[CAS](#) [PubMed](#) [PubMed Central](#) [Google Scholar](#)

42. 42.

Jin, Y. et al. Genome-wide association studies of autoimmune vitiligo identify 23 new risk loci and highlight key pathways and regulatory variants. *Nat. Genet.* **48**, 1418–1424 (2016).

[CAS](#) [PubMed](#) [PubMed Central](#) [Google Scholar](#)

43. 43.

Paternoster, L. et al. Multi-ancestry genome-wide association study of 21,000 cases and 95,000 controls identifies new risk loci for atopic dermatitis. *Nat. Genet.* **47**, 1449–1456 (2015).

[PubMed](#) [PubMed Central](#) [Google Scholar](#)

44. 44.

López-Isac, E. et al. GWAS for systemic sclerosis identifies multiple risk loci and highlights fibrotic and vasculopathy pathways. *Nat. Commun.* **10**, 4955 (2019).

[PubMed](#) [PubMed Central](#) [Google Scholar](#)

45. 45.

Jansen, I. E. et al. Genome-wide meta-analysis identifies new loci and functional pathways influencing Alzheimer's disease risk. *Nat. Genet.* **51**, 404–413 (2019).

[CAS](#) [PubMed](#) [PubMed Central](#) [Google Scholar](#)

46. 46.

Mahajan, A. et al. Fine-mapping type 2 diabetes loci to single-variant resolution using high-density imputation and islet-specific epigenome maps. *Nat. Genet.* **50**, 1505–1513 (2018).

[CAS](#) [PubMed](#) [PubMed Central](#) [Google Scholar](#)

47. 47.

Nelson, C. P. et al. Association analyses based on false discovery rate implicate new loci for coronary artery disease. *Nat. Genet.* **49**, 1385–1391 (2017).

[CAS](#) [PubMed](#) [Google Scholar](#)

48. 48.

Stahl, E. A. et al. Genome-wide association study identifies 30 loci associated with bipolar disorder. *Nat. Genet.* **51**, 793–803 (2019).

[CAS](#) [PubMed](#) [PubMed Central](#) [Google Scholar](#)

49. 49.

Wray, N. R. et al. Genome-wide association analyses identify 44 risk variants and refine the genetic architecture of major depression. *Nat. Genet.* **50**, 668–681 (2018).

[CAS](#) [PubMed](#) [PubMed Central](#) [Google Scholar](#)

50. 50.

Grove, J. et al. Identification of common genetic risk variants for autism spectrum disorder. *Nat. Genet.* **51**, 431–444 (2019).

[CAS](#) [PubMed](#) [PubMed Central](#) [Google Scholar](#)

51. 51.

Watson, H. J. et al. Genome-wide association study identifies eight risk loci and implicates metabo-psychiatric origins for anorexia nervosa. *Nat. Genet.* **51**, 1207–1214 (2019).

[CAS](#) [PubMed](#) [PubMed Central](#) [Google Scholar](#)

52. 52.

Schizophrenia Working Group of the Psychiatric Genomics Consortium. Biological insights from 108 schizophrenia-associated genetic loci. *Nature* **511**, 421–427 (2014).

[ADS](#) [PubMed Central](#) [Google Scholar](#)

53. 53.

Wuttke, M. et al. A catalog of genetic loci associated with kidney function from analyses of a million individuals. *Nat. Genet.* **51**, 957–972 (2019).

[CAS](#) [PubMed](#) [PubMed Central](#) [Google Scholar](#)

54. 54.

Nielsen, J. B. et al. Biobank-driven genomic discovery yields new insight into atrial fibrillation biology. *Nat. Genet.* **50**, 1234–1239 (2018).

[CAS](#) [PubMed](#) [PubMed Central](#) [Google Scholar](#)

55. 55.

Tachmazidou, I. et al. Identification of new therapeutic targets for osteoarthritis through genome-wide analyses of UK Biobank data. *Nat. Genet.* **51**, 230–236 (2019).

[CAS](#) [PubMed](#) [PubMed Central](#) [Google Scholar](#)

56. 56.

Wheeler, E. et al. Impact of common genetic determinants of hemoglobin A1c on type 2 diabetes risk and diagnosis in ancestrally diverse populations: a transethnic genome-wide meta-analysis. *PLoS Med.* **14**, e1002383 (2017).

[PubMed](#) [PubMed Central](#) [Google Scholar](#)

57. 57.

Horikoshi, M. et al. Genome-wide associations for birth weight and correlations with adult disease. *Nature* **538**, 248–252 (2016).

[CAS](#) [PubMed](#) [PubMed Central](#) [Google Scholar](#)

58. 58.

Yengo, L. et al. Meta-analysis of genome-wide association studies for height and body mass index in ~ 700000 individuals of European ancestry. *Hum. Mol. Genet.* **27**, 3641–3649 (2018).

[CAS](#) [PubMed](#) [PubMed Central](#) [Google Scholar](#)

59. 59.

Jiang, X. et al. Genome-wide association study in 79,366 European-ancestry individuals informs the genetic architecture of 25-hydroxyvitamin D levels. *Nat. Commun.* **9**, 260 (2018).

[ADS](#) [PubMed](#) [PubMed Central](#) [Google Scholar](#)

60. 60.

Manning, A. K. et al. A genome-wide approach accounting for body mass index identifies genetic variants influencing fasting glycemic traits and insulin resistance. *Nat. Genet.* **44**, 659–669 (2012).

[CAS](#) [PubMed](#) [PubMed Central](#) [Google Scholar](#)

61. 61.

Day, F. R. et al. Large-scale genomic analyses link reproductive aging to hypothalamic signaling, breast cancer susceptibility and BRCA1-mediated DNA repair. *Nat. Genet.* **47**, 1294–1303 (2015).

[CAS](#) [PubMed](#) [PubMed Central](#) [Google Scholar](#)

62. 62.

Day, F. R. et al. Genomic analyses identify hundreds of variants associated with age at menarche and support a role for puberty timing in cancer risk. *Nat. Genet.* **49**, 834–841 (2017).

[CAS](#) [PubMed](#) [PubMed Central](#) [Google Scholar](#)

63. 63.

Savage, J. E. et al. Genome-wide association meta-analysis in 269,867 individuals identifies new genetic and functional links to intelligence. *Nat. Genet.* **50**, 912–919 (2018).

[CAS](#) [PubMed](#) [PubMed Central](#) [Google Scholar](#)

64. 64.

Strawbridge, R. J. et al. Genome-wide association identifies nine common variants associated with fasting proinsulin levels and provides new insights into the pathophysiology of type 2 diabetes. *Diabetes* **60**, 2624–2634 (2011).

[CAS](#) [PubMed](#) [PubMed Central](#) [Google Scholar](#)

65. 65.

Saxena, R. et al. Genetic variation in GIPR influences the glucose and insulin responses to an oral glucose challenge. *Nat. Genet.* **42**, 142–148 (2010).

[CAS](#) [PubMed](#) [PubMed Central](#) [Google Scholar](#)

66. 66.

Tobacco and Genetics Consortium. Genome-wide meta-analyses identify multiple loci associated with smoking behavior. *Nat. Genet.* **42**, 441–447 (2010).

[Google Scholar](#)

67. 67.

Shungin, D. et al. New genetic loci link adipose and insulin biology to body fat distribution. *Nature* **518**, 187–196 (2015).

[CAS](#) [PubMed](#) [PubMed Central](#) [Google Scholar](#)

68. 68.

Cousminer, D. L. et al. Genome-wide association and longitudinal analyses reveal genetic loci linking pubertal height growth, pubertal

timing and childhood adiposity. *Hum. Mol. Genet.* **22**, 2735–2747 (2013).

[CAS](#) [PubMed](#) [PubMed Central](#) [Google Scholar](#)

69. 69.

Taal, H. R. et al. Common variants at 12q15 and 12q24 are associated with infant head circumference. *Nat. Genet.* **44**, 532–538 (2012).

[CAS](#) [PubMed](#) [PubMed Central](#) [Google Scholar](#)

70. 70.

Teumer, A. et al. Genome-wide analyses identify a role for SLC17A4 and AADAT in thyroid hormone regulation. *Nat. Commun.* **9**, 4455 (2018).

[ADS](#) [PubMed](#) [PubMed Central](#) [Google Scholar](#)

71. 71.

Jansen, P. R. et al. Genome-wide analysis of insomnia in 1,331,010 individuals identifies new risk loci and functional pathways. *Nat. Genet.* **51**, 394–403 (2019).

[CAS](#) [PubMed](#) [Google Scholar](#)

72. 72.

van der Valk, R. J. P. et al. A novel common variant in DCST2 is associated with length in early life and height in adulthood. *Hum. Mol. Genet.* **24**, 1155–1168 (2015).

[PubMed](#) [Google Scholar](#)

73. 73.

Willer, C. J. et al. Discovery and refinement of loci associated with lipid levels. *Nat. Genet.* **45**, 1274–1283 (2013).

[CAS](#) [PubMed](#) [PubMed Central](#) [Google Scholar](#)

74. 74.

Felix, J. F. et al. Genome-wide association analysis identifies three new susceptibility loci for childhood body mass index. *Hum. Mol. Genet.* **25**, 389–403 (2016).

[CAS](#) [PubMed](#) [Google Scholar](#)

75. 75.

Chiou, J. et al. Single cell chromatin accessibility identifies pancreatic islet cell type- and state-specific regulatory programs of diabetes risk. *Nat. Genet.* **53**, 455–466 (2021).

[CAS](#) [PubMed](#) [Google Scholar](#)

76. 76.

Preissl, S. et al. Single-nucleus analysis of accessible chromatin in developing mouse forebrain reveals cell-type-specific transcriptional regulation. *Nat. Neurosci.* **21**, 432–439 (2018).

[CAS](#) [PubMed](#) [PubMed Central](#) [Google Scholar](#)

77. 77.

Cusanovich, D. A. et al. Multiplex single cell profiling of chromatin accessibility by combinatorial cellular indexing. *Science* **348**, 910–914 (2015).

[ADS](#) [CAS](#) [PubMed](#) [PubMed Central](#) [Google Scholar](#)

78. 78.

Li, H. & Durbin, R. Fast and accurate long-read alignment with Burrows-Wheeler transform. *Bioinformatics* **26**, 589–595 (2010).

[PubMed](#) [PubMed Central](#) [Google Scholar](#)

79. 79.

Li, H. et al. The sequence alignment/map format and SAMtools. *Bioinformatics* **25**, 2078–2079 (2009).

[PubMed](#) [PubMed Central](#) [Google Scholar](#)

80. 80.

Wolf, F. A., Angerer, P. & Theis, F. J. SCANPY: large-scale single-cell gene expression data analysis. *Genome Biol.* **19**, 15 (2018).

[PubMed](#) [PubMed Central](#) [Google Scholar](#)

81. 81.

Korsunsky, I. et al. Fast, sensitive and accurate integration of single-cell data with Harmony. *Nat. Methods* **16**, 1289–1296 (2019).

[CAS](#) [PubMed](#) [PubMed Central](#) [Google Scholar](#)

82. 82.

Traag, V. A., Waltman, L. & van Eck, N. J. From Louvain to Leiden: guaranteeing well-connected communities. *Sci. Rep.* **9**, 5233 (2019).

[ADS](#) [CAS](#) [PubMed](#) [PubMed Central](#) [Google Scholar](#)

83. 83.

Franzén, O., Gan, L.-M. & Björkegren, J. L. M. PanglaoDB: a web server for exploration of mouse and human single-cell RNA sequencing data. *Database* **2019**, baz046 (2019).

[PubMed](#) [PubMed Central](#) [Google Scholar](#)

84. 84.

Xin, Y. et al. Pseudotime ordering of single human β -cells reveals states of insulin production and unfolded protein response. *Diabetes* **67**, 1783–1794 (2018).

[CAS](#) [PubMed](#) [Google Scholar](#)

85. 85.

Zhang, Y. et al. Model-based analysis of ChIP-seq (MACS). *Genome Biol.* **9**, R137 (2008).

[PubMed](#) [PubMed Central](#) [Google Scholar](#)

86. 86.

Amemiya, H. M., Kundaje, A. & Boyle, A. P. The ENCODE blacklist: identification of problematic regions of the genome. *Sci. Rep.* **9**, 9354 (2019).

[ADS](#) [PubMed](#) [PubMed Central](#) [Google Scholar](#)

87. 87.

Quinlan, A. R. & Hall, I. M. BEDTools: a flexible suite of utilities for comparing genomic features. *Bioinformatics* **26**, 841–842 (2010).

[CAS](#) [PubMed](#) [PubMed Central](#) [Google Scholar](#)

88. 88.

Arda, H. E. et al. A chromatin basis for cell lineage and disease risk in the human pancreas. *Cell Syst.* **7**, 310–322 (2018).

[CAS](#) [PubMed](#) [Google Scholar](#)

89. 89.

Calderon, D. et al. Landscape of stimulation-responsive chromatin across diverse human immune cells. *Nat. Genet.* **51**, 1494–1505 (2019).

[CAS](#) [PubMed](#) [PubMed Central](#) [Google Scholar](#)

90. 90.

McLean, C. Y. et al. GREAT improves functional interpretation of cis-regulatory regions. *Nat. Biotechnol.* **28**, 495–501 (2010).

[CAS](#) [PubMed](#) [PubMed Central](#) [Google Scholar](#)

91. 91.

Schep, A. N., Wu, B., Buenrostro, J. D. & Greenleaf, W. J. chromVAR: inferring transcription-factor-associated accessibility from single-cell epigenomic data. *Nat. Methods* **14**, 975–978 (2017).

[CAS](#) [PubMed](#) [PubMed Central](#) [Google Scholar](#)

92. 92.

Khan, A. et al. JASPAR 2018: update of the open-access database of transcription factor binding profiles and its web framework. *Nucleic Acids Res.* **46**, D260–D266 (2018).

[CAS](#) [PubMed](#) [Google Scholar](#)

93. 93.

Wingender, E., Schoeps, T., Haubrock, M. & Dönitz, J. TFClass: a classification of human transcription factors and their rodent orthologs. *Nucleic Acids Res.* **43**, D97–D102 (2015).

[CAS](#) [PubMed](#) [Google Scholar](#)

94. 94.

Pliner, H. A. et al. Cicero predicts *cis*-regulatory DNA interactions from single-cell chromatin accessibility data. *Mol. Cell* **71**, 858–871 (2018).

[CAS](#) [PubMed](#) [PubMed Central](#) [Google Scholar](#)

95. 95.

Harrow, J. et al. GENCODE: the reference human genome annotation for The ENCODE Project. *Genome Res.* **22**, 1760–1774 (2012).

[CAS](#) [PubMed](#) [PubMed Central](#) [Google Scholar](#)

96. 96.

Finucane, H. K. et al. Partitioning heritability by functional annotation using genome-wide association summary statistics. *Nat. Genet.* **47**, 1228–1235 (2015).

[CAS](#) [PubMed](#) [PubMed Central](#) [Google Scholar](#)

97. 97.

Cusanovich, D. A. et al. A single-cell atlas of in vivo mammalian chromatin accessibility. *Cell* **174**, 1309–1324 (2018).

[CAS](#) [PubMed](#) [PubMed Central](#) [Google Scholar](#)

98. 98.

Wakefield, J. Bayes factors for genome-wide association studies: comparison with P-values. *Genet. Epidemiol.* **33**, 79–86 (2009).

[PubMed](#) [Google Scholar](#)

99. 99.

Pickrell, J. K. Joint analysis of functional genomic data and genome-wide association studies of 18 human traits. *Am. J. Hum. Genet.* **94**, 559–573 (2014).

[CAS](#) [PubMed](#) [PubMed Central](#) [Google Scholar](#)

100. 100.

Namkung, W. et al. Ca²⁺ activates cystic fibrosis transmembrane conductance regulator- and Cl⁻-dependent HCO3⁻ transport in pancreatic duct cells. *J. Biol. Chem.* **278**, 200–207 (2003).

[CAS](#) [PubMed](#) [Google Scholar](#)

101. 101.

Doench, J. G. et al. Optimized sgRNA design to maximize activity and minimize off-target effects of CRISPR–Cas9. *Nat. Biotechnol.* **34**, 184–191 (2016).

[CAS](#) [PubMed](#) [PubMed Central](#) [Google Scholar](#)

102. 102.

Hsu, P. D. et al. DNA targeting specificity of RNA-guided Cas9 nucleases. *Nat. Biotechnol.* **31**, 827–832 (2013).

[CAS](#) [PubMed](#) [PubMed Central](#) [Google Scholar](#)

103. 103.

Horlbeck, M. A. et al. Compact and highly active next-generation libraries for CRISPR-mediated gene repression and activation. *eLife* **5**, e19760 (2016).

[PubMed](#) [PubMed Central](#) [Google Scholar](#)

104. 104.

Giambartolomei, C. et al. Bayesian test for colocalisation between pairs of genetic association studies using summary statistics. *PLoS Genet.* **10**, e1004383 (2014).

[PubMed](#) [PubMed Central](#) [Google Scholar](#)

105. 105.

Hormozdiari, F. et al. Colocalization of GWAS and eQTL signals detects target genes. *Am. J. Hum. Genet.* **99**, 1245–1260 (2016).

[CAS](#) [PubMed](#) [PubMed Central](#) [Google Scholar](#)

106. 106.

Wang, X., Park, J., Susztak, K., Zhang, N. R. & Li, M. Bulk tissue cell type deconvolution with multi-subject single-cell expression reference. *Nat. Commun.* **10**, 380 (2019).

[ADS](#) [CAS](#) [PubMed](#) [PubMed Central](#) [Google Scholar](#)

[Download references](#)

Acknowledgements

This work was supported by NIH grants DK112155, DK120429 and DK122607 to K.J.G. and M.S., and T32 GM008666 to R.J.G. We thank S. Kuan for assistance with sequencing. Additional acknowledgements for each cohort are listed in the Supplementary Information.

Author information

Author notes

1. Joshua Chiou

Present address: Internal Medicine Research Unit, Pfizer Worldwide Research, Cambridge, MA, USA

2. David U. Gorkin

Present address: Department of Biology, Emory University, Atlanta, GA, USA

Affiliations

1. Biomedical Sciences Graduate Program, University of California San Diego, La Jolla, CA, USA

Joshua Chiou, Ryan J. Geusz & Rebecca Melton

2. Department of Pediatrics, Pediatric Diabetes Research Center, University of California San Diego, La Jolla, CA, USA

Mei-Lin Okino, Elisha Beebe, Paola Benaglio, Serina Huang, Katha Korgaonkar, Maike Sander & Kyle J. Gaulton

3. Center for Epigenomics, Department of Cellular and Molecular Medicine, University of California San Diego, La Jolla, CA, USA

Jee Yun Han, Michael Miller, Sebastian Preissl & David U. Gorkin

4. Department of Internal Medicine I, Ulm University, Ulm, Germany

Sandra Heller & Alexander Kleger

5. Department of Cellular and Molecular Medicine, University of California San Diego, La Jolla, CA, USA

Maike Sander

6. Institute for Genomic Medicine, University of California San Diego, La Jolla, CA, USA

Maike Sander & Kyle J. Gaulton

Authors

1. Joshua Chiou

[View author publications](#)

You can also search for this author in [PubMed](#) [Google Scholar](#)

2. Ryan J. Geusz

[View author publications](#)

You can also search for this author in [PubMed](#) [Google Scholar](#)

3. Mei-Lin Okino

[View author publications](#)

You can also search for this author in [PubMed](#) [Google Scholar](#)

4. Jee Yun Han

[View author publications](#)

You can also search for this author in [PubMed](#) [Google Scholar](#)

5. Michael Miller

[View author publications](#)

You can also search for this author in [PubMed](#) [Google Scholar](#)

6. Rebecca Melton

[View author publications](#)

You can also search for this author in [PubMed](#) [Google Scholar](#)

7. Elisha Beebe

[View author publications](#)

You can also search for this author in [PubMed](#) [Google Scholar](#)

8. Paola Benaglio

[View author publications](#)

You can also search for this author in [PubMed](#) [Google Scholar](#)

9. Serina Huang

[View author publications](#)

You can also search for this author in [PubMed](#) [Google Scholar](#)

10. Katha Korgaonkar

[View author publications](#)

You can also search for this author in [PubMed](#) [Google Scholar](#)

11. Sandra Heller

[View author publications](#)

You can also search for this author in [PubMed](#) [Google Scholar](#)

12. Alexander Kleger

[View author publications](#)

You can also search for this author in [PubMed](#) [Google Scholar](#)

13. Sebastian Preissl

[View author publications](#)

You can also search for this author in [PubMed](#) [Google Scholar](#)

14. David U. Gorkin

[View author publications](#)

You can also search for this author in [PubMed](#) [Google Scholar](#)

15. Maike Sander

[View author publications](#)

You can also search for this author in [PubMed](#) [Google Scholar](#)

16. Kyle J. Gaulton

[View author publications](#)

You can also search for this author in [PubMed](#) [Google Scholar](#)

Contributions

K.J.G. and J.C. designed the study and wrote the manuscript. J.C. performed genetic association and single-cell genomics analyses. R.J.G. performed molecular experiments on enhancer function. M.-L.O. and S. Huang performed molecular experiments on variant function. R.M. and E.B. contributed to analyses of single-cell gene expression. J.Y.H. and M.M. generated single-cell accessible chromatin data. P.B. and K.K. contributed to single-cell motif enrichment analysis. D.U.G. and S.P. supervised the generation of single-cell accessible chromatin data and contributed to data interpretation and analyses. M.S. supervised experiments related to enhancer function and contributed to data interpretation. S. Heller and A.K. contributed to the design and interpretation of enhancer experiments.

Corresponding authors

Correspondence to [Joshua Chiou](#) or [Kyle J. Gaulton](#).

Ethics declarations

Competing interests

K.J.G is a consultant for Genentech and holds stock in Vertex Pharmaceuticals; neither is related to the work in this study. The other

authors declare no competing interests.

Additional information

Peer review information *Nature* thanks Jason Torres, Anna Hutchinson, Chris Wallace and the other, anonymous, reviewer(s) for their contribution to the peer review of this work.

Publisher's note Springer Nature remains neutral with regard to jurisdictional claims in published maps and institutional affiliations.

Extended data figures and tables

[Extended Data Fig. 1 Independent association signals at T1D risk loci.](#)

Bayes factors (natural log-transformed) for independent association signals at the known *PTPN2* locus (left) and the novel *BCL11A* locus (right). Variants are coloured by linkage disequilibrium (r^2) with the index variant for each signal.

[Extended Data Fig. 2 Rare variants with large effects on T1D risk.](#)

a, The relationship between minor allele frequency and T1D odds ratios (OR) for index variants at 136 T1D signals. Signals with common index variants and larger effect size estimates (PTPN22 1:114,377,568 A:G and INS 11:2,182,224 A:T) or rare index variants (MAF < 0.005) are labelled. Points and lines represent estimates for OR and 95% CI. **b**, Comparison of OR across cohorts for rare variants. Missing values indicate that the variant was not tested in the cohort. Points and lines represent estimates for OR and 95% CI.

[Extended Data Fig. 3 Genetic correlations between T1D and other traits.](#)

Genetic correlations between T1D and immune-related diseases (left), other diseases (middle), and non-disease traits (right); adj., adjusted; circ., circumference. Two-sided P values are adjusted for multiple comparisons with false discovery rate (FDR). Colours indicate significance: red, correlation is significant after FDR correction ($FDR < 0.1$); black, correlation is nominally significant ($P < 0.05$) but not significant after FDR correction; grey, correlation is not significant. Points and lines represent genetic correlation estimates and 95% CI.

Extended Data Fig. 4 Annotations derived from single-cell chromatin accessibility of T1D-relevant tissues.

a, Relative gene accessibility (column-normalized chromatin accessibility reads in gene bodies) showing examples of marker genes used to identify cluster labels. Aggregated chromatin accessibility profiles in a 50-kb window around selected marker genes (bottom). **b**, Single-cell motif enrichment z-scores (left) and expression of motif subfamily members (right) for examples of TFs with lineage-, cell-type-, or cell-state-specific motif enrichment and expression. TFs with matching motif enrichment and expression are highlighted. **c**, Co-accessibility between *AQPI* and cCREs in ductal cells (left) and *CEL* and cCREs in acinar cells (right).

Extended Data Fig. 5 Single-cell RNA-seq reference map of PBMCs and pancreatic islets.

a, Clustering of 90,495 expression profiles from scRNA-seq experiments of peripheral blood mononuclear cells and pancreatic islets from published studies. Cells are plotted on the first two UMAP components and coloured according to cluster assignment. The number of cells in each cluster is shown next to its corresponding label. HSC, haematopoietic stem cell; $\gamma\delta$ T, gamma delta T cell; pDC, plasmacytoid dendritic cell. **b**, Relative gene expression (average expression for all cells within a cluster and scaled from 0–100 across clusters) showing examples of marker genes used to assign cluster labels. **c**, Pearson correlation coefficient between gene expression and promoter accessibility specificity scores using a list containing the top 100 most specific genes for each scRNA-seq cluster found in snATAC-seq.

Extended Data Fig. 6 GWAS enrichment for T1D compared to other diseases and traits.

Stratified LD score regression coefficient z -scores for autoimmune and inflammatory diseases (top), other diseases (middle), and non-disease quantitative endophenotypes (bottom) for cCREs that are active in immune and pancreatic cell types. Two sided P values were calculated from z -scores and multiple test correction was performed using FDR. ***FDR < 0.001, **FDR < 0.01, *FDR < 0.1.

[Source data](#)

Extended Data Fig. 7 Fine-mapped variants linked to exocrine-specific genes.

a, The *GP2* locus contains three variants in a distal cCRE that is co-accessible with the *GP2* promoter in acinar cells, which account for the majority of the causal probability (cPPA = 0.98). Chromatin accessibility at both the distal cCRE and the *GP2* promoter is highly specific to acinar cells. **b**, Variant rs72802342 at the *CTRBI/2/BCARI* locus overlaps a distal cCRE that is co-accessible with the *CTRBI* and *CTRBI2* promoters in acinar cells. Chromatin accessibility at the *CTRBI* and *CTRBI2* promoters is highly specific to acinar cells. Variants contained in the 99% credible set are circled in black.

Extended Data Fig. 8 rs7795896 has allelic effects on ductal enhancer activity.

a, Relative luciferase units (RLU) for reporter containing 594-bp sequence surrounding rs7795896 in Capan-1 cells ($n = 6$; 2 batches \times 3 transfections). Centre line, median; box limits, 25th and 75th percentiles; whiskers extend to $1.5 \times$ the interquartile range from the 25th and 75th percentiles. P value by two-sided, two-way ANOVA. **b**, Luciferase reporter assay in Capan-1 cells transfected with pGL4.23 minimal promoter plasmids containing rs7795896 in the forward orientation. Relative luciferase units (RLU) represent Firefly:Renilla ratios normalized to control cells transfected with

the empty pGL4.23 vector. P value by two-sided Student's t -test. **c**, Electrophoretic mobility shift assay with nuclear extract from Capan-1 cells using probes for rs7795896 alleles, with or without 200 \times unlabelled competitor probe (200 \times comp.). Quantification of the bound fraction (specific binding/free probe). Data are from $n = 1$ experiment. **d**, rs7795896 overlaps histone marks of active enhancers (H3K4me1, H3K27ac; region: chr7:117,050,000–117,125,000, hg19) but not promoters (H3K4me3) in pancreatic ductal adenocarcinoma (PDAC) cell lines (Capan-1, Capan-2, and CFPAC-1). rs7795896 overlaps a ChIP-seq peak for the transcription factor HNF1B in CFPAC-1 cells and a predicted HNF1B motif. **e**, Relative expression for genes in a 2-Mb window around rs7795896 with non-zero expression and the puromycin resistance and dCas9 genes. Ctrl, control, $n = 3$ biological replicates; Enh, enhancer, $n = 9$, 3 sgRNAs \times 3 biological replicates; Prom, promoter, $n = 3$ biological replicates. Data are mean \pm 95% CI. P values by two-sided Student's t -test (Prom versus Ctrl) or two-sided ANOVA (Enh versus Ctrl); NS, not significant.

Source data

Extended Data Fig. 9 rs7795896 affects *CFTR* expression levels in ductal cells.

a, Bayesian colocalization of T1D signal and *CFTR* pancreas eQTL. Variants in the T1D credible set are circled. **b**, Expression of pancreatic cell type marker genes from scRNA-seq. **c**, Proportions of selected pancreatic cell types estimated by MuSiC for 220 bulk pancreas RNA-seq samples from the GTEx v7 release using single-cell expression profiles. **d**, $-\log_{10}$ -transformed two-sided uncorrected P values from linear regression interaction between dosage and cell-type proportion for the *CFTR* pancreas eQTL.

Extended Data Fig. 10 Relationship between T1D and other pancreatic diseases.

a, rs7795896 GWAS association for T1D (from full meta-analysis), pancreatic disease, and autoimmune disease. Points and lines represent OR

estimates and 95% CI. Two-sided P values from GWAS meta-analysis are unadjusted for multiple comparisons. **b**, Variants that regulate genes with specialized exocrine pancreas function influence T1D risk, and we hypothesize that these effects are mediated through inflammation and immune infiltration.

Supplementary information

Supplementary Information

This file contains Supplementary Figs. 1-9 and the Supplementary Note.

Reporting Summary

Supplementary Tables

This file contains Supplementary Tables 1-11.

Supplementary Data 1

This file contains the 99% credible sets for 136 independent T1D risk signals.

Supplementary Data 2

This file contains cell type-resolved TPM-normalized gene expression for pancreatic and immune cell types.

Supplementary Data 3

This file contains the catalog of 448,142 cCREs.

Supplementary Data 4

This file contains the subset of 25,436 cCREs elements with the most cell type-specific accessibility.

Supplementary Data 5

This file contains cell type-resolved chromVAR motif enrichment z-scores.

Supplementary Data 6

This file contains co-accessibility links between distal cCREs and gene promoters.

Source data

Source Data Fig. 4

Source Data Extended Data Fig. 6

Source Data Extended Data Fig. 8

Rights and permissions

Reprints and Permissions

About this article



Check for
updates

Cite this article

Chiou, J., Geusz, R.J., Okino, M.L. *et al.* Interpreting type 1 diabetes risk with genetics and single-cell epigenomics. *Nature* **594**, 398–402 (2021).
<https://doi.org/10.1038/s41586-021-03552-w>

Download citation

- Received: 21 June 2020
- Accepted: 14 April 2021
- Published: 19 May 2021
- Issue Date: 17 June 2021
- DOI: <https://doi.org/10.1038/s41586-021-03552-w>

Comments

By submitting a comment you agree to abide by our [Terms](#) and [Community Guidelines](#). If you find something abusive or that does not comply with our terms or guidelines please flag it as inappropriate.

[Download PDF](#)

Associated Content

Milestone

[**Diabetes**](#)

Advertisement

This article was downloaded by **calibre** from <https://www.nature.com/articles/s41586-021-03552-w>

- Article
- [Published: 26 May 2021](#)

Intercalated amygdala clusters orchestrate a switch in fear state

- [Kenta M. Hagihara](#) [ORCID: orcid.org/0000-0003-0064-0852^{1,2 na1}](#),
- [Olena Bukalo^{3 na1}](#),
- [Martin Zeller^{4,5}](#),
- [Ayla Aksoy-Aksel^{4,5,6}](#),
- [Nikolaos Karalis¹](#),
- [Aaron Limoges](#) [ORCID: orcid.org/0000-0002-7987-7045³](#),
- [Tanner Rigg³](#),
- [Tiffany Campbell³](#),
- [Adriana Mendez](#) [ORCID: orcid.org/0000-0003-0418-9608³](#),
- [Chase Weinholtz](#) [ORCID: orcid.org/0000-0001-9785-9273³](#),
- [Mathias Mahn](#) [ORCID: orcid.org/0000-0002-8951-1530¹](#),
- [Larry S. Zweifel](#) [ORCID: orcid.org/0000-0003-3465-5331^{7,8}](#),
- [Richard D. Palmiter](#) [ORCID: orcid.org/0000-0001-6587-0582^{9,10,11}](#),
- [Ingrid Ehrlich](#) [ORCID: orcid.org/0000-0001-9078-2429^{4,5,6}](#),
- [Andreas Lüthi](#) [ORCID: orcid.org/0000-0002-1859-4252^{1,2 na2}](#) &
- [Andrew Holmes](#) [ORCID: orcid.org/0000-0001-7308-1129^{3 na2}](#)

[Nature](#) volume 594, pages 403–407 (2021) [Cite this article](#)

- 10k Accesses
- 232 Altmetric
- [Metrics details](#)

Subjects

- [Amygdala](#)
- [Classical conditioning](#)
- [Extinction](#)

Abstract

Adaptive behaviour necessitates the formation of memories for fearful events, but also that these memories can be extinguished. Effective extinction prevents excessive and persistent reactions to perceived threat, as can occur in anxiety and ‘trauma- and stressor-related’ disorders¹. However, although there is evidence that fear learning and extinction are mediated by distinct neural circuits, the nature of the interaction between these circuits remains poorly understood^{2,3,4,5,6}. Here, through a combination of in vivo calcium imaging, functional manipulations, and slice physiology, we show that distinct inhibitory clusters of intercalated neurons (ITCs) in the mouse amygdala exert diametrically opposed roles during the acquisition and retrieval of fear extinction memory. Furthermore, we find that the ITC clusters antagonize one another through mutual synaptic inhibition and differentially access functionally distinct cortical- and midbrain-projecting amygdala output pathways. Our findings show that the balance of activity between ITC clusters represents a unique regulatory motif that orchestrates a distributed neural circuitry, which in turn regulates the switch between high- and low-fear states. These findings suggest that the ITCs have a broader role in a range of amygdala functions and associated brain states that underpins the capacity to adapt to salient environmental demands.

Access options

Subscribe to Journal

Get full journal access for 1 year

\$199.00

only \$3.90 per issue

Subscribe

All prices are NET prices.
VAT will be added later in the checkout.
Tax calculation will be finalised during checkout.

Rent or Buy article

Get time limited or full article access on ReadCube.

from \$8.99

Rent or Buy

All prices are NET prices.

Additional access options:

- [Log in](#)
- [Access through your institution](#)
- [Learn about institutional subscriptions](#)

Fig. 1: ITC clusters differentially signal the presence and absence of an aversive stimulus.

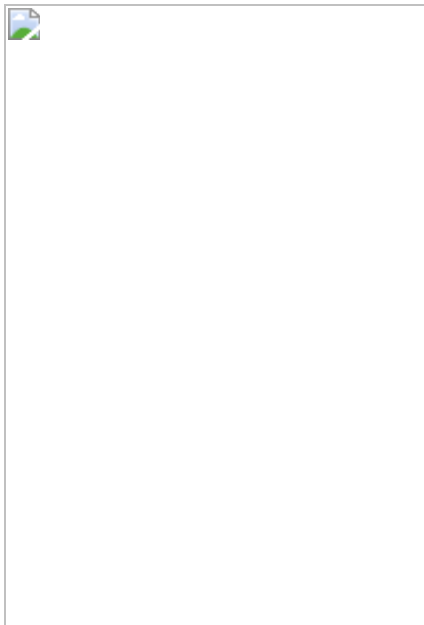


Fig. 2: CS responses of ITC clusters parallel the switch from high- to low-fear state.

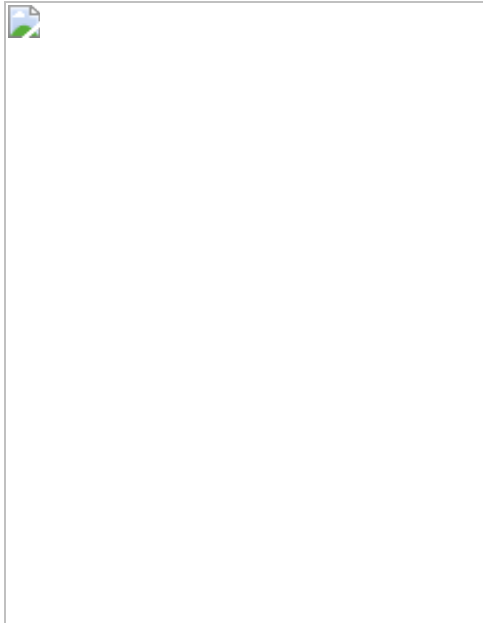


Fig. 3: ITC clusters differentially and bidirectionally regulate fear extinction.

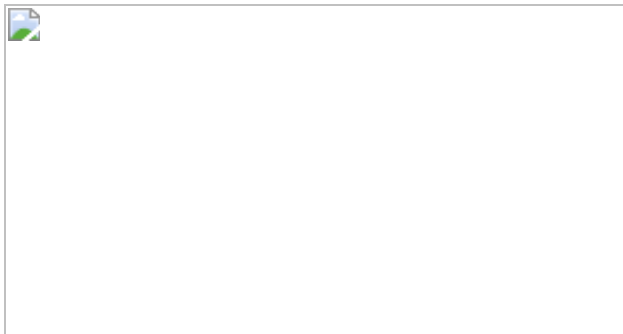
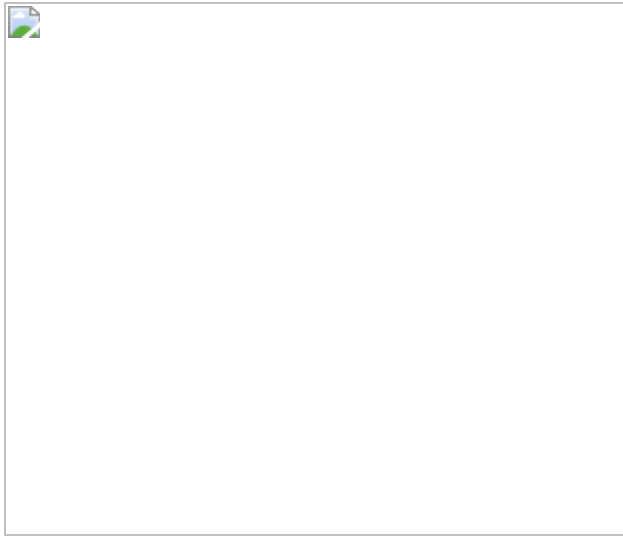


Fig. 4: ITC clusters exert reciprocal inhibition and selective control over extinction-regulating amygdala outputs.



Data availability

The data that support the findings of this study are available at: <https://data.fmi.ch/PublicationSupplementRepo/>. Source data are provided with this paper.

Code availability

Custom-written codes used to analyse data from this study are available upon reasonable request from the corresponding authors.

References

1. 1.

Craske, M. G. et al. Anxiety disorders. *Nat. Rev. Dis. Primers* **3**, 17024 (2017).

[PubMed](#) [Google Scholar](#)

2. 2.

Duvarci, S. & Pare, D. Amygdala microcircuits controlling learned fear. *Neuron* **82**, 966–980 (2014).

[CAS](#) [PubMed](#) [PubMed Central](#) [Google Scholar](#)

3. 3.

Milad, M. R. & Quirk, G. J. Fear extinction as a model for translational neuroscience: ten years of progress. *Annu. Rev. Psychol.* **63**, 129–151 (2012).

[PubMed](#) [PubMed Central](#) [Google Scholar](#)

4. 4.

Orsini, C. A. & Maren, S. Neural and cellular mechanisms of fear and extinction memory formation. *Neurosci. Biobehav. Rev.* **36**, 1773–1802 (2012).

[PubMed](#) [PubMed Central](#) [Google Scholar](#)

5. 5.

Tovoye, P., Fadok, J. P. & Lüthi, A. Neuronal circuits for fear and anxiety. *Nat. Rev. Neurosci.* **16**, 317–331 (2015).

[CAS](#) [PubMed](#) [Google Scholar](#)

6. 6.

Li, B. Central amygdala cells for learning and expressing aversive emotional memories. *Curr. Opin. Behav. Sci.* **26**, 40–45 (2019).

[PubMed](#) [Google Scholar](#)

7. 7.

LeDoux, J. E. Emotion circuits in the brain. *Annu. Rev. Neurosci.* **23**, 155–184 (2000).

[CAS](#) [PubMed](#) [Google Scholar](#)

8. 8.

Bouton, M. E. Context, ambiguity, and unlearning: sources of relapse after behavioral extinction. *Biol. Psychiatry* **52**, 976–986 (2002).

[PubMed](#) [Google Scholar](#)

9. 9.

Herry, C. et al. Neuronal circuits of fear extinction. *Eur. J. Neurosci.* **31**, 599–612 (2010).

[PubMed](#) [Google Scholar](#)

10. 10.

Busti, D. et al. Different fear states engage distinct networks within the intercalated cell clusters of the amygdala. *J. Neurosci.* **31**, 5131–5144 (2011).

[CAS](#) [PubMed](#) [PubMed Central](#) [Google Scholar](#)

11. 11.

Collins, D. R. & Paré, D. Spontaneous and evoked activity of intercalated amygdala neurons. *Eur. J. Neurosci.* **11**, 3441–3448 (1999).

[CAS](#) [PubMed](#) [Google Scholar](#)

12. 12.

Millhouse, O. E. The intercalated cells of the amygdala. *J. Comp. Neurol.* **247**, 246–271 (1986).

[CAS](#) [PubMed](#) [Google Scholar](#)

13. 13.

Waclaw, R. R., Ehrman, L. A., Pierani, A. & Campbell, K. Developmental origin of the neuronal subtypes that comprise the amygdalar fear circuit in the mouse. *J. Neurosci.* **30**, 6944–6953 (2010).

[CAS](#) [PubMed](#) [PubMed Central](#) [Google Scholar](#)

14. 14.

Royer, S., Martina, M. & Paré, D. An inhibitory interface gates impulse traffic between the input and output stations of the amygdala. *J. Neurosci.* **19**, 10575–10583 (1999).

[CAS](#) [PubMed](#) [PubMed Central](#) [Google Scholar](#)

15. 15.

Amano, T., Unal, C. T. & Paré, D. Synaptic correlates of fear extinction in the amygdala. *Nat. Neurosci.* **13**, 489–494 (2010).

[CAS](#) [PubMed](#) [PubMed Central](#) [Google Scholar](#)

16. 16.

Likhtik, E., Popa, D., Apergis-Schoute, J., Fidacaro, G. A. & Paré, D. Amygdala intercalated neurons are required for expression of fear extinction. *Nature* **454**, 642–645 (2008).

[ADS](#) [CAS](#) [PubMed](#) [PubMed Central](#) [Google Scholar](#)

17. 17.

Asede, D., Bosch, D., Lüthi, A., Ferraguti, F. & Ehrlich, I. Sensory inputs to intercalated cells provide fear-learning modulated inhibition to the basolateral amygdala. *Neuron* **86**, 541–554 (2015).

[CAS](#) [PubMed](#) [Google Scholar](#)

18. 18.

Mańko, M., Geracitano, R. & Capogna, M. Functional connectivity of the main intercalated nucleus of the mouse amygdala. *J. Physiol. (Lond.)* **589**, 1911–1925 (2011).

[Google Scholar](#)

19. 19.

Grewé, B. F. et al. Neural ensemble dynamics underlying a long-term associative memory. *Nature* **543**, 670–675 (2017).

[ADS](#) [CAS](#) [PubMed](#) [PubMed Central](#) [Google Scholar](#)

20. 20.

Luo, R. et al. A dopaminergic switch for fear to safety transitions. *Nat. Commun.* **9**, 2483 (2018).

[ADS](#) [PubMed](#) [PubMed Central](#) [Google Scholar](#)

21. 21.

Salinas-Hernández, X. I. et al. Dopamine neurons drive fear extinction learning by signaling the omission of expected aversive outcomes. *eLife* **7**, e38818 (2018).

[PubMed](#) [PubMed Central](#) [Google Scholar](#)

22. 22.

Strobel, C., Marek, R., Gooch, H. M., Sullivan, R. K. P. & Sah, P. Prefrontal and auditory input to intercalated neurons of the amygdala. *Cell Rep.* **10**, 1435–1442 (2015).

[CAS](#) [PubMed](#) [Google Scholar](#)

23. 23.

Herry, C. et al. Switching on and off fear by distinct neuronal circuits. *Nature* **454**, 600–606 (2008).

[ADS](#) [CAS](#) [PubMed](#) [Google Scholar](#)

24. 24.

Paré, D. & Smith, Y. GABAergic projection from the intercalated cell masses of the amygdala to the basal forebrain in cats. *J. Comp. Neurol.* **344**, 33–49 (1994).

[PubMed](#) [Google Scholar](#)

25. 25.

Tovote, P. et al. Midbrain circuits for defensive behaviour. *Nature* **534**, 206–212 (2016).

[ADS](#) [CAS](#) [PubMed](#) [Google Scholar](#)

26. 26.

Senn, V. et al. Long-range connectivity defines behavioral specificity of amygdala neurons. *Neuron* **81**, 428–437 (2014).

[CAS](#) [PubMed](#) [Google Scholar](#)

27. 27.

McGarry, L. M. & Carter, A. G. Inhibitory gating of basolateral amygdala inputs to the prefrontal cortex. *J. Neurosci.* **36**, 9391–9406 (2016).

[CAS](#) [PubMed](#) [PubMed Central](#) [Google Scholar](#)

28. 28.

Arruda-Carvalho, M. & Clem, R. L. Prefrontal-amamygdala fear networks come into focus. *Front. Syst. Neurosci.* **9**, 145 (2015).

[PubMed](#) [PubMed Central](#) [Google Scholar](#)

29. 29.

Koyama, M. & Pujala, A. Mutual inhibition of lateral inhibition: a network motif for an elementary computation in the brain. *Curr. Opin. Neurobiol.* **49**, 69–74 (2018).

[CAS](#) [PubMed](#) [Google Scholar](#)

30. 30.

Machens, C. K., Romo, R. & Brody, C. D. Flexible control of mutual inhibition: a neural model of two-interval discrimination. *Science* **307**, 1121–1124 (2005).

[ADS](#) [CAS](#) [PubMed](#) [Google Scholar](#)

31. 31.

Felsenberg, J. et al. Integration of parallel opposing memories underlies memory extinction. *Cell* **175**, 709–722.e15 (2018).

[CAS](#) [PubMed](#) [PubMed Central](#) [Google Scholar](#)

32. 32.

Solomon, R. L. & Corbit, J. D. An opponent-process theory of motivation. I. Temporal dynamics of affect. *Psychol. Rev.* **81**, 119–145 (1974).

[CAS](#) [PubMed](#) [Google Scholar](#)

33. 33.

Zhang, X., Kim, J. & Tonegawa, S. Amygdala reward neurons form and store fear extinction memory. *Neuron* **105**, 1077–1093.e7 (2020).

[CAS](#) [PubMed](#) [Google Scholar](#)

34. 34.

Braak, H. & Braak, E. Neuronal types in the basolateral amygdaloid nuclei of man. *Brain Res. Bull.* **11**, 349–365 (1983).

[CAS](#) [PubMed](#) [Google Scholar](#)

35. 35.

Roussos, D. L. et al. Two pairs of ON and OFF retinal ganglion cells are defined by intersectional patterns of transcription factor expression. *Cell Rep.* **15**, 1930–1944 (2016).

[CAS](#) [PubMed](#) [PubMed Central](#) [Google Scholar](#)

36. 36.

Guenthner, C. J., Miyamichi, K., Yang, H. H., Heller, H. C. & Luo, L. Permanent genetic access to transiently active neurons via TRAP: targeted recombination in active populations. *Neuron* **78**, 773–784 (2013).

[CAS](#) [PubMed](#) [PubMed Central](#) [Google Scholar](#)

37. 37.

Chen, T. W. et al. Ultrasensitive fluorescent proteins for imaging neuronal activity. *Nature* **499**, 295–300 (2013).

[ADS](#) [CAS](#) [PubMed](#) [PubMed Central](#) [Google Scholar](#)

38. 38.

Vardy, E. et al. A new DREADD facilitates the multiplexed chemogenetic interrogation of behavior. *Neuron* **86**, 936–946 (2015).

[CAS](#) [PubMed](#) [PubMed Central](#) [Google Scholar](#)

39. 39.

Armbruster, B. N., Li, X., Pausch, M. H., Herlitze, S. & Roth, B. L. Evolving the lock to fit the key to create a family of G protein-coupled receptors potently activated by an inert ligand. *Proc. Natl Acad. Sci. USA* **104**, 5163–5168 (2007).

[ADS](#) [PubMed](#) [PubMed Central](#) [Google Scholar](#)

40. 40.

Shemesh, O. A. et al. Temporally precise single-cell-resolution optogenetics. *Nat. Neurosci.* **20**, 1796–1806 (2017).

[CAS](#) [PubMed](#) [PubMed Central](#) [Google Scholar](#)

41. 41.

Dana, H. et al. Sensitive red protein calcium indicators for imaging neural activity. *eLife* **5**, e12727 (2016).

[PubMed](#) [PubMed Central](#) [Google Scholar](#)

42. 42.

Dana, H. et al. High-performance calcium sensors for imaging activity in neuronal populations and microcompartments. *Nat. Methods* **16**, 649–657 (2019).

[CAS](#) [PubMed](#) [Google Scholar](#)

43. 43.

Renier, N. et al. iDISCO: a simple, rapid method to immunolabel large tissue samples for volume imaging. *Cell* **159**, 896–910 (2014).

[CAS](#) [PubMed](#) [Google Scholar](#)

44. 44.

Susaki, E. A. et al. Whole-brain imaging with single-cell resolution using chemical cocktails and computational analysis. *Cell* **157**, 726–739 (2014).

[CAS](#) [PubMed](#) [Google Scholar](#)

45. 45.

Claudi, F. et al. Visualizing anatomically registered data with brainrender. *eLife* **10**, e65751 (2020).

[Google Scholar](#)

46. 46.

Ghosh, K. K. et al. Miniaturized integration of a fluorescence microscope. *Nat. Methods* **8**, 871–878 (2011).

[CAS](#) [PubMed](#) [PubMed Central](#) [Google Scholar](#)

47. 47.

Franklin, K. B. J. & Paxinos, G. *The Mouse Brain in Stereotaxic Coordinates* (Academic, 1997).

48. 48.

Bukalo, O. et al. Prefrontal inputs to the amygdala instruct fear extinction memory formation. *Sci. Adv.* **1**, e1500251 (2015).

[ADS](#) [PubMed](#) [PubMed Central](#) [Google Scholar](#)

49. 49.

Petreanu, L., Huber, D., Sobczyk, A. & Svoboda, K. Channelrhodopsin-2-assisted circuit mapping of long-range callosal projections. *Nat. Neurosci.* **10**, 663–668 (2007).

[CAS](#) [PubMed](#) [Google Scholar](#)

50. 50.

Tanaka, Y., Tanaka, Y., Furuta, T., Yanagawa, Y. & Kaneko, T. The effects of cutting solutions on the viability of GABAergic interneurons in cerebral cortical slices of adult mice. *J. Neurosci. Methods* **171**, 118–125 (2008).

[CAS](#) [PubMed](#) [Google Scholar](#)

51. 51.

Ting, J. T., Daigle, T. L., Chen, Q. & Feng, G. Acute brain slice methods for adult and aging animals: application of targeted patch clamp analysis and optogenetics. *Methods Mol. Biol.* **1183**, 221–242 (2014).

[PubMed](#) [PubMed Central](#) [Google Scholar](#)

52. 52.

Lerner, T. N. et al. Intact-brain analyses reveal distinct information carried by SNc dopamine subcircuits. *Cell* **162**, 635–647 (2015).

[CAS](#) [PubMed](#) [PubMed Central](#) [Google Scholar](#)

53. 53.

Gunaydin, L. A. et al. Natural neural projection dynamics underlying social behavior. *Cell* **157**, 1535–1551 (2014).

[CAS](#) [PubMed](#) [PubMed Central](#) [Google Scholar](#)

54. 54.

Lopes, G. et al. Bonsai: an event-based framework for processing and controlling data streams. *Front. Neuroinform.* **9**, 7 (2015).

[PubMed](#) [PubMed Central](#) [Google Scholar](#)

55. 55.

An, B. et al. Amount of fear extinction changes its underlying mechanisms. *eLife* **6**, e25224 (2017).

[PubMed](#) [PubMed Central](#) [Google Scholar](#)

56. 56.

Baek, J. et al. Neural circuits underlying a psychotherapeutic regimen for fear disorders. *Nature* **566**, 339–343 (2019).

[ADS](#) [CAS](#) [PubMed](#) [Google Scholar](#)

57. 57.

Pnevmatikakis, E. A. & Giovannucci, A. NoRMCorre: an online algorithm for piecewise rigid motion correction of calcium imaging data. *J. Neurosci. Methods* **291**, 83–94 (2017).

[CAS](#) [PubMed](#) [Google Scholar](#)

58. 58.

Hagihara, K. M., Murakami, T., Yoshida, T., Tagawa, Y. & Ohki, K. Neuronal activity is not required for the initial formation and maturation of visual selectivity. *Nat. Neurosci.* **18**, 1780–1788 (2015).

[CAS](#) [PubMed](#) [Google Scholar](#)

59. 59.

Kerlin, A. M., Andermann, M. L., Berezovskii, V. K. & Reid, R. C. Broadly tuned response properties of diverse inhibitory neuron subtypes in mouse visual cortex. *Neuron* **67**, 858–871 (2010).

[CAS](#) [PubMed](#) [PubMed Central](#) [Google Scholar](#)

60. 60.

Gründemann, J. et al. Amygdala ensembles encode behavioral states. *Science* **364**, eaav8736 (2019).

[PubMed](#) [Google Scholar](#)

[Download references](#)

Acknowledgements

We thank F. Ferraguti for discussions on ITC cluster nomenclature; J. Felsenberg, P. Tovote and A. Uematsu for reading and commenting on earlier versions of the manuscript; T. Mrsic-Flogel, M. Häusser and B. Roska for discussion and serving as thesis committee members for K.M.H.; E. Susaki for sharing the CUBIC protocol; Y. Tanaka for sharing the NMDG-based slice preparation protocol; L. Choo for slice physiology demonstration; the GENIE Project for making GCaMP6f, jGCaMP7f and jRGECO1a materials available; B. Roth for making KORD and DREADD materials available; K. Deisseroth for making the ChR2 material available; E. Boyden for making the soCoChR material available; all members of the Lüthi, Holmes, and Ehrlich laboratories for discussion and support, especially T. Eichlisberger for excellent animal care; and the FMI animal facility and microscopy core facility (FAIM), especially L. Gelman and J. Eglinger, and the IT department for constant support. This work was supported by the European Research Council (ERC) under the European Union's Horizon 2020 research and innovation program (grant agreement no. 669582), and a Swiss National Science Foundation core grant (310030B_170268) (all to A. Lüthi); by the NIAAA Intramural Research Program (to A.H.); by the German Research Foundation DFG EH 197/3-1 (to I.E.); and by the Novartis Research Foundation.

Author information

Author notes

1. These authors contributed equally: Kenta M. Hagihara, Olena Bukalo

2. These authors jointly supervised this work: Andreas Lüthi, Andrew Holmes

Affiliations

1. Friedrich Miescher Institute for Biomedical Research, Basel, Switzerland

Kenta M. Hagihara, Nikolaos Karalis, Mathias Mahn & Andreas Lüthi

2. University of Basel, Basel, Switzerland

Kenta M. Hagihara & Andreas Lüthi

3. Laboratory of Behavioral and Genomic Neuroscience, National Institute on Alcohol Abuse and Alcoholism, NIH, Bethesda, MD, USA

Olena Bukalo, Aaron Limoges, Tanner Rigg, Tiffany Campbell, Adriana Mendez, Chase Weinholtz & Andrew Holmes

4. Hertie Institute for Clinical Brain Research, Tübingen, Germany

Martin Zeller, Ayla Aksoy-Aksel & Ingrid Ehrlich

5. Centre for Integrative Neuroscience, Tübingen, Germany

Martin Zeller, Ayla Aksoy-Aksel & Ingrid Ehrlich

6. Department of Neurobiology, Institute of Biomaterials and Biomolecular Systems, University of Stuttgart, Stuttgart, Germany

Ayla Aksoy-Aksel & Ingrid Ehrlich

7. Department of Psychiatry and Behavioral Sciences, University of Washington, Seattle, WA, USA

Larry S. Zweifel

8. Department of Pharmacology, University of Washington, Seattle, WA, USA

Larry S. Zweifel

9. Howard Hughes Medical Institute, University of Washington, Seattle, WA, USA

Richard D. Palmiter

10. Department of Biochemistry, University of Washington, Seattle, WA, USA

Richard D. Palmiter

11. Department of Genome Sciences, University of Washington, Seattle, WA, USA

Richard D. Palmiter

Authors

1. Kenta M. Hagihara

[View author publications](#)

You can also search for this author in [PubMed](#) [Google Scholar](#)

2. Olena Bukalo

[View author publications](#)

You can also search for this author in [PubMed](#) [Google Scholar](#)

3. Martin Zeller

[View author publications](#)

You can also search for this author in [PubMed](#) [Google Scholar](#)

4. Ayla Aksoy-Aksel

[View author publications](#)

You can also search for this author in [PubMed](#) [Google Scholar](#)

5. Nikolaos Karalis

[View author publications](#)

You can also search for this author in [PubMed](#) [Google Scholar](#)

6. Aaron Limoges

[View author publications](#)

You can also search for this author in [PubMed](#) [Google Scholar](#)

7. Tanner Rigg

[View author publications](#)

You can also search for this author in [PubMed](#) [Google Scholar](#)

8. Tiffany Campbell

[View author publications](#)

You can also search for this author in [PubMed](#) [Google Scholar](#)

9. Adriana Mendez

[View author publications](#)

You can also search for this author in [PubMed](#) [Google Scholar](#)

10. Chase Weinholtz

[View author publications](#)

You can also search for this author in [PubMed](#) [Google Scholar](#)

11. Mathias Mahn

[View author publications](#)

You can also search for this author in [PubMed](#) [Google Scholar](#)

12. Larry S. Zweifel

[View author publications](#)

You can also search for this author in [PubMed](#) [Google Scholar](#)

13. Richard D. Palmiter

[View author publications](#)

You can also search for this author in [PubMed](#) [Google Scholar](#)

14. Ingrid Ehrlich

[View author publications](#)

You can also search for this author in [PubMed](#) [Google Scholar](#)

15. Andreas Lüthi

[View author publications](#)

You can also search for this author in [PubMed](#) [Google Scholar](#)

16. Andrew Holmes

[View author publications](#)

You can also search for this author in [PubMed](#) [Google Scholar](#)

Contributions

K.M.H., O.B., A. Lüthi and A.H. conceived the project. K.M.H. performed all the calcium imaging experiments, virus-based circuit mapping, and the slice experiments in Fig. 4e–j, Extended Data Figs. 11, 12 and analysed the data. O.B. performed chemogenetic manipulation experiments and analysed the data with A. Limoges, T.R., T.C., A.M. and C.W. M.Z. and A.A.-A. performed the slice experiments in Fig. 4a–d, Extended Data Figs. 7, 10 and analysed the data. I.E. conceived the slice experiments and supervised M.Z. and A.A.-A. N.K. performed fibre photometry with K.M.H. M.M. helped to establish the slice physiology setup and provided K.M.H. with technical training and advice on opsin selection. L.S.Z. and R.D.P. provided the *Foxp2*-Cre mouse line. K.M.H. prepared figures and drafted the manuscript. K.M.H., A. Lüthi and A.H. wrote the manuscript. All the authors commented on and finalized the manuscript and figures. A. Lüthi and A.H. supervised the entire project.

Corresponding authors

Correspondence to [Andreas Lüthi](#) or [Andrew Holmes](#).

Ethics declarations

Competing interests

The authors declare no competing interests.

Additional information

Peer review information *Nature* thanks Vadim Bolshakov and the other, anonymous, reviewer(s) for their contribution to the peer review of this work. Peer reviewer reports are available.

Publisher's note Springer Nature remains neutral with regard to jurisdictional claims in published maps and institutional affiliations.

Extended data figures and tables

[Extended Data Fig. 1 3D reconstruction of individual ITC clusters.](#)

a, Schematic of a mouse brain volume. R, rostral; C, caudal; D, dorsal; V, ventral. **b**, 3D reconstructions were separately obtained via 1) anti-FOXP2 immunostaining; 2) a *FoxP2-Cre* × Ai14 mouse; and 3) a *D1R-Cre* × Ai14 mouse, in triplicate for each method. ITC_{ap}, apical ITC; ITC_l, lateral ITC; ITC_{av}, anteroventral ITC; ITC_{int}, internal ITC; ITC_{pv}, posteroventral ITC; M, medial; L, lateral; Scale bar, 300 µm. **c**, Example planes of cleared 3D tissue obtained from a wild-type mouse stained with an anti-FOXP2 antibody covering the anterior–posterior axis of ITC clusters. Bregma levels are indicated above each panel. Scale bar, 300 µm. See also Supplementary Video 1 and Supplementary Table 1.

Extended Data Fig. 2 Ca²⁺ imaging from ITC_{dm} and ITC_{vm}.

a–c, Histological validation of GCaMP6f expression. Wild-type mice (not used for in vivo imaging; $n = 2$) were injected with AAV-CaMK2-GCaMP6f and killed after 1 month of expression. Thin slices (120 μm) were cut and stained with an anti-FOXP2 antibody. In addition to BLA and CeA neurons, most of the FOXP2-positive ITC_{dm} neurons expressed GCaMP6f. Blue arrow shows a putative large, FOXP2-negative ITC neuron. Scale bars, 500 μm (**a**), 100 μm (**b**), and 10 μm (**c**). **d**, Example Ca²⁺ traces from neurons in the CeA, ITC_{dm}, and BLA that were simultaneously imaged with a miniature microscope during fear conditioning. Data obtained from the same mice as in Fig. [1d–g](#). Grey shading indicates CS presentation (30 s); red line indicates footshock US presentation (1 s). **e, f**, Histological validation of GCaMP6f expression in ITC_{vm} neurons. *Foxp2*-Cre mice were injected with an AAV encoding Cre-dependent GCaMP6f, implanted with a GRIN lens, and killed after behavioural experiments. Thin slices (120 μm) were cut and stained with an anti-FOXP2 antibody. Scale bars, 200 μm (**e**), 50 μm (**f**). Similar results were obtained with all six mice. **g**, Summary of histologically confirmed GRIN lens implantation locations for ITC_{vm} recordings. Animals with off-target implantations were excluded from analysis. **h**, Example Ca²⁺ traces from neurons in the ITC_{vm} cluster during fear conditioning. Grey shading indicates CS presentation (30 s); red line indicates footshock US presentation (1 s). Images of GCaMP6f expression from the same mouse are shown in **e, f**. **i, j**, Correlation matrices of all simultaneously recorded neuron pairs in CeA, ITC_{dm}, and BLA (**i**), or in ITC_{vm} (**j**) from representative animals. The entire recording session (11 min) was used. **k**, Distributions of correlation coefficients from CeA–CeA, ITC_{dm}–ITC_{dm}, and BLA–BLA pairs. Arrowheads indicate medians of the distributions. **l**, Distribution of correlation coefficients from ITC_{vm}–ITC_{vm} pairs. Arrowhead indicates median of the distribution. **m**, Summary of medians of correlation coefficient distributions shown in **k**. Solid lines indicate individual animals in which CeA, the ITC_{dm} cluster, and BLA were simultaneously imaged ($n = 3$). Dotted lines indicate animals in which only

the ITC_{dm} cluster and BLA were simultaneously imaged ($n = 5$).

* $P = 0.007$, one-way ANOVA followed by Tukey–Kramer test. **n**, Medians of correlation coefficient distribution. The same analysis as in **m** was applied to data from home-cage recording sessions. ITC_{dm} neurons also show a trend towards a higher correlation in the absence of CS or US stimulation. * $P = 0.12$, one-way ANOVA.

Source data

Extended Data Fig. 3 Two-photon imaging and fibre photometry.

a, Schematic showing dual-colour in vivo 2-photon imaging through the implanted GRIN lens. ITC_{dm} neurons were labelled by co-injection of an AAV expressing Cre-dependent tdTomato in *Foxp2*-Cre mice. A GRIN lens was implanted above ITC_{dm} and surrounding BLA and CeA to record Ca²⁺ responses to aversive skin shocks (USs). **b**, Mean projected FOV. Green, GCaMP6; magenta, tdTomato. Dashed lines indicate the intermediate capsule surrounding ITC_{dm}. **c**, Heatplot of Ca²⁺ responses ($\Delta F/F$) to US presentations showing clustered activation of ITC_{dm} neurons. **d**, Regions of interest (ROIs) corresponding to ITC_{dm} (magenta) and BLA (blue) neurons. ROI numbers correspond to traces shown in **e**. **e**, Example Ca²⁺ traces from ITC_{dm} and BLA neurons. Red lines indicate US presentations (1 s). We confirmed that face skin shock used in this experiment and footshock similarly activated ITC_{dm} neurons (data not shown). **f**, Schematic illustrating in vivo fibre photometry in a freely moving mouse. **g**, ITC_{dm} and ITC_{vm} clusters were targeted with AAVs encoding Cre-dependent jRGECO1a and jGCaMP7f, respectively. Recording fibres were placed in BLA to simultaneously monitor axon terminal Ca²⁺ dynamics of ITC_{dm} and ITC_{vm} axons. Isosbestic control signals were recorded in the blue channel. **h**, Example traces of simultaneously recorded dual-colour Ca²⁺ signals and a control signal during a fear conditioning session. **i**, Cross-correlation traces between two simultaneously recorded Ca²⁺ signals. Dark grey lines represent five-trial averaged traces and light grey lines represent individual

trials. **j**, Top, minimum peak values of cross correlation. Bottom, lags of the minimum peak points ($n = 2$ mice). **k, l**, Activity heatplot of trial-averaged responses (left, first 5 trials; right, last 5 trials) to footshock US omissions of all the recorded ITC_{dm} (**k**; $n = 271$ neurons, from 9 mice) or ITC_{vm} neurons (**l**; $n = 372$ neurons, from 6 mice) aligned by CS offset. Cells were sorted according to their averaged $\Delta F/F$ responses in the first five trials.

[Source data](#)

[Extended Data Fig. 4 Population activity of ITC_{dm} and ITC_{vm} neurons.](#)

a, b, Heatplots of all recorded neurons: **a**, 271 ITC_{dm} neurons from 9 mice and **b**, 372 ITC_{vm} neurons from 6 mice throughout the entire 5-day fear conditioning–extinction paradigm. Neurons were sorted by their classification into fear, extinction, extinction resistant, and non-responsive neurons. **c**, Example Ca²⁺ traces from a fear neuron and an extinction neuron from ITC_{dm} and ITC_{vm}, respectively, for all time points indicated in **a, b**. Habituation, Ext1: 1–5, Ext2: 21–25, and Retrieval time points are duplicated in Fig. [2c](#). **d**, Scatter plots visualizing distributions of tone responses of all the recorded ITC_{dm} neurons (left) and ITC_{vm} neurons (middle and right) during Ext1: 1–5 and Ext 2: 21–25 trials. Functional cell-types (fear, extinction, and extinction-resistant neurons) are plotted with different colours; non-responsive neurons in grey (compare with Fig. [2d](#)).

[Source data](#)

[Extended Data Fig. 5 Properties of ITC_{dm} and ITC_{vm} neurons during fear extinction.](#)

a, Trial-averaged $\Delta F/F$ Ca²⁺ responses of ITC_{dm} fear and ITC_{vm} extinction neurons aligned to freezing onset and offset. **b**, Schematics illustrating the analysis shown **c**. Correlation coefficients between trial-by-trial (in total, 50 CS trials) freezing levels and CS-response amplitudes of all the recorded neurons across two days of extinction. Distributions of those correlation

coefficients (one value from each neuron) were first normalized in each animal, then mean \pm s.e.m. values were acquired from all ITC_{dm} and ITC_{vm} recordings and visualized. **c**, The distribution of correlation coefficients for ITC_{dm} neurons was skewed towards 1, indicating that a larger fraction showed a CS response pattern positively correlated with freezing behaviour. By contrast, ITC_{vm} neurons exhibited the opposite tendency; a response pattern anti-correlated with freezing behaviour. $*P = 1.64 \times 10^{-40}$, Kolmogorov–Smirnov test. **d**, Trial-averaged $\Delta F/F$ Ca²⁺ responses of ITC_{vm} neurons aligned to tone on habituation (day 1). **e**, Left, averaged Ca²⁺ responses to tone CS onset in ITC_{dm}. Vertical dotted lines indicate onsets and 2-s time-window of CSs for AUC analysis. Middle, single-trial average of all the ITC_{dm} neurons. Right, AUC quantification of single-trial responses shown in the middle panel. $P = 0.027$, one-way ANOVA. **f**, Trial-averaged $\Delta F/F$ Ca²⁺ responses of ITC_{dm} fear and ITC_{vm} extinction neurons aligned to US omission on day 3. Early, CS1–5; late, CS21–25. Dotted red boxes indicate the expected timing of US delivery. **g**, Trial-averaged $\Delta F/F$ Ca²⁺ responses of all recorded ITC_{vm} neurons aligned to US omission on day 5. The dotted red box indicates the expected timing of US delivery. **h**, Relationship between CS responses during last five trials of extinction training on day 4 and US omission responses on day 3 in ITC_{vm} extinction neurons shows a weak positive correlation.

[Source data](#)

[Extended Data Fig. 6 Simultaneous photometry recordings from ITC_{dm} and ITC_{vm} during state transition.](#)

a, Schematic of an elevated zero-maze apparatus. **b**, Top, example Z-scored Ca²⁺ traces of simultaneously recorded ITC_{dm} (magenta) and ITC_{vm} (green) neurons with the corresponding location in the maze indicated with grey (closed quadrant) and blue (open quadrant) shading. Bottom, difference between the ITC_{dm} and ITC_{vm} signals. **c**, Left, percentage of time spent in closed and open quadrants. Right, total number of transitions from closed to open quadrants (15 ± 3.9 , mean \pm s.e.m.) or from open to closed quadrants.

$n = 5$ mice. Centre line, median; box limits, 25th and 75th percentiles; whiskers, range. **d**, Averaged activity of ITC_{dm} or ITC_{vm} neurons in the closed or open quadrants did not correlate with the total time spent in open quadrants. Regarding the larger variability in ITC activities in open quadrants, we note that the time an animal spent in open quadrants was, on average, much shorter than that in closed quadrants (**c**). As such, activity in open quadrants was to a lesser extent averaged out, resulting in higher variability. Eight sessions from $n = 5$ mice. **e**, Top, averaged Ca²⁺ traces during transitions between quadrants. Changes in the balance between ITC_{dm} and ITC_{vm} parallel a transition from a closed to an open quadrant. Bottom, difference between the ITC_{dm} and ITC_{vm} signals. Briefly stated, the results of this experiment make at least three points: 1) the role of the ITC clusters extends beyond signalling acute, cue-triggered fear states to conditioned fear stimuli to encompass state transitions during exploration of a potentially threatening environment; 2) the clusters exhibit markedly divergent, opposing responses to transitions between protected and unprotected environments, as they do in response to conditioned and extinguished fear cues; and 3) the pattern of results shows that increased ITC_{vm} activity occurs when the animal moves from the protected, closed, to the unprotected, open, quadrants. Potentially, this increase in ITC_{vm} neuron activity may serve to inhibit defensive behaviour and thereby enable exploration of the unprotected open quadrants, analogous to the inhibition of freezing behaviour following extinction. Such cross-task neuronal function is not without precedent; for example, BLA neuronal activity during exploration of the open arm in an elevated plus-maze is anti-correlated with conditioned freezing behaviour in the same mice⁶⁰.

Source data

Extended Data Fig. 7 Ex vivo validation of KORD.

a, Fluorescence (mCitrine, left) and infrared (IR, right) images from a slice used for recordings in a *Foxp2*-Cre mouse injected with AAV-DIO-KORD-mCitrine into ITC_{dm} and ITC_{vm}. Inset, infrared image from a recorded ITC_{dm} neuron. Scale bars, 200 μ m. **b**, Representative current-clamp traces illustrating supra-threshold responses to a +60-pA current injection and

continuous recording of the resting membrane potential (RMP) during application of Salvinorin B (SalB, 100 nM) from control (mCitrine⁻) and KORD-infected (mCitrine⁺) ITC neurons. Scale bars, RMP, 5 mV, 1 min; current steps, 20 mV, 200 ms. **c**, SalB application induced significant hyperpolarization of the membrane in mCitrine⁺ neurons ($n = 10$ neurons from 4 mice) at both time points versus baseline (12.5 min, $*P = 0.003$; 17.5 min, $*P = 0.0001$; two-sided Dunnett's test). Changes in membrane potential were not significant in the mCitrine⁻ control neurons ($n = 5$ neurons from 3 mice) at both time points versus baseline (12.5 min, $P = 0.99$; 17.5 min, $P = 0.84$; Dunnett's test). Mean \pm s.e.m. **d**, Comparison of membrane potential changes (Δ RMP) 17.5 min after application of SalB. Changes in KORD-infected neurons (mCitrine⁺) were significantly different from control ($*P = 0.013$, Wilcoxon rank-sum test; $n = 5$ neurons from 3 mice and $n = 11$ neurons from 5 mice for mCitrine⁻ and mCitrine⁺, respectively). Mean \pm s.e.m. **e**, Comparisons of spike rates in response to +60-pA current injections before and 17.5 min after application of SalB. KORD-infected neurons (mCitrine⁺, $n = 11$) significantly reduced spike rate (from 26.2 ± 1.69 Hz to 20.1 ± 3.30 Hz; $*P = 0.016$, Wilcoxon signed-rank test). By contrast, mCitrine⁻ neurons ($n = 4$ neurons from 3 mice) did not show a significant reduction in spike rate (from 25.3 ± 2.89 Hz to 23.7 ± 2.27 Hz; $P = 0.25$, Wilcoxon signed-rank test). Mean \pm s.e.m.

[Source data](#)

[**Extended Data Fig. 8 Histology for chemogenetic manipulations of distinct ITC clusters.**](#)

a, Examples of histological validation of KORD–mCitrine expression in ITC_{vm} neurons across multiple anterior-to-posterior coronal sections. Following all the behavioural experiments (Fig. 3), mice were killed and slices (50 μ m) cut and stained with an anti-FOXP2 antibody. Scale bar, 200 μ m. **b**, Examples of histological validation of hM3Dq–mCherry expression in ITC_{vm} neurons across multiple anterior-to-posterior coronal sections. Scale bar, 200 μ m. **c**, Heatmaps illustrating virus expression aggregated across Cre⁺ mice in **a** and **b**. Scale bar indicates the fraction of animals exhibiting expression at each locus (0: no mice expressed; 1: all

mice expressed). **d**, Examples of histological validation of KORD–mCitrine expression in ITC_{dm} neurons across multiple anterior-to-posterior coronal sections. Scale bar, 200 µm. **e**, Examples of histological validation of hM3Dq–mCherry expression in ITC_{dm} neurons across multiple anterior-to-posterior coronal sections. Scale bar, 200 µm. **f**, Heatmaps illustrating virus expression aggregated across Cre⁺ mice in **d** and **e**. Scale bar indicates the fraction of animals exhibiting expression at each locus (0: no mice expressed; 1: all mice expressed). Bregma levels are noted above the panels in **a** and **d**.

Extended Data Fig. 9 Additional chemogenetic manipulations of ITC_{dm} and ITC_{vm} clusters.

a, Chemogenetic manipulations. AAV encoding Cre-dependent hM3Dq was targeted to ITC_{dm} neurons in *Foxp2*-Cre mice. **b**, ITC_{dm} activation. Freezing on retrieval: Cre⁺, 45.7 ± 7.6%; Cre⁻, 28.5 ± 3.3%; *P = 0.0044. **c**, Schematic showing the dual-cluster chemogenetic manipulation experiment. An AAV encoding Cre-dependent KORD was targeted to both ITC_{vm} and ITC_{dm} neurons in *Foxp2*-Cre mice. **d**, Freezing behaviour of experimental (Cre⁺) and control (Cre⁻) mice; controls were injected with the AAV and administered the ligand. Arrows and colour-shadings indicate the timing of SalB administration before extinction retrieval. Freezing levels on extinction retrieval (day 3): Cre⁺, 46.4 ± 4.3%; Cre⁻, 27.3 ± 2.7%; *P < 0.0001, repeated-measures ANOVA followed by Sidak post hoc test. N.S., not significantly different on day 1 or day 2 freezing. Mean ± s.e.m. **e**, Examples of histological validation of KORD–mCitrine expression in ITC_{vm} and ITC_{dm} neurons across multiple anterior-to-posterior coronal sections. Following behavioural experiments, mice were killed and slices (50 µm) cut and stained with an anti-FOXP2 antibody. Scale bar, 200 µm. **f**, Heatmaps illustrating virus expression aggregated across Cre⁺ mice. Scale bar indicates the fraction of animals exhibiting expression at each locus (0: no mice expressed; 1: all mice expressed).

[Source data](#)

Extended Data Fig. 10 Reciprocal inhibitory connections between ITC clusters.

a, Inter-cluster virus-based tracing (ITC_{dm}-targeted example shown, same strategy for ITC_{vm} targeting). AAV encoding Cre-dependent synaptophysin–GFP targeted to ITC_{dm} or ITC_{vm} neurons in *Foxp2*-Cre mice. **b, c**, Confocal images from ITC_{dm} (**b**) or ITC_{vm} (**c**) injections. FOXP2 expression visualized using immunohistochemistry (IHC). Injections repeated in five (ITC_{dm}), and four (ITC_{vm}) mice. Scale bars: 500 µm (**b1, c1**); 200 µm (**b2, 3, c2, 3**). **d, e**, Histological validation of selective ChR2 expression in ITC_{dm} (**d1–3**) and ITC_{vm} (**e1–3**). Scale bars: 500 µm (**d1, e1**); 50 µm (**d3, e3**). Repeated for all mice shown in Fig. 4. **f**, Representative example of IPSCs recorded at different holding potentials from an ITC_{dm} neuron upon photostimulation of ChR2-EYFP fibers from ITC_{vm}. **g, i**, Schematics illustrating ex vivo slice electrophysiological experiments with direct cluster stimulation. The ITC_{vm} (**g**) or ITC_{dm} (**i**) cluster was targeted with an AAV encoding Cre-dependent ChR2. Recordings were performed in the other cluster while the ChR2-positive cluster or the surrounding area was selectively stimulated with aperture-restricted stimulation (see [Methods](#)). **h, j**, Images taken from the recording setup illustrating positions of on- and off-cluster stimulation for ITC_{vm} while recording in ITC_{dm} and vice versa. **k**, Summary of PTX application experiments ($n = 3$ from 3 mice). Magenta lines represent ITC_{vm}→ITC_{dm} connections and green lines represent ITC_{dm}→ITC_{vm} connections.

* $P = 0.005$, paired *t*-test. **l**, Summary of experiments shown in **g–j**. On-cluster photostimulation evoked significantly larger IPSCs than off-cluster stimulation. Note that we used the highest value out of the four off-cluster stimulation sites. * $P = 0.0016$, paired *t*-test.

[Source data](#)

Extended Data Fig. 11 Selective ex vivo ITC cluster stimulation.

a, Histological validation of selective soCoChR expression. Scale bars, 50 μm . Repeated for $n = 3$ mice. **b**, Schematic illustrating ex vivo slice electrophysiological experiments. ITC_{dm} and ITC_{vm} neurons were targeted with an AAV encoding Cre-dependent soCoChR. Two optical fibres for photostimulation were placed above the ITC clusters. Whole-cell recordings were performed from neurons in the ITC_{dm}, ITC_{vm}, and ITC_l clusters. To block synaptic currents, CPP (10 μM), CNQX (10 μM) and PTX (100 μM) were applied. **c–e**, Example responses to photostimulation of ITC_{dm} or ITC_{vm} clusters recorded under current-clamp configuration from ITC_{dm} (**c**), ITC_{vm} (**d**), and ITC_l (**e**) neurons. **f**, Summary of experiments shown in **b–e**. All recorded ITC_{dm} and ITC_{vm} neurons fired action potentials selectively in response to photostimulation with the corresponding fibre. ITC_l neurons did not fire action potentials upon photostimulation of ITC_{dm} or ITC_{vm} clusters. **g**, Schematic illustrating experiments wherein the position of the optical fibre was systematically moved away from the optimal location ($X = 0 \mu\text{m}$). To block synaptic currents, CPP (10 μM), CNQX (10 μM), and PTX (100 μM) were applied. These experiments further confirmed the spatial resolution of the photostimulation configuration. **h**, Example voltage-clamp recordings from an ITC neuron showing IPSCs evoked at different positions of the optical fibre. **i**, Left, quantification of peak IPSC amplitudes of the neuron shown in **h**. Right, normalized by the value at $X = 0 \mu\text{m}$. **j**, Summary of all recorded neurons ($n = 3$ from 3 mice). **k**, Summary of additionally performed current-clamp recordings ($n = 3$ from 3 mice).

[Source data](#)

[**Extended Data Fig. 12 ITC to CeM connectivity.**](#)

a, Schematic illustrating the experimental design used to assess connectivity between ITC_{dm} or ITC_{vm} neurons and CeM neurons. To isolate IPSCs, CPP (10 μM) and CNQX (10 μM) were applied. **b**, Example voltage-clamp recording from a CeM neuron showing selective IPSC elicited by stimulation of the ITC_{vm} but not ITC_{dm}. **c**, Summary of connectivity from ITC_{dm} and ITC_{vm} to CeM ($n = 11$ neurons from 4 mice). * $P = 7.5 \times 10^{-3}$, Fisher's exact test. **d**, Evoked IPSC amplitudes recorded

from CeM neurons (at -70 mV holding potential) in response to stimulation of ITC_{dm} or ITC_{vm} clusters. **e**, Synaptic conductance calculated based on IPSC amplitudes recorded at three different holding potentials (-60 , -70 , and -80 mV). **f**, Example injections of CTB555 targeted to the ventrolateral periaqueductal grey (vlPAG). Scale bar, 200 μm . **g**, Schematic illustrating the experimental design used to assess connectivity between ITC_{dm} or ITC_{vm} neurons and CeM neurons projecting to the vlPAG. vlPAG-projecting CeM neurons were retrogradely labelled with CTB injections into the vlPAG. Whole-cell recordings were performed in CTB⁺ CeM neurons while photostimulating incoming axons expressing ChR2-EYFP from either ITC_{dm} or ITC_{vm}. **h**, Summary of connectivity from ITC_{dm} and ITC_{vm} to vlPAG-projecting CeM neurons ($n = 15$ neurons from 4 mice and $n = 10$ neurons from 4 mice). * $P = 0.0001$, Fisher's exact test. **i**, Evoked IPSC amplitudes recorded from CTB⁺ CeM neurons (at 0 mV holding potential) in response to stimulation of axons from ITC_{dm} or ITC_{vm}. **j**, Example injections of CTB555 and CTB647 targeted to the PL or IL, respectively. Scale bar, 500 μm . **k**, Example BLA histology showing PLp and ILp BLA neurons. Both subpopulations are located in the medial part of the BLA. Scale bar, 200 μm . **l**, Mostly non-overlapping PLp and ILp subpopulations; orange arrow indicates an example of a double-labelled neuron. Scale bar, 50 μm . **m**, Quantification of double-labelled neurons ($n = 3$ mice). Mean \pm s.e.m. **n**, State-dependent functional changes in amygdala circuitry regulated by ITC clusters. Node size indicates activity level, connection width represents putative functional connection strength.

[Source data](#)

Supplementary information

[Supplementary Tables](#)

This file contains Supplementary Table 1, a cross-study comparison of ITC cluster nomenclature and Supplementary Table 2, statistical analyses summary for chemogenetic experiments.

Reporting Summary

Peer Review File

Video 1

: 3D-reconstruction of individual ITC clusters. An example 3D-reconstruction of ITC clusters from a cleared FoxP2-Cre crossed with tdTomato reporter mouse brain. The same sample as shown in Extended Data Fig.1b is presented. Note, this intercross mouse line shows tdTomato signal in some CeA neurons and blood vessels in addition to ITCs, likely because of developmental transient expression of FoxP2.

Video 2

: Post-hoc identification of ITCdm in a 3D confocal image of a cleared tissue. An example confocal 3D image stack of cleared and stained tissue acquired with a 20x objective. The same sample as shown in Fig.1d, e is presented.

Video 3

: Spatially clustered robust aversive shock responses in ITCdm Example Ca2+ movies from simultaneously recorded BLA, CeA, and ITCdm regions. ITCdm shows spatially clustered and robust responses to 5 trials of aversive footshock presentation. The video was sped up 2x. The timing of shock presentation is indicated with red ‘shock’ text. The same sample as shown in Fig.1f, g is presented.

Source data

Source Data Fig. 1

Source Data Fig. 2

[Source Data Fig. 3](#)

[Source Data Fig. 4](#)

[Source Data Extended Data Fig. 2](#)

[Source Data Extended Data Fig. 3](#)

[Source Data Extended Data Fig. 4](#)

[Source Data Extended Data Fig. 5](#)

[Source Data Extended Data Fig. 6](#)

[Source Data Extended Data Fig. 7](#)

[Source Data Extended Data Fig. 9](#)

[Source Data Extended Data Fig. 10](#)

[Source Data Extended Data Fig. 11](#)

[Source Data Extended Data Fig. 12](#)

Rights and permissions

[Reprints and Permissions](#)

About this article



Check for
updates

Cite this article

Hagihara, K.M., Bukalo, O., Zeller, M. *et al.* Intercalated amygdala clusters orchestrate a switch in fear state. *Nature* **594**, 403–407 (2021).
<https://doi.org/10.1038/s41586-021-03593-1>

[Download citation](#)

- Received: 21 May 2020
- Accepted: 28 April 2021
- Published: 26 May 2021
- Issue Date: 17 June 2021
- DOI: <https://doi.org/10.1038/s41586-021-03593-1>

Comments

By submitting a comment you agree to abide by our [Terms](#) and [Community Guidelines](#). If you find something abusive or that does not comply with our terms or guidelines please flag it as inappropriate.

[Access through your institution](#)

[Change institution](#)

[Buy or subscribe](#)

Advertisement

This article was downloaded by **calibre** from <https://www.nature.com/articles/s41586-021-03593-1>

The epidemiological impact of the NHS COVID-19 app

[Download PDF](#)

- Article
- [Published: 12 May 2021](#)

The epidemiological impact of the NHS COVID-19 app

- [Chris Wymant](#) [ORCID: orcid.org/0000-0002-9847-8226](#)^{1 na1},
- [Luca Ferretti](#)^{1 na1},
- [Daphne Tsallis](#) [ORCID: orcid.org/0000-0002-0968-2744](#)²,
- [Marcos Charalambides](#)³,
- [Lucie Abeler-Dörner](#)¹,
- [David Bonsall](#)¹,
- [Robert Hinch](#) [ORCID: orcid.org/0000-0003-3169-698X](#)¹,
- [Michelle Kendall](#) [ORCID: orcid.org/0000-0001-7344-7071](#)^{1,4},
- [Luke Milsom](#)⁵,
- [Matthew Ayres](#)³,
- [Chris Holmes](#)^{1,3,6},
- [Mark Briers](#)³ &
- [Christophe Fraser](#) [ORCID: orcid.org/0000-0003-2399-9657](#)¹

[Nature](#) volume 594, pages 408–412 (2021) [Cite this article](#)

- 23k Accesses
- 1 Citations
- 1298 Altmetric
- [Metrics details](#)

Subjects

- [Epidemiology](#)
- [Infectious diseases](#)
- [SARS-CoV-2](#)

Abstract

The COVID-19 pandemic has seen the emergence of digital contact tracing to help to prevent the spread of the disease. A mobile phone app records proximity events between app users, and when a user tests positive for COVID-19, their recent contacts can be notified instantly. Theoretical evidence has supported this new public health intervention^{1,2,3,4,5,6}, but its epidemiological impact has remained uncertain⁷. Here we investigate the impact of the National Health Service (NHS) COVID-19 app for England and Wales, from its launch on 24 September 2020 to the end of December 2020. It was used regularly by approximately 16.5 million users (28% of the total population), and sent approximately 1.7 million exposure notifications: 4.2 per index case consenting to contact tracing. We estimated that the fraction of individuals notified by the app who subsequently showed symptoms and tested positive (the secondary attack rate (SAR)) was 6%, similar to the SAR for manually traced close contacts. We estimated the number of cases averted by the app using two complementary approaches: modelling based on the notifications and SAR gave an estimate of 284,000 (central 95% range of sensitivity analyses 108,000–450,000), and statistical comparison of matched neighbouring local authorities gave an estimate of 594,000 (95% confidence interval 317,000–914,000). Approximately one case was averted for each case consenting to notification of their contacts. We estimated that for every percentage point increase in app uptake, the number of cases could be reduced by 0.8% (using modelling) or 2.3% (using statistical analysis). These findings support the continued development and deployment of such apps in populations that are awaiting full protection from vaccines.

[Download PDF](#)

Main

The United Kingdom has been severely affected by the COVID-19 pandemic, recording one of the highest confirmed death rates in the world in 2020. The NHS COVID-19 app for England and Wales was launched on 24 September 2020 to help to reduce the spread of the virus. The app has been downloaded on 21 million unique devices, out of a population of 34.3 million eligible people with compatible smartphones, and is regularly used by at least 16.5 million people. The main function of the app is digital contact tracing^{1,2,3,4,5,6} using the privacy-preserving Google Apple Exposure Notification system, which is embedded in the Android and iOS operating systems^{8,9}, supplemented with custom Bluetooth processing algorithms¹⁰. App users are notified and instructed to quarantine if they have been in contact with another user later confirmed to have COVID-19 if the exposure had characteristics that exceed a risk threshold. Digital tracing is a novel public health measure with unknown

epidemiological impact⁷. Other functions of the NHS app include providing locally appropriate information on COVID-19 prevention, checking into venues using a custom QR-code scanner (allowing later notification if users have visited risky venues), and a symptom checker linked to the booking of tests. For tests booked through the app, the test result triggers a set of actions automatically, including notification of the tested individual through the app and digital contact tracing for positive results (upon the user's approval).

When installing the app, users enter their postcode district (the first half of the postcode), which enables analysis of geographical variation in app use. We aggregated data at the level of lower tier local authorities (LTLAs), of which there are 338 in England and Wales, to match case data. App uptake—the fraction of active users in the population—was variable between LTLAs (Fig. 1a, c), with an interquartile range of 24.2–32.4%. We defined three phases for the analysis, annotated in Fig. 1d: phase 0 before app launch, phase 1 from 1 October to early November 2020 (first version of the app) and phase 2 from early November to 31 December 2020 (improved version of the app). These are described in greater detail in Extended Data Table 1. Phases in the app precede phases in the resulting cases: there is a lag between changes in transmission rates and changes in confirmed cases, which we assumed to be 8 days. Other factors besides the app changed during these phases, including locally targeted control measures, a national lockdown and a surge in cases in December, mostly driven by the new SARS-CoV-2 variant B.1.1.7.

Fig. 1: Geographical variability of app uptake and cases of COVID-19.

 **figure1**

a, c, Map (**a**) and histogram (**c**) of app uptake by LTLA. Colours in **a** indicate app uptake as shown in **c**. **b**, Cumulative cases of COVID-19 per 100,000 population over analysis phases 1 and 2. **d**, Seven-day rolling mean of daily cases of COVID-19 per 100,000 population. Each line represents an LTLA, coloured by app uptake as shown in **c**. Values for England and Wales are also shown. Black horizontal arrows indicate our analysis phases. In **b, d**, case numbers are for the whole LTLA population, not just app users.

[Full size image](#)

Roughly 1.7 million notifications were sent as a result of 560,000 app users testing positive over the entire time period: a mean number of notifications per index case of 3.1. Seventy-two per cent of app-using index cases consented to digital tracing upon

testing positive, resulting in a mean number of notifications per tracing event of 4.2. Numbers of notifications over time are shown in Extended Data Fig. [1b](#).

We estimated the SAR in individuals notified by the app; this is the probability that someone who is notified will report a positive test during the recommended quarantine or in the following two weeks. We estimated an SAR of 6.02%, with confidence interval 5.96–6.09%, although sensitivity analyses suggest a precision of roughly 5–7%. These results indicate that the app is functioning at a technical level, as also recently demonstrated for the Swiss and Spanish apps[11,12](#).

To evaluate the epidemiological impact of the app, we first used a modelling approach. We estimated the number of cases averted with a model linking the number of notifications, the probability that notified individuals had COVID-19, the timing of notification relative to transmission, and the adherence to quarantine. Adherence to quarantine is critical but difficult to assess reliably. UK surveys found that only 11% of individuals in quarantine declared proper adherence to quarantine rules, but 65% of individuals intended to adhere to quarantine[13](#), albeit imperfectly. Recent surveys found a high adherence to quarantine (greater than 80%)[14](#), and this behaviour may be more representative of app users. We considered an intermediate scenario corresponding to 61% overall effectiveness of quarantine in preventing transmissions as our central estimate, leading to 284,000 cases averted. The estimated number of cases averted was higher in areas of high app uptake (Fig. [2](#)). The slope of the regression in Fig. [2b](#) indicates that the fraction of cases averted (among all cases observed or averted) increased by 0.8% for 1% increase in app uptake (Table [1](#)).

Fig. 2: The link between app use and cases averted in each LTLA.

 [figure2](#)

a, b, Estimated number (**a**) and percentage (**b**) of cases averted in phases 1 and 2 combined versus number of app users. **c,** Unadjusted relationship between difference in app uptake and difference in number of cases per capita in phases 1 and 2 combined. In **b, c**, the blue line shows the least-squares fit of the y -axis variable to the x -axis variable, and the shaded grey area shows the associated 95% confidence interval.

[Full size image](#)

Table 1 The estimated effect of the NHS COVID-19 app
[Full size table](#)

We used a second approach to evaluate the epidemiological impact of the app, linking variation in app uptake between LTLAs with variation in cumulative cases. We addressed strong confounding factors with a stratified approach, only comparing LTLAs with similar socio-economic properties and geography. We used several different ways of grouping LTLAs into comparable units, with similar results; one method is described below (with full results in Extended Data Table 2) and the other methods are described in the [Supplementary Information](#) (their results are presented in Extended Data Fig. 2, Extended Data Tables 3, 4).

Increased app use is associated with more rural areas, less poverty and greater local gross domestic product (GDP) (Supplementary Table 4); we therefore adjusted for these measured confounding variables. Unmeasured confounders could include adherence to social distancing and face-mask use; since these factors affected transmission before app release, app uptake should have some correlation with case numbers even before app release (phase 0). To test this, we regressed phase 0 case numbers on several covariates, including later uptake of the app; app uptake was indeed associated with case numbers (pure confounding). To adjust for this confounding, we stratified LTLAs into quintiles on the basis of the number of cases in phase 0 and compared them only within these strata. This stratification removed the correlation between app uptake and pre-app cases, indicating that this at least partially adjusted for unmeasured confounders (Extended Data Table 2; details on confounding and placebo regression are in the [Supplementary Information](#)). Case numbers in an LTLA are also confounded by those in neighbouring LTLAs; we therefore compared only neighbouring (adjacent) LTLAs. We found that the difference in case numbers per capita between neighbouring LTLAs, matched by phase 0 case number quintile, was strongly and robustly associated with differences in app use, regardless of adjustment for other demographic confounders (Fig. 2, Table 1, Extended Data Table 2).

Disaggregating the effect by phase, we found that it was larger during phase 2 (Table 1). This is consistent with the increased number of notifications sent per index case implemented at the start of phase 2 (Extended Data Fig. 1b). Table 1 shows the estimated effect size replicated in different statistical analyses (described in the [Supplementary Information](#)).

We estimated the numbers of cases averted during phases 1 and 2 combined: 284,000 (108,000–450,000) using the modelling approach, and 594,000 (317,000–914,000) using the statistical approach. The ranges show a sensitivity analysis exploring 2.5–97.5% of the variability in modelling estimates, and a 95% confidence interval for the statistical one. These estimates are comparable to the number of app users who tested positive and consented for notifications to be sent: roughly 400,000. This suggests that

on average, each confirmed COVID-19-positive individual who consented to notification of their contacts through the app prevented one new case; that is, the whole transmission chain following each such case was reduced by one individual. We translated these estimates to deaths averted during phases 1 and 2 using the case fatality rate observed for this period: 1.47% (Methods). This gave an estimate of 4,200 (1,600–6,600) deaths averted using the modelling approach, and 8,700 (4,700–13,500) using the statistical approach. For comparison, the total number of cases and deaths that actually occurred in this period were 1,892,000 and 32,500, respectively. Cases averted over this period are shown in Extended Data Fig. 3.

Finally, we extrapolated the findings to explore different ways in which the app could be improved, by re-running scenarios with different parameters (Table 2). These are retrospective projections; however, the expected reductions in cases are relevant when considering forward projections.

Table 2 Scenarios for improvements

[Full size table](#)

Discussion

Our analyses suggest that a large number of cases of COVID-19 were averted by contact tracing through the NHS app, with estimates ranging from approximately 100,000 to 900,000, depending on the details of the analysis. For comparison, there were 1.9 million actual cases of COVID-19 over the same period. Averted cases were concentrated in phase 2, during November and December 2020, after a major upgrade to the app's risk-scoring function¹⁰. This finding is similar to previous results from modelling: using our individual-based model¹⁵, a 30% app uptake was estimated to avert approximately 1 infection for every 4 infections that arose⁴ during 4.5 months.

Although it is informative to estimate effects on quantities such as the time-varying reproduction number¹⁶, we did not pursue such an analysis here. The dynamics of the epidemic for individual LTLAs are difficult to interpret: the period of analysis coincided with staggered introductions of locally targeted restrictions, a short national lockdown, the Christmas holiday season and the emergence of the B.1.1.7 SARS-CoV-2 variant, which is more infectious and spread rapidly across the country^{17,18,19,20}. Future work could perhaps model all of these effects in a single hierarchical model, permitting joint estimation of the app's effects over LTLAs with linked drivers and dynamics. Our simpler approaches have the benefit of transparency, and we hypothesize that under negative-feedback dynamics (greater local spread triggering greater local control measures), appropriately constructed comparisons of total case counts over an appropriate period may reveal the underlying propensity for disease spread.

The main limitation of our analysis is that it is an observational study: no randomized or systematic experiment resulted in different rates of app uptake in different locations. Interpreting observational analyses requires particular care owing to the risk of confounding. We therefore used two approaches: mechanistically modelling the app's function, and a statistical approach. Our statistical approach was stratified to focus only on differences between directly comparable areas, emulating how a cluster randomized trial would have been conducted²¹. Our placebo analysis suggested that our adjustment for confounders largely removed their effect; however, it is still possible that changes in app use over time and across geographies reflect changes in other interventions, and that our analysis incorrectly attributes the effects to the app. Such residual confounding, if present, would mean that our statistical estimate for cases averted is too high and thus our modelling estimate is more accurate.

Conversely, there could be a genuine, albeit indirect effect of the app, whereby users maintain a greater distance from others than they otherwise would have done, being aware that the app monitors distance and could later advise quarantine. This would mean that our modelling estimate (derived solely from the app's direct effect, proportional to the SAR) is too low, and that our statistical estimate is more accurate. On balance, an effect size between the two estimates seems most likely. We discuss the expected effects of further biases in the [Supplementary Information](#).

The app is best understood as part of a system of non-pharmaceutical interventions, and not in isolation⁷. It is not a substitute for social distancing or face masks: control of the epidemic requires all available interventions to work together. Isolation and quarantine can only be effective when supported financially. All contact tracing requires identification of cases, and is therefore a follow-up to effective, widespread and rapid testing. The specific role of digital tracing is to speed up tracing, and to reach more people per index case. An advantage of the NHS app compared with other digital tracing apps is its full integration with testing: tests ordered through the app trigger actions automatically, without requiring the user to enter their results in the app. Further improvement could potentially be achieved with increased use of location-specific QR-code scanning: notifications were issued for 226 venue events designated as risky as of 20 January 2021. Backwards contact tracing²² could help to identify risky venue events. The COVID-19 response policy concerning the hospitality sector—restaurants, pubs and so on—required visitors to ‘check in’ to facilitate outbreak analysis when needed. Scanning the venue QR code with the app provided a more convenient way of doing this than writing the contact details of the individual, and hence individuals visiting such venues may have been more likely than average to use the app, giving a greater epidemiological effect than expected.

Digital tracing is not a substitute for manual tracing—both are valuable. We compare the two approaches in Supplementary Table 1. In summary, the SAR of 6% that we estimated for the app is similar to the SAR of 6.9% for manual contact tracing of close

contacts during December 2020 and January 2021²³. The mean number of contacts traced per consenting index case was 4.2 for digital tracing, compared with 1.8 for manual tracing, and a larger fraction of these traced contacts is expected to be outside of the household of the index case for the app. Contacts outside the household have a smaller probability of having already been notified informally by the index case, and so obtain greater benefit of having been traced. This increased coverage and the speed of notification by the app (Extended Data Fig. 4) suggest that the effect of digital tracing was mostly additional to that of manual tracing. We confirmed this with an analysis that included adjustment for quality of manual tracing, which did not affect our conclusions.

The surest ways to increase the effectiveness of the digital tracing programme are to increase uptake of the app and to provide material support to individuals undergoing isolation and quarantine. Special efforts may be needed to reach underserved communities. It is well established that testing should be as rapid as possible to help to prevent transmission. This could perhaps be facilitated by point-of-care antigen tests and integration of self-testing with the app, however this would need investigation to establish accuracy and usability. Widespread vaccination will eventually reduce the need for non-pharmaceutical interventions, but vaccination is unlikely to achieve global reach within the coming months, during which time improved non-pharmaceutical interventions could still prevent many infections^{24,25}. Smartphone use is already global, and thus privacy-preserving contact-tracing apps should be further integrated into the public health toolkit.

Methods

No statistical methods were used to predetermine sample size. The experiments were not randomized. The investigators were not blinded to allocation during experiments and outcome assessment.

Estimating app uptake

To monitor the safe function of the app and enable its evaluation, a limited amount of data are shared with a secure NHS server. Each active app sends a single data packet daily. The fields in these packets contain no sensitive or identifying information, and are approved and publicly listed by the Information Commissioner

(<https://www.gov.uk/government/publications/nhs-covid-19-app-privacy-information>).

The raw data fields we used are described in Supplementary Table 2; further variables derived from these are described in Supplementary Table 3. A schematic illustration of data gathering is shown in Extended Data Fig. 5. For the reported numbers of downloads, repeat downloads to the same phone are counted only once. The number of active users each day is defined as the number of data packets received by the NHS

server; for a single representative value of this quantity, we took the mean over all days from 1 November to 11 December 2020 (earlier data was deemed less reliable). We note that there continue to be unexplained fluctuations in reported user numbers on Android phones. To estimate uptake within an LTLA, each postcode district was mapped to the LTLA in which the majority of its population reside, and we took the ratio (number of active users in postcode districts mapped to this LTLA)/(total population in postcode districts mapped to this LTLA). The population of England and Wales is 59.4 million, of whom 48.1 million are 16 or over and thus eligible to use the app (<https://www.ons.gov.uk/peoplepopulationandcommunity/populationandmigration/populationestimates/datasets/lowersuperoutputareamidyearpopulationestimates>). We assumed that England and Wales are representative of the UK, in which 82% of people aged 16 years and over have smartphones (OFCOM, personal communication), and that of smartphones in circulation, 87% support the Google Apple Exposure Notification system (Department of Health and Social Care, personal communication). The denominators for measuring uptake at the national level are therefore 59.4 million (total population) and 34.3 million (eligible population with compatible phones).

Defining numbers of cases

The COVID-19 case numbers per day we used here are those reported at <https://coronavirus.data.gov.uk/>, by specimen date and LTLA. We obtained per-capita case numbers at the LTLA level by dividing by LTLA populations reported by ONS. These per capita case numbers by phase are shown in Extended Data Fig. 6. Testing has been available through the NHS Test and Trace system in all areas throughout the period, with a median delay of less than 2 days from booking a test to receiving the result. Testing capacity has mostly exceeded demand, except for two weeks in early September. We assumed that case ascertainment has been relatively constant over the period of analysis, an assumption qualitatively supported by the unbiased ONS and REACT studies^{26,27}.

Estimating the SAR

We focused on a period in December 2020 and January 2021 when the number of positive test results in app users could be disaggregated by whether the user had been recently notified or not. Even with this data, successive data packets sent by the same device are not linked to each other. This means that when a given number of notifications are sent on a particular day, the exact number of those individuals notified who later receive a positive test result is unknown, because of the lack of linkage over time. We therefore used a probabilistic model for how many positive test results we would expect among those recently notified, as a function of the number of notifications on previous days, of the estimated delay from notification to testing

positive, and of the SAR. We estimated the SAR by maximising the likelihood of this model. In detail: let $f_{NP}(t)$ be the probability that an individual notified on a given day then tests positive t days later (conditional on their testing positive at some later time, that is, the function is normalized to 1). Let $N(t)$ be the number of individuals notified on day t , and $I_N(t)$ the number of individuals reporting a positive test on day t having been notified recently (either they are currently in the quarantine period recommended by the app, or the following 14 days). The number expected for the latter is $\sum_t N(t) f_{NP}(t)$, and we maximised a Poisson likelihood for the number observed, $I_N(t)$ (shown in Extended Data Fig. 1d), given the number expected, treating observations from different days as independent. The confidence interval was obtained by likelihood profiling; however, sensitivity analyses suggested greater uncertainty (see [Supplementary Information](#)). $f_{NP}(t)$ was calculated as a convolution of the distributions for times from exposure to symptoms, from symptoms to testing positive, and from exposure to notification ([Supplementary Information](#)). Our SAR calculation used only data from iPhones, excluding Android phones, for more stable daily numbers of analysis packets.

Modelling cases averted based on notifications and SAR

The effect of notifications received at time t on cases averted can be modelled as the product of (i) the number of notifications, (ii) the secondary attack rate, that is, a conservative underestimate of the probability that notified individuals are actually infected, (iii) the expected fraction of transmissions preventable by strict quarantine of an infectious individual after a notification, (iv) the actual adherence to quarantine, and (v) the expected size of the full transmission chain that would be originated by the contact if not notified. Before each notification, the contact's app sends a request for permission to the central NHS server. We estimated the total number of notifications per day on each operating system (OS; being either Android or iOS) from these requests. We estimated the number of notifications per LTLA from the number of partial days of quarantine (typically corresponding to the first day of quarantine, that is, the day of notification) per day, OS and LTLA, rescaling it by a time- and OS-dependent factor to match the number of notifications per day and OS. The geographical variability in notifications after summing over time is shown in Supplementary Fig. 1. The delay between last exposure and notification is assumed to follow a normal distribution, with time-dependent parameters estimated via least squares from the daily number of notifications and individuals in quarantine. The fraction of preventable transmissions is estimated from the delay distribution using the generation time distribution in ²⁸ with mean 5.5 days. For the effectiveness of quarantine in reducing transmission from traced contacts, we assumed as our central value that 45.5% of traced contacts quarantine perfectly (100% reduction in

transmission), 31% of traced contacts quarantine imperfectly with 50% reduction in transmission, and 23.5% of traced contacts do not quarantine at all (0% reduction in transmission). This is equivalent to an average effectiveness of quarantine of 61%. Finally, the size of the epidemic chain triggered by a single case is computed assuming that local epidemics do not mix and that the extra cases do not affect the epidemic dynamic. See [Supplementary Information](#) for further details.

Statistical analysis

The main statistical analysis compared statistics for each LTLA, labelled x , to those of the set comprising all of its ‘matched’ neighbours $N(x) = \{n_1, n_2, n_3, \dots\}$, and so on. The matched neighbours $N(x)$ were defined as other LTLAs that share a border with x and were in the same quintile for number of cases per capita in phase 0. Distributions showing the variability between LTLAs in the number of neighbours and number of matched neighbours are shown in Supplementary Fig. 2. Stratification into quintiles (as opposed to deciles and so on) was chosen to balance power and sufficient adjustment; no other possibility was tried, to guard against investigator bias.

Each statistic of interest was averaged over the matched neighbours, weighting by population size, to obtain the mean value in the matched neighbours of x . This was compared to the statistic for x . Linear regression was carried out using, for each statistic of interest, the difference between its value in x and in its matched neighbours $N(x)$. The statistics we considered were: per capita number of cases in each phase; the fraction of the population using the app; a measure of rural/urban mix on a scale from 1 to 5, from the Office of National Statistics (ONS); a measure of local GDP per capita from the ONS, adjusted for rural/urban score; and a measure of the fraction of the population living in poverty before housing costs, from the ONS.

Our main regression was

$$\begin{aligned} \log(\text{cumulative cases per capita in } x) - \log(\text{cumulative cases per capita in } N(x)) &= \\ \text{beta_rural_urban} \times (\text{rural/urban score of } x - \text{rural/urban score of } N(x)) + \\ \text{beta_gdp_band} \times (\text{local GDP band of } x - \text{local GDP band of } N(x)) + \\ \text{beta_poverty} \times (\text{per cent of the population living in poverty in } x - \text{per cent of the population living in poverty in } N(x)) + \\ \text{beta_users} \times (\text{per cent of the population using the app in } x - \text{per cent of the population using the app in } N(x)) + \\ \text{epsilon_residual} \end{aligned}$$

where the different data points for the regression (the different values of x) were the set of LTLAs with at least one matched neighbour, excluding LTLAs with no matched neighbours. Cumulative cases were considered in each of the three phases separately or with phases 1 and 2, as reported in our results. The values of the beta coefficients we estimated are shown in Extended Data Table 2. We used a logarithmic transform for the response variable in our regression, because cases are generated by an exponential process (transmission) and so the rate at which the number of cases varies with the dose of a treatment (that is, the extent of an intervention) is highly confounded with the absolute number of cases. A regression with quadratic effect of uptake and intercept at 0 produced very similar findings to the above regression with linear effect of uptake (not shown). We considered additional uncertainty in the regression due to redundancy in the differences approach, for example, in comparing both LTLA x with LTLA n and LTLA n with LTLA x , described in the bootstrapping section of [Supplementary Information](#).

Predictions for cases averted were found using the regression coefficient beta_uptake to linearly extrapolate log(cumulative cases per capita) for each LTLA to that expected for an uptake of 15% (or keeping cases counts as they were, if uptake was already less than 15%). Here we assumed that there is negligible benefit of app uptake below 15% (though this is not expected to be the case in settings where usage is clustered into high-uptake communities²⁹). The definition of beta_users in the regression equation above means it is the expected increase in log(cumulative cases per capita) associated with a one-percentage-point increase in app uptake, when keeping constant GDP, rural/urban mix, and level of poverty. Our central estimate of beta_users in this analysis was -0.023 for phase 1 and 2 combined; this means an increase in uptake of p percentage points is expected to be associated with an increase by the factor $e^{-0.023p}$ in the cumulative number of cases per capita in phases 1 and 2. An increase of $p = 1$ percentage points in uptake means a decrease of 2.3% in cases as we reported above. We estimated the number of deaths averted by multiplying the number of cases averted by the crude case fatality rate.

Alternative regressions are described in [Supplementary Information](#); their results are in Extended Data Tables 3 and 4, and Extended Data Fig. 2.

Case fatality rate

The case fatality rate was estimated as the ratio of total deaths (27,922) to cases (1,891,777) for phases 1 and 2 combined. To test for heterogeneity, it was also estimated as the regression of local deaths to cases, but no substantial heterogeneity was observed (not shown). It is a lower-bound due to right censoring of the time series of deaths.

Reporting summary

Further information on research design is available in the [Nature Research Reporting Summary](#) linked to this paper.

Data availability

Data access is managed by the DHSC. An application is underway to make all data necessary to reproduce our analyses available to accredited researchers through the Office for National Statistics

(<https://www.ons.gov.uk/aboutus/whatwedo/statistics/requestingstatistics/approvedresearcherscheme>). Data aggregated spatially and temporally are available at <https://stats.app.covid19.nhs.uk/>; note that we applied correction factors to early numbers of notifications based on analysis of data available later (see [Supplementary Information](#), ‘Estimate of the number of notifications’).

Code availability

The analysis was performed with custom R (version 4.0.2) code, available on GitHub at https://github.com/BDI-pathogens/nhs_covid_app_evaluation.

References

1. 1.

Ferretti, L. et al. Quantifying SARS-CoV-2 transmission suggests epidemic control with digital contact tracing. *Science* **368**, eabb6936 (2020).

[CAS Article](#) [Google Scholar](#)

2. 2.

Kretzschmar, M. E. et al. Impact of delays on effectiveness of contact tracing strategies for COVID-19: a modelling study. *Lancet Public Health* **5**, e452–e459 (2020).

[Article](#) [Google Scholar](#)

3. 3.

Lunz, D., Batt, G. & Ruess, J. To quarantine, or not to quarantine: a theoretical framework for disease control via contact tracing. *Epidemics* **34**, 100428 (2021).

[Article](#) [Google Scholar](#)

4. 4.

Abueg, M. et al. Modeling the combined effect of digital exposure notification and non-pharmaceutical interventions on the COVID-19 epidemic in Washington state. *npj Digit. Med.* **4**, 49 (2021).

[Article](#) [Google Scholar](#)

5. 5.

Lambert, A. A mathematically rigorous assessment of the efficiency of quarantining and contact tracing in curbing the COVID-19 epidemic. Preprint at <https://doi.org/10.1101/2020.05.04.20091009> (2020).

6. 6.

Cencetti, G. et al. Digital proximity tracing in the COVID-19 pandemic on empirical contact networks. *Nat. Commun.* **12**, 1655 (2021).

[ADS](#) [CAS](#) [Article](#) [Google Scholar](#)

7. 7.

Colizza, V. et al. Time to evaluate COVID-19 contact-tracing apps. *Nat. Med.* **27**, 361–362 (2021).

[CAS](#) [Article](#) [Google Scholar](#)

8. 8.

Google & Apple. Exposure notifications: using technology to help public health authorities fight COVID-19. *Google* https://www.google.com/intl/en_us/covid19/exposurenotifications/ (2020).

9. 9.

Troncoso, C. et al. Decentralized privacy-preserving proximity tracing. Preprint at <https://arxiv.org/abs/2005.12273> (2020).

10. 10.

Lovett, T. et al. Inferring proximity from Bluetooth low energy RSSI with unscented Kalman smoothers. Preprint at <https://arxiv.org/abs/2007.05057> (2020).

11. 11.

Salathé, M. et al. Early evidence of effectiveness of digital contact tracing for SARS-CoV-2 in Switzerland. *Swiss Med. Wkly.* **150**, w20457 (2020).

[PubMed](#) [PubMed Central](#) [Google Scholar](#)

12. 12.

Rodríguez, P. et al. A population-based controlled experiment assessing the epidemiological impact of digital contact tracing. *Nat. Commun.* **12**, 587 (2021).

[ADS](#) [Article](#) [Google Scholar](#)

13. 13.

Smith, L. E. et al. Adherence to the test, trace and isolate system: results from a time series of 21 nationally representative surveys in the UK (the COVID-19 Rapid Survey of Adherence to Interventions and Responses [CORSAIR] study). <https://doi.org/10.1101/2020.09.15.20191957> (2020).

14. 14.

Fancourt, D., Bu, F., Wan Mak, H. & Steptoe, A. *Covid-19 Social Study: Results Release 28* (UCL, 2020);
http://allcatsrgrey.org.uk/wp/download/public_health/mental_health/3d9db5_bf013154aed5484b970c0cf84ff109e9.pdf

15. 15.

Hinch, R. et al. OpenABM-Covid19—an agent-based model for non-pharmaceutical interventions against COVID-19 including contact tracing. Preprint at <https://doi.org/10.1101/2020.09.16.20195925> (2020).

16. 16.

Flaxman, S. et al. Estimating the effects of non-pharmaceutical interventions on COVID-19 in Europe. *Nature* **584**, 257–261 (2020).

[ADS](#) [CAS](#) [Article](#) [Google Scholar](#)

17. 17.

Volz, E. et al. Assessing transmissibility of SARS-CoV-2 lineage B.1.1.7 in England. *Nature* **593**, 266–269 (2021).

[ADS](#) [CAS](#) [Article](#) [Google Scholar](#)

18. 18.

Davies, N. G. et al. Estimated transmissibility and impact of SARS-CoV-2 lineage B.1.1.1.7 in England. *Science* **372**, eabg3055 (2021).

[CAS](#) [Article](#) [Google Scholar](#)

19. 19.

Vöhringer, H. et al. *Lineage-Specific Growth of SARS-CoV-2 B.1.1.7 During the English National Lockdown* (Virological, 2020); <https://virological.org/t/lineage-specific-growth-of-sars-cov-2-b-1-1-7-during-the-english-national-lockdown/575>

20. 20.

Investigation of Novel SARS-CoV-2 Variant: Variant of Concern 202012/01 Technical Briefing 2 (Public Health England, 2020);
https://assets.publishing.service.gov.uk/government/uploads/system/uploads/attachment_data/file/959361/Technical_Briefing_VOC202012-2_Briefing_2.pdf

21. 21.

Hernán, M. A. & Robins, J. M. Using big data to emulate a target trial when a randomized trial is not available. *Am. J. Epidemiol.* **183**, 758–764 (2016).

[Article](#) [Google Scholar](#)

22. 22.

Endo, A. et al. Implication of backward contact tracing in the presence of overdispersed transmission in COVID-19 outbreaks. *Wellcome Open Res.* **5**, 239 (2021).

[Article](#) [Google Scholar](#)

23. 23.

Investigation of Novel SARS-CoV-2 Variant: Variant of Concern 202012/01
Technical Briefing 3 (Public Health England, 2020);
https://assets.publishing.service.gov.uk/government/uploads/system/uploads/attachment_data/file/950823/Variant_of_Concern_VOC_202012_01_Technical_Briefing_3_-_England.pdf

24. 24.

Galanti, M. et al. The importance of continued non-pharmaceutical interventions during the upcoming SARS-CoV-2 vaccination campaign. Preprint at <https://doi.org/10.1101/2020.12.23.20248784> (2020).

25. 25.

Moore, S., Hill, E. M., Tildesley, M. J., Dyson, L. & Keeling, M. J. Vaccination and non-pharmaceutical interventions: when can the UK relax about COVID-19? Preprint at <https://doi.org/10.1101/2020.12.27.2024896> (2021).

26. 26.

Steel, K. & Donnarumma, H. *Coronavirus (COVID-19) Infection Survey, UK 8 January 2021* (Office For National Statistics, 2020);
<https://www.ons.gov.uk/peoplepopulationandcommunity/healthandsocialcare/conditionsanddiseases/bulletins/coronaviruscovid19infectionssurveypilot/8january2021>

27. 27.

Riley, S. et al. REACT-1 round 7 updated report: regional heterogeneity in changes in prevalence of SARS-CoV-2 infection during the second national COVID-19 lockdown in England. Preprint at <https://doi.org/10.1101/2020.12.15.20248244> (2020).

28. 28.

Ferretti, L. et al. The timing of COVID-19 transmission. Preprint at <https://doi.org/10.1101/2020.09.04.20188516> (2020).

29. 29.

Farronato, C. et al. How to get people to actually use contact-tracing apps. *Harvard Business Review* <https://hbr.org/2020/07/how-to-get-people-to-actually-use-contact-tracing-apps> (2020).

[Download references](#)

Acknowledgements

We thank R. Hayes, M. Kraemer, S. Bhatt, S. Mishra, J. Scott, S. Flaxman, A. Gandy, C. Jewell and W. Probert for helpful comments. This work was funded by a Li Ka Shing Foundation award to C.F., and by research grant funding from the UK Department of Health and Social Care (DHSC) to M.B., C.H. and C.F. The funders had no role in the design and conduct of the analysis.

Author information

Author notes

1. These authors contributed equally: Chris Wymant, Luca Ferretti

Affiliations

1. Big Data Institute, Li Ka Shing Centre for Health Information and Discovery, Nuffield Department of Medicine, University of Oxford, Oxford, UK

Chris Wymant, Luca Ferretti, Lucie Abeler-Dörner, David Bonsall, Robert Hinch, Michelle Kendall, Chris Holmes & Christophe Fraser

2. Zühlke Engineering Ltd, London, UK

Daphne Tsallis

3. The Alan Turing Institute, London, UK

Marcos Charalambides, Matthew Ayres, Chris Holmes & Mark Briers

4. Department of Statistics, University of Warwick, Coventry, UK

Michelle Kendall

5. Department of Economics, University of Oxford, Oxford, UK

Luke Milsom

6. Department of Statistics, University of Oxford, Oxford, UK

Chris Holmes

Authors

1. Chris Wymant

[View author publications](#)

You can also search for this author in [PubMed](#) [Google Scholar](#)

2. Luca Ferretti

[View author publications](#)

You can also search for this author in [PubMed](#) [Google Scholar](#)

3. Daphne Tsallis

[View author publications](#)

You can also search for this author in [PubMed](#) [Google Scholar](#)

4. Marcos Charalambides

[View author publications](#)

You can also search for this author in [PubMed](#) [Google Scholar](#)

5. Lucie Abeler-Dörner

[View author publications](#)

You can also search for this author in [PubMed](#) [Google Scholar](#)

6. David Bonsall

[View author publications](#)

You can also search for this author in [PubMed](#) [Google Scholar](#)

7. Robert Hinch

[View author publications](#)

You can also search for this author in [PubMed](#) [Google Scholar](#)

8. Michelle Kendall

[View author publications](#)

You can also search for this author in [PubMed](#) [Google Scholar](#)

9. Luke Milsom

[View author publications](#)

You can also search for this author in [PubMed](#) [Google Scholar](#)

10. Matthew Ayres

[View author publications](#)

You can also search for this author in [PubMed](#) [Google Scholar](#)

11. Chris Holmes

[View author publications](#)

You can also search for this author in [PubMed](#) [Google Scholar](#)

12. Mark Briers

[View author publications](#)

You can also search for this author in [PubMed](#) [Google Scholar](#)

13. Christophe Fraser

[View author publications](#)

You can also search for this author in [PubMed](#) [Google Scholar](#)

Contributions

Contributions have been categorized according to the CRediT taxonomy (<https://casrai.org/credit/>). Conceptualization: C.W., L.F., M.B. and C.F. Data curation: C.W., D.T., M.C., L.M. and M.A. Formal analysis: C.W., L.F. and C.F. Funding acquisition: C.H., M.B. and C.F. Investigation: C.W., L.F., D.T., M.C., L.M. and C.F. Methodology: C.W., L.F., R.H., L.M. and C.F. Project administration: D.B., L.A.-D., C.H., M.B. and C.F. Resources: M.A., C.H., M.B. and C.F. Supervision: C.H., M.B. and C.F. Visualization: C.W., D.T. and M.K. Writing—original draft: C.W., L.F. and C.F. Writing—review and editing: all authors.

Corresponding author

Correspondence to [Christophe Fraser](#).

Ethics declarations

Competing interests

D.T., M.C. and M.A. are part of the app data analytics team. D.T. is employed by Zühlke and M.A. is employed by Accenture; Zühlke and Accenture are contracted by the DHSC for app development and analytics. M.B. is lead scientist for the app. C.W., L.F., R.H., L.A.-D., D.B., M.K., C.H. and C.F. have acted as advisors for the DHSC on the app. DHSC runs the app, and manages the secure data environment where the analyses conducted here were performed. DHSC led dissemination of the findings in the UK.

Additional information

Peer review information *Nature* thanks Chiara Poletto, Jason Wang and the other, anonymous, reviewer(s) for their contribution to the peer review of this work.

Publisher's note Springer Nature remains neutral with regard to jurisdictional claims in published maps and institutional affiliations.

Extended data figures and tables

Extended Data Fig. 1 Characterizing the behaviour of the app.

a, The total number of app downloads and active users over time. Fluctuations in app users are artefactual, driven by reporting issues on Android handsets, such that the estimate of ‘active users’ is a lower bound estimate. **b**, The seven-day rolling mean of the total number of notifications triggered each day. **c**, The daily number of app users receiving a confirmed positive test. **d**, The daily number of app users recording a positive test result in the app, having recently received an exposure notification.

Extended Data Fig. 2 Results for the secondary statistical analysis based on clusters.

Regression coefficients for app effect for each cluster, and aggregate variance-weighted estimate (labelled ‘meta’). Error bars show 95% confidence intervals. Panels are labelled for phase 1 and 2 combined, and phase 1 and phase 2 separately. Aggregate estimates are reported in main text Table 1.

Extended Data Fig. 3 Estimated cases averted over time.

Plotted is the rolling 7-day average of the number of cases observed and predicted number of cases averted due to the notifications sent by the app, for different values of adherence to imperfect quarantine (25%, 50%, 75%) for the 31% of notified

individuals who we assumed adhere imperfectly, in addition to 45.5% of notified individuals assumed to adhere perfectly.

Extended Data Fig. 4 Estimated delay from exposure to notification.

The black line shows the mean, and the grey ribbon around the mean shows points within 1 standard deviation of the mean. For comparison, deciles of the generation time distribution (the probability density function for the time from becoming infected to infecting others) are shown in blue; for example the first decile (tenth percentile) is greater than the mean time to notification in December, that is, the mean time to notification comes before 90% of when transmission would normally happen.

Extended Data Fig. 5 Summarizing app data.

We show the relationship between epidemiological events, and the data gathered about these by the app on individual phones and in the central database. The so-called circuit breaker monitors and processes in real time requests by the app to notify (our quantity $N(t)$ in Methods, ‘Estimate of the number of notifications’.).

Extended Data Fig. 6 Maps of per-capita numbers of cases in LTLAs over time.

a, Per-capita case numbers in phase 0 grouped into quintiles, showing the stratification used for the main statistical analysis. **b–d**, Actual per capita case numbers are shown, using a shared colour scale (shown once), for phases 0 (**b**), 1 (**c**) and 2 (**d**), respectively.

Extended Data Table 1 Phases of our analysis

[Full size table](#)

Extended Data Table 2 Coefficients for the main regression

[Full size table](#)

Extended Data Table 3 Regression results for the matched pairs analysis

[Full size table](#)

Extended Data Table 4 Results for regression adjusting for quality of manual contact tracing

[Full size table](#)

Supplementary information

Supplementary Information

This file contains Supplementary Information, including Supplementary Figures 1-3 and Supplementary Tables 1-4.

Reporting Summary

Rights and permissions

Reprints and Permissions

About this article



Check for
updates

Cite this article

Wymant, C., Ferretti, L., Tsallis, D. *et al.* The epidemiological impact of the NHS COVID-19 app. *Nature* **594**, 408–412 (2021). <https://doi.org/10.1038/s41586-021-03606-z>

Download citation

- Received: 10 February 2021
- Accepted: 03 May 2021
- Published: 12 May 2021
- Issue Date: 17 June 2021
- DOI: <https://doi.org/10.1038/s41586-021-03606-z>

Further reading

- [Contact-tracing app curbed the spread of COVID in England and Wales](#)
 - C. Jason Wang

Nature (2021)

Comments

By submitting a comment you agree to abide by our [Terms](#) and [Community Guidelines](#). If you find something abusive or that does not comply with our terms or guidelines please flag it as inappropriate.

[Download PDF](#)

Associated Content

Collection

[**Coronavirus**](#)

[**Contact-tracing app curbed the spread of COVID in England and Wales**](#)

- C. Jason Wang

Advertisement

This article was downloaded by **calibre** from <https://www.nature.com/articles/s41586-021-03606-z>

| [Section menu](#) | [Main menu](#) |

- Article
- [Published: 12 May 2021](#)

Thymic development of gut-microbiota-specific T cells

- [Daniel F. Zegarra-Ruiz](#) ORCID: orcid.org/0000-0003-0752-7238¹,
- [Dasom V. Kim](#)^{1,2},
- [Kendra Norwood](#)³,
- [Myunghoo Kim](#)³ nAff12,
- [Wan-Jung H. Wu](#)^{1,4},
- [Fatima B. Saldana-Morales](#) ORCID: orcid.org/0000-0001-5192-5722^{1,5},
- [Andrea A. Hill](#)⁶,
- [Shubhabrata Majumdar](#)^{4,7},
- [Stephanie Orozco](#)⁷,
- [Rickesha Bell](#)⁷,
- [June L. Round](#)⁷,
- [Randy S. Longman](#)^{8,9,10},
- [Takeshi Egawa](#) ORCID: orcid.org/0000-0001-7489-1051¹¹,
- [Matthew L. Bettini](#) ORCID: orcid.org/0000-0001-9479-657X⁷ &
- [Gretchen E. Diehl](#) ORCID: orcid.org/0000-0002-1841-2842^{1,2,3}

[Nature](#) volume **594**, pages 413–417 (2021) [Cite this article](#)

- 12k Accesses
- 243 Altmetric
- [Metrics details](#)

Subjects

- [Adaptive immunity](#)
- [Mucosal immunology](#)

Abstract

Humans and their microbiota have coevolved a mutually beneficial relationship in which the human host provides a hospitable environment for the microorganisms and the microbiota provides many advantages for the host, including nutritional benefits and protection from pathogen infection¹. Maintaining this relationship requires a careful immune balance to contain commensal microorganisms within the lumen while limiting inflammatory anti-commensal responses^{1,2}. Antigen-specific recognition of intestinal microorganisms by T cells has previously been described^{3,4}. Although the local environment shapes the differentiation of effector cells^{3,4,5} it is unclear how microbiota-specific T cells are educated in the thymus. Here we show that intestinal colonization in early life leads to the trafficking of microbial antigens from the intestine to the thymus by intestinal dendritic cells, which then induce the expansion of microbiota-specific T cells. Once in the periphery, microbiota-specific T cells have pathogenic potential or can protect against related pathogens. In this way, the developing microbiota shapes and expands the thymic and peripheral T cell repertoire, allowing for enhanced recognition of intestinal microorganisms and pathogens.

Access options

Subscribe to Journal

Get full journal access for 1 year

\$199.00

only \$3.90 per issue

[Subscribe](#)

All prices are NET prices.
VAT will be added later in the checkout.
Tax calculation will be finalised during checkout.

Rent or Buy article

Get time limited or full article access on ReadCube.

from \$8.99

[Rent or Buy](#)

All prices are NET prices.

Additional access options:

- [Log in](#)
- [Access through your institution](#)
- [Learn about institutional subscriptions](#)

Fig. 1: Commensal colonization leads to an expansion of bacteria-specific T cells in the thymus.



Fig. 2: Enrichment of CX3CR1⁺ DCs in the thymus after colonization with commensal microorganisms.

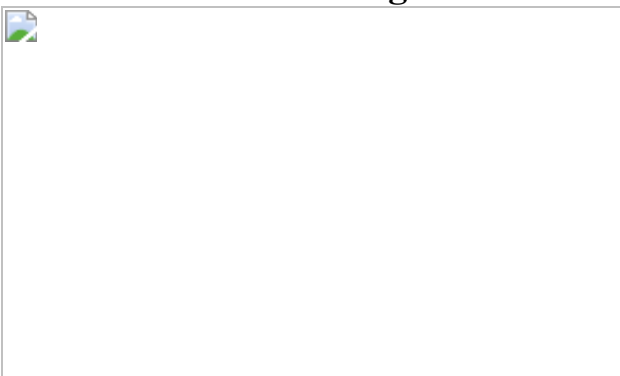
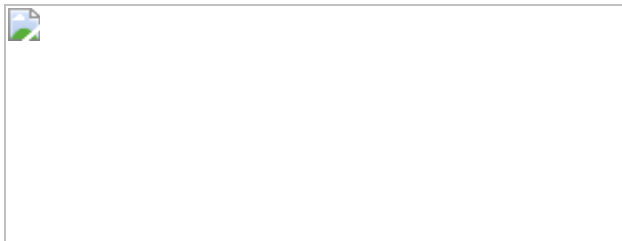


Fig. 3: Thymic microbiota-specific T cells are functional in distal tissues.



Data availability

All data generated and supporting the findings of this study are available within the paper. The RNA-seq data have been deposited in the Gene Expression Omnibus (GEO) under accession number [GSE171279](#). The 16S sequencing data have been submitted to the Sequence Read Archive (SRA) under the BioProject ID [718898](#). Additional information and materials will be made available upon request. [Source data](#) are provided with this paper.

References

1. 1.

Hooper, L. V., Littman, D. R. & Macpherson, A. J. Interactions between the microbiota and the immune system. *Science* **336**, 1268–1273 (2012).

[ADS](#) [CAS](#) [PubMed](#) [PubMed Central](#) [Google Scholar](#)

2. 2.

Zegarra-Ruiz, D. F. et al. A diet-sensitive commensal *Lactobacillus* strain mediates TLR7-dependent systemic autoimmunity. *Cell Host Microbe* **25**, 113–127 (2019).

[CAS](#) [PubMed](#) [Google Scholar](#)

3. 3.

Xu, M. et al. c-MAF-dependent regulatory T cells mediate immunological tolerance to a gut pathobiont. *Nature* **554**, 373–377 (2018).

[ADS](#) [CAS](#) [PubMed](#) [PubMed Central](#) [Google Scholar](#)

4. 4.

Yang, Y. et al. Focused specificity of intestinal T_H17 cells towards commensal bacterial antigens. *Nature* **510**, 152–156 (2014).

[ADS](#) [CAS](#) [PubMed](#) [PubMed Central](#) [Google Scholar](#)

5. 5.

Lathrop, S. K. et al. Peripheral education of the immune system by colonic commensal microbiota. *Nature* **478**, 250–254 (2011).

[ADS](#) [CAS](#) [PubMed](#) [PubMed Central](#) [Google Scholar](#)

6. 6.

Bäckhed, F. et al. Dynamics and stabilization of the human gut microbiome during the first year of life. *Cell Host Microbe* **17**, 690–703 (2015).

[PubMed](#) [Google Scholar](#)

7. 7.

Boehm, T. & Swann, J. B. Thymus involution and regeneration: two sides of the same coin? *Nat. Rev. Immunol.* **13**, 831–838 (2013).

[CAS](#) [PubMed](#) [Google Scholar](#)

8. 8.

Cebula, A. et al. Thymus-derived regulatory T cells contribute to tolerance to commensal microbiota. *Nature* **497**, 258–262 (2013).

[ADS](#) [CAS](#) [PubMed](#) [PubMed Central](#) [Google Scholar](#)

9. 9.

Kotov, D. I. & Jenkins, M. K. Peptide:MHCII tetramer-based cell enrichment for the study of epitope-specific CD4⁺ T cells. *Curr. Protoc. Immunol.* **125**, e75 (2019).

[PubMed](#) [PubMed Central](#) [Google Scholar](#)

10. 10.

Sakaguchi, S. Naturally arising Foxp3-expressing CD25⁺CD4⁺ regulatory T cells in immunological tolerance to self and non-self. *Nat. Immunol.* **6**, 345–352 (2005).

[CAS](#) [PubMed](#) [Google Scholar](#)

11. 11.

Egawa, T. & Littman, D. R. ThPOK acts late in specification of the helper T cell lineage and suppresses Runx-mediated commitment to the cytotoxic T cell lineage. *Nat. Immunol.* **9**, 1131–1139 (2008).

[CAS](#) [PubMed](#) [PubMed Central](#) [Google Scholar](#)

12. 12.

Hogquist, K. A., Xing, Y., Hsu, F.-C. & Shapiro, V. S. T cell adolescence: maturation events beyond positive selection. *J. Immunol.* **195**, 1351–1357 (2015).

[CAS](#) [PubMed](#) [PubMed Central](#) [Google Scholar](#)

13. 13.

Anderson, K. G. et al. Intravascular staining for discrimination of vascular and tissue leukocytes. *Nat. Protocols* **9**, 209–222 (2014).

[CAS](#) [PubMed](#) [Google Scholar](#)

14. 14.

Owen, D. L. et al. Thymic regulatory T cells arise via two distinct developmental programs. *Nat. Immunol.* **20**, 195–205 (2019).

[CAS](#) [PubMed](#) [PubMed Central](#) [Google Scholar](#)

15. 15.

Chopp, L. B. et al. An integrated epigenomic and transcriptomic map of mouse and human $\alpha\beta$ T cell development. *Immunity* **53**, 1182–1201 (2020).

[CAS](#) [PubMed](#) [Google Scholar](#)

16. 16.

Diehl, G. E. et al. Microbiota restricts trafficking of bacteria to mesenteric lymph nodes by CX₃CR1^{hi} cells. *Nature* **494**, 116–120 (2013).

[ADS](#) [CAS](#) [PubMed](#) [PubMed Central](#) [Google Scholar](#)

17. 17.

Varol, C., Zigmond, E. & Jung, S. Securing the immune tightrope: mononuclear phagocytes in the intestinal lamina propria. *Nat. Rev. Immunol.* **10**, 415–426 (2010).

[CAS](#) [PubMed](#) [Google Scholar](#)

18. 18.

Longman, R. S. et al. CX₃CR1⁺ mononuclear phagocytes support colitis-associated innate lymphoid cell production of IL-22. *J. Exp. Med.* **211**, 1571–1583 (2014).

[CAS](#) [PubMed](#) [PubMed Central](#) [Google Scholar](#)

19. 19.

Kim, M. et al. Critical role for the microbiota in CX₃CR1⁺ intestinal mononuclear phagocyte regulation of intestinal T cell responses. *Immunity* **49**, 151–163 (2018).

[CAS](#) [PubMed](#) [PubMed Central](#) [Google Scholar](#)

20. 20.

Hadeiba, H. & Butcher, E. C. Thymus-homing dendritic cells in central tolerance. *Eur. J. Immunol.* **43**, 1425–1429 (2013).

[CAS](#) [PubMed](#) [PubMed Central](#) [Google Scholar](#)

21. 21.

Nowotschin, S. & Hadjantonakis, A.-K. Use of KikGR a photoconvertible green-to-red fluorescent protein for cell labeling and lineage analysis in ES cells and mouse embryos. *BMC Dev. Biol.* **9**, 49 (2009).

[PubMed](#) [PubMed Central](#) [Google Scholar](#)

22. 22.

Sohy, D. et al. Hetero-oligomerization of CCR2, CCR5, and CXCR4 and the protean effects of “selective” antagonists. *J. Biol. Chem.* **284**, 31270–31279 (2009).

[CAS](#) [PubMed](#) [PubMed Central](#) [Google Scholar](#)

23. 23.

Coombes, J. L., Robinson, N. J., Maloy, K. J., Uhlig, H. H. & Powrie, F. Regulatory T cells and intestinal homeostasis. *Immunol. Rev.* **204**, 184–194 (2005).

[CAS](#) [PubMed](#) [Google Scholar](#)

24. 24.

Di Padova, F. E. et al. A broadly cross-protective monoclonal antibody binding to *Escherichia coli* and *Salmonella* lipopolysaccharides. *Infect. Immun.* **61**, 3863–3872 (1993).

[PubMed](#) [PubMed Central](#) [Google Scholar](#)

25. 25.

Bensinger, S. J., Bandeira, A., Jordan, M. S., Caton, A. J. & Laufer, T. M. Major histocompatibility complex class II-positive cortical epithelium mediates the selection of CD4⁺25⁺ immunoregulatory T cells. *J. Exp. Med.* **194**, 427–438 (2001).

[CAS](#) [PubMed](#) [PubMed Central](#) [Google Scholar](#)

26. 26.

Klein, L., Kyewski, B., Allen, P. M. & Hogquist, K. A. Positive and negative selection of the T cell repertoire: what thymocytes see (and don't see). *Nat. Rev. Immunol.* **14**, 377–391 (2014).

[CAS](#) [PubMed](#) [PubMed Central](#) [Google Scholar](#)

27. 27.

Leech, J. M. et al. Toxin-triggered interleukin-1 receptor signaling enables early-life discrimination of pathogenic versus commensal skin bacteria. *Cell Host Microbe* **26**, 795–809 (2019).

[CAS](#) [PubMed](#) [PubMed Central](#) [Google Scholar](#)

28. 28.

Scharschmidt, T. C. et al. A wave of regulatory T cells into neonatal skin mediates tolerance to commensal microbes. *Immunity* **43**, 1011–

1021 (2015).

[CAS](#) [PubMed](#) [PubMed Central](#) [Google Scholar](#)

29. 29.

Hashimoto, K., Joshi, S. K. & Koni, P. A. A conditional null allele of the major histocompatibility IA-beta chain gene. *Genesis* **32**, 152–153 (2002).

[CAS](#) [PubMed](#) [Google Scholar](#)

30. 30.

Jung, S. et al. Analysis of fractalkine receptor CX₃CR1 function by targeted deletion and green fluorescent protein reporter gene insertion. *Mol. Cell. Biol.* **20**, 4106–4114 (2000).

[CAS](#) [PubMed](#) [PubMed Central](#) [Google Scholar](#)

31. 31.

Parkhurst, C. N. et al. Microglia promote learning-dependent synapse formation through brain-derived neurotrophic factor. *Cell* **155**, 1596–1609 (2013).

[CAS](#) [PubMed](#) [PubMed Central](#) [Google Scholar](#)

32. 32.

Sano, T. et al. An IL-23R/IL-22 circuit regulates epithelial serum amyloid A to promote local effector Th17 responses. *Cell* **163**, 381–393 (2015).

[CAS](#) [PubMed](#) [PubMed Central](#) [Google Scholar](#)

33. 33.

Buchan, A., Hadden, M. & Suzuki, M. T. Development and application of quantitative-PCR tools for subgroups of the *Roseobacter* clade. *Appl. Environ. Microbiol.* **75**, 7542–7547 (2009).

[CAS](#) [PubMed](#) [PubMed Central](#) [Google Scholar](#)

34. 34.

Chern, E. C., Siefring, S., Paar, J., Doolittle, M. & Haugland, R. A. Comparison of quantitative PCR assays for *Escherichia coli* targeting ribosomal RNA and single copy genes. *Lett. Appl. Microbiol.* **52**, 298–306 (2011).

[CAS](#) [PubMed](#) [Google Scholar](#)

35. 35.

Valdez, Y. et al. Nramp1 expression by dendritic cells modulates inflammatory responses during *Salmonella* Typhimurium infection. *Cell. Microbiol.* **10**, 1646–1661 (2008).

[CAS](#) [PubMed](#) [PubMed Central](#) [Google Scholar](#)

36. 36.

Moon, J. J. et al. Tracking epitope-specific T cells. *Nat. Protocols* **4**, 565–581 (2009).

[CAS](#) [PubMed](#) [Google Scholar](#)

37. 37.

Moon, J. J. et al. Naive CD4⁺ T cell frequency varies for different epitopes and predicts repertoire diversity and response magnitude. *Immunity* **27**, 203–213 (2007).

[CAS](#) [PubMed](#) [PubMed Central](#) [Google Scholar](#)

38. 38.

Chu, H. H., Moon, J. J., Kruse, A. C., Pepper, M. & Jenkins, M. K. Negative selection and peptide chemistry determine the size of naive foreign peptide-MHC class II-specific CD4⁺ T cell populations. *J. Immunol.* **185**, 4705–4713 (2010).

[CAS](#) [PubMed](#) [PubMed Central](#) [Google Scholar](#)

39. 39.

Viladomiu, M. et al. IgA-coated *E. coli* enriched in Crohn's disease spondyloarthritis promote T_H17-dependent inflammation. *Sci. Transl. Med.* **9**, eaaf9655 (2017).

[PubMed](#) [PubMed Central](#) [Google Scholar](#)

40. 40.

Dobin, A. et al. STAR: ultrafast universal RNA-seq aligner. *Bioinformatics* **29**, 15–21 (2013).

[CAS](#) [PubMed](#) [Google Scholar](#)

41. 41.

Engström, P. G. et al. Systematic evaluation of spliced alignment programs for RNA-seq data. *Nat. Methods* **10**, 1185–1191 (2013).

[PubMed](#) [PubMed Central](#) [Google Scholar](#)

42. 42.

Anders, S., Pyl, P. T. & Huber, W. HTSeq—a Python framework to work with high-throughput sequencing data. *Bioinformatics* **35**, 166–169 (2015).

[Google Scholar](#)

43. 43.

Huang, W., Sherman, B. T. & Lempicki, R. A. Systematic and integrative analysis of large gene lists using DAVID bioinformatics resources. *Nat. Protocols* **4**, 44–57 (2009).

[CAS](#) [Google Scholar](#)

44. 44.

Berg, D. J. et al. Enterocolitis and colon cancer in interleukin-10-deficient mice are associated with aberrant cytokine production and CD4⁺ TH1-like responses. *J. Clin. Invest.* **98**, 1010–1020 (1996).

[CAS](#) [PubMed](#) [PubMed Central](#) [Google Scholar](#)

[Download references](#)

Acknowledgements

This work was supported by NIH grants R01AI136963 (G.E.D. and M.L.B.), R01AI125264 (G.E.D.), R01DK114456 (M.L.B.), R01AI130152 (T.E.) and R01 DK114252 (R.S.L.); the Kleberg Foundation (G.E.D. and M.L.B); the Kenneth Rainin Foundation (G.E.D.); the Leukemia and Lymphoma Society Scholar Award (T.E.); and the Cytometry and Cell Sorting Core at Baylor College of Medicine, with funding from the CPRIT Core Facility Support Award (CPRIT-RP180672) and the NIH (P30 CA125123 and S10 RR024574) and with the assistance of J. M. Sederstrom. We thank the Baylor College of Medicine Genetically Engineered Mouse Core supported by the Cancer Center Grant (P30 CA125123); the Mouse Embryonic Stem Cell Core at Baylor College of Medicine; D. Littman and C.-S. Hsieh for critical reading of the manuscript; N. Ajami for advice on 16S; and the NIH Tetramer Facility, which is supported by contract HHSN272201300006C from the NIAID.

Author information

Author notes

1. Myunghoo Kim

Present address: Department of Animal Science, Pusan National University, Pusan, South Korea

Affiliations

1. Immunology Program, Memorial Sloan Kettering Cancer Center, New York, NY, USA

Daniel F. Zegarra-Ruiz, Dasom V. Kim, Wan-Jung H. Wu, Fatima B. Saldana-Morales & Gretchen E. Diehl

2. Immunology and Microbial Pathogenesis Program, Weill Cornell Graduate School of Medical Sciences, New York, NY, USA

Dasom V. Kim & Gretchen E. Diehl

3. Department of Molecular Virology and Microbiology, Baylor College of Medicine, Houston, TX, USA

Kendra Norwood, Myunghoo Kim & Gretchen E. Diehl

4. Immunology Program, Baylor College of Medicine, Houston, TX, USA

Wan-Jung H. Wu & Shubhabrata Majumdar

5. Neuroscience Program, Baylor College of Medicine, Houston, TX, USA

Fatima B. Saldana-Morales

6. Department of Pathology and Immunology, Baylor College of Medicine, Houston, TX, USA

Andrea A. Hill

7. Department of Pathology, University of Utah School of Medicine, Salt Lake City, UT, USA

Shubhabrata Majumdar, Stephanie Orozco, Rickesha Bell, June L. Round & Matthew L. Bettini

8. Division of Gastroenterology and Hepatology, Department of Medicine, Weill Cornell Medicine, New York, NY, USA

Randy S. Longman

9. Jill Roberts Institute for Research in Inflammatory Bowel Disease, Weill Cornell Medicine, New York, NY, USA

Randy S. Longman

10. Jill Roberts Center for Inflammatory Bowel Disease, Weill Cornell Medicine, New York, NY, USA

Randy S. Longman

11. Department of Pathology, Washington University School of Medicine in St Louis, St Louis, MO, USA

Takeshi Egawa

Authors

1. Daniel F. Zegarra-Ruiz

[View author publications](#)

You can also search for this author in [PubMed](#) [Google Scholar](#)

2. Dasom V. Kim

[View author publications](#)

You can also search for this author in [PubMed](#) [Google Scholar](#)

3. Kendra Norwood

[View author publications](#)

You can also search for this author in [PubMed](#) [Google Scholar](#)

4. Myunghoo Kim

[View author publications](#)

You can also search for this author in [PubMed](#) [Google Scholar](#)

5. Wan-Jung H. Wu

[View author publications](#)

You can also search for this author in [PubMed](#) [Google Scholar](#)

6. Fatima B. Saldana-Morales

[View author publications](#)

You can also search for this author in [PubMed](#) [Google Scholar](#)

7. Andrea A. Hill

[View author publications](#)

You can also search for this author in [PubMed](#) [Google Scholar](#)

8. Shubhabrata Majumdar

[View author publications](#)

You can also search for this author in [PubMed](#) [Google Scholar](#)

9. Stephanie Orozco

[View author publications](#)

You can also search for this author in [PubMed](#) [Google Scholar](#)

10. Rickesha Bell

[View author publications](#)

You can also search for this author in [PubMed](#) [Google Scholar](#)

11. June L. Round

[View author publications](#)

You can also search for this author in [PubMed](#) [Google Scholar](#)

12. Randy S. Longman

[View author publications](#)

You can also search for this author in [PubMed](#) [Google Scholar](#)

13. Takeshi Egawa

[View author publications](#)

You can also search for this author in [PubMed](#) [Google Scholar](#)

14. Matthew L. Bettini

[View author publications](#)

You can also search for this author in [PubMed](#) [Google Scholar](#)

15. Gretchen E. Diehl

[View author publications](#)

You can also search for this author in [PubMed](#) [Google Scholar](#)

Contributions

D.F.Z.-R., T.E., R.S.L., M.L.B. and G.E.D. designed the experiments and analysed data. D.F.Z.-R. and G.E.D. wrote the manuscript with input from all co-authors. D.F.Z.-R., D.V.K., K.N., M.K, W.-J.H.W., F.B.S.-M., A.A.H., S.M., S.O., M.L.B. and G.E.D. conducted experiments and analysed data. R.B. and J.L.R. were responsible for germ-free mouse experiments.

Corresponding authors

Correspondence to [Matthew L. Bettini](#) or [Gretchen E. Diehl](#).

Ethics declarations

Competing interests

The authors declare no competing interests.

Additional information

Peer review information *Nature* thanks Dennis Kasper and the other, anonymous, reviewer(s) for their contribution to the peer review of this work.

Publisher's note Springer Nature remains neutral with regard to jurisdictional claims in published maps and institutional affiliations.

Extended data figures and tables

Extended Data Fig. 1 Characterization of SFB-tetramer⁺ CD4⁺ T cells.

a, Gating strategy used to identify SFB-tetramer⁺ CD4⁺ T cells after magnetic enrichment. Live, CD45⁺ single cells negative for CX3CR1, Ly6G, B220, Ly6C, MHCII and CD8 were further analysed. From the CD3⁺CD4⁺ population, SFB-specific cells were identified as double positive for APC- and PE- (Fig. 1) or single positive for APC- or PE-conjugated tetramers specific for SFB peptide QFSGAVPNKTD (all other figures). **b**, Mice were colonized with SFB at weaning and two weeks later thymic T cells were compared to age-matched control (CTRL) mice. Frequencies and counts of SFB-tetramer⁺ cells in thymic flow-through after magnetic enrichment ($n = 3$ per group). **c**, 7B8 TCR transgenic mice were left uncolonized or SFB-colonized at weaning and two weeks later CD4⁺ counts in the thymus were compared (control $n = 6$; SFB $n = 7$). **d–f**, Mice were colonized with SFB at weaning and two weeks later thymic T cells were compared to age-matched control mice. **d**, Frequencies and counts of

SFB-tetramer⁺ cells in CD8⁺ (single-positive; SP) and CD4⁺CD8⁺ (double-positive; DP) T cells ($n = 10$ per group). **e**, Frequencies and counts of no tetramer (NT), 2W1S, *H. hepaticus* (HH) and human (HU) tetramer⁺ cells in CD4⁺ T cells ($n = 5$ per group). **f**, Frequencies and counts of CD4⁺, CD8⁺ and CD4⁺CD8⁺ thymic subsets. **g–k**, Representative flow plots of control and SFB CD4⁺ T cells for ROR γ t and FOXP3 (**g**), CD25 (**h**), CD44 (**i**); CD24 and TCR β (**j**) and CD69 and TCR β (**k**). In **f–k**, $n = 15$ per group. Each replicate is a biologically independent sample. Data are shown as individual values and mean; P values by two-tailed unpaired *t*-test (**b, c**) or two-way ANOVA with Sidak's post hoc test (**d–f**).

[Source data](#)

[**Extended Data Fig. 2 Thymic expansion of bacteria-specific T cells after colonization with commensal microorganisms at weaning.**](#)

a–c, Thymic SFB-tetramer⁺ cells from young mice were analysed by flow cytometry ($n = 15$). **a**, CD24 and TCR β . **b**, CD44. **c**, CD69 and TCR β . **d**, Mice were colonized with SFB at weaning for two weeks and were injected intravenously with anti-CD45 before euthanasia. Flow cytometry of CD45 in thymic SFB-tetramer⁺ cells and spleen ($n = 5$). **e**, RAG2-GFP mice were colonized with SFB at weaning and two weeks later thymi were collected. Flow cytometry of thymic CD4⁺ cells ($n = 7$). **f, g**, Thymic SFB-non-specific and SFB-specific CD4⁺ T cells from young mice two weeks after colonization were analysed by RNA-seq. **f**, Principal component analysis of SFB-non-specific and SFB-specific CD4⁺ T cells (circled) compared to thymocytes at different developmental stages (GSE148973). **g**, Heat map showing row-standardized z -scores of mRNA expression for genes in enriched KEGG pathways ($P < 0.05$). In **f, g**, $n = 5$ (SFB-non-specific T cells); $n = 3$ (SFB-specific T cells). Each SFB-specific T cell replicate is a pool of 10 thymi. **h–j**, Mice were colonized with SFB at weaning and were compared four weeks later to age-matched control mice. **h**, Flow cytometry and counts of SFB-tetramer⁺ cells in the MLNs ($n = 5$ (CTRL; $n = 15$ (SFB)), spleen (SPL; $n = 5$ per group), ileum ($n = 5$ (CTRL); $n = 10$ (SFB)) and colon ($n = 5$ per group). **i, j**, Flow cytometry (**i**) and counts (**j**) of

thymic SFB-tetramer⁺ cells ($n = 5$ (CTRL); $n = 15$ (SFB)). **k**, RAG2-GFP mice were colonized with SFB at weaning and four weeks later thymi were collected. Flow cytometry of thymic CD4⁺ cells ($n = 7$). **l, m**, SPF and germ-free mice were treated with antibiotics (ABX) at weaning and compared two weeks later to age-matched control mice. Counts of total thymocytes, CD4⁺, CD8⁺ and thymic T_{reg} cells in SPF mice (**l**; $n = 15$ (CTRL); $n = 9$ (ABX)) and germ-free mice (**m**; $n = 3$ (CTRL); $n = 4$ (ABX)). Each replicate is a biologically independent sample. Data are shown as individual values and mean; P values by two-tailed unpaired t -test (**j, l, m**) or two-way ANOVA with Sidak's post hoc test (**h**).

Source data

Extended Data Fig. 3 Bacterial DNA is found in the thymus after early-life colonization.

a, b, h–j, Mice were colonized with SFB or *E. coli* at weaning (young) or at 12 weeks of age (adult) and one week later were compared to age-matched control mice. **a, b**, SFB-specific qPCR in faecal pellets (FP) (**a**; young: CTRL, SFB $n = 8$; adult: CTRL, SFB $n = 6$); and MLNs (**b**; young: CTRL, SFB $n = 9$; adult: CTRL, SFB $n = 7$). **h–j**, *E. coli*-specific qPCR in the thymus (**h**; young: CTRL $n = 10$, EC $n = 15$; adult: CTRL, EC $n = 15$), MLNs (**i**; young: CTRL, EC $n = 8$; adult: CTRL, EC $n = 7$) and faecal pellets (**j**; young: CTRL, EC $n = 8$; adult: CTRL, EC $n = 10$). Mice were colonized with SFB at weaning and compared one week later to age-matched control mice. **c, e**, SFB-specific qPCR (**c**; $n = 6$ per group) and 16S qPCR (**e**) in the thymus, MLNs, liver, spleen, heart and lungs (in **e**, thymus, MLNs: CTRL, SFB $n = 12$; liver, SPL, heart, lungs: CTRL, SFB $n = 6$). **d, g**, Mice were colonized with SFB at weaning and analysed up to three weeks later. SFB-specific PCR (**d**) and 16S qPCR (**g**) in the thymus, MLNs and faecal pellets ($n = 5$ per group). **f**, Mice were colonized with SFB at 12 weeks of age and compared one week later to age-matched control mice. 16S qPCR in thymus and MLNs (thymus: CTRL $n = 16$, SFB $n = 11$; MLNs CTRL, SFB $n = 7$). **k**, Mice were euthanized at 4 weeks of age, tissues were collected, DNA was isolated and 16S rDNA sequencing was performed. Bacterial phyla and class relative abundance in the thymus,

MLNs and caecum ($n = 5$ per group; thymus and MLNs were pooled). **I–n**, Mice were treated with antibiotics at weaning and compared one week later to age-matched control mice. 16S qPCR in the thymus (**I**; $n = 7$ (CTRL), $n = 8$ (ABX)); MLNs (**m**; $n = 16$ (CTRL), $n = 9$ (ABX)) and faecal pellets (**n**; $n = 10$ per group). Each replicate is a biologically independent sample. Data are shown as mean \pm s.e.m. (**d, g**) or as individual values and mean; P values by two-tailed unpaired t -test (**I–n**) or two-way ANOVA with Tukey's (**a, b, f, h–j**), Sidak's (**c, e**) or Fisher's LSD (**e**) post hoc test.

Source data

Extended Data Fig. 4 CX3CR1 $^{\pm}$ DCs are enriched in the thymus after colonization with commensal microorganisms in young mice.

a–c, g, Thymic cell populations were analysed at weaning (W3), one (W4) and two (W5) weeks after weaning, and at 12 weeks of age (W12). Frequencies and counts of CD4 $^{+}$, CD8 $^{+}$ and CD4 $^{+}$ CD8 $^{+}$ subsets (**a**); T $_{\text{reg}}$ cells (**b**) (in **a, b**, W3 $n = 5$; W4 $n = 11$; W5 $n = 15$; W12 $n = 8$); CD11c $^{+}$ MHCII $^{+}$ DCs (**c**); and CD103 $^{+}$ and CX3CR1 $^{+}$ DC subsets (**g**) (in **c, g**, $n = 10$ (W3); $n = 15$ (W4, W5, W12)). **d, m, p, q**, Mice were treated with antibiotics at weaning and thymi were compared two weeks later to age-matched control mice. **d, m**, Frequencies and counts of CD11c $^{+}$ MHCII $^{+}$ DCs (**d**) and CD103 $^{+}$ and CX3CR1 $^{+}$ DC subsets (**m**) ($n = 23$ per group). **p, q**, Frequencies of plasmacytoid DCs (pDCs) (**p**) and B cells (**q**) ($n = 15$ per group). **e, f, i–l, n, o**, Mice were colonized with SFB or *E. coli* at weaning (young) or at 12 weeks of age (adult) and thymi were compared two weeks later to age-matched control mice. **e, f**, Flow cytometry (**e**) and counts (**f**) of CD11c $^{+}$ MHCII $^{+}$ DCs. **i**, Representative flow plot of CX3CR1 $^{+}$ DCs. **j**, Frequencies and counts of CD103 $^{+}$ DCs in the thymus (in **e, f, i, j**, young: CTRL $n = 15$; SFB $n = 20$; EC $n = 12$. Adult: CTRL $n = 20$; SFB $n = 20$; EC $n = 16$). **k, l**, Frequencies of CD11c $^{+}$ MHCII $^{+}$ DCs (**k**) and CX3CR1 $^{+}$ DC subsets (**l**) in the MLNs (young: CTRL $n = 12$; SFB $n = 15$; EC $n = 10$. Adult: CTRL $n = 8$; SFB $n = 12$; EC $n = 8$). **n, o**, Frequencies of pDCs (**n**) and B cells (**o**) in the thymus ($n = 12$ per group). **h**, Mice were colonized with SFB at weaning for two weeks and were injected intravenously with

anti-CD45 before euthanasia. Flow cytometry of CD45 in thymic CX3CR1⁺ DCs and spleen ($n = 5$). Each replicate is a biologically independent sample. Data are shown as individual values and mean; P values by two-tailed unpaired t -test (**d**, **p**, **q**), one-way ANOVA with Tukey's post hoc test (**b**, **c**) or two-way ANOVA with Tukey's (**a**, **f**, **g**, **j–l**, **n**, **o**) or Sidak's (**m**) post hoc test.

[Source data](#)

[**Extended Data Fig. 5 MHCII expression on CX3CR1[±] cells is required for the thymic expansion of bacteria-specific T cells.**](#)

a–g, Wild-type and CX3-DTR mice were colonized with SFB or *E. coli* at weaning or left untreated and tissues were compared one week (qPCR) or two weeks (flow cytometry analysis) later. **a**, Flow cytometry of thymic SFB-tetramer⁺ cells (CTRL: $n = 5$; SFB: WT $n = 6$; CX3-DTR $n = 8$). **b**, **c**, 16S qPCR in the thymus (**b**; $n = 8$ (WT); $n = 9$ (CX3-DTR)); and MLNs (**c**; $n = 13$ (WT); $n = 12$ (CX3-DTR)). **d**, **e**, SFB-specific qPCR in the thymus (**d**; $n = 5$ per group) and faecal pellets (**e**; $n = 10$ (WT); $n = 5$ (CX3-DTR)). **f**, **g**, *E. coli*-specific qPCR in the thymus (**f**; WT $n = 7$; CX3-DTR $n = 12$) and faecal pellets (**g**; $n = 10$). **h**, Diphtheria-toxin-treated littermate wild-type mice and mice depleted of CD103⁺ DCs (CD103-DTR CD11c-Cre) were analysed two weeks after weaning. Flow cytometry of CD103⁺ and CX3CR1⁺ DC subsets in colon lamina propria ($n = 5$). **i**, **j**, Diphtheria-toxin-treated littermate wild-type, CX3-DTR CD11c-Cre and CD103-DTR CD11c-Cre mice were colonized with *E. coli* at weaning and thymi were compared one week later. **i**, *E. coli*-specific qPCR ($n = 8$ (WT); $n = 10$ (CX3-DTR); $n = 8$ (CD103-DTR)). **j**, 16S qPCR ($n = 24$ (WT); $n = 10$ (CX3-DTR); $n = 8$ (CD103-DTR)). **k–m**, 4-OHT-treated MHCII^{fl/+} (WT) and MHCII^{fl/-} (KO) CX3-Cre mice were colonized with SFB at weaning and thymi were compared two weeks later. **k**, Frequencies and counts of SFB-tetramer⁺ cells ($n = 10$ per group). **l**, SFB-specific qPCR ($n = 5$ per group). **m**, Frequencies of CD103⁺ and CX3CR1⁺ DC subsets ($n = 10$ per group). Each replicate is a biologically independent sample. Data are shown as individual values and mean P values by two-tailed unpaired t -test (**b–g**, **k**, **l**) or one-way ANOVA with Tukey's (**i**, **j**) or Sidak's (**m**) post hoc test.

[Source data](#)

[Extended Data Fig. 6 Intestinal CX3CR1 \$\pm\$ DCs migrate to the thymus.](#)

a, Thymic DCs were analysed at two weeks after weaning for XCR1 and SIRP α . Flow cytometry of total DCs, CX3CR1 $^+$ DCs, CD103 $^+$ DCs and pDCs ($n = 5$). **b–f**, Caeca from KikGR33 transgenic mice were exposed to 405-nm-wavelength light or left untreated at 5 (young) or 14 (adult) weeks of age and two days later the thymus, MLNs and spleen were collected. **b**, Flow cytometry of RFP $^+$ MHCII $^+$ cells in KikGR33 mice without light exposure ($n = 5$). **c**, Frequencies and counts of RFP $^+$ MHCII $^+$ cells in young mice. **d, e**, Flow cytometry (**d**) and counts (**e**) of RFP $^+$ MHCII $^+$ cells in adult mice. **f**, Flow cytometry of RFP $^+$ MHCII $^+$ cells subsets in young and adult thymi. In **c–f**, $n = 5$ (young); $n = 9$ (adult). **g–i**, Mice were analysed at weaning (young) or at 12 weeks of age (adult) and thymus chemokine gene expression or colon lamina propria DC populations were analysed. **g**, Relative expression of chemokines in the thymus ($n = 5$ (young); $n = 15$ (adult)). **h**, CCR5 $^+$ cell frequencies of CX3CR1 $^+$ DCs in the colon ($n = 10$ per group). Wild-type and CX3CR1^{GFP/GFP} (KO) mice were colonized with SFB at weaning and treated with TAK-779 or anti-CCL2 antibody and thymi were compared one week later. **i**, SFB-specific qPCR ($n = 17$ (WT); $n = 13$ (anti-CCR5 + anti-CCR2); $n = 5$ (WT anti-CCR2); $n = 10$ (KO); $n = 5$ (KO anti-CCR5 + anti-CCR2)). Each replicate is a biologically independent sample. Data are shown as individual values and mean; P values by two-tailed unpaired t -test (**g, h**) or one-way ANOVA with Fisher's LSD post hoc test (**i**).

[Source data](#)

[Extended Data Fig. 7 Bacteria-specific T cells from the thymus of young mice are functional in distal tissues.](#)

Wild-type donor mice were colonized with SFB or *E. coli* at weaning and two weeks later CD4 $^+$ T cells from the thymus were sorted and transferred to SFB- or *E. coli*-colonized *Rag2* $^{-/-}$ recipient mice. Recipient mice were

followed for four weeks and disease severity was compared to *Rag2*^{-/-} mice receiving age-matched control donor thymocytes. **a–f**, SFB ($n = 8$ (CTRL); $n = 13$ (SFB)). **a**, Colon length. **b**, Immune infiltration in colon lamina propria. **c, d**, Flow cytometry (**c**) and counts (**d**) of T_H17 cells. **e**, Representative flow plot of SFB-tetramer⁺ cells. **f**, Flow cytometry of RORyt and T-bet expression in SFB-tetramer⁺ cells. **g–i**, *E. coli* ($n = 8$ (CTRL); $n = 15$ (EC)). **g**, Colon length. **h**, Immune infiltration in colon lamina propria. **i**, Representative flow plot of T_H1 cells. Each replicate is a biologically independent sample. Data are shown as individual values and mean; P values by two-tailed unpaired *t*-test (**a, b, d, g, h**).

[Source data](#)

[**Extended Data Fig. 8 Bacteria-specific T cells from the thymus of adult mice do not increase pathology in distal tissues.**](#)

Wild-type donor mice were colonized with SFB or *E. coli* at 12 weeks of age and two weeks later CD4⁺ T cells from the thymus were sorted and transferred to SFB- or *E. coli*-colonized *Rag2*^{-/-} recipient mice. Recipient mice were followed for four weeks and disease severity was compared to *Rag2*^{-/-} mice receiving age-matched control donor thymocytes. **a–h**, SFB. **a**, Relative weight change after transfer ($n = 5$ (CTRL); $n = 7$ (SFB)). **b**, Colon length. **c, d**, Representative H&E (**c**) and colitis score (**d**). **e**, Immune infiltration in colon lamina propria. **f, g**, Frequencies and counts of T_H17 cells (**f**) and SFB-tetramer⁺ cells (**g**). **h**, Flow cytometry of RORyt and T-bet expression in SFB-tetramer⁺ cells. In **b–h**, $n = 4$ (CTRL); $n = 7$ (SFB). **i–n**, *E. coli* ($n = 7$ (CTRL); $n = 9$ (EC)). **i**, Relative weight change after transfer. **j**, Colon length. **k, l**, Representative H&E (**k**) and colitis score (**l**). **m**, Immune infiltration in colon lamina propria. **n**, Frequencies and counts of T_H1 cells. Each replicate is a biologically independent sample. Data are shown as mean \pm s.e.m., with P values by two-way ANOVA with Fisher's LSD post hoc test (**a, i**), or are shown as individual values and mean, with P values by two-tailed unpaired *t*-test (**b, d–g, j, l–n**). Scale bars, 100 μ m (**c, k**).

[Source data](#)

Extended Data Fig. 9 Requirement for antigen presentation by CX3CR1+ cells for thymic T cell pathogenicity in distal tissues.

a–d, Diphtheria-toxin-treated littermate SPF wild-type and CX3-DTR donor mice were colonized with SFB at weaning and two weeks later CD4⁺ T cells from the thymus were sorted and transferred to SFB-colonized *Rag2*^{-/-} recipient mice. Recipient mice were followed for four weeks and disease severity was assessed. **a**, Colon length ($n = 12$ (WT); $n = 13$ (CX3-DTR)). **b**, Immune infiltration in colon lamina propria. **c**, **d**, Flow cytometry (**c**) and counts (**d**) of SFB-tetramer⁺ cells. In **b–d**, $n = 8$ per group. **e–k**, 4-OHT-treated MHCII^{fl/+} (WT) and MHCII^{fl/-} (KO) CX3-Cre mice were colonized with SFB at weaning and two weeks later CD4⁺ T cells from the thymus were sorted and transferred to SFB-colonized *Rag2*^{-/-} recipient mice. Recipient mice were followed for four weeks and disease severity was assessed. **e**, Relative weight change after transfer. **f**, Colon length. **g**, **h**, Representative H&E (**g**) and colitis score (**h**). **i**, Immune infiltration in colon lamina propria. **j**, **k**, Flow cytometry (**j**) and counts (**k**) of SFB-tetramer⁺ cells. In **e–k**, $n = 8$ (WT); $n = 10$ (KO). **l–q**, SPF wild-type donor mice were treated with antibiotics at weaning and two weeks later CD4⁺ T cells from the thymus were sorted and transferred to untreated *Rag2*^{-/-} recipient mice. Recipient mice were followed for eight weeks and disease severity was compared to *Rag2*^{-/-} mice receiving age-matched control donor thymocytes. **l**, Relative weight change after transfer. **m**, Colon length. **n**, **o**, Representative H&E (**n**) and colitis score (**o**). **p**, Immune infiltration in colon lamina propria. **q**, Frequencies and counts of T_H1 cells. In **l–q**, $n = 7$ (CTRL); $n = 9$ (ABX). **r**, Wild-type mice were infected at 5 weeks of age with *S. Typhimurium*. MLNs were collected and cells restimulated with *S. Typhimurium* or *E. coli*. IFN- γ levels in culture supernatants ($n = 7$ (ST); $n = 5$ (EC)). Each replicate is a biologically independent sample. Data are shown as mean \pm s.e.m., with P values by two-way ANOVA with Fisher's LSD post hoc test (**e**, **l**), or are shown as individual values and mean, with P values by two-tailed unpaired *t*-test (**a**, **b**, **d**, **f**, **h**, **i**, **k**, **m**, **o–r**). Scale bars, 100 μ m (**g**, **n**).

[Source data](#)

Extended Data Fig. 10 Proposed model for early-life thymic expansion of microbiota-specific T cells.

At weaning we propose that CX3CR1⁺ DCs take up intestinal commensal microorganisms (1) and migrate to the thymus (2), where they present bacterial antigens to CD4⁺ T cells. This induces the expansion of bacteria-specific CD4⁺T cells (3) that are later exported to peripheral organs (4).

Supplementary information

Reporting Summary

Supplementary Table 1

Normalized gene counts of SFB-specific and non-specific CD4 SP thymocytes as determined by RNA-seq. Normalized gene counts obtained by DESeq.

Supplementary Table 2

Differential Gene Expression between SFB-specific and non-specific CD4 SP thymocytes by RNA-seq. Differential gene expression analyzed by DESeq. Two-tailed P-values generated by the Wald test were corrected for multiple testing using the Benjamini and Hochberg method.

Supplementary Table 3

KEGG Pathways identified as differentially enriched between SFB-specific and non-specific CD4 SP thymocytes. Top 200 differentially expressed genes were analyzed in DAVID v6.8 using KEGG PATHWAY as a reference database. Significantly gene-enriched terms ($p < 0.05$) are shown. One-sided P value was obtained by Fisher's exact test (EASE score).

Supplementary Table 4

Bacteria-specific T cells from the thymus are functional in distal tissues.
Experimental groups for transfer of thymic T cells to RAG-/ recipients.

Source data

[Source Data Fig. 1](#)

[Source Data Fig. 2](#)

[Source Data Fig. 3](#)

[Source Data Extended Data Fig. 1](#)

[Source Data Extended Data Fig. 2](#)

[Source Data Extended Data Fig. 3](#)

[Source Data Extended Data Fig. 4](#)

[Source Data Extended Data Fig. 5](#)

[Source Data Extended Data Fig. 6](#)

[Source Data Extended Data Fig. 7](#)

[Source Data Extended Data Fig. 8](#)

[Source Data Extended Data Fig. 9](#)

Rights and permissions

[Reprints and Permissions](#)

About this article



Check for
updates

Cite this article

Zegarra-Ruiz, D.F., Kim, D.V., Norwood, K. *et al.* Thymic development of gut-microbiota-specific T cells. *Nature* **594**, 413–417 (2021).
<https://doi.org/10.1038/s41586-021-03531-1>

[Download citation](#)

- Received: 27 January 2020
- Accepted: 12 April 2021
- Published: 12 May 2021
- Issue Date: 17 June 2021
- DOI: <https://doi.org/10.1038/s41586-021-03531-1>

Comments

By submitting a comment you agree to abide by our [Terms](#) and [Community Guidelines](#). If you find something abusive or that does not comply with our terms or guidelines please flag it as inappropriate.

[Access through your institution](#)

[Change institution](#)

[Buy or subscribe](#)

Advertisement

| [Section menu](#) | [Main menu](#) |

- Article
- [Published: 05 May 2021](#)

ARAF mutations confer resistance to the RAF inhibitor belvarafenib in melanoma

- [Ivana Yen¹ na1](#),
- [Frances Shanahan¹ na1](#),
- [Jeeyun Lee](#) [ORCID: orcid.org/0000-0002-4911-6165^{2,3} na1](#),
- [Yong Sang Hong⁴ na1](#),
- [Sang Joon Shin⁵ na1](#),
- [Amanda R. Moore](#) [ORCID: orcid.org/0000-0003-3864-6387¹](#),
- [Jawahar Sudhamsu](#) [ORCID: orcid.org/0000-0003-0737-2299^{1,6}](#),
- [Matthew T. Chang⁷](#),
- [Inhwan Bae](#) [ORCID: orcid.org/0000-0001-5390-2401⁸](#),
- [Darlene Dela Cruz⁹](#),
- [Thomas Hunsaker⁹](#),
- [Christiaan Klijn⁷](#),
- [Nicholas P. D. Liau](#) [ORCID: orcid.org/0000-0002-3887-899X⁶](#),
- [Eva Lin¹](#),
- [Scott E. Martin¹](#),
- [Zora Modrusan¹⁰](#),
- [Robert Piskol](#) [ORCID: orcid.org/0000-0001-8942-9943⁷](#),
- [Ehud Segal⁹](#),
- [Avinashnarayan Venkatanarayan¹](#),
- [Xin Ye¹](#),
- [Jianping Yin⁶](#),
- [Liangxuan Zhang¹¹](#),
- [Jin-Soo Kim¹²](#),

- [Hyeong-Seok Lim](#)¹³,
- [Kyu-Pyo Kim](#)⁴,
- [Yu Jung Kim](#)¹⁴,
- [Hye Sook Han](#)¹⁵,
- [Soo Jung Lee](#)¹⁶,
- [Seung Tae Kim](#)²,
- [Minkyu Jung](#)⁵,
- [Yoon-hee Hong](#) ORCID: orcid.org/0000-0002-8224-4396¹⁷,
- [Young Su Noh](#) ORCID: orcid.org/0000-0002-4204-2503¹⁷,
- [Munjeong Choi](#)¹⁷,
- [Oakpil Han](#)¹⁷,
- [Malgorzata Nowicka](#)¹¹,
- [Shrividhya Srinivasan](#)¹¹,
- [Yibing Yan](#)¹¹,
- [Tae Won Kim](#) ORCID: orcid.org/0000-0001-9522-1997⁴ &
- [Shiva Malek](#) ORCID: orcid.org/0000-0002-9526-7968¹

Nature volume **594**, pages 418–423 (2021) [Cite this article](#)

- 6932 Accesses
- 21 Altmetric
- [Metrics details](#)

Subjects

- [Drug discovery](#)
- [Melanoma](#)

Abstract

Although RAF monomer inhibitors (type I.5, BRAF(V600)) are clinically approved for the treatment of *BRAF^{V600}*-mutant melanoma, they are ineffective in non-*BRAF^{V600}* mutant cells^{1,2,3}. Belvarafenib is a potent and

selective RAF dimer (type II) inhibitor that exhibits clinical activity in patients with *BRAF^{V600E}*- and *NRAS*-mutant melanomas. Here we report the first-in-human phase I study investigating the maximum tolerated dose, and assessing the safety and preliminary efficacy of belvarafenib in *BRAF^{V600E}*- and *RAS*-mutated advanced solid tumours (NCT02405065, NCT03118817). By generating belvarafenib-resistant *NRAS*-mutant melanoma cells and analysing circulating tumour DNA from patients treated with belvarafenib, we identified new recurrent mutations in *ARAF* within the kinase domain. *ARAF* mutants conferred resistance to belvarafenib in both a dimer- and a kinase activity-dependent manner. Belvarafenib induced *ARAF* mutant dimers, and dimers containing mutant *ARAF* were active in the presence of inhibitor. *ARAF* mutations may serve as a general resistance mechanism for RAF dimer inhibitors as the mutants exhibit reduced sensitivity to a panel of type II RAF inhibitors. The combination of RAF plus MEK inhibition may be used to delay *ARAF*-driven resistance and suggests a rational combination for clinical use. Together, our findings reveal specific and compensatory functions for the *ARAF* isoform and implicate *ARAF* mutations as a driver of resistance to RAF dimer inhibitors.

Access options

Subscribe to Journal

Get full journal access for 1 year

\$199.00

only \$3.90 per issue

[Subscribe](#)

All prices are NET prices.

VAT will be added later in the checkout.

Tax calculation will be finalised during checkout.

Rent or Buy article

Get time limited or full article access on ReadCube.

from \$8.99

[Rent or Buy](#)

All prices are NET prices.

Additional access options:

- [Log in](#)
- [Access through your institution](#)
- [Learn about institutional subscriptions](#)

Fig. 1: Belvarafenib is a potent RAF dimer inhibitor.

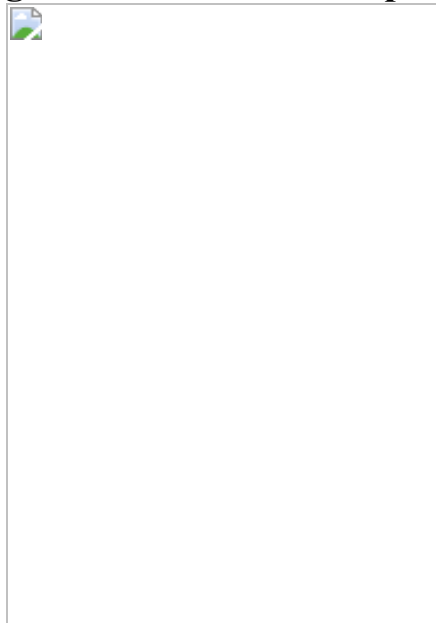


Fig. 2: Generation of belvarafenib-resistant cell lines results in ARAF mutations.

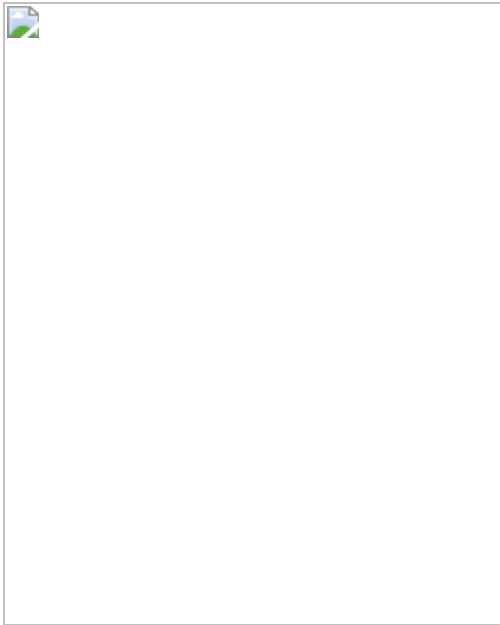


Fig. 3: ARAF mutations confer belvarafenib resistance in a kinase- and dimer-dependent manner.

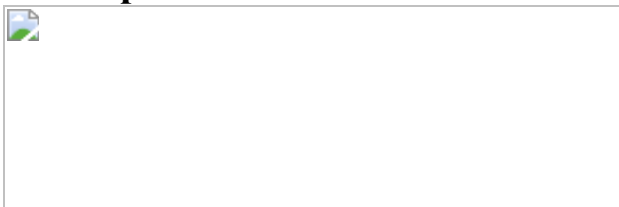
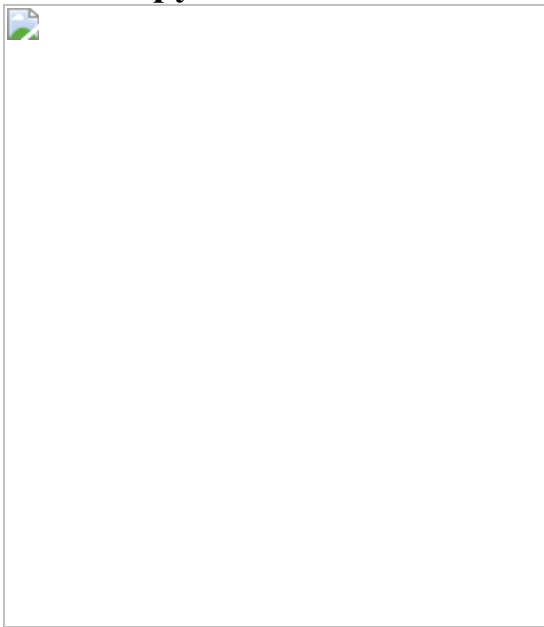


Fig. 4: Clinical data confirm belvarafenib activity in *BRAF^{V600E}*- and *NRAS*-mutant melanoma and the mechanism of resistance to monotherapy.



Data availability

The coordinates of the BRAF^{KD}–belvarafenib complex have been deposited in the Protein Data Bank (PDB) with accession code [6XFP](#). Raw data from exome sequencing were deposited in the European Genome-phenome Archive (EGA) hosted by EBI, with accession number EGAS00001005086. An overview of the clinical protocol (also found at <https://clinicaltrials.gov/>) and details of patient demographics, subject information and dose information are included in the Supplementary Information. Information on the full kinase selectivity data, cell line profiling IC₅₀ values, raw gels for all western blot figures, and all mouse experiments have been provided. [Source data](#) are provided with this paper.

References

1. 1.

Hatzivassiliou, G. et al. RAF inhibitors prime wild-type RAF to activate the MAPK pathway and enhance growth. *Nature* **464**, 431–435 (2010).

[ADS](#) [CAS](#) [PubMed](#) [Google Scholar](#)

2. 2.

Poulikakos, P. I., Zhang, C., Bollag, G., Shokat, K. M. & Rosen, N. RAF inhibitors transactivate RAF dimers and ERK signalling in cells with wild-type BRAF. *Nature* **464**, 427–430 (2010).

[ADS](#) [CAS](#) [PubMed](#) [PubMed Central](#) [Google Scholar](#)

3. 3.

Peng, S. B. et al. Inhibition of RAF isoforms and active dimers by LY3009120 leads to anti-tumor activities in RAS or BRAF mutant cancers. *Cancer Cell* **28**, 384–398 (2015).

[CAS](#) [PubMed](#) [Google Scholar](#)

4. 4.

Solit, D. B. et al. BRAF mutation predicts sensitivity to MEK inhibition. *Nature* **439**, 358–362 (2006).

[ADS](#) [CAS](#) [PubMed](#) [Google Scholar](#)

5. 5.

Poulikakos, P. I. & Rosen, N. Mutant BRAF melanomas—dependence and resistance. *Cancer Cell* **19**, 11–15 (2011).

[CAS](#) [PubMed](#) [Google Scholar](#)

6. 6.

Heidorn, S. J. et al. Kinase-dead BRAF and oncogenic RAS cooperate to drive tumor progression through CRAF. *Cell* **140**, 209–221 (2010).

[CAS](#) [PubMed](#) [PubMed Central](#) [Google Scholar](#)

7. 7.

Davies, H. et al. Mutations of the BRAF gene in human cancer. *Nature* **417**, 949–954 (2002).

[ADS](#) [CAS](#) [PubMed](#) [PubMed Central](#) [Google Scholar](#)

8. 8.

Sekulic, A. et al. Malignant melanoma in the 21st century: the emerging molecular landscape. *Mayo Clin. Proc.* **83**, 825–846 (2008).

[CAS](#) [PubMed](#) [PubMed Central](#) [Google Scholar](#)

9. 9.

Dorard, C. et al. RAF proteins exert both specific and compensatory functions during tumour progression of NRAS-driven melanoma. *Nat. Commun.* **8**, 15262 (2017).

[ADS](#) [CAS](#) [PubMed](#) [PubMed Central](#) [Google Scholar](#)

10. 10.

Moore, A. R., Rosenberg, S. C., McCormick, F. & Malek, S. RAS-targeted therapies: is the undruggable drugged? *Nat. Rev. Drug Discov.* **19**, 533–552 (2020).

[CAS](#) [PubMed](#) [PubMed Central](#) [Google Scholar](#)

11. 11.

Wang, T. et al. Gene essentiality profiling reveals gene networks and synthetic lethal interactions with oncogenic Ras. *Cell* **168**, 890–903 (2017).

[CAS](#) [PubMed](#) [PubMed Central](#) [Google Scholar](#)

12. 12.

Marais, R., Light, Y., Paterson, H. F., Mason, C. S. & Marshall, C. J. Differential regulation of Raf-1, A-Raf, and B-Raf by oncogenic ras and tyrosine kinases. *J. Biol. Chem.* **272**, 4378–4383 (1997).

[CAS](#) [PubMed](#) [Google Scholar](#)

13. 13.

Fransén, K. et al. Mutation analysis of the BRAF, ARAF and RAF-1 genes in human colorectal adenocarcinomas. *Carcinogenesis* **25**, 527–533 (2004).

[PubMed](#) [Google Scholar](#)

14. 14.

Lee, J. W. et al. Mutational analysis of the *ARAF* gene in human cancers. *APMIS* **113**, 54–57 (2005).

[ADS](#) [CAS](#) [PubMed](#) [Google Scholar](#)

15. 15.

Nelson, D. S. et al. Somatic activating ARAF mutations in Langerhans cell histiocytosis. *Blood* **123**, 3152–3155 (2014).

[CAS](#) [PubMed](#) [Google Scholar](#)

16. 16.

Emuss, V., Garnett, M., Mason, C. & Marais, R. Mutations of C-RAF are rare in human cancer because C-RAF has a low basal kinase activity compared with B-RAF. *Cancer Res.* **65**, 9719–9726 (2005).

[CAS](#) [PubMed](#) [Google Scholar](#)

17. 17.

Blasco, R. B. et al. c-Raf, but not B-Raf, is essential for development of K-Ras oncogene-driven non-small cell lung carcinoma. *Cancer Cell* **19**, 652–663 (2011).

[CAS](#) [PubMed](#) [PubMed Central](#) [Google Scholar](#)

18. 18.

Karreth, F. A., DeNicola, G. M., Winter, S. P. & Tuveson, D. A. C-Raf inhibits MAPK activation and transformation by B-Raf(V600E). *Mol. Cell* **36**, 477–486 (2009).

[CAS](#) [PubMed](#) [Google Scholar](#)

19. 19.

Rebocho, A. P. & Marais, R. ARAF acts as a scaffold to stabilize BRAF:CRAF heterodimers. *Oncogene* **32**, 3207–3212 (2013).

[CAS](#) [PubMed](#) [Google Scholar](#)

20. 20.

Chapman, P. B. et al. Improved survival with vemurafenib in melanoma with BRAF V600E mutation. *N. Engl. J. Med.* **364**, 2507–2516 (2011).

[CAS](#) [PubMed](#) [PubMed Central](#) [Google Scholar](#)

21. 21.

Ramurthy, S. et al. Design and discovery of *N*-(3-(2-(2-Hydroxyethoxy)-6-morpholinopyridin-4-yl)-4-methylphenyl)-2-(trifluoromethyl)isonicotinamide, a selective, efficacious, and well-tolerated RAF inhibitor targeting RAS mutant cancers: the path to the clinic. *J. Med. Chem.* **63**, 2013–2027 (2020).

[CAS](#) [PubMed](#) [Google Scholar](#)

22. 22.

Sun, Y. et al. A brain-penetrant RAF dimer antagonist for the noncanonical BRAF oncoprotein of pediatric low-grade astrocytomas. *Neuro-Oncol.* **19**, 774–785 (2017).

[CAS](#) [PubMed](#) [PubMed Central](#) [Google Scholar](#)

23. 23.

Tang, Z. et al. BGB-283, a novel RAF kinase and EGFR inhibitor, displays potent antitumor activity in BRAF-mutated colorectal cancers. *Mol. Cancer Ther.* **14**, 2187–2197 (2015).

[CAS](#) [PubMed](#) [Google Scholar](#)

24. 24.

Yuan, X. et al. RAF dimer inhibition enhances the antitumor activity of MEK inhibitors in K-RAS mutant tumors. *Mol. Oncol.* **14**, 1833–1849 (2020).

[CAS](#) [PubMed](#) [PubMed Central](#) [Google Scholar](#)

25. 25.

Desai, J. et al. Phase I, open-label, dose-escalation/dose-expansion study of Lifirafenib (BGB-283), an RAF family kinase inhibitor, in patients with solid tumors. *J. Clin. Oncol.* **38**, 2140–2150 (2020).

[CAS](#) [PubMed](#) [PubMed Central](#) [Google Scholar](#)

26. 26.

Poulikakos, P. I. et al. RAF inhibitor resistance is mediated by dimerization of aberrantly spliced BRAF(V600E). *Nature* **480**, 387–390 (2011).

[ADS](#) [CAS](#) [PubMed](#) [PubMed Central](#) [Google Scholar](#)

27. 27.

Yaeger, R. et al. Mechanisms of acquired resistance to BRAF V600E inhibition in colon cancers converge on RAF dimerization and are sensitive to its inhibition. *Cancer Res.* **77**, 6513–6523 (2017).

[CAS](#) [PubMed](#) [PubMed Central](#) [Google Scholar](#)

28. 28.

Corcoran, R. B. et al. EGFR-mediated re-activation of MAPK signaling contributes to insensitivity of BRAF mutant colorectal cancers to RAF inhibition with vemurafenib. *Cancer Discov.* **2**, 227–235 (2012).

[CAS](#) [PubMed](#) [PubMed Central](#) [Google Scholar](#)

29. 29.

Prahallad, A. et al. Unresponsiveness of colon cancer to BRAF(V600E) inhibition through feedback activation of EGFR. *Nature* **483**, 100–103 (2012).

[ADS](#) [CAS](#) [PubMed](#) [Google Scholar](#)

30. 30.

Montagut, C. et al. Elevated CRAF as a potential mechanism of acquired resistance to BRAF inhibition in melanoma. *Cancer Res.* **68**, 4853–4861 (2008).

[CAS](#) [PubMed](#) [PubMed Central](#) [Google Scholar](#)

31. 31.

Martinez Molina, D. et al. Monitoring drug target engagement in cells and tissues using the cellular thermal shift assay. *Science* **341**, 84–87 (2013).

[ADS](#) [PubMed](#) [Google Scholar](#)

32. 32.

Zhao, Z. et al. Exploration of type II binding mode: A privileged approach for kinase inhibitor focused drug discovery? *ACS Chem. Biol.* **9**, 1230–1241 (2014).

[CAS](#) [PubMed](#) [PubMed Central](#) [Google Scholar](#)

33. 33.

Treiber, D. K. & Shah, N. P. Ins and outs of kinase DFG motifs. *Chem. Biol.* **20**, 745–746 (2013).

[CAS](#) [PubMed](#) [Google Scholar](#)

34. 34.

Waterhouse, A. et al. SWISS-MODEL: homology modelling of protein structures and complexes. *Nucleic Acids Res.* **46**, W296–W303 (2018).

[CAS](#) [PubMed](#) [PubMed Central](#) [Google Scholar](#)

35. 35.

Ascierto, P. A. et al. Cobimetinib combined with vemurafenib in advanced BRAF(V600)-mutant melanoma (coBRIM): updated efficacy results from a randomised, double-blind, phase 3 trial. *Lancet Oncol.* **17**, 1248–1260 (2016).

[CAS](#) [PubMed](#) [Google Scholar](#)

36. 36.

Dummer, R. et al. Encorafenib plus binimatinib versus vemurafenib or encorafenib in patients with BRAF-mutant melanoma (COLUMBUS): a multicentre, open-label, randomised phase 3 trial. *Lancet Oncol.* **19**, 603–615 (2018).

[CAS](#) [PubMed](#) [Google Scholar](#)

37. 37.

Long, G. V. et al. Dabrafenib and trametinib versus dabrafenib and placebo for Val600 BRAF-mutant melanoma: a multicentre, double-blind, phase 3 randomised controlled trial. *Lancet* **386**, 444–451 (2015).

[CAS](#) [PubMed](#) [Google Scholar](#)

38. 38.

Kim, T. W. et al. Belvarafenib, a novel pan-RAF inhibitor, in solid tumor patients harboring BRAF, KRAS, or NRAS mutations: Phase I study. *J. Clin. Oncol.* **37**, 3000–3000 (2019).

[Google Scholar](#)

39. 39.

Van Allen, E. M. et al. The genetic landscape of clinical resistance to RAF inhibition in metastatic melanoma. *Cancer Discov.* **4**, 94–109 (2014).

[PubMed](#) [Google Scholar](#)

40. 40.

Bean, J. et al. MET amplification occurs with or without T790M mutations in EGFR mutant lung tumors with acquired resistance to gefitinib or erlotinib. *Proc. Natl Acad. Sci. USA* **104**, 20932–20937 (2007).

[ADS](#) [CAS](#) [PubMed](#) [Google Scholar](#)

41. 41.

Engelman, J. A. et al. MET amplification leads to gefitinib resistance in lung cancer by activating ERBB3 signaling. *Science* **316**, 1039–1043 (2007).

[ADS](#) [CAS](#) [PubMed](#) [Google Scholar](#)

42. 42.

Villanueva, J. et al. Acquired resistance to BRAF inhibitors mediated by a RAF kinase switch in melanoma can be overcome by cotargeting MEK and IGF-1R/PI3K. *Cancer Cell* **18**, 683–695 (2010).

[CAS](#) [PubMed](#) [PubMed Central](#) [Google Scholar](#)

43. 43.

Johannessen, C. M. et al. COT drives resistance to RAF inhibition through MAP kinase pathway reactivation. *Nature* **468**, 968–972 (2010).

[ADS](#) [CAS](#) [PubMed](#) [PubMed Central](#) [Google Scholar](#)

44. 44.

Sharma, S. V. et al. A chromatin-mediated reversible drug-tolerant state in cancer cell subpopulations. *Cell* **141**, 69–80 (2010).

[CAS](#) [PubMed](#) [PubMed Central](#) [Google Scholar](#)

45. 45.

Hata, A. N. et al. Tumor cells can follow distinct evolutionary paths to become resistant to epidermal growth factor receptor inhibition. *Nat. Med.* **22**, 262–269 (2016).

[CAS](#) [PubMed](#) [PubMed Central](#) [Google Scholar](#)

46. 46.

Monaco, K. A. et al. LXH254, a potent and selective ARAF-sparing inhibitor of BRAF and CRAF for the treatment of MAPK-driven tumors. *Clin. Cancer Res.* (2020).

47. 47.

Bhang, H. E. et al. Studying clonal dynamics in response to cancer therapy using high-complexity barcoding. *Nat. Med.* **21**, 440–448 (2015).

[CAS](#) [PubMed](#) [Google Scholar](#)

48. 48.

Meerbrey, K. L. et al. The pINDUCER lentiviral toolkit for inducible RNA interference in vitro and in vivo. *Proc. Natl Acad. Sci. USA* **108**, 3665–3670 (2011).

[ADS](#) [CAS](#) [PubMed](#) [Google Scholar](#)

49. 49.

Fellmann, C. et al. An optimized microRNA backbone for effective single-copy RNAi. *Cell Rep.* **5**, 1704–1713 (2013).

[CAS](#) [PubMed](#) [Google Scholar](#)

50. 50.

Haling, J. R. et al. Structure of the BRAF–MEK complex reveals a kinase activity independent role for BRAF in MAPK signaling. *Cancer Cell* **26**, 402–413 (2014).

[CAS](#) [PubMed](#) [Google Scholar](#)

51. 51.

Liau, N. P. D. et al. Negative regulation of RAF kinase activity by ATP is overcome by 14-3-3-induced dimerization. *Nat. Struct. Mol. Biol.* **27**, 134–141 (2020).

[CAS](#) [PubMed](#) [Google Scholar](#)

52. 52.

McCoy, A. J. et al. Phaser crystallographic software. *J. Appl. Crystallogr.* **40**, 658–674 (2007).

[CAS](#) [PubMed](#) [PubMed Central](#) [Google Scholar](#)

53. 53.

Emsley, P., Lohkamp, B., Scott, W. G. & Cowtan, K. Features and development of Coot. *Acta Crystallogr. D* **66**, 486–501 (2010).

[CAS](#) [PubMed](#) [Google Scholar](#)

54. 54.

Adams, P. D. et al. PHENIX: a comprehensive Python-based system for macromolecular structure solution. *Acta Crystallogr. D* **66**, 213–221 (2010).

[CAS](#) [PubMed](#) [Google Scholar](#)

55. 55.

Bueno, R. et al. Comprehensive genomic analysis of malignant pleural mesothelioma identifies recurrent mutations, gene fusions and splicing alterations. *Nat. Genet.* **48**, 407–416 (2016).

[CAS](#) [PubMed](#) [Google Scholar](#)

56. 56.

Eisenhauer, E. A. et al. New response evaluation criteria in solid tumours: revised RECIST guideline (version 1.1). *Eur. J. Cancer* **45**, 228–247 (2009).

[CAS](#) [PubMed](#) [PubMed Central](#) [Google Scholar](#)

57. 57.

US Food & Drug Administration. *S9 Nonclinical Evaluation for Anticancer Pharmaceuticals* <https://www.fda.gov/regulatory-information/search-fda-guidance-documents/s9-nonclinical-evaluation-anticancer-pharmaceuticals> (2010).

58. 58.

Clark, T. A. et al. Analytical validation of a hybrid capture-based next-generation sequencing clinical assay for genomic profiling of cell-free circulating tumor DNA. *J. Mol. Diagn.* **20**, 686–702 (2018).

[CAS](#) [PubMed](#) [PubMed Central](#) [Google Scholar](#)

[Download references](#)

Acknowledgements

We thank patients, their families, and investigators for participation in this trial. We also thank members of the Hanmi and Genentech clinical study teams. We are grateful to S. A. Foster and S. Gendreau for discussions and critical reading of the manuscript, and B. N. Park at NALA CnT and J. S. Lim at the Clinical Research Center of Asan Medical Center for medical writing assistance. We thank the BioMolecular Resources (BMR) group at Genentech for construct generation. We thank the Next Generation Sequencing (NGS) group at Genentech for support with exome sequencing. We thank the gCell and Genentech Cell Screening Initiative (gCSI) groups at Genentech for cell line validation and screening.

Author information

Author notes

1. These authors contributed equally: Ivana Yen, Frances Shanahan, Jeeyun Lee, Yong Sang Hong, Sang Joon Shin

Affiliations

1. Department of Discovery Oncology, Genentech Inc., South San Francisco, CA, USA

Ivana Yen, Frances Shanahan, Amanda R. Moore, Jawahar Sudhamsu, Eva Lin, Scott E. Martin, Avinashnarayan Venkatanarayan, Xin Ye & Shiva Malek

2. Division of Hematology-Oncology, Samsung Medical Center,
Sungkyunkwan University School of Medicine, Seoul, South Korea

Jeeyun Lee & Seung Tae Kim

3. Department of Intelligence Precision Healthcare Convergence,
Samsung Medical Center, Sungkyunkwan University School of
Medicine, Suwon, South Korea

Jeeyun Lee

4. Department of Oncology, Asan Medical Center, University of Ulsan
College of Medicine, Seoul, South Korea

Yong Sang Hong, Kyu-Pyo Kim & Tae Won Kim

5. Division of Medical Oncology, Department of Internal Medicine,
Yonsei University College of Medicine, Seoul, South Korea

Sang Joon Shin & Minkyu Jung

6. Department of Structural Biology, Genentech Inc., South San
Francisco, CA, USA

Jawahar Sudhamasu, Nicholas P. D. Liau & Jianping Yin

7. Department of Bioinformatics, Genentech Inc., South San Francisco,
CA, USA

Matthew T. Chang, Christiaan Klijn & Robert Piskol

8. Department of New Chemical Entity Discovery, Hanmi Research
Center, Hanmi Pharmaceutical Co., Ltd., Seoul, South Korea

Inhwan Bae

9. Department of Translational Oncology, Genentech Inc., South San
Francisco, CA, USA

Darlene Dela Cruz, Thomas Hunsaker & Ehud Segal

10. Department of Microchemistry, Proteomics and Lipidomics,
Genentech Inc., South San Francisco, CA, USA

Zora Modrusan

11. Department of Oncology Biomarker Development, Genentech Inc.,
South San Francisco, CA, USA

Liangxuan Zhang, Małgorzata Nowicka, Shrividhya
Srinivasan & Yibing Yan

12. Department of Internal Medicine, Seoul National University Boramae
Medical Center, Seoul, South Korea

Jin-Soo Kim

13. Department of Clinical Pharmacology and Therapeutics, Asan Medical
Center, University of Ulsan College of Medicine, Seoul, South Korea

Hyeong-Seok Lim

14. Division of Hematology and Medical Oncology, Department of
Internal Medicine, Seoul National University Bundang Hospital, Seoul
National University College of Medicine, Seongnam, South Korea

Yu Jung Kim

15. Department of Internal Medicine, Chungbuk National University
Hospital, Chungbuk National University College of Medicine,
Cheongju, South Korea

Hye Sook Han

16. Department of Oncology/Hematology, Kyungpook National
University Chilgok Hospital, Kyungpook National University, Daegu,
South Korea

Soo Jung Lee

17. Department of Clinical Research and Development, Hanmi Pharmaceutical Co., Ltd., Seoul, South Korea

Yoon-hee Hong, Young Su Noh, Munjeong Choi & Oakpil Han

Authors

1. Ivana Yen

[View author publications](#)

You can also search for this author in [PubMed](#) [Google Scholar](#)

2. Frances Shanahan

[View author publications](#)

You can also search for this author in [PubMed](#) [Google Scholar](#)

3. Jeeyun Lee

[View author publications](#)

You can also search for this author in [PubMed](#) [Google Scholar](#)

4. Yong Sang Hong

[View author publications](#)

You can also search for this author in [PubMed](#) [Google Scholar](#)

5. Sang Joon Shin

[View author publications](#)

You can also search for this author in [PubMed](#) [Google Scholar](#)

6. Amanda R. Moore

[View author publications](#)

You can also search for this author in [PubMed](#) [Google Scholar](#)

7. Jawahar Sudhamsu

[View author publications](#)

You can also search for this author in [PubMed](#) [Google Scholar](#)

8. Matthew T. Chang

[View author publications](#)

You can also search for this author in [PubMed](#) [Google Scholar](#)

9. Inhwan Bae

[View author publications](#)

You can also search for this author in [PubMed](#) [Google Scholar](#)

10. Darlene Dela Cruz

[View author publications](#)

You can also search for this author in [PubMed](#) [Google Scholar](#)

11. Thomas Hunsaker

[View author publications](#)

You can also search for this author in [PubMed](#) [Google Scholar](#)

12. Christiaan Klijn

[View author publications](#)

You can also search for this author in [PubMed](#) [Google Scholar](#)

13. Nicholas P. D. Liau

[View author publications](#)

You can also search for this author in [PubMed](#) [Google Scholar](#)

14. Eva Lin

[View author publications](#)

You can also search for this author in [PubMed](#) [Google Scholar](#)

15. Scott E. Martin

[View author publications](#)

You can also search for this author in [PubMed](#) [Google Scholar](#)

16. Zora Modrusan

[View author publications](#)

You can also search for this author in [PubMed](#) [Google Scholar](#)

17. Robert Piskol

[View author publications](#)

You can also search for this author in [PubMed](#) [Google Scholar](#)

18. Ehud Segal

[View author publications](#)

You can also search for this author in [PubMed](#) [Google Scholar](#)

19. Avinashnarayan Venkatanarayan

[View author publications](#)

You can also search for this author in [PubMed](#) [Google Scholar](#)

20. Xin Ye

[View author publications](#)

You can also search for this author in [PubMed](#) [Google Scholar](#)

21. Jianping Yin

[View author publications](#)

You can also search for this author in [PubMed](#) [Google Scholar](#)

22. Liangxuan Zhang

[View author publications](#)

You can also search for this author in [PubMed](#) [Google Scholar](#)

23. Jin-Soo Kim

[View author publications](#)

You can also search for this author in [PubMed](#) [Google Scholar](#)

24. Hyeong-Seok Lim

[View author publications](#)

You can also search for this author in [PubMed](#) [Google Scholar](#)

25. Kyu-Pyo Kim

[View author publications](#)

You can also search for this author in [PubMed](#) [Google Scholar](#)

26. Yu Jung Kim

[View author publications](#)

You can also search for this author in [PubMed](#) [Google Scholar](#)

27. Hye Sook Han

[View author publications](#)

You can also search for this author in [PubMed](#) [Google Scholar](#)

28. Soo Jung Lee

[View author publications](#)

You can also search for this author in [PubMed](#) [Google Scholar](#)

29. Seung Tae Kim

[View author publications](#)

You can also search for this author in [PubMed](#) [Google Scholar](#)

30. Minkyu Jung

[View author publications](#)

You can also search for this author in [PubMed](#) [Google Scholar](#)

31. Yoon-hee Hong

[View author publications](#)

You can also search for this author in [PubMed](#) [Google Scholar](#)

32. Young Su Noh

[View author publications](#)

You can also search for this author in [PubMed](#) [Google Scholar](#)

33. Munjeong Choi

[View author publications](#)

You can also search for this author in [PubMed](#) [Google Scholar](#)

34. Oakpil Han

[View author publications](#)

You can also search for this author in [PubMed](#) [Google Scholar](#)

35. Małgorzata Nowicka

[View author publications](#)

You can also search for this author in [PubMed](#) [Google Scholar](#)

36. Shrividhya Srinivasan

[View author publications](#)

You can also search for this author in [PubMed](#) [Google Scholar](#)

37. Yibing Yan

[View author publications](#)

You can also search for this author in [PubMed](#) [Google Scholar](#)

38. Tae Won Kim

[View author publications](#)

You can also search for this author in [PubMed](#) [Google Scholar](#)

39. Shiva Malek

[View author publications](#)

You can also search for this author in [PubMed](#) [Google Scholar](#)

Contributions

S.M. conceived the project, and T.W.K. coordinated the clinical trial. I.Y. and F.S. led the project, designed experiments, and interpreted the results. J.L., Y.S.H., S.J.S. and T.W.K. were the lead clinical investigators on the study, collected plasma samples from patients for ctDNA analysis, and reviewed and interpreted the clinical computerized axial tomography scans. S.M. and I.Y. wrote the manuscript. A.R.M., F.S., J.L. and T.W.K. provided revisions of the manuscript. F.S., I.Y., A.R.M., A.V., N.P.D.L., Y.S.N., Y.-H.H., I.B., E.L., J.Y., X.Y., E.S., D.D.C., T.H., S.E.M. and J.S. established the experimental systems, performed laboratory experiments, and analysed the results. J.Y. and J.S. conducted the structural studies, and J.S. conducted the structural analysis. Z.M., C.K., M.T.C. and R.P. acquired and analysed the in vitro sequencing data. C.K., M.T.C. and R.P. conducted the bioinformatics analyses. J.-S.K., K.-P.K., Y.J.K., H.S.H., S.J.L., S.T.K. and M.J. were clinical investigators on the study. Y.-H.H., Y.S.N., M.C. and O.H. established the trial design, analysed the clinical data, and interpreted the results. H.-S.L., M.N. and S.S. analysed the clinical pharmacokinetic data and interpreted the results. L.Z. and Y.Y. analysed the ctDNA data.

Corresponding authors

Correspondence to [Tae Won Kim](#) or [Shiva Malek](#).

Ethics declarations

Competing interests

Hanmi Pharmaceutical Co., Ltd. funded the clinical study and assisted in preparation of the manuscript. S.M., I.Y. and Y.Y. are employees and stockholders of Genentech/Roche, and inventors of the patent application

on belvarafenib. F.S., A.R.M., A.V., C.K., J.Y., N.P.D.L., E.L., L.Z., X.Y., E.S., D.D.C., T.H., Z.M., S.E.M., J.S., M.T.C., R.P., M.N. and S.S. are employees and stockholders of Genentech/Roche. T.W.K. is an inventor of the patent application on belvarafenib and received research funding from Sanofi-Aventis. J.L. is a consultant for Oncologie and Seattle Genetics and received research funding from AstraZeneca, Merck Sharp & Dohme, and Lilly. J.-S.K. is a stockholder of Dae Hwa Pharmaceutical and a consultant for Lilly and CJ Healthcare, provided expert testimony for CJ Healthcare, received honoraria from Merck, CJ Healthcare, Lilly, Boehringer Ingelheim, AstraZeneca, and Dae Hwa Pharmaceutical, and received research funding from AstraZeneca, Boehringer Ingelheim, Sanofi, Lilly, CJ Healthcare, Hanmi Pharmaceutical, Chong Kun Dang Pharmaceutical, Ono Pharmaceutical, Pfizer, Novotech, Astellas Pharma, Merck, Aslan Pharmaceuticals, Alphabiopharma, Yuhan, MSD, and Il-Yang Pharmiceutical. Y.-H.H. and Y.S.N. are employees of Hanmi Pharmaceutical and inventors of the patent application on belvarafenib. M.C. and O.H. are employees of Hanmi Pharmaceutical. The remaining authors have no conflicts of interest to disclose.

Additional information

Peer review information *Nature* thanks Rene Bernards, Helen Rizos and Frank Sicheri for their contribution to the peer review of this work.

Extended data figures and tables

[Extended Data Fig. 1 Belvarafenib effectively inhibits NRAS-mutant melanoma cells.](#)

a, Cell lysate treated with 10 µM belvarafenib or DMSO for 1 h before performing thermal-shift CETSA assay. **b**, Inhibition of pMEK by belvarafenib after treatment for 24 h in A549 cells engineered to express a single RAF isoform. Ratio of phosphorylated and total MEK plotted after treatment. Data are mean ± s.e.m., $n = 2$ replicates. **c**, Representation of RAF inhibitor binding for vemurafenib (left) or belvarafenib (right). **d, e**, Inhibition of pMEK by belvarafenib or vemurafenib after 24 h in Hec-1-A

$\text{BRAF}^{\text{null}}$ cells transiently transfected with BRAF(V600E) or BRAF(V600E/E568K). Ratio of phosphorylated and total MEK plotted. Data are mean \pm s.e.m., $n = 2$ replicates. **f–h**, MAPK signalling in SK-MEL-28 (**f**), SK-MEL-2 (**g**), or human melanocytes, HEMn-LP (**h**) after treatment with serial titration of vemurafenib or belvarafenib for 24 h. **i**, Sensitivity of melanoma cell lines to vemurafenib or belvarafenib. In vitro IC₅₀ screening data for a panel of 25 melanoma cell lines. **j**, Cell viability of a panel of melanoma cell lines treated with belvarafenib (left) or cobimetinib (right) for 3 days. Data are mean \pm s.e.m., $n = 2$ replicates. **k**, Clonogenic assay of panel of *BRAF^{V600E}*, *NRAS*, and *BRAF* non-canonical mutant melanoma cells treated with vemurafenib or belvarafenib. Cells were cultured for 8 days then stained with crystal violet. **l**, Cell viability of Ba/F3 cells expressing *RAS*-mutations treated with belvarafenib (left) or vemurafenib (right) for 3 days. Data are mean \pm s.e.m., $n = 6$ replicates. **m**, Confirmation of RAS overexpression in Ba/F3 cells by western blot. Tubulin was stained on a separate gel as a sample processing control. **n**, Mice with established A431 tumours treated with vemurafenib, dabrafenib or belvarafenib. Data are mean \pm s.e.m., $n = 6$ mice per group. * $P = 0.0374$ (Belva 30 versus vehicle), ** $P = 0.0003$ (Belva versus vem), one-way ANOVA, followed by Dunnett's multiple-comparisons test.

[Source data](#)

[Extended Data Fig. 2 ARAF p.G387 mutations confer mutational specific belvarafenib resistance.](#)

a, Cellular viability of IPC-298 belvarafenib-resistant clones (round 2) treated with belvarafenib for 3 days. Data are mean \pm s.e.m., $n = 3$ replicates. **b**, Clonogenic assay of IPC-298 parental, BRC9 and BRC9-WO cells treated with increasing concentrations of belvarafenib. Cells were cultured for 8 days then stained with crystal violet. **c**, Cell growth in IPC-298 parental or BRC9 cells treated with DMSO or 10 μM belvarafenib. **d**, MAPK signalling in parental, BRC9 or BRC9-WO cells after 24 h treatment with 10 μM belvarafenib. **e**, Relative ARAF expression in BRC cells compared to parental IPC-298 cells. Data are mean \pm s.e.m. ($\Delta\Delta C_t$), $n = 4$ replicates. *** $P < 0.0001$, one-way ANOVA, followed by Dunnett's

multiple-comparisons test. **f**, Cellular viability of BRC or parental cells treated with vemurafenib for 3 days, $n = 5$ BRCs. Data are mean \pm s.e.m., $n = 3$ replicates. **g**, IGV view of exome sequencing reads from BRCs around *ARAF* p.Gly387 (c.1168G>C or c.1169G>A). Wild-type G in orange, mutant C allele in blue, mutant A allele in green. **h**, Allelic frequency of *ARAF* p.G387 in a panel of BRCs and BRC9-WO. **i**, IGV view of exome sequencing reads from IPC-298 parental, BRC9 and BRC9-WO cells around *ARAF* p.Gly387 (c.1169G>A). **j**, Clonality of belvarafenib-resistant cells assessed by high-complexity genomic barcoding using Collecta CloneTracker 50M library. **k**, Sanger sequencing reads of *ARAF* p.Gly387 of BRC1-1 and BRC6-3. **l**, Cellular viability of IPC-298 belvarafenib-resistant clones (Collecta CloneTracker) treated with belvarafenib for 3 days. Data are mean \pm s.e.m., $n = 3$ replicates. **m**, **n**, Deep sequencing nucleotide reads of *ARAF* p.Gly387 in BRC9, IPC-298 parental, and MelJuso. **o**, Cellular growth of IPC-298 or BRC9 doxycycline-inducible shRNA knockdown cells against *ARAF*, *BRAF* or *CRAF* for 128 h in the presence of doxycycline treated with DMSO. **p**, MAPK signalling and RAF protein levels after shRNA knockdown in the presence of doxycycline for 24 h (pre-seeding levels for **o**, **q**). **q**, Cellular growth of doxycycline-inducible IPC-298 or BRC9 cells after shRNA knockdown of *ARAF*, *BRAF* or *CRAF* for 128 h in the presence of doxycycline treated 10 μ M belvarafenib. **r**, MAPK signalling and RAF protein levels in doxycycline-inducible IPC-298 or BRC9 cells after shRNA knockdown of *ARAF* and treatment with serial titrations of belvarafenib for 24 h in the presence of doxycycline. **s**, *ARAF* protein levels after shRNA knockdown, as shown in Fig. 2e.

Extended Data Fig. 3 Corresponding glycine substitutions in BRAF and CRAF confer belvarafenib resistance.

a, Homology model of the *ARAF* kinase domain (KD) bound to belvarafenib based on the *BRAF*^{KD}-belvarafenib co-crystal structure. Highlighted residues are mutated in *ARAF* in belvarafenib-resistant cells. **b**, Confirmation of *BRAF*- and *CRAF*-mutant overexpression in doxycycline-inducible IPC-298 cell lines treated with doxycycline, assayed by Flag-*BRAF* or Flag-*CRAF* western blot. **c**, Cellular viability of doxycycline-inducible IPC-298 cells expressing wild-type *BRAF*, *BRAF*(G534D), wild-

type CRAF, or CRAF(G426D) and treated with belvarafenib for 3 days \pm doxycycline. Data are mean \pm s.e.m., $n = 3$ replicates. **d**, MAPK signalling in doxycycline-inducible IPC-298 cells expressing wild-type BRAF, BRAF(G534D), wild-type CRAF, or CRAF(G426D) and treated with 0.1, 1 or 10 μ M belvarafenib for 24 h. **e**, Dimer interface of BRAF (PDB code 4MNF). E586 from each BRAF monomer (yellow and cyan) forms hydrogen bonds across the dimer interface with E586 and T589 from the interacting protomer *in trans*. E586 and T589 are shown as stick models, G534 is shown as spheres. **f**, MAPK signalling in IPC-298 cells transiently transfected with ARAF(G387D), ARAF(G387D/R362H), ARAF(G387D/E439K), ARAF(G387D/K336M), wild-type ARAF or empty vector (EV). After 24 h, cells were treated with 0.1, 1 or 10 μ M belvarafenib for 24 h. **g**, MAPK signalling in IPC-298 and BRC9 cells after 24-h treatment with 1 μ M belvarafenib.

Extended Data Fig. 4 Participant selection, baseline characteristics, and safety for belvarafenib phase I study.

a, b, Flow diagram indicating selection of study participants for dose-escalation (**a**) and dose-expansion (**b**) phases. In the dose-escalation phase (**a**), the full analysis set (FAS) included 67 out of 72 patients. Five patients without any post-dose tumour response assessments due to withdrawal of consent ($n = 2$), adverse event ($n = 2$), or progression of disease or lack of treatment effect ($n = 1$) were excluded from the FAS. In the dose-expansion phase (**b**), FAS included 59 out of 63 patients. Four patients without any post-dose tumour response assessments due to violation of inclusion/exclusion criteria ($n = 1$) or confirmed progressive disease or lack of efficacy in the judgement of the investigator ($n = 3$) were excluded from the FAS. QD, once daily; DLT, dose-limiting toxicity. **c**, Patient demographics and baseline characteristics. ECOG, Eastern Cooperative Oncology Group; GIST, gastrointestinal stromal tumour. **d**, Overall safety summary and treatment-emergent adverse events occurring in >10% of patients. TEAE, treatment-emergent adverse event. Result analysed with pooled data from dose-escalation and dose-expansion phases.

Extended Data Fig. 5 Pharmacokinetic properties of belvarafenib.

a, b, Pharmacokinetic assessment of belvarafenib after first administration (day 1) (**a**) or multiple administration (day 22*) (**b**). Area under the curve (AUC) was calculated based on the concentrations measured from 0 (pre-dose) to 48 h in cohort 1, and from 0 to 168 h in other cohorts. Mean and coefficient of variation are presented except where indicated (*day 17 for cohort 1). **c**, Plasma AUC of belvarafenib on multiple doses by cohort. * $N = 83$, dose-escalation and dose-expansion phases; **plasma AUC of all 450 mg BID patients from dose-escalation and dose-expansion phases. Yellow box indicates target exposure of belvarafenib, 50,000–100,000 $\mu\text{g h l}^{-1}$ of $\text{AUC}_{0\sim 24}$.

Extended Data Fig. 6 Clinical activity of belvarafenib.

a, Tumour responses in the dose-escalation phase. Best percentage changes in size of target lesions from baseline and specific genetic mutations in each evaluable patient are shown. Others include: NSCLC, bladder, GIST, and sarcoma. Two patients with only non-target lesions at baseline were excluded. **b**, Tumour response in efficacy-evaluable patients from the dose-escalation and dose-expansion phases. DCR, disease control rate; PFS, progression-free survival; DOR, duration of response; NE, not estimable. Note that BORR (%) = (number of subjects with best overall response as complete or partial response/total number of subjects) $\times 100$. ORR (%) = (number of subjects with confirmed best overall response as complete or partial response/total number of subjects) $\times 100$. DCR (%) = (number of subjects with best overall response as complete or partial response or stable disease/total number of subjects) $\times 100$. **c–f**, Progression-free survival plot of all patients (**c**) and patients with *NRAS*-mutant melanoma (**d**) in dose-escalation phase, and all patients (**e**) and patients with *NRAS*-mutant melanoma (**f**) in dose-expansion phase. **g**, Patients with *NRAS*-mutant melanoma with previous immunotherapy treatments. BOR, best overall response; CPI, check-point inhibitor; PD, progression of disease; PR, partial response; SD, stable disease; uPR, unconfirmed partial response. Confirmed partial response is claimed only if patient achieved partial or complete

responses at a subsequent time point as specified in the protocol. **h**, Patients with *BRAF^{V600E}*-mutant melanoma and CRC with previous *BRAF^{V600E}* inhibitor treatments. **i, j**, Responses and treatment durations of patients in dose-escalation (**i**) and dose-expansion (**j**) phases. In the dose-escalation and dose-expansion phases, one patient with both *BRAF* and *NRAS* mutations enrolled in each phase as indicated in the swimmer plot.

Extended Data Fig. 7 Patient ARAF mutations confirm resistance in BRAF- and NRAS-mutant cell lines.

a, Confirmation of ARAF-mutant overexpression in doxycycline-inducible cell lines (IPC-298, A375, WM-266-4, MelJuso) treated with doxycycline, assayed by Flag–ARAF western blot. **b–e**, Cellular viability of IPC-298 (**b**), A375 (**c**), WM-266-4 (**d**), or MelJuso (**e**) doxycycline-inducible expression of patient derived *ARAF* mutations (G387N, P462L, G377R) or wild-type treated with belvarafenib for 3 days ± doxycycline. Data are mean ± s.e.m., $n = 3$ replicates. IC₅₀ values are indicated. **f**, Confirmation of ARAF double-mutation overexpression in doxycycline-inducible IPC-298 cells treated with doxycycline, assayed by Flag–ARAF western blot. **g**, Cellular viability of IPC-298 doxycycline-inducible expression of *ARAF* double mutations treated with belvarafenib for 3 days ± doxycycline. Data are mean ± s.e.m., $n = 3$ replicates. IC₅₀ values are indicated. **h**, MAPK signalling in IPC-298 cells transiently transfected with ARAF constructs, treated with serial titration of belvarafenib for 24 h. **i**, Cellular viability of IPC-298 doxycycline-inducible cells expressing ARAF patient-derived mutations or wild-type ARAF, treated with AZ-628, LXH-254, cobimetinib or GDC-0994 for 3-days ± doxycycline. Data are mean ± s.e.m., $n = 3$ replicates.

Extended Data Fig. 8 Belvarafenib and cobimetinib combination in NRAS- and BRAF-mutant models delays resistance.

a–c, Clonogenic assay of IPC-298 (**a**), MelJuso (**b**) or WM-266-4 (**c**) cells treated with 100 nM belvarafenib, 50 nM cobimetinib, 100 nM belvarafenib + 50 nM cobimetinib, 100 nM vemurafenib, or 100 nM vemurafenib + 50

nM cobimetinib. Cells were cultured for 7, 14 or 21 days then stained with crystal violet. **d**, Body weight change of mice xenografted with IPC-298 tumours treated with belvarafenib, cobimetinib, or a combination of both. $n = 10$ mice per group; data are mean \pm s.e.m. **e**, Percentage change in mRNA of *DUSP6* and *SPRY4* of IPC-298 tumours treated with belvarafenib, cobimetinib, or their combination. $n = 5$ mice per group; data are mean \pm s.e.m.

[Source data](#)

Extended Data Table 1 Single point screening data of 187 kinases with 1 μ M belvarafenib (percentage inhibition of in vitro kinase panel)

[Full size table](#)

Extended Data Table 2 Data collection and refinement statistics for the BRAF^{KD}–belvarafenib complex

[Full size table](#)

Supplementary information

[Supplementary Information](#)

This file contains: Supplementary methods; Clinical study information; Supplementary Figure 1 (Uncropped and unprocessed western blots); and Preliminary full wwPDB X-ray structure validation report.

[Reporting Summary](#)

Source data

[Source Data Fig. 1](#)

[Source Data Fig. 4](#)

[Source Data Extended Data Fig. 1](#)

[Source Data Extended Data Fig. 8](#)

Rights and permissions

[Reprints and Permissions](#)

About this article



Check for
updates

Cite this article

Yen, I., Shanahan, F., Lee, J. *et al.* *ARAF* mutations confer resistance to the RAF inhibitor belvarafenib in melanoma. *Nature* **594**, 418–423 (2021).
<https://doi.org/10.1038/s41586-021-03515-1>

[Download citation](#)

- Received: 16 August 2020
- Accepted: 05 April 2021
- Published: 05 May 2021
- Issue Date: 17 June 2021
- DOI: <https://doi.org/10.1038/s41586-021-03515-1>

Comments

By submitting a comment you agree to abide by our [Terms](#) and [Community Guidelines](#). If you find something abusive or that does not comply with our terms or guidelines please flag it as inappropriate.

[Access through your institution](#)

[Change institution](#)

[Buy or subscribe](#)

Advertisement

This article was downloaded by **calibre** from <https://www.nature.com/articles/s41586-021-03515-1>

| [Section menu](#) | [Main menu](#) |

- Article
- [Published: 26 May 2021](#)

A phase-separated nuclear GBPL circuit controls immunity in plants

- [Shuai Huang](#) ORCID: [orcid.org/0000-0002-8903-122X^{1,2,3,4}](https://orcid.org/0000-0002-8903-122X),
- [Shiwei Zhu](#) ORCID: [orcid.org/0000-0003-1145-1192^{1,2,3,4}](https://orcid.org/0000-0003-1145-1192),
- [Pradeep Kumar^{1,2,3,4}](#) &
- [John D. MacMicking](#) ORCID: [orcid.org/0000-0002-1734-135X^{1,2,3,4}](https://orcid.org/0000-0002-1734-135X)

[Nature](#) volume 594, pages 424–429 (2021) [Cite this article](#)

- 5534 Accesses
- 66 Altmetric
- [Metrics details](#)

Subjects

- [Biotic](#)
- [Plant cell biology](#)
- [Plant genetics](#)
- [Plant immunity](#)

Abstract

Liquid–liquid phase separation (LLPS) has emerged as a central paradigm for understanding how membraneless organelles compartmentalize diverse cellular activities in eukaryotes^{1,2,3}. Here we identify a superfamily of plant

guanylate-binding protein (GBP)-like GTPases (GBPLs) that assemble LLPS-driven condensates within the nucleus to protect against infection and autoimmunity. In *Arabidopsis thaliana*, two members of this family—GBPL1 and GBPL3—undergo phase-transition behaviour to control transcriptional responses as part of an allosteric switch that is triggered by exposure to biotic stress. GBPL1, a pseudo-GTPase, sequesters catalytically active GBPL3 under basal conditions but is displaced by GBPL3 LLPS when it enters the nucleus following immune cues to drive the formation of unique membraneless organelles termed GBPL defence-activated condensates (GDACs) that we visualized by *in situ* cryo-electron tomography. Within these mesoscale GDAC structures, native GBPL3 directly bound defence-gene promoters and recruited specific transcriptional coactivators of the Mediator complex and RNA polymerase II machinery to massively reprogram host gene expression for disease resistance. Together, our study identifies a GBPL circuit that reinforces the biological importance of phase-separated condensates, in this case, as indispensable players in plant defence.

Access options

Subscribe to Journal

Get full journal access for 1 year

\$199.00

only \$3.90 per issue

[Subscribe](#)

All prices are NET prices.

VAT will be added later in the checkout.

Tax calculation will be finalised during checkout.

Rent or Buy article

Get time limited or full article access on ReadCube.

from \$8.99

[Rent or Buy](#)

All prices are NET prices.

Additional access options:

- [Log in](#)
- [Access through your institution](#)
- [Learn about institutional subscriptions](#)

Fig. 1: IDR-containing GBPLs are essential for plant defence.

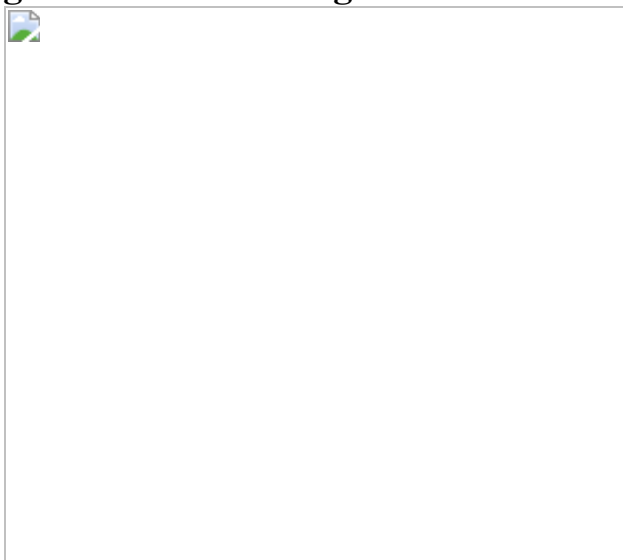


Fig. 2: Defence activation triggers a GBPL1–GBPL3 chromatin switch for immune condensates in the nucleus.

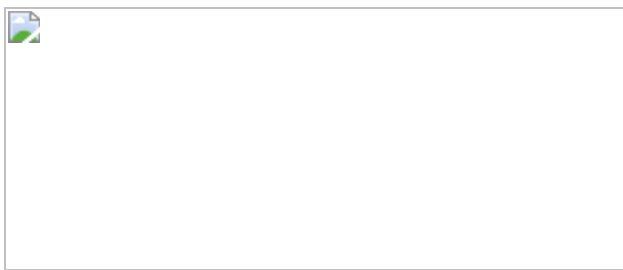


Fig. 3: *Arabidopsis* GBPL3 immune condensates are assembled via LLPS.

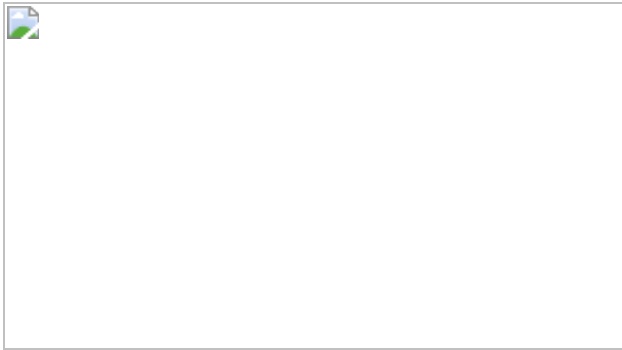
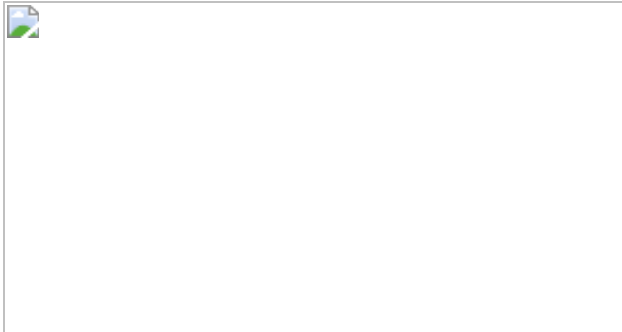


Fig. 4: GDACs concentrate RNAPII coactivators and nuclear GBPL3 on promoters of *Arabidopsis* defence genes.



Data availability

The original raw RNA-seq data that support the findings of this study have been deposited and made publicly available in the NCBI Gene Expression Omnibus with accession number [GSE134651](#). RNA-seq data are provided in Supplementary Tables 4 and 5. Full versions of all gels and blots are provided in Supplementary Fig. 1. The phylogenetic source data related to Extended Data Fig. 1b and high-resolution images of Fig. 4c are available on Dryad from <https://doi.org/10.5061/dryad.g1jwstqqv>. [Source data](#) are provided with this paper.

References

1. 1.

Boeynaems, S. et al. Protein phase separation: a new phase in cell biology. *Trends Cell Biol.* **28**, 420–435 (2018).

[CAS](#) [PubMed](#) [PubMed Central](#) [Google Scholar](#)

2. 2.

Shin, Y. & Brangwynne, C. P. Liquid phase condensation in cell physiology and disease. *Science* **357**, eaaf4382 (2017).

[PubMed](#) [Google Scholar](#)

3. 3.

Alberti, S., Gladfelter, A. & Mittag, T. Considerations and challenges in studying liquid–liquid phase separation and biomolecular condensates. *Cell* **176**, 419–434 (2019).

[CAS](#) [PubMed](#) [PubMed Central](#) [Google Scholar](#)

4. 4.

Randow, F., MacMicking, J. D. & James, L. C. Cellular self-defense: how cell-autonomous immunity protects against pathogens. *Science* **340**, 701–706 (2013).

[ADS](#) [CAS](#) [PubMed](#) [Google Scholar](#)

5. 5.

Bar-On, Y. M., Phillips, R. & Milo, R. The biomass distribution on Earth. *Proc. Natl Acad. Sci. USA* **115**, 6506–6511 (2018).

[CAS](#) [PubMed](#) [Google Scholar](#)

6. 6.

Jones, J. D. & Dangl, J. L. The plant immune system. *Nature* **444**, 323–329 (2006).

[ADS](#) [CAS](#) [Google Scholar](#)

7. 7.

Jones, J. D., Vance, R. E. & Dangl, J. L. Intracellular innate immune surveillance devices in plants and animals. *Science* **354**, aaf6395 (2016).

[PubMed](#) [Google Scholar](#)

8. 8.

Jung, J.-H. et al. A prion-like domain in ELF3 functions as a thermosensor in *Arabidopsis*. *Nature* **585**, 256–260 (2020).

[CAS](#) [PubMed](#) [Google Scholar](#)

9. 9.

Fang, X. et al. *Arabidopsis* FLL2 promotes liquid–liquid phase separation of polyadenylation complexes. *Nature* **569**, 265–269 (2019).

[ADS](#) [CAS](#) [PubMed](#) [PubMed Central](#) [Google Scholar](#)

10. 10.

Bailey-Serres, J., Parker, J. E., Ainsworth, E. A., Oldroyd, G. E. D. & Schroeder, J. I. Genetic strategies for improving crop yields. *Nature* **575**, 109–118 (2019).

[ADS](#) [CAS](#) [PubMed](#) [PubMed Central](#) [Google Scholar](#)

11. 11.

Frottin, F. et al. The nucleolus functions as a phase-separated protein quality control compartment. *Science* **365**, 342–347 (2019).

[ADS](#) [CAS](#) [PubMed](#) [Google Scholar](#)

12. 12.

Feric, M. et al. Coexisting liquid phases underlie nucleolar subcompartments. *Cell* **165**, 1686–1697 (2016).

[CAS](#) [PubMed](#) [PubMed Central](#) [Google Scholar](#)

13. 13.

Gibson, B. A. et al. Organization of chromatin by intrinsic and regulated phase separation. *Cell* **179**, 470–484 (2019).

[CAS](#) [PubMed](#) [PubMed Central](#) [Google Scholar](#)

14. 14.

Sabari, B. R. et al. Coactivator condensation at super-enhancers links phase separation and gene control. *Science* **361**, eaar3958 (2018).

[PubMed](#) [PubMed Central](#) [Google Scholar](#)

15. 15.

Cho, W. K. et al. Mediator and RNA polymerase II clusters associate in transcription-dependent condensates. *Science* **361**, 412–415 (2018).

[ADS](#) [CAS](#) [PubMed](#) [PubMed Central](#) [Google Scholar](#)

16. 16.

Shin, Y. et al. liquid nuclear condensates mechanically sense and restructure the genome. *Cell* **175**, 1481–1491 (2018).

[CAS](#) [PubMed](#) [PubMed Central](#) [Google Scholar](#)

17. 17.

Kim, B. H. et al. A family of IFN- γ -inducible 65-kD GTPases protects against bacterial infection. *Science* **332**, 717–721 (2011).

[ADS](#) [CAS](#) [PubMed](#) [Google Scholar](#)

18. 18.

Shenoy, A. R. et al. GBP5 promotes NLRP3 inflammasome assembly and immunity in mammals. *Science* **336**, 481–485 (2012).

[ADS](#) [CAS](#) [PubMed](#) [Google Scholar](#)

19. 19.

Kim, B. H. et al. Interferon-induced guanylate-binding proteins in inflammasome activation and host defense. *Nat. Immunol.* **17**, 481–489 (2016).

[CAS](#) [PubMed](#) [PubMed Central](#) [Google Scholar](#)

20. 20.

Merchant, S. S. et al. The *Chlamydomonas* genome reveals the evolution of key animal and plant functions. *Science* **318**, 245–250 (2007).

[ADS](#) [CAS](#) [PubMed](#) [PubMed Central](#) [Google Scholar](#)

21. 21.

Henikoff, S., Henikoff, J. G., Sakai, A., Loeb, G. B. & Ahmad, K. Genome-wide profiling of salt fractions maps physical properties of chromatin. *Genome Res.* **19**, 460–469 (2009).

[CAS](#) [PubMed](#) [PubMed Central](#) [Google Scholar](#)

22. 22.

Yang, L., Gal, J., Chen, J. & Zhu, H. Self-assembled FUS binds active chromatin and regulates gene transcription. *Proc. Natl Acad. Sci. USA* **111**, 17809–17814 (2014).

[ADS](#) [CAS](#) [PubMed](#) [Google Scholar](#)

23. 23.

Zipfel, C. et al. Bacterial disease resistance in *Arabidopsis* through flagellin perception. *Nature* **428**, 764–767 (2004).

[ADS](#) [CAS](#) [PubMed](#) [Google Scholar](#)

24. 24.

Knuesel, M. T., Meyer, K. D., Bernecke, C. & Taatjes, D. J. The human CDK8 subcomplex is a molecular switch that controls Mediator coactivator function. *Genes Dev.* **23**, 439–451 (2009).

[CAS](#) [PubMed](#) [PubMed Central](#) [Google Scholar](#)

25. 25.

Bergeron-Sandoval, L. P., Safaei, N. & Michnick, S. W. Mechanisms and consequences of macromolecular phase separation. *Cell* **165**, 1067–1079 (2016).

[CAS](#) [PubMed](#) [Google Scholar](#)

26. 26.

Álvarez-Aragón, R., Haro, R., Benito, B. & Rodríguez-Navarro, A. Salt intolerance in *Arabidopsis*: shoot and root sodium toxicity, and inhibition by sodium-plus-potassium overaccumulation. *Planta* **243**, 97–114 (2016).

[PubMed](#) [Google Scholar](#)

27. 27.

Huang, S., Meng, Q., Maminska, A. & MacMicking, J. D. Cell-autonomous immunity by IFN-induced GBPs in animals and plants. *Curr. Opin. Immunol.* **60**, 71–80 (2019).

[CAS](#) [PubMed](#) [PubMed Central](#) [Google Scholar](#)

28. 28.

Riechmann, J. L. et al. *Arabidopsis* transcription factors: genome-wide comparative analysis among eukaryotes. *Science* **290**, 2105–2110 (2000).

[ADS](#) [CAS](#) [PubMed](#) [Google Scholar](#)

29. 29.

Allen, B. L. & Taatjes, D. J. The Mediator complex: a central integrator of transcription. *Nat. Rev. Mol. Cell Biol.* **16**, 155–166 (2015).

[CAS](#) [PubMed](#) [PubMed Central](#) [Google Scholar](#)

30. 30.

Mathur, S., Vyas, S., Kapoor, S. & Tyagi, A. K. The Mediator complex in plants: structure, phylogeny, and expression profiling of representative genes in a dicot (*Arabidopsis*) and a monocot (rice) during reproduction and abiotic stress. *Plant Physiol.* **157**, 1609–1627 (2011).

[CAS](#) [PubMed](#) [PubMed Central](#) [Google Scholar](#)

31. 31.

McWhite, C. D. et al. A pan-plant protein complex map reveals deep conservation and novel assemblies. *Cell* **181**, 460–474 (2020).

[CAS](#) [PubMed](#) [PubMed Central](#) [Google Scholar](#)

32. 32.

Tsai, K. L. et al. A conserved Mediator–CDK8 kinase module association regulates Mediator–RNA polymerase II interaction. *Nat. Struct. Mol. Biol.* **20**, 611–619 (2013).

[CAS](#) [PubMed](#) [PubMed Central](#) [Google Scholar](#)

33. 33.

Kitsios, G., Alexiou, K. G., Bush, M., Shaw, P. & Doonan, J. H. A cyclin-dependent protein kinase, CDKC2, colocalizes with and modulates the distribution of spliceosomal components in *Arabidopsis*. *Plant J.* **54**, 220–235 (2008).

[CAS](#) [PubMed](#) [Google Scholar](#)

34. 34.

Oates, M. E. et al. D²P²: database of disordered protein predictions. *Nucleic Acids Res.* **41**, D508–D516 (2013).

[CAS](#) [PubMed](#) [Google Scholar](#)

35. 35.

Jiao, X. et al. DAVID-WS: a stateful web service to facilitate gene/protein list analysis. *Bioinformatics* **28**, 1805–1806 (2012).

[CAS](#) [PubMed](#) [PubMed Central](#) [Google Scholar](#)

36. 36.

Ronquist, F. & Huelsenbeck, J. P. MrBayes 3: Bayesian phylogenetic inference under mixed models. *Bioinformatics* **19**, 1572–1574 (2003).

[CAS](#) [PubMed](#) [Google Scholar](#)

37. 37.

Jones, D. T., Taylor, W. R. & Thornton, J. M. The rapid generation of mutation data matrices from protein sequences. *Comput. Appl. Biosci.* **8**, 275–282 (1992).

[CAS](#) [PubMed](#) [Google Scholar](#)

38. 38.

Stamatakis, A. RAxML version 8: a tool for phylogenetic analysis and post-analysis of large phylogenies. *Bioinformatics* **30**, 1312–1313 (2014).

[CAS](#) [PubMed](#) [PubMed Central](#) [Google Scholar](#)

39. 39.

Yang, J. et al. The I-TASSER suite: protein structure and function prediction. *Nat. Methods* **12**, 7–8 (2015).

[CAS](#) [PubMed](#) [PubMed Central](#) [Google Scholar](#)

40. 40.

Clough, S. J. & Bent, A. F. Floral dip: a simplified method for *Agrobacterium*-mediated transformation of *Arabidopsis thaliana*. *Plant J.* **16**, 735–743 (1998).

[CAS](#) [PubMed](#) [Google Scholar](#)

41. 41.

Wang, Z. P. et al. Egg cell-specific promoter-controlled CRISPR/Cas9 efficiently generates homozygous mutants for multiple target genes in *Arabidopsis* in a single generation. *Genome Biol.* **16**, 144 (2015).

[PubMed](#) [PubMed Central](#) [Google Scholar](#)

42. 42.

Kim, D., Langmead, B. & Salzberg, S. L. HISAT: a fast spliced aligner with low memory requirements. *Nat. Methods* **12**, 357–360 (2015).

[CAS](#) [PubMed](#) [PubMed Central](#) [Google Scholar](#)

43. 43.

Li, H. et al. The Sequence Alignment/Map format and SAMtools. *Bioinformatics* **25**, 2078–2079 (2009).

[PubMed](#) [PubMed Central](#) [Google Scholar](#)

44. 44.

Anders, S., Pyl, P. T. & Huber, W. HTSeq—a Python framework to work with high-throughput sequencing data. *Bioinformatics* **31**, 166–169 (2015).

[CAS](#) [PubMed](#) [PubMed Central](#) [Google Scholar](#)

45. 45.

Love, M. I., Huber, W. & Anders, S. Moderated estimation of fold change and dispersion for RNA-seq data with DESeq2. *Genome Biol.* **15**, 550 (2014).

[PubMed](#) [PubMed Central](#) [Google Scholar](#)

46. 46.

Huang, S. et al. Plant TRAF proteins regulate NLR immune receptor turnover. *Cell Host Microbe* **19**, 204–215 (2016).

[CAS](#) [PubMed](#) [Google Scholar](#)

47. 47.

Cheng, Y. T. et al. Nuclear pore complex component MOS7/Nup88 is required for innate immunity and nuclear accumulation of defense regulators in *Arabidopsis*. *Plant Cell* **21**, 2503–2516 (2009).

[CAS](#) [PubMed](#) [PubMed Central](#) [Google Scholar](#)

48. 48.

Schindelin, J. et al. Fiji: an open-source platform for biological-image analysis. *Nat. Methods* **9**, 676–682 (2012).

[CAS](#) [Google Scholar](#)

49. 49.

Moissiard, G. et al. MORC family ATPases required for heterochromatin condensation and gene silencing. *Science* **336**, 1448–1451 (2012).

[ADS](#) [CAS](#) [PubMed](#) [PubMed Central](#) [Google Scholar](#)

50. 50.

Freeman Rosenzweig, E. S. et al. The eukaryotic CO₂-concentrating organelle is liquid-like and exhibits dynamic reorganization. *Cell* **171**, 148–162 (2017).

[CAS](#) [PubMed](#) [PubMed Central](#) [Google Scholar](#)

51. 51.

Thévenaz, P., Ruttimann, U. E. & Unser, M. A pyramid approach to subpixel registration based on intensity. *IEEE Trans. Image Process.* **7**, 27–41 (1998).

[ADS](#) [PubMed](#) [Google Scholar](#)

52. 52.

Li, X. et al. Symmetrical organization of proteins under docked synaptic vesicles. *FEBS Lett.* **593**, 144–153 (2019).

[CAS](#) [PubMed](#) [PubMed Central](#) [Google Scholar](#)

53. 53.

Zhu, S., Qin, Z., Wang, J., Morado, D. R. & Liu, J. In situ structural analysis of the spirochetal flagellar motor by cryo-electron tomography. *Methods Mol. Biol.* **1593**, 229–242 (2017).

[CAS](#) [PubMed](#) [Google Scholar](#)

54. 54.

Schorb, M. & Briggs, J. A. Correlated cryo-fluorescence and cryo-electron microscopy with high spatial precision and improved sensitivity. *Ultramicroscopy* **143**, 24–32 (2014).

[CAS](#) [PubMed](#) [Google Scholar](#)

55. 55.

Schaffer, M. et al. Optimized cryo-focused ion beam sample preparation aimed at in situ structural studies of membrane proteins. *J. Struct. Biol.* **197**, 73–82 (2017).

[CAS](#) [PubMed](#) [Google Scholar](#)

56. 56.

Mastronarde, D. N. & Held, S. R. Automated tilt series alignment and tomographic reconstruction in IMOD. *J. Struct. Biol.* **197**, 102–113 (2017).

[PubMed](#) [Google Scholar](#)

57. 57.

Mastronarde, D. N. Automated electron microscope tomography using robust prediction of specimen movements. *J. Struct. Biol.* **152**, 36–51 (2005).

[Google Scholar](#)

58. 58.

Hagen, W. J. H., Wan, W. & Briggs, J. A. G. Implementation of a cryo-electron tomography tilt-scheme optimized for high resolution subtomogram averaging. *J. Struct. Biol.* **197**, 191–198 (2017).

[PubMed](#) [PubMed Central](#) [Google Scholar](#)

59. 59.

Li, X. et al. Electron counting and beam-induced motion correction enable near-atomic-resolution single-particle cryo-EM. *Nat. Methods* **10**, 584–590 (2013).

[CAS](#) [PubMed](#) [PubMed Central](#) [Google Scholar](#)

60. 60.

Zheng, S. Q. et al. MotionCor2: anisotropic correction of beam-induced motion for improved cryo-electron microscopy. *Nat. Methods* **14**, 331–332 (2017).

[CAS](#) [PubMed](#) [PubMed Central](#) [Google Scholar](#)

61. 61.

Kremer, J. R., Mastronarde, D. N. & McIntosh, J. R. Computer visualization of three-dimensional image data using IMOD. *J. Struct. Biol.* **116**, 71–76 (1996).

[CAS](#) [PubMed](#) [Google Scholar](#)

62. 62.

Agulleiro, J. I. & Fernandez, J. J. Tomo3D 2.0—exploitation of advanced vector extensions (AVX) for 3D reconstruction. *J. Struct. Biol.* **189**, 147–152 (2015).

[PubMed](#) [Google Scholar](#)

63. 63.

Chen, M. et al. Convolutional neural networks for automated annotation of cellular cryo-electron tomograms. *Nat. Methods* **14**, 983–985 (2017).

[CAS](#) [PubMed](#) [PubMed Central](#) [Google Scholar](#)

64. 64.

Pettersen, E. F. et al. UCSF Chimera—a visualization system for exploratory research and analysis. *J. Comput. Chem.* **25**, 1605–1612 (2004).

[CAS](#) [PubMed](#) [PubMed Central](#) [Google Scholar](#)

65. 65.

Khoshouei, M., Pfeffer, S., Baumeister, W., Förster, F. & Danev, R. Subtomogram analysis using the Volta phase plate. *J. Struct. Biol.* **197**, 94–101 (2017).

[PubMed](#) [Google Scholar](#)

66. 66.

Sun, T. et al. ChIP-seq reveals broad roles of SARD1 and CBP60g in regulating plant immunity. *Nat. Commun.* **6**, 10159 (2015).

[ADS](#) [CAS](#) [PubMed](#) [PubMed Central](#) [Google Scholar](#)

[Download references](#)

Acknowledgements

We thank all members of the MacMicking laboratory for feedback and discussions; X. Liu for TEM assistance; members of the J. Liu laboratory (R. Park, M. Shao and Y. Chang) for instruction on CLEM and FIB milling; S. Wu for cryo-ET data collection advice; and X. Li, N. Clay, J. Parker, X. Dong, J. Zhou, Q. Wu, L. Wu, F. Xu and others for sharing materials and

tools. The MacMicking laboratory is supported by grants from NIH NIAID (R01AI068041-12, R01AI108834-05). J.D.M. is an Investigator of the Howard Hughes Medical Institute.

Author information

Affiliations

1. Howard Hughes Medical Institute, New Haven, CT, USA

Shuai Huang, Shiwei Zhu, Pradeep Kumar & John D. MacMicking

2. Yale Systems Biology Institute, West Haven, CT, USA

Shuai Huang, Shiwei Zhu, Pradeep Kumar & John D. MacMicking

3. Department of Immunobiology, Yale University School of Medicine, New Haven, CT, USA

Shuai Huang, Shiwei Zhu, Pradeep Kumar & John D. MacMicking

4. Department of Microbial Pathogenesis, Yale University School of Medicine, New Haven, CT, USA

Shuai Huang, Shiwei Zhu, Pradeep Kumar & John D. MacMicking

Authors

1. Shuai Huang

[View author publications](#)

You can also search for this author in [PubMed](#) [Google Scholar](#)

2. Shiwei Zhu

[View author publications](#)

You can also search for this author in [PubMed](#) [Google Scholar](#)

3. Pradeep Kumar

[View author publications](#)

You can also search for this author in [PubMed](#) [Google Scholar](#)

4. John D. MacMicking

[View author publications](#)

You can also search for this author in [PubMed](#) [Google Scholar](#)

Contributions

S.H. performed most experiments and analyses throughout with the following exceptions. P.K. purified human GBP1 and GBP5 proteins and undertook TLC assays. S.Z. performed negative-stain electron microscopy and cryo-ET (including FIB and CLEM). J.D.M. and S.H. conceived the project, designed experiments and wrote the manuscript with input from all authors.

Corresponding author

Correspondence to [John D. MacMicking](#).

Ethics declarations

Competing interests

The authors declare no competing interests.

Additional information

Peer review information *Nature* thanks Yoji Kawano and the other, anonymous, reviewer(s) for their contribution to the peer review of this work. Peer reviewer reports are available.

Publisher's note Springer Nature remains neutral with regard to jurisdictional claims in published maps and institutional affiliations.

Extended data figures and tables

Extended Data Fig. 1 Retrieval and structural characteristics of plant IDR-containing GBPLs.

a, Pipeline of IDP-based in silico screening of the *Arabidopsis* proteome. **b**, Phylogenetic tree inferred by Bayesian analysis. Support value: Left, Nodal posterior probabilities; Right, Maximum likelihood bootstrap values. Scale bar, substitutions per site. Number of amino acid (#aa) not drawn to scale. **c**, 3D structure prediction of *Arabidopsis* GBPLs performed on I-TASSER web server and projected with PyMOL software. GD, GTPase domain. HD, helical domain. IDR, intrinsically disordered region. hGBP1, 1F5N.PDB. **d**, Domain configuration and size of the *Arabidopsis* GBPL family versus human GBP1. **e**, GBPL disorder and hydrophobicity plots carried out using ProtScale and PONDR servers, respectively. Charged amino acids (red, glutamate/ aspartate; blue, arginine/lysine) displayed as vertical lines atop panels. IDRs are shaded.

Extended Data Fig. 2 Generation and characterization of *Arabidopsis gbpl* mutants.

a, Immunoblot of GBPL3 protein level using α -GBPL3 rabbit polyclonal antibody in wild type (WT) (Col-0) and four independent T1 transformants generated via CRISPR/Cas9 targeting GBPL3 (predicted molecular weight 122 kDa). Ponceau S staining of a non-specific band (nsb) serves as a loading control. Proteins extracted from five-week-old plants. Experiment performed once only due to the limit of tissue materials from sterile plants. **b**, PAM sequences of gRNAs and the consequences of CRISPR-Cas cleavages in T1 generation. Line 15 is biallelic and line 16 is heterozygous. **c**, Chromatograms of sanger sequencing of the mutation sites in CRISPR lines in **b**. **d**, Fresh weight of plants (mean \pm SD) shown above (top-right graph the same as Fig. 1b for comparison with left). **e**, Gene expression of *GBPL1* and *GBPL2* in T-DNA mutants. **f**, Immunoblot (α -GBPL3) of

GBPL3 and EGFP–GBPL3 levels in complemented plants. Ponceau S staining of RbcL serves as a loading control. **g**, Growth of *Psm* ES4326 (*Psm*) at day 3 of infection. Inoculum, bottom left. **h**, *Hpa* Noco2 sporulation in 2~3-week-old plants at day 7. Inoculum, bottom left. **i**, GBPL proteins are not required for *Pst* DC3000 *Avr* challenge using *gbpl* mutant lines. Growth of *Pst*-*Avr* at day 3 of infection. Inoculum, bottom left. **g–i**, Box = 25th and 75th percentiles; bars = min and max values. Statistical analysis, comparison of mean via one-way ANOVA test (Bonferroni post hoc correction). ns, not significant. Individual data points represent biologically independent samples (**d**, **g–i**).

[Source data](#)

[Extended Data Fig. 3 RNA-seq and defence-gene expression analysis in transgenic plants.](#)

a, Comparative heat map of the top 1,000 differentially expressed genes (RNA-seq; base log2) across *Arabidopsis* genotypes from two biologically independent replicates. **b**, GO enrichment of upregulated genes in *Col-0/pGBPL3::GBPL3 (GBPL3^{OX})* (left) and *gbpl1-1* (right) plants versus WT. Top 25 significantly enriched GO terms are shown. Red, enriched GO-terms found in both *GBPL3^{OX}* and *gbpl1-1* plants. **c**, **d**, Defence-gene expression (mean ± SD) in under basal and induced conditions. RNA extracted 4 h after mock ($MgCl_2$) or *Psm* ES4326 ($OD_{600} = 0.1$) infection. Expression normalized to *ACTIN7*. **e**, **f**, Defence-gene expression (mean ± SD) under basal and induced conditions shown as \log_2 transformations for comparison. **g**, **h**, Relative expression (mean ± SD, normalized to *ACTIN7*) in two different *gbpl3* mutants. RNA extracted 24 h after mock ($MgCl_2$) or *Psm* ES4326 ($OD_{600} = 0.001$) infection from 4-week-old plants. Statistical analysis, two-tailed Student's *t*-test (**c**, **e**), one-way ANOVA with Holm–Sidak post hoc test (**g**) and two-way ANOVA with Holm–Sidak post hoc test (**d**, **f**, **h**). Individual data points represent biologically independent samples with experiments undertaken twice with similar results (**c–h**).

[Source data](#)

Extended Data Fig. 4 Nuclear GBPL1–GBPL3 analysis in *Arabidopsis* and *N. benthamiana*.

a, Live imaging of EGFP–GBPL3 in the nucleus of 2-week-old transgenic Col-0 or *gbpl1-1* plants under basal conditions. Bar, 5 μm. **b**, Sequential fractionation strategy to examine chromatin binding properties of GBPL1 and GBPL3 in Fig. 2, using Col-0/*pGBPL1:GBPL1-3×Flag* plants to ensure physiological expression. **c**, Nuclear co-immunoprecipitation of GBPL3 with FLAG-M2 agarose (bottom) and GBPL1 with α-GBPL3 antibody (top). Streptavidin agarose and rabbit normal IgG served as negative controls. **d**, Split luciferase complementation assay in *N. benthamiana*. (top) Luminescence image of *N. benthamiana* leaves co-infiltrated with agrobacterial strains containing plasmids shown below. (bottom) Quantification of LUC activity (mean ± SD, $n = 4$ biologically independent leaf discs). **e**, Time course of total GBPL3 levels by immunoblot after salicylic acid treatment (0.5 mM). Ponceau S stained RbcL serves as loading control. **f**, Immunoblot of total GBPL3 protein levels 24 h after *Psm* ES4326 ($OD_{600} = 0.01$) infection from 4-week old plants. **g**, Top, Exclusion of mRFP-GBPL1 to the periphery of EGFP–GBPL3 nuclear condensates when co-expressed in *N. benthamiana* leaves. Scale bar, 2 μm. Inset bar used for average line profiling. Bottom, Average line profile (2 μm) of fluorescence intensity spanning GBPL3 condensates. Bar = mean ± s.d. ($n = 5$ biologically independent condensates). Shaded area with arrows, GBPL3 condensate core.

[Source data](#)

Extended Data Fig. 5 GBPL droplets are unique LLPS structures conserved across plant species, cell types and during development.

a, Coomassie staining of purified rEGFP protein. **b**, Standard curve of rEGFP via confocal microscopy. **c**, Quantitative measurement (mean ± SD) of EGFP–GBPL3 concentration 24 h after salicylic acid (0.5 mM), *Psm* ($OD_{600} = 0.001$) and *Pst* ($OD_{600} = 0.001$) from multiple 4-week-old plant nuclei. Comparison of mean via one-way ANOVA test with Holm–Sidak

post hoc test. Individual data points represent biologically independent samples. **d, e**, Colocalization analysis of EGFP–GBPL3 in *N. benthamiana* (**d**, live cell) and HeLa cells (**e**, fixed cell). The latter enabled parallel antibody detection of subnuclear structures. DSB, double strand break. DNA stained with Hoechst 33342 dye. Bar, 5 µm (**d**, *N.B.*) and 2 µm (**e**, HeLa). **f**, Immunofluorescence of native GBPL3 in Col-0 and Col-0/GBPL3^{*OX*} plants. Nuclei were isolated from 3-week-old soil-grown plants and DNA stained with Hoechst 33342. chr, chromocentre (white arrows). Bar, 2 µm. Experiment repeated once with similar results. **g**, Left, GBPL3 condensates in *Arabidopsis* cotyledons stably expressing 35S::EGFP-GBPL3. Shown are maximum projection images. Dashed circle, nuclear boundary. Bar, 5 µm. Right, salicylic acid-induced GBPL3 condensates (mean ± SD, Student's *t*-test, two-tailed) in guard cells from 10-day-old *Arabidopsis* cotyledons ($n = 4$ biologically independent plants with 100 guard cells each). Mock, water treatment. **h**, Localization of EGFP-tagged tomato and maize GBPs in HeLa cells. DNA stained with Hoechst 33342 dye. Bar, 5 µm (SlGBP2 and ZmGBP1) and 2 µm (SlGBP1 and ZmGBP2). **i**, Maximum intensity projection images of EGFP–GBPL3 transiently expressed in *N. benthamiana* (*N.B.*), human HeLa and HEK 293T cells. Bar, 2 µm. **j**, Immunogold transmission electron microscopy of spheroid GDACs (dashed circles) expressed in HEK 293T cells. NE, nuclear envelope. NPC, nuclear pore complex. Bar, 500 nm. **k**, GBPL3 condensates were sensitive to 1,6-hexanediol (5%) but not 1,2,6-hexanetriol (5%). Digitonin (10 µg/ml) was used to facilitate chemical delivery.

[Source data](#)

[**Extended Data Fig. 6 Comparative LLPS behaviour of GBPLs in cells and cell-free systems.**](#)

a, A 3D volume view of rEGFP–GBPL3 droplets (10% Ficoll) depicted in (Fig. 3d). Bar, 2 µm. **b**, Phase separation (PS) diagram of rEGFP–GBPL3 across NaCl concentrations 30 min after reconstitution. **c**, Confocal images showing GBPL3 condensates fusion behaviours every 100 s in vitro. Images collected 30 min after reconstitution in droplet buffer (20 mM HEPES [pH 7.5], 200 mM NaCl, 1 mM TCEP, 10% Ficoll). Bar, 5 µm. **d**, RFP-GBPL1 does not generate LLPS nuclear condensates *in situ* in *N.*

benthamiana. **e**, in vitro phase separation of rRFP–GBPL1 (375 nM) in droplet buffer (20 mM HEPES [pH 7.5], 150 mM NaCl, 1 mM TCEP). Coomassie brilliant blue (CBB) of rRFP–GBPL1 is shown on the left. Bar, 10 µm. **f**, Co-condensation assay of rEGFP–GBPL3 and rRFP–GBPL1 in vitro. Below, quantification of EGFP–GBPL3 droplet size. Median (solid line) and quartile (dashed line) values. Comparison of mean via one-way ANOVA with Holm–Sidak post hoc test ($****P < 1.0 \times 10^{-15}$, n = number of biologically independent droplets). **g**, Native PAGE of rEGFP–GBPL3 in the presence of increasing concentrations of rRFP–GBPL1 leads to GBPL3 displacement. Same loading controls below the original (anti-GFP) and re-probed (anti-RFP) native gel separated by SDS–PAGE. **h**, Exclusion of rRFP–GBPL1 from larger rEGFP–GBPL3 droplets in co-condensation assays. **i**, Representative negative stain EM images of rGBPL3 droplets at 24 h. Bar, 2 µm. Inset at right. Bar, 100 nm. **j**, FRAP analysis of 2 h old rEGFP–GBPL3 droplets in vitro. Bar, 5 µm. Fluorescence recovery of 5 individual droplets shown. Insert, representative images of a bleached droplet over 10 min recovery.

[Source data](#)

[Extended Data Fig. 7 In situ cryo-ET analysis of GDACs including CLEM corroboration.](#)

a, Flow chart of in situ cryo-ET analysis. **b**, **c**, CLEM images of EM grids seeded with HEK 293T cells transfected with *CMV-EGFP-GBPL3*. Single cell view of (**b**) shown below (**c**). These nuclear GDAC structures form in a species- and kingdom-independent manner with similar structures generated by GBPL3 plant orthologues; hence they appear to share conserved features with those directly generated in *Plantae*. **d**, Schema of FIB-milled lamella. **e**, CLEM images of FIB-milled lamella and overlay with Cryo-ET montage images. **f**, Left, Selected regions for tomograph collection. Right, Slice tomogram of GDACs and the corresponding CLEM fluorescence of GDACs overlap. **g**, **h**, Enlarged and higher resolution (binning factor 1) view of the GDAC in tomographic overlays with CLEM for region 1 of the cryo-ET montage image.

Extended Data Fig. 8 In situ cryo-ET analysis of GDACs in larger tomographic slices.

a, Shared similarities of CLEM-verified GDACs (from Extended Data Fig. 7h) with GDACs identified in tomographic images harbouring the nearby nuclear envelope for validating its intranuclear location (right, from Fig. 3e for comparison). Possible chromatin boundaries also depicted in both independently identified GDAC structures. **b**, CLEM images of EM grids seeded with HEK 293T cells transfected with *CMV-EGFP-GBPL3* used to generate the tomogram in (a, right) above. Single cell view of the nucleus used to detect GDACs in far-right panel. Bar, 20 μ m. **c**, FIB-milled lamella of the chosen nucleus from the CLEM above. **d**, Tomographic slice of the demarcated rectangular area 62 yielded a single demarcated GDAC near the nuclear envelope boundary shown in (a, right) and yielded 3D segmented images in Fig. 3e.

Extended Data Fig. 9 GBPL3 IDR contributes to LLPS-driven defence.

a, Top, domain structures of the *Arabidopsis* GBPL3 protein. Sites for mutagenesis are shown below. Bottom, GTP-binding pocket with conserved G-boxes (hGBP1 surface representation; 1F5N.PDB). GBPL3 hydrophobicity and disorder plots on right. Charged amino acids (red, glutamate and aspartate; blue, arginine and lysine) displayed as vertical lines atop panels. IDRs are shaded light green. **b**, Amino acid compositions of GBPL3 full length protein. Each row represents information for a single amino acid. Vertical bars, occurrence of indicated amino acid at that position. Right, amino acid percentage. **c**, Immunofluorescence of EGFP–GBPL3 mutant variants in HeLa cells 36 h after transfection. DNA stained with Hoechst 33342 dye. Arrows, nucleus. **d**, Growth of *Psm* ES4326 (*Psm*) and *Pst* DC3000 (*Pst*) at day 3 of infection. Inoculum, bottom left. Statistical analysis, comparison of mean via one-way ANOVA test (Bonferroni post hoc correction). ns, not significant. Box = 25th and 75th percentiles; bars = min and max values. Individual data points represent biologically independent samples. **e**, In vitro phase separation of rEGFP–GBPL3^{IDR} and rEGFP. Equimolar (400 nM) amounts incubated at

22 °C for 16 h in droplet buffer (20 mM HEPES, pH 7.5, 150 mM NaCl, 1 mM TCEP, 10% Ficoll). Bar, 20 µm. Left, Coomassie stain. **f**, Immunofluorescence of plant–human GBP-IDR chimeras performed as in **c**.

[Source data](#)

Extended Data Fig. 10 GBPL3 GTPase activity is required for LLPS-driven defence.

a, Alignment of conserved G-boxes in animal GBPs and plant GBPLs. Red outline denotes non-functional G2 box alterations in GBPL1. **b**, GTP hydrolysis assay of recombinant proteins along with tag controls. Bottom, percent GTP conversion. **c**, Malachite green phosphate assay (mean ± SD, $n = 2$ biologically independent samples) of recombinant GBPL proteins. **d**, Top, Immunoblot (α -GBPL3) of GBPL3 and EGFP–GBPL3^{K83A,S84A} levels in Col-0 and Col-0/35S::EGFP–GBPL3^{K83A,S84A} plants. T1-6 used in Extended Data Fig. [9d](#). Ponceau S staining of RbcL serves as a loading control. Bottom, Nuclear fractionation and immunoblot analysis of EGFP–GBPL3^{K83A,S84A} in HEK 293T cells shows the DN GTPase mutant still enters the nucleus and binds chromatin but cannot phase separate. Sn, nuclear soluble. CB, chromatin bound. **e**, Live imaging of 35S::EGFP–GBPL3 and 35S::EGFP–GBPL3^{K83A,S84A} in *N. benthamiana* and *Arabidopsis* plants. *Arabidopsis* imaging 24 h after salicylic acid (0.5 mM) treatment. Arrows, nucleolus. Bars, 5 µm (N.B.) and 2 µm (*Arabidopsis*). **f**, Effect of EGFP–GBPL3^{K83A,S84A} (ks mt) on wild-type (WT) GBPL3 in confocal microscopy. Plasmids were co-transfected in HeLa cells and analysed 36 h post transfection. Bar, 2 µm. **g**, GBPL3 self-assembly co-IP in HEK 293T cells reveal GBPL3^{K83A,S84A} can bind WT GBPL3 to interfere with its nuclear LLPS function in **f**. Cells were collected 36 h post transfection.

[Source data](#)

Extended Data Fig. 11 GBPL3 enlists a monopartite NLS motif to target the nucleus where it engages Mediator subunits and

excludes CDK8 for LLPS-driven immunity.

a, NLS motifs in GBPL3. Monopartite and bipartite NLS motifs were predicted via two web servers (SeqNLS and cNLS mapper). Shared sequences in red. **b**, Subcellular fractionation of *gbpl3-3/35S::EGFP-GBPL3^{ΔNLS}* plants. RbcL (Ponceau staining) and Histone H3 are cytosol and nuclear controls, respectively. **c**, Live cell imaging of *gbpl3-3/35S::EGFP-GBPL3^{ΔNLS}* plant leaves under basal conditions. Image overlay of GFP and DIC channels. Arrows, cytosolic condensates formed by EGFP–GBPL3^{ΔNLS}. Bar, 10 µm. **d**, Immunofluorescence of *CMV::EGFP-GBPL3^{ΔNLS}* in HeLa cells. Bar, 20 µm (top) and 5 µm (bottom). **e**, Spatiotemporal model derived from GBPL3 functional mutagenesis analysis. **f**, Combinatory GBPL3 interactome in *Arabidopsis* from co-IP candidates using Col-GBPL3-Flag plants under basal conditions and publicly available data sets (<http://plants.proteincomplexes.org/>). Node size denotes degree of protein–protein interactions. Classes of GBPL3 interactors grouped by colour-coding. Bracket denotes Mediator complex interactions. **g**, Different subunits associated with each region of the *Arabidopsis* Mediator complex (head [yellow], middle [green] and tail [blue] modules) and CDK8 kinase module. **h**, Line profile (colocalization) of fluorescence intensity for CDK8, MED15, MED19a and MED21 co-expressed with GBPL3 in (Fig. 4b). These head, middle and tail Mediator subunits directly overlap and interact with GBPL3 in leaf cell PPI profiling. CDK8 is excluded and surrounds GBPL3, as seen in line profiling. **i**, Effects of digitonin (10 µg/ml), digitonin plus 1,6-hexanediol (Hex, 5%), DRB (100 µM) and JQ1 (1 µM) on GBPL3 LLPS in live HeLa cells 2 h after treatment ($n = 30$ biologically independent cells/treatment). One-way ANOVA test with Bonferroni post hoc correction.

Source data

Supplementary information

Supplementary Figure 1

This file contains the gel source data.

Reporting Summary

Supplementary Table 1

NLS sequences of candidate nuclear IDPs (only one NLS is shown).

Supplementary Table 2

Gene family classification of candidate nuclear IDPs.

Supplementary Table 3

Domain accretion of plant GBPLs uncovered from NCBI.

Supplementary Table 4

Differentially expressed genes in GBPL3-OX plants compared with WT (padj-value < 0.05 and log₂(Fold change) > 1.5).

Supplementary Table 5

Differentially expressed genes in *gbpl1-1* plants compared with WT (padj-value < 0.05 and log₂(Fold change) > 1.5).

Supplementary Table 6

Reported mediator activities in *Arabidopsis* immunity.

Supplementary Table 7

A list of primers used in this study.

Peer Review File

Video 1 : Live cell imaging of *in situ* formation of GBPL3 nuclear condensates (event 1).

Soil-grown *gbpl3-3/35S::EGFP-GBPL3* plants were treated with 0.5 mM SA and imaging of *in situ* GBPL3 condensates formation in leaf nuclei was performed 5 h after treatment. Frame interval, 15 s. Bar, 2 μ m.

Video 2 : Live cell imaging of *in situ* formation of GBPL3 nuclear condensates (event 2).

Soil-grown *gbpl3-3/35S::EGFP-GBPL3* plants were treated with 0.5 mM SA and imaging of *in situ* GBPL3 condensates formation in leaf nuclei was performed 5 h after treatment. Frame interval, 10 s. Bar, 2 μ m.

Video 3 : Live cell imaging of *in situ* formation of GBPL3 nuclear condensates (event 3, GFP channel).

Soil-grown *gbpl3-3/35S::EGFP-GBPL3* plants were treated with 0.5 mM SA and imaging of *in situ* GBPL3 condensates formation in leaf guard cell nuclei was performed 5 h after treatment. Frame interval, 10 s. Bar, 2 μ m.

Video 4 : Live cell imaging of *in situ* formation of GBPL3 nuclear condensates (event 3, merged channels).

Soil-grown *gbpl3-3/35S::EGFP-GBPL3* plants were treated with 0.5 mM SA and imaging of *in situ* GBPL3 condensates formation in leaf guard cell nuclei was performed 5 h after treatment. Frame interval, 10 s. Bar, 2 μ m.

Video 5 : Live cell imaging of fusion events of GDACs in *Arabidopsis*.

Confocal imaging (GFP channel) of GBPL3 condensates fusion (arrows) was performed in 10 d-old *Arabidopsis* cotyledon guard cells expressing *EGFP-GBPL3*. Frame interval, 5 s. Bar, 5 μ m.

Video 6

: 3D tomographic reconstruction of cryo-ET analysis of GDACs. Scale bar, 200 nm.

Video 7 : 3D tomographic reconstruction and overlay of the segmented structures.

Ribosomes and vesicles are evident in the cytoplasm whereas GDAC is detected only in the nucleoplasm region. NE, Nuclear envelope. NPC, Nuclear pore complex.

Source data

[Source Data Fig. 1](#)

[Source Data Fig. 2](#)

[Source Data Fig. 3](#)

[Source Data Fig. 4](#)

[Source Data Extended Data Fig. 2](#)

[Source Data Extended Data Fig. 3](#)

[Source Data Extended Data Fig. 4](#)

[Source Data Extended Data Fig. 5](#)

[Source Data Extended Data Fig. 6](#)

[Source Data Extended Data Fig. 9](#)

[Source Data Extended Data Fig. 10](#)

[Source Data Extended Data Fig. 11](#)

Rights and permissions

[Reprints and Permissions](#)

About this article



Check for
updates

Cite this article

Huang, S., Zhu, S., Kumar, P. *et al.* A phase-separated nuclear GBPL circuit controls immunity in plants. *Nature* **594**, 424–429 (2021).
<https://doi.org/10.1038/s41586-021-03572-6>

[Download citation](#)

- Received: 10 October 2020
- Accepted: 21 April 2021
- Published: 26 May 2021
- Issue Date: 17 June 2021
- DOI: <https://doi.org/10.1038/s41586-021-03572-6>

Comments

By submitting a comment you agree to abide by our [Terms](#) and [Community Guidelines](#). If you find something abusive or that does not comply with our terms or guidelines please flag it as inappropriate.

[Access through your institution](#)

[Change institution](#)

[Buy or subscribe](#)

Advertisement

This article was downloaded by **calibre** from <https://www.nature.com/articles/s41586-021-03572-6>

| [Section menu](#) | [Main menu](#) |

- Article
- [Published: 02 June 2021](#)

NOTUM from *Apc*-mutant cells biases clonal competition to initiate cancer

- [Dustin J. Flanagan](#)¹,
- [Nalle Penttikä](#) [ORCID: orcid.org/0000-0003-3578-1073](#)^{2,3},
- [Kalle Luopajarvi](#)^{2,3},
- [Nicky J. Willis](#) [ORCID: orcid.org/0000-0003-3245-5280](#)⁴,
- [Kathryn Gilroy](#)^{1,5},
- [Alexander P. Raven](#)^{1,5},
- [Lynn McGarry](#) [ORCID: orcid.org/0000-0002-7055-2615](#)¹,
- [Johanna I. Englund](#) [ORCID: orcid.org/0000-0001-9637-6843](#)^{2,3},
- [Anna T. Webb](#)⁶,
- [Sandra Scharaw](#) [ORCID: orcid.org/0000-0001-9428-3213](#)⁶,
- [Nadia Nasreddin](#) [ORCID: orcid.org/0000-0002-3025-6213](#)⁷,
- [Michael C. Hodder](#)^{1,8},
- [Rachel A. Ridgway](#) [ORCID: orcid.org/0000-0003-0198-8244](#)¹,
- [Emma Minnee](#)¹ nAff17,
- [Nathalie Sphyris](#)¹,
- [Ella Gilchrist](#) [ORCID: orcid.org/0000-0003-3972-4121](#)^{1,8},
- [Arafath K. Najumudeen](#) [ORCID: orcid.org/0000-0002-3764-5721](#)¹,
- [Beatrice Romagnolo](#)⁹,
- [Christine Perret](#) [ORCID: orcid.org/0000-0003-4710-7051](#)⁹,
- [Ann C. Williams](#) [ORCID: orcid.org/0000-0002-6009-7137](#)¹⁰,
- [Hans Clevers](#) [ORCID: orcid.org/0000-0002-3077-5582](#)^{5,11},
- [Pirjo Nummela](#) [ORCID: orcid.org/0000-0002-2768-8816](#)¹²,
- [Marianne Lähde](#)^{13,14},

- [Kari Alitalo](#) [ORCID: orcid.org/0000-0002-7331-0902](#)^{13,14},
- [Ville Hietakangas](#)^{2,3},
- [Ann Hedley](#)¹,
- [William Clark](#)¹,
- [Colin Nixon](#) [ORCID: orcid.org/0000-0002-8085-2160](#)¹,
- [Kristina Kirschner](#) [ORCID: orcid.org/0000-0001-7607-8670](#)⁸,
- [E. Yvonne Jones](#) [ORCID: orcid.org/0000-0002-3834-1893](#)¹⁵,
- [Ari Ristimäki](#)¹²,
- [Simon J. Leedham](#)⁷,
- [Paul V. Fish](#)^{4,16},
- [Jean-Paul Vincent](#) [ORCID: orcid.org/0000-0003-2305-5744](#)¹⁶,
- [Pekka Katajisto](#) [ORCID: orcid.org/0000-0002-3033-4189](#)^{2,3,6} &
- [Owen J. Sansom](#) [ORCID: orcid.org/0000-0001-9540-3010](#)^{1,5,8}

[Nature](#) volume **594**, pages 430–435 (2021) [Cite this article](#)

- 7547 Accesses
- 1 Citations
- 187 Altmetric
- [Metrics details](#)

Subjects

- [Cancer stem cells](#)
- [Colon cancer](#)
- [Growth factor signalling](#)
- [Intestinal stem cells](#)

Abstract

The tumour suppressor *APC* is the most commonly mutated gene in colorectal cancer. Loss of *Apc* in intestinal stem cells drives the formation of adenomas in mice via increased WNT signalling¹, but reduced secretion

of WNT ligands increases the ability of *Apc*-mutant intestinal stem cells to colonize a crypt (known as fixation)². Here we investigated how *Apc*-mutant cells gain a clonal advantage over wild-type counterparts to achieve fixation. We found that *Apc*-mutant cells are enriched for transcripts that encode several secreted WNT antagonists, with *Notum* being the most highly expressed. Conditioned medium from *Apc*-mutant cells suppressed the growth of wild-type organoids in a NOTUM-dependent manner. Furthermore, NOTUM-secreting *Apc*-mutant clones actively inhibited the proliferation of surrounding wild-type crypt cells and drove their differentiation, thereby outcompeting crypt cells from the niche. Genetic or pharmacological inhibition of NOTUM abrogated the ability of *Apc*-mutant cells to expand and form intestinal adenomas. We identify NOTUM as a key mediator during the early stages of mutation fixation that can be targeted to restore wild-type cell competitiveness and provide preventative strategies for people at a high risk of developing colorectal cancer.

Access options

Subscribe to Journal

Get full journal access for 1 year

\$199.00

only \$3.90 per issue

[Subscribe](#)

All prices are NET prices.

VAT will be added later in the checkout.

Tax calculation will be finalised during checkout.

Rent or Buy article

Get time limited or full article access on ReadCube.

from \$8.99

[Rent or Buy](#)

All prices are NET prices.

Additional access options:

- [Log in](#)
- [Access through your institution](#)
- [Learn about institutional subscriptions](#)

Fig. 1: *Apc*-mutant cells impair the growth of WT ISCs via NOTUM.

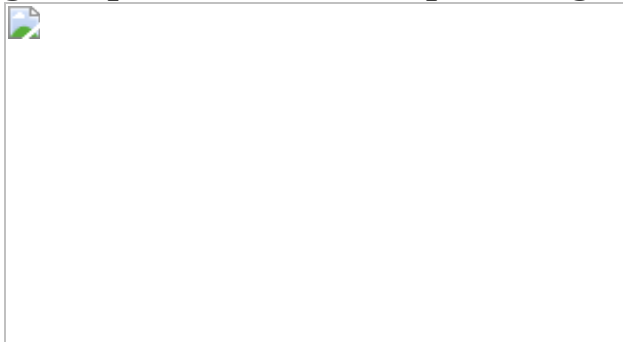


Fig. 2: NOTUM is required for *Apc*-mutant fixation in vivo.

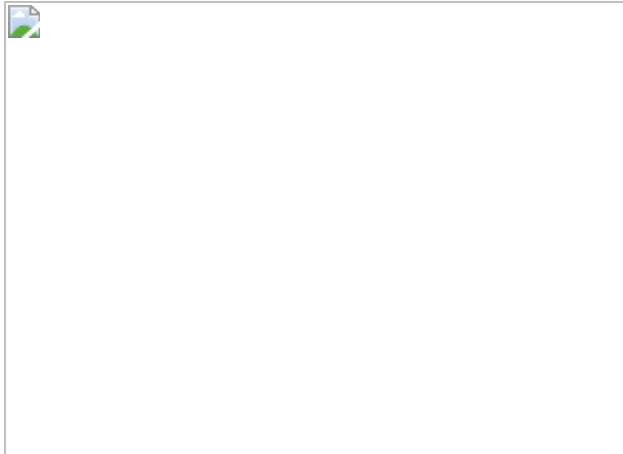


Fig. 3: NOTUM inhibits cell proliferation and drives differentiation of WT ISCs.

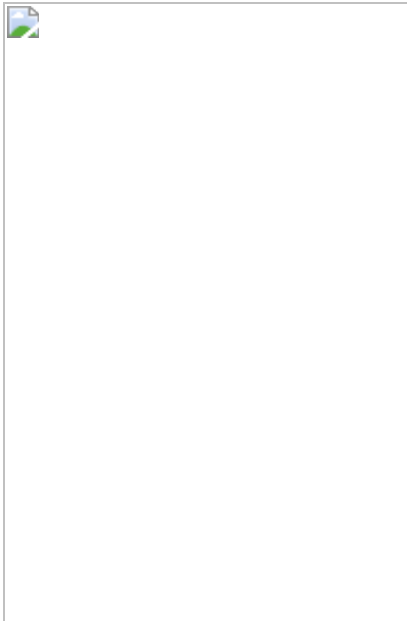
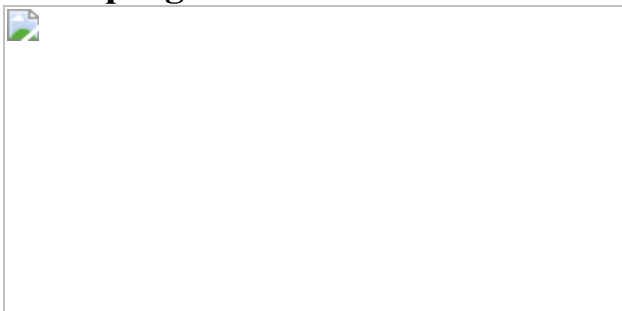


Fig. 4: Inhibition of NOTUM limits *Apc*-mutant fixation and intestinal tumour progression.



Data availability

The RNA sequencing data generated in this study are publicly available through the Gene Expression Omnibus (GEO) with the accession code [GSE167008](#). All other data are available from the corresponding authors on reasonable request. [Source data](#) are provided with this paper.

References

1. 1.

- Barker, N. et al. Crypt stem cells as the cells-of-origin of intestinal cancer. *Nature* **457**, 608–611 (2009).

[ADS](#) [CAS](#) [Article](#) [Google Scholar](#)

2. 2.

Huels, D. J. et al. Wnt ligands influence tumour initiation by controlling the number of intestinal stem cells. *Nat. Commun.* **9**, 1132 (2018).

[ADS](#) [CAS](#) [Article](#) [Google Scholar](#)

3. 3.

Powell, S. M. et al. APC mutations occur early during colorectal tumorigenesis. *Nature* **359**, 235–237 (1992).

[ADS](#) [CAS](#) [Article](#) [Google Scholar](#)

4. 4.

Snippert, H. J. et al. Intestinal crypt homeostasis results from neutral competition between symmetrically dividing Lgr5 stem cells. *Cell* **143**, 134–144 (2010).

[CAS](#) [Article](#) [Google Scholar](#)

5. 5.

Vermeulen, L. et al. Defining stem cell dynamics in models of intestinal tumor initiation. *Science* **342**, 995–998 (2013).

[ADS](#) [CAS](#) [Article](#) [Google Scholar](#)

6. 6.

Snippert, H. J., Schepers, A. G., van Es, J. H., Simons, B. D. & Clevers, H. Biased competition between Lgr5 intestinal stem cells driven by oncogenic mutation induces clonal expansion. *EMBO Rep.* **15**, 62–69 (2014).

[CAS](#) [Article](#) [Google Scholar](#)

7. 7.

Morin, P. J. et al. Activation of β -catenin–Tcf signalling in colon cancer by mutations in β -catenin or APC. *Science* **275**, 1787–1790 (1997).

[CAS](#) [Article](#) [Google Scholar](#)

8. 8.

Cammareri, P. et al. TGF β pathway limits dedifferentiation following WNT and MAPK pathway activation to suppress intestinal tumourigenesis. *Cell Death Differ.* **24**, 1681–1693 (2017).

[CAS](#) [Article](#) [Google Scholar](#)

9. 9.

Moser, A. R., Pitot, H. C. & Dove, W. F. A dominant mutation that predisposes to multiple intestinal neoplasia in the mouse. *Science* **247**, 322–324 (1990).

[ADS](#) [CAS](#) [Article](#) [Google Scholar](#)

10. 10.

Kakugawa, S. et al. Notum deacylates Wnt proteins to suppress signalling activity. *Nature* **519**, 187–192 (2015).

[ADS](#) [CAS](#) [Article](#) [Google Scholar](#)

11. 11.

Pentimikko, N. et al. Notum produced by Paneth cells attenuates regeneration of aged intestinal epithelium. *Nature* **571**, 398–402 (2019).

[CAS](#) [Article](#) [Google Scholar](#)

12. 12.

Barker, N. et al. Identification of stem cells in small intestine and colon by marker gene Lgr5. *Nature* **449**, 1003–1007 (2007).

[ADS](#) [CAS](#) [Article](#) [Google Scholar](#)

13. 13.

Vincent, J. P., Kolahgar, G., Gagliardi, M. & Piddini, E. Steep differences in wingless signaling trigger Myc-independent competitive cell interactions. *Dev. Cell* **21**, 366–374 (2011).

[CAS](#) [Article](#) [Google Scholar](#)

14. 14.

van Neerven, S. M. et al. *Apc*-mutant cells act as supercompetitors in intestinal tumour initiation. *Nature*, <https://doi.org/10.1038/s41586-021-03558-4> (2021).

15. 15.

Tarver, J. E. Jr et al. Stimulation of cortical bone formation with thienopyrimidine based inhibitors of Notum pectinacetylesterase. *Bioorg. Med. Chem. Lett.* **26**, 1525–1528 (2016).

[CAS](#) [Article](#) [Google Scholar](#)

16. 16.

Brommage, R. et al. NOTUM inhibition increases endocortical bone formation and bone strength. *Bone Res.* **7**, 2 (2019).

[CAS](#) [Article](#) [Google Scholar](#)

17. 17.

Canal, F. et al. Generation of mice with hepatocyte-specific conditional deletion of Notum. *PLoS ONE* **11**, e0150997 (2016).

[Article](#) [Google Scholar](#)

18. 18.

Blache, P. et al. SOX9 is an intestine crypt transcription factor, is regulated by the Wnt pathway, and represses the CDX2 and MUC2 genes. *J. Cell Biol.* **166**, 37–47 (2004).

[CAS](#) [Article](#) [Google Scholar](#)

19. 19.

Roche, K. C. et al. SOX9 maintains reserve stem cells and preserves radioresistance in mouse small intestine. *Gastroenterology* **149**, 1553–1563.e10 (2015).

[CAS](#) [Article](#) [Google Scholar](#)

20. 20.

Kleeman, S. O. et al. Exploiting differential Wnt target gene expression to generate a molecular biomarker for colorectal cancer stratification. *Gut* **69**, 1092–1103 (2020).

[CAS](#) [Article](#) [Google Scholar](#)

21. 21.

Hao, H. X. et al. ZNRF3 promotes Wnt receptor turnover in an R-spondin-sensitive manner. *Nature* **485**, 195–200 (2012).

[ADS](#) [CAS](#) [Article](#) [Google Scholar](#)

22. 22.

Koo, B. K. et al. Tumour suppressor RNF43 is a stem-cell E3 ligase that induces endocytosis of Wnt receptors. *Nature* **488**, 665–669 (2012).

[ADS](#) [CAS](#) [Article](#) [Google Scholar](#)

23. 23.

Moreno, E. & Basler, K. dMyc transforms cells into super-competitors. *Cell* **117**, 117–129 (2004).

[CAS](#) [Article](#) [Google Scholar](#)

24. 24.

el Marjou, F. et al. Tissue-specific and inducible Cre-mediated recombination in the gut epithelium. *Genesis* **39**, 186–193 (2004).

[CAS](#) [Article](#) [Google Scholar](#)

25. 25.

Shibata, H. et al. Rapid colorectal adenoma formation initiated by conditional targeting of the Apc gene. *Science* **278**, 120–123 (1997).

[CAS](#) [Article](#) [Google Scholar](#)

26. 26.

Pollard, P. et al. The Apc 1322T mouse develops severe polyposis associated with submaximal nuclear β-catenin expression. *Gastroenterology* **136**, 2204–2213.e13 (2009).

[CAS](#) [Article](#) [Google Scholar](#)

27. 27.

Harada, N. et al. Intestinal polyposis in mice with a dominant stable mutation of the β-catenin gene. *EMBO J.* **18**, 5931–5942 (1999).

[CAS](#) [Article](#) [Google Scholar](#)

28. 28.

Madisen, L. et al. A robust and high-throughput Cre reporting and characterization system for the whole mouse brain. *Nat. Neurosci.* **13**, 133–140 (2010).

[CAS](#) [Article](#) [Google Scholar](#)

29. 29.

Takeuchi, O. et al. Essential role of BAX,BAK in B cell homeostasis and prevention of autoimmune disease. *Proc. Natl Acad. Sci. USA* **102**, 11272–11277 (2005).

[ADS](#) [CAS](#) [Article](#) [Google Scholar](#)

30. 30.

Midgley, R. S. et al. Phase III randomized trial assessing rofecoxib in the adjuvant setting of colorectal cancer: final results of the VICTOR trial. *J. Clin. Oncol.* **28**, 4575–4580 (2010).

[CAS](#) [Article](#) [Google Scholar](#)

31. 31.

Sato, T. et al. Single Lgr5 stem cells build crypt-villus structures in vitro without a mesenchymal niche. *Nature* **459**, 262–265 (2009).

[ADS](#) [CAS](#) [Article](#) [Google Scholar](#)

32. 32.

Schmidt, S. et al. A MYC–GCN2–eIF2 α negative feedback loop limits protein synthesis to prevent MYC-dependent apoptosis in colorectal cancer. *Nat. Cell Biol.* **21**, 1413–1424 (2019).

[CAS](#) [Article](#) [Google Scholar](#)

33. 33.

Gay, D. M. et al. Loss of BCL9/9l suppresses Wnt driven tumourigenesis in models that recapitulate human cancer. *Nat. Commun.* **10**, 723 (2019).

[ADS](#) [CAS](#) [Article](#) [Google Scholar](#)

[Download references](#)

Acknowledgements

We thank the Core Services and Advanced Technologies at the Cancer Research UK Beatson Institute (C596/A17196 and A31287), and particularly the Biological Services Unit, Histology Service and Molecular Technologies; members of the Sansom and Katajisto laboratories for discussions of the data and manuscript; and BRC Oxford for supplying patient material. O.J.S. and his laboratory members were supported by Cancer Research UK (A28223, A21139, A12481 and A17196). D.J.F. and M.C.H. were supported by the UK Medical Research Council (MR/R017247/1 and MR/J50032X/1, respectively). SpeciCancer CRUK Grand Challenge (C7932/A29055) is funded by Cancer Research UK and the Mark Foundation for Cancer Research. P.K. and his laboratory members were supported by the Academy of Finland Centre of Excellence MetaStem (266869, 304591 and 320185), the ERC Starting Grant 677809, the Swedish Research Council 2018-03078, the Cancerfonden 190634, the Jane and Aatos Erkko Foundation and the Cancer Foundation Finland. N.P. was supported by the Finnish Cultural Foundation, the Biomedicum Helsinki Foundation, the Orion Research Foundation sr and The Paulo Foundation. P.V.F. was supported by Alzheimer's Research UK and The Francis Crick Institute. The ARUK UCL Drug Discovery Institute receives its core funding from Alzheimer's Research UK (520909). The Francis Crick Institute receives its core funding from Cancer Research UK (FC001002), the UK Medical Research Council (FC001002) and the Wellcome Trust (FC001002).

Author information

Author notes

1. Emma Minnee

Present address: Vrije Universiteit Amsterdam, Amsterdam, The Netherlands

Affiliations

1. Cancer Research UK Beatson Institute, Glasgow, UK

Dustin J. Flanagan, Kathryn Gilroy, Alexander P. Raven, Lynn Mcgarry, Michael C. Hodder, Rachel A. Ridgway, Emma Minnee, Nathalie Sphyris, Ella Gilchrist, Arafath K. Najumudeen, Ann Hedley, William Clark, Colin Nixon & Owen J. Sansom

2. Institute of Biotechnology, HiLIFE, University of Helsinki, Helsinki, Finland

Nalle Penttämäkki, Kalle Luopajarvi, Johanna I. Englund, Ville Hietakangas & Pekka Katajisto

3. Molecular and Integrative Bioscience Research Programme, Faculty of Biological and Environmental Sciences, University of Helsinki, Helsinki, Finland

Nalle Penttämäkki, Kalle Luopajarvi, Johanna I. Englund, Ville Hietakangas & Pekka Katajisto

4. Alzheimer's Research UK UCL Drug Discovery Institute, University College London, London, UK

Nicky J. Willis & Paul V. Fish

5. SpeciCancer CRUK Grand Challenge Team (C7932/A29055), Department of Genetics, Harvard Medical School, Boston, MA, USA

Kathryn Gilroy, Alexander P. Raven, Hans Clevers & Owen J. Sansom

6. Department of Cell and Molecular Biology (CMB), Karolinska Institutet, Stockholm, Sweden

Anna T. Webb, Sandra Scharaw & Pekka Katajisto

7. Intestinal Stem Cell Biology Lab, Wellcome Trust Centre Human Genetics, University of Oxford, Oxford, UK

Nadia Nasreddin & Simon J. Leedham

8. Institute of Cancer Sciences, University of Glasgow, Glasgow, UK

Michael C. Hodder, Ella Gilchrist, Kristina Kirschner & Owen J. Sansom

9. Université de Paris, Institut Cochin, INSERM, CNRS, Paris, France

Beatrice Romagnolo & Christine Perret

10. Colorectal Tumour Biology Group, School of Cellular and Molecular Medicine, Faculty of Life Sciences, University of Bristol, Bristol, UK

Ann C. Williams

11. Hubrecht Institute, Royal Netherlands Academy of Arts and Sciences, Utrecht, The Netherlands

Hans Clevers

12. Department of Pathology, Applied Tumor Genomics, Research Programs Unit and HUSLAB, HUS Diagnostic Center, University of Helsinki and Helsinki University Hospital, Helsinki, Finland

Pirjo Nummela & Ari Ristimäki

13. Translational Cancer Medicine Program, Faculty of Medicine, University of Helsinki, Helsinki, Finland

Marianne Lähde & Kari Alitalo

14. Wihuri Research Institute, University of Helsinki, Helsinki, Finland

Marianne Lähde & Kari Alitalo

15. Division of Structural Biology, Wellcome Centre for Human Genetics,
University of Oxford, Oxford, UK

E. Yvonne Jones

16. The Francis Crick Institute, London, UK

Paul V. Fish & Jean-Paul Vincent

Authors

1. Dustin J. Flanagan

[View author publications](#)

You can also search for this author in [PubMed](#) [Google Scholar](#)

2. Nalle Penttilä

[View author publications](#)

You can also search for this author in [PubMed](#) [Google Scholar](#)

3. Kalle Luopajarvi

[View author publications](#)

You can also search for this author in [PubMed](#) [Google Scholar](#)

4. Nicky J. Willis

[View author publications](#)

You can also search for this author in [PubMed](#) [Google Scholar](#)

5. Kathryn Gilroy

[View author publications](#)

You can also search for this author in [PubMed](#) [Google Scholar](#)

6. Alexander P. Raven

[View author publications](#)

You can also search for this author in [PubMed](#) [Google Scholar](#)

7. Lynn McGarry

[View author publications](#)

You can also search for this author in [PubMed](#) [Google Scholar](#)

8. Johanna I. Englund

[View author publications](#)

You can also search for this author in [PubMed](#) [Google Scholar](#)

9. Anna T. Webb

[View author publications](#)

You can also search for this author in [PubMed](#) [Google Scholar](#)

10. Sandra Scharaw

[View author publications](#)

You can also search for this author in [PubMed](#) [Google Scholar](#)

11. Nadia Nasreddin

[View author publications](#)

You can also search for this author in [PubMed](#) [Google Scholar](#)

12. Michael C. Hodder

[View author publications](#)

You can also search for this author in [PubMed](#) [Google Scholar](#)

13. Rachel A. Ridgway

[View author publications](#)

You can also search for this author in [PubMed](#) [Google Scholar](#)

14. Emma Minnee

[View author publications](#)

You can also search for this author in [PubMed](#) [Google Scholar](#)

15. Nathalie Sphyris

[View author publications](#)

You can also search for this author in [PubMed](#) [Google Scholar](#)

16. Ella Gilchrist

[View author publications](#)

You can also search for this author in [PubMed](#) [Google Scholar](#)

17. Arafath K. Najumudeen

[View author publications](#)

You can also search for this author in [PubMed](#) [Google Scholar](#)

18. Beatrice Romagnolo

[View author publications](#)

You can also search for this author in [PubMed](#) [Google Scholar](#)

19. Christine Perret

[View author publications](#)

You can also search for this author in [PubMed](#) [Google Scholar](#)

20. Ann C. Williams

[View author publications](#)

You can also search for this author in [PubMed](#) [Google Scholar](#)

21. Hans Clevers

[View author publications](#)

You can also search for this author in [PubMed](#) [Google Scholar](#)

22. Pirjo Nummela

[View author publications](#)

You can also search for this author in [PubMed](#) [Google Scholar](#)

23. Marianne Lähde

[View author publications](#)

You can also search for this author in [PubMed](#) [Google Scholar](#)

24. Kari Alitalo

[View author publications](#)

You can also search for this author in [PubMed](#) [Google Scholar](#)

25. Ville Hietakangas

[View author publications](#)

You can also search for this author in [PubMed](#) [Google Scholar](#)

26. Ann Hedley

[View author publications](#)

You can also search for this author in [PubMed](#) [Google Scholar](#)

27. William Clark

[View author publications](#)

You can also search for this author in [PubMed](#) [Google Scholar](#)

28. Colin Nixon

[View author publications](#)

You can also search for this author in [PubMed](#) [Google Scholar](#)

29. Kristina Kirschner

[View author publications](#)

You can also search for this author in [PubMed](#) [Google Scholar](#)

30. E. Yvonne Jones

[View author publications](#)

You can also search for this author in [PubMed](#) [Google Scholar](#)

31. Ari Ristimäki

[View author publications](#)

You can also search for this author in [PubMed](#) [Google Scholar](#)

32. Simon J. Leedham

[View author publications](#)

You can also search for this author in [PubMed](#) [Google Scholar](#)

33. Paul V. Fish

[View author publications](#)

You can also search for this author in [PubMed](#) [Google Scholar](#)

34. Jean-Paul Vincent

[View author publications](#)

You can also search for this author in [PubMed](#) [Google Scholar](#)

35. Pekka Katajisto

[View author publications](#)

You can also search for this author in [PubMed](#) [Google Scholar](#)

36. Owen J. Sansom

[View author publications](#)

You can also search for this author in [PubMed](#) [Google Scholar](#)

Contributions

D.J.F., N.P., P.K. and O.J.S. designed and interpreted the results of all experiments. D.J.F., N.P., K.L., A.P.R., L.M., J.I.E., A.T.W., S.S., N.N., E.G., E.M., M.C.H. and R.A.R. performed all of the experiments and analysed the results. D.J.F. performed and analysed the organoid experiments. K.G., K.K., A.H. and W.C. processed and analysed the RNA sequencing data. C.N. performed ISH. N.S. provided advice on manuscript preparation. A.K.N., N.J.W., B.R., C.P., A.C.W., H.C., P.V.F., P.N., M.L., V.H., K.A., A.R., S.J.L., E.Y.J. and J.-P.V. provided advice and reagents. D.J.F., N.S., N.P., P.K. and O.J.S. wrote the paper.

Corresponding authors

Correspondence to [Pekka Katajisto](#) or [Owen J. Sansom](#).

Ethics declarations

Competing interests

The authors declare no competing interests.

Additional information

Peer review information *Nature* thanks James DeGregori, Toshiro Sato and the other, anonymous, reviewer(s) for their contribution to the peer review of this work. Peer reviewer reports are available.

Publisher's note Springer Nature remains neutral with regard to jurisdictional claims in published maps and institutional affiliations.

Extended data figures and tables

[Extended Data Fig. 1 Notum secreted by *Apc*-mutant clones inhibits WT organoid growth.](#)

a, Volcano plot of significantly differentially expressed Wnt-target genes in *Apc*-mutant (*VilCre^{ER}*; *Apc*^{fl/+}) tumour tissue compared to WT small intestine ($n = 3$ WT mice, $n = 5$ *VilCre^{ER}*; *Apc*^{fl/+} mice). This is the same data set as in Fig. 1a but with different Wnt-target genes highlighted (green dots) using Wald test (two-tailed). **b**, *Notum*-ISH shows high levels of *Notum* expression in the intestine of multiple Wnt-driven tumour models of the indicated genotypes (*Ctnnbl*^{Ex3/+}, 30 days; *Apc*^{1322T/+}, 98 days; *Apc*^{Min/+}, 125 days). Sections from $n = 4$ mice per genotype were stained. Scale bar, 200 μm . **c**, ISH of serial en face sections of intestinal tissue from *Lgr5Cre^{ER}*; *Apc*^{fl/fl} mice 10 days after tamoxifen induction. BaseScope ISH for recombined *Apc* (*Apc*^{Ex14}-ISH) and *Notum* (*Notum*-ISH) shows exclusive expression of *Notum* in cells that have recombined *Apc* (cells lacking pink RNA dots in right panel). The boxed areas show a close-up of *Notum*⁺ *Apc*-mutant crypts, demarcated by a dashed line. Sections from $n = 4$ mice per genotype were stained. Scale bar, 20 μm . **d**, *Notum*-ISH timecourse (days 6, 28, 60 and >100) after tamoxifen induction in *Lgr5Cre^{ER}*; *Apc*^{fl/fl} mice shows specific *Notum* expression in progressively dysplastic epithelium. Sections from $n = 4$ mice per genotype were stained. Scale bar, 100 μm . **e**, Quantification of the number of crypt domains per WT organoid following indicated treatments. Each data point represents a single mouse; $n = 6$ mice. **f**, Relative WT organoid viability measured at passage 3 following treatments as indicated. $n = 5$ mice per condition. **g**, Schematic illustrating the mouse breeding scheme to generate *Lgr5Cre^{ER}*; *Apc*^{fl/fl}; *Notum*^{fl/fl} mice for treatment of WT organoids with *Apc*^{-/-}; *Notum*^{-/-} CM (*Apc*^{-/-}; *Notum*^{-/-} CM) (top). Representative images of WT organoids grown in *Apc*^{-/-}; *Notum*^{-/-} CM for 5 days and supplemented with recombinant NOTUM (bottom). Treatments were repeated twice on WT organoids derived from $n = 3$ mice. Scale bar, 200 μm . Data are mean \pm s.e.m. In e, f, Mann–Whitney two-tailed *U*-test; *P* values are shown in the corresponding panels.

Source data

Extended Data Fig. 2 *Apc*-mutant cells upregulate negative regulators of Wnt signalling.

a, Raw sequence reads for transcripts encoding Wnt-negative regulators, *Wif1* and *Dkk3*, in *Apc*-mutant (*VilCre^{ER};Apc^{fl/+}*) tumour tissue compared to WT small intestine ($n = 3$ WT mice, $n = 5$ *VilCre^{ER};Apc^{fl/+}* mice). **b**, Representative ISH for *Wif1* and *Dkk3* in *Lgr5Cre^{ER};Apc^{fl/fl}* tumour (top panels) and WT small intestine (bottom panels). $n = 3$ mice. Images of mice shown aged 3–4 months. The boxed areas show close-ups of WT crypts. Scale bar, 200 μm . **c**, Quantification and representative images of WT organoids, formed over multiple passages (P1, P2 and P3), during culture supplemented with recombinant WIF1, DKK3 and NOTUM. WT organoids treated with recombinant proteins were derived from $n = 3$ mice. Images taken at P2. Mann–Whitney one-tailed *U*-test. Scale bar, 200 μm . **d**, Quantitative PCR (qPCR) for Wnt antagonists expressed by tamoxifen-induced *Lgr5Cre^{ER};Apc^{fl/fl}* (*Notum^{+/+}*) and *Lgr5Cre^{ER};Apc^{fl/fl};Notum^{fl/fl}* (*Notum^{fl/fl}*) small intestinal organoids. $n = 4$ mice per genotype. **e**, qPCR for Wnt targets expressed in WT organoids 3 days following treatment with indicated recombinant Wnt antagonists. $n = 3$ mice per treatment. Mann–Whitney one-tailed *U*-test. **f**, Quantification of *VilCre^{ER};Apc^{fl/fl}* organoids 3 days after culture with recombinant WIF1, DKK3 and NOTUM. $n = 3$ mice per condition. **g**, Relative organoid viability and representative images of *VilCre^{ER};Apc^{fl/fl}* intestinal organoids treated with vehicle or NOTUMi for 3 days. $n = 3$ mice/condition. Scale bar, 100 μm . Data are mean \pm s.e.m. In **d**, Mann–Whitney two-tailed *U*-test; *P* values are shown in the corresponding panels.

Source data

Extended Data Fig. 3 Notum is required for *Apc*-mutant cells to form intestinal tumours.

a, Survival plot for *Lgr5Cre^{ER};Apc^{fl/fl};Notum^{+/+}* (*Notum^{+/+}*) and *Lgr5Cre^{ER};Apc^{fl/fl};Notum^{fl/fl}* (*Notum^{fl/fl}*) mice aged until clinical end point following induction with 0.15 mg tamoxifen. ($n = 10$ *Notum^{+/+}* mice, $n = 10$ *Notum^{fl/fl}* mice). $P = 0.12$, log-rank test. **b**, Total small intestinal tumour burden (area) per mouse from mice in **a** ($n = 10$ *Notum^{+/+}* mice, $n = 9$ *Notum^{fl/fl}* mice). **c**, Small intestinal tumour number per mouse from mice in **a** ($n = 10$ *Notum^{+/+}* mice, $n = 10$ *Notum^{fl/fl}* mice). **d**, Representative H&E

and *Notum*-ISH staining on serial sections from *Notum*^{+/+} and *Notum*^{fl/fl} mice in **a**. The asterisks denote intestinal adenomas. The boxed areas are close-ups of adenomas stained for *Notum*. Note that adenomas grow out as *Notum*-positive lesions in *Notum*^{fl/fl} mice, suggesting that retaining *Notum* confers a survival advantage during adenoma development. Scale bars, 200 μm . Data are mean \pm s.e.m. In, **b**, **c**, Mann–Whitney *U*-test; *P* values are shown in the corresponding panels.

[Source data](#)

Extended Data Fig. 4 Generation and characterization of novel *Notum* conditional knockout.

a, Schematic of the *Notum* locus and recombined *Notum*^c allele with relevant genome editing sites indicated. **b**, Southern blot analysis of embryonic stem (ES) cell *Notum*^c clones and WT genomic DNA showing successful recombination at the *Notum* locus (4.7-kb product). The 13.6-kb band and 4.7-kb band represent endogenous and recombined alleles, respectively (arrows). **c**, Schematic of tamoxifen treatment regimen and tissue analysis 7 and 14 d.p.i. of *Lgr5Cre^{ER};Apc*^{fl/fl}; *Notum*^{+/+} (*Notum*^{WT}) and *Lgr5Cre^{ER};Apc*^{fl/fl}; *Notum*^{c/c} (*Notum*^{cKO}) mice (top). Representative images of small intestinal sections stained for β -catenin from *Notum*^{WT} and *Notum*^{cKO} mice 14 days following induction with 120 mg/kg (3 mg) tamoxifen are also shown (bottom). The arrows indicate dysplastic crypts with nuclear β -catenin (magenta border). The boxed area shows a close-up of β -catenin⁺ crypts. Sections from $n = 4$ mice per genotype were stained. Scale bar, 50 μm . **d**, Representative agarose gel electrophoresis of products from conventional PCR showing relative recombination of *Apc*^{fl} and *Notum*^c alleles 5 days after tamoxifen induction. The 250-bp and 513-bp bands represent recombined *Apc* and *Notum*, respectively. For gel source data, see Supplementary Fig. 2. $n = 3$ mice. **e**, Quantification of small intestinal β -catenin⁺ lesions in *Notum*^{WT} and *Notum*^{cKO} mice, induced with 3 mg tamoxifen, and sampled at 7 and 14 d.p.i. $n = 4$ per genotype at 7 d.p.i; $n = 18$ *Notum*^{WT} mice and $n = 12$ *Notum*^{cKO} mice at 14 d.p.i. **f**, Quantification of large intestinal β -catenin⁺ lesions at 14 d.p.i ($n = 18$ *Notum*^{WT} mice, $n = 12$ *Notum*^{cKO} mice). **g**, Representative images of β -

catenin IHC depicting fully and partially fixed *Apc*-mutant crypts in *Notum*^{WT} and *Notum*^{cKO} mice, respectively (left). Mice were induced with 3 mg tamoxifen and sampled at 14 d.p.i ($n = 4$ per genotype). The ratio of fully to partially fixed crypts in *Notum*^{WT} and *Notum*^{cKO} mice is also shown (right). Scale bar, 100 μ m. **h**, Relative percentages of clonal crypt classification (clonal crypt phenotype) from mice described in **g**. **i**, Analysis of *Notum*^{WT} and *Notum*^{cKO} adenomas at 14 d.p.i. Representative confocal images (left). Ki67 (magenta), Lgr5–EGFP (green), nuclei (cyan), β -catenin (white) and adenomas (yellow dashed line). Quantification of *Lgr5*⁺ cell frequency within β -catenin⁺ *Apc*-mutant clones (middle). Proliferation of *Lgr5*⁺ and *Lgr5*⁻ *Apc*-mutant cells (β -catenin⁺) (right). $n = 5$ mice/genotype. Scale bar, 20 μ m. In the box plots, the line represents the median, the box shows the interquartile range and the whiskers represent the range. Data are mean \pm s.e.m. In **e–g, i**, Mann–Whitney two-tailed *U*-test; *P* values are shown in the corresponding panels.

Source data

Extended Data Fig. 5 Deletion of *Notum* does not disrupt intestinal homeostasis.

a, Schematic of the tamoxifen (TMX) treatment regimen and analysis of tissues from *Lgr5Cre^{ER};Notum^{c/c}* mice (top). Representative agarose gel electrophoresis of products from conventional PCR detecting alleles for non-recombined and recombined *Notum*^c (238 and 513 bp, respectively) in *Lgr5*^{hi} cells isolated from *Lgr5Cre^{ER};Notum^{c/c}* mice with or without tamoxifen induction (bottom). Cells were isolated from $n = 3$ mice/genotype per time point. **b**, H&E staining of WT (*Notum*^{WT}) and *Notum*^{cKO} tissue collected 8 months after tamoxifen induction. The right panels show regular crypt-villus architecture in both cohorts. Sections from $n = 4$ mice per genotype were stained. Scale bar, 5 mm. **c**, Cellular frequencies of crypt cells, analysed by flow cytometry, remain unchanged after *Notum* deletion (WT, $n = 5$; *Notum*^{cKO}, $n = 6$). ISCs (*Lgr5*^{hi}), transit-amplifying cells (*Lgr5*^{med} and *Lgr5*^{lo}), Paneth cells and enteroendocrine cells (Endo). For FACS gating strategy, see Supplementary Fig. 1. In the box plots, the line represents the median, the box shows the interquartile

range and the whiskers represent the range. **d**, Representative images and quantification of organoid regeneration (shown as the number of crypt domains per organoid) of WT and *Notum*^{cKO} (cKO) organoid cultures, (WT, $n = 3$; *Notum*^{cKO}, $n = 4$). Scale bar, 100 μm . **e**, Clonogenic growth of isolated Lgr5^{hi} cells is increased in *Notum*^{cKO} (cKO) compared to WT. Colonies were quantified 7 days post-seeding; $n = 3$ independent organoid lines per genotype. Mann–Whitney one-tailed *U*-test. Scale bar, 100 μm . Data are mean \pm s.e.m. In **d**, Mann–Whitney two-tailed *U*-test; *P* values are shown in the corresponding panels. Representative images taken at day 6 (**d**) and day 7 (**e**) of culture. For gel source data, see Supplementary Fig. 1.

[Source data](#)

Extended Data Fig. 6 Notum drives the elimination of WT cells from the crypt independent of apoptosis.

a, Quantification and representative confocal imaging of cleaved caspase-3⁺ cells (CC3) within clonal crypts and the surrounding non-mutant epithelium in *Notum*^{WT} and *Notum*^{cKO} mice at 14 d.p.i. $n = 4$ per genotype. Crypts adjacent (Adj.) to or remote (Rem.) from *Apc*-mutant (clone) crypts were scored as non-mutant epithelia. The red arrows indicate CC3⁺ cells (green) in areas of *Apc*-mutant clones (purple border) and surrounding epithelia. Scale bar, 50 μm . Data are mean \pm s.e.m.; Mann–Whitney two-tailed *U*-test.

[Source data](#)

Extended Data Fig. 7 Cells that escape *Notum* deletion upregulate *Wif1*, but not *Dkk3*.

a, Quantification of the relative percentage of *Notum*⁺ adenomas (as detected via *Notum*-ISH) in *VilCre*^{ER}; *Apc*^{Min/+}; *Notum*^{+/+} (+/+) and *VilCre*^{ER}; *Apc*^{Min/+}; *Notum*^{fl/fl} (fl/fl) mice aged 85 days. Mice were induced with 2 mg tamoxifen at 6 and 8 weeks of age. $n = 11$ *Notum*^{+/+} and $n = 8$ *Notum*^{fl/fl} mice. **b**, Representative RFP-IHC of *VilCre*^{ER}; *Apc*^{Min/+}; *tdTom*⁺ tumour tissue to show recombination efficiency at 85 days of age. Mice were induced with 2 mg tamoxifen at 6 and 8 weeks of age. The boxed area

shows a close-up of recombined (dark brown cells) and non-recombined (light brown cells) tumour epithelium from a single *VilCre^{ER};Apc^{Min/+};tdTom⁺* mouse. Sections from $n = 4$ mice were stained. Scale bar, 10 mm. **c**, Serial sections of intestinal tumour tissue stained via ISH for *Notum*, *Wifl* and *Dkk3* from two separate *VilCre^{ER};Apc^{Min/+};Notum^{fl/fl}* mice described in **a**. Note, *Wifl* is upregulated in *Notum*-negative epithelial cells (boxed area). Scale bar, 50 μm . Data are mean \pm s.e.m.

Source data

Extended Data Fig. 8 *Notum* is expressed by ligand-independent and not ligand-dependent tumours.

a, Relative percentages of clonal crypt classification (clonal crypt phenotype) from *Lgr5Cre^{ER};Apc^{fl/fl}* mice induced with 0.15 mg tamoxifen followed by twice-daily treatment with vehicle or NOTUMi (30 mg/kg) and sampled 21 days post-induction. $n = 4$ mice per treatment group. **b**, Quantification of β -catenin⁺ lesions from mice described in **a**. **c**, Representative examples of high, moderate and low *NOTUM* expression (as shown via ISH) within human colonic adenoma tissue. The arrows indicate single NOTUM-positive cells. Staining was performed on more than 10 patient samples. Scale bar, 20 μm . **d**, Representative *NOTUM* expression, as shown by fluorescent ISH (FISH) on human colonic adenoma tissue. Of note, *NOTUM* expression is minimally expressed in known RSPO1 fusion mutant adenoma tissue (traditional serrated adenoma (TSA)). Staining was performed on more than 10 patient samples. Scale bar, 50 μm . TVA, tubulovillous adenoma. **e**, Representative *Notum*-ISH and β -catenin-IHC on *VilCre^{ER};Rnf43^{fl/fl};Znrf3^{fl/fl}* mice 14 d.p.i. (2 mg tamoxifen). The boxed areas show close-ups of nuclear β -catenin⁺/*Notum*⁻ epithelium (right panels). Sections from $n = 4$ mice per genotype were stained. Scale bar, 50 μm . **f**, Quantification and representative images of WT organoids treated for 5 days with CM collected from *VilCre^{ER};Rnf43^{fl/fl};Znrf3^{fl/fl}* organoids ($R/Z^{-/-}$ CM) \pm recombinant NOTUM. $R/Z^{-/-}$ CM was collected from organoids derived from $n = 3$ mice. WT organoids treated with CM \pm NOTUM were derived from $n = 3$ mice. Treatments were repeated twice. Mann–Whitney

one-tailed U -test. Scale bar, 100 μm . Data are mean \pm s.e.m. In **b**, Mann–Whitney two-tailed U -test; P values are shown in the corresponding panels.

[Source data](#)

Supplementary information

[Supplementary Information](#)

This file includes Supplementary Figures 1-2 which contain the FACS gating strategy (Supplementary Fig. 1) and the uncropped scans of gel electrophoresis (Supplementary Fig. 2).

[Reporting Summary](#)

[Peer Review File](#)

Source data

[Source Data Fig. 1](#)

[Source Data Fig. 2](#)

[Source Data Fig. 3](#)

[Source Data Fig. 4](#)

[Source Data Extended Data Fig. 1](#)

[Source Data Extended Data Fig. 2](#)

[Source Data Extended Data Fig. 3](#)

[Source Data Extended Data Fig. 4](#)

[**Source Data Extended Data Fig. 5**](#)

[**Source Data Extended Data Fig. 6**](#)

[**Source Data Extended Data Fig. 7**](#)

[**Source Data Extended Data Fig. 8**](#)

Rights and permissions

[Reprints and Permissions](#)

About this article



Check for
updates

Cite this article

Flanagan, D.J., Pentimikko, N., Luopajarvi, K. *et al.* NOTUM from *Apc*-mutant cells biases clonal competition to initiate cancer. *Nature* **594**, 430–435 (2021). <https://doi.org/10.1038/s41586-021-03525-z>

[Download citation](#)

- Received: 05 March 2020
- Accepted: 07 April 2021
- Published: 02 June 2021
- Issue Date: 17 June 2021
- DOI: <https://doi.org/10.1038/s41586-021-03525-z>

Further reading

- [Apc-mutant cells act as supercompetitors in intestinal tumour initiation](#)

- Sanne M. van Neerven
- , Nina E. de Groot
- , Lisanne E. Nijman
- , Brendon P. Scicluna
- , Milou S. van Driel
- , Maria C. Lecca
- , Daniël O. Warmerdam
- , Vaishali Kakkar
- , Leandro F. Moreno
- , Felipe A. Vieira Braga
- , Delano R. Sanches
- , Prashanthi Ramesh
- , Sanne ten Hoorn
- , Arthur S. Aelvoet
- , Marouska F. van Boxel
- , Lianne Koens
- , Przemek M. Krawczyk
- , Jan Koster
- , Evelien Dekker
- , Jan Paul Medema
- , Douglas J. Winton
- , Maarten F. Bijlsma
- , Edward Morrissey
- , Nicolas L'Veillé
- & Louis Vermeulen

Nature (2021)

Comments

By submitting a comment you agree to abide by our [Terms](#) and [Community Guidelines](#). If you find something abusive or that does not comply with our terms or guidelines please flag it as inappropriate.

[Access through your institution](#)

[Change institution](#)

[Buy or subscribe](#)

Associated Content

[Cancer stem cells in the gut have a bad influence on neighbouring cells](#)

- Shi Biao Chia
- James DeGregori

Advertisement

This article was downloaded by **calibre** from <https://www.nature.com/articles/s41586-021-03525-z>

| [Section menu](#) | [Main menu](#) |

- Article
- [Published: 02 June 2021](#)

Apc-mutant cells act as supercompetitors in intestinal tumour initiation

- [Sanne M. van Neerven](#) [ORCID: orcid.org/0000-0003-2599-5756^{1,2}](#),
- [Nina E. de Groot^{1,2}](#),
- [Lisanne E. Nijman^{1,2}](#),
- [Brendon P. Scicluna^{3,4}](#),
- [Milou S. van Driel](#) [ORCID: orcid.org/0000-0002-3253-2971^{1,2}](#),
- [Maria C. Lecca^{1,2}](#),
- [Daniël O. Warmerdam](#) [ORCID: orcid.org/0000-0003-1606-7448^{1,2,5}](#),
- [Vaishali Kakkar^{1,2}](#),
- [Leandro F. Moreno^{1,2}](#),
- [Felipe A. Vieira Braga](#) [ORCID: orcid.org/0000-0003-0206-9258^{1,2}](#),
- [Delano R. Sanches^{1,2}](#),
- [Prashanthi Ramesh^{1,2}](#),
- [Sanne ten Hoorn^{1,2}](#),
- [Arthur S. Aelvoet⁶](#),
- [Marouska F. van Boxel](#) [ORCID: orcid.org/0000-0001-5845-1494^{1,2}](#),
- [Lianne Koens⁷](#),
- [Przemek M. Krawczyk⁸](#),
- [Jan Koster](#) [ORCID: orcid.org/0000-0002-0890-7585⁹](#),
- [Evelien Dekker⁶](#),
- [Jan Paul Medema^{1,2}](#),
- [Douglas J. Winton](#) [ORCID: orcid.org/0000-0001-6067-7927¹⁰](#),
- [Maarten F. Bijlsma^{1,2}](#),
- [Edward Morrissey](#) [ORCID: orcid.org/0000-0003-1021-5358¹¹](#),

- [Nicolas Léveillé^{1,2}](#) &
- [Louis Vermeulen](#) [ORCID: orcid.org/0000-0002-6066-789X^{1,2}](#)

[Nature](#) volume **594**, pages 436–441 (2021) [Cite this article](#)

- 7700 Accesses
- 1 Citations
- 147 Altmetric
- [Metrics details](#)

Subjects

- [Colorectal cancer](#)
- [Intestinal stem cells](#)

Abstract

A delicate equilibrium of WNT agonists and antagonists in the intestinal stem cell (ISC) niche is critical to maintaining the ISC compartment, as it accommodates the rapid renewal of the gut lining. Disruption of this balance by mutations in the tumour suppressor gene *APC*, which are found in approximately 80% of all human colon cancers, leads to unrestrained activation of the WNT pathway^{1,2}. It has previously been established that *Apc*-mutant cells have a competitive advantage over wild-type ISCs³. Consequently, *Apc*-mutant ISCs frequently outcompete all wild-type stem cells within a crypt, thereby reaching clonal fixation in the tissue and initiating cancer formation. However, whether the increased relative fitness of *Apc*-mutant ISCs involves only cell-intrinsic features or whether *Apc* mutants are actively involved in the elimination of their wild-type neighbours remains unresolved. Here we show that *Apc*-mutant ISCs function as bona fide supercompetitors by secreting WNT antagonists, thereby inducing differentiation of neighbouring wild-type ISCs. Lithium chloride prevented the expansion of *Apc*-mutant clones and the formation of adenomas by rendering wild-type ISCs insensitive to WNT antagonists.

through downstream activation of WNT by inhibition of GSK3 β . Our work suggests that boosting the fitness of healthy cells to limit the expansion of pre-malignant clones may be a powerful strategy to limit the formation of cancers in high-risk individuals.

Access options

Subscribe to Journal

Get full journal access for 1 year

\$199.00

only \$3.90 per issue

[Subscribe](#)

All prices are NET prices.

VAT will be added later in the checkout.

Tax calculation will be finalised during checkout.

Rent or Buy article

Get time limited or full article access on ReadCube.

from \$8.99

[Rent or Buy](#)

All prices are NET prices.

Additional access options:

- [Log in](#)
- [Access through your institution](#)
- [Learn about institutional subscriptions](#)

Fig. 1: Apc-mutant cells actively impair outgrowth of WT organoids.

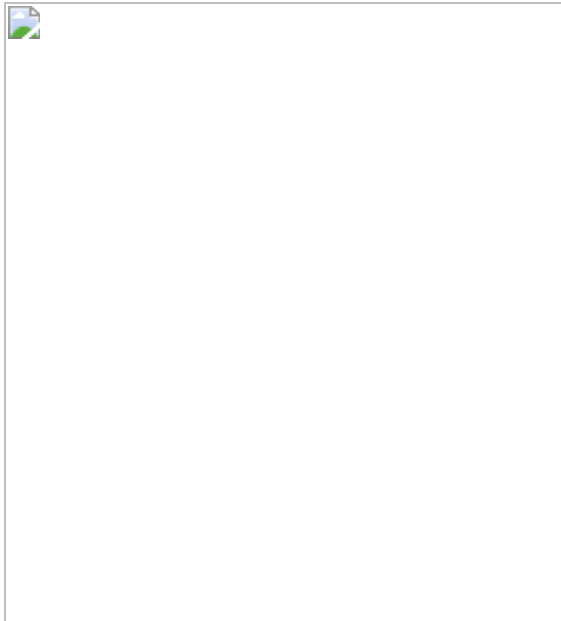


Fig. 2: *Apc* mutants induce differentiation in adjacent WT cells.

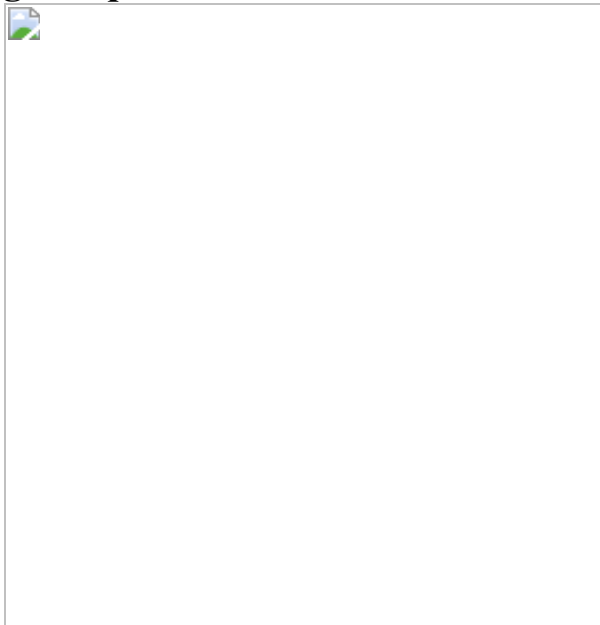


Fig. 3: *Apc*-mutant cells secrete Wnt antagonists.

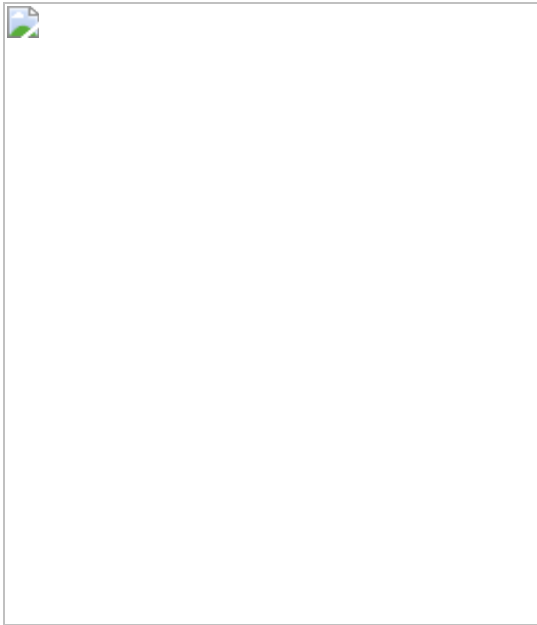


Fig. 4: LiCl neutralizes biased drift and reduces adenoma formation in *Apc*^{-/-} mice.



Data availability

The sequence libraries generated in this study are publicly available through the National Center for Biotechnology Information (NCBI) Gene Expression Omnibus (GEO) under accession [GSE144325](#). Other data sets used in this study are also publicly available via the NCBI GEO under

accession numbers [GSE145308](#), [GSE65461](#) and [GSE8671](#). For information regarding stem cell drift modelling, contact E.M. (edward.morrissey@imm.ox.ac.uk). All source data can be explored via the online data sharing platform Figlinq: <https://create.figlinq.com/~vermeulen.lab/272>. [Source data](#) are provided with this paper.

Code availability

The clone data were modelled using an R package implementing the model and are available at <https://github.com/MorrisseyLab/CryptDriftR>.

References

1. 1.

Fearnhead, N. S., Britton, M. P. & Bodmer, W. F. The ABC of APC. *Hum. Mol. Genet.* **10**, 721–733 (2001).

[CAS](#) [PubMed](#) [PubMed Central](#) [Google Scholar](#)

2. 2.

Cancer Genome Atlas Network. Comprehensive molecular characterization of human colon and rectal cancer. *Nature* **487**, 330–337 (2012).

[ADS](#) [Google Scholar](#)

3. 3.

Vermeulen, L. et al. Defining stem cell dynamics in models of intestinal tumor initiation. *Science* **342**, 995–998 (2013).

[ADS](#) [CAS](#) [PubMed](#) [PubMed Central](#) [Google Scholar](#)

4. 4.

Fearon, E. R. & Vogelstein, B. A genetic model for colorectal tumorigenesis. *Cell* **61**, 759–767 (1990).

[CAS](#) [PubMed](#) [PubMed Central](#) [Google Scholar](#)

5. 5.

Morin, P. J., Vogelstein, B. & Kinzler, K. W. Apoptosis and APC in colorectal tumorigenesis. *Proc. Natl Acad. Sci. USA* **93**, 7950–7954 (1996).

[ADS](#) [CAS](#) [PubMed](#) [PubMed Central](#) [Google Scholar](#)

6. 6.

Fevr, T., Robine, S., Louvard, D. & Huelsken, J. Wnt/β-catenin is essential for intestinal homeostasis and maintenance of intestinal stem cells. *Mol. Cell. Biol.* **27**, 7551–7559 (2007).

[CAS](#) [PubMed](#) [PubMed Central](#) [Google Scholar](#)

7. 7.

Boone, P. G. et al. A cancer rainbow mouse for visualizing the functional genomics of oncogenic clonal expansion. *Nat. Commun.* **10**, 5490 (2019).

[ADS](#) [CAS](#) [PubMed](#) [PubMed Central](#) [Google Scholar](#)

8. 8.

Albuquerque, C. et al. The ‘just-right’ signaling model: APC somatic mutations are selected based on a specific level of activation of the β-catenin signaling cascade. *Hum. Mol. Genet.* **11**, 1549–1560 (2002).

[CAS](#) [PubMed](#) [PubMed Central](#) [Google Scholar](#)

9. 9.

Crabtree, M. et al. Refining the relation between ‘first hits’ and ‘second hits’ at the APC locus: the ‘loose fit’ model and evidence for differences in somatic mutation spectra among patients. *Oncogene* **22**, 4257–4265 (2003).

[CAS](#) [PubMed](#) [PubMed Central](#) [Google Scholar](#)

10. 10.

Sato, T. et al. Single Lgr5 stem cells build crypt-villus structures *in vitro* without a mesenchymal niche. *Nature* **459**, 262–265 (2009)

[ADS](#) [CAS](#) [Google Scholar](#)

11. 11.

Flanagan, D. J. et al. NOTUM from *Apc*-mutant cells biases clonal competition to initiate cancer. *Nature* <https://doi.org/10.1038/s41586-021-03525-z> (2021).

12. 12.

Pentimikko, N. et al. Notum produced by Paneth cells attenuates regeneration of aged intestinal epithelium. *Nature* **571**, 398–402 (2019).

[CAS](#) [PubMed](#) [PubMed Central](#) [Google Scholar](#)

13. 13.

Snippert, H. J., Schepers, A. G., van Es, J. H., Simons, B. D. & Clevers, H. Biased competition between Lgr5 intestinal stem cells driven by oncogenic mutation induces clonal expansion. *EMBO Rep.* **15**, 62–69 (2014).

[CAS](#) [PubMed](#) [PubMed Central](#) [Google Scholar](#)

14. 14.

Morata, G. & Ripoll, P. Minutes: mutants of *Drosophila* autonomously affecting cell division rate. *Dev. Biol.* **42**, 211–221 (1975).

[CAS](#) [PubMed](#) [PubMed Central](#) [Google Scholar](#)

15. 15.

de la Cova, C. et al. *Drosophila* Myc regulates organ size by inducing cell competition. *Cell* **117**, 107–116 (2004).

[PubMed](#) [PubMed Central](#) [Google Scholar](#)

16. 16.

Moreno, E., Basler, K. & Morata, G. Cells compete for decapentaplegic survival factor to prevent apoptosis in *Drosophila* wing development. *Nature* **416**, 755–759 (2002).

[ADS](#) [CAS](#) [PubMed](#) [PubMed Central](#) [Google Scholar](#)

17. 17.

Moreno, E. & Basler, K. dMyc transforms cells into super-competitors. *Cell* **117**, 117–129 (2004).

[CAS](#) [PubMed](#) [PubMed Central](#) [Google Scholar](#)

18. 18.

Suijkerbuijk, S. J. E., Kolahgar, G., Kucinski, I. & Piddini, E. Cell competition drives the growth of intestinal adenomas in *Drosophila*. *Curr. Biol.* **26**, 428–438 (2016).

[CAS](#) [PubMed](#) [PubMed Central](#) [Google Scholar](#)

19. 19.

Jin, Z. et al. Differentiation-defective stem cells outcompete normal stem cells for niche occupancy in the *Drosophila* ovary. *Cell Stem Cell*

2, 39–49 (2008).

[CAS](#) [PubMed](#) [PubMed Central](#) [Google Scholar](#)

20. 20.

Liu, N. et al. Stem cell competition orchestrates skin homeostasis and ageing. *Nature* **568**, 344–350 (2019).

[ADS](#) [CAS](#) [PubMed](#) [PubMed Central](#) [Google Scholar](#)

21. 21.

Ellis, S. J. et al. Distinct modes of cell competition shape mammalian tissue morphogenesis. *Nature* **569**, 497–502 (2019).

[ADS](#) [CAS](#) [PubMed](#) [PubMed Central](#) [Google Scholar](#)

22. 22.

Vincent, J. P., Kolahgar, G., Gagliardi, M. & Piddini, E. Steep differences in wingless signaling trigger Myc-independent competitive cell interactions. *Dev. Cell* **21**, 366–374 (2011).

[CAS](#) [PubMed](#) [PubMed Central](#) [Google Scholar](#)

23. 23.

Kakugawa, S. et al. Notum deacylates Wnt proteins to suppress signalling activity. *Nature* **519**, 187–192 (2015).

[ADS](#) [CAS](#) [PubMed](#) [PubMed Central](#) [Google Scholar](#)

24. 24.

Koo, B. K. et al. Tumour suppressor RNF43 is a stem-cell E3 ligase that induces endocytosis of Wnt receptors. *Nature* **488**, 665–669 (2012).

[ADS](#) [CAS](#) [PubMed](#) [PubMed Central](#) [Google Scholar](#)

25. 25.

De Robertis, M. et al. Novel insights into Notum and glypicans regulation in colorectal cancer. *Oncotarget* **6**, 41237–41257 (2015).

[PubMed](#) [PubMed Central](#) [Google Scholar](#)

26. 26.

González-Sancho, J. M. et al. The Wnt antagonist DICKKOPF-1 gene is a downstream target of β-catenin/TCF and is downregulated in human colon cancer. *Oncogene* **24**, 1098–1103 (2005).

[PubMed](#) [PubMed Central](#) [Google Scholar](#)

27. 27.

Niida, A. et al. DKK1, a negative regulator of Wnt signaling, is a target of the β-catenin/TCF pathway. *Oncogene* **23**, 8520–8526 (2004).

[CAS](#) [PubMed](#) [PubMed Central](#) [Google Scholar](#)

28. 28.

Gould, T. D., Gray, N. A. & Manji, H. K. Effects of a glycogen synthase kinase-3 inhibitor, lithium, in adenomatous polyposis coli mutant mice. *Pharmacol. Res.* **48**, 49–53 (2003).

[CAS](#) [PubMed](#) [PubMed Central](#) [Google Scholar](#)

29. 29.

Martinsson, L., Westman, J., Hällgren, J., Ösby, U. & Backlund, L. Lithium treatment and cancer incidence in bipolar disorder. *Bipolar Disord.* **18**, 33–40 (2016).

[CAS](#) [PubMed](#) [PubMed Central](#) [Google Scholar](#)

30. 30.

Huang, R.-Y., Hsieh, K.-P., Huang, W.-W. & Yang, Y.-H. Use of lithium and cancer risk in patients with bipolar disorder: population-based cohort study. *Br. J. Psychiatry* **209**, 393–399 (2016).

[PubMed](#) [PubMed Central](#) [Google Scholar](#)

31. 31.

Barker, N. et al. Identification of stem cells in small intestine and colon by marker gene Lgr5. *Nature* **449**, 1003–1007 (2007).

[ADS](#) [CAS](#) [PubMed](#) [PubMed Central](#) [Google Scholar](#)

32. 32.

el Marjou, F. et al. Tissue-specific and inducible Cre-mediated recombination in the gut epithelium. *Genesis* **39**, 186–193 (2004).

[CAS](#) [PubMed](#) [PubMed Central](#) [Google Scholar](#)

33. 33.

Shibata, H. et al. Rapid colorectal adenoma formation initiated by conditional targeting of the APC gene. *Science* **278**, 120–133 (1997).

[CAS](#) [PubMed](#) [PubMed Central](#) [Google Scholar](#)

34. 34.

Muzumdar, M. D., Tasic, B., Miyamichi, K., Li, L. & Luo, L. A global double-fluorescent Cre reporter mouse. *Genesis* **45**, 593–605 (2007).

[CAS](#) [PubMed](#) [PubMed Central](#) [Google Scholar](#)

35. 35.

Johnson, L. et al. Somatic activation of the K-ras oncogene causes early onset lung cancer in mice. *Nature* **410**, 1111–1116 (2001).

[ADS](#) [CAS](#) [PubMed](#) [PubMed Central](#) [Google Scholar](#)

36. 36.

van der Heijden, M. et al. Bcl-2 is a critical mediator of intestinal transformation. *Nat. Commun.* **7**, 10916 (2016).

[PubMed](#) [PubMed Central](#) [Google Scholar](#)

37. 37.

Sato, T. et al. Long-term expansion of epithelial organoids from human colon, adenoma, adenocarcinoma, and Barrett's epithelium. *Gastroenterology* **141**, 1762–1772 (2011).

[CAS](#) [PubMed](#) [Google Scholar](#)

38. 38.

Adam, R. S. et al. Intestinal region-specific Wnt signalling profiles reveal interrelation between cell identity and oncogenic pathway activity in cancer development. *Cancer Cell Int.* **20**, 578 (2020).

[CAS](#) [PubMed](#) [PubMed Central](#) [Google Scholar](#)

39. 39.

Fessler, E. et al. TGF β signaling directs serrated adenomas to the mesenchymal colorectal cancer subtype. *EMBO Mol. Med.* **8**, 745–760 (2016).

[CAS](#) [PubMed](#) [PubMed Central](#) [Google Scholar](#)

40. 40.

Brinkman, E. K., Chen, T., Amendola, M. & van Steensel, B. Easy quantitative assessment of genome editing by sequence trace decomposition. *Nucleic Acids Res.* **42**, e168 (2014).

[PubMed](#) [PubMed Central](#) [Google Scholar](#)

41. 41.

Bankhead, P. et al. QuPath: open source software for digital pathology image analysis. *Sci. Rep.* **7**, 16878 (2017).

[ADS](#) [PubMed](#) [PubMed Central](#) [Google Scholar](#)

42. 42.

Bolger, A. M., Lohse, M. & Usadel, B. Trimmomatic: a flexible trimmer for Illumina sequence data. *Bioinformatics* **30**, 2114–2120 (2014).

[CAS](#) [PubMed](#) [PubMed Central](#) [Google Scholar](#)

43. 43.

Harrow, J. et al. GENCODE: producing a reference annotation for ENCODE. *Genome Biol.* **7** (Suppl. 1), S4 (2006).

[PubMed](#) [PubMed Central](#) [Google Scholar](#)

44. 44.

Kim, D., Langmead, B. & Salzberg, S. L. HISAT: a fast spliced aligner with low memory requirements. *Nat. Methods* **12**, 357–360 (2015).

[CAS](#) [PubMed](#) [PubMed Central](#) [Google Scholar](#)

45. 45.

Anders, S., Pyl, P. T. & Huber, W. HTSeq—a Python framework to work with high-throughput sequencing data. *Bioinformatics* **31**, 166–

169 (2015).

[CAS](#) [PubMed](#) [Google Scholar](#)

46. 46.

Love, M. I., Huber, W. & Anders, S. Moderated estimation of fold change and dispersion for RNA-seq data with DESeq2. *Genome Biol.* **15**, 550 (2014).

[PubMed](#) [PubMed Central](#) [Google Scholar](#)

47. 47.

R Core Team. R: a language and environment for statistical computing (R Foundation for Statistical Computing, 2014).

48. 48.

Ringel, T. et al. Genome-scale CRISPR screening in human intestinal organoids identifies drivers of TGF- β resistance. *Cell Stem Cell* **26**, 431–440.e8 (2020).

[CAS](#) [PubMed](#) [PubMed Central](#) [Google Scholar](#)

49. 49.

Reed, K. R. et al. Hunk/Mak-v is a negative regulator of intestinal cell proliferation. *BMC Cancer* **15**, 110 (2015).

[ADS](#) [PubMed](#) [PubMed Central](#) [Google Scholar](#)

50. 50.

Sabates-Bellver, J. et al. Transcriptome profile of human colorectal adenomas. *Mol. Cancer Res.* **5**, 1263–1275 (2007).

[CAS](#) [PubMed](#) [PubMed Central](#) [Google Scholar](#)

51. 51.

R2 database: Genomic Analysis And Visualization Platform. *AMC* <http://r2.amc.nl> (Amsterdam Medical Centre, 2019).

52. 52.

Van der Flier, L. G. et al. The intestinal Wnt/TCF signature. *Gastroenterology* **132**, 628–632 (2007).

[PubMed](#) [PubMed Central](#) [Google Scholar](#)

53. 53.

Muñoz, J. et al. The Lgr5 intestinal stem cell signature: robust expression of proposed quiescent '+4' cell markers. *EMBO J.* **31**, 3079–3091 (2012).

[PubMed](#) [PubMed Central](#) [Google Scholar](#)

54. 54.

Merlos-Suárez, A. et al. The intestinal stem cell signature identifies colorectal cancer stem cells and predicts disease relapse. *Cell Stem Cell* **8**, 511–524 (2011).

[PubMed](#) [PubMed Central](#) [Google Scholar](#)

55. 55.

Lopez-Garcia, C., Klein, A. M., Simons, B. D. & Winton, D. J. Intestinal stem cell replacement follows a pattern of neutral drift. *Science* **330**, 822–825 (2010).

[ADS](#) [CAS](#) [PubMed](#) [Google Scholar](#)

56. 56.

Carpenter, B. et al. Stan: a probabilistic programming language. *J. Stat. Softw.* (2017).

57. 57.

Schindelin, J. et al. Fiji: an open-source platform for biological-image analysis. *Nat. Methods* **9**, 676–682 (2012).

[CAS](#) [PubMed](#) [PubMed Central](#) [Google Scholar](#)

[Download references](#)

Acknowledgements

S.M.v.N. is supported by a NWO OOA PhD scholarship (022.005.002). This work is supported by The New York Stem Cell Foundation and grants from KWF (UVA2014-7245), the Maurits en Anna de Kock Stichting (2015-2), Worldwide Cancer Research (14-1164), the Maag Lever Darm Stichting (MLDS-CDG 14-03), the European Research Council (ERC-StG 638193) and ZonMw (Vidi 016.156.308) to L.V. L.V. is a New York Stem Cell Foundation–Robertson Investigator. We thank the AMC laboratory for clinical chemistry (LAKC), the mouse breeding and research facilities, and the core facilities for genomics, cellular imaging and pathology for their technical support.

Author information

Affiliations

1. Laboratory for Experimental Oncology and Radiobiology, Center for Experimental and Molecular Medicine, Cancer Center Amsterdam, Amsterdam Gastroenterology Endocrinology Metabolism, Amsterdam University Medical Centers, Amsterdam, The Netherlands

Sanne M. van Neerven, Nina E. de Groot, Lisanne E. Nijman, Milou S. van Driel, Maria C. Lecca, Daniël O. Warmerdam, Vaishali Kakkar, Leandro F. Moreno, Felipe A. Vieira Braga, Delano R.

Sanches, Prashanthi Ramesh, Sanne ten Hoorn, Marouska F. van Boxel, Jan Paul Medema, Maarten F. Bijlsma, Nicolas Léveillé & Louis Vermeulen

2. Oncode Institute, Amsterdam, The Netherlands

Sanne M. van Neerven, Nina E. de Groot, Lisanne E. Nijman, Milou S. van Driel, Maria C. Lecca, Daniël O. Warmerdam, Vaishali Kakkar, Leandro F. Moreno, Felipe A. Vieira Braga, Delano R. Sanches, Prashanthi Ramesh, Sanne ten Hoorn, Marouska F. van Boxel, Jan Paul Medema, Maarten F. Bijlsma, Nicolas Léveillé & Louis Vermeulen

3. Center for Experimental Molecular Medicine, Amsterdam Infection & Immunity, Amsterdam UMC, Amsterdam, The Netherlands

Brendon P. Scicluna

4. Department of Clinical Epidemiology, Biostatistics and Bioinformatics, Amsterdam UMC, Amsterdam, The Netherlands

Brendon P. Scicluna

5. CRISPR Platform, University of Amsterdam, Cancer Center Amsterdam, Amsterdam UMC, Amsterdam, The Netherlands

Daniël O. Warmerdam

6. Department of Gastroenterology and Hepatology, Amsterdam University Medical Centers, Amsterdam, The Netherlands

Arthur S. Aelvoet & Evelien Dekker

7. Department of Pathology, Amsterdam University Medical Centers, Amsterdam, The Netherlands

Lianne Koens

8. Department of Medical Biology, Amsterdam University Medical Centers, Amsterdam, The Netherlands

Przemek M. Krawczyk

9. Department of Oncogenomics, Amsterdam University Medical Centers, Amsterdam, The Netherlands

Jan Koster

10. Cancer Research UK, Cambridge Institute, University of Cambridge, Cambridge, UK

Douglas J. Winton

11. MRC Weatherall Institute of Molecular Medicine, University of Oxford, John Radcliffe Hospital, Oxford, UK

Edward Morrissey

Authors

1. Sanne M. van Neerven

[View author publications](#)

You can also search for this author in [PubMed](#) [Google Scholar](#)

2. Nina E. de Groot

[View author publications](#)

You can also search for this author in [PubMed](#) [Google Scholar](#)

3. Lisanne E. Nijman

[View author publications](#)

You can also search for this author in [PubMed](#) [Google Scholar](#)

4. Brendon P. Scicluna

[View author publications](#)

You can also search for this author in [PubMed](#) [Google Scholar](#)

5. Milou S. van Driel

[View author publications](#)

You can also search for this author in [PubMed](#) [Google Scholar](#)

6. Maria C. Lecca

[View author publications](#)

You can also search for this author in [PubMed](#) [Google Scholar](#)

7. Daniël O. Warmerdam

[View author publications](#)

You can also search for this author in [PubMed](#) [Google Scholar](#)

8. Vaishali Kakkar

[View author publications](#)

You can also search for this author in [PubMed](#) [Google Scholar](#)

9. Leandro F. Moreno

[View author publications](#)

You can also search for this author in [PubMed](#) [Google Scholar](#)

10. Felipe A. Vieira Braga

[View author publications](#)

You can also search for this author in [PubMed](#) [Google Scholar](#)

11. Delano R. Sanches

[View author publications](#)

You can also search for this author in [PubMed](#) [Google Scholar](#)

12. Prashanthi Ramesh

[View author publications](#)

You can also search for this author in [PubMed](#) [Google Scholar](#)

13. Sanne ten Hoorn

[View author publications](#)

You can also search for this author in [PubMed](#) [Google Scholar](#)

14. Arthur S. Aelvoet

[View author publications](#)

You can also search for this author in [PubMed](#) [Google Scholar](#)

15. Marouska F. van Boxel

[View author publications](#)

You can also search for this author in [PubMed](#) [Google Scholar](#)

16. Lianne Koens

[View author publications](#)

You can also search for this author in [PubMed](#) [Google Scholar](#)

17. Przemek M. Krawczyk

[View author publications](#)

You can also search for this author in [PubMed](#) [Google Scholar](#)

18. Jan Koster

[View author publications](#)

You can also search for this author in [PubMed](#) [Google Scholar](#)

19. Evelien Dekker

[View author publications](#)

You can also search for this author in [PubMed](#) [Google Scholar](#)

20. Jan Paul Medema

[View author publications](#)

You can also search for this author in [PubMed](#) [Google Scholar](#)

21. Douglas J. Winton

[View author publications](#)

You can also search for this author in [PubMed](#) [Google Scholar](#)

22. Maarten F. Bijlsma

[View author publications](#)

You can also search for this author in [PubMed](#) [Google Scholar](#)

23. Edward Morrissey

[View author publications](#)

You can also search for this author in [PubMed](#) [Google Scholar](#)

24. Nicolas Léveillé

[View author publications](#)

You can also search for this author in [PubMed](#) [Google Scholar](#)

25. Louis Vermeulen

[View author publications](#)

You can also search for this author in [PubMed](#) [Google Scholar](#)

Contributions

S.M.v.N. and L.V. conceptualized the project. S.M.v.N. and L.V. designed the experiments. S.M.v.N., N.E.d.G., L.E.N., M.S.v.D. and D.R.S. performed the in vitro organoid (co-)culture experiments, the DNA, RNA and protein assays, stainings and RNA-ISH. V.K. performed the in vitro organoid recombination assays. F.A.V.B. assisted with the FACS assays. P.R. and A.S.A. assisted with the human organoid cultures and the FAP adenoma data. M.F.v.B. generated the fluorescent organoid cultures. N.L. designed and generated the overexpression constructs. N.E.d.G., L.E.N., M.S.v.D. and M.C.L. performed the in vivo experiments and tissue

processing. D.O.W. developed the CRISPR strategies. L.F.M. and S.t.H. generated the clone size plots. P.M.K. generated the spider plots and helped with visualization of the data. L.K. and E.D. provided human materials. B.P.S. and J.K. analysed the RNA sequencing data. E.M. designed and performed the mathematical modelling. S.M.v.N. and L.V. wrote the manuscript, with help from B.P.S., J.K., E.M. and N.L. J.P.M., D.J.W. and M.F.B. advised on the project.

Corresponding author

Correspondence to [Louis Vermeulen](#).

Ethics declarations

Competing interests

L.V. received consultancy fees from Bayer, MSD, Genentech, Servier and Pierre Fabre, but these had no relation to the content of this publication.

Additional information

Peer review information *Nature* thanks Hans Clevers, James DeGregori and Toshiro Sato for their contribution to the peer review of this work.

Publisher's note Springer Nature remains neutral with regard to jurisdictional claims in published maps and institutional affiliations.

Extended data figures and tables

[Extended Data Fig. 1 \$Apc^{-/-}\$ cells actively impair outgrowth of \$Apc^{+/-}\$ organoids.](#)

a, Schematic workflow for in vitro co-cultures. **b**, Representative images of full wells containing $WT/Apc^{+/-}$ co-cultures; scale bar, 1 mm. **c**, Relative

surface contribution in *WT/Apc*^{+/−} co-cultures ($P = 0.3771$, day 1–day 7, two-tailed paired *t*-test). **d**, Organoid expansion in *WT/Apc*^{+/−} co-cultures. $n = 4$ independent experiments. **e**, Representative images of full wells containing *Apc*^{+/−}/*Apc*^{−/−} co-cultures; scale bar, 1 mm. **f**, Reduction in surface contribution of *Apc*^{+/−} and *Apc*^{−/−} organoids in *Apc*^{+/−}/*Apc*^{−/−} co-culture ($P = 0.0012$, day 1–day 4; $P = 0.0016$, day 1–day 7, two-tailed paired *t*-test). **g**, Organoid expansion of *Apc*^{+/−} and *Apc*^{−/−} organoids in *Apc*^{+/−}/*Apc*^{−/−} co-culture. **h**, Full well images of *Apc*^{+/−} organoids with *Apc*^{+/−} or *Apc*^{−/−} CM at day 7; scale bar, 1 mm. Zoom panel right, 250 μm. **i**, *Apc*^{+/−} organoid expansion in CM ($P = 0.0322$, day 4; $P = 0.0006$, day 7). Data are mean ± s.d., $n = 3$ independent experiments, analysed using two-sided Student's *t*-test, unless otherwise specified. * $P \leq 0.05$, ** $P \leq 0.01$, *** $P \leq 0.001$, ns, not significant.

[Source data](#)

[**Extended Data Fig. 2 *Apc* mutants induce differentiation in adjacent *WT* cells through Wnt inhibition.**](#)

a–d, Signature scores for Wnt signatures (**a**, **b**) and stem cell signatures (**c**, **d**) for *WT* organoids treated with CM for 2 or 4 days. Signature scores were calculated by summing the standardized expression of the genes within each signature. Box plots are minimum to maximum values, the box shows the 25th to the 75th percentiles, the median is indicated with a line; $n = 3$ biological replicates. **e–h**, Effect of 10x concentrated *WT* or *Apc*^{−/−} CM on *WT* organoid growth (**e**; scale bar, 250 μm), *Lgr5* expression ($P = 0.0033$; data are mean ± s.e.m.) (**f**), the percentage of *Lgr5*–GFP^{high} cells ($P = 0.0371$; data are mean ± s.e.m.) (**g**) and the clonogenicity ($P = 0.0044$) of *WT* organoids (**h**). $n = 4$ independent experiments. **i**, Schematic illustration of the TOP-GFP construct. **j**, FACS histograms showing TOP-GFP expression in mouse embryonic fibroblasts (MEFs) in the absence (unstimulated) or presence of Wnt3a. **k–m**, Mean fluorescent intensity (MFI) of TOP-GFP upon upstream stimulation with Wnt3a (WT CM versus *Apc*^{−/−} CM, $P < 0.0001$) (**k**), or upon downstream pathway activation with 5 mM LiCl (WT CM versus *Apc*^{−/−} CM, $P = 0.9812$) (**l**) or 2.5 μM CHIR99021 (WT CM versus *Apc*^{−/−} CM, $P = 0.8082$) (**m**); $n = 4$.

independent experiments. Data are mean \pm s.d.; $n = 3$ independent experiments, analysed using two-sided Student's *t*-test, unless otherwise specified. FACS gating can be found in Supplementary File 2. * $P \leq 0.05$, ** $P \leq 0.01$, **** $P \leq 0.0001$, ns, not significant.

[Source data](#)

Extended Data Fig. 3 Apc-mutant cells secrete Wnt antagonists.

a, mRNA expression of Wnt antagonists in a time course following tamoxifen-mediated recombination. $n = 3$ technical replicates from a representative experiment performed 3 times ($P = 0.0039$ (*Notum*), $P = 0.0115$ (*Wifl*), $P = 0.0252$ (*Dkk2*), 72 h versus control). **b**, Protein levels of NOTUM and WIF1 ($P < 0.0001$) detected in CM of *WT* or *Apc*^{-/-} organoids. **c**, Volcano plot for significantly upregulated Wnt antagonists in pooled normal or adenoma murine tissue (GSE65461; 2,483 DEGs). **d**, Expression of Wnt antagonists *Notum*, *Wifl* and *Dkk2* in mouse adenoma tissue by RNA-ISH. Scale bar, 100 μ m. $n = 3$ mice per ISH probe. **e**, Volcano plot for significantly upregulated Wnt antagonists in human matched normal or adenoma tissue (GSE8671; 9,478 DEGs). **f**, NOTUM expression in FAP adenomas. Scale bar, 100 μ m. **g**, *APC*-mutant crypts, marked with asterisk. Scale bar, 100 μ m. *APC*-mutant crypts are recognized as low-grade dysplasia by their enlarged pellate nuclei (H&E staining, right panel). Scale bar, 50 μ m. **h**, Protein levels of NOTUM in CM of *WT* or *APC*-mutant organoids ($P = 0.0291$). Data are mean \pm s.e.m., $n = 2$ *WT* organoid lines, $n = 6$ *APC*-mutant organoid lines. Data are mean \pm s.d., $n = 3$ independent experiments, analysed using two-sided Student's *t*-test, unless otherwise specified. * $P \leq 0.05$, ** $P \leq 0.01$, **** $P \leq 0.0001$.

[Source data](#)

Extended Data Fig. 4 Characterization of the role of individual Wnt antagonists.

a, Schematic illustration of overexpression (OE) constructs for *Notum*, *Wifl* and *Dkk2*. **b**, mRNA expression of Wnt antagonists in OE lines; $n = 3$ technical replicates. **c**, Protein concentration in CM of OE lines; $n = 3$

technical replicates. **d–f**, Fluorescent images (**d**), relative organoid expansion (**e**) and clonogenic potential (**f**) of *WT* organoids incubated with recombinant NOTUM (2 µg/ml), WIF1 (5 µg/ml) and DKK2 (1 µg/ml) protein. Scale bar, 250 µm. $P = 0.0011$ (rNotum), $P = 0.0006$ (rWif1), $P = 0.0144$ (rDkk2) and $P = 0.0003$ (combination) all relative to the control. Data are mean ± s.e.m. **g**, Representative image of *WT/Apc^{-/-}Notum KO* co-culture at day 4. Scale bar, 1 mm. **h**, Relative expansion of *WT* organoids in co-culture with *Apc^{-/-}* organoids that contain CRISPR-based modifications in Wnt antagonist genes *Notum*, *Wif1* or *Dkk2*. $n = 2$ single-cell *Apc^{-/-}* KO clones per Wnt antagonist. **i**, MFI for TOP-GFP expression in the presence of *Wnt3a* and *Apc^{-/-}* KO CM ($P = 0.3606$, one-way ANOVA, between all *Apc*-mutant conditions). Data are mean ± s.e.m., each dot represents a single-cell *Apc^{-/-}* KO clone. **j**, Clonogenic potential of *WT* organoids that are incubated with a titration of *Apc^{-/-}* KO CM; $n = 2$ independent experiments. **k, l**, Phase images (**k**), and clonogenicity (**l**) of *WT* human organoids incubated with recombinant NOTUM ($P = 0.0113$ (1:200, 0.5 µg/ml), $P = 0.0059$ (1:100, 1 µg/ml)) Data are mean ± s.e.m. All data are mean ± s.d., $n = 3$ independent experiments, analysed using two-sided Student's *t*-test, unless otherwise specified. * $P \leq 0.05$, ** $P \leq 0.01$, *** $P \leq 0.001$, ns, not significant.

Source data

Extended Data Fig. 5 Downstream activation of the Wnt pathway rescues the *Apc*-mutant supercompetitor phenotype in vitro.

a, Relative clonogenic potential of *WT* organoids incubated with *Apc^{-/-}* CM in the absence or presence of 2.5 µM CHIR ($P = 0.0040$, P3). **b**, Validation of overexpression of a non-degradable variant of β-catenin, *Ctnnb^s*, on mRNA ($P < 0.0001$, for *Ctnnb1* versus WT and *Ctnnb1* vs *Apc^{-/-}*; $n = 3$ biological replicates; data are mean ± s.e.m.) and protein level. Full western blot images can be found in Supplementary File 1. **c, d**, Fluorescent image (**c**) and relative surface contribution (**d**) of co-culture between *Ctnnb^s* (purple) and *Apc^{-/-}* (green) ($P = 0.4604$ day 1–day 4, $P = 0.2734$ day 1–day 7; two-tailed paired *t*-test). Scale bar, 500 µm. **e**, Relative LGR5 expression

of human colon organoids incubated with CM in the absence or presence of LiCl ($P = 0.0012$, FAP CM \pm LiCl). Data are mean \pm s.e.m. **f**, Relative clonogenic potential of human colon organoids incubated with *WT* or FAP CM in the absence or presence of LiCl ($n = 4$ biological replicates; $P < 0.0001$, one-way ANOVA). Data are mean \pm s.d., $n = 3$ independent experiments, analysed using two-sided Student's *t*-test, unless otherwise specified. ** $P \leq 0.01$, *** $P \leq 0.0001$, ns, not significant.

[Source data](#)

Extended Data Fig. 6 Biallelic *Apc* mutants exclusively express Wnt antagonists.

a, mRNA expression of Wnt antagonists *Notum*, *Wifl* and *Dkk2* in *Apc*^{+/+}, *Apc*^{+/-} and *Apc*^{-/-} organoids. $P < 0.0001$ (*Notum*), $P = 0.006$ (*Wifl*) and $P = 0.0004$ (*Dkk2*). Data are mean \pm s.e.m., $n = 3$ biological replicates, two-sided Student's *t*-test. **b**, RNA-ISH on consecutive tissue slices for detection of recombined *Apc* alleles (*Apc*^{E14-16}) and *Notum* in *Apc*^{+/+}, *Apc*^{+/-} and *Apc*^{-/-} tissues. Scale bar, 50 μ m for *Apc*^{+/+} and *Apc*^{+/-} crypt base images, and 100 μ m for *Apc*^{-/-} adenoma. **c**, Expression of *Notum* in ageing Paneth cells is not detected in young mice (upper panel, <100 days old). *Notum*⁺ Paneth cells are observed in old mice (middle panel, >800 days old); positive cells are marked with arrowheads. *Notum*⁺ Paneth cells do not interfere with *Notum*⁺/*Apc*^{-/-} clonal analysis and are not detected in *Apc*^{-/-} mice (lower panel, <100 days old). Scale bar, 10 μ m. All RNA-ISH has been performed on $n = 3$ mice per condition. ** $P \leq 0.01$, *** $P \leq 0.001$, *** $P \leq 0.0001$.

[Source data](#)

Extended Data Fig. 7 Effects of LiCl on the *WT* mouse intestine.

a, Detection of lithium (Li⁺) levels in mouse serum; $n = 4$ mice per condition, data are mean \pm s.d. **b**, mRNA expression of Wnt target gene *Lgr5* in isolated crypts of control ($n = 8$) or LiCl-treated ($n = 10$) mice

($P = 0.0037$). **c**, Percentage of *Lgr5*-GFP expressing cells in isolated crypts from control ($n = 11$) or LiCl-treated ($n = 12$) mice, as measured by FACS ($P = 0.0140$). **d**, Fluorescent images of *Lgr5*-GFP⁺ ISCs in crypt bases of control or LiCl-treated mice, adjacent quantification is the frequency distribution of *Lgr5*-GFP⁺ cells per half (2D) crypt; $n = 125$ crypts per condition, each data point is a crypt base. Scale bar, 50 μm . **e**, Schematic illustration of the in vivo treatment scheme with tamoxifen and LiCl in *Lgr5-Cre^{Ert2};Rosa26^{mTmG}* (*WT*) mice. **f**, Box plot for Cre-reporter activity as measured by the percentage of induced crypts at day 4 ($n = 5$ mice, $P = 0.3322$). **g**, Scatter dot plots for tdTomato^{neg}/GFP^{pos} clone induction per intestinal region as measured by FACS ($P = 0.6335$ (proximal SI), 0.5171 (distal SI) and 0.7804 (colon)). **h**, Fluorescent images of representative clone sizes of *WT* crypts of mice treated with or without LiCl, mTmGFP⁺ clones are visualized in white. Scale bar, 20 μm . **i**, Respective box plots of clone size distributions of *WT* mice in the presence or absence of LiCl; data points indicate fractional crypt sizes per time point, with random x and y jitter added for visualization. The mean is indicated with a dashed line. **j**, **k**, Relative clone sizes ($P = 0.7749$, day 21) (**j**) and the relative amount of fixed clones (**k**) remain unaffected by LiCl ($P = 0.8668$, day 21). **l**, No effect of LiCl on the probability of replacement for *WT* drift. All box plots are minimum to maximum, the box shows the 25th to the 75th percentiles, and the median is indicated with a line. Data are mean \pm s.e.m.; $n = 3$ control mice, $n = 2$ LiCl mice, unless otherwise specified. All data are analysed using two-sided Student's *t*-test. For FACS gating data, see Supplementary File 2. * $P \leq 0.05$, ** $P \leq 0.01$, ns, not significant.

Source data

Extended Data Fig. 8 Notum influences Lgr5 expression in adjacent crypt bases.

a, b, Duplex RNA-ISH of *Lgr5* (magenta) and *Notum* (blue) in crypt bases (scale bar, 50 μm) (**a**) and relative *Lgr5* expression in crypts adjacent to *Notum^{pos}* crypts (**b**) ($P < 0.0001$, one-way ANOVA). **c, d**, Duplex RNA-ISH of *Lgr5* (magenta) and *Notum* (blue) in crypt bases in the presence of LiCl (scale bar, 50 μm) (**c**) and relative *Lgr5* expression in crypts adjacent

to *Notum*^{pos} crypts in the presence of LiCl (**d**) ($P = 0.4032$, one-way ANOVA). Box plots are the minimum to maximum values, the box shows the 25th to the 75th percentiles, and the median is indicated with a line; each data point represents a crypt; $n = 3$ mice per condition. *** $P \leq 0.0001$, ns, not significant.

[Source data](#)

Extended Data Fig. 9 LiCl influences stem cell dynamics and reduces adenoma formation.

a, b, The effect of LiCl on *WT* stem cell dynamics based on the inferred replacement probability (P_R) (**a**) or when the number of *WT* stem cells (N^{WT}) is determined (**b**). **c, d**, Fits of clone size distributions for the adapted stem cells model (N^{WT}) for *WT* and *Apc*^{-/-} clone dynamics in the absence (**c**) or presence (**d**) of LiCl. Each data point indicates the average clone size proportion of that particular time point, and the error bars are the 95% credible interval for the proportion. Modelling is based on crypt data from $n = 12$ mice for both the control group and the LiCl-treated group. **e**, The amount of adenomas counted per intestinal region in the absence or presence of LiCl ($P = 0.0037$ (proximal SI), $P < 0.0001$ (distal SI) and $P = 0.0077$ (colon)); $n = 9$ (control) and $n = 12$ (LiCl). The box plot is the minimum to maximum values, the box shows the 25th to the 75th percentiles, and the median is indicated with a line; each data point represents a mouse. All data are analysed using two-sided Student's *t*-test. ** $P \leq 0.01$, *** $P \leq 0.0001$.

[Source data](#)

Extended Data Fig. 10 LiCl does not influence *Kras*^{G12D} stem cell dynamics.

a, Schematic illustration of PCR strategy to detect *WT* (*Kras*^{WT}) and mutant (*Kras*^{G12D}) alleles. **b**, Successful recombination of *Kras*^{G12D} organoids after tamoxifen administration results in loss of Lox-Stop-Lox band, which means transcription of *Kras*^{G12D}. **c–e**, Fluorescent images (**c**), relative *Lgr5*

expression ($P = 0.0013$) (**d**) and clonogenicity ($P = 0.0007$, data are mean \pm s.d.) (**e**) of $Kras^{G12D}$ organoids incubated in the absence or presence of 5 mM LiCl. Scale bar, 250 μ m. $n = 3$ independent experiments. **f**, Schematic illustration of in vivo treatment scheme with tamoxifen and LiCl in $Lgr5-Cre^{Ert2}$; $Rosa26^{mTmG}$; $Kras^{G12D}$ mice. **g**, Sorting strategy of crypts isolated from $Kras^{G12D}$ mice 7 days after tamoxifen administration for $Kras^{WT}$ (tdTom $^+$) and $Kras^{G12D}$ (GFP $^+$) cells. **h**, Validation of recombination (= loss of LSL-site) of the $Kras^{G12D}$ locus shows complete recombination in the GFP $^+$ -sorted fraction. **i**, Representative clone sizes of $Kras^{G12D}$ mice treated with or without LiCl; mTmGFP $^+$ clones are visualized in white. Scale bar, 20 μ m. **j**, Respective box plots of clone size distributions of $Kras^{G12D}$ mice in the presence or absence of LiCl. The box plot is the minimum to maximum values, the box shows the 25th to the 75th percentiles, and the median/mean is indicated with a dashed/straight line respectively; the data points indicate fractional crypt sizes per time point, with random x and y jitter added for visualization. The mean is indicated with a dashed line. $n = 2$ mice per time point. **k**, **l**, Relative clone sizes ($P = 0.5861$, day 21, $n = 2$ mice per time point) (**k**) and the relative number of fixed clones remain unaffected by LiCl ($P = 0.6718$, day 21, $n = 2$ mice per time point). **m**, Modelling the probability of replacement (P_R) of $Kras^{G12D}$ LiCl mice (versus WT LiCl mice) compared to untreated $Kras^{G12D}$ mice (versus WT control mice). Data are mean \pm s.e.m.; $n = 3$ independent experiments, analysed using two-sided Student's t -test, unless otherwise specified. PCRs on gel (**b**, **h**) have been repeated three times. For gel source data, see Supplementary File [1](#). For FACS gating data, see Supplementary File [2](#). ** $P \leq 0.01$, *** $P \leq 0.001$, ns, not significant.

[Source data](#)

Supplementary information

[Supplementary Information](#)

This file contains supplementary text, supplementary figures 1-2 and supplementary tables 1 – 3.

Reporting Summary

Source data

Source Data Fig. 1

Source Data Fig. 2

Source Data Fig. 3

Source Data Fig. 4

Source Data Extended Data Fig. 1

Source Data Extended Data Fig. 2

Source Data Extended Data Fig. 3

Source Data Extended Data Fig. 4

Source Data Extended Data Fig. 5

Source Data Extended Data Fig. 6

Source Data Extended Data Fig. 7

Source Data Extended Data Fig. 8

Source Data Extended Data Fig. 9

Source Data Extended Data Fig. 10

Rights and permissions

[Reprints and Permissions](#)

About this article



Check for
updates

Cite this article

van Neerven, S.M., de Groot, N.E., Nijman, L.E. *et al.* *Apc*-mutant cells act as supercompetitors in intestinal tumour initiation. *Nature* **594**, 436–441 (2021). <https://doi.org/10.1038/s41586-021-03558-4>

[Download citation](#)

- Received: 31 January 2020
- Accepted: 15 April 2021
- Published: 02 June 2021
- Issue Date: 17 June 2021
- DOI: <https://doi.org/10.1038/s41586-021-03558-4>

Further reading

- [**NOTUM from Apc-mutant cells biases clonal competition to initiate cancer**](#)
 - Dustin J. Flanagan
 - , Nalle Penttinenmikko
 - , Kalle Luopajarvi
 - , Nicky J. Willis
 - , Kathryn Gilroy

- , Alexander P. Raven
- , Lynn McGarry
- , Johanna I. Englund
- , Anna T. Webb
- , Sandra Scharaw
- , Nadia Nasreddin
- , Michael C. Hodder
- , Rachel A. Ridgway
- , Emma Minnee
- , Nathalie Sphyris
- , Ella Gilchrist
- , Arafath K. Najumudeen
- , Beatrice Romagnolo
- , Christine Perret
- , Ann C. Williams
- , Hans Clevers
- , Pirjo Nummela
- , Marianne LÃ¤hde
- , Kari Alitalo
- , Ville Hietakangas
- , Ann Hedley
- , William Clark
- , Colin Nixon
- , Kristina Kirschner
- , E. Yvonne Jones
- , Ari RistimÃ¤ki
- , Simon J. Leedham
- , Paul V. Fish
- , Jean-Paul Vincent
- , Pekka Katajisto
- & Owen J. Sansom

Nature (2021)

Comments

By submitting a comment you agree to abide by our [Terms](#) and [Community Guidelines](#). If you find something abusive or that does not comply with our terms or guidelines please flag it as inappropriate.

[Access through your institution](#)

[Change institution](#)

[Buy or subscribe](#)

Associated Content

[Cancer stem cells in the gut have a bad influence on neighbouring cells](#)

- Shi Biao Chia
- James DeGregori

Advertisement

This article was downloaded by **calibre** from <https://www.nature.com/articles/s41586-021-03558-4>

| [Section menu](#) | [Main menu](#) |

- Article
- [Published: 02 June 2021](#)

Tracing oncogene-driven remodelling of the intestinal stem cell niche

- [Min Kyu Yum](#)^{1,2 na1},
- [Seungmin Han](#)^{1,2 na1},
- [Juergen Fink](#)²,
- [Szu-Hsien Sam Wu](#) ORCID: orcid.org/0000-0002-6377-608X^{3,4},
- [Catherine Dabrowska](#)^{2,5},
- [Teodora Trendafilova](#)²,
- [Roxana Mustata](#)²,
- [Lemonia Chatzeli](#)^{1,2},
- [Roberta Azzarelli](#) ORCID: orcid.org/0000-0002-8160-7538^{2,6},
- [Irina Pshenichnaya](#)²,
- [Eunmin Lee](#)⁷,
- [Frances England](#) ORCID: orcid.org/0000-0003-0821-8015^{2,5},
- [Jong Kyoung Kim](#) ORCID: orcid.org/0000-0002-0257-0547⁷,
- [Daniel E. Stange](#) ORCID: orcid.org/0000-0003-4246-2230⁸,
- [Anna Philpott](#) ORCID: orcid.org/0000-0003-3789-2463^{2,6},
- [Joo-Hyeon Lee](#) ORCID: orcid.org/0000-0002-7364-6422^{2,5},
- [Bon-Kyoung Koo](#) ORCID: orcid.org/0000-0002-4134-8033^{2,3 na2} &
- [Benjamin D. Simons](#) ORCID: orcid.org/0000-0002-3875-7071^{1,2,9 na2}

[Nature](#) volume 594, pages 442–447 (2021) [Cite this article](#)

- 11k Accesses

- 180 Altmetric
- [Metrics details](#)

Subjects

- [Cancer microenvironment](#)
- [Colorectal cancer](#)
- [Intestinal stem cells](#)
- [Stem-cell niche](#)
- [Stochastic modelling](#)

Abstract

Interactions between tumour cells and the surrounding microenvironment contribute to tumour progression, metastasis and recurrence^{1,2,3}. Although mosaic analyses in *Drosophila* have advanced our understanding of such interactions^{4,5}, it has been difficult to engineer parallel approaches in vertebrates. Here we present an oncogene-associated, multicolour reporter mouse model—the Red2Onco system—that allows differential tracing of mutant and wild-type cells in the same tissue. By applying this system to the small intestine, we show that oncogene-expressing mutant crypts alter the cellular organization of neighbouring wild-type crypts, thereby driving accelerated clonal drift. Crypts that express oncogenic KRAS or PI3K secrete BMP ligands that suppress local stem cell activity, while changes in PDGFR^{lo}CD81⁺ stromal cells induced by crypts with oncogenic PI3K alter the WNT signalling environment. Together, these results show how oncogene-driven paracrine remodelling creates a niche environment that is detrimental to the maintenance of wild-type tissue, promoting field transformation dominated by oncogenic clones.

Access options

Subscribe to Journal

Get full journal access for 1 year

\$199.00

only \$3.90 per issue

[Subscribe](#)

All prices are NET prices.

VAT will be added later in the checkout.

Tax calculation will be finalised during checkout.

Rent or Buy article

Get time limited or full article access on ReadCube.

from \$8.99

[Rent or Buy](#)

All prices are NET prices.

Additional access options:

- [Log in](#)
- [Access through your institution](#)
- [Learn about institutional subscriptions](#)

Fig. 1: Red2Onco system: an oncogene-associated multicolour reporter.

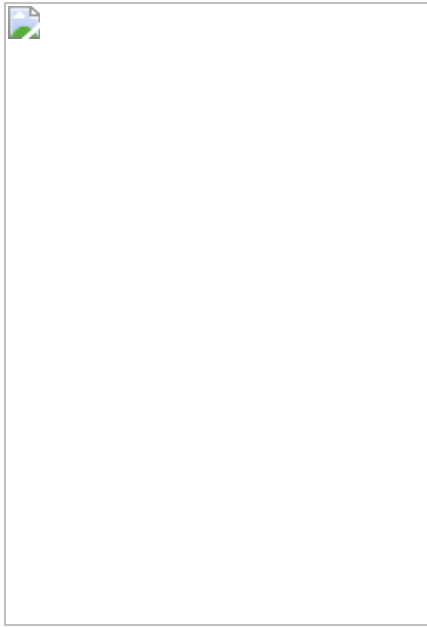


Fig. 2: Reduced effective stem cell number leads to accelerated drift of WT clones in crypts that neighbour mutant crypts.

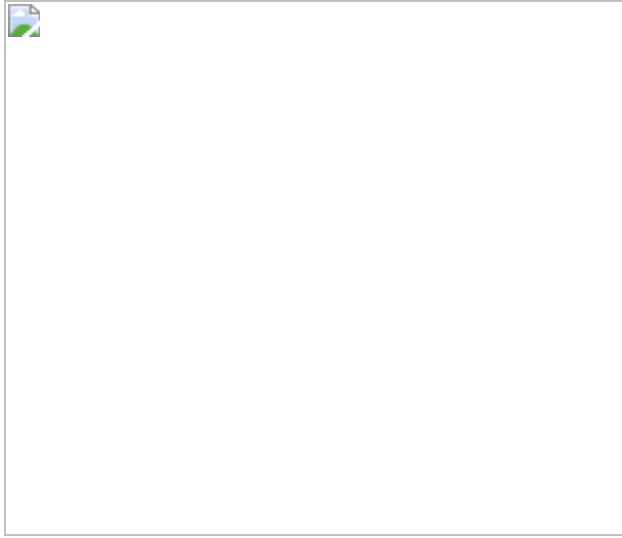
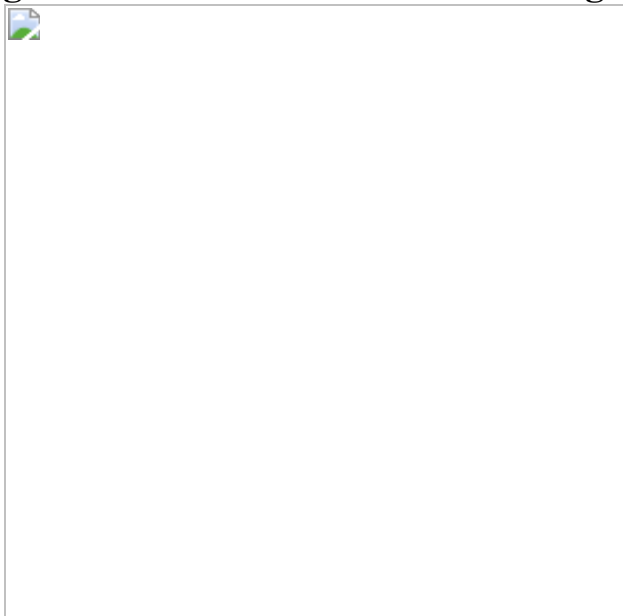


Fig. 3: Comparative single-cell analysis identifies oncogene-driven niche changes.



Fig. 4: Functional validation of oncogene-driven niche remodelling.



Data availability

The scRNA-seq data generated for this study have been deposited in ArrayExpress under [E-MTAB-8656](#). The reference genome sequence was downloaded from Ensembl (http://www.ensembl.org/Mus_musculus) and used for alignment of the scRNA-seq data. To evaluate stem cell priming, scRNA-seq data were obtained from the Single Cell Portal (https://portals.broadinstitute.org/single_cell/study/small-intestinal-epithelium) and used to define gene sets for differentiated sub-lineages of

epithelial cells. The lists of marker genes used to annotate types of epithelial, mesenchymal and immune cells in Fig. 3b, f and Extended Data Figs. 6d, 8a–c are given in Supplementary Tables 1, 3. Gene sets used in Fig. 3d, e and Extended Data Fig. 7a, b, k–m are provided in Supplementary Table 2. [Source data](#) are provided with this paper.

Code availability

The statistical analysis of the clone fate data, based on a fit to the established modelling scheme, was performed using a FORTRAN (G95 compiler) code developed for this study. The scRNA-seq data were analysed using publicly available R packages. The codes and data used for clonal analysis and scRNA-seq data analysis have been deposited in GitHub (available at https://github.com/BenSimonsLab/Yum_Nature_2021).

References

1. 1.

Hanahan, D. & Weinberg, R. A. Hallmarks of cancer: the next generation. *Cell* **144**, 646–674 (2011).

[CAS](#) [Article](#) [Google Scholar](#)

2. 2.

Medema, J. P. & Vermeulen, L. Microenvironmental regulation of stem cells in intestinal homeostasis and cancer. *Nature* **474**, 318–326 (2011).

[CAS](#) [PubMed](#) [PubMed Central](#) [Google Scholar](#)

3. 3.

Quail, D. F. & Joyce, J. A. Microenvironmental regulation of tumor progression and metastasis. *Nat. Med.* **19**, 1423–1437 (2013).

[CAS](#) [PubMed](#) [PubMed Central](#) [Google Scholar](#)

4. 4.

Clavería, C. & Torres, M. Cell competition: mechanisms and physiological roles. *Annu. Rev. Cell Dev. Biol.* **32**, 411–439 (2016).

[PubMed](#) [PubMed Central](#) [Google Scholar](#)

5. 5.

Di Gregorio, A., Bowling, S. & Rodriguez, T. A. Cell competition and its role in the regulation of cell fitness from development to cancer. *Dev. Cell* **38**, 621–634 (2016).

[PubMed](#) [PubMed Central](#) [Google Scholar](#)

6. 6.

Moreno, E. & Rhiner, C. Darwin’s multicellularity: from neurotrophic theories and cell competition to fitness fingerprints. *Curr. Opin. Cell Biol.* **31**, 16–22 (2014).

[CAS](#) [PubMed](#) [PubMed Central](#) [Google Scholar](#)

7. 7.

Maruyama, T. & Fujita, Y. Cell competition in mammals — novel homeostatic machinery for embryonic development and cancer prevention. *Curr. Opin. Cell Biol.* **48**, 106–112 (2017).

[CAS](#) [PubMed](#) [PubMed Central](#) [Google Scholar](#)

8. 8.

Egeblad, M., Nakasone, E. S. & Werb, Z. Tumors as organs: complex tissues that interface with the entire organism. *Dev. Cell* **18**, 884–901 (2010).

[CAS](#) [PubMed](#) [PubMed Central](#) [Google Scholar](#)

9. 9.

Bjerknes, M. & Cheng, H. Colossal crypts bordering colon adenomas in *Apc*^{Min} mice express full-length Apc. *Am. J. Pathol.* **154**, 1831–1834 (1999).

[CAS](#) [PubMed](#) [PubMed Central](#) [Google Scholar](#)

10. 10.

Curtius, K., Wright, N. A. & Graham, T. A. An evolutionary perspective on field cancerization. *Nat. Rev. Cancer* **18**, 19–32 (2018).

[CAS](#) [PubMed](#) [PubMed Central](#) [Google Scholar](#)

11. 11.

Vermeulen, L. & Snippert, H. J. Stem cell dynamics in homeostasis and cancer of the intestine. *Nat. Rev. Cancer* **14**, 468–480 (2014).

[CAS](#) [PubMed](#) [PubMed Central](#) [Google Scholar](#)

12. 12.

Baron, C. S. & van Oudenaarden, A. Unravelling cellular relationships during development and regeneration using genetic lineage tracing. *Nat. Rev. Mol. Cell Biol.* **20**, 753–765 (2019).

[CAS](#) [PubMed](#) [PubMed Central](#) [Google Scholar](#)

13. 13.

Zong, H., Espinosa, J. S., Su, H. H., Muzumdar, M. D. & Luo, L. Mosaic analysis with double markers in mice. *Cell* **121**, 479–492 (2005).

[CAS](#) [PubMed](#) [PubMed Central](#) [Google Scholar](#)

14. 14.

Pontes-Quero, S. et al. Dual ifgMosaic: a versatile method for multispectral and combinatorial mosaic gene-function analysis. *Cell* **170**, 800–814 (2017).

[CAS](#) [PubMed](#) [PubMed Central](#) [Google Scholar](#)

15. 15.

Snippert, H. J. et al. Intestinal crypt homeostasis results from neutral competition between symmetrically dividing Lgr5 stem cells. *Cell* **143**, 134–144 (2010).

[CAS](#) [PubMed](#) [PubMed Central](#) [Google Scholar](#)

16. 16.

Sheng, H., Shao, J., Townsend, C. M., Jr & Evers, B. M. Phosphatidylinositol 3-kinase mediates proliferative signals in intestinal epithelial cells. *Gut* **52**, 1472–1478 (2003).

[CAS](#) [PubMed](#) [PubMed Central](#) [Google Scholar](#)

17. 17.

Haigis, K. M. et al. Differential effects of oncogenic K-Ras and N-Ras on proliferation, differentiation and tumor progression in the colon. *Nat. Genet.* **40**, 600–608 (2008).

[CAS](#) [PubMed](#) [PubMed Central](#) [Google Scholar](#)

18. 18.

Stanger, B. Z., Datar, R., Murtaugh, L. C. & Melton, D. A. Direct regulation of intestinal fate by Notch. *Proc. Natl Acad. Sci. USA* **102**, 12443–12448 (2005).

[ADS](#) [CAS](#) [PubMed](#) [PubMed Central](#) [Google Scholar](#)

19. 19.

Lopez-Garcia, C., Klein, A. M., Simons, B. D. & Winton, D. J. Intestinal stem cell replacement follows a pattern of neutral drift. *Science* **330**, 822–825 (2010).

[ADS](#) [CAS](#) [PubMed](#) [PubMed Central](#) [Google Scholar](#)

20. 20.

Ritsma, L. et al. Intestinal crypt homeostasis revealed at single-stem-cell level by in vivo live imaging. *Nature* **507**, 362–365 (2014).

[ADS](#) [CAS](#) [PubMed](#) [PubMed Central](#) [Google Scholar](#)

21. 21.

Cancer Genome Atlas Network. Comprehensive molecular characterization of human colon and rectal cancer. *Nature* **487**, 330–337 (2012).

[ADS](#) [Google Scholar](#)

22. 22.

Fearon, E. R. Molecular genetics of colorectal cancer. *Annu. Rev. Pathol.* **6**, 479–507 (2011).

[CAS](#) [PubMed](#) [PubMed Central](#) [Google Scholar](#)

23. 23.

Nicholson, A. M. et al. Fixation and spread of somatic mutations in adult human colonic epithelium. *Cell Stem Cell* **22**, 909–918 (2018).

[CAS](#) [PubMed](#) [PubMed Central](#) [Google Scholar](#)

24. 24.

Leedham, S. J. et al. Clonality, founder mutations, and field cancerization in human ulcerative colitis-associated neoplasia. *Gastroenterology* **136**, 542–550 (2009).

[PubMed](#) [PubMed Central](#) [Google Scholar](#)

25. 25.

Galandiuk, S. et al. Field cancerization in the intestinal epithelium of patients with Crohn's ileocolitis. *Gastroenterology* **142**, 855–864 (2012).

[PubMed](#) [PubMed Central](#) [Google Scholar](#)

26. 26.

Vermeulen, L. et al. Defining stem cell dynamics in models of intestinal tumor initiation. *Science* **342**, 995–998 (2013).

[ADS](#) [CAS](#) [PubMed](#) [PubMed Central](#) [Google Scholar](#)

27. 27.

Snippert, H. J., Schepers, A. G., van Es, J. H., Simons, B. D. & Clevers, H. Biased competition between Lgr5 intestinal stem cells driven by oncogenic mutation induces clonal expansion. *EMBO Rep.* **15**, 62–69 (2014).

[CAS](#) [PubMed](#) [PubMed Central](#) [Google Scholar](#)

28. 28.

Kozar, S. et al. Continuous clonal labeling reveals small numbers of functional stem cells in intestinal crypts and adenomas. *Cell Stem Cell* **13**, 626–633 (2013).

[CAS](#) [PubMed](#) [PubMed Central](#) [Google Scholar](#)

29. 29.

Huels, D. J. et al. Wnt ligands influence tumour initiation by controlling the number of intestinal stem cells. *Nat. Commun.* **9**, 1132 (2018).

[ADS](#) [CAS](#) [PubMed](#) [PubMed Central](#) [Google Scholar](#)

30. 30.

Bruens, L., Ellenbroek, S. I. J., van Rheenen, J. & Snippert, H. J. In vivo imaging reveals existence of crypt fission and fusion in adult mouse intestine. *Gastroenterology* **153**, 674–677 (2017).

[PubMed](#) [PubMed Central](#) [Google Scholar](#)

31. 31.

Grün, D. et al. Single-cell messenger RNA sequencing reveals rare intestinal cell types. *Nature* **525**, 251–255 (2015).

[ADS](#) [PubMed](#) [PubMed Central](#) [Google Scholar](#)

32. 32.

Haber, A. L. et al. A single-cell survey of the small intestinal epithelium. *Nature* **551**, 333–339 (2017).

[ADS](#) [CAS](#) [PubMed](#) [PubMed Central](#) [Google Scholar](#)

33. 33.

Ayyaz, A. et al. Single-cell transcriptomes of the regenerating intestine reveal a revival stem cell. *Nature* **569**, 121–125 (2019).

[ADS](#) [CAS](#) [PubMed](#) [PubMed Central](#) [Google Scholar](#)

34. 34.

Cheng, C. W. et al. Ketone body signaling mediates intestinal stem cell homeostasis and adaptation to diet. *Cell* **178**, 1115–1131 (2019).

[CAS](#) [PubMed](#) [PubMed Central](#) [Google Scholar](#)

35. 35.

Gehart, H. & Clevers, H. Tales from the crypt: new insights into intestinal stem cells. *Nat. Rev. Gastroenterol. Hepatol.* **16**, 19–34 (2019).

[PubMed](#) [PubMed Central](#) [Google Scholar](#)

36. 36.

Stzepourginski, I. et al. CD34⁺ mesenchymal cells are a major component of the intestinal stem cells niche at homeostasis and after injury. *Proc. Natl Acad. Sci. USA* **114**, E506–E513 (2017).

[CAS](#) [PubMed](#) [PubMed Central](#) [Google Scholar](#)

37. 37.

Greicius, G. et al. *PDGFRα*⁺ pericyctal stromal cells are the critical source of Wnts and RSPO3 for murine intestinal stem cells in vivo. *Proc. Natl Acad. Sci. USA* **115**, E3173–E3181 (2018).

[CAS](#) [PubMed](#) [PubMed Central](#) [Google Scholar](#)

38. 38.

McCarthy, N. et al. Distinct mesenchymal cell populations generate the essential intestinal BMP signaling gradient. *Cell Stem Cell* **26**, 391–402 (2020).

[CAS](#) [PubMed](#) [PubMed Central](#) [Google Scholar](#)

39. 39.

Jin, Z. et al. Differentiation-defective stem cells outcompete normal stem cells for niche occupancy in the *Drosophila* ovary. *Cell Stem Cell* **2**, 39–49 (2008).

[CAS](#) [PubMed](#) [PubMed Central](#) [Google Scholar](#)

40. 40.

Ellis, S. J. et al. Distinct modes of cell competition shape mammalian tissue morphogenesis. *Nature* **569**, 497–502 (2019).

[ADS](#) [CAS](#) [PubMed](#) [PubMed Central](#) [Google Scholar](#)

41. 41.

Kinross, K. M. et al. An activating *Pik3ca* mutation coupled with *Pten* loss is sufficient to initiate ovarian tumorigenesis in mice. *J. Clin. Invest.* **122**, 553–557 (2012).

[CAS](#) [PubMed](#) [PubMed Central](#) [Google Scholar](#)

42. 42.

Murtaugh, L. C., Stanger, B. Z., Kwan, K. M. & Melton, D. A. Notch signaling controls multiple steps of pancreatic differentiation. *Proc. Natl Acad. Sci. USA* **100**, 14920–14925 (2003).

[ADS](#) [CAS](#) [PubMed](#) [PubMed Central](#) [Google Scholar](#)

43. 43.

Orsulic, S. et al. Induction of ovarian cancer by defined multiple genetic changes in a mouse model system. *Cancer Cell* **1**, 53–62 (2002).

[CAS](#) [PubMed](#) [PubMed Central](#) [Google Scholar](#)

44. 44.

Zhao, J. J. et al. The oncogenic properties of mutant p110 α and p110 β phosphatidylinositol 3-kinases in human mammary epithelial cells. *Proc. Natl Acad. Sci. USA* **102**, 18443–18448 (2005).

[ADS](#) [CAS](#) [PubMed](#) [PubMed Central](#) [Google Scholar](#)

45. 45.

Susaki, E. A. et al. Advanced CUBIC protocols for whole-brain and whole-body clearing and imaging. *Nat. Protocols* **10**, 1709–1727 (2015).

[CAS](#) [PubMed](#) [PubMed Central](#) [Google Scholar](#)

46. 46.

Snippert, H. J., Schepers, A. G., Delconte, G., Siersema, P. D. & Clevers, H. Slide preparation for single-cell-resolution imaging of fluorescent proteins in their three-dimensional near-native environment. *Nat. Protocols* **6**, 1221–1228 (2011).

[CAS](#) [PubMed](#) [PubMed Central](#) [Google Scholar](#)

47. 47.

Stzepourginski, I., Eberl, G. & Peduto, L. An optimized protocol for isolating lymphoid stromal cells from the intestinal lamina propria. *J. Immunol. Methods* **421**, 14–19 (2015).

[CAS](#) [PubMed](#) [PubMed Central](#) [Google Scholar](#)

48. 48.

Sato, T. et al. Single Lgr5 stem cells build crypt-villus structures in vitro without a mesenchymal niche. *Nature* **459**, 262–265 (2009).

[ADS](#) [CAS](#) [Google Scholar](#)

49. 49.

Lun, A. T., Bach, K. & Marioni, J. C. Pooling across cells to normalize single-cell RNA sequencing data with many zero counts. *Genome Biol.* **17**, 75 (2016).

[PubMed](#) [Google Scholar](#)

50. 50.

Feng, Y. et al. Mutant *Kras* promotes hyperplasia and alters differentiation in the colon epithelium but does not expand the presumptive stem cell pool. *Gastroenterology* **141**, 1003–1013 (2011).

[CAS](#) [PubMed](#) [PubMed Central](#) [Google Scholar](#)

51. 51.

Herman, J. S., Sagar, & Grün, D. FateID infers cell fate bias in multipotent progenitors from single-cell RNA-seq data. *Nat. Methods* **15**, 379–386 (2018).

[CAS](#) [PubMed](#) [PubMed Central](#) [Google Scholar](#)

52. 52.

Pinto, D., Gregorieff, A., Begthel, H. & Clevers, H. Canonical Wnt signals are essential for homeostasis of the intestinal epithelium. *Genes Dev.* **17**, 1709–1713 (2003).

[CAS](#) [PubMed](#) [PubMed Central](#) [Google Scholar](#)

53. 53.

Qi, Z. et al. BMP restricts stemness of intestinal Lgr5⁺ stem cells by directly suppressing their signature genes. *Nat. Commun.* **8**, 13824 (2017).

[ADS](#) [CAS](#) [PubMed](#) [PubMed Central](#) [Google Scholar](#)

54. 54.

Sansom, O. J. et al. Myc deletion rescues Apc deficiency in the small intestine. *Nature* **446**, 676–679 (2007).

[ADS](#) [CAS](#) [PubMed](#) [PubMed Central](#) [Google Scholar](#)

55. 55.

Kim, T. H. et al. Broadly permissive intestinal chromatin underlies lateral inhibition and cell plasticity. *Nature* **506**, 511–515 (2014).

[ADS](#) [CAS](#) [PubMed](#) [PubMed Central](#) [Google Scholar](#)

56. 56.

Skinnider, M. A. et al. Cell type prioritization in single-cell data. *Nat. Biotechnol.* **39**, 30–34 (2021).

[CAS](#) [PubMed](#) [PubMed Central](#) [Google Scholar](#)

57. 57.

Huang, W., Sherman, B. T. & Lempicki, R. A. Systematic and integrative analysis of large gene lists using DAVID bioinformatics resources. *Nat. Protocols* **4**, 44–57 (2009).

[CAS](#) [Google Scholar](#)

[Download references](#)

Acknowledgements

We thank S. Alexandrova and members of the Simons laboratory for discussions, C. J. Hindley for reading the manuscript, S. Bae for assistance with graphic illustrations, the Gurdon Institute Imaging Facility for microscopy and image analysis support, and the Cancer Research UK Cambridge Institute Genomics Core Facility for sequencing and library generation. This work was supported by a Cancer Research UK Multidisciplinary Project Award to B.-K.K. and B.D.S. (C52767/A23363), and grants to A.P. (Cancer Research UK, A25636), J.-H.L. (Wellcome Trust, 107633/Z/15/Z; ERC Starting Grant, 679411), B.-K.K. (ERC Starting Grant, 639050; Human Frontier Science Program, RGY0071/2018;

Interpark Bio-Convergence Center Grant Program, IBCC-IMBA-2020-01) and B.D.S. (Wellcome Trust, 098357/Z/12/Z and 219478/Z/19/Z), as well as by studentships and fellowships to J.F. (Wellcome Trust), S.-H.S.W. (DOC Fellowship of the Austrian Academy of Sciences), L.C. (Herchel Smith Fund), S.H. (Human Frontier Science Program, LT000092/2016-L; Basic Science Research Program NRF-2014R1A6A3A01005675) and B.D.S. (Royal Society EP Abraham Research Professorship, RP\R1\180165). The research team also acknowledges core grant support from the Austrian Academy of Sciences to the Institute of Molecular Biotechnology, the Wellcome Trust and MRC to the Wellcome–MRC Cambridge Stem Cell Institute, and the Wellcome Trust (092096) and CRUK (C6946/A14492) to the Gurdon Institute.

Author information

Author notes

1. These authors contributed equally: Min Kyu Yum, Seungmin Han
2. These authors jointly supervised this work: Bon-Kyoung Koo, Benjamin D. Simons

Affiliations

1. Wellcome Trust–Cancer Research UK Gurdon Institute, University of Cambridge, Cambridge, UK

Min Kyu Yum, Seungmin Han, Lemonia Chatzeli & Benjamin D. Simons

2. Wellcome Trust–Medical Research Council Cambridge Stem Cell Institute, Jeffrey Cheah Biomedical Centre, University of Cambridge, Cambridge, UK

Min Kyu Yum, Seungmin Han, Juergen Fink, Catherine Dabrowska, Teodora Trendafilova, Roxana Mustata, Lemonia Chatzeli, Roberta Azzarelli, Irina Pshenichnaya, Frances

England, Anna Philpott, Joo-Hyeon Lee, Bon-Kyoung Koo & Benjamin D. Simons

3. Institute of Molecular Biotechnology of the Austrian Academy of Sciences (IMBA), Vienna Biocenter (VBC), Vienna, Austria

Szu-Hsien Sam Wu & Bon-Kyoung Koo

4. Vienna BioCenter PhD Program, Doctoral School at the University of Vienna and Medical University of Vienna, Vienna, Austria

Szu-Hsien Sam Wu

5. Department of Physiology, Development and Neuroscience, University of Cambridge, Cambridge, UK

Catherine Dabrowska, Frances England & Joo-Hyeon Lee

6. Department of Oncology, University of Cambridge, Hutchison–MRC Research Centre, Cambridge, UK

Roberta Azzarelli & Anna Philpott

7. Department of New Biology, DGIST, Daegu, Republic of Korea

Eunmin Lee & Jong Kyoung Kim

8. Department of Visceral, Thoracic and Vascular Surgery, University Hospital Carl Gustav Carus, Medical Faculty, Technische Universität Dresden, Dresden, Germany

Daniel E. Stange

9. Department of Applied Mathematics and Theoretical Physics, Centre for Mathematical Sciences, University of Cambridge, Cambridge, UK

Benjamin D. Simons

Authors

1. Min Kyu Yum

[View author publications](#)

You can also search for this author in [PubMed](#) [Google Scholar](#)

2. Seungmin Han

[View author publications](#)

You can also search for this author in [PubMed](#) [Google Scholar](#)

3. Juergen Fink

[View author publications](#)

You can also search for this author in [PubMed](#) [Google Scholar](#)

4. Szu-Hsien Sam Wu

[View author publications](#)

You can also search for this author in [PubMed](#) [Google Scholar](#)

5. Catherine Dabrowska

[View author publications](#)

You can also search for this author in [PubMed](#) [Google Scholar](#)

6. Teodora Trendafilova

[View author publications](#)

You can also search for this author in [PubMed](#) [Google Scholar](#)

7. Roxana Mustata

[View author publications](#)

You can also search for this author in [PubMed](#) [Google Scholar](#)

8. Lemonia Chatzeli

[View author publications](#)

You can also search for this author in [PubMed](#) [Google Scholar](#)

9. Roberta Azzarelli

[View author publications](#)

You can also search for this author in [PubMed](#) [Google Scholar](#)

10. Irina Pshenichnaya

[View author publications](#)

You can also search for this author in [PubMed](#) [Google Scholar](#)

11. Eunmin Lee

[View author publications](#)

You can also search for this author in [PubMed](#) [Google Scholar](#)

12. Frances England

[View author publications](#)

You can also search for this author in [PubMed](#) [Google Scholar](#)

13. Jong Kyoung Kim

[View author publications](#)

You can also search for this author in [PubMed](#) [Google Scholar](#)

14. Daniel E. Stange

[View author publications](#)

You can also search for this author in [PubMed](#) [Google Scholar](#)

15. Anna Philpott

[View author publications](#)

You can also search for this author in [PubMed](#) [Google Scholar](#)

16. Joo-Hyeon Lee

[View author publications](#)

You can also search for this author in [PubMed](#) [Google Scholar](#)

17. Bon-Kyoung Koo

[View author publications](#)

You can also search for this author in [PubMed](#) [Google Scholar](#)

18. Benjamin D. Simons

[View author publications](#)

You can also search for this author in [PubMed](#) [Google Scholar](#)

Contributions

M.K.Y., S.H., J.F., B.-K.K. and B.D.S. planned and designed the experiments. M.K.Y. performed lineage tracing, tissue imaging and quantification, flow cytometry and cell sorting, which were supervised by A.P., J.-H.L., B.-K.K. and B.D.S. B.-K.K. conceived the Red2Onco design and the Red2Onco mouse models were established by M.K.Y., S.H., J.F., C.D., T.T., R.M., J.-H.L. and B.-K.K. M.K.Y. and B.D.S. performed the quantitative statistical analysis of the clone size data. M.K.Y. and S.-H.S.W. performed organoid experiments. M.K.Y., L.C. and I.P. performed *in situ* hybridization experiments. C.D., L.C., R.A. and F.E. performed lineage tracing with oesophagus, stomach corpus, pancreas and lung tissue, respectively. E.L. and J.K.K. aligned raw sequencing data from scRNA-seq experiments. M.K.Y. and S.H. analysed scRNA-seq data, supervised by J.K.K., B.-K.K. and B.D.S. S.H. devised the algorithm for statistical analysis of transcriptomic changes with scRNA-seq data. S.-H.S.W. performed lineage tracing and tissue preparation of *LSL-Kras^{G12D}*, *PIK3CA^{Lat-H1047R}* and *Apc^{f/f}* mice, which were provided by D.E.S. M.K.Y., S.H., B.-K.K. and B.D.S. wrote the manuscript with input from all authors. These authors contributed equally: J.F., S.-H.S.W., C.D., T.T.

Corresponding authors

Correspondence to [Bon-Kyoung Koo](#) or [Benjamin D. Simons](#).

Ethics declarations

Competing interests

The authors declare no competing interests.

Additional information

Peer review information *Nature* thanks Hans Clevers, James DeGregori, Dominic Grün and Toshiro Sato for their contribution to the peer review of this work. Peer reviewer reports are available.

Publisher's note Springer Nature remains neutral with regard to jurisdictional claims in published maps and institutional affiliations.

Extended data figures and tables

[Extended Data Fig. 1 Red2Onco system: an oncogene-associated multicolour reporter.](#)

a, Representative confocal images of mutant clones from sections (*Red2-Notch1^{ICD}*) or whole mounts (*Red2-Kras^{G12D}* and *Red2-PIK3CA^{H1047R}*) of small intestine from *Villin-CreERT2;Red2Onco* mice 2 w after tamoxifen administration. Crypt borders are marked with a grey dashed outline. **b**, Average clone numbers collected from a single field of image (0.15 mm²) of whole-mount small intestine from *Villin-CreERT2;R26R-Confetti* or *Red2Onco* mice 2 d after tamoxifen administration. **c–e**, Representative confocal images (left) and quantification (right) of EdU⁺ proliferating crypt cells (**c**), LYZ⁺ Paneth cells (**d**) and MUC2⁺ goblet cells (**e**) from sections of small intestine from *Villin-CreERT2;R26R-Confetti* or *Red2Onco* mice 4 w after tamoxifen administration. **f**, Representative confocal images of 100-μm-thick sections or whole mounts of tissues from adult *R26R-CreERT2; Red2Onco* mice (skin and stomach corpus), *Sftpc-CreERT2; Red2Onco* mice (lung) or *Krt5-CreERT2; Red2Onco* mice (oesophagus) at 1, 2 and 4 w after tamoxifen administration. White dashed line, epithelial lining. β-catenin stained as a cell membrane marker. SPC marks alveolar type II cells in lung. **g**, Representative confocal images of sectioned mouse

embryonic pancreas tissue from the *R26R-CreERT2; Red2-Kras*^{G12D} mouse on embryonic day (E)18.5, 6 d after tamoxifen administration. Magnified panel to the right shows an example of acinar cell expansion in developing pancreas. CPA1 marks acinar cells. * $P < 0.05$, ** $P < 0.01$, *** $P < 0.0001$ by one-way ANOVA with Games-Howell's multiple comparisons test (**b**, **c**) or unpaired two-tailed *t*-test (**d**, **e**) from biological replicates. Data are mean ± s.d. (**b**) or mean ± s.e.m. (**c–e**). Exact *P* values are presented in Source Data. Scale bars: 50 μm (**a**, **c–f**) or 200 μm (**g**).

[Source data](#)

[Extended Data Fig. 2 Oncogenes drive non-neutral clone expansion in the mouse intestinal crypt.](#)

a, Schematic illustration of clonal events within the Red2Onco system (left) and representative tile scan images (right). Images are representative of tissues quantified in **h–k**. Arrow, WT crypt; arrowheads, fixed mutant crypts. **b**, Representative confocal images of the base and neck of crypts. Images are representative of tissues quantified in **c**. **c–e**, Strong correlation between clone size at the base and neck of a crypt from *Villin-CreERT2;R26R-Confetti* (2 w after tamoxifen administration) or *Red2Onco* mice (1 w after tamoxifen administration). **f**, Average number of clones per 100 crypts. **g**, Schematic illustration of mutant (RFP⁺) and WT (YFP⁺) clones in crypts, remote from each other. **h**, Representative confocal images at 4 d, 1 w, 2 w and 3 w after tamoxifen administration. Images are representative of tissues quantified in **i–k**. Red2-Wild-type: remote YFP⁺ clones; Red2-Mutant: RFP⁺ clones. **i**, Heat maps indicate the relative clone fractions of the indicated sizes (columns) at various time points after induction (rows). Data are mean ± s.e.m. **j**, **k**, Average clone size (**j**) and percentage of monoclonal crypts (**k**) at different time points after tamoxifen administration. Asterisks for statistical significance omitted in graphs in **j**, **k** for better visualization. Confocal images of small intestine are from *Villin-CreERT2;R26R-Confetti* (**a**, **b**, **h**) or *Red2Onco* mice (**a**, **h**). Crypt borders are marked with a white dashed outline (**a**, **b**). Significance (* $P < 0.05$; ** $P < 0.01$; *** $P < 0.0001$) was determined by unpaired two-tailed Pearson's correlation test (**c–e**), one-way ANOVA with Games-Howell's multiple comparisons test (**j**) or unpaired two-tailed *t*-test (**k**) from

biological replicates. Data are mean \pm s.d. (**f**) or mean \pm s.e.m. (**j, k**). For exact P values, see Source Data. Scale bars: 100 μm (**a, b**) or 50 μm (**h**).

[Source data](#)

Extended Data Fig. 3 Biophysical modelling of mutant clone expansion.

a, d, Contour plots showing mean-square differences of clone size distribution between neutral drift model and YFP clone data from *Confetti* (left), WT crypts remote from mutant crypts in R2KR (middle) and R2P3 (right) in **a**; and between biased drift model and RFP mutant (MT) clone data from R2KR (left), R2P3 (middle) and R2N1 (right) in **d**. Plots: scan of loss/replacement rate λ against time delay between injection and induction in **a**; and drift bias δ with time delay of 0.29 w (R2KR), 0 w (R2P3), and 0.43 w (R2N1) in **d**. Blue lines in **d**, constraint $\lambda(1 - \delta) = \lambda_{\text{WT}}$, where λ_{WT} is the loss/replacement rate inferred from *Confetti* ([Supplementary Theory](#)). Analysis in **a, d** based on data in **c, f**, respectively. **b, e**, Average clone size (effective stem cell number) from **a, d**, respectively. Points show data, lines show model prediction at optimal parameter values. In each case, total effective stem cell number $N = 5$, so that an average clone size of, for example, 2 corresponds to circumferential angle of $360^\circ \times 2/5$. **c, f**, Distribution of clone sizes for models from **a, d**, respectively. Points show data; lines show model prediction at optimal parameter values. **g**, Representative confocal images of cleaved caspase-3⁺ apoptotic cells. A single cleaved caspase-3⁺ apoptotic cell in the villus tip is indicated by the white arrow as a positive control. **h, i**, Representative confocal images (**h**) and quantification (**i**) of EdU⁺ proliferating crypt base columnar cells. Whole mount of small intestine from *Villin-CreERT2;R26R-Confetti* or *Red2Onco* 1 w (**g**) or 2 w (**h, i**) after tamoxifen administration. * $P < 0.05$, ** $P < 0.01$, *** $P < 0.0001$; unpaired two-tailed t -test (**i**) from biological replicates. Data are mean \pm s.e.m. (**b, c, e, f, i**). Exact P values in Source Data. Scale bars: 50 μm (**g**) or 25 μm (**h**).

[Source data](#)

Extended Data Fig. 4 Mutant crypts perturb clonal dynamics of WT cells in neighbouring crypts.

a, Representative confocal images of tissues quantified in **b**. Fixed (monoclonal) WT crypts are indicated by white arrows. **b**, Percentage of monoclonal WT small intestinal crypts. **c**, **d**, Average clone size (**c**) and percentage of monoclonal crypts (**d**) of remote and proximate WT (YFP^+) clones at different time points after tamoxifen administration. **e**, Schematic illustration of proximate WT clones in relation to fixed mutant crypts. **f**, Heat maps indicate the relative clone fractions of the indicated sizes (columns) at various time points after induction (rows). Data are mean \pm s.e.m. **g**, Average clone size of proximate (inner and outer) WT (YFP^+) clones at different time points after tamoxifen administration. **h**, Average clone size $\langle \theta \rangle / 360^\circ$ of WT (YFP^+) clones in crypts neighbouring fixed mutant crypts as a function of time t after induction. Data are mean \pm s.e.m. Blue line shows a fit to the square root dependence predicted by the neutral drift model ([Supplementary Theory](#)). Orange line shows the 95% confidence interval. **i**, Schematic illustration of factors that affect rate of clonal drift ([Supplementary Theory](#)). **j**, Representative images (left) and quantification (right) of OLFM4^+ ISCs. Arrows, proximate WT crypts; arrowheads, fixed mutant crypts; grey dashed outlines, crypt borders. Confocal images of whole-mount small intestine are from *Villin-CreERT2;R26R-Confetti* or *Red2Onco* mice (**a**) and *Lgr5-EGFP-IRES-CreERT2;Red2Onco* mice (**j**) 2 w after tamoxifen administration.
* $P < 0.05$, ** $P < 0.01$, *** $P < 0.0001$; one-way ANOVA with Games-Howell's multiple comparisons test (**c**, **g**) and unpaired two-tailed t -test (**b**, **d**, **j**) from biological replicates. Data are mean \pm s.e.m. (**b-d**, **f-h**) or mean \pm s.d. (**j**). For exact P values, see Source Data. Asterisks for statistical significance omitted in graphs in **c**, **d**, **g** for better visualization. Scale bars, 50 μm (**a**, **j**).

[Source data](#)

Extended Data Fig. 5 Reduced effective stem cell number leads to accelerated drift dynamics.

a, Original image (left) was thresholded (top right) and outlined (bottom right) to measure crypt size and circularity. Image representative of tissues quantified in **b–e**. **b–e**, Scatter and violin plots display size (**b, c**) and circularity (**d, e**) of WT crypts against distance from nearest fixed mutant (RFP^+) crypt. **f, g**, Illustration (**f**) and confocal images (**g**) of clones representative of tissues quantified in **h, i**. **h**, Heat maps indicate relative clone fractions of given sizes. Data are mean \pm s.e.m. **i**, Percentage of monoclonal crypts of proximate WT (YFP^+) clones. **j, k**, Confocal images (**j**) and quantification (**k**) of EGFP^+ (LGR5^+) ISCs. Images representative of tissues quantified in **k, l**. White dashed lines, EGFP^+ cells in WT crypts. **l**, Violin plots display size of WT crypts in relation to multiplicity of neighbouring mutant crypts. n for each group is shown. **m, n**, Representative confocal images of *Red2Onco* intestine (**m**) and fractions of WT crypts from single field (0.15 mm^2 ; **n**). **o**, Illustration (left) and representative images (right) of crypt fission and fusion event in ‘8-shaped crypts’³⁰. Images representative of tissues quantified in **p**. **p**, Percentage of crypts undergoing crypt fission (upper) or fusion (lower). Whole mount of small intestine from *Villin-CreERT2;R26R-Confetti* or *Red2Onco* mice (**a–i**, **m, o, p**), and *Lgr5-EGFP-IRES-CreERT2;Red2Onco* mice (**j, k**) at indicated time points. Proximate WT crypts and fixed mutant crypts indicated by white arrows and arrowheads, respectively (**g, j**). Crypt borders marked by dashed grey outlines (**g, j, o**). In **b, d**, blue shaded area and red dashed line indicate 95% confidence interval of *R26R-Confetti* controls and average distance between the centre of fixed mutant crypt and proximate WT crypts, respectively. $*P < 0.05$, $**P < 0.01$, $***P < 0.0001$; unpaired two-tailed *t*-test (**c, e, i, k, l, p**). Data are mean \pm s.d. (**i, k, n**) or mean \pm s.e.m. (**h, p**). For exact *P* values, see Source Data. Scale bars, $50 \mu\text{m}$ (**a, g, j, m, o**).

Source data

Extended Data Fig. 6 Oncogene-driven signalling changes.

a, FACS sorting strategy to isolate cells from *Confetti* and *Red2Onco* tissue. R1, live; R2, singlet; R3, mesenchymal/immune (EPCAM^-); R4, epithelial (EPCAM^+); R5, mutant-epithelial (RFP^+); R6, WT epithelial (YFP^+); R7,

immune ($CD45^+$); R8, mesenchymal ($CD45^-$). **b**, Box plots showing distributions of Pearson correlation coefficients in averaged \log_2 -transformed normalized UMIs for cell types across all pairs of mice from the same (white) and between different (grey) conditions. **c**, UMAP of epithelial cells detected by Louvain. k , k nearest-neighbour value. **d**, UMAPs showing distribution of averaged expression of marker genes. Colour bars, average \log_2 -transformed normalized UMIs. Top left from Fig. [3b](#). **e**, Heat map representing marker expression for epithelial cells. Coloured panel (left) groups marker genes (right) for cell types. Colour bar, auto-scaled \log_2 -transformed normalized UMIs. **f**, Heat maps representing differential gene expression for epithelial cells in *Red2Onco* compared to *Confetti*. Parentheses, number of differentially expressed genes. Colour bar, \log_2 (fold change) (Supplementary Table [1](#)). **g**, UMAPs showing distributions of mutant (RFP^+) and WT (YFP^+) epithelial cells for *Confetti* and *Red2Onco* mice. **h**, **i**, Fractions of mutant (**h**) and WT (**i**) epithelial cells in *Red2Onco* and *Confetti* mice. See Fig. [3c](#) for other WT data. **j–l**, Confocal images (**j**) of EGFP $^+$ cells, representative of tissues quantified for stem cell number (**k**) and fraction (**l**). In **j**, white arrows indicate WT crypts proximate to mutant (MT) crypts. White dashed lines mark crypts. Scale bars, 25 μ m. **m**, **n**, FACS plots (**m**) and quantification (**n**) of EGFP hi stem cell fractions from R5 or R6 (**a**). Small intestine from *Lgr5-EGFP-IRES-CreERT2;Red2Onco* 2 w after induction (clonal dosage (0.2 mg per 20 g body weight) for **j–l**, mosaic dosage (4 mg per 20 g body weight) for **m**, **n**). * $P < 0.05$, ** $P < 0.01$, *** $P < 0.0001$; n.s., statistically not significant, $P > 0.05$; two-sided Kolmogorov–Smirnov test (**b**), two-sided likelihood ratio test (**h**, **i**) and one-way ANOVA with Games-Howell’s multiple comparisons test (**k**, **l**, **n**). Data are mean \pm s.e.m. (**h**, **i**, **k**, **l**) or mean \pm s.d. (**n**). For exact P values, see Source Data.

[Source data](#)

[Extended Data Fig. 7 Mutant crypt induces primed differentiation.](#)

a, b, Priming scores of stem (SC) and transit-amplifying (TA) cells of mutant (**a**) and WT (**b**) crypts towards secretory and enterocyte lineages in

Red2Onco and *Confetti* mice. Black line, 50th percentile; dashed lines, 25th and 75th percentiles. Green and black asterisks, higher and lower in *Red2Onco* than in *Confetti*, respectively. **c**, qPCR of lineage markers (*Lgr5*, ISC; *Clcal*, goblet cell; *Fabp1*, enterocyte; *Mki67*, proliferation) using sorted RFP⁺ and YFP⁺ cells from *Villin-CreERT2;R26R-Confetti* or *Red2Onco* mice 2 w after tamoxifen administration. **d, e**, Confocal images (**d**) and quantification (**e**) of MUC2⁺ goblet cells. **f, h–j**, Images (**f**) from RNA in situ hybridization of enterocyte marker *Fabp1* and quantification in remote WT (Remote_R2KR, Remote_R2P3; **h**), proximate WT (Prox_R2KR, Prox_R2P3; **i**) and mutant crypts (MT_R2KR or MT_R2P3; **j**) along crypt axis. In **f**, *Fabp1*⁺ cells in lower crypts (below +8) marked by white arrow. **g**, Illustration of cellular localization along crypt axis. Position 0 is crypt base cell. **k, l**, UMAPs showing distributions of enrichment scores for BMP (**k**, left), WNT (**k**, right), and NOTCH (**l**) pathways in epithelial cells of *Red2Onco* and *Confetti* mice. Colour bars, enrichment scores. **m**, Fractions of ‘active’ cells with high enrichment scores for NOTCH pathway in mutant (MT) and WT epithelial cells from *Red2Onco* and *Confetti* mice. Small intestine sections from *Villin-CreERT2;R26R-Confetti* or *Red2Onco* 2 w after tamoxifen administration (**d, f**). WT and mutant crypts marked with white and grey dashed outlines, respectively (**d, f**). Remote WT in crypts separated by >3 crypt diameters from mutant crypts. Proximate WT in crypts neighbouring fixed mutant crypts. * $P < 0.05$, ** $P < 0.01$, *** $P < 0.0001$; two-sided Kolmogorov–Smirnov test (**a, b**), unpaired two-tailed *t*-test (**c, e, h–j**) and two-sided likelihood ratio test (**m**). Data are mean ± s.e.m. (**c, e, m**) or mean ± s.d. (**h–j**). For exact *P* values, see Source Data. Scale bars, 50 μm (**d, f**).

[Source data](#)

[Extended Data Fig. 8 Mutation-induced environmental changes.](#)

a, t-SNE representing immune cells from *Confetti* and *Red2Onco* mice. **b, c**, Heat maps representing differential expression (DE) patterns for mesenchymal (**b**) and immune (**c**) cells from *Red2Onco* and *Confetti* mice: top 300 genes or less (FDR < 0.05, pairwise *t*-test). Colour bar, averaged Z-

scores of \log_2 -transformed normalized UMIs. **d**, Secretion factor expression in stromal clusters for *Confetti*. In **d**, **f**, dot size denotes percentage of cells expressing gene; colour shows average expression. **e**, UMAPs showing expression of *Bmprla* and *Fzd7* in epithelial cells. Colour bar, \log_2 -transformed normalized UMIs. Inset from Fig. [3b](#). **f**, Dot plots showing expression of receptors upstream of BMP and WNT pathways for epithelial cells. **g**, **h**, Fractions of mesenchymal (**g**) and immune (**h**) cells in *Red2Onco* and *Confetti* mice. Data are mean \pm s.e.m. Two-sided likelihood ratio test: * $P < 0.05$, ** $P < 0.01$; n.s., statistically not significant ($P > 0.05$). **i**, Degree of transcriptomic change for immune cells estimated by cell-to-cell variability (P_{VAR}) or separability of perturbed and unperturbed cells (P_{AUGUR}). Dotted lines show $-\log_{10}(0.01)$. Dot colour denotes cell type; dot shape shows *Red2Onco*. **j**, Enriched biological processes from gene ontology (GO) analysis of DE genes in STC2 of *Red2-PIK3CA^{H1047R}* mice relative to *Confetti*. One-sided Fisher's exact test. Dotted line, $-\log_{10}(0.05)$. **k**, **l**, Heat maps representing DE genes and their numbers (in parentheses) for mesenchymal (**k**) and immune (**l**) cells in *Red2Onco* mice compared to *Confetti*. Colour bar, $\log_2(\text{fold change})$ (Supplementary Table [3](#)). **m**, Volcano plot representing DE genes in STC2 of *Red2-PIK3CA^{H1047R}* mice relative to *Confetti*. Two-sided pairwise *t*-test. Red dots, genes for biological processes in **j**. Vertical dotted lines, absolute value of $\log_2(\text{fold change}) = 0.259$; horizontal, $-\log_{10}(0.05)$. **n**, Model of direct and indirect cross-talk between mutant and WT crypts in *Red2Onco* mice. BC, B cell; DC, dendritic cell; Mono, monocyte; MP1, 2, macrophage 1, 2; PLC, plasma cell; TC, T cell. For exact *P* values, see Source Data.

Source data

Extended Data Fig. 9 Mutant clones secrete functional BMP ligands.

a–d, Representative *in situ* hybridization images and quantification of *Axin2* (**a**, **b**) and *Id1* (**c**, **d**) on sections of small intestine from *Villin-CreERT2;R26R-Confetti* or *Red2Onco* mice 2 w after tamoxifen administration. Arrowheads, fixed mutant crypts. Crypts are marked with dashed outlines. **e**, **f**, qPCR analysis of *Axin2* (**e**), and *Id1* (**f**). **g**,

Experimental set-up for **h–j**. **h**, Bright-field images of intestinal organoids after 2 days of treatment. The number and size of crypt-like budding structures are reduced in treated organoids. **i**, qPCR analysis of lineage markers. **j**, Representative images of LGR5–EGFP organoids show that the number of LGR5⁺ cells decreases following treatment. **k**, Experimental set-up for **l, m**. **l, m**, Bright-field images (**l**) and quantification (**m**) of intestinal organoids after 6 days of culture in WENR medium. **n**, qPCR analysis of BMP ligands (*Bmp2* and *Bmp7*). **o**, Experimental set-up for **p**. **p**, qPCR analysis of *Id1* using WT organoids after the CM treatment. **q**, Bright-field images of intestinal organoids from *Villin-CreERT2;R26R-Confetti* or *Red2Onco* mice 1 month after tamoxifen administration. Insets, RFP expression in the mutant organoids. **r**, qPCR analysis of WT and mutant organoids cultured in ENR medium. In **e, f, n, r**, sorted RFP⁺ or YFP⁺ cells from *Villin-CreERT2;R26R-Confetti* or *Red2Onco* mice 2 w after tamoxifen administration (4 mg per 20 g body weight, mosaic dosage) were analysed. * $P < 0.05$, ** $P < 0.01$, *** $P < 0.0001$; one-way ANOVA with Games-Howell's multiple comparisons test (**b, d**) and unpaired two-tailed *t*-test (**e, f, i, m, n, p, r**). Quantification graphs show data from three independent experiments (**i, m, p, r**). Data are mean \pm s.d. (**b, d, i, m, p**) or mean \pm s.e.m. (**e, f, n, r**). For exact *P* values, see Source Data. Scale bars: 50 μm (**a, c, h**), 100 μm (**j, q**) and 500 μm (**l**).

Source data

Extended Data Fig. 10 Mutant clones drive niche stromal remodelling.

a, Heat map showing marker gene expression for STC2 among mesenchymal cells. Colour bar, averaged Z-scores of log₂-transformed normalized UMIs over all cells within a cell type in *Confetti* mice. **b, c**, Representative multiplexed *in situ* hybridization images (**b**) and quantification (**c**) of *Sfrp2* in *Grem1*⁺ cells on small intestine sections from *Villin-CreERT2;R26R-Confetti* or *Red2Onco* mice 2 w after tamoxifen administration. Arrowheads, fixed mutant crypts; grey dashed outlines indicate crypts; arrows, *Grem1*⁺ STC2 cells. **d**, Heat map showing expression of marker genes and secreted factors in STC1, 2 from *Red2Onco*

and *Confetti* mice. Colour bar, averaged Z-scores of log₂-transformed normalized UMIs over all cells within a cell type and condition. **e**, Projection of *Pdgfra* expression (middle) onto UMAP from Fig. 3f (left) for comparison. Projection of *Cd81* expression onto *Pdgfra*^{lo} cell clusters (STC1, 2) (right). Colour bar, log₂-transformed normalized UMIs. **f**, Sorting strategy to isolate STC2 from intestinal mesenchymal cells by FACS. R1, non-immune cells (CD45⁻); R2, mesenchymal cells (EPCAM⁻); R3, PDGFRA^{lo} population. **g**, qPCR of STC2 markers (*Cd81*, *Grem1*), STC1 marker (*Frzb*) and secreted WNT modulators (*Rspo3*, *Sfrp2*, *Sfrp4*) using sorted CD45⁻EPCAM⁻PDGFRA^{lo}CD81⁻ cells (STC1) or CD45⁻EPCAM⁻PDGFRA^{lo}CD81⁺ cells (STC2) from *Villin-CreERT2;R26R-Confetti* or *Red2Onco* mice 2 w after tamoxifen administration. **h**, qPCR of telocyte markers (*Pdgfra*, *Foxl1*) using sorted STC1, 2 and PDGFRA^{hi} telocytes. **P* < 0.05, ***P* < 0.01, ****P* < 0.0001; one-way ANOVA with Games-Howell's multiple comparisons test (**c**) and unpaired two-tailed *t*-test (**g**, **h**). Data are mean ± s.d. (**c**, **g**) or mean ± s.e.m. (**h**). For exact *P* values, see Source Data. Scale bars, 25 μm (**b**).

[Source data](#)

[Extended Data Fig. 11 Functional validation of oncogene-driven niche remodelling.](#)

a, b, qPCR analysis of *Id1* (**a**), *Axin2* and *Lgr5* (**b**) after administration of indicated inhibitor. **c**, Fraction of monoclonal WT (YFP⁺) crypts remote from (Remote) or proximate to (Prox) mutant crypts in *Red2Onco* mice. **d**, Heat maps indicate relative clone fractions of the indicated sizes. Data are mean ± s.e.m. **e**, Fraction of monoclonal (RFP⁺) mutant crypts in *Red2Onco* mice. **f**, **g**, Representative confocal images (**f**) and quantification (**g**) of EGFP⁺ (LGR5⁺) ISCs. Images are representative of tissues quantified in **g**. Arrows, proximate WT crypts; arrowheads, fixed mutant crypts. **h**, Representative confocal images of whole-mount small intestine. Images are representative of tissues quantified in **i**. Arrowheads, fixed mutant crypts. **i**, Violin plots of proximate WT crypt size. **j**, **k**, RNA in situ hybridization (**j**) and quantification (**k**) of *Bmp2*. Arrowheads, fixed mutant crypts. **l**, **m**, Representative multiplexed in situ hybridization images (**l**) and

quantification (**m**) of *Rspo3* in *Cd81⁺* cells. Arrow: *Cd81*-positive STC2 cells; Arrowheads, fixed mutant crypts. Whole mount (**f–i**) and sections (**j–m**) of small intestine from *Lgr5-EGFP-IRES-CreERT2* control (L5), *Lgr5-EGFP-IRES-CreERT2; LSL-Kras^{G12D}* (enKR) or *PIK3CA^{Lat-H1047R}* (enP3) mice 2 w after tamoxifen administration. In **c–e**, graphs show data collected 2 w after concomitant administration of indicated drug and tamoxifen. Crypt borders are marked by dashed outlines (**f, h, j, l**). In **f, h, j, l**, white (**f, h**) or red (**j, l**): immunostaining for mutant KRAS(G12D) in enKR, or p-AKT in enP3. **P* < 0.05, ***P* < 0.01, ****P* < 0.0001; one-way ANOVA with Games-Howell's multiple comparisons test (**k, m**) and unpaired two-tailed *t*-test (**c, e, g, i**). Data are mean ± s.d. (**a, b, g, k, m**) or mean ± s.e.m. (**c, e**). For exact *P* values, see Source Data. Scale bars: 50 µm (**f, h, j**) and 25 µm (**l**).

Source data

Extended Data Fig. 12 *Apc* mutation induces reduction of stem cells in neighbouring wild-type crypts.

a, b, Representative confocal images of small intestine from *Villin-CreERT2; Apc^{ff}* mice at 2 w after tamoxifen administration (**a**) and from *Apc^{Min/+}* mice at 12 weeks of age (**b**). Images are representative of two independent experiments. OLFM4 staining shows a reduced number of stem cells in wild-type crypts neighbouring mutant crypts. Grey dashed outlines, *Apc* mutant foci (*Villin-CreERT2; Apc^{ff}*) or polyps (*Apc^{Min/+}*); white dashed outlines, crypt borders. Scale bars, 50 µm. **c**, Bright-field images of intestinal organoids after 7 days of culture in ENR medium. Images are representative of three independent experiments. Note that organoids from *Villin-CreERT2; Apc^{ff}* mice form spheroids in ENR medium. Scale bars, 500 µm. **d**, qPCR analysis of WNT target gene (*Axin2*) and secreted WNT inhibitory factors (*Dkk2*, *Wif1* and *Notum*) following *Apc* deletion. Data are mean ± s.d. *n* = 3 independent experiments. **P* < 0.05, ***P* < 0.01, ****P* < 0.0001; unpaired two-tailed *t*-test. **e, f**, Representative multiplexed *in situ* hybridization images of *Axin2* and *Wif1* (**e**) and *Lgr5* and *Notum* (**f**) on sections of small intestine from *Villin-CreERT2; Apc^{ff}* mice 2 w after tamoxifen administration. Images are

representative of two independent experiments. *Axin2* (**e**) and *Lgr5* (**f**) staining shows a reduced number of stem cells in wild-type crypts neighbouring *Apc* mutant crypts. Grey dashed outlines, *Apc* mutant foci (*Villin-CreERT2; Apc^{fl/fl}*); white dashed outlines, crypt borders. Scale bars, 50 µm.

[Source data](#)

Supplementary information

[Supplementary Information](#)

This file contains gene set enrichment analysis (GSEA) for senescence-associated secretory phenotype (SASP) and inflammation, and theory for clonal analysis, related to Figs 1–3 and Extended Data Figs 2–4 and 8. This consists of two parts: 1) **Supplementary Methods** describing GSEA for SASP and inflammation, and 2) **Supplementary Theory** explaining clonal analysis and modelling.

[Reporting Summary](#)

[Peer Review File](#)

[Supplementary Table 1](#)

Marker genes and differentially expressed genes of epithelial cells in Red2Onco models, related to Fig. 3 and Extended Data Fig. 6. This table lists marker genes for epithelial cell types and differentially expressed genes for all epithelial cells or individual cell types in *Red2Onco* samples compared to *Confetti* control.

[Supplementary Table 2](#)

Gene sets for evaluating stem cell priming and enrichment scores for signalling pathways, related to Fig. 3 and Extended Data Fig. 7. This table shows the gene sets for: 1) differentiated sub-lineages of epithelial cells; 2)

BMP, Wnt and Notch signalling pathways, and 3) senescence-associated secretory phenotype (SASP) and inflammation.

Supplementary Table 3

Cell type markers and differentially expressed genes of mesenchymal and immune cells, related to Fig. 3 and Extended Data Figs 8 and 10. The table lists marker genes for mesenchymal and immune cell types and differentially expressed genes for each of their cell types in *Red2Onc* samples compared to *Confetti* control.

Supplementary Table 4

List of expressed ligands regulating BMP and Wnt signalling pathways, related to Fig. 3 and Extended Data Figs 8 and 10. This table shows the expression of ligands regulating BMP and Wnt signalling pathways that are secreted from mutant epithelial cells and mesenchymal and immune cells.

Video 1

: Whole mount z-stack imaging of *Villin-CreERT2; Red2-KrasG12D* small intestine, related to Figure 1 Representative z-stack imaging of *Villin-CreERT2; Red2-KrasG12D* small intestine 2 weeks post-tamoxifen administration. The video is representative of 3 biologically independent samples analysed.

Source data

Source Data Fig. 1

Source Data Fig. 2

Source Data Fig. 3

Source Data Fig. 4

[Source Data Extended Data Fig. 1](#)

[Source Data Extended Data Fig. 2](#)

[Source Data Extended Data Fig. 3](#)

[Source Data Extended Data Fig. 4](#)

[Source Data Extended Data Fig. 5](#)

[Source Data Extended Data Fig. 6](#)

[Source Data Extended Data Fig. 7](#)

[Source Data Extended Data Fig. 8](#)

[Source Data Extended Data Fig. 9](#)

[Source Data Extended Data Fig. 10](#)

[Source Data Extended Data Fig. 11](#)

[Source Data Extended Data Fig. 12](#)

Rights and permissions

[Reprints and Permissions](#)

About this article



Check for
updates

Cite this article

Yum, M.K., Han, S., Fink, J. *et al.* Tracing oncogene-driven remodelling of the intestinal stem cell niche. *Nature* **594**, 442–447 (2021).
<https://doi.org/10.1038/s41586-021-03605-0>

[Download citation](#)

- Received: 22 October 2020
- Accepted: 30 April 2021
- Published: 02 June 2021
- Issue Date: 17 June 2021
- DOI: <https://doi.org/10.1038/s41586-021-03605-0>

Comments

By submitting a comment you agree to abide by our [Terms](#) and [Community Guidelines](#). If you find something abusive or that does not comply with our terms or guidelines please flag it as inappropriate.

[Access through your institution](#)

[Change institution](#)

[Buy or subscribe](#)

Associated Content

[Cancer stem cells in the gut have a bad influence on neighbouring cells](#)

- Shi Biao Chia
- James DeGregori

Advertisement

This article was downloaded by **calibre** from <https://www.nature.com/articles/s41586-021-03605-0>

| [Section menu](#) | [Main menu](#) |

- Article
- [Published: 12 May 2021](#)

Hippocampal AMPA receptor assemblies and mechanism of allosteric inhibition

- [Jie Yu¹ na1](#),
- [Prashant Rao](#) [ORCID: orcid.org/0000-0003-0132-5571](#)¹ na1,
- [Sarah Clark¹](#),
- [Jaba Mitra](#) [ORCID: orcid.org/0000-0001-6569-6203](#)^{2,3},
- [Taekjip Ha](#) [ORCID: orcid.org/0000-0003-2195-6258](#)^{3,4,5,6} &
- [Eric Gouaux](#) [ORCID: orcid.org/0000-0002-8549-2360](#)^{1,7}

[Nature](#) volume **594**, pages 448–453 (2021) [Cite this article](#)

- 6301 Accesses
- 103 Altmetric
- [Metrics details](#)

Subjects

- [Cryoelectron microscopy](#)
- [Ion channels in the nervous system](#)

Abstract

AMPA-selective glutamate receptors mediate the transduction of signals between the neuronal circuits of the hippocampus¹. The trafficking,

localization, kinetics and pharmacology of AMPA receptors are tuned by an ensemble of auxiliary protein subunits, which are integral membrane proteins that associate with the receptor to yield bona fide receptor signalling complexes². Thus far, extensive studies of recombinant AMPA receptor–auxiliary subunit complexes using engineered protein constructs have not been able to faithfully elucidate the molecular architecture of hippocampal AMPA receptor complexes. Here we obtain mouse hippocampal, calcium-impermeable AMPA receptor complexes using immunoaffinity purification and use single-molecule fluorescence and cryo-electron microscopy experiments to elucidate three major AMPA receptor–auxiliary subunit complexes. The GluA1–GluA2, GluA1–GluA2–GluA3 and GluA2–GluA3 receptors are the predominant assemblies, with the auxiliary subunits TARP- γ 8 and CNIH2–SynDIG4 non-stochastically positioned at the B'/D' and A'/C' positions, respectively. We further demonstrate how the receptor–TARP- γ 8 stoichiometry explains the mechanism of and submaximal inhibition by a clinically relevant, brain-region-specific allosteric inhibitor.

Access options

Subscribe to Journal

Get full journal access for 1 year

\$199.00

only \$3.90 per issue

[Subscribe](#)

All prices are NET prices.

VAT will be added later in the checkout.

Tax calculation will be finalised during checkout.

Rent or Buy article

Get time limited or full article access on ReadCube.

from \$8.99

[Rent or Buy](#)

All prices are NET prices.

Additional access options:

- [Log in](#)
- [Access through your institution](#)
- [Learn about institutional subscriptions](#)

Fig. 1: Cryo-EM and single-molecule fluorescence analysis of hpAMPAR complexes.

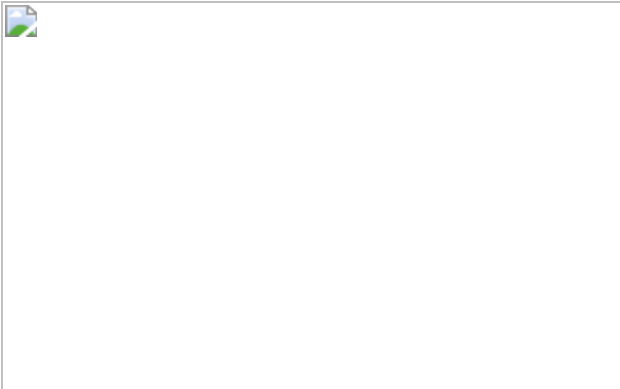


Fig. 2: Architecture and subunit arrangement of LBD–TMD_{A1/A2} complexes.

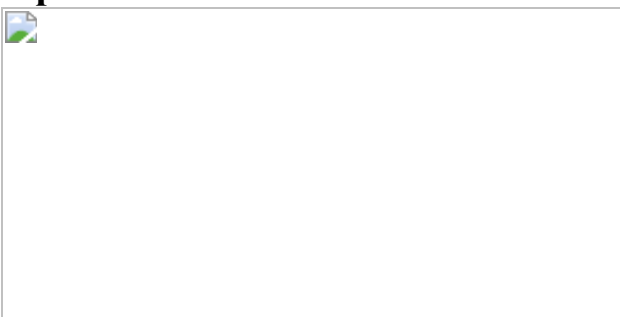


Fig. 3: JNJ-binding site and mechanism of inhibition.

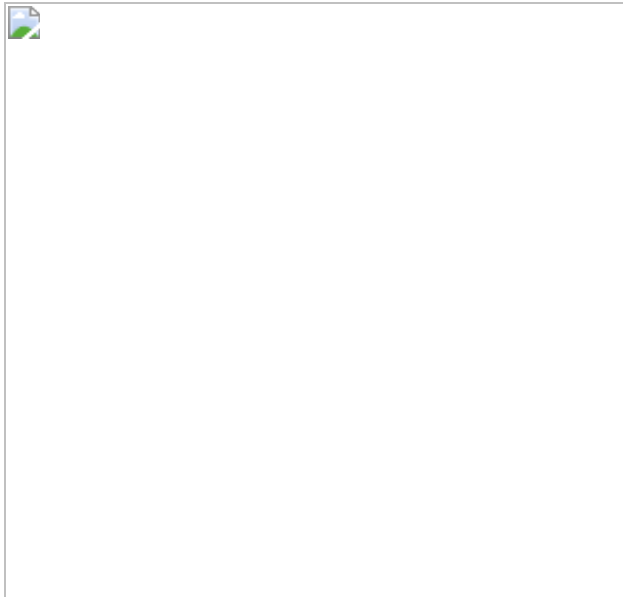
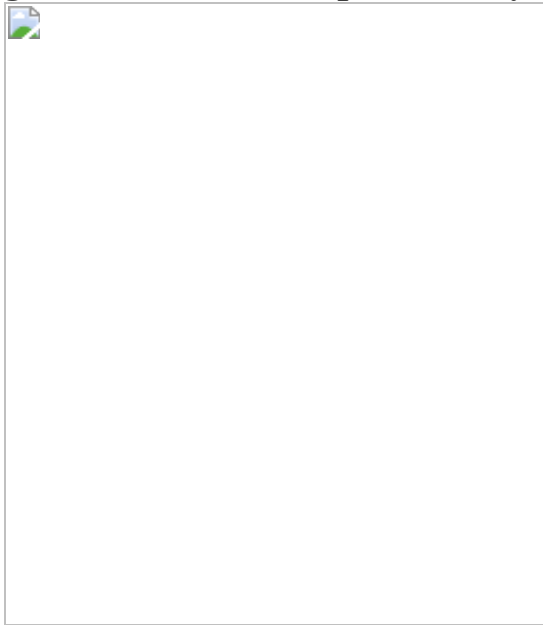


Fig. 4: Elucidation of putative SynDIG4 density and interaction sites.



Data availability

The cryo-EM maps and coordinates for overall, the ATD layer and the LBD-TMD layer of the A1A2A1A2 symmetric (S) and A1A2A1A2 asymmetric (AS) complexes have been deposited in the Electron Microscopy Data Bank (EMDB) under accession numbers [EMD-23283](#) and [EMD-23284](#) and in the Protein Data Bank (PDB) under accession codes [7LDD](#) and [7LDE](#), respectively. The cryo-EM maps for overall, the ATD

layer and the LBD–TMD layer of the A1A2A3A2 (AS1), A1A2A3A2 (AS2), A3A2A3A2 (S) and A3A2A3A2 (AS) complexes have been deposited in the EMDB under accession numbers [EMD-23285](#), [EMD-23286](#), [EMD-23287](#) and [EMD-23288](#), respectively. The cryo-EM maps of A1A2A3A2 (AS3) and A1A2AXA2 have been deposited in the EMDB under accession numbers [EMD-23289](#) and [EMD-23290](#), respectively. The cryo-EM map and coordinates for the LBD-TMD_{mix} complex have been deposited in the EMDB and PDB under accession codes [EMD-23292](#) and [7LEP](#), respectively.

References

1. 1.

Diering, G. H. & Huganir, R. L. The AMPA receptor code of synaptic plasticity. *Neuron* **100**, 314–329 (2018).

[CAS](#) [PubMed](#) [PubMed Central](#) [Google Scholar](#)

2. 2.

Jackson, A. C. & Nicoll, R. A. The expanding social network of ionotropic glutamate receptors: TARPs and other transmembrane auxiliary subunits. *Neuron* **70**, 178–199 (2011).

[CAS](#) [PubMed](#) [PubMed Central](#) [Google Scholar](#)

3. 3.

Collingridge, G. L., Kehl, S. J. & McLennan, H. Excitatory amino acids in synaptic transmission in the Schaffer collateral-commissural pathway of the rat hippocampus. *J. Physiol.* **334**, 33–46 (1983).

[CAS](#) [PubMed](#) [PubMed Central](#) [Google Scholar](#)

4. 4.

Bliss, T. V. & Lomo, T. Long-lasting potentiation of synaptic transmission in the dentate area of the anaesthetized rabbit following stimulation of the perforant path. *J. Physiol.* **232**, 331–356 (1973).

[CAS](#) [PubMed](#) [PubMed Central](#) [Google Scholar](#)

5. 5.

Rosenmund, C., Stern-Bach, Y. & Stevens, C. F. The tetrameric structure of a glutamate receptor channel. *Science* **280**, 1596–1599 (1998).

[ADS](#) [CAS](#) [PubMed](#) [PubMed Central](#) [Google Scholar](#)

6. 6.

Sobolevsky, A. I., Rosconi, M. P. & Gouaux, E. X-ray structure, symmetry and mechanism of an AMPA-subtype glutamate receptor. *Nature* **462**, 745–756 (2009).

[ADS](#) [CAS](#) [PubMed](#) [PubMed Central](#) [Google Scholar](#)

7. 7.

Traynelis, S. F. et al. Glutamate receptor ion channels: structure, regulation, and function. *Pharmacol. Rev.* **62**, 405–496 (2010).

[CAS](#) [PubMed](#) [PubMed Central](#) [Google Scholar](#)

8. 8.

Keinanen, K. et al. A family of AMPA-selective glutamate receptors. *Science* **249**, 556–560 (1990).

[ADS](#) [CAS](#) [PubMed](#) [PubMed Central](#) [Google Scholar](#)

9. 9.

Schwenk, J. et al. Regional diversity and developmental dynamics of the AMPA-receptor proteome in the mammalian brain. *Neuron* **84**, 41–54 (2014).

[CAS](#) [PubMed](#) [PubMed Central](#) [Google Scholar](#)

10. 10.

Wenthold, R. J., Petralia, R. S., Blahos J, I. I. & Niedzielski, A. S. Evidence for multiple AMPA receptor complexes in hippocampal CA1/CA2 neurons. *J. Neurosci.* **16**, 1982–1989 (1996).

[CAS](#) [PubMed](#) [PubMed Central](#) [Google Scholar](#)

11. 11.

Kamalova, A. & Nakagawa, T. AMPA receptor structure and auxiliary subunits. *J. Physiol.* **599**, 453–469 (2021).

[CAS](#) [PubMed](#) [PubMed Central](#) [Google Scholar](#)

12. 12.

Tomita, S. et al. Functional studies and distribution define a family of transmembrane AMPA receptor regulatory proteins. *J. Cell Biol.* **161**, 805–816 (2003).

[CAS](#) [PubMed](#) [PubMed Central](#) [Google Scholar](#)

13. 13.

Schwenk, J. et al. Functional proteomics identify cornichon proteins as auxiliary subunits of AMPA receptors. *Science* **323**, 1313–1319 (2009).

[ADS](#) [CAS](#) [PubMed](#) [PubMed Central](#) [Google Scholar](#)

14. 14.

Chen, L. et al. Stargazin regulates synaptic targeting of AMPA receptors by two distinct mechanisms. *Nature* **408**, 936–943 (2000).

[ADS](#) [CAS](#) [PubMed](#) [PubMed Central](#) [Google Scholar](#)

15. 15.

Herguedas, B. et al. Architecture of the heteromeric GluA1/2 AMPA receptor in complex with the auxiliary subunit TARP γ 8. *Science* **364**, eaav9011 (2019).

[CAS](#) [PubMed](#) [PubMed Central](#) [Google Scholar](#)

16. 16.

Nakagawa, T. Structures of the AMPA receptor in complex with its auxiliary subunit cornichon. *Science* **366**, 1259–1263 (2019).

[ADS](#) [CAS](#) [PubMed](#) [PubMed Central](#) [Google Scholar](#)

17. 17.

Jain, A. et al. Probing cellular protein complexes using single-molecule pull-down. *Nature* **473**, 484–488 (2011).

[ADS](#) [CAS](#) [PubMed](#) [PubMed Central](#) [Google Scholar](#)

18. 18.

Zhao, Y., Chen, S., Swensen, A. C., Qian, W. J. & Gouaux, E. Architecture and subunit arrangement of native AMPA receptors elucidated by cryo-EM. *Science* **364**, 355–362 (2019).

[ADS](#) [CAS](#) [PubMed](#) [PubMed Central](#) [Google Scholar](#)

19. 19.

Maher, M. P. et al. Discovery and characterization of AMPA receptor modulators selective for TARP- γ 8. *J. Pharmacol. Exp. Ther.* **357**, 394–

414 (2016).

[CAS](#) [PubMed](#) [PubMed Central](#) [Google Scholar](#)

20. 20.

Lu, W. et al. Subunit composition of synaptic AMPA receptors revealed by a single-cell genetic approach. *Neuron* **62**, 254–268 (2009).

[CAS](#) [PubMed](#) [PubMed Central](#) [Google Scholar](#)

21. 21.

Jacobi, E. & von Engelhardt, J. Diversity in AMPA receptor complexes in the brain. *Curr. Opin. Neurobiol.* **45**, 32–38 (2017).

[CAS](#) [PubMed](#) [PubMed Central](#) [Google Scholar](#)

22. 22.

Morise, J. et al. Distinct cell surface expression patterns of *N*-glycosylation site mutants of AMPA-type glutamate receptor under the homo-oligomeric expression conditions. *Int. J. Mol. Sci.* **21**, 5101 (2020).

[CAS](#) [Google Scholar](#)

23. 23.

Fukaya, M. et al. Abundant distribution of TARP γ -8 in synaptic and extrasynaptic surface of hippocampal neurons and its major role in AMPA receptor expression on spines and dendrites. *Eur. J. Neurosci.* **24**, 2177–2190 (2006).

[PubMed](#) [PubMed Central](#) [Google Scholar](#)

24. 24.

Rouach, N. et al. TARP γ -8 controls hippocampal AMPA receptor number, distribution and synaptic plasticity. *Nat. Neurosci.* **8**, 1525–1533 (2005).

[CAS](#) [PubMed](#) [PubMed Central](#) [Google Scholar](#)

25. 25.

Kato, A. S. et al. Hippocampal AMPA receptor gating controlled by both TARP and cornichon proteins. *Neuron* **68**, 1082–1096 (2010).

[CAS](#) [PubMed](#) [PubMed Central](#) [Google Scholar](#)

26. 26.

Carrillo, E. et al. Mechanism of modulation of AMPA receptors by TARP- γ 8. *J. Gen. Physiol.* **152**, jgp.201912451 (2020).

[PubMed](#) [PubMed Central](#) [Google Scholar](#)

27. 27.

Plested, A. J. & Mayer, M. L. AMPA receptor ligand binding domain mobility revealed by functional cross linking. *J. Neurosci.* **29**, 11912–11923 (2009).

[CAS](#) [PubMed](#) [PubMed Central](#) [Google Scholar](#)

28. 28.

Baranovic, J. et al. Dynamics of the ligand binding domain layer during AMPA receptor activation. *Biophys. J.* **110**, 896–911 (2016).

[ADS](#) [CAS](#) [PubMed](#) [PubMed Central](#) [Google Scholar](#)

29. 29.

Harmel, N. et al. AMPA receptors commandeer an ancient cargo exporter for use as an auxiliary subunit for signaling. *PLoS ONE* **7**,

e30681 (2012).

[ADS](#) [CAS](#) [PubMed](#) [PubMed Central](#) [Google Scholar](#)

30. 30.

Boudkkazi, S., Brechet, A., Schwenk, J. & Fakler, B. Cornichon2 dictates the time course of excitatory transmission at individual hippocampal synapses. *Neuron* **82**, 848–858 (2014).

[CAS](#) [PubMed](#) [PubMed Central](#) [Google Scholar](#)

31. 31.

Gill, M. B., Kato, A. S., Wang, H. & Bredt, D. S. AMPA receptor modulation by cornichon-2 dictated by transmembrane AMPA receptor regulatory protein isoform. *Eur. J. Neurosci.* **35**, 182–194 (2012).

[PubMed](#) [PubMed Central](#) [Google Scholar](#)

32. 32.

Herring, B. E. et al. Cornichon proteins determine the subunit composition of synaptic AMPA receptors. *Neuron* **77**, 1083–1096 (2013).

[CAS](#) [PubMed](#) [PubMed Central](#) [Google Scholar](#)

33. 33.

Sommer, B., Köhler, M., Sprengel, R. & Seuberg, P. H. RNA editing in brain controls a determinant of ion flow in glutamate-gated channels. *Cell* **67**, 11–19 (1991).

[CAS](#) [PubMed](#) [PubMed Central](#) [Google Scholar](#)

34. 34.

Burnashev, N., Villarroel, A. & Sakmann, B. Dimensions and ion selectivity of recombinant AMPA and kainate receptor channels and their dependence on Q/R site residues. *J. Physiol.* **496**, 165–173 (1996).

[CAS](#) [PubMed](#) [PubMed Central](#) [Google Scholar](#)

35. 35.

Swanson, G. T., Kamboj, S. K. & Cull-Candy, S. G. Single-channel properties of recombinant AMPA receptors depend on RNA editing, splice variation, and subunit composition. *J. Neurosci.* **17**, 58–69 (1997).

[CAS](#) [PubMed](#) [PubMed Central](#) [Google Scholar](#)

36. 36.

Bowie, D. & Mayer, M. L. Inward rectification of both AMPA and kainate subtype glutamate receptors generated by polyamine-mediated ion channel block. *Neuron* **15**, 453–462 (1995).

[CAS](#) [PubMed](#) [PubMed Central](#) [Google Scholar](#)

37. 37.

Lomeli, H. et al. Control of kinetic properties of AMPA receptor channels by nuclear RNA editing. *Science* **266**, 1709–1713 (1994).

[ADS](#) [CAS](#) [PubMed](#) [PubMed Central](#) [Google Scholar](#)

38. 38.

Kirk, L. M. et al. Distribution of the SynDIG4/proline-rich transmembrane protein 1 in rat brain. *J. Comp. Neurol.* **524**, 2266–2280 (2016).

[CAS](#) [PubMed](#) [PubMed Central](#) [Google Scholar](#)

39. 39.

Matt, L. et al. SynDIG4/Prrt1 is required for excitatory synapse development and plasticity underlying cognitive function. *Cell Rep.* **22**, 2246–2253 (2018).

[CAS](#) [PubMed](#) [PubMed Central](#) [Google Scholar](#)

40. 40.

Troyano-Rodriguez, E., Mann, S., Ullah, R. & Ahmad, M. PRRT1 regulates basal and plasticity-induced AMPA receptor trafficking. *Mol. Cell. Neurosci.* **98**, 155–163 (2019).

[CAS](#) [PubMed](#) [PubMed Central](#) [Google Scholar](#)

41. 41.

Penn, A. C. et al. Hippocampal LTP and contextual learning require surface diffusion of AMPA receptors. *Nature* **549**, 384–388 (2017).

[ADS](#) [CAS](#) [PubMed](#) [PubMed Central](#) [Google Scholar](#)

42. 42.

Goehring, A. et al. Screening and large-scale expression of membrane proteins in mammalian cells for structural studies. *Nat. Protocols* **9**, 2574–2585 (2014).

[CAS](#) [PubMed](#) [PubMed Central](#) [Google Scholar](#)

43. 43.

Coleman, J. A., Green, E. M. & Gouaux, E. X-ray structures and mechanism of the human serotonin transporter. *Nature* **532**, 334–339 (2016).

[ADS](#) [CAS](#) [PubMed](#) [PubMed Central](#) [Google Scholar](#)

44. 44.

Kawate, T. & Gouaux, E. Fluorescence-detection size-exclusion chromatography for precrystallization screening of integral membrane proteins. *Structure* **14**, 673–681 (2006).

[CAS](#) [PubMed](#) [PubMed Central](#) [Google Scholar](#)

45. 45.

Sultan, F. A. Dissection of different areas from mouse hippocampus. *Bio-Protocol* **3**, e955 (2013).

[PubMed](#) [PubMed Central](#) [Google Scholar](#)

46. 46.

Mastronarde, D. N. Automated electron microscope tomography using robust prediction of specimen movements. *J. Struct. Biol.* **152**, 36–51 (2005).

[PubMed](#) [Google Scholar](#)

47. 47.

Punjani, A., Rubinstein, J. L., Fleet, D. J. & Brubaker, M. A. cryoSPARC: algorithms for rapid unsupervised cryo-EM structure determination. *Nat. Methods* **14**, 290–296 (2017).

[CAS](#) [PubMed](#) [Google Scholar](#)

48. 48.

Zivanov, J. et al. New tools for automated high-resolution cryo-EM structure determination in RELION-3. *eLife* **7**, e42166 (2018).

[PubMed](#) [PubMed Central](#) [Google Scholar](#)

49. 49.

Punjani, A., Zhang, H. & Fleet, D. J. Non-uniform refinement: adaptive regularization improves single-particle cryo-EM reconstruction. *Nat. Methods* **17**, 1214–1221 (2020).

[CAS](#) [PubMed](#) [PubMed Central](#) [Google Scholar](#)

50. 50.

Pettersen, E. F. et al. UCSF Chimera—a visualization system for exploratory research and analysis. *J. Comput. Chem.* **25**, 1605–1612 (2004).

[CAS](#) [PubMed](#) [Google Scholar](#)

51. 51.

Emsley, P. & Cowtan, K. Coot: model-building tools for molecular graphics. *Acta Crystallogr. D* **60**, 2126–2132 (2004).

[PubMed](#) [PubMed Central](#) [Google Scholar](#)

52. 52.

Afonine, P. V. et al. Real-space refinement in PHENIX for cryo-EM and crystallography. *Acta Crystallogr. D* **74**, 531–544 (2018).

[CAS](#) [Google Scholar](#)

53. 53.

The PyMOL Molecular Graphics System v.2.1 (Schrödinger, 2020).

54. 54.

Biedermann, J., Braunbeck, S., Plested, A. J. & Sun, H. Non-selective cation permeation in an AMPA-type glutamate receptor. *Proc. Natl Acad. Sci. USA* **118**, e2012843118 (2021).

[PubMed](#) [PubMed Central](#) [Google Scholar](#)

55. 55.

Chen, V. B. et al. MolProbity: all-atom structure validation for macromolecular crystallography. *Acta Crystallogr. D* **66**, 12–21 (2010).

[CAS](#) [PubMed](#) [PubMed Central](#) [Google Scholar](#)

56. 56.

Goddard, T. D. et al. UCSF ChimeraX: meeting modern challenges in visualization and analysis. *Protein Sci.* **27**, 14–25 (2018).

[CAS](#) [Google Scholar](#)

57. 57.

Jain, A., Liu, R., Xiang, Y. K. & Ha, T. Single-molecule pull-down for studying protein interactions. *Nat. Protocols* **7**, 445–452 (2012).

[CAS](#) [PubMed](#) [PubMed Central](#) [Google Scholar](#)

58. 58.

Reeves, P. J., Callewaert, N., Contreras, R. & Khorana, H. G. Structure and function in rhodopsin: high-level expression of rhodopsin with restricted and homogeneous N-glycosylation by a tetracycline-inducible *N*-acetylglucosaminyltransferase I-negative HEK293S stable mammalian cell line. *Proc. Natl Acad. Sci. USA* **99**, 13419–13424 (2002).

[ADS](#) [CAS](#) [PubMed](#) [PubMed Central](#) [Google Scholar](#)

[Download references](#)

Acknowledgements

We thank the Pacific Northwest Cryo-EM Center (PNCC) and OHSU MMC for microscope use, D. Cawley, P. Streeter, Y. Zhong and N. Sheldon for generating antibodies, A. Goehring for mouse dissections, M. Mayer for his guidance and advice on electrophysiology experiments, J. Elferich for help writing SiMPull processing scripts, S. Chen for help initiating the project, L. Vaskalis for assistance with figures, F. Jalali-Yazdi and H. Owen for help with manuscript preparation and R. Nicoll and members of the Gouaux laboratory for discussions. PNCC is supported by NIH grant U24GM129547 and accessed through EMSL (grid.436923.9), a DOE Office of Science User Facility sponsored by the Office of Biological and Environmental Research. T.H. and J.M. were supported by the NIGMS grant R35GM122569. This work was supported by the NINDS grant R01NS038631 to E.G. T.H. and E.G. are investigators of the Howard Hughes Medical Institute. The content is solely the responsibility of the authors and does not necessarily represent the official views of National Institutes of Health.

Author information

Author notes

1. These authors contributed equally: Jie Yu, Prashant Rao

Affiliations

1. Vollum Institute, Oregon Health & Science University, Portland, OR, USA

Jie Yu, Prashant Rao, Sarah Clark & Eric Gouaux

2. Department of Materials Science and Engineering, University of Illinois at Urbana-Champaign, Urbana, IL, USA

Jaba Mitra

3. Department of Biophysics and Biophysical Chemistry, Johns Hopkins University, Baltimore, MD, USA

Jaba Mitra & Taekjip Ha

4. Department of Biophysics, Johns Hopkins University, Baltimore, MD, USA

Taekjip Ha

5. Department of Biomedical Engineering, Johns Hopkins University, Baltimore, MD, USA

Taekjip Ha

6. Howard Hughes Medical Institute, Baltimore, MD, USA

Taekjip Ha

7. Howard Hughes Medical Institute, Portland, OR, USA

Eric Gouaux

Authors

1. Jie Yu

[View author publications](#)

You can also search for this author in [PubMed](#) [Google Scholar](#)

2. Prashant Rao

[View author publications](#)

You can also search for this author in [PubMed](#) [Google Scholar](#)

3. Sarah Clark

[View author publications](#)

You can also search for this author in [PubMed](#) [Google Scholar](#)

4. Jaba Mitra

[View author publications](#)

You can also search for this author in [PubMed](#) [Google Scholar](#)

5. Taekjip Ha

[View author publications](#)

You can also search for this author in [PubMed](#) [Google Scholar](#)

6. Eric Gouaux

[View author publications](#)

You can also search for this author in [PubMed](#) [Google Scholar](#)

Contributions

J.Y., P.R. and E.G. designed the project. J.Y. and P.R. performed the sample preparation for cryo-EM and biochemistry studies. J.Y. and P.R. performed the cryo-EM data collection, data analysis and model building. J.Y. performed the patch-clamp recording experiments. S.C. performed all of the SiMPull experiments with T.H and J.M. providing training and comments. E.G., J.Y., P.R. and S.C. wrote the manuscript with input from T.H. and J.M.

Corresponding author

Correspondence to [Eric Gouaux](#).

Ethics declarations

Competing interests

The authors declare no competing interests.

Additional information

Peer review information *Nature* thanks Sudha Chakrapani, Vasanthi Jayaraman and Andrew Plested for their contribution to the peer review of

this work. Peer reviewer reports are available.

Publisher's note Springer Nature remains neutral with regard to jurisdictional claims in published maps and institutional affiliations.

Extended data figures and tables

Extended Data Fig. 1 Biochemical characterization and cryo-EM analysis of hpAMPAR complexes.

a, Representative SEC profile of hippocampal AMPAR complexes. Inset shows an SDS-PAGE gel of AMPAR complexes and antibody fragments used for cryo-EM grid preparation, visualized by silver staining. The gel was repeated three times from different batches of purification with similar results. **b**, Western blot analysis of isolated AMPAR complexes using antibodies against GluA1, GluA2, GluA3, GluA4, PSD95, TARP- γ 8 and CNIH2. The uncropped blot can be found in Supplementary Fig. 1 and blotting was repeated three times with similar results. **c**, A representative cryo-EM micrograph of hpAMPAR complexes. The experiments were repeated four times with similar results. **d**, Selected two-dimensional class averages. Protrusions extending out of the detergent micelle are indicated by arrows, corresponding to the extracellular domain of TARP- γ 8. Similar results were obtained from experiments repeated four times.

Extended Data Fig. 2 Characterization of monoclonal antibodies 13A8 and E3.

a, Octet measurements of the 13A8 monoclonal antibody binding to TARP- γ 8. Concentrations of the 13A8 monoclonal antibody ranging from 25 nM to 200 nM were applied. **b–f**, FSEC profiles of recombinant GFP-tagged TARP- γ 8 (**b**), TARP- γ 2 (**c**), TARP- γ 3 (**d**), TARP- γ 4 (**e**) and TARP- γ 7 (**f**) with 13A8 monoclonal antibody (green traces) and without 13A8 monoclonal antibody (black traces), detecting GFP fluorescence. Only the TARP- γ 8 trace is shifted by the 13A8 monoclonal antibody. **g**, Octet measurements of the E3 monoclonal antibody binding to GluA4. **h–k**, FSEC profiles of recombinant mKalama-tagged GluA1 (**h**), GFP-tagged

GluA2 (**i**), GFP-tagged GluA3 (**j**) and GFP-tagged GluA4 (**k**) with E3 monoclonal antibody (green traces) and without E3 monoclonal antibody (black traces), detecting mKalama or GFP fluorescence. Only GluA4 receptors are shifted by the E3 monoclonal antibody.

Extended Data Fig. 3 A representative flow chart of data processing focused on the whole receptor and ATD layer using data-processing strategy 1.

A total of 2,893,667 particles was picked from 46,927 motion-corrected micrographs in cryoSPARC v.2.14. Classes showing clear receptor features were kept after several rounds of two-dimensional classification, resulting in the retention of 2,893,667 particles. Next, three-dimensional classification with a large sampling degree was performed to further remove junk classes in RELION 3.0. Another round of three-dimensional classification was carried out to sort receptors with the same Fab and scFv combination. Classes with the same ATD labelling and orientation were combined and subjected to ATD-focused classification without alignment. For the A1A2A1A2 symmetric subtype, the ATD layer was classified into eight classes, of which one class, which occupied the largest population (55%), had the least well-resolved secondary structure features. Another round of ATD-focused classification was performed on this class, producing a subtype with one unlabelled subunit, denoted as A1A2AXA2. The three remaining classes showing the most well-defined secondary structure features were selected for final refinement with C2 symmetry, producing a map at a resolution of 4 Å. ATD-focused refinement with C2 symmetry was carried out to improve map density in the ATD, yielding an ATD–A1A2A1A2 symmetric map at a resolution of 3.4 Å.

Extended Data Fig. 4 Data-processing workflow to determine AMPAR subtypes using data-processing strategy 2.

Motion-corrected micrographs were first curated on the basis of ice thickness, motion correction, CTF fit and astigmatism. Template-based picking was used to autopick 6,002,517 particles in cryoSPARC v.2.14. To remove junk particles and false positives, multiple rounds of two-

dimensional and three-dimensional classification were performed, selecting only classes that showed discernible receptor features, resulting in a particle stack of 1,844,956 particles. To sort receptors based on subtype (AMPAR subunit stoichiometry and tilting), multiple rounds of three-dimensional classification were performed without symmetry imposed or masking. Particles from classes showing clear labelling with antibodies were grouped into distinct subtypes. Each of the AMPAR subtypes were refined separately. This strategy elucidated three different heteromeric AMPAR subtypes comprising both symmetric and asymmetric conformations.

Extended Data Fig. 5 Three-dimensional reconstructions of dimeric GluA1–GluA2 and dimeric GluA2–GluA3 complexes.

a, c, e, g, i, Local resolution estimates of the entire GluA1–GluA2 symmetric map (**a**), ATD layer of the GluA1–GluA2 symmetric map (**c**), entire GluA1–GluA2 asymmetric map (**e**), the ATD layer of GluA1–GluA2 asymmetric map (**g**) and the LBD–TMD layers of the GluA1–GluA2 map (**i**). **d, h, k**, FSC curves before and after masking and between the model and the final maps of the ATD layer of the GluA1–GluA2 symmetric map (**d**), the ATD layer of the GluA1–GluA2 asymmetric map (**h**) and the LBD–TMD layers of the GluA1–GluA2 map (**k**). **j**, Angular distribution of the LBD–TMD layers of the GluA1–GluA2 map. **l, n, p, r, t**, Local resolution estimates of the entire GluA2–GluA3 symmetric map (**l**), the ATD layer of the GluA2–GluA3 symmetric map (**n**), the entire GluA2–GluA3 asymmetric map (**p**), the ATD layers of the GluA2–GluA3 asymmetric map (**r**) and LBD–TMD layers of the GluA2–GluA3 map (**t**). **b, f, m, o, q, s, v**, FSC curves before and after masking of the whole GluA1–GluA2 symmetric map (**b**), the entire GluA1–GluA2 asymmetric map (**f**), the entire GluA2–GluA3 symmetric map (**m**), the ATD layer of GluA2–GluA3 symmetric map (**o**), the entire GluA2–GluA3 asymmetric map (**q**), the ATD layer of the GluA2–GluA3 asymmetric map (**s**) and the LBD–TMD layers of the GluA2–GluA3 map (**v**). **u**, Angular distribution of the LBD–TMD layers of the GluA2–GluA3 map.

Extended Data Fig. 6 Three-dimensional reconstructions of trimeric GluA1–GluA2–GluA3 complexes and the LBD–

TMD_{mix} map.

a, c, e, g, i, l, o, Local resolution estimates of the entire GluA1–GluA2–GluA3 asymmetric 1 map (**a**), the ATD layer of the GluA1–GluA2–GluA3 asymmetric 1 map (**c**), the entire GluA1–GluA2–GluA3 asymmetric 2 map (**e**), the ATD layer of the GluA1–GluA2–GluA3 asymmetric 2 map (**g**), the LBD–TMD layers of GluA1–GluA2–GluA3 without symmetry (**i**), the LBD–TMD layers of GluA1–GluA2–GluA3 with C2 symmetry imposed (**l**), and the LBD–TMD_{mix} map (**o**). **b, d, f, h, k, n**, FSC curves before and after masking the entire GluA1–GluA2–GluA3 asymmetric 1 receptor map (**b**), the ATD layer of the GluA1–GluA2–GluA3 asymmetric 1 map (**d**), the entire GluA1–GluA2–GluA3 asymmetric 1 map (**f**), the ATD layer of the GluA1–GluA2–GluA3 asymmetric 2 map (**h**), the LBD–TMD layers of GluA1–GluA2–GluA3 map without symmetry (**k**) and with C2 symmetry (**n**). **j, m, p**, Angular distribution of the LBD–TMD layers of the GluA1–GluA2–GluA3 maps with C1 symmetry (**j**) or C2 symmetry (**m**), and the LBD–TMD_{mix} map (**p**). **q**, FSC curves before and after masking and between the model and the final maps of the LBD–TMD_{mix} map.

Extended Data Fig. 7 Representative TIRF images for native AMPAR complexes captured with the 15F1 monoclonal antibody.

a–e, Fluorescence detection with the anti-GluA1-Alexa488 monoclonal antibody (α GluA1) and anti-GluA3-Alexa594 monoclonal antibody (α GluA3) (**a**), the anti-GluA1-Alexa488 monoclonal antibody, anti-GluA3-Alexa594 monoclonal antibody and anti-GluA4-Alexa594 monoclonal antibody (α GluA4) (**b**), the anti-GluA1-Alexa488 monoclonal antibody, anti-GluA3-Alexa594 monoclonal antibody and anti-TARP- γ 8 monoclonal antibody (α TARP- γ 8) (for each colocalization experiment) (**c**), anti-TARP- γ 8 (α TARP- γ 8) Fab–GFP (**d**) and the anti-SynDIG4–Alexa594 monoclonal antibody (α SynDIG4) and anti-TARP- γ 8–Alexa647 monoclonal antibody (α TARP- γ 8) (**e**). Scale bars, 5 μ m. For each SiMPull experiment, images were acquired from two independent samples on different days.

Extended Data Fig. 8 Structures of the dimeric GluA1–GluA2 receptor, trimeric GluA1–GluA2–GluA3 receptor and dimeric GluA2–GluA3 receptor complexes in symmetric and asymmetric conformations.

a, c, Cryo-EM structures of the GluA1–GluA2 subtype in symmetric (**a**) and asymmetric (**c**) conformations viewed parallel to the membrane. GluA1, GluA2, TARP- γ 8 and CNIH2 are shown in grey, red, green and blue, respectively. Antibody fragments 11B8 scFv and 15F1 Fab are shown in pink and cyan, respectively. **b**, ATD layer analysis of symmetric and asymmetric conformations. Top, the ATD model of the symmetric state, in which the centre of mass (COM) of each subunit is indicated by a black circle. Bottom, the distances (in Ångstrom) and angles determined by the COMs of the symmetric (left) and asymmetric (right) conformations. **d, e**, Close contacts between the ATD layer and LBD layer in the asymmetric conformations. Magnified views of the ‘left’ side (**d**) and ‘right’ side (**e**) of the ATD–LBD interfaces as indicated in the black and cyan rectangles. **f–h**, Cryo-EM structures of the trimeric GluA1–GluA2–GluA3 subtype in asymmetric conformations with different tilted angles and orientations viewed parallel to the membrane. GluA1, GluA2, GluA3, TARP- γ 8 and CNIH2 are coloured in grey, red, orange, green and blue, respectively. Antibody fragments 11B8 scFv, 15F1 Fab, 5B2 Fab are shown in pink, cyan and light yellow colours, respectively. **i, j**, Magnified views of ATD–LBD interfaces in the asymmetric states (**f, h**) as indicated in the black and red rectangles. The distances are defined by the $\text{C}\alpha$ atoms of the indicated residues. **k, l**, Cryo-EM structures of the dimeric GluA2–GluA3 subtype in symmetric (**k**) and asymmetric (**l**) conformations viewed parallel to the membrane. **m**, The ATD layer analysis of the symmetric and asymmetric conformations. Top, an ATD model of the symmetric state. The COM of each subunit is shown as a black circle. Bottom, the distances (in Ångstrom) and angles determined by the COMs of the symmetric (left) and asymmetric (right) conformations. **n, o**, Close contacts between the ATD layer and LBD layer in the asymmetric conformations. Magnified views of the left side (**n**) and right side (**o**) of the ATD–LBD interfaces as indicated in the green and cyan rectangles.

Extended Data Fig. 9 Flow chart of data processing for hpAMPAR complexes focused on the LBD–TMD layers.

Particles corresponding to both the symmetric and the asymmetric GluA1–GluA2 subtypes were combined and subjected to LBD–TMD focused three-dimensional classification with alignment in RELION 3.0, resulting in three good classes with continuous transmembrane helical densities. Another round of classification without alignment was carried out for classes 1 and 8. Classes displaying strong density for TMD and auxiliary proteins were combined for refinement in cryoSPARC v.2.14, yielding the LBD–TMD_{A1/A2} map at a resolution of 3.63 Å.

Extended Data Fig. 10 Conformational differences in the LBD and TMD layers between native and recombinant AMPAR–auxiliary protein complexes.

a, Reference model and orientation of the hippocampal LBD–TMD_{A1/A2} complex. GluA1, GluA2, TARP-γ8 and CNIH2 are shown in grey, red, green and blue, respectively. **b–e**, Superposition of hippocampal LBD–TMD_{A1/A2} with recombinant GluA1–GluA2–TARP-γ8 complexes (PDB code: 6QKC) to show the differences in the LBD (**b**, **d**) and TMD (**c**, **e**) layers. Recombinant GluA1–GluA2–TARP-γ8 is shown in blue. COMs of LBD and TMD layers of each subunit are shown in coloured circles. The schematic diagrams illustrate the subunit arrangement differences in the distance (Ångstrom) of the LBD (**d**) and TMD (**e**) layers of these two complexes. **f–i**, Superposition of the hippocampal LBD–TMD_{A1/A2} structure with the recombinant GluA2–CNIH3 complex (PDB code: 6PEQ) to show the differences in the LBD (**f**, **h**) and TMD (**g**, **i**) layers. Recombinant GluA2–CNIH3 is shown in yellow. COMs of the LBD and TMD layers of each subunit are shown in coloured circles. The schematic diagrams illustrate the subunit arrangement differences in the distance (Ångstrom) of the LBD (**h**) and TMD (**i**) layers of these two complexes. **j**, The B/C LBD dimers from the hippocampal LBD–TMD_{A1/A2} structure and the GluA2–CNIH3 complex (PDB code: 6PEQ) were superimposed, exhibiting a 3.2 Å shift in the COM (black circles) between the opposing

A/D LBD dimers. **k**, Superposition of the M1, M3 and M4 helices of the hippocampal LBD–TMD_{A1/A2} structure with the recombinant GluA2–CNIH3 complex (PDB code: 6PEQ), highlighting the rotation and compression of the GluA2–CNIH3 TMD layer. Equivalent positions of the Cα atoms from the M1 (Val538), M3 (Ile600) and M4 (Leu805) helices of the GluA2–CNIH3 structure are shifted by 4.5 Å, 5.7 Å and 4.7 Å, respectively.

Extended Data Fig. 11 Representative densities of the maps of the LBD–TMD_{A1/A2} or LBD–TMD_{mix} complexes.

a, The S1–M1, M2–pore loop, R/G site and MPQX from GluA1 are isolated from LBD–TMD_{A1/A2}, contoured at 0.085σ. **b**, S1–M1, M2–pore loop and R/G site from GluA2 are isolated from LBD–TMD_{A1/A2}, contoured at 0.085σ. **c**, Comparison of the differences by fitting Arg and Gln into the GluA2 Q/R site density. **d**, Four transmembrane helices (TM1–TM4) in TARP-γ8 are isolated from LBD–TMD_{mix}, contoured at 0.15σ. **e**, Four transmembrane helices (TM1–TM4) in CNIH2 are isolated from LBD–TMD_{mix}, contoured at 0.13σ.

Extended Data Fig. 12 Electrophysiological recordings of GluA1–TARP-γ8 mutant proteins.

a, Current responses of wild-type GluA1–TARP-γ8 complexes evoked by repeated application of 10 mM glutamate with 10 pulses, each for a duration time of 1 s to reach a plateau of the steady-state current. To measure the inhibition of glutamate-induced currents, 10 μM JNJ-55511118 was applied before and during glutamate application for 1 s. Bottom insets illustrate the inhibition effect of JNJ-55511118 on the steady-state current by overlaying the currents without (the last application) and with JNJ-55511118 at timescales of 500 ms (left) and 20 ms (right). **b–h**, Representative recordings for the indicated GluA1 (**b–e**) and TARP-γ8 (**f–h**) mutant proteins with the same recording conditions as for the wild-type proteins.

Extended Data Fig. 13 LBD–TMD_{mix} data-processing strategy 2.

Particles after two-dimensional and three-dimensional classification clean-up using data-processing strategy 2 were combined into a single stack and refined, and unless otherwise specified, all subsequent processing was performed in cryoSPARC v.2.14. Signal subtraction was implemented using the consensus refinement and a soft mask created around the ATD layer and all possible binding sites of the antibodies. Several rounds of two-dimensional classification were used to remove false positives and particles that still contained the ATD layer. This cleaned stack of particles underwent three-dimensional classification (C1 symmetry), which resulted in a single class displaying continuous transmembrane density features. Particles from this class were subject to two-dimensional classification to remove a small subset of junk particles. An iterative, sequential, refinement procedure consisting of (1) homogenous refinement, (2) non-uniform refinement, (3) local CTF refinement and (4) non-uniform refinement, was used to improve the resolution of the stack of 151,141 particles. This procedure was iterated twice until no resolution improvement was obtained, resulting in a 3.45 Å map. Particles from this map were then subjected to ab initio classification permitting the removal of junk particles. A new stack of 132,427 particles was then subjected to the previously described four-step refinement procedure for one iteration, before three-dimensional classification was performed in RELION 3.0 to remove junk particles. This final particle stack was subjected to non-uniform refinement in cryoSPARC to obtain the LBD–TMD_{mix} map at 3.25 Å.

Supplementary information

Supplementary Information

This file contains Supplementary Figure 1 and Supplementary Tables 1-2.

Reporting Summary

Peer Review File

Rights and permissions

Reprints and Permissions

About this article



Check for
updates

Cite this article

Yu, J., Rao, P., Clark, S. *et al.* Hippocampal AMPA receptor assemblies and

mechanism of allosteric inhibition. *Nature* **594**, 448–453 (2021).

<https://doi.org/10.1038/s41586-021-03540-0>

Download citation

- Received: 31 January 2021
- Accepted: 12 April 2021
- Published: 12 May 2021
- Issue Date: 17 June 2021
- DOI: <https://doi.org/10.1038/s41586-021-03540-0>

Comments

By submitting a comment you agree to abide by our [Terms](#) and [Community Guidelines](#). If you find something abusive or that does not comply with our terms or guidelines please flag it as inappropriate.

[Access through your institution](#)

[Change institution](#)

[Buy or subscribe](#)

Associated Content

[Glutamate receptor complexes open up and reveal their molecular dialect](#)

- Andrew J. R. Plested

Advertisement

This article was downloaded by **calibre** from <https://www.nature.com/articles/s41586-021-03540-0>

| [Section menu](#) | [Main menu](#) |

- Article
- [Published: 02 June 2021](#)

Gating and modulation of a hetero-octameric AMPA glutamate receptor

- [Danyang Zhang¹](#),
- [Jake F. Watson](#) [ORCID: orcid.org/0000-0002-8698-3823¹](#) nAff2,
- [Peter M. Matthews¹](#),
- [Ondrej Cais¹](#) &
- [Ingo H. Greger](#) [ORCID: orcid.org/0000-0002-7291-2581¹](#)

[Nature](#) volume **594**, pages 454–458 (2021) [Cite this article](#)

- 3993 Accesses
- 48 Altmetric
- [Metrics details](#)

Subjects

- [Cryoelectron microscopy](#)
- [Ion channels in the nervous system](#)

Abstract

AMPA receptors (AMPARs) mediate the majority of excitatory transmission in the brain and enable the synaptic plasticity that underlies learning¹. A diverse array of AMPAR signalling complexes are established

by receptor auxiliary subunits, which associate with the AMPAR in various combinations to modulate trafficking, gating and synaptic strength². However, their mechanisms of action are poorly understood. Here we determine cryo-electron microscopy structures of the heteromeric GluA1–GluA2 receptor assembled with both TARP- γ 8 and CNIH2, the predominant AMPAR complex in the forebrain, in both resting and active states. Two TARP- γ 8 and two CNIH2 subunits insert at distinct sites beneath the ligand-binding domains of the receptor, with site-specific lipids shaping each interaction and affecting the gating regulation of the AMPARs. Activation of the receptor leads to asymmetry between GluA1 and GluA2 along the ion conduction path and an outward expansion of the channel triggers counter-rotations of both auxiliary subunit pairs, promoting the active-state conformation. In addition, both TARP- γ 8 and CNIH2 pivot towards the pore exit upon activation, extending their reach for cytoplasmic receptor elements. CNIH2 achieves this through its uniquely extended M2 helix, which has transformed this endoplasmic reticulum-export factor into a powerful AMPAR modulator that is capable of providing hippocampal pyramidal neurons with their integrative synaptic properties.

Access options

Subscribe to Journal

Get full journal access for 1 year

\$199.00

only \$3.90 per issue

[Subscribe](#)

All prices are NET prices.

VAT will be added later in the checkout.

Tax calculation will be finalised during checkout.

Rent or Buy article

Get time limited or full article access on ReadCube.

from \$8.99

[Rent or Buy](#)

All prices are NET prices.

Additional access options:

- [Log in](#)
- [Access through your institution](#)
- [Learn about institutional subscriptions](#)

Fig. 1: Physiology and architecture of the GluA1–A2 γ 8–CNIH2 complex.



Fig. 2: Gating transitions of the GluA1–A2 γ 8–CNIH2 octamer.

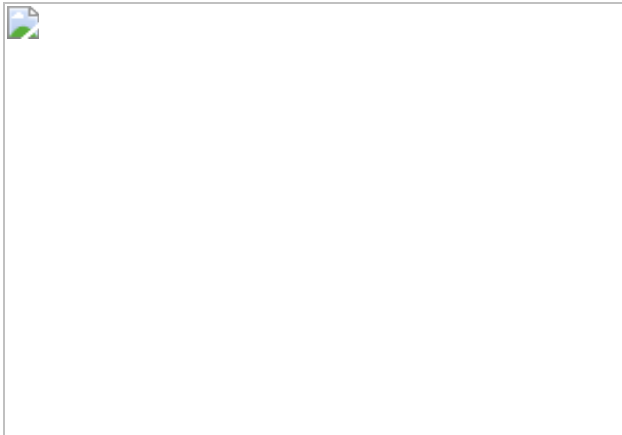
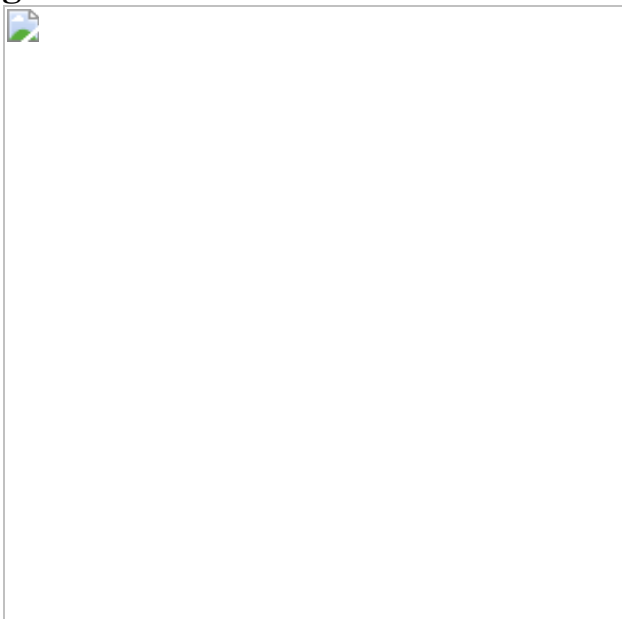


Fig. 3: Mechanism of AMPAR modulation by CNIH2.



Data availability

Cryo-EM coordinates are deposited in the PDB under the accession codes [7OCA](#) (resting state full-length AMPAR octamer), [7OCC](#) (NTD of the resting state octamer), [7OCD](#) (resting state LBD-TMD with TARP- γ 8 only), [7OCE](#) (resting state LBD-TMD of the octamer), [7OCF](#) (active state LBD-TMD of the octamer); the corresponding EM maps are deposited in the EMDB under accession codes [EMD-12802](#), [EMD-12803](#), [EMD-12804](#), [EMD-12805](#) and [EMD-12806](#). Source data are provided with this paper.

References

1. 1.

Traynelis, S. F. et al. Glutamate receptor ion channels: structure, regulation, and function. *Pharmacol. Rev.* **62**, 405–496 (2010).

[CAS](#) [PubMed](#) [PubMed Central](#) [Google Scholar](#)

2. 2.

Greger, I. H., Watson, J. F. & Cull-Candy, S. G. Structural and functional architecture of AMPA-type glutamate receptors and their auxiliary proteins. *Neuron* **94**, 713–730 (2017).

[CAS](#) [PubMed](#) [PubMed Central](#) [Google Scholar](#)

3. 3.

Jonas, P. The time course of signaling at central glutamatergic synapses. *News Physiol. Sci.* **15**, 83–89 (2000).

[ADS](#) [CAS](#) [PubMed](#) [PubMed Central](#) [Google Scholar](#)

4. 4.

Schwenk, J. et al. High-resolution proteomics unravel architecture and molecular diversity of native AMPA receptor complexes. *Neuron* **74**, 621–633 (2012).

[CAS](#) [PubMed](#) [PubMed Central](#) [Google Scholar](#)

5. 5.

Shanks, N. F. et al. Differences in AMPA and kainate receptor interactomes facilitate identification of AMPA receptor auxiliary subunit GSG1L. *Cell Rep.* **1**, 590–598 (2012).

[CAS](#) [PubMed](#) [PubMed Central](#) [Google Scholar](#)

6. 6.

Lu, W. et al. Subunit composition of synaptic AMPA receptors revealed by a single-cell genetic approach. *Neuron* **62**, 254–268 (2009).

[CAS](#) [PubMed](#) [PubMed Central](#) [Google Scholar](#)

7. 7.

Schwenk, J. et al. Regional diversity and developmental dynamics of the AMPA-receptor proteome in the mammalian brain. *Neuron* **84**, 41–54 (2014).

[CAS](#) [PubMed](#) [PubMed Central](#) [Google Scholar](#)

8. 8.

Schwenk, J. et al. Functional proteomics identify cornichon proteins as auxiliary subunits of AMPA receptors. *Science* **323**, 1313–1319 (2009).

[ADS](#) [CAS](#) [PubMed](#) [PubMed Central](#) [Google Scholar](#)

9. 9.

Boudkkazi, S., Brechet, A., Schwenk, J. & Fakler, B. Cornichon2 dictates the time course of excitatory transmission at individual hippocampal synapses. *Neuron* **82**, 848–858 (2014).

[CAS](#) [PubMed](#) [PubMed Central](#) [Google Scholar](#)

10. 10.

Rouach, N. et al. TARP γ -8 controls hippocampal AMPA receptor number, distribution and synaptic plasticity. *Nat. Neurosci.* **8**, 1525–1533 (2005).

[CAS](#) [PubMed](#) [PubMed Central](#) [Google Scholar](#)

11. 11.

Gill, M. B. et al. Cornichon-2 modulates AMPA receptor–transmembrane AMPA receptor regulatory protein assembly to dictate gating and pharmacology. *J. Neurosci.* **31**, 6928–6938 (2011).

[CAS](#) [PubMed](#) [PubMed Central](#) [Google Scholar](#)

12. 12.

Herring, B. E. et al. Cornichon proteins determine the subunit composition of synaptic AMPA receptors. *Neuron* **77**, 1083–1096 (2013).

[CAS](#) [PubMed](#) [PubMed Central](#) [Google Scholar](#)

13. 13.

Kato, A. S. et al. Hippocampal AMPA receptor gating controlled by both TARP and cornichon proteins. *Neuron* **68**, 1082–1096 (2010).

[CAS](#) [PubMed](#) [PubMed Central](#) [Google Scholar](#)

14. 14.

Chen, S. et al. Activation and desensitization mechanism of AMPA receptor-TARP complex by cryo-EM. *Cell* **170**, 1234–1246.e14 (2017).

[CAS](#) [PubMed](#) [PubMed Central](#) [Google Scholar](#)

15. 15.

Herguedas, B. et al. Architecture of the heteromeric GluA1/2 AMPA receptor in complex with the auxiliary subunit TARP $\gamma 8$. *Science* **364**, eaav9011 (2019).

[CAS](#) [PubMed](#) [PubMed Central](#) [Google Scholar](#)

16. 16.

Twomey, E. C., Yelshanskaya, M. V., Grassucci, R. A., Frank, J. & Sobolevsky, A. I. Channel opening and gating mechanism in AMPA-subtype glutamate receptors. *Nature* **549**, 60–65 (2017).

[ADS](#) [CAS](#) [PubMed](#) [PubMed Central](#) [Google Scholar](#)

17. 17.

Nakagawa, T. Structures of the AMPA receptor in complex with its auxiliary subunit cornichon. *Science* **366**, 1259–1263 (2019).

[ADS](#) [CAS](#) [PubMed](#) [PubMed Central](#) [Google Scholar](#)

18. 18.

Dancourt, J. & Barlowe, C. Protein sorting receptors in the early secretory pathway. *Annu. Rev. Biochem.* **79**, 777–802 (2010).

[CAS](#) [PubMed](#) [PubMed Central](#) [Google Scholar](#)

19. 19.

Shi, Y., Lu, W., Milstein, A. D. & Nicoll, R. A. The stoichiometry of AMPA receptors and TARPs varies by neuronal cell type. *Neuron* **62**, 633–640 (2009).

[CAS](#) [PubMed](#) [PubMed Central](#) [Google Scholar](#)

20. 20.

Khodosevich, K. et al. Coexpressed auxiliary subunits exhibit distinct modulatory profiles on AMPA receptor function. *Neuron* **83**, 601–615 (2014).

[CAS](#) [PubMed](#) [PubMed Central](#) [Google Scholar](#)

21. 21.

Zhao, Y., Chen, S., Swensen, A. C., Qian, W. J. & Gouaux, E. Architecture and subunit arrangement of native AMPA receptors elucidated by cryo-EM. *Science* **364**, 355–362 (2019).

[ADS](#) [CAS](#) [PubMed](#) [PubMed Central](#) [Google Scholar](#)

22. 22.

Sobolevsky, A. I., Rosconi, M. P. & Gouaux, E. X-ray structure, symmetry and mechanism of an AMPA-subtype glutamate receptor. *Nature* **462**, 745–756 (2009).

[ADS](#) [CAS](#) [PubMed](#) [PubMed Central](#) [Google Scholar](#)

23. 23.

Twomey, E. C., Yelshanskaya, M. V., Grassucci, R. A., Frank, J. & Sobolevsky, A. I. Structural bases of desensitization in AMPA receptor-auxiliary subunit complexes. *Neuron* **94**, 569–580.e5 (2017).

[CAS](#) [PubMed](#) [PubMed Central](#) [Google Scholar](#)

24. 24.

Armstrong, N. & Gouaux, E. Mechanisms for activation and antagonism of an AMPA-sensitive glutamate receptor: crystal structures of the GluR2 ligand binding core. *Neuron* **28**, 165–181 (2000).

[CAS](#) [PubMed](#) [PubMed Central](#) [Google Scholar](#)

25. 25.

Yelshansky, M. V., Sobolevsky, A. I., Jatzke, C. & Wollmuth, L. P. Block of AMPA receptor desensitization by a point mutation outside the ligand-binding domain. *J. Neurosci.* **24**, 4728–4736 (2004).

[CAS](#) [PubMed](#) [PubMed Central](#) [Google Scholar](#)

26. 26.

Burnashev, N., Monyer, H., Seeburg, P. H. & Sakmann, B. Divalent ion permeability of AMPA receptor channels is dominated by the edited form of a single subunit. *Neuron* **8**, 189–198 (1992).

[CAS](#) [PubMed](#) [PubMed Central](#) [Google Scholar](#)

27. 27.

Hume, R. I., Dingledine, R. & Heinemann, S. F. Identification of a site in glutamate receptor subunits that controls calcium permeability. *Science* **253**, 1028–1031 (1991).

[ADS](#) [CAS](#) [PubMed](#) [PubMed Central](#) [Google Scholar](#)

28. 28.

Twomey, E. C., Yelshanskaya, M. V., Vassilevski, A. A. & Sobolevsky, A. I. Mechanisms of channel block in calcium-permeable AMPA receptors. *Neuron* **99**, 956–968.e4 (2018).

[CAS](#) [PubMed](#) [PubMed Central](#) [Google Scholar](#)

29. 29.

Bowie, D. Polyamine-mediated channel block of ionotropic glutamate receptors and its regulation by auxiliary proteins. *J. Biol. Chem.* **293**, 18789–18802 (2018).

[CAS](#) [PubMed](#) [PubMed Central](#) [Google Scholar](#)

30. 30.

Coombs, I. D. et al. Cornichons modify channel properties of recombinant and glial AMPA receptors. *J. Neurosci.* **32**, 9796–9804 (2012).

[CAS](#) [PubMed](#) [PubMed Central](#) [Google Scholar](#)

31. 31.

Alsaloum, M., Kazi, R., Gan, Q., Amin, J. & Wollmuth, L. P. A molecular determinant of subtype-specific desensitization in ionotropic glutamate receptors. *J. Neurosci.* **36**, 2617–2622 (2016).

[PubMed](#) [PubMed Central](#) [Google Scholar](#)

32. 32.

McDaniel, M. J. et al. NMDA receptor channel gating control by the pre-M1 helix. *J. Gen. Physiol.* **152**, e201912362 (2020).

[PubMed](#) [PubMed Central](#) [Google Scholar](#)

33. 33.

Yelshanskaya, M. V., Mesbahi-Vasey, S., Kurnikova, M. G. & Sobolevsky, A. I. Role of the ion channel extracellular collar in AMPA receptor gating. *Sci. Rep.* **7**, 1050 (2017).

[ADS](#) [PubMed](#) [PubMed Central](#) [Google Scholar](#)

34. 34.

Dawe, G. B. et al. Distinct structural pathways coordinate the activation of AMPA receptor-auxiliary subunit complexes. *Neuron* **89**, 1264–1276 (2016).

[CAS](#) [PubMed](#) [PubMed Central](#) [Google Scholar](#)

35. 35.

Krieger, J., Lee, J. Y., Greger, I. H. & Bahar, I. Activation and desensitization of ionotropic glutamate receptors by selectively triggering pre-existing motions. *Neurosci. Lett.* **700**, 22–29 (2019).

[CAS](#) [PubMed](#) [PubMed Central](#) [Google Scholar](#)

36. 36.

Eyal, E., Lum, G. & Bahar, I. The anisotropic network model web server at 2015 (ANM 2.0). *Bioinformatics* **31**, 1487–1489 (2015).

[CAS](#) [PubMed](#) [PubMed Central](#) [Google Scholar](#)

37. 37.

Shanks, N. F. et al. Molecular dissection of the interaction between the AMPA receptor and cornichon homolog-3. *J. Neurosci.* **34**, 12104–12120 (2014).

[CAS](#) [PubMed](#) [PubMed Central](#) [Google Scholar](#)

38. 38.

Bakan, A., Meireles, L. M. & Bahar, I. ProDy: protein dynamics inferred from theory and experiments. *Bioinformatics* **27**, 1575–1577 (2011).

[CAS](#) [PubMed](#) [PubMed Central](#) [Google Scholar](#)

39. 39.

García-Nafría, J., Watson, J. F. & Greger, I. H. IVA cloning: a single-tube universal cloning system exploiting bacterial *in vivo* assembly. *Sci. Rep.* **6**, 27459 (2016).

[ADS](#) [PubMed](#) [PubMed Central](#) [Google Scholar](#)

40. 40.

Stoppini, L., Buchs, P. A. & Muller, D. A simple method for organotypic cultures of nervous tissue. *J. Neurosci. Methods* **37**, 173–182 (1991).

[CAS](#) [PubMed](#) [PubMed Central](#) [Google Scholar](#)

41. 41.

Elegheert, J. et al. Lentiviral transduction of mammalian cells for fast, scalable and high-level production of soluble and membrane proteins. *Nat. Protocols* **13**, 2991–3017 (2018).

[CAS](#) [PubMed](#) [PubMed Central](#) [Google Scholar](#)

42. 42.

Zheng, S. Q. et al. MotionCor2: anisotropic correction of beam-induced motion for improved cryo-electron microscopy. *Nat. Methods* **14**, 331–332 (2017).

[CAS](#) [PubMed](#) [PubMed Central](#) [Google Scholar](#)

43. 43.

Zhang, K. Gctf: real-time CTF determination and correction. *J. Struct. Biol.* **193**, 1–12 (2016).

[ADS](#) [CAS](#) [PubMed](#) [PubMed Central](#) [Google Scholar](#)

44. 44.

Zivanov, J. et al. New tools for automated high-resolution cryo-EM structure determination in RELION-3. *eLife* **7**, e42166 (2018).

[PubMed](#) [PubMed Central](#) [Google Scholar](#)

45. 45.

Emsley, P., Lohkamp, B., Scott, W. G. & Cowtan, K. Features and development of Coot. *Acta Crystallogr. D* **66**, 486–501 (2010).

[CAS](#) [PubMed](#) [PubMed Central](#) [Google Scholar](#)

46. 46.

Murshudov, G. N. et al. REFMAC5 for the refinement of macromolecular crystal structures. *Acta Crystallogr. D* **67**, 355–367 (2011).

[CAS](#) [PubMed](#) [PubMed Central](#) [Google Scholar](#)

47. 47.

Liebschner, D. et al. Macromolecular structure determination using X-rays, neutrons and electrons: recent developments in Phenix. *Acta Crystallogr. D* **75**, 861–877 (2019).

[CAS](#) [Google Scholar](#)

48. 48.

Williams, C. J. et al. MolProbity: more and better reference data for improved all-atom structure validation. *Protein Sci.* **27**, 293–315 (2018).

[CAS](#) [PubMed](#) [PubMed Central](#) [Google Scholar](#)

49. 49.

Smart, O. S., Neduvvelil, J. G., Wang, X., Wallace, B. A. & Sansom, M. S. HOLE: a program for the analysis of the pore dimensions of ion channel structural models. *J. Mol. Graph.* **14**, 354–360 (1996).

[CAS](#) [PubMed](#) [PubMed Central](#) [Google Scholar](#)

50. 50.

Bakan, A. et al. Evol and ProDy for bridging protein sequence evolution and structural dynamics. *Bioinformatics* **30**, 2681–2683 (2014).

[CAS](#) [PubMed](#) [PubMed Central](#) [Google Scholar](#)

51. 51.

Zhang, S., Li, H., Krieger, J. M. & Bahar, I. Shared signature dynamics tempered by local fluctuations enables fold adaptability and specificity. *Mol. Biol. Evol.* **36**, 2053–2068 (2019).

[CAS](#) [PubMed](#) [PubMed Central](#) [Google Scholar](#)

52. 52.

Schindelin, J. et al. Fiji: an open-source platform for biological-image analysis. *Nat. Methods* **9**, 676–682 (2012).

[CAS](#) [PubMed](#) [PubMed Central](#) [Google Scholar](#)

[Download references](#)

Acknowledgements

We thank members of the Greger laboratory, B. Herguedas, J. Krieger and J.-N. Dohrke for comments on the manuscript; J. Krieger and J.-N. Dohrke for discussion, J. Krieger for help with the normal mode analysis, B. Köhegyi for help with cryo-EM imaging, V. Chang and K. Suzuki for helping to generate the CNIH2-1D4-HA stable cell line, M. Carvalho for assistance at early stages of this project, the LMB scientific computing and the cryo-EM facility for support, P. Emsley for help with model building, T. Nakane for helpful comments with RELION 3.1 and R. Warshamamanage for helping with EMDA cryo-EM-map processing. We acknowledge the Diamond Light Source for access and support of the Cryo-EM facilities at the UK national electron bio10 imaging centre (eBIC), proposal EM17434, funded by the Wellcome Trust, MRC and BBSRC. This work was supported by grants from the Medical Research Council, as part of United Kingdom Research and Innovation (also known as UK Research and Innovation) (MC_U105174197) and BBSRC (BB/N002113/1) to I.H.G.

Author information

Author notes

1. Jake F. Watson

Present address: IST Austria, Klosterneuburg, Austria

Affiliations

1. Neurobiology Division, MRC Laboratory of Molecular Biology, Cambridge, UK

Danyang Zhang, Jake F. Watson, Peter M. Matthews, Ondrej
Cais & Ingo H. Greger

Authors

1. Danyang Zhang

[View author publications](#)

You can also search for this author in [PubMed](#) [Google Scholar](#)

2. Jake F. Watson

[View author publications](#)

You can also search for this author in [PubMed](#) [Google Scholar](#)

3. Peter M. Matthews

[View author publications](#)

You can also search for this author in [PubMed](#) [Google Scholar](#)

4. Ondrej Cais

[View author publications](#)

You can also search for this author in [PubMed](#) [Google Scholar](#)

5. Ingo H. Greger

[View author publications](#)

You can also search for this author in [PubMed](#) [Google Scholar](#)

Contributions

I.H.G. conceptualized and supervised the study, and wrote the paper with input from J.F.W. D.Z. performed protein purification, cryo-EM data collection, data processing and model building. J.F.W. and O.C. designed and performed electrophysiological experiments. P.M.M. and J.F.W. performed confocal imaging and data analysis.

Corresponding author

Correspondence to [Ingo H. Greger](#).

Ethics declarations

Competing interests

The authors declare no competing interests.

Additional information

Peer review information *Nature* thanks Sudha Chakrapani, Yael Stern-Bach and the other, anonymous, reviewer(s) for their contribution to the peer review of this work.

Publisher's note Springer Nature remains neutral with regard to jurisdictional claims in published maps and institutional affiliations.

Extended data figures and tables

[Extended Data Fig. 1 Properties of neuronal and recombinant AMPAR complexes.](#)

a, Electrophysiological properties of neuronal and recombinant AMPAR complexes. Top left, hippocampus schematic indicating selected cell types. Bottom left, rise time of fast-application glutamate responses of

recombinant and neuronal AMPAR patches. The 20–80% rise time (ms) was as follows. Recombinant receptors: GluA1–GluA2, 0.46 ± 0.03 ms, $n = 9$; $+\gamma 8$, 0.55 ± 0.03 ms, $n = 11$; $+\gamma 8+CNIH2$, 0.59 ± 0.04 ms, $n = 8$. Neuronal receptors: CA1 pyramidal (pyr), 0.52 ± 0.02 ms, $n = 14$; CA3 pyramidal, 0.60 ± 0.05 ms, $n = 5$; DG granule (gran) cell (GC), 0.42 ± 0.02 ms, $n = 6$; CA1 stratum pyramidale interneurons (str rad IN), 0.51 ± 0.03 ms, $n = 8$. Welch's ANOVA with Dunnett's multiple comparison tests; recombinant, $W_{2,15.11} = 4.25$, $P = 0.03$; neurons, $W_{3,12.12} = 5.40$, $P = 0.014$ (further details in Supplementary Table 1). Top middle, example trace of rectification index recording from CA1 pyramidal neuron normalized to -100 mV peak amplitude. Bottom middle, quantified rectification index from recorded surface patches. Recombinant receptors: GluA1–GluA2, 0.70 ± 0.04 , $n = 8$; $+\gamma 8$, 0.60 ± 0.02 , $n = 12$; $+\gamma 8+CNIH2$, 0.63 ± 0.01 , $n = 12$. Neuronal receptors: CA1 pyramidal, 0.58 ± 0.01 , $n = 13$; CA3 pyramidal, 0.56 ± 0.01 , $n = 4$; DG granule cell, 0.55 ± 0.04 , $n = 4$; CA1 stratum pyramidale interneurons, 0.42 ± 0.08 , $n = 5$. Welch's ANOVA with Dunnett's multiple comparisons test; recombinant, $W_{2,15.01} = 2.47$, $P = 0.12$; neurons, $W_{3,7.57} = 1.5$, $P = 0.29$ (further details in Supplementary Table 1). Top right, strong correlation between equilibrium current and desensitization rate are observed (individual neuronal patches plotted). Bottom right, equilibrium current for patch responses show auxiliary protein dependent modulation and neuronal heterogeneity. Percentage of peak current. Recombinant receptors: GluA1–GluA2, 1.81 ± 0.34 , $n = 9$; $+\gamma 8$, 4.72 ± 1.09 , $n = 11$; $+\gamma 8+CNIH2$, 10.97 ± 2.03 , $n = 8$. Neuronal receptors: CA1 pyramidal, 4.86 ± 0.71 , $n = 14$; CA3 pyramidal, 5.78 ± 1.00 , $n = 5$; DG granule cell, 0.75 ± 0.22 , $n = 6$; CA1 stratum pyramidale interneurons, 0.59 ± 0.29 , $n = 8$. Welch's ANOVA tests with Dunnett's multiple comparisons test; recombinant, $W_{2,12.09} = 11.93$, $P = 0.002$; neurons, $W_{3,12.42} = 16.74$, $P = 0.0001$ (further details in Supplementary Table 1).

b, Purification and cryo-EM images of the GluA1–A2 $-\gamma 8$ –CNIH2 complex. Left, representative 4–12% Bis-Tris gel stained with Coomassie blue, indicating elution of GluA1–A2 $-\gamma 8$ –CNIH2 complex from Flag beads. CNIH2 expression from the same purification is detected by probing for the C-terminal HA tag using western blotting. Purification was performed reproducibly (four times); uncropped blots are shown in Supplementary Fig. 1. Middle, a representative motion-corrected

micrograph of the resting state GluA1–A2 γ 8–CNIH2 complex among collected data. Scale bar, 50 nm. Right, representative two-dimensional class averages of the resting state GluA1–A2 γ 8–CNIH2 complex. **c**, Left, cryo-EM maps of the full-length AMPAR octamer, depicting the three domain layers—NTD, LBD and TMD—composed of the GluA1 (blue) and GluA2 (red) heteromer associated with TARP- γ 8 (green) and CNIH2 (orange). Right, schematic of the plasmid constructs and the secondary protein structure of auxiliary subunits.

[Source data](#)

[Extended Data Fig. 2 Cryo-EM data-processing workflow of the resting-state GluA1–A2 \$\gamma\$ 8–CNIH2 complex.](#)

Two datasets were first processed individually to remove particles lacking AMPAR features. Next, classifications focused on the LBD–TMD region were performed to separate CNIH-containing and CNIH-free particles, meanwhile classifications for full-length receptors were conducted to elucidate particles with a stable NTD signal. Subsequently, particles from the two datasets were combined together for refinement. Focused refinements were performed separately on the LBD–TMD gating core and the NTD region. To further improve the resolution, LBD and TMD are refined separately. A structure of A1/A2 γ 8 (lacking CNIH2) was also resolved from the same dataset (containing only TARP- γ 8 observed in three-dimensional slice). CNIH2 density was further enhanced by first applying symmetry expansion on aligned particles from the TMD reconstruction, following by focused classification and refinement on only CNIH2 and the surrounding receptor transmembrane helices. Inset, top view slices of the GluA1–A2 γ 8–CNIH2 (left) and GluA1–A2 γ 8 (right). Three-dimensional maps of the TMD region show signal for transmembrane helices of TARP- γ 8 (green) and CNIH2 (orange).

[Extended Data Fig. 3 Cryo-EM data-processing workflow of the active-state GluA1–A2 \$\gamma\$ 8–CNIH2 complex.](#)

The overall data-processing procedure for the active-state complex is similar to that of the resting-state complexes. Focused refinement was

performed on the LBD–TMD gating core and individual LBD and TMD domain layers of the receptor. CNIH2 density was further improved by first applying symmetry expansion on aligned particles from the TMD reconstruction, followed by focused classification on CNIH2 alone, and finally focused refinement on CNIH2 together with surrounding receptor transmembrane helices. Particles lacking CNIH2 found in these datasets were not of high enough quality to provide a high-resolution structure.

Extended Data Fig. 4 Cryo-EM analysis of GluA1–A2 γ 8–CNIH2 and GluA1–A2 γ 8 complexes.

a, Local resolution and Fourier shell correlation (FSC) of focused refinement maps at the TMD, CNIH2, LBD and NTD. Euler angle distribution of particles for cryo-EM reconstruction of the resting state GluA1–A2 γ 8–CNIH2 complex. Three-dimensional maps are coloured based on the local resolution estimation. Masked (red) or unmasked (blue) FSCs of corresponding maps are both shown where FSC = 0.143 (black line). **b**, Local resolution and FSC of focused refinements at the TMD and LBD. Euler angle distribution of particles for cryo-EM reconstruction of the resting state GluA1–A2 γ 8 complex. **c**, Local resolution, FSC of focused refinements at the TMD, CNIH2 and LBD. Euler angle distribution of particles for cryo-EM reconstruction of the active state GluA1–A2 γ 8–CNIH2 complex. **d**, Model to map FSCs of GluA1–A2 γ 8–CNIH2 LBD–TMD models in resting and active states, resting-state NTD model and resting-state GluA1–A2 γ 8 LBD–TMD model.

Extended Data Fig. 5 Features of GluA1–A2 γ 8–CNIH2 NTD and LBD layers and quality of the density in the TMD region.

a, Cryo-EM density and model of the resting state GluA1 (blue) and GluA2 (red) NTD dimer. GluA1-specific N-linked glycans are observed at N45 and N239 (green sticks). **b**, Cryo-EM density and model of GluA1–GluA2 LBD dimer in the resting state. Density and model for the competitive antagonist NBQX bound to its orthosteric site in the LBD cleft. **c**, Top view of cryo-EM density and model of GluA1–GluA2 LBD tetramer in the resting state. **d**, Cryo-EM density and model of GluA1–GluA2 LBD dimer in the active

state demonstrating a closure of the LBD ‘clamshell’. **e**, Top view of cryo-EM density and model of GluA1–GluA2 LBD tetramer in the active state. Density and model of desensitization blocker cyclothiazide (CTZ) bound at the LBD dimer interface are shown in the inset. **f**, Cryo-EM density and model of transmembrane helices of GluA1–A2_{γ8}–CNIH2 in the resting state.

Extended Data Fig. 6 Cryo-EM data processing workflow of A2_{γ8} homomeric complex.

Automatic particle picking was first applied on the raw images which had similar features to the GluA1–A2_{γ8}–CNIH2 heteromeric complex. Scale bar, 50 nm. Two-dimensional classifications were then performed to remove particles lacking AMPAR features. In several side-view two-dimensional class averages, an additional layer of density (marked by a red arrowhead) beneath the micelle can be observed. Next, selected particles were used for separate three-dimensional classifications on the full-length receptor (left) or on masked-out LBD–TMD regions (right). In each of the two classifications, around 10% of low-quality particles were removed and the remaining AMPAR-shaped class averages are presented (side and bottom views). An additional layer was observed in the full-length classification in all five classes (indicated by a red arrowhead). Three-dimensional refinement was performed on all classes individually, slices of the TMD region from the refined maps are also shown, with TARP-γ8 densities only apparent at the B'/D' sites (indicated by green arrowheads).

Extended Data Fig. 7 TARP-γ8 and CNIH2 receptor-binding sites and their relevant bound lipids.

a, Overlay of the A'/C' and B'/D' binding sites, showing reorientations of five residues along the M1 helices (GluA1 M1, red; GluA2 M1, blue). These changes are likely mediated by TARP-γ8 engaging GluA1 M1. **b**, Strong lipid densities (light blue, density shown in grey mesh) line the cavity between GluA2 M1 and M4. F515, F517 and L518 from GluA2 pre-M1 interact with the lipids from the upper leaflet. Other residues from GluA2 M1, M2 and GluA1 M3 involved in these interactions are shown as

sticks. **c**, LL1 binds to the TARP- γ 8(N224) side chain, connecting TARP- γ 8 to the GluA1 M2 pore helix. LL2 bridges between CNIH2 and the GluA2 M1 and M2 helices. **d**, ‘Open book’ view of the A’/C’ binding site, displaying how the UL1, LL2 and LL3 lipids engage the receptor (left) and the CNIH2 M1 and M2 helices (right). Side chains in close proximity to lipids are shown. **e**, Superposition of CNIHs and their binding peripheral helices from the resting-state GluA1–A2 γ 8–CNIH2 (orange) and GluA2–CNIH3 (grey, PDB 6PEQ) complexes. Although the upper parts of the M1 and M2 helices of the CNIHs are aligned together, the lower part of CNIH2 is kinked away from the receptor relative to CNIH3—this permits the accommodation of three CNIH2 binding-relevant lipids. The distance between W26 (CNIH2) and C811 (GluA1) in GluA1–A2 γ 8–CNIH2 and W26 (CNIH3) and C815 (GluA2) in GluA2–CNIH3 are measured. M1 and M4 from GluA1–A2 γ 8–CNIH2 resting state are coloured as in Fig. 1. M1 and M4 for GluA2–CNIH3 (PDB 6PEQ) are coloured in grey. Three CNIH2 binding-relevant lipids LL2, LL3 and UL1 are shown as pink sticks. **f**, A density modelled as cholesterol occupies the pocket between CNIH2 M3 and M4, observed after focused refinement.

Extended Data Fig. 8 Features of the GluA1–A2 γ 8–CNIH2 and GluA1–A2 γ 8 conduction pore.

a, Density of M2/M3 gating regions and their fit against models in the resting and active state. **b**, Pore dimensions of resting state GluA1–A2 γ 8 (left) and the resting (middle) and active (right) state of GluA1–A2 γ 8–CNIH2 depicted by space-filling representation (HOLE program) with relevant side chains indicated as sticks. A comparison of the pore radius across these three structures indicates a similar diameter of the receptor gate in resting state GluA1–A2 γ 8 (grey) and GluA1–A2 γ 8–CNIH2 (orange), with a clear expansion observed in the active-state GluA1–A2 γ 8–CNIH2 (red) complex. Diameter differences at the Q/R site are mainly caused by conformational variations at the R586 side chain among these three models. **c**, Pore dimensions measured between C α of GluA1 Q582 and GluA2 R586 in resting-state GluA1–A2 γ 8 (left), GluA1–A2 γ 8–CNIH2 (middle) and active-state GluA1–A2 γ 8–CNIH2 (right). Upon receptor activation, the distance between GluA2 R586 is increased by around 1 Å in GluA1–A2 γ 8–CNIH2. **d**, Distance measured between C α of GluA1 C585 and

GluA2 C589 of GluA1–A2_γ8 resting state (left) and GluA1–A2_γ8–CNIH2 resting (middle) and active (right) state. The corresponding cryo-EM densities are shown as mesh. Upon receptor activation, the distance between the GluA2 subunits at C589 also increased by around 1.5 Å in GluA1–A2_γ8–CNIH2. All diameter labels are measured in ångström. **e**, Charge distribution maps of the intracellular face of GluA1–A2_γ8–CNIH2 (red: $-5 k_B T/e$; blue, $5 k_B T/e$) in the resting (top) and active (bottom) state indicate a dilation of the pore entrance in the direction of GluA2, but not GluA1, during receptor activation.

Extended Data Fig. 9 Conformational changes of GluA1–A2_γ8–CNIH2 during receptor activation.

a, The top-view superposition along the pore axis of GluA1–A2_γ8–CNIH2 in resting (grey) and active (red) states shows the dilation of the receptor and rotation of TARP- γ 8 and CNIH2 during activation. **b**, Superposition of GluA1–A2_γ8–CNIH2 in resting (grey) and active (coloured) states along the pore axis shows the conformational change in the GluA2 M1 and M3 linkers as well as the LBD region upon receptor activation. The GluA2 M3 linker moves towards the M1 linker, while the latter approaches the acidic β4 loop in TARP- γ 8. The LBD ‘KGK’ motif also moves towards the acidic loop in TARP- γ 8. **c, d**, Conformational change in TARP- γ 8 and CNIH2 during receptor activation. Models are aligned along the pore axis. The translation of the Cα atoms from the resting to active state is indicated as arrows for every second residue. Arrows indicate the direction and distance of helical movements; these were determined for all Cα atoms between the two states relative to the centre of mass (COM) of a given auxiliary subunit. Auxiliary subunits come together on the GluA1 pre-M1 side (**c**), but are separated on the GluA2 pre-M1 side (**d**). The magnification in **c** shows a contact between the TARP- γ 8 M4 helix and the base of the GluA1 M1/M2 cytoplasmic loop formed during receptor activation.

Extended Data Fig. 10 Flag immunoprecipitation, immunostaining and electrophysiology of CNIH homologues and CNIH2 mutants in complex with GluA1 or GluA2 homomers.

a, Flag immunoprecipitation of CNIH homologues and CNIH2 mutants in complex with Flag-tagged GluA2 homomers. CNIH1_{2CHIM}, CNIH1–CNIH2 chimera with a fragment of CNIH2 (51-RERLKNIERICCLLRK-66) inserted into CNIH1 between P50 and L51; F3L, CNIH2 F3L; F5L, CNIH2 F5L; F8L, CNIH2 F8L; CNIH2 3FL, all three phenylalanines at positions 3, 5 and 8 in CNIH2 are mutated to leucine; FT, flow through. Immunoprecipitations were performed reproducibly (three times); uncropped blots are shown in Supplementary Fig. 1. **b**, Surface CNIH fluorescence (left), total CNIH fluorescence (middle) and surface/total ratio (right) for CNIH homologues and CNIH2 mutants in complex with GluA2. Surface CNIH (AU): no CNIH, 0.21 ± 0.15 , $n = 80$; CNIH1, 6.60 ± 0.63 , $n = 46$; CNIH2, 7.54 ± 0.56 , $n = 55$; CNIH3, 8.07 ± 0.64 , $n = 61$; CNIH1_{2CHIM}, 8.56 ± 0.69 , $n = 61$; F3L, 4.42 ± 0.80 , $n = 17$; F5L, 4.25 ± 0.40 , $n = 50$; F8L, 8.36 ± 0.75 , $n = 34$; 3FL, 1.67 ± 0.22 , $n = 50$. Kruskal–Wallis test, $H_8 = 256.3$, $P < 0.0001$. Total CNIH (AU): no CNIH, 0.02 ± 0.06 , $n = 80$; CNIH1, 21.5 ± 2.03 , $n = 46$; CNIH2, 25.8 ± 2.08 , $n = 55$; CNIH3, 25.2 ± 2.19 , $n = 61$; CNIH1_{2CHIM}, 25.0 ± 1.49 , $n = 61$; F3L, 12.7 ± 1.85 , $n = 17$; F5L, 16.2 ± 1.97 , $n = 50$; F8L, 24.6 ± 2.00 , $n = 34$; 3FL, 27.3 ± 2.42 , $n = 50$. Kruskal–Wallis test: $H_8 = 230.1$, $P < 0.0001$. Surface/Total: CNIH1, 0.34 ± 0.03 , $n = 46$; CNIH2, 0.39 ± 0.04 , $n = 55$; CNIH3, 0.42 ± 0.04 , $n = 61$; CNIH1_{2CHIM}, 0.36 ± 0.02 , $n = 61$; F3L, 0.41 ± 0.08 , $n = 17$; F5L, 0.35 ± 0.03 , $n = 50$; F8L, 0.39 ± 0.04 , $n = 34$; 3FL, 0.07 ± 0.01 , $n = 50$. One-sample Wilcoxon signed-rank test (median = 0), $P < 0.0001$; further details in Supplementary Table 3.

Homologues CNIH1, CNIH2 and CNIH3 show robust surface expression. CNIH2 mutants F3L, F5L and F8L, as well as the CNIH1_{2CHIM} chimera, also traffic to the cell surface, whereas 3FL does not. F3L and F5L CNIH2 mutants show decreased total and, consequently, surface expression levels; to ensure that the AMPARs in our electrophysiology experiments were still saturated with CNIHs, we used a 1:2 AMPAR:CNIH co-transfection ratio. Increasing this ratio further to 1:4 for F3L and F5L did not affect the gating properties, suggesting that the observed change in AMPAR modulation by these mutants is not caused by their lower (surface) expression. **c**, Representative images showing surface CNIH (green), total CNIH (magenta) and total GluA2 (blue). **d**, Equilibrium current (Fig. 3a dataset) (percentage of peak). GluA2 alone: 1.03 ± 0.19 , $n = 15$; CNIH2 wild type

(WT), 24.72 ± 4.55 , $n = 9$; F3L, 9.25 ± 1.16 , $n = 7$; F5L, 8.96 ± 1.16 , $n = 9$; F8L, 8.05 ± 1.00 , $n = 6$; 3FL, 2.01 ± 0.28 , $n = 9$. Welch's ANOVA with Dunnett's multiple comparisons test; $W_{5,17.48} = 27.95$, $P < 0.0001$. e, Equilibrium current (Fig. 3c dataset). GluA2 alone, 1.33 ± 0.50 , $n = 6$; CNIH1, 3.52 ± 0.56 , $n = 12$; CNIH1_{2CHIM}, 10.93 ± 1.16 , $n = 11$; CNIH2, 19.77 ± 1.93 , $n = 7$. Welch's ANOVA with Dunnett's multiple comparisons test; $W_{3,15.36} = 40.08$, $P < 0.0001$; further details in Supplementary Table 2.

Source data

Extended Data Table 1 Cryo-EM data collection, refinement and validation statistics

[Full size table](#)

Supplementary information

Supplementary Information

This file contains Supplementary Fig. 1 (the uncropped gels and immunoblots) and Supplementary Tables 1-4 which list P values from statistical tests used in the study.

Reporting Summary

Video 1

: Cryo-EM map of the full-length A1/2 γ 8/C2 complex. The complex is composed of the GluA1 (blue), GluA2 (red) heteromer associated with γ 8 (green) and CNIH2 (orange).

Video 2

: Conformational changes at gate and selectivity filter of A1/2 γ 8/C2 during receptor activation. Conformational changes of GluA1 and GluA2 from resting to active state are shown first from side view and then from top view. The model is coloured with the same scheme in Fig1.

Video 3

: Movements of auxiliary subunits in A1/2_γ8/C2 during receptor activation Movements of γ8 and CNIH2 from resting to active state are shown first from side view and then from bottom view. The model is coloured with the same scheme in Fig1.

Video 4

: Normal model analysis of A1/2_γ8/C2 at active state Energetically favorable motion modes of A1/2_γ8/C2 at active state via normal mode analysis are shown from side view (top) and bottom view (bottom). The model is coloured with the same scheme in Fig. 1.

Source data

[Source Data Fig. 1](#)

[Source Data Fig. 3](#)

[Source Data Extended Data Fig. 1](#)

[Source Data Extended Data Fig. 10](#)

Rights and permissions

[Reprints and Permissions](#)

About this article



Check for
updates

Cite this article

Zhang, D., Watson, J.F., Matthews, P.M. *et al.* Gating and modulation of a hetero-octameric AMPA glutamate receptor. *Nature* **594**, 454–458 (2021). <https://doi.org/10.1038/s41586-021-03613-0>

[Download citation](#)

- Received: 01 December 2020
- Accepted: 05 May 2021
- Published: 02 June 2021
- Issue Date: 17 June 2021
- DOI: <https://doi.org/10.1038/s41586-021-03613-0>

Comments

By submitting a comment you agree to abide by our [Terms](#) and [Community Guidelines](#). If you find something abusive or that does not comply with our terms or guidelines please flag it as inappropriate.

[Access through your institution](#)

[Change institution](#)

[Buy or subscribe](#)

Associated Content

[Glutamate receptor complexes open up and reveal their molecular dialect](#)

- Andrew J. R. Plested

Advertisement

This article was downloaded by **calibre** from <https://www.nature.com/articles/s41586-021-03613-0>

| [Section menu](#) | [Main menu](#) |

- Matters Arising
- [Published: 16 June 2021](#)

Clusters of flowstone ages are not supported by statistical evidence

- [Philip Hopley](#) ORCID: orcid.org/0000-0001-8138-3813¹,
- [Pieter Vermeesch](#)²,
- [Randall Parrish](#)³ &
- [Alfred Latham](#)⁴

[Nature](#) volume 594, page E10 (2021)[Cite this article](#)

- 604 Accesses
- 13 Altmetric
- [Metrics details](#)

Subjects

- [Biological anthropology](#)
- [Palaeoclimate](#)

[Matters Arising](#) to this article was published on 16 June 2021

The [Original Article](#) was published on 21 November 2018

arising from R. Pickering et al. *Nature* <https://doi.org/10.1038/s41586-018-0711-0> (2019)

Access options

Subscribe to Journal

Get full journal access for 1 year

\$199.00

only \$3.90 per issue

[Subscribe](#)

All prices are NET prices.

VAT will be added later in the checkout.

Tax calculation will be finalised during checkout.

Rent or Buy article

Get time limited or full article access on ReadCube.

from \$8.99

[Rent or Buy](#)

All prices are NET prices.

Additional access options:

- [Log in](#)
- [Access through your institution](#)
- [Learn about institutional subscriptions](#)

References

1. 1.

Pickering, R. et al. U–Pb-dated flowstones restrict South African early hominin record to dry climate phases. *Nature* **565**, 226–229 (2019).

[ADS](#) [CAS](#) [Article](#) [Google Scholar](#)

2. 2.

Vermeesch, P. On the visualisation of detrital age distributions. *Chem. Geol.* **312–313**, 190–194 (2012).

[ADS](#) [Article](#) [Google Scholar](#)

3. 3.

Stratford, D. et al. Comments on ‘U-Pb dated flowstones restrict South African early hominin record to dry climate phases’ (Pickering et al. *Nature* 2018;565:226–229). *S. Afr. J. Sci.* **116**, 7094 (2020).

[Article](#) [Google Scholar](#)

[Download references](#)

Author information

Affiliations

1. Department of Earth & Planetary Sciences, Birkbeck, University of London, London, UK

Philip Hopley

2. Earth Sciences, University College London, London, UK

Pieter Vermeesch

3. Earth & Environmental Sciences, University of Portsmouth, Portsmouth, UK

Randall Parrish

4. Department of Archaeology, Classics and Egyptology, University of Liverpool, Liverpool, UK

Alfred Latham

Authors

1. Philip Hopley

[View author publications](#)

You can also search for this author in [PubMed](#) [Google Scholar](#)

2. Pieter Vermeesch

[View author publications](#)

You can also search for this author in [PubMed](#) [Google Scholar](#)

3. Randall Parrish

[View author publications](#)

You can also search for this author in [PubMed](#) [Google Scholar](#)

4. Alfred Latham

[View author publications](#)

You can also search for this author in [PubMed](#) [Google Scholar](#)

Contributions

All authors contributed to writing the manuscript and interpreting the results. P.V. undertook the statistical analysis.

Corresponding author

Correspondence to [Philip Hopley](#).

Ethics declarations

Competing interests

The authors declare no competing interests.

Rights and permissions

[Reprints and Permissions](#)

About this article



Check for
updates

Cite this article

Hopley, P., Vermeesch, P., Parrish, R. *et al.* Clusters of flowstone ages are not supported by statistical evidence. *Nature* **594**, E10 (2021).
<https://doi.org/10.1038/s41586-021-03586-0>

[Download citation](#)

- Received: 27 June 2019
- Accepted: 27 April 2021
- Published: 16 June 2021
- Issue Date: 17 June 2021
- DOI: <https://doi.org/10.1038/s41586-021-03586-0>

Comments

By submitting a comment you agree to abide by our [Terms](#) and [Community Guidelines](#). If you find something abusive or that does not comply with our terms or guidelines please flag it as inappropriate.

[Access through your institution](#)

[Change institution](#)

[Buy or subscribe](#)

Advertisement

This article was downloaded by **calibre** from <https://www.nature.com/articles/s41586-021-03586-0>

| [Section menu](#) | [Main menu](#) |

- Matters Arising
- [Published: 16 June 2021](#)

Reply to: Clusters of flowstone ages are not supported by statistical evidence

- [Robyn Pickering](#) ORCID: [orcid.org/0000-0002-2663-7574^{1,2}](https://orcid.org/0000-0002-2663-7574),
- [Andy I. R. Herries](#) ORCID: [orcid.org/0000-0002-2905-2002^{3,4}](https://orcid.org/0000-0002-2905-2002),
- [Jon D. Woodhead](#) ORCID: [orcid.org/0000-0002-7614-0136⁵](https://orcid.org/0000-0002-7614-0136),
- [John C. Hellstrom⁵](#),
- [Helen E. Green⁵](#),
- [Bence Paul](#) ORCID: [orcid.org/0000-0001-6559-0759⁵](https://orcid.org/0000-0001-6559-0759),
- [Terrence Ritzman^{2,6,7}](#),
- [David S. Strait](#) ORCID: [orcid.org/0000-0002-3572-1663^{4,7}](https://orcid.org/0000-0002-3572-1663),
- [Benjamin J. Schoville^{2,8}](#) &
- [John Hancox⁹](#)

[Nature](#) volume 594, page E11 (2021)[Cite this article](#)

- 372 Accesses
- 5 Altmetric
- [Metrics details](#)

Subjects

- [Geochemistry](#)
- [Palaeontology](#)

The [Original Article](#) was published on 16 June 2021

replying to P. Hopley et al. *Nature* <https://doi.org/10.1038/s41586-021-03586-0> (2021)

Access options

Subscribe to Journal

Get full journal access for 1 year

\$199.00

only \$3.90 per issue

[Subscribe](#)

All prices are NET prices.

VAT will be added later in the checkout.

Tax calculation will be finalised during checkout.

Rent or Buy article

Get time limited or full article access on ReadCube.

from \$8.99

[Rent or Buy](#)

All prices are NET prices.

Additional access options:

- [Log in](#)
- [Access through your institution](#)
- [Learn about institutional subscriptions](#)

References

1. 1.

Hopley, P., Vermeesch, P., Parrish, R. & Latham, A. Clusters of flowstone ages are not supported by statistical evidence. *Nature*, <https://doi.org/10.1038/s41586-021-03586-0> (2021).

2. 2.

Pickering, R. et al. U–Pb-dated flowstones restrict South African early hominin record to dry climate phases. *Nature* **565**, 226–229 (2019).

[ADS](#) [CAS](#) [Article](#) [Google Scholar](#)

3. 3.

Vermeesch, P. On the visualisation of detrital age distributions. *Chem. Geol.* **312–313**, 190–194 (2012).

[ADS](#) [Article](#) [Google Scholar](#)

4. 4.

Vermeesch, P. & Garzanti, E. Making geological sense of ‘Big Data’ in sedimentary provenance analysis. *Chem. Geol.* **409**, 20–27 (2015).

[ADS](#) [CAS](#) [Article](#) [Google Scholar](#)

[Download references](#)

Author information

Affiliations

1. Department of Geological Sciences, University of Cape Town, Cape Town, South Africa

Robyn Pickering

2. Human Evolution Research Institute, University of Cape Town, Cape Town, South Africa

Robyn Pickering, Terrence Ritzman & Benjamin J. Schoville

3. The Australian Archaeomagnetism Laboratory, Department of Archaeology and History, La Trobe University, Bundoora, Victoria, Australia

Andy I. R. Herries

4. Palaeo-Research Institute, University of Johannesburg, Johannesburg, South Africa

Andy I. R. Herries & David S. Strait

5. School of Geography, Earth and Atmospheric Sciences, The University of Melbourne, Melbourne, Victoria, Australia

Jon D. Woodhead, John C. Hellstrom, Helen E. Green & Bence Paul

6. Department of Neuroscience, Washington University School of Medicine, St Louis, MO, USA

Terrence Ritzman

7. Department of Anthropology, Washington University in St Louis, St Louis, MO, USA

Terrence Ritzman & David S. Strait

8. School of Social Science, University of Queensland, Brisbane, Queensland, Australia

Benjamin J. Schoville

9. Evolutionary Science Institute, University of the Witwatersrand, Johannesburg, South Africa

John Hancox

Authors

1. Robyn Pickering

[View author publications](#)

You can also search for this author in [PubMed](#) [Google Scholar](#)

2. Andy I. R. Herries

[View author publications](#)

You can also search for this author in [PubMed](#) [Google Scholar](#)

3. Jon D. Woodhead

[View author publications](#)

You can also search for this author in [PubMed](#) [Google Scholar](#)

4. John C. Hellstrom

[View author publications](#)

You can also search for this author in [PubMed](#) [Google Scholar](#)

5. Helen E. Green

[View author publications](#)

You can also search for this author in [PubMed](#) [Google Scholar](#)

6. Bence Paul

[View author publications](#)

You can also search for this author in [PubMed](#) [Google Scholar](#)

7. Terrence Ritzman

[View author publications](#)

You can also search for this author in [PubMed](#) [Google Scholar](#)

8. David S. Strait

[View author publications](#)

You can also search for this author in [PubMed](#) [Google Scholar](#)

9. Benjamin J. Schoville

[View author publications](#)

You can also search for this author in [PubMed](#) [Google Scholar](#)

10. John Hancox

[View author publications](#)

You can also search for this author in [PubMed](#) [Google Scholar](#)

Contributions

R.P. coordinated the team effort, and all authors equally contributed to the drafting and reviewing of this Reply.

Corresponding author

Correspondence to [Robyn Pickering](#).

Ethics declarations

Competing interests

The authors declare no competing interests.

Rights and permissions

[Reprints and Permissions](#)

About this article



Check for
updates

Cite this article

Pickering, R., Herries, A.I.R., Woodhead, J.D. *et al.* Reply to: Clusters of flowstone ages are not supported by statistical evidence. *Nature* **594**, E11 (2021). <https://doi.org/10.1038/s41586-021-03587-z>

[Download citation](#)

- Published: 16 June 2021
- Issue Date: 17 June 2021
- DOI: <https://doi.org/10.1038/s41586-021-03587-z>

Comments

By submitting a comment you agree to abide by our [Terms](#) and [Community Guidelines](#). If you find something abusive or that does not comply with our terms or guidelines please flag it as inappropriate.

[Access through your institution](#)

[Change institution](#)

[Buy or subscribe](#)

Associated Content

[**U–Pb-dated flowstones restrict South African early hominin record to dry climate phases**](#)

- Robyn Pickering
- Andy I. R. Herries
- Phillip J. Hancox

Advertisement

This article was downloaded by **calibre** from <https://www.nature.com/articles/s41586-021-03587-z>

| [Section menu](#) | [Main menu](#) |